# PROCEEDINGS

## of the

# 16th MINI CONFERENCE ON VEHICLE SYSTEM DYNAMICS, IDENTIFICATION AND ANOMALIES

Held at the

Faculty of Transportation Engineering and Vehicle Engineering
Budapest University of Technology and Economics, H u n g a r y
BUDAPEST, 5-7 November, 2018

Edited by Prof. I. Zobory

**VSDIA 2018**

BUDAPEST UNIVERSITY OF TECHNOLOGY AND ECONOMICS

# PROCEEDINGS

## of the

## 16th MINI CONFERENCE ON VEHICLE SYSTEM DYNAMICS, IDENTIFICATION AND ANOMALIES

Held at the

Faculty of Transportation Engineering and Vehicle Engineering
Budapest University of Technology and Economics, H u n g a r y
BUDAPEST, 5-7 November, 2018

Edited by Prof. I. Zobory

*VSDIA 2018*

BUDAPEST UNIVERSITY OF TECHNOLOGY AND ECONOMICS

## THE CONFERENCE ORGANISING COMMITTEE GRATEFULLY ACKNOWLEDGES THE GENEROSITY OF THE FOLLOWING ***MAJOR SPONSORS*** AND SPONSORS:

*BME Faculty of Transportation and Vehicle Engineering* (H)
*BME Intelligent Transportation and Vehicle Systems Co.* (ITS ZRt.) (H)
*Knorr Bremse Brake Systems Ltd.* (H)
*Knorr Bremse Brake R&D Institute Budapest* (H).
*Knorr-Bremse Railway Vehicle Systems Hungaria Ltd.* (H).
AVL Autokut Ltd. (H)
Stadlertrains Hungary Ltd. (H)
Ganz Motor Ltd. (H)
Hungarian Transport Federation (H)
Grampet Debrecen Vagon Factory Kft. (H)
Siemens ZRt (H)


## CONFERENCE PRESIDENT


**Prof. Isván ZOBORY,**
Group of Railway Vehicles and
Vehicle System Analysis,
BME, Budapest, Hungary


## INTERNATIONAL SCIENTIFIC COMMITTEE




The Organising Committee thanks the authors for their efforts providing the electronic version of the full paper manuscripts. Issued by the ***BME ITS ZRt***. Budapest, 2019. ISBN 978-963-421-804-3

Participants of the VSDIA 2018 International Scientific Conference in front of the Vehicle Engineering Building of the Faculty of Transportation Engineering and Vehicle Engineering at the Budapest University of Technology and Economics

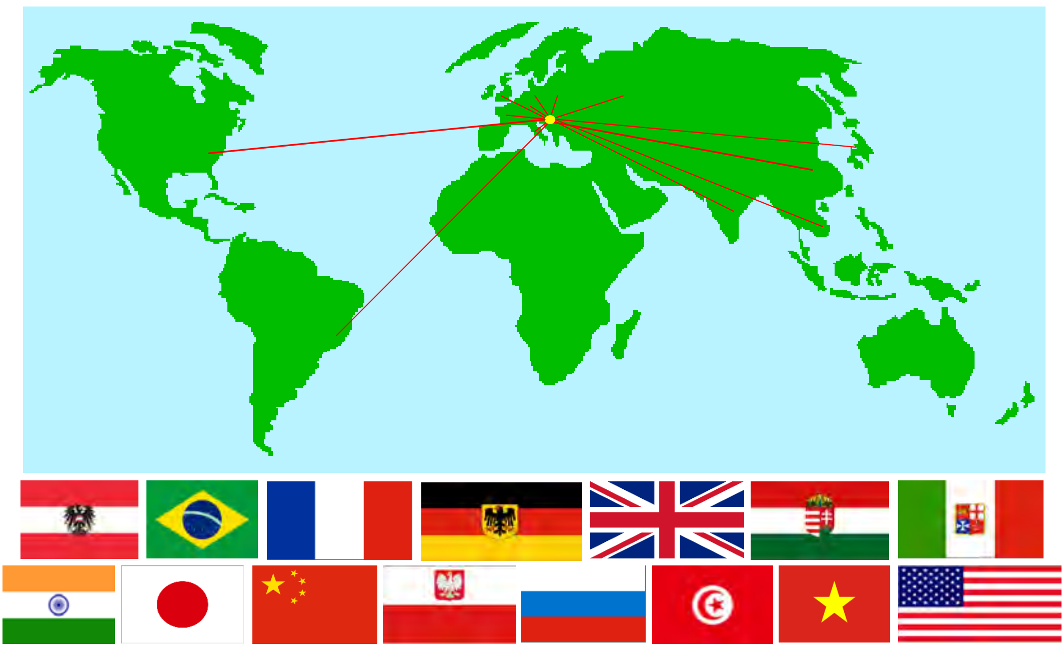

The 15 Countries interested in VSDIA 2018

Editor in Chief:
Prof. István Zobory

This volume was prepared using files submitted by the authors.
No scientific or linguistic revisions were provided by the Organisers.

## CONTENTS

**PREFACE**.......................................................................................................... 9

**PLENARY SESSION** .......................................................................................... 11

**GÁTI, B. – VASS, G.** (Hungary + USA)
Investigation of Airfoils in Jet Flow.................................................................... 13

**PITTNER, CH. – EDELMANN, J. – PLÖCHL, M.** (Austria)
Reference Models for Torque-Vectoring Electric Vehicles ........................................ 23

**MONTROUGE, A. – BIROUCHE, A. – TORRES, G. – LAMY,CH. – PARSONS, A. – BASSET, M.** (France + Luxemburg)
Identification of Tire Model Parameters from Vehicle Measurements Using Sensitivity Analysis ............................................................................................ 31

**MÜLLER, G. – LUBER, B. – SORRIBES-PALMER, F. – PIETSCH, L. – SIX, K.** (Austria)
Influence of the Wheel Profile Condition on the Dynamics of Wheel-Rail Interface Quantities ............................................................................................ 39

**VU, V.T. – ZOLOTAS, A. – SENAME, O. – DUGARD, L**.
(Vietnam + France)
Towards Robust Linear Parameter Varying Control of Active Rail-Vehicle Wheel-Sets ............................................................................................ 45

**HEGEDŰS, F. – BÉCSI, T.** (Hungary)
Evaluation of Trajectories for Automated Road Vehicles in Sense of Dynamical Feasibility............................................................................................ 57

**BENEDA, K. – NAGY, A.** (Hungary)
Introduction, Identification and Control of a New Fuel Metering System on a Micro Turbo Jet Engine ............................................................................................ 65

**VANDANJON, P.-O. – VINOT, E. – EL ALMI, T.** (France)
Slope Optimisation (Sloop): Tailor-Made Optimisation for Road Longitudinal Profile Eco-design Considering the Dynamics of Vehicles ......................................... 75

**SESSION FOR DYNAMICS, IDENTIFICATION AND ANOMALIES OF RAILWAY VEHICLES** ............................................................................................ 83

**ZOLLER, V.** (Hungary)
Analysis of the Track/Vehicle Interaction with Regard to the Coupling with the Subgrade Dynamics ............................................................................................ 85

**CHUDZIKIEWICZ, A. – STELMACH, A.** (Poland)
Evaluation of the Process of Placing in Service of a Rail Vehicle with Regard to Safety of Transport Operation ............................................................................ 91

**JAKUSHEV, A. – HOMONETS, I.** (Russia)
Impact of Residual Stresses on the Railcar Wheel Strength........................................ 93

**ALBON, A.** (France)
On Wheel Profile Optimization by Generic Algorithm............................................. 101

**SZABÓ A. – ZOBORY, I.** (Hungary)
Vertical Dynamical Loading Conditions of Driven Wheel-Set................................. 109

**ZOBORY, I. – NAGY, D.** (Hungary)
Creep Control in Brake Operation to Avoid Wheel Sliding and Flattening............... 121

**NÉMETH, I.** (Hungary)
How to Avoid Dynamical Instability in Disc-Brake System by Using Additional Linear Damping ........................................................................................ 131

**KRÉMER, M.** (Hungary)
Knorr-Bremse Results in Adhesion Management and Participating in PINTA Project ......................................................................................................... 143

**LIN, S. – SUDA, J.** (Japan)
Vehicle Condition Monitor System Considering Vehicle and Track Maintenance........ 151

**ALFI, S. – BRUNI, S. – FU, B.** (Italy + China)
Condition Monitoring and Fault Detection of Suspension Components in Freight Wagons Using Acceleration Measurements ................................................ 157

**CSIBA, J.** (Hungary)
Numerical Analysis of the Failures, Reliabilities and Availabilities Concerning a Given Family of Railway Carriages under Different Operation and Maintenance Circumstances...................................................................................... 165

**ZÁBORI, Z. – ZOBORY, I.** (Hungary)
Track Qualification Method by Using System Dynamics Based Parameter Identification ....... 173

**MALATINSZKY, S.** (Hungary)
Conformity Assessment of Modernised Locomotive Bogie and Body Connection ...... 187

**DI GIALLEONARDO, E. – BIONDA, S. – BRAGHIN, F. – SOMASCHINI, C.** (Italy)
Design of Experiment Approaches for the Calibration of Instrumented Wheel-Set ....... 193

**SOMASCHINI, C**. – **D I GIALLEONARDO, E. – COLLINA, A. – BOCCIOLONE, M**. (Italy)
Algorithm Development to Classify the Deterioration of Insulated Rail Joints by Means of on Board Measurements ...................................................................... 201

**CARNEVALE, M – COLLINA, A. – ZUIN, A.** (Italy)
A Rolling Stock Based System for Pantograph and Catenary Condition Monitoring: Validation through Numerical Simulations on Rigid Catenary...................... 209

**SZŐKE, D. – ZOBORY, I.** (Hungary)
Investigation into the Structure of the Railway Track/Vehicle Connection .............. 219

**SESSION FOR DYNAMICS, IDENTIFICATION AND ANOMALIES OF ROAD VEHICLES**.......................................................................................... 229

**COSTA, L. – PERRIN, CH. – DUBOIS-LOUNIS, M. – SERRE, T. – M'SIRDI, N.K.** (France)
Modelling of the Two-Wheeler Dynamic Behaviour for Emergency Situations Analyses ........ 231

**KOKREHEL, Cs. – NÉMETH, H.** (Hungary)
Wheel-brake Design for Heavy Duty Electric Vehicles............................................ 239

**SZŰCS, G. – BÁRI, G.** (Hungary)
Tire Data Analysis Method for Finding Grip-Optimal Slip and Camber Values ........... 247

**WIDNER, A. – BÁRI, G.** (Hungary)
Investigating the Effects of Roll Centre Height, during Transient Vehicle Manoeuvres .......... 255
**ERŐSDI, Z. – BÁRI, G.** (Hungary)
Yaw Rate Control for Enhancing Vehicle Steering Behaviour ................................. 261
**BÁRDOS, Á. - NÉMETH, H.** (Hungary)
Diesel Engine Cylinder-Charge Composition Control with HpEGr and Exhaust Throttling .......... 269
**NAKANO, K. – SEKI, M. – KAIZUKA, T. – ZHENG, R. – SAKURA, T. – MAKI, T.** (Japan)
Design of Haptic Steering Guidance Controller Considering Look-ahead Distance ........ 277
**LENGYEL, H. – SZALAY, ZS.** (Hungary)
Potential Weak Points of Environment Sensors in Autonomous Vehicles ............... 285
**SIMON, T. S. – MELEGH, G – SZALAY, ZS.** (Hungary)
Automated Vehicles' Accidents – Uber Self-Driving Vehicle Accident ................... 293
**NYERGES, Á. – TIHANYI, V.** (Hungary)
Environment Sensing and Parking Place Detection for Automated Vehicles ............ 303
**ARADI, SZ. – TARI, B. – BÉCSI, T.– GÁSPÁR, P.** (Hungary)
Reinforcement Learning Based Racing Car Control ................................. 313
**KONCZ, A.** (Hungary)
Failure Mode and Effect Analysis Types in the Automotive Industry ....................... 321

**SESSION FOR DYNAMICS, IDENTIFICATION AND ANOMALIES OF AIRCRAFT AND SHIPS** .......... 329
**SZONDA, G. – VERESS, Á.** (Hungary)
CFD Analysis and Redesign of Main Landing Gear Unit on Skycruiser Sc-200 Autogyro for Drag Reduction .......... 331
**BÍRÓ, O. – SZABÓ, G.** (Hungary)
Integrating Large Remotely Piloted Vehicles into the Controlled Airspace .............. 349
**URBAN, A.X.C. – MOLNAR, I.T. - VERESS, A.** (Mexico+Hungary)
Investigation of Hybrid Propulsion Systems Applied on Small Sized Aircraft ......... 357
**BENEDA, K. – DERBEL, K.** (Hungary+Tunesia)
Identification of Single Spool Micro Turbojet Engine with Fixed Exhaust Nozzle at Multiple Operating Points for Linear Parameter Varying Control............. 371
**HARGITAI, CS. – SIMONGÁTI, GY. – ZALACKÓ, R.** (Hungary)
Operational Profile of Inland Public Transport .......................................... 381

**SESSION FOR VEHICLE CONTROL THEORY AND INTERDISCIPLINARY SCIENCES** .......... 393
**FÉNYES, D. – NÉMETH, B. – GÁSPÁR, P. – ASSZONYI, M.** (Hungary)
Possibilities of Vehicle State Estimation Using Big Data Approaches...................... 395
**SZŐTS, D. – NÉMETH, B.** (Hungary)
Challenges and Problems in the Design of Smart Intersections ................................ 403
**DALVÁRI, M. – FÉNYES, D. – MIHÁLY, A. – NÉMETH, B. – GÁSPÁR, P.** (Hungary)
Camera-Based Lateral Driver Modelling for Vehicle Control Design Purposes ....... 409

**SZALAY, J. – KŐVÁRY, B. – ARADI, SZ. – GÁSPÁR, P. –BÉCSI, T.** (Hungary)
Highway Behaviour Training through Learning Based State Choice Model............ 417
**DO, M. H. – KOENIG, D. – THEILLIOL, D.** (France+Vietnam)
Robust $H_\infty$ Proportional-Integral Observer Design for Actuator Fault Estimation ......... 425
**VU, V. T. – SENAME, O. – DUGARD, L. – PHAM, T. P. – DINH,V. P.** (France+Vietnam)
$H_\infty$/LPD Active Braking Control System to Prevent Rollover of Heavy Vehicles ........ 437
**RATHAI, K.M.M. – SENAME, O. – ALAMIR, M.** (France)
A Comparative Study of Different NMPC Schemes for Control of Semi-Active Suspension System ........................................................................... 447
**VARGA, B.** (Hungary)
Energy Aware Cruise Control for Urban Public Transport Buses ............................ 455
**HEGEDŰS, T. – NÉMETH, B. – BEDE, ZS.** (Hungary)
Control and Decision Method for Overtaking Problem in Autonomous Vehicles ......... 463
**PAPP, J. – BÁRI, G.** (Hungary)
Hardware in the Loop Test System for Teaching Model Based Design for Automotive Control ........................................................................................ 471
**PHAM, T.P. – SENAME, O. – DUGARD, L. – VU, V.T.** (France +Vietnam)
Real-Time Estimation of the Damping Force of Vehicle Electrorheological Suspension ........ 477
**DOMINA, Á. – TIHANYI, V.** (Hungary)
Comparison of Controller Systems and Motion Modelling Methods for Autonomous Vehicle Trajectory Following Practice........................................................... 487
**KOLONITS, F.** (Hungary)
Possible Cause of an Internal Level Crash, '95 Kobe Eq......................................... 497
**KISS, CS.** (Hungary)
Some Remarks on Designing Crankshafts................................................................ 507
**HIDAS, A.** (Hungary)
Thermal Simulation to Ensure Heat Management of Vehicle Ecus with Plastic Enclosure.................................................................................................... 517
**POKORÁDI, L. – LÁZÁR-FÜLEP, T.** (Hungary)
Dependability of Vehicle Systems with Complex Interconnections ......................... 519
**POKORÁDI, L. – SOMOSI, V.** (Hungary)
Graph-Theoretical Investigation into Vehicle and Transportation Systems ............. 529
**FERENCZ, P.** (Hungary)
The Question of Lifetime: Extension Possibilities of Bogie Force Transmission Elements on the Basis of Condition Test Results ............................................... 539
**TULIPANT, G. – SZABÓ, A. – ZOBORY, I.** (Hungary)
Laboratory Investigation into the Noise Generated by Sliding Friction for Cast Iron and Steel Friction Pair ........................................................................ 549

**ADVERTISEMENTS** .......................................................................... 557

# PREFACE

The Budapest VSDIA MINI Conference series on *Vehicle System Dynamics, Identification and Anomalies* began in 1988 on the basis of the initiative of the academic staff members of the *Faculty of Transportation Engineering* dealing with railway vehicle, road vehicle, aerospace vehicle, as well as ship dynamics and control at the *Technical University of Budapest*. The rapid development in this special field and the great interest of industrial/transport enterprises in the intensive research and development made it reasonable to think of widening the possibilities in Central Europe for the international exchange of views and experience on *dynamics, identification and parameter anomaly problems* of vehicle systems.

Since 1988 the Faculty of Transportation Engineering methodically organises the VSDIA Conferences *in a biannual order* under increasing international interest. By 2018, the Conference series achieved its 30th birthday. The VSDIA conferences became world-wide known among the representatives of the special field, first of all in Europe but the published conference proceedings volumes are known in a rather wide circle all through the world due to the intensive dissemination realised by the organisers.

Considering the thirsty-year-long history of the VSDIA Conferences and the fact that also the 16th Conference of Jubilee character on Vehicle System Dynamics, Identification and Anomalies has been successfully realised, it can be stated that the original strategic goals of the initiators, namely to give a scene of high scientific level for the treatment of all dynamical/control system and operation process models commonly valid for both ground vehicles and flying/floating vehicles have been fulfilled. Parallely, the intended integration of the recent results of modern control theory, as well as those of applied mechanics and mathematics have been successfully realised in the contributions received in the vehicle control/interdisciplinary sessions of the Conferences.

The VSDIA 2018 Conference was held at the Budapest University of Technology and Economics between 5 and 7 November, 2018. The International Scientific Committee accepted 62 paper offers from 15 countries, while the final number of participants was 85. High quality papers were presented in all the five Sessions. The atmosphere of the Conference was as usual excellent, and provided an outstanding opportunity for direct communication and exchange of ideas on an international level between researchers and specialists working in industry or practising as executive engineers. Theory and praxis could meet and fertilise each other.

In this volume the electronic versions of the camera-ready manuscripts received from the authors at the end and after the Conference are published. The members of the Organising Committee are convinced that the material represented will provide a wide-scale view of the latest developments in the special field over the past two years.

Budapest, 31 December, 2018

***Prof. István Zobory***
Conference President

## PLENARY SESSION

**GÁTI, B. – VASS, G.** (Hungary + USA)
Investigation of Airfoils in Jetstream ..... 13

**PITTNER, CH. – EDELMANN, J. – PLÖCHL, M.** (Austria)
Reference Models for Torque-Vectoring Electric Vehicles ..... 23

**MONTROUGE, A. – BIROUCHE, A. – TORRES, G. – LAMY,CH. – PARSONS, A. – BASSET, M.** (France + Luxemburg)
Identification of Tire Model Parameters from Vehicle Measurements Using Sensitivity Analysis ..... 31

**MÜLLER, G. – LUBER, B. – SORRIBES-PALMER, F. – PIETSCH, L. – SIX, K.** (Austria)
Influence of the Wheel Profile Condition on the Dynamic Behaviour of Wheel-Rail Interface Quantities ..... 39

**VU, V.T. – ZOLOTAS, A. – SENAME, O. – DUGARD, L.**
(Vietnam + France)
Towards Robust Linear Parameter Varying Control of Active Rail-Vehicle Wheel-Sets ..... 45

**HEGEDŰS, F. – BÉCSI, T.** (Hungary)
Evaluation of Trajectories for Automated Road Vehicles in Sense of Dynamical Feasibility ..... 57

**BENEDA, K. – NAGY, A.** (Hungary)
Introduction, Identification and Control of a New Fuel Metering System on a Micro Turbo Jet Engine ..... 65

**VANDANJON, P.-O. – El ALMI TAHA, V. E.** (France)
Slope Optimisation (Sloop): Tailor-Made Optimisation for Road Longitudinal Profile Ecodesign Considering the Dynamics of Vehicles ..... 75

# INVESTIGATION OF AIRFOILS IN JET FLOW

**Balázs GATI and Gábor VASS**

Department of Aeronautics, Naval Architecture and Railway Vehicles
Faculty of Transportation Engineering and Vehicle Engineering
Budapest University of Technology and Economics
H-1111 Budapest, Hungary

*Received: November 5, 2018*

## ABSTRACT

Airfoils are optimized for lift and drag in free airflow like flow around wings or rotorblades. They provide significantly more performance than an arbitrary wing section. However if the boundary conditions are changing, airfoils can lose their advantage. Our investigation resulted that a high lift airfoil (S1223) and a curved plate in a jet flow will generate approximately the same maximum lift. We examined the effect of Reynolds number, vertical position, size and angle of attack of airfoil on the lift and introduced the Theoretical Maximum Lift Coefficient for an airfoil in jet flow.

*Keywords:* OpenFOAM, airfoil, jet flow, batch analysis

## 1. INTRODUCTION

The best airfoils are the result of a sophisticated optimization process in which the cost function considers lift, drag and some additional parameters such the moment around the Aerodynamic Center or Reynolds and Mach number range. These processes assume an infinitive and undisturbed on-flow to the airfoil in most cases. The shape of a resulted airfoil is sensitive to the changes in the cost function. That is the reason why different airfoils are used for different purposes and why sometimes carefully designed airfoils can be fully neglected.

## 2. METHOD

### 2.1 OpenFOAM

The effect of the geometry on the performance of a wing section is mostly investigated with a CFD method. [1] For the investigation we decided to use OpenFOAM [2]. This framework of 250 open-source, pre-built application is licensed under the GNU General Public License, freely accessible and is a well-known tool for solving finite volume problems in academic and in some special industrial research.

OpenFOAM contains different solvers for different investigations. SimpleFoam is a Reynolds Averaged Navier-Stock Solver (RANS) for steady-state, incompressible flows with turbulence modelling, its name is an acronym for Semi-Implicit Method for Pressure Linked Equations and OpenFOAM.

### 2.2 Salome Meca

Every CFD simulation requires the proper discretization of the flow field. For this purpose we used another open-source application, the SALOME distributed under the terms of the GNU LGPL license. [3] This application has got a user-friendly graphical user interface, but provides the opportunity to define the geometry with a Python-based script language and use a CLI command to generate the mesh demanded by the CFD application without using the graphical user interface.

### 2.3 MATLAB

The well known commercial application MATLAB is mostly used for complex calculation of computation demanding investigation, because it provides a broad variety of numerical methods. In our case the core calculations were performed by SALOME and openFoam, however MATLAB M-files were used to prepare the required files and directories for these applications and post process the result of the large number of calculations. For this purpose can be used open source solutions such Python or Scilab, too.

### 2.4 ParaView

To visually check the result of a simulation we used ParaView, an open-source, multi-platform data analysis and visualization application. [4] ParaView supports quick visualizations and quantitative techniques interactively or programmatically. ParaView uses a permissive BSD license that enables the usage of the software, royalty free, for most purposes.

### 2.5 Procedure

The performance of a wing section is investigated in most cases at different Angle of Attack (AoA), which is the angle between its chord and the direction of the main direction of the undisturbed airflow before the wing section. This requires a large number of similar simulation, that vary only in the initial orientation of the given wing section. To avoid the huge amount of manual work we created a MATLAB script (M-file), which realized the procedure shown in Figure 1.

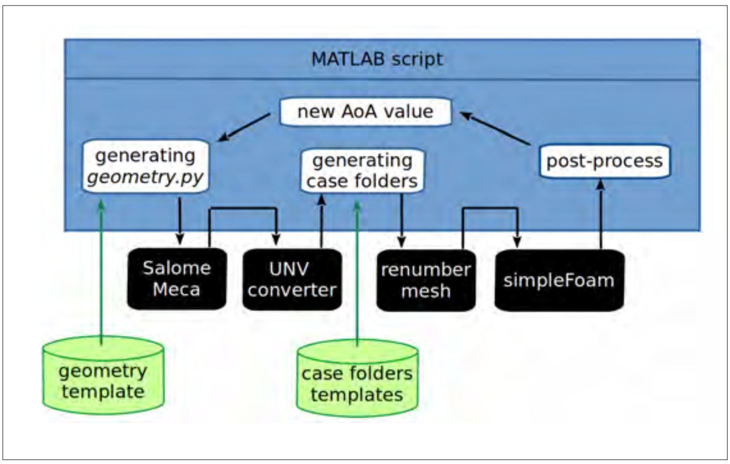


Fig. 1 Scheme to perform batch of runs

As the first step the script chooses a value from a predefined array of Angle of Attacks and generates an actual Python script for the subsequent simulation. The Python script defines the detailed geometry of the flow field and commands for generating the mesh based on a geometry template. The template includes the values and commands common for each mesh generation. As the next step the MATLAB scripts initiates the mesh generation by executing the proper SALOME command in a terminal window that processes the generated actual Python script. The mesh is resulted in a form of a UNV file.

OpenFoam is a CFD application that requires its inputs in many different files – mainly text files - in a given directory structure named case folders. The preparation of the case folders is not obvious, but very beneficial in case an automatic process is applied to generate it. First the MATLAB script executes the conversion of the UNV file into the required files, then merges them into the copy of the template case folders containing the additional inputs common for all simulation. To complete the preparations of the case folders the MATLAB script edits some additional input files according to the specific case.

Before the simulation our MATLAB script executes an openFoam command line tool that renumbers the cell list and all fields from all the time directories in order to reduce the calculation bandwidth. When renumbering has been finished the script can execute the solver simpleFoam in a terminal window and wait for the simulation results.

Postprocessing starts with the extraction of the specific results relevant for our investigation, then generates and saves figures for verification and evaluation later.

These steps are done for each subsequent simulation for different Angle of Attacks without human intervention, thus a given batch of simulation can be performed automatically.

## 3. VALIDATION

To demonstrate the lost advantage of airfoils we focused only on lift and choose the high lift airfoil Selig S1223. In order to validate our method the first step was to compare our results to published measurement in the case of a normal wind tunnel test. We applied meshing commands generating an unstructured hexagonal mesh refined in the proximity of the airfoil. (Figure 2)

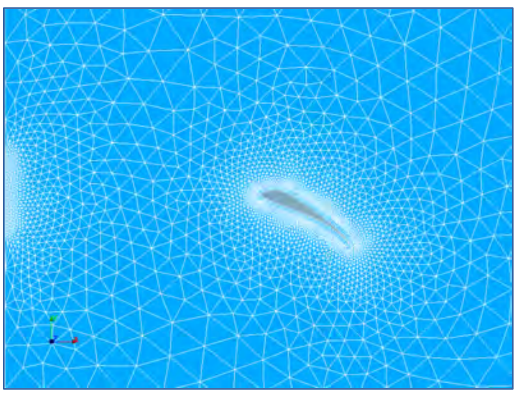

Fig. 2 Mesh around the airfoil

We omitted the definition of a detailed boundary layer mesh because the drag and flow separation were out of the scope of our investigation. The boundary conditions consisted an inlet, an outlet and slip walls below and over the airfoil similar to a wind tunnel. We applied the Spalart-Allmaras turbulence model often used by investigation of airplane lifting surfaces [5].

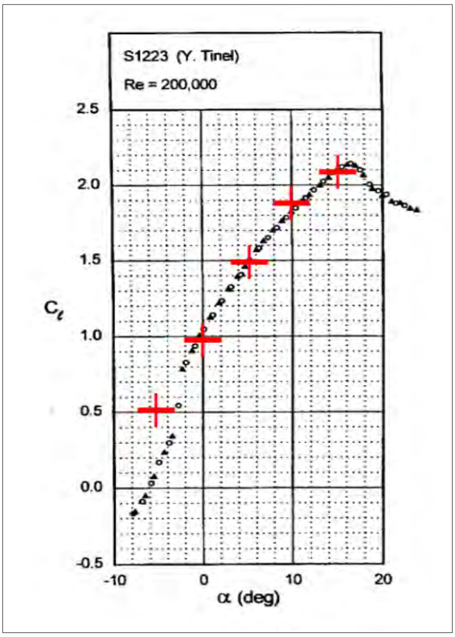


Fig. 3 Comparing calculations (+) to wind tunnel measurements (o)

The results are shown in Figure 3. by red crosses. In the normal AoA range between 0° and 15° the results correlates to the wind tunnel tests [6], thus proved that the method is suitable for the investigation. Out of this range the airflow separates from airfoil and the simulation was unable to provide proper prediction, but post-stall behavior was out of the scope of our investigation.

## 4. BASELINE ANALYSIS

The investigation focused on generating maximum lift with different wing sections assuming an airflow exiting from a nozzle. Figure 4 shows the geometry of the baseline case.

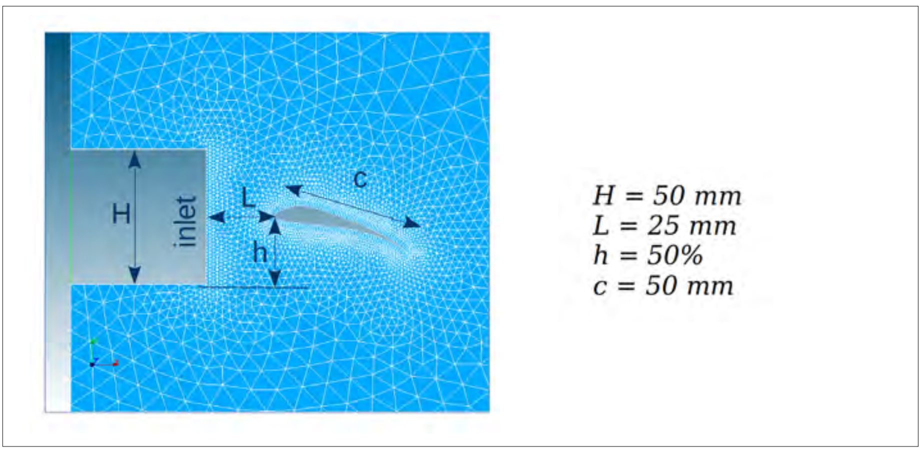


Fig. 4 Geometry of the baseline analysis

According to the actual investigation we applied the inlet boundary condition only on the nozzle, entrainment boundary condition on the upper, lower and right border of the mesh, wall boundary on the wing section. Slip wall boundary condition was applied on the remaining borders.

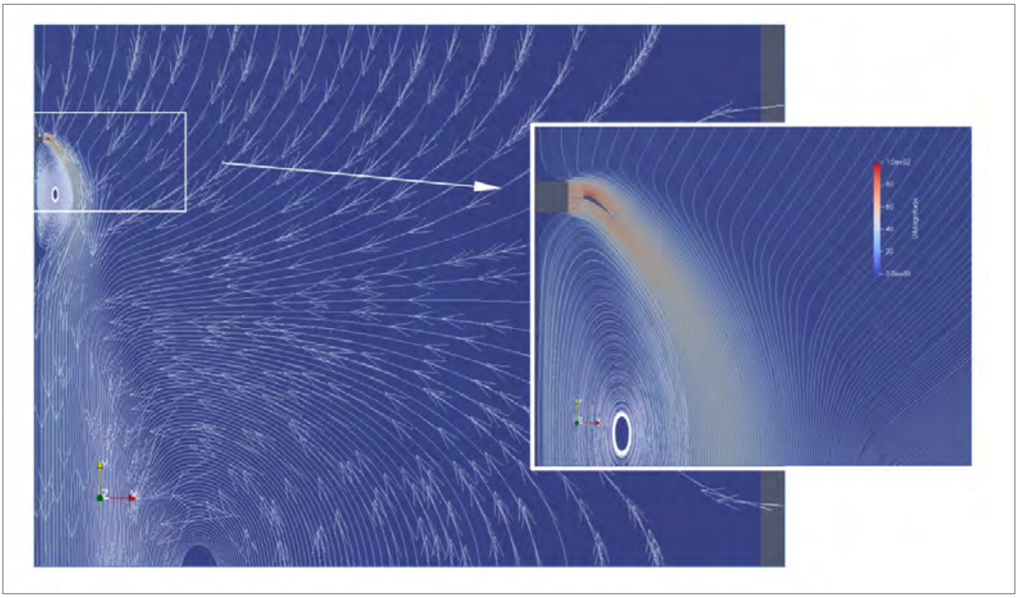

Fig. 5 The flow field at *AoA=40°*

In the baseline analysis the Angle of Attack was changed from 5° to 60° in steps of 5°, thus 12 simulation was performed in one batch of simulations.

A typical example for the resulted flow fields can be seen on figure 5. In the proximity of the wing section the streamlines are showing similar airflow to the wind tunnel tests, but the global structure of the flow is significantly different from the wind tunnel tests.

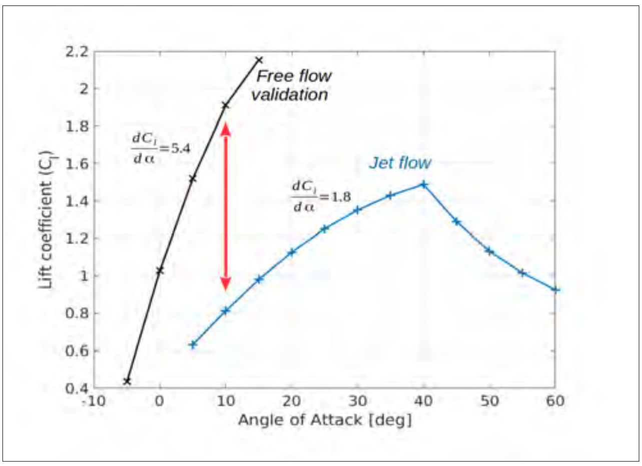


Fig. 6 Comparison of lift coefficient curves in case of the validation and the baseline analysis

Figure 6 shows the lift coefficient curves resulted by the validation and the baseline analysis. The lift coefficient and the Reynolds number were calculated in both analyses with the airspeed at the inlet. In case of the validation the inlet was the complete left border of the flow field, while in the baseline analysis the inlet was reduced to the nozzle. The nominal Reynolds number was about 100.000 in both cases. The comparison shows significant difference in the slope of the lift coefficient and in itself the maximum lift coefficient, too.
The explanation can be found based on the global structure of the flow field. The suction provided by the jet flow caused a significant onflow to the upper surface of the wing section that reduced the depression there. This resulted much lower lift and lift coefficient compared to wind tunnel tests assuming the same Angle of Attack. This is also the reason why signs of flow separation can't be observed until 40° of Angle of Attack, which is a much higher value than common in wind tunnel experiments and higher that could be explained with the coarse modeling of the boundary layer.

## 5. SENSITIVITY ANALYSIS

In order to better understand the phenomenon a sensitivity analysis was performed considering the Reynolds number, vertical position *h*, distance *L*, and the height of the nozzle *H*. (See figure 4.)

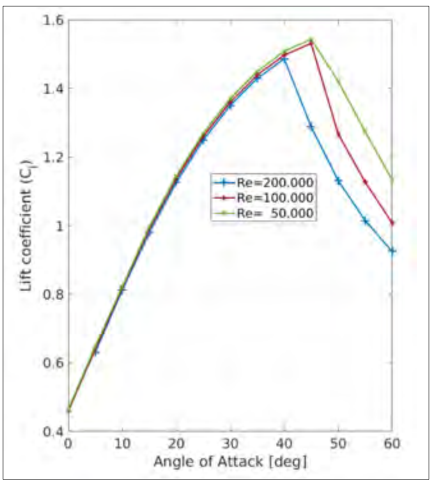


Fig. 7 Sensitivity on Reynolds number

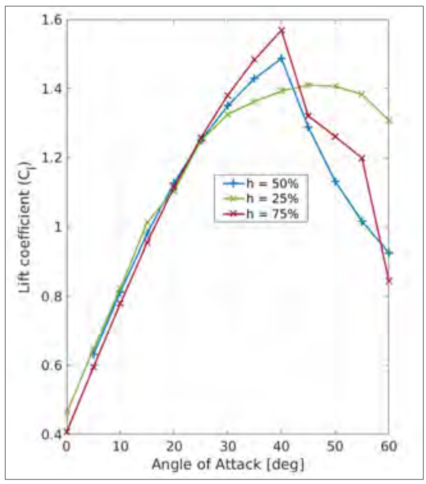


Fig. 8 Sensitivity on vertical position

Figure 7 shows the results in case of three different Reynold numbers. The slope of the lift coefficient seems insensitive to this parameter. The maximum lift coefficient is slightly different, but this value is limited by the phenomenon of the flow separation, that isn't well modeled in our simulations. Figure 8 proves the same in case of different vertical position of the wing section in front of the nozzle. It could be interesting to perform later a detailed analysis because this preliminary result predicts different ways of flow separation at different position. Figure 9 shows observable vertical shift of the lift curve depending on the distance between the nozzle and the leading edge of the airfoil, but the slope of the lift curve seems still insensitive.

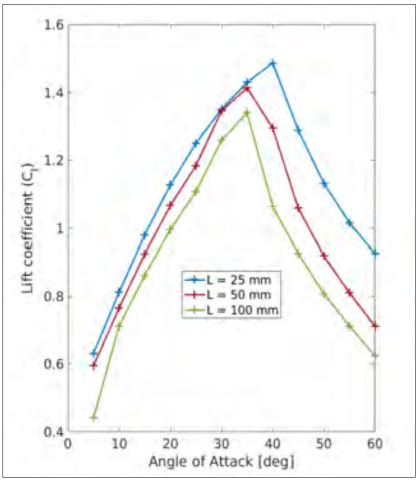


Fig. 9 Sensitivity on distance

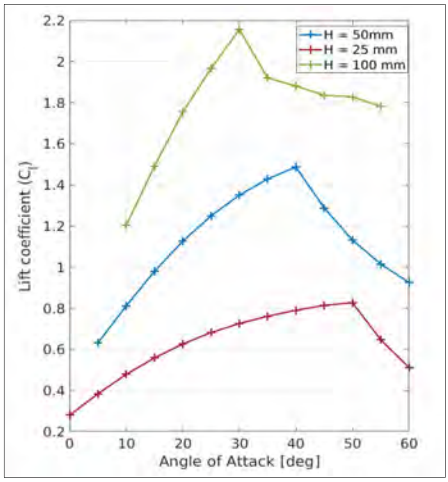


Fig. 10 Sensitivity on nozzle height

Opposite to the three geometry parameters mentioned before the height of the nozzle influences significantly the slope of the lift curve as shown on figure 10. This result can’t be expected based on common airfoil investigations, where the lift assumed to be function of airspeed (Reynolds number, Mach number), density, wing surface and Angle of Attack. The momentum conservation theory, however, explains the phenomenon: increasing nozzle height results higher amount of air involved in lift generation and more air has more momentum, thus generating more lift.

## 6. THEORETICAL MAXIMUM LIFT COEFFICIENT

The momentum theory is the Newton's second law of motion applied to a control volume and is a statement that any change in momentum of the fluid within that control volume will be due to the net flow of momentum into the volume and the action of external forces acting on the fluid. This statement written in form of a general equation:

$$\int_A \underline{v}\rho\underline{v}\,d\underline{A}=\int_A \underline{\underline{\Phi}}\,d\underline{A}+\int_V \rho g dV+\underline{F} \tag{1}$$

Let us assume, that an ideal fluid exits the nozzle and the wing section deflects all of them by 90° downward and the streamlines exiting at the circumference of the nozzle form a pipe elbow. (Figure 11) If the control volume defined as this ideal pipe elbow, the absolute value of the momentum entering and exiting the control volume are equal (conservation of mass), while their directions are perpendicular to each other resulting maximum possible change in direction of momentum. This results the maximal possible lift *F* assuming a given amount of mass flow.

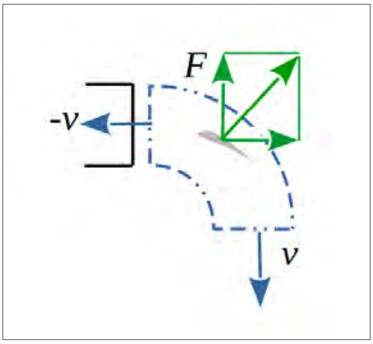


Fig. 11  Case of theoretical maximum lift

In this very special case (1) can be simplified to the following form considering only the vertical direction:

$$\Delta(\dot{m}v) = \dot{m}\Delta v = F \tag{2}$$

Defining the lift on a common way:

$$F = C_{ITM}\frac{\rho}{2}v^2 S \tag{3}$$

,

where $C_{ITM}$ is the Theoretical Maximum Lift Coefficient. Using the letters introduced in figure 4 the Theoretical Maximum Lift Coefficient can be calculated:

$$C_{ITM} = 2\frac{H}{c} \tag{4}$$

that gives a quantitative approximation on the effect of increasing nozzle height on lift. In the baseline analysis the value of the Theoretical Maximum Lift Coefficient is 2, while the maximum lift coefficient calculated by the simulations is 1.5 (figure 6), that means 25% loss compared to the ideal value. We created a simulation with a wing section formed by a simple curved arc similar to a deflector, too. Figure 12 shows the resulted streamlines in this case.

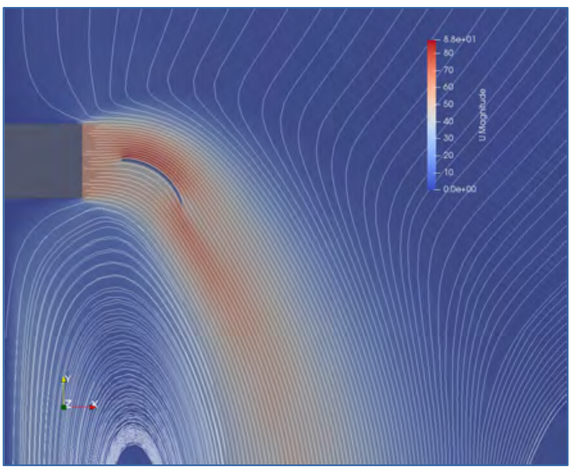


Fig. 12  Streamlines around a simple deflector

The value of the resulted lift coefficients can be seen in Table 1 and can be compared to all other cases.

| | $C_{lmax}$ | $C_{lTM}$ |
|---|---|---|
| Deflector | 1.62 | 2 |
| h = 75% | 1.58 | 2 |
| Re = 50.000 | 1.56 | 2 |
| Re = 100.000 | 1.55 | 2 |
| Baseline | 1.48 | 2 |
| h = 25% | 1.42 | 2 |
| L = 50mm | 1.41 | 2 |
| L = 100mm | 1.36 | 2 |
| H = 25mm | 0.82 | 1 |
| H = 100mm | 2.16 | 4 |

Table 1 Comparison of calculated and Theoretical Maximum Lift Coefficients

The geometry of the flow field resulted a Theoretical Maximum Lift Coefficient of 2 in most of our analysis. It is obvious that in none of these analyses the special high lift airfoil S1223 provided better performance than the simple deflector. The last two rows require some more detailed interpretation. In case of the nozzle height *H=25mm* the calculated maximum lift coefficient is very low though, because of the low amount air involved in lift generation, but the ratio $C_{lmax}/C_{lTM}$ is practically equal to the case of the deflector. In case of the nozzle height *H=100mm* the calculated maximum lift coefficient is significant higher than in any other cases, because of the higher amount of air, but the ratio $C_{lmax}/C_{lTM}$ is the worst of all cases.
We have to remark, that the precise value of the maximum lift coefficient depends on the phenomena in the boundary layer, and the boundary layer wasn't modeled detailed enough in our investigation to accept the quantitative results without further investigations.

## 7. CONCLUDING REMARKS

135 simulations were performed during the investigation with a special high lift airfoil. This was possible because we developed a process that can run batch of similar CFD simulations with the help of features provided by open source applications. These simulations proved that in cases where drag has low importance, the usage of airfoils is less important or even less optimal than much less sophisticated, conventional geometries. Additionally we found an explanation to the phenomenon, that the flow separates at much higher Angle of Attacks in case of jet flow, than in normal wind tunnel tests.

## 8. REFERENCES


[1] **Veress, A.:** Numerikus módszerek és alkalmazások a hő- és áramlástechnikai gépekben lezajló folyamatok modellezésére, PhD thesis, 2004, Budapest University of Technology and Economics

[2] **Cardiff, P.:** Introduction to Meshing in OpenFOAM; 5th UK & Éire FOAM/ OpenFOAM User Day; 2017; University College Dublin, Dublin, Ireland

[3] **Kortelainen, J.**: Meshing Tools for Open Source CFD – A Practical Point of View; 2009; VTT Technical Research Centre of Finland; VTT-R-02440-09

[4] **Ahrens, James, Geveci, Berk, Law, Charles:** ParaView: An End-User Tool for Large Data Visualization, Visualization Handbook, Elsevier, 2005, ISBN-13: 978-0123875822

[5] **Pizzarelli, M.:** Effectiveness of Spalart–Allmaras Turbulence Model in Analysis of Curved Cooling Channels, AIAA Journal, Vol. 51, No. 9, 2013, p.2158-2167.

[6] **Selig, M. S. – Lyon, Ch. A. – Giguere, Philippe – Ninham, C.P. – Guglielmo J. J.**: Summary of Low-Speed Airfoil Data. SoarTech Publications, Virginia Beach, 1996, ISBN 0-9646747-2-6, p.129.

# REFERENCE MODELS FOR TORQUE-VECTORING ELECTRIC VEHICLES

**Christian PITTNER, Johannes EDELMANN and Manfred PLÖCHL**

Institute of Mechanics and Mechatronics
Technische Universität Wien
A-1060 Vienna, Austria

*Received: November 5, 2018*

## ABSTRACT

Various hardware components and software modules predetermine the performance of torque-vectoring control systems for electric vehicles. Regarding control design, the focus is often put on the feed-forward and/or feedback control scheme and control approaches, as well as torque allocation and tyre slip control. However, rather little attention is paid to the desired handling reference behaviour of the vehicle. The aim of this paper is to present an approach to adapt the handling reference properties for torque-vectoring systems, adapted to the driver's skills and awareness. Thus, different categories of drivers are defined, where the handling and stability properties of the vehicle are adapted to meet their demands and expectations. Novice, skilled and expert drivers are considered to represent 'typical' categories, and respective heuristic reference models are presented in more detail. Simulation results from a critical highway exit scenario are discussed for these references, applying appropriate driver models.

*Keywords:* torque-vectoring, electric vehicle, reference model

## 1. INTRODUCTION

Up to now, torque-vectoring (TV) systems to enhance handling behaviour in ordinary driving conditions are rarely found in production cars. However, the promotion of electric vehicles – with drive trains of reduced (mechanical) complexity – boosts research on both fundamentals of TV, e.g. [1], as well as practical application, e.g. [2]. While active differentials to apply a desired yaw moment are regarded in [3, 4], four individual electric motors are considered in [2, 5].

Various control approaches have been investigated and adapted for TV systems, [2, 4, 5, 6, 7, 8, 9, 10], where the focus of the reference behaviour is most often put on extending the linear range of steady-state handling behaviour and increased maximum lateral acceleration, improved agility and stability. Optimal TV yaw reference for minimum-time manoeuvring is studied in [9].

However, the expectations and limitations of the individual driver with respect to a desirable reference behaviour of the vehicle are rarely addressed in literature. In [11], the yaw rate reference for a lane-keeping manoeuvre is selected from two pre-sets, based on the identified driver steering behaviour from a hidden *Markov* model and camera-based lane-maker detection, to give an example.

The aim of this paper is to present a basic approach to adopt the reference behaviour of the vehicle, depending on the (identified) driving style and the condition of the driver, to meet the driver's expectations and demands, as well as to guarantee for desired controllability of the vehicle in the advent of unexpected disturbances.

First, the overall system 'driver–controlled vehicle–environment' and the general idea of different reference models will be presented, followed by three examples of possible types of drivers. Respective vehicle reference behaviours will be introduced next.

Finally, critical highway exit scenario results from driver–vehicle–environment closed loop simulations will be discussed, and concluding remarks are given.

## 2. DRIVER–CONTROLLED VEHICLE–ENVIRONMENT

The schematic of the overall system is presented in Fig. 1. The driver may apply steering wheel commands $\delta_s$ as well as accelerator and brake pedal inputs $x_a$ and $x_b$ to the vehicle in order to track a desired trajectory. From these commands, as well as from driver drowsiness detection systems, [12], his/her driving skills, driving style, and current condition are evaluated in the decision maker module of the reference generator. Based on the characterisation of the driver, as well as from current road (friction) conditions and driving task, appropriate vehicle handling properties are selected to guarantee safety, low physical and mental workload on the driver, and pleasure to drive. Exemplifying driver characterisations and respective heuristic reference models are presented in the subsequent section. Reference models may also be selected manually.

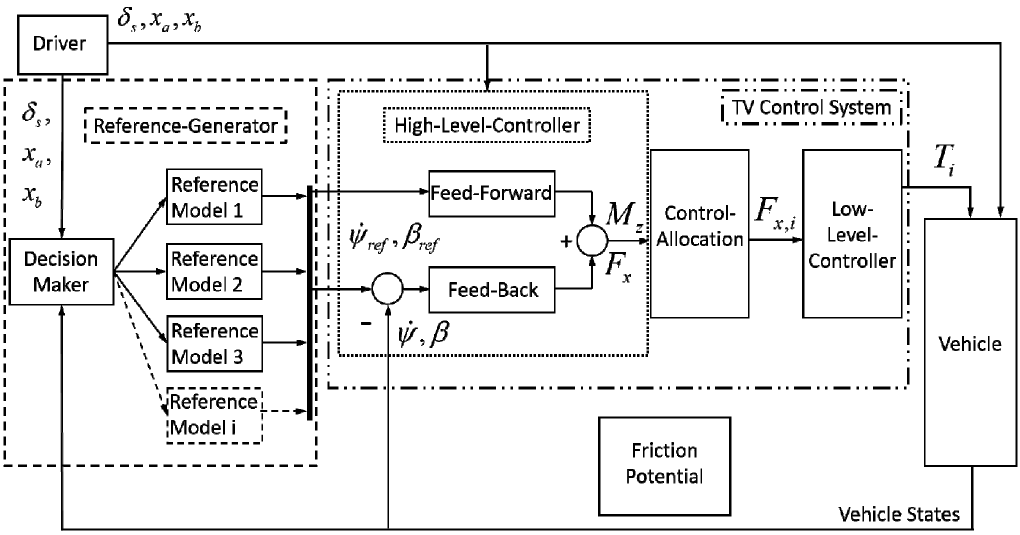


Fig. 1 Schematic of the driver–controlled vehicle–environment system

Since the TV control system is not in focus here, a ‘typical’ TV control approach consisting of high-level control, control allocation and low-level control is taken from literature, see e.g. [9]. The high-level control consists of a quasi-steady-state inverse-model based feed-forward contribution, [13, 14], and a PID-control, [15], with yaw rate feed-back, and vehicle side slip angle control at large side slip angles. Desired effective yaw moment $M_z$ and traction force $F_x$ are processed and longitudinal forces $F_{x,i}$ assigned to the wheels by the control allocation that ensures uniform levels of utilised tyre force potential at the four individual tyres. At very high levels of utilised tyre force potential, drive torque will be moved to front tyres, to allow for a certain margin from force saturation of the rear tyres. Thus, loss of stability is less likely in the case of certain road friction disturbances. The low level control includes wheel dynamics as well as basic ABS/TCS control strategies, and maps the individual desired longitudinal tyres forces to (electric motor) torques, [16]. These torques are applied to the drive shafts of the wheels.

## 3. REFERENCE MODELS

Novice, skilled and expert drivers are selected in this paper to serve as 'typical' categories of drivers, to give some examples. These categories relate to different steady-state and transient reference handling properties of the TV controlled vehicle, considering the drivers' demands and expectations. However, additional categories and driving scenarios may be defined, and individual drivers that have been recognised as skilled in the decision maker in the first place may step down to the novice category, for instance, due to degraded awareness at long-range drives. In the following, representative steady-state and transient reference handing properties will be presented, as well as the respective modelling approach.

The novice driver represents the average driver, who has no ambition to exploit high lateral accelerations, and who requires save and predictable handling behaviour. Since the novice driver is aware of the linear range of handling only, [17], this range is extended to higher lateral accelerations of the vehicle, see Fig. 2. Considering tyre wear and energy consumption, the understeer gradient of the proper designed passive vehicle is maintained, as well as the respective maximum steady-state lateral acceleration, thus providing a similar grip margin at the rear axle for the passive and novice TV vehicle. However, a severe increase of steering demand is predefined to indicate the limits of handling, depending on the known actual road (friction) conditions. The transient behaviour of the passive vehicle remains basically unchanged, however, the steering response is slightly increased as well as the baseline level of yaw damping, to support a faster lane change, for example.

In contrast, the skilled driver aims at driving faster and more 'dynamic' through bends. The focus in this category is put – in addition to safety – on pleasure to drive. Again, the understeer gradient of the passive vehicle is maintained. However, the skilled driver takes advantage of the TV system from a further increased linear range of handling, as well as increased maximum lateral acceleration, compared to the passive vehicle (while the grip margin at the rear axle is degraded). In the transient domain of handling, the pleasure-to-drive aspect is addressed by defining a faster response to steering wheel inputs by higher gains and slightly reducing the phase lag and yaw damping. Both takes effect in particular at higher steering input frequencies.

The expert driver is considered to be a professional (race) driver, who can handle demanding driving situations, such as large vehicle side slip angles and sudden changes in steering (stability) behaviour, for instance due to external disturbances. The aim of the expert driver is to drive fast. The steady-state reference handling is purely linear up to the sudden appearance of the limit of handling. Compared to the skilled driver, gains are increased and phase lag is reduced further, as well as yaw damping, resulting in a very fast response of the vehicle to steering inputs.

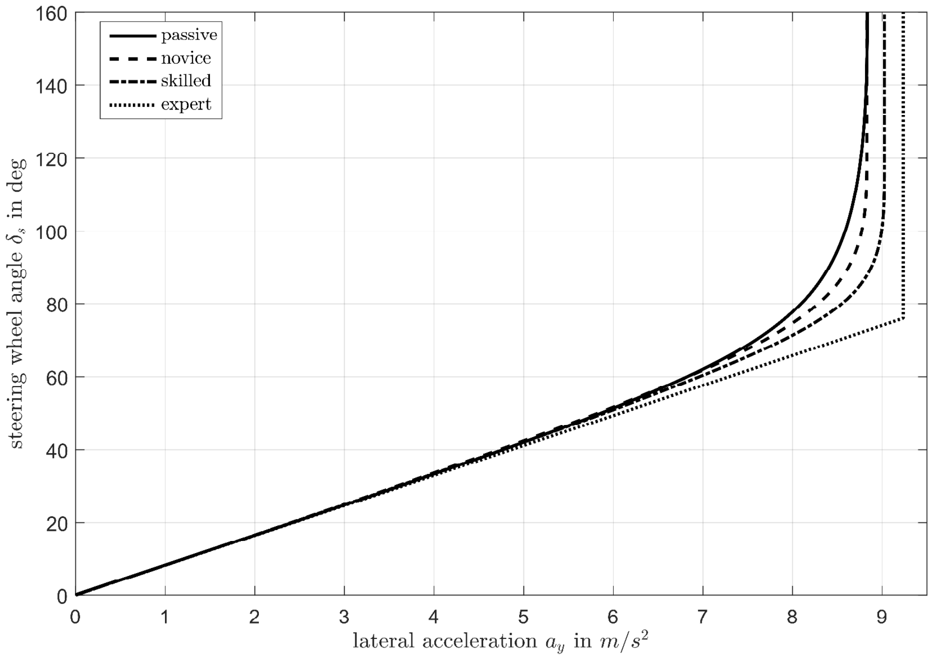


Fig. 2 Steady-state references and passive vehicle ramp steer at 80 km/h

The steady-state reference handling characteristics, hence reference yaw rate $\psi\dot{\psi}_{ss}$ (and respective vehicle side slip angle $\beta_{ss}$), is derived online from the (steady state) two-wheel vehicle model

$$0 = -\dot{\psi}_{ss} + \frac{F_{y,F}(\alpha_F) + F_{y,R}(\alpha_R)}{m \cdot v_x} \quad \text{and} \quad 0 = F_{y,F}(\alpha_F) l_F - F_{y,R}(\alpha_R) l_R \tag{1}$$

with

$$\alpha_F = \frac{\delta_s}{i_l} - \beta_{ss} - l_F \frac{\dot{\psi}_{ss}}{v_x}, \quad \alpha_R = -\beta_{ss} + l_R \frac{\dot{\psi}_{ss}}{v_x}, \tag{2}$$

and brush-type tyre/axle characteristics [17] for all drivers except the expert, applying linear tyre/axle characteristics in the later test manoeuvre. Thus, only few parameters need to be changed to switch between several reference models and road (friction) conditions, to prevent the need to store predefined respective 4D-look-up tables. Reference changes due to longitudinal acceleration are not considered here, but might be easily integrated in the reference models.

Transient reference handling properties are most often disregarded in literature. However, to ensure natural handling behaviour perception by the driver, the reference yaw rate $\dot{\psi}$ is derived from a linear two-wheel vehicle model,

$$G_{yaw} = \left(\frac{\dot{\psi}_{ss}}{\delta_S}\right) \frac{1 + T_1 s}{1 + \frac{2\sigma_f}{v_f^2} s + \frac{1}{v_f^2} s^2} \tag{3}$$

Linear transient behaviour guarantees for predicable and easy handling, since the human driver has been identified to be a linear controller only, see e.g. Refs. in [18]. Again, only (up to) three parameters need to be changed to adapt for several categories of drivers. In general, parameters should not deviate considerably from those of the proper designed passive vehicle, at least in the linear range of handling, to avoid excessive actuation effort and thus energy consumption and tyre wear.

## 4. HIGHWAY EXIT SCENARIO

Critical highway exit scenario simulations have been selected to demonstrate the idea of adapting reference models at TV systems to different categories of drivers. A four-wheel vehicle model including heave, pitch and roll dynamics, four individual (simplified) electric motors and the combined Magic Formula tyre model, [17], is used. The selected categories of drivers are modelled by applying the ‘internal model family’ (IMF) concept proposed in [19] to the (human) driver model presented in [18]. Following the IMF concept, the novice driver is aware of the linear range of handling only, while the skilled driver benefits from the knowledge on several locally linearized ‘internal’ vehicle models. The expert driver is fully aware of the overall handling behaviour of the vehicle.

The rather narrow highway exit is presented in Fig. 3, where a 40 m clothoid (marked with ‘x’) is followed from a constant 65 m radius curve, a second clothoid and a straight line.

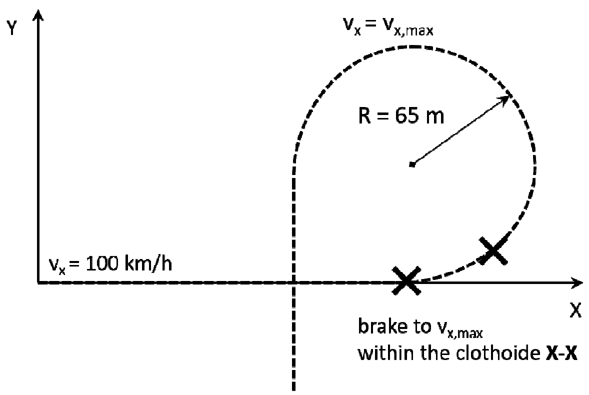


Fig. 3 Road trajectory of the highway exit

The different drivers approach the exit at a forward speed of 100 km/h, and realise rather late that the vehicle is too fast to pass the curve. Hence, they brake (late) at entering the clothoid. Skilled and expert driver operate appropriately tuned TV vehicles, Fig. 4, where the novice driver is driving both the ‘passive’ vehicle (with equally distributed drive torque to the four wheels) and the adapted ‘novice’ vehicle.

Due to the (needed) hard braking in the clothoid, the driver is struggling with the passive vehicle, but may stabilize the motion with considerable steering inputs and passes through the curve with severe path deviations. In contrast, when operating the adapted TV vehicle, the novice passes the highway exit smoothly. However, path deviations exceed those from the skilled and expert driver. Since the steady-state lateral acceleration of the vehicle is increased at the skilled driver category, less braking is needed to negotiate the curve. Although the TV vehicle is at the limit of handling, rather small path deviations appear, however, substantial vehicle side slip angles result from TV system intervention, see also e.g. [5]. Since the expert driver is fully aware of the combined longitudinal and lateral tyre force potential, (softer) braking until the end of the clothoid, based on [10], allows for very smooth steering commands. However, controllability is reduced remarkably due to very large (steady-state) vehicle side slip angles, [20], resulting from the expert driver category reference for TV control.

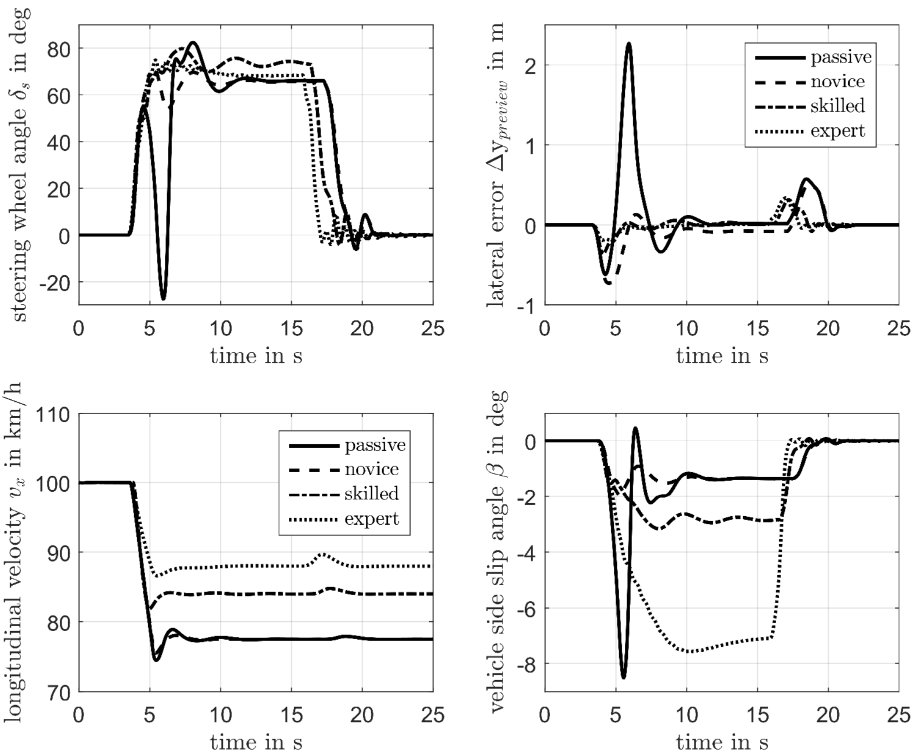


Fig. 4 critical highway exit scenario: driver steering wheel input $\delta_s$, previewed lateral path deviation $\Delta y_{preview}$, vehicle speed $v_x$, and vehicle side slip angle $\beta$

## 5. SUMMARY

In this paper, the idea of adapting the reference handling properties for TV controlled vehicles to the driving skills and condition of the individual driver as well as driving tasks was presented, to allow for safe and enjoyable driving. A ‘decision maker’ module is considered to select appropriate reference handling properties, based on identified driver steering behaviour, drowsiness detection systems, etc. Three heuristic steady-state and transient handling reference models, for ‘novice’, ‘skilled’, and ‘expert’ drivers, have been chosen to illustrate this approach. Respective advantages have been demonstrated by simulations of a critical highway exit scenarios, where driver models have been employed to track a desired road trajectory. Future work will include tyre-road friction and road conditions.

## 6. REFERENCES


[1] **Horiuchi, S.**: Evaluation of chassis control method through optimisation-based controllability region computation Vehicle System Dynamics, Vol. 50, Supplement, 2012. (p. 19-31)

[2] **Sakai, S-I. - Sado, H. - Hori, Y.**: Motion control in an electric vehicle with four independently driven in-wheel motors. IEEE/ASME Transactions on mechatronics, Vol. 4, No. 1, 1999. (p. 9-16)

[3] **Canale, M. - Fagiano, L. - Milanese, M. - Borodani, P.**: Robust vehicle yaw control using an active differential and IMC techniques. Control Engineering Practice, Vol. 15, 2007. (p. 923-941)

[4] **Rahimi Fetrati, S. - Kandler, C. - Kärcher, C. - Schramm, D.**: Inversion based feedforward design to improve the lateral dynamics of high performance sports cars. Proc. of AVEC'16, 2016. (p. 625-630)

[5] **De Novellis, L. - Sorniotti, A. - Gruber, P. - Shead, L. - Ivanov, V. - Hoepping, K.**: Torque vectoring for electric vehicles with individually controlled motors: State-of-the-Art and future developments. Proc. of the 26th International Electric Vehicle Symposium ESV26, 2012.

[6] **Metzler, M. - Tavernini, D. - Sorniotti, A. - Gruber, P.**: An Explicit Nonlinear MPC Approach to Vehicle Stability Control. Proc. of AVEC'18, 2018. 6p.

[7] **Braghin, F. - Sabbioni, E. - Sironi, G. - Vignati, M.**: A feedback control strategy for torque-vectoring of IWM vehicles. Proc. of the ASME Conference IDETC/CIE, 2014. 11p.

[8] **Bünte, T. - Kaspar, S. - Hohmann, S. - Brembeck, J.**: Inverse model based torque vectoring control for a rear wheel driven battery electric vehicle. Proc. of the 19th World Congress, The International Federation of Automatic Control IFAC, 2014. (p. 12016-12022)

[9] **Smith, E. N. - Velenis, E. - Cao, D. - Tavernini, D.**: Evaluation of optimal yaw rate reference for electric vehicle torque vectoring. Proc. of AVEC'16, 2016. (p. 619-624)

[10] **Yamakado, M. - Takahashi, J. - Saito, S. - Yokoyama, A - Abe, M.**: Improvement in vehicle agility and stability by G-vectoring control. Vehicle System Dynamics, Vol. 48, Supplement, 2010. (p. 231-254)

[11] **Raksincharoensak, P. - Mizushima, T. - Nagai, M.**: Direct yaw moment control system based on driver behaviour recognition, Vehicle System Dynamics, Vol. 46, Supplement, 2008. (p. 911–921)

[12] **Tokutake, H.**: Drowsiness estimation from identified driver model. Systems Science & Control Engineering, Vol. 3, 2015. (p. 381-390)

[13] **Bächle, T. - Graichen, K. - Buchholz - M., Dietmayer, K.**: Vehicle dynamics control in challenging driving situations using model predictive control allocation. Proc. of the IEEE Conference on Control Applications (CCA), 2014. (p. 346-351)

[14] **De Novellis, L. - Sorniotti, A. - Gruber, P.**: Wheel torque distribution criteria for electric vehicles with torque-vectoring differentials. IEEE Transactions on Vehicular Technology, Vol. 63, No. 4, 2014. (p. 1593-1602)

[15] **De Novellis, L. - Sorniotti, A. - Gruber, P. - Pennycott, A.**: Comparison of feedback control techniques for torque-Vectoring control of fully electric vehicles. IEEE Transactions on Vehicular Technology, Vol. 63, No. 8, 2014. (p. 3612-3623)

[16] **de Castro, R. - Araujo, R. E. - Freitas, D.**: Wheel slip control of EVs based on sliding mode technique with conditional integrators. IEEE Transactions on Industrial Electronics, Vol. 60, No. 8, 2014. (p. 3256-3271)

[17] **Pacejka, H. B.**: Tire and vehicle dynamics. Butterworth-Heinemann, 2012.

[18] **Edelmann, J. - Plöchl, M. - Reinalter, W. - Tieber, W.**: A passenger car driver model for higher lateral accelerations. Vehicle Systems Dynamics, Vol. 45, No. 12, 2007. (p. 1117-1129)

[19] **Keen, S. D. - Cole, D. J.**: Application of time-variant predictive control to modelling driver steering skill. Vehicle Systems Dynamics, Vol. 49, No. 4, 2011. (p. 527-559)

[20] **Shibahata, Y. - Shimada, K. - Tomari, T.**: Improvement of vehicle maneuverability by direct yaw moment control. Vehicle System Dynamics, Vol. 22, No. 5-6, 1993 (p. 465-481)

# IDENTIFICATION OF TIRE MODEL PARAMETERS FROM VEHICLE MEASUREMENTS USING SENSITIVITY ANALYSIS

**Arnaud MONTROUGE**[*,**], **Abderazik BIROUCHE**[*], **Guillaume TORRES**[**], **Christophe LAMY**[**], **Anthony PARSONS**[**] **and Michel BASSET**[*]

[*] University of Haute Alsace
12 Rue des Frères Lumières
68093 MULHOUSE Cedex, France
email : firstname.name@uha.fr

[**] Goodyear Innovation Center
Avenue Gordon Smith
7750 COLMAR BERG, Luxembourg
email : firstname_name@goodyear.com

*Received: November 5, 2018*

## ABSTRACT

Vehicle handling performance simulation is subject to many different tire models existing to estimate tire lateral forces. However, even with complex and accurate vehicle/tire models, significant differences appear between actual measurements of vehicle performance and simulation results. The non-consideration of actual operating conditions such as tire/road temperatures when using empirical tire models could be a significant contributor to these observations. A solution envisaged to reduce these differences is to identify new tire model parameters directly from vehicle track tests and to make a comparison with the parameters identified from indoor bench testing.

*Keywords:* Tire, Pacejka, Sensitivity Analysis, Identification, Modeling, Instrumented Test, Tire Temperature

## 1. INTRODUCTION

### 1.1 Context and Motivations

Today, simulation models are widely used in the industry to reduce vehicle development time. For the prediction of vehicle ride and handling performance the accuracy of the tire models used is especially important since the tire is the only vehicle component in contact with the road. For vehicle handling performance simulation different tire models exist to calculate tire lateral forces, ranging from physical models [1],[2] (high degree of insight but with high complexity and low accuracy) to empirical models [3], which is the type used here. Currently, the tire model parameters integrated in vehicle simulation models are identified from indoor bench testing, where the tire is tested under known and fixed ambient conditions (temperature and surface adherence). In contrast, when a tire is operating on a vehicle driven on a test track, it undergoes the influence of both the vehicle behavior and the

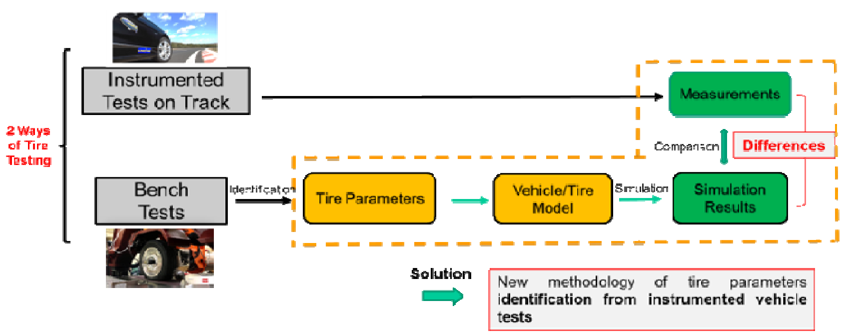


Fig. 1 Problem illustration

track conditions.

Consequently, some phenomena are not considered, resulting in differences appearing between simulation and measurements of vehicle performance criteria such as lateral acceleration/yaw rate when using tire empirical model, as shown in Fig.1. To correct that and reduce these differences, a new procedure of tire parameters identification is proposed here.

### 1.2 Proposed Solution: A new Parameter Identification Procedure

The aim of this paper is to propose a solution to identify the tire model parameters directly from vehicle measurements (lateral acceleration/yaw rate) obtained on track, and then make a comparison with the parameters identified from indoor bench testing. The objective is to link the differences in identified tire parameters to the variations in tire operating conditions, including temperature variation, between laboratory and road test conditions. In order to reach this objective, the identification procedure of tire model parameters from road measurements is proposed, which presents an high difficulty objective since no direct measurement of tire lateral forces is desired due to the complexity of sensors installation. In the literature, [4] and [5] propose identification methods for Pacejka model [3] coefficients from instrumented road tests. This paper innovates by adding the parameters sensitivity analysis to the identification procedure, to define necessary maneuvers and give information of parameters influence on input, and their identifiability (cartography), used to improve the identification algorithm. The goal being to identify Pacejka tire model parameters using only the measurement of vehicle performance criteria such as lateral acceleration $A_y$ and yaw rate $\dot{\psi}$. The objective function used in the optimization algorithm is improved thanks to the sensitivity indexes of the parameters, selecting the right measurement data where the considered tire parameter is influent and consequently identifiable. Fig.2 illustrates the methodology proposed.

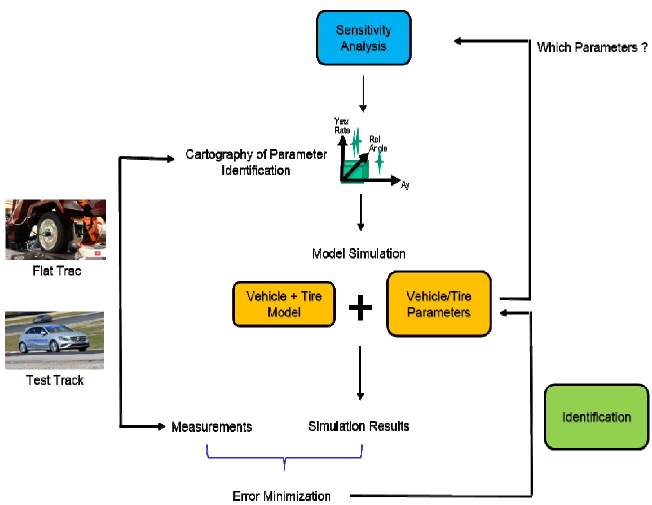


Fig. 2 Solution proposed

The identification from track measurements gives a new set of tire parameters values, then compared with those identified on test bench: a correlation with measured tire surface temperature variation is then done in order to estimate effects on the Pacejka tire parameters identified, to develop a new expression of these parameters as functions of tire temperature.

## 2. SENSITIVITY ANALYSIS TO IDENTIFY PARAMETERS

Before introducing the sensitivity analysis method, the tire model on which it is applied needs to be introduced.

### 2.1 Analyzed Tire Model: Pacejka Magic Formula

The tire model from Hans Pacejka, called Magic Formula (MF) [3], is a non-linear and empirical model, and expresses the tire lateral force as:

$$F_y(\alpha) = D_y.\sin(C_y.\arctan(B_y.\alpha - E_y.(B_y.\alpha - \arctan(B_y.\alpha)))) \quad (5)$$

with $\alpha$ the slip angle, and the parameters expressed as $K_y = B_y C_y D_y$ the cornering stiffness, $B_y$ the stiffness factor, $C_y$ the shape factor, $D_y = \mu_y.F_z$ the peak value ($F_z$ the load, $F_{z_0}$ nominal load and $\mu_y$ the friction factor) and $E_y$ the curvature factor.

These parameters called macro coefficients can be expressed using numerous independent micro coefficients (refer to [3] for details), to make them have a more physical meaning and dependent on the inputs applied to the tire such as tire load and camber angle. In this paper, the study focuses on eight micro coefficients $p_{K_{y1}}, p_{K_{y2}}, p_{K_{y3}}, p_{D_{y1}}, p_{D_{y2}}, p_{C_{y1}}, p_{E_{y1}}, p_{E_{y2}}$ affecting $D_y$, $K_y$, $C_y$ and $E_y$.

The next section explains the sensitivity method used. The purpose is to study the sensitivity of vehicle lateral acceleration and yaw rate to these 8 parameters variations, in order to know their potential of identifiability.

### 2.1 Chaos Polynomials Estimation of Sobol Indexes

The sensitivity analysis consists in the evaluation of the effect of parameters variation on output variation. In fact, it can be used in a context of parameters identification (which parameter is the most influent on output and consequently can be identified), test definition, performance optimization or command. It can be divided into local or global category, depending if the analysis focuses on a small variation of parameter value around nominal or if the entire variation range is studied. To evaluate the influence of parameters, static sensitivity indexes are calculated thanks to Sobol approach [6]. These indexes stay difficult to calculate, and their estimation can be done thanks to several methods. In this paper, these indexes are estimated using a Chaos Polynomials decomposition of the model output [7],[8] which does not need knowledge of parameters distribution functions and model structure, making it applicable on measurements.

Following this approach, the vehicle dynamics (lateral acceleration $A_y$ and yaw rate $\dot{\psi}$) can be decomposed as a finite sum of polynomials, whose coefficients are used to estimate the sensitivity indexes:

$$A_y \approx \sum_{j=0}^{M} a_j \psi_j(p_1, p_2, ...., p_n) \text{ with } \psi_j(p_1, p_2, ...., p_n) = \prod_{i=1}^{n} \phi_{\alpha_i^j}(p_i) \quad (1)$$

where $\phi_{\alpha_i^j}(p_i)$ Hermite polynomials with the $n$ parameters $(p_1, p_2, ...., p_n)$ of Pacejka model for which the sensitivity analysis is applied on. $(a_0, a_1, ..., a_j)$ the $M+1 = \frac{(n+b)!}{n!b!}$ Chaos Polynomials coefficients to be determined, $b$ the degree of Chaos Polynomials chosen to obtain a good approximation of the lateral acceleration $A_y$. For details of the decomposition, see [7].

Since the micro parameters of Pacejka model are independent, there are no interactions between each other and they affect the lateral acceleration independently. Consequently, only their first order sensitivity indexes $\dot{S}_{p_i}$ is needed and defined by:

$$\dot{S}_{p_i} = \frac{\sum_{j \in \Gamma_{p_i}} \hat{a}_j^2 E(\psi_j^2(p_i))}{\sum_{j=1}^{M} \hat{a}_j^2 E(\psi_j^2(p_1, ..., p_n))}$$ , with $\Gamma_i$ the polynomials function only of variable $p_i$ (4)

These indexes $\dot{S}_{p_i}$ are static, and they give the influence of a parameter at one state point of the model. To obtain dynamical indexes, the sensitivity index $\dot{S}_{p_i}(t_k)$ is calculated at each time index $t_k = k.\Delta T$, with $\Delta T$ the sampling rate, as seen in [9]. $\dot{S}_{p_i}(t_k)$ corresponds to the sensitivity of the parameter $p_i$ at this specific sample time $t_k$, and then all the $\dot{S}_{p_i}(t_k)$ are extrapolated in order to make them function of the time, or the output: $S_{p_i}(A_y)$ and $S_{p_i}(\dot{\psi})$ .

Thanks to that, the sensitivity of Pacejka parameters can be obtained at each moment of the maneuver, allowing to observe their influence evolution along the maneuver.

## 2.3 Application and Results

The sensitivity analysis presented in the section 2.1 is applied on the 8 previous independent parameters, and their 1st order Sobol static index is calculated at each time of a steady state maneuver, a steering wheel ramp at constant longitudinal velocity. The lateral acceleration $A_y$ and yaw rate $\dot{\psi}$ of the vehicle are generated thanks to a vehicle model [10], and the sensitivity of the eight Pacejka parameters is studied on these two outputs. Then, an extrapolation is applied to obtain the sensitivity function of lateral acceleration and yaw rate variation along time, which is used in the identification. It allows to know, following the value of lateral acceleration and yaw rate reached, which Pacejka parameters are influent. To obtain these sensitivity results, the parameters follow an arbitrary distribution, with a variation of $\pm 40\%$ of their nominal value (hypothesis that, when the parameters are identified on outside track, the difference in test conditions cannot make vary them more than $\pm 40\%$ of their value identified on test bench).

Fig.4 shows the evolution of sensitivity of Pacejka parameters function of the lateral acceleration $A_y$ :

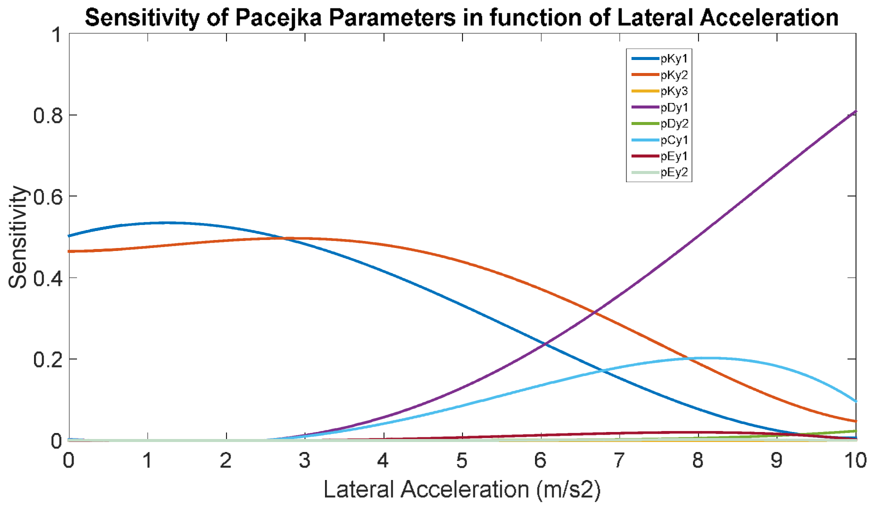


Fig. 4 Pacejka Sensitivity Functions

It is possible to see that the parameters $p_{K_{y1}}, p_{K_{y2}}$ of Pacejka (for the tire cornering stiffness $K_y$, equation (5)) are influent on the lateral acceleration for $A_y < 5m/s^2$, which confirms that for these values of $A_y$ corresponding to linear tire behavior (small slip angles $\alpha$), the lateral force $F_y$ can be approximated by $F_y \vdots \alpha.K_y$. At the contrary, for high lateral acceleration values, $p_{D_{y1}}, p_{D_{y2}}$ become more and more influent since they correspond to the coefficients of friction factor $\mu_y$, and it is known that in this zone, the lateral force is approximated by its peak value $D_y = \mu_y.F_z$. Similar sensitivity functions have been obtained for the yaw rate $\dot{\psi}$.
These sensitivity functions are then used in the identification, which is detailed thereafter.

## 3. IDENTIFICATION OF PACEJKA PARAMETERS

### 3.1 Cost Function Definition

We recall that the parameters to be identified are the same eight parameters of the Pacejka model studied previously, $p_{K_{y1}}, p_{K_{y2}}, p_{K_{y3}}, p_{D_{y1}}, p_{D_{y2}}, p_{C_{y1}}, p_{E_{y1}}, p_{E_{y2}}$. First, they are identified from indoor test bench testing, by measuring the tire lateral force for different slip angles, loads and camber angles. The values obtained give to the identification algorithm proposed here its initial starting condition $P_{init}$ (see Fig.3). The objective is to quantify the variation in their identified values when the identification is done on the measurements of vehicle lateral acceleration and yaw rate from outdoor vehicle on-track tests.
The choice has been made to find their optimal values to reduce the error between simulation and measurements, explained in Fig.1 and Fig.2, by minimizing the cost functions defined here: eight cost functions $C_{i\in\{1...8\}}$ defined for each Pacejka parameter

$p_i$. They rely on a modified least square criterion, weighted by the sensitivity functions $S_{p_i}(A_y)$ and $S_{p_i}(\dot{\psi})$ of $p_i$:

$$C_i = \frac{\sqrt{\sum_{j=1}^{N} S_{p_i}(A_{y_{measured}}).[A_{y_{measured}} - A_{y_{simulated}}]^2}}{\sqrt{\sum_{j=1}^{N} S_{p_i}(A_{y_{measured}}).A_{y_{measured}}{}^2}} + \frac{\sqrt{\sum_{j=1}^{N} S_{p_i}(\dot{\psi}_{measured}).[\dot{\psi}_{measured} - \dot{\psi}_{simulated}]^2}}{\sqrt{\sum_{j=1}^{N} S_{p_i}(\dot{\psi}_{measured}).\dot{\psi}_{measured}{}^2}} \qquad (6)$$

with $N$ the number of output samples.

The advantage of this cost function definition is that only the parts of the output where the parameter $p_i$ is influent are considered for its identification.

Finally, the final cost function $C$ is obtained as the sum of each individual cost function $C_i$. Once the cost functions are proposed, their minimization is discussed in the next section.

### 3.2 Proposed Identification Methodology

Since the cost functions defined previously are not known, their convexity and continuity are not guaranteed, and consequently it is recommended to use identification methods relying on derivative free calculation. Furthermore, the cost functions are unconstrainted since the objective is to identify the tire parameters without initial condition in the future (so without having to test them on test bench initially), making the Nelder-Mead simplex method [11] (also called downhill simplex), the most adapted to minimize the cost functions defined in (6). Here, it is decided to use the downhill simplex inside a developed identification algorithm, and not alone. By this way, the minimization of error is done on less parameters since they are grouped following their influence on the output, making it easier to identify separately less parameters in different groups. The objective is to orientate the direction of parameters research in order to reduce $C$: whereas a downhill simplex method is searching in every direction of parameters to minimize the cost function (sometimes making the parameter reached values not eligible for the model), the algorithm proposed here is oriented thanks to the sensitivity information of each of its parameters. For each cost function $C_{i\in\{1,2,....,n\}}$ (here $n$ = 8), a minimization is processed to find the optimal parameter $p_i$ which reduces $C_i$. Then, the maximum of the $n$ derivatives of each $C_i$ is searched, its corresponding parameter $p_i$ is replaced by the new identified value, and its index is used to calculate the new optimal parameters vector $P^j = [p_1{}^j,....,p_n{}^j]$ (with $\{p_2{}^j,...,p_n{}^j\} = \{p_2{}^{j-1},...,p_n{}^{j-1}\}$ if for example i =1). When the cost function $C_j$ is smaller than the condition defined, then the algorithm is stopped.

### 3.3 Results of Identification

The proposed identification algorithm gives consistent results for the identification of the Pacejka parameters. The obtained values from identification on test track measurements show important variation compared to the values obtained on test bench. Table.1 gives the values:

| | test bench | track | variation |
|---|---|---|---|
| $p_{K_{y1}}$ | -30 | -21 | -30% |
| $p_{K_{y2}}$ | 2.3 | 2.1 | -8% |
| $p_{K_{y3}}$ | 0.03 | 0.03 | 0% |
| $p_{D_{y1}}$ | 1.18 | 1.33 | +12% |
| $p_{D_{y2}}$ | -0.22 | -0.25 | +13% |
| $p_{C_{y1}}$ | 1.8 | 1.9 | +5% |
| $p_{E_{y1}}$ | -0.3 | -0.3 | 0% |
| $p_{E_{y2}}$ | -1.33 | -1.29 | -3% |

Table 1 Pacejka Parameters Identified Values

The results of fit on lateral acceleration are shown on Fig.5, corresponding to a fit ratio of 95% on steering wheel angles $STW < 50°$ (same results for yaw rate). Other sensibility analyzes have been done in parallel to identify the other vehicle parameters influent on the studied outputs $A_y$ and $\dot{\psi}$: these influent parameters have consequently been correctly identified before starting the identification of the Pacejka parameters. The model has been correctly validated and calibrated in consequence to be sure that the differences observed come from the tire parameters only.

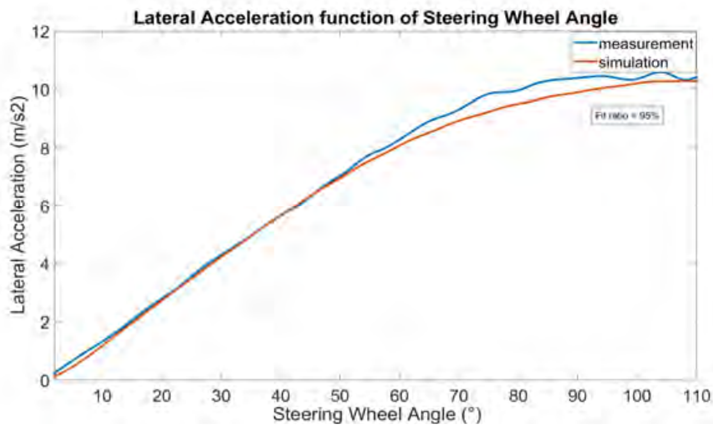


Fig. 5 Identification Result of Lateral Acceleration

The model has then been validated on a similar maneuver to verify the acceptability of this identification, giving a good fit ratio of 94% on lateral acceleration and yaw rate.

## 4. PERSPECTIVES AND CONCLUSION

In this paper, an innovative methodology to identify Pacejka tire parameters directly from usual vehicle on-track measurements (lateral acceleration and yaw rate) has been developed. It stands on an identification algorithm relying on the sensitivity information of the parameters to the outputs. This methodology has given promising results of identification, validated on track measurements. The parameters show non-negligible variations from test bench identification, supposed to be explainable thanks to differences in tire temperature.

The next work is to use a tire temperature model developed in parallel to correlate the variation in parameters with the variations in temperature, thanks to a tire temperature estimation model and a modified Pacejka model taking into account the temperature.

## 5. REFERENCES

[1] **Gipser, M.:** FTire a the tire simulation model for all applications related to vehicle dynamics. Vehicle System Dynamics, 45(sup1): January 2007, p.139–151.

[2] **Pearson, M. – Blanco-Hague, O. – Pawlowski, R.:** TameTire: Introduction to the Model. Tire Science and Technology, 44(2):, April 2016, p.102–119.

[3] **Pacejka, H.B. – Bakker, E.**: The Magic Formula Tyre Model. Vehicle System Dynamics, 21 (sup001):, January 1992, p.1–18.

[4] **Arosio, D. – Braghin, F. – Cheli, F. – Sabbioni, E.**: Identification of Pacejkas scaling factors from full-scale experimental tests, Vehicle System Dynamics, vol. 43, no. sup1, Jan. 2005. p. 457–474.

[5] **Farroni, F. – Lamberti, R. – Mancinelli, N. – Timpone, F.:** TRIP-ID: A tool for a smart and interactive identification of Magic Formula tyre model parameters from experimental data acquired on track or test rig, Mechanical Systems and Signal Processing, vol. 102, Mar. 2018, p.1–22.

[6] **Sobol, I.M.**: Global sensitivity indices for nonlinear mathematical models and their monte carlo estimates. Mathematics and computers in simulation, 2001.

[7] **Blatman, G.**: Adaptive sparse polynomial chaos expansions for uncertainty propagation and sensitivity analysis," ResearchGate, Oct. 2009.

[8] **Hamza, S. – Anstett-Collin, F. - Kiébré, R. et al**.: Analyse de sensibilité basée sur les polynômes du chaos pour des modèles de type boîte noire. CIFA 2012. 2012.

[9] **Sandoval, E.H. – Anstett-Collin, F. – Basset, M.:** Sensitivity study of dynamic systems using polynomial chaos. Reliability Engineering & System Safety, 2012, vol. 104, p.15-26.

[10] **Rajamani, R.:** Vehicle dynamics and control. Springer Science & Business Media, 2011.

[11] **Lagarias, J.C. – Reeds, J.A. – Wright, M.H. – Wright, P.E.:** Convergence Properties of the Nelder-Mead Simplex Method in Low Dimensions. SIAM Journal of Optimization. Vol. 9, Number 1, 1998, p.112–147.

# INFLUENCE OF THE WHEEL PROFILE CONDITION ON THE VEHICLE DYNAMICS

**Gabor MÜLLER[1)], Bernd LUBER[1)], Felix SORRIBES-PALMER[1)], Lorenz PIETSCH[2)] and Klaus SIX[1)]**

[1)]Virtual Vehicle Research Center
Inffeldgasse 21a, A-8010 Graz, Austria
[2)] PJ Messtechnik GmbH
*Waagner Biro Str. 125, A-8020 Graz, Austria*

*Received: November 5, 2018*

## ABSTRACT

The wheel-rail contact has a large influence on the vehicle dynamics which is highly influenced by the shape of the wheel profile. The main goal of this work is to investigate the influence of the wheel profile condition on the vehicle dynamics taking into account stochastic parameters occurring in operation. Multi-Body-Dynamics (MBD) simulations have been carried out to analyse the vehicle dynamic behaviour under different conditions. The simulation object was a model of a freight wagon. Two types of wheel profiles have been used during the simulation, a new one and a worn wheel profile with hollow worn characteristic. The shape of the rail profile has also been varied between a new and a measured worn shape. A framework in Matlab has been built up to steer the simulation and analysis process. After defining the constant and stochastic parameters – with their distribution and range – the simulations in SIMPACK are automatically started and after that the output channels are loaded to a predefined object and analysed in time and frequency domain. The results have shown that the relative displacement between wheel and rail is quite different in case of worn and new wheel profiles. If the wheel is worn, under certain conditions the variation of this displacement can be larger while if the wheel is new the distance can be more concentrated due to an increased number of distinct two-point contacts. This concentration drives the wheel, and it follows the track irregularities much more than a worn wheel, where a filtering due to the wheel-rail contact works more effective. This phenomenon has been observed on the lateral axle-box accelerations as well.

*Keywords:* multibody dynamics, stochastic parameter variation, railway wheel-profile

## 1. INTRODUCTION

Freight wagons are equipped mostly with composite brake blocks – so called “K-Sohlen” (German). These brake blocks can increase wheel wear on the centre of the wheel tread. Such so-called hollow worn wheels lead to shorter inspection intervals because of the increased risk of instability. The global goal of this research work is to elongate the inspection intervals with the help of continuous on-board monitoring of the wheel wear state. To reach this aim a methodology has to be found to estimate the wheel profile condition based on the vehicle’s running behaviour (mainly in lateral direction).

To investigate the physical effects the Multi-Body-Dynamics (MBD) simulation software SIMPACK has been used. First, the parameters have to be defined which can have an influence on the vehicle dynamics of the vehicle and can also be considered in the MBD simulation. The most important one is the wheel profile whose influence will be investigated. In the MBD simulation a new and a measured hollow worn profile are considered. A very important factor is the friction between wheel and rail, such as the rail profile with its wear status. The wagons are not the same even though they have the same type because of the production tolerances of the parts and of the car. The vehicle rolls on different tracks with different irregularities and layouts. The load can have a wide range at freight wagons, such as the vehicle speed (see Fig. 1). These parameters have been defined based on pre-knowledge or measurements and a sensitivity analysis has been carried out to analyse the main influencing effects. The focus was laid on the wheel-rail contact and on the resulting accelerations measured at the axle-box.

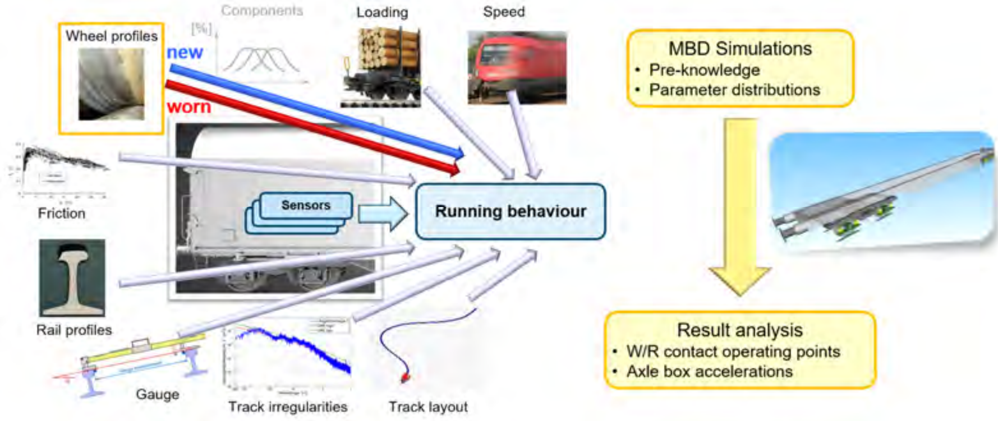


Fig. 1 Physical parameters influencing the vehicle dynamics of a freight wagon

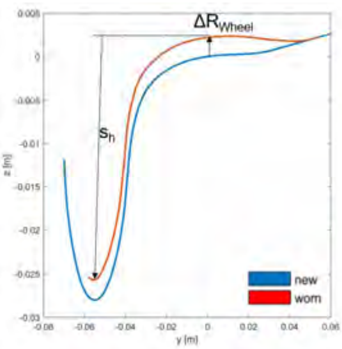


| | Simulation Parameters | | | | | | |
|---|---|---|---|---|---|---|---|
| ShortName | WP | mue | CV | LD | Exc | G | RP |
| Name | Wheel Profile | Coefficient of friction | Curvature | Loading | Track Irreg. Quality | Gauge | Rail Profile |
| Level 0 | New Profile (S1002) | Low (0.2) | Straight track | Tare/Empty (axle load 4 t) | Good quality | Nominal (1435 mm) | New Profile (UIC60) |
| Level 1 | Worn Profile (500tkm) | High (0.4) | Curved track (R = 700 m) | Loaded (axle load 22.5 t) | Bad quality | Wide (1445 mm) | Worn Profile |

| DOE-ID | WP-Level | mue-Level | CV-Level | LD-Level | Exc-Level | G-Level | RP-Level |
|---|---|---|---|---|---|---|---|
| 0 | 0 | 0 | 0 | 0 | 0 | 0 | 0 |
| 1 | 0 | 0 | 0 | 0 | 0 | 0 | 1 |
| 2 | 0 | 0 | 0 | 0 | 0 | 1 | 0 |
| 126 | 1 | 1 | 1 | 1 | 1 | 1 | 0 |
| 127 | 1 | 1 | 1 | 1 | 1 | 1 | 1 |

Fig. 2 Hollow worn vs. new wheel profile (left), table of varied parameters for the two-level factorial DoE (right)

## 2. METHODOLOGY

### 2.1 MBD simulations to investigate the physical effects

The main parameter is the condition of the wheel profile. A hollow worn and a new wheel profile have been considered in the simulations, the worn one has run approximately 500t km (see Fig. 2, left).

In the first investigation, a two-level full-factorial DoE (Design of Experiment) has been carried out: the two conditions of the wheel profiles, a lower and a higher coefficient of friction, a curved and a tangent track, two loading conditions, two different qualities of measured track irregularities, two gauges and a new and a worn rail profiles (see Fig. 2, right).

### 2.2 Simulation results – DoE

After carrying out the two-level full-factorial DoE, the influence of the considered parameters on the target value – axle-box accelerations – has been investigated and the dependency on the wear status of the wheel profile has been analysed. The scatter plot shown in Fig. 3 shows the standard deviation of the vertical axle-box accelerations over the lateral ones. In the case where the wagon runs on a curved track without loading, an effect can be observed in case of DoE-variations 54 and 118, where the only difference between the runs is the wheel profile. In the case of run 54 it is a new one and in case of run 118 it is a worn one. In this case, the standard deviations of the accelerations can be separated well. Higher accelerations occur in the case of a new wheel profile compared to the case of a run with hollow worn wheel profile. It has also been observed that if the track gauge is wider than normally, a reverse effect occurs, which can be seen in case 55 vs. 119. The next step is to analyse the physics, or in other words the vehicle dynamic behaviour behind these effects.

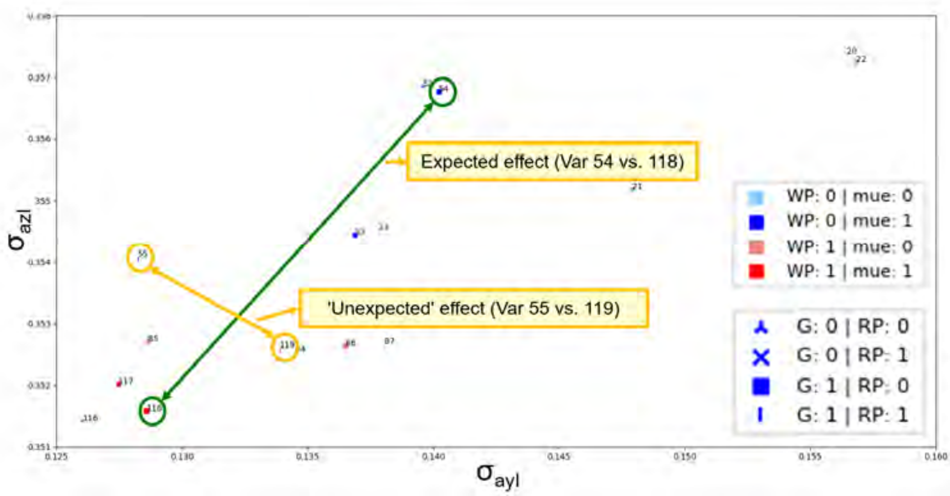


Fig. 3  Standard deviations of the vertical axle-box accelerations over the lateral axle-box accelerations, DoE, curved track, tare vehicle

With the help of MBD simulations a more detailed insight into the wheel-rail contact effects is possible compared to measurement analysis. Taking the DoE-cases 54 vs. 118, where a good separation was possible, the relative distance between wheel and rail and the contact position of the patches on the wheel surface have been analysed (see Fig. 4). The figure on the top describes the lateral contact point positions over the relative distance between wheel and rail on the high rail. It can be seen in the figure on the top, that in the case of the new wheel profile (blue points) distinctive two point contacts occur, while in the case of the hollow worn wheel profile (red) more likely one point contact takes place. Analysing the distribution of the relative distance between wheel and rail (bottom figure) it can be seen that in case of an increased number of two point contact conditions (blue) the distribution is narrower because the wheel follows the rail and its irregularities most of the time due to the geometric constrained introduced by the two-point contact. In the case with the worn wheel profile, this distribution is wider, because more movement is possible between wheel and rail.

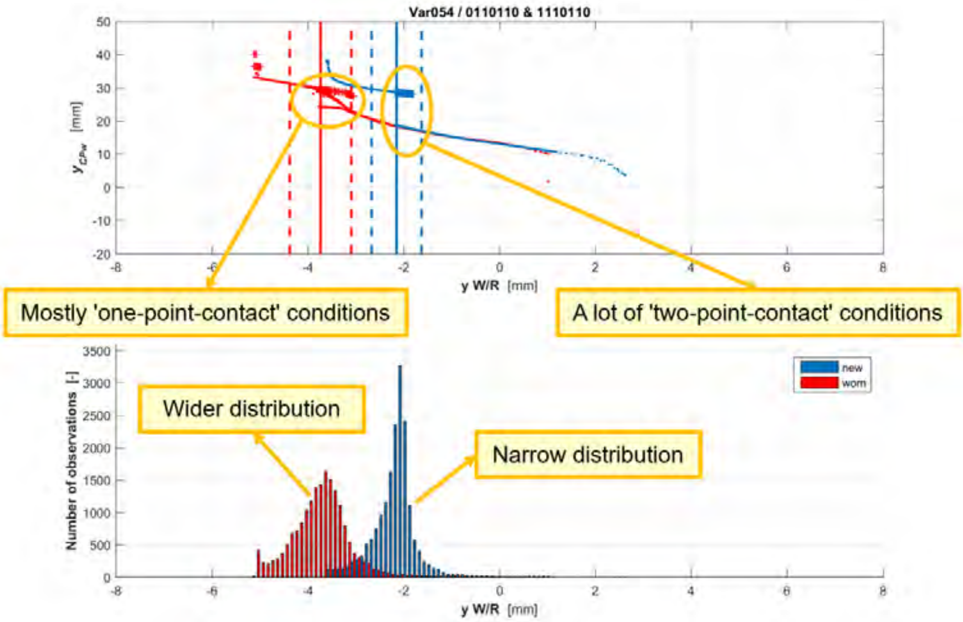


Fig. 4 Analysis of the contact patch positions regarding the relative distance between wheel and rail

The hypothesis after analysing the two-level full-factorial DoE results is that in case of a new wheel profile decisive two point contacts occur. This leads to a geometric constraint between wheel and rail and can cause higher lateral wheelset accelerations. In case of worn wheel profiles, the one point contact is prestigious, giving the wheelset flexibility in lateral direction, which causes lower lateral accelerations. In the next step further simulations have been carried out to analyse the vehicle dynamic behaviour under more realist stochastic conditions, where the distribution of the parameters has been determined due to measured values and due to knowledge of operating conditions.

This more detailed analysis with stochastic parameter sets has confirmed the appearance of distinctive two-point contacts in the case of the new wheel profile. The distributions of the relative wheel-rail positions and the lateral axle-box accelerations show the same characteristic as before, namely narrower distribution of the relative wheel-rail positions in the case of the new wheel profile. Due to more direct guiding more energy is transferred to the wheelset which leads to a wider distribution of the lateral axle-box accelerations (see Fig. 5).

It can also be concluded that the stochastically varying parameters makes the separation more complex. Therefore, additional features are necessary to separate the wheel profile effects from all other parameter effects. Therefore, for example machine-learning algorithms will be applied in future research.

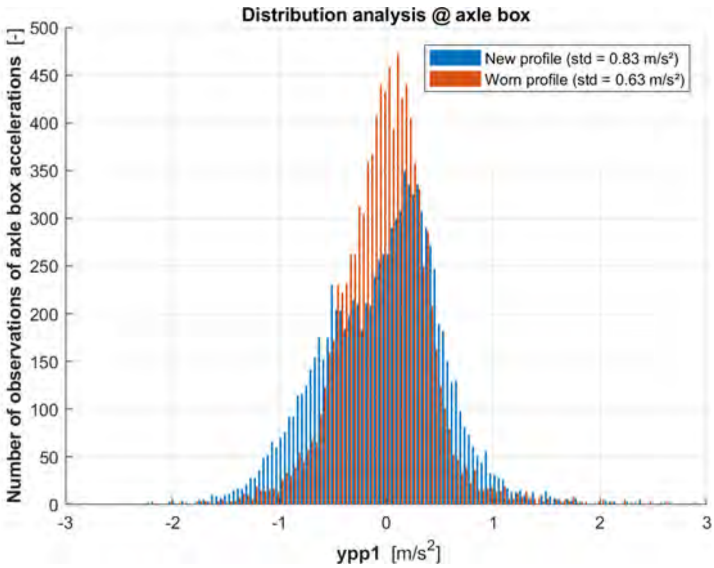


Fig. 5 Standard deviation of the lateral axle-box accelerations (new vs. worn wheel profile)

## 3. CONCLUDING REMARKS

The wear status of the wheel has a significant influence on the vehicle dynamic behaviour in lateral direction dependent on the operating conditions. Wheel wear can increase the lateral vehicle accelerations because of the “impact-like” flange contact, but it also can decrease the lateral vehicle accelerations because of a wider distribution of the contact points on the wheel.

Further investigations are needed to isolate the scenarios – like radius, high/low friction – under real conditions, to get more knowledge of operating conditions and finally to find additional relevant features to separate the influence of the wheel profile. According to the experience from this investigation it is concluded, that the knowledge of physical effects is essential for the development of on-board profile monitoring algorithms. From the current point of view pure data driven approaches are not sufficient to develop reliable monitoring systems.

## 4. ACKNOWLEDGEMENT

This work has been partly financed within the European Horizon 2020 Joint Technology Initiative Shift2Rail through contract n° 730617 (FR8RAIL).

The publication was written at VIRTUAL VEHICLE Research Center in Graz, Austria. The authors would like to acknowledge the financial support of the COMET K2 – Competence Centers for Excellent Technologies Programme of the Federal Ministry for Transport, Innovation and Technology (bmvit), the Federal Ministry for Digital, Business and Enterprise (bmdw), the Austrian Research Promotion Agency (FFG), the

Province of Styria and the Styrian Business Promotion Agency (SFG). We also want to thank for the support from PJ MESSTECHNIK GMBH (PJM).

## 5. REFERENCES

[1] **Zobory, I.:** Prediction of Wheel/Rail Profile Wear. Vehicle System Dynamics, Swets & Zeitlinger, Vol. 28, 1997, p.221-259.

# TOWARDS ROBUST LINEAR PARAMETER VARYING CONTROL FOR ACTIVE RAIL VEHICLE WHEELSETS

**Van Tan VU[1], Argyrios ZOLOTAS[2], Olivier SENAME[3] and Luc DUGARD[3]**

[1]Department of Automotive Mechanical Engineering,
University of Transport and Communications, Hanoi, Vietnam
E-mail: vvtan@utc.edu.vn
[2]School of Engineering, College of Science, Univ. of Lincoln, Lincoln LN6 7TS, UK
E-mail: azolotas@lincoln.ac.uk
[3]Univ. Grenoble Alpes, CNRS, Grenoble INP*, GIPSA-lab, 38000 Grenoble, France
*Institute of Engineering Univ. Grenoble Alpes
E-mail: {olivier.sename, luc.dugard}@gipsa-lab.grenoble-inp.fr

*Received: November 5, 2018*

## ABSTRACT

The complexity of railway vehicle structures has been part of an evolutionary process for almost two hundred years. Issues such as increased weight, increased maintenance, higher costs and energy consumption have arisen. The vision for future railway vehicles is to alleviate issues of complexity, hence enable simpler structures and reduce maintenance and cost issues, and of course various research challenges arising from this. In fact, a number of papers in the railway engineering literature have presented practical ways to control steering of railway vehicles to improve performance. The model at the railway wheelset level is highly nonlinear, mainly due to the nature of the wheelset structure and the related wheel-rail contact forces involved during operation. Here the simplest in terms of retrofitting, the actuated solid-axle wheelset is considered, we investigate actively controlled wheelsets from a Linear Parameter Varying (LPV) control aspect. We use the grid-based LPV approach to synthesize the $H_\infty$/LPV controller, which is self-scheduled by the forward velocity, as well as the longitudinal and lateral creep coefficients. The aim of the controller is to reduce the lateral displacement and yaw angle of the wheelset. Simulation results show that the proposed controller ensures the above targets' achievement in the considered frequency domain up to 100 rad/s.

*Keywords*: Railways, Active steering, Active control, $H_\infty$ control, Linear Parameter Varying (LPV) system.

## 1. INTRODUCTION

### 1.1 Context

Some of the railways' most important features include high speed, relatively cheap operation and relatively low maintenance cost as well as safe and environmentally friendly service. Therefore, railways play an essential transport role in the 21st century. The cost efficiency in railway operations can be explored from different points of view such as running speed, ride comfort, safety, rail/wheel contact wear, maintenance cost and so forth. The bogie system of high speed trains contains primary and secondary suspension components which can significantly affect the overall dynamic behaviour of railway vehicles in different operational scenarios [1]. The kinematic and dynamic characteristics of railway wheelsets are now well understood. Although passive suspension systems might provide satisfactory running behaviour at low to medium speeds, application of such systems at high speeds might lead to poor ride comfort and steering problems such as instability and lack of excellent curving performance [2].

In order to overcome the drawback of the passive system, special attention has been paid to the bogie suspension system with the active control design. Active elements are often used in substitution of, or in combination with passive components to improve the train's dynamics. The mainstream of the active control design in railway applications is considered for the secondary suspension system. However, the increasing interest in the idea of actively-controlled wheelsets gives a new perspective to the possibilities for achieving better stability [3], and it is therefore valuable to re- evaluate the dynamic equations in a manner which will facilitate a control engineering approach. Several active systems have been developed during the past few decades in order to meet various design requirements and improve railway vehicles' performance from different perspectives such as ride comfort, safety, and wheel/rail contact wear [4-6]. This paper presents a new LPV control design for an active wheelset system in order to improve wheelset stability.

### 1.2 Related works

In the literature some related works are listed as below:

- In [1], a robust controller is designed for active steering of a high speed train bogie with solid axle wheelsets to reduce track irregularity effects on the train's dynamics and to improve stability and curving performance. A half-car railway model with seven degrees of freedom equipped with practical accelerometers and angular velocity sensors is considered for the $H_\infty$ control design. The results showed that for the case of nonlinear wheel and rail profiles, significant improvements in the active control performance can be achieved using the proposed compensation technique.
- In [2], the authors present the unconstrained wheelset equations in a block diagram form, illustrating the feedback action created by a combination of creep and conicity. It then identifies a re-structuring and simplification from which the basic kinematic oscillation can readily be predicted, and also helps to expose the issues relating to stabilisation through passive means. The analysis is extended using a similar approach to a wheelset with independently rotating wheels, including the effect of longitudinal creep upon the relative speed of the two wheels.
- In [7], an improvement of the curving behaviour of conventional railway vehicles mounting bogies and solid wheelsets through active control was investigated. Various possible control goals are considered and implemented using optimal control techniques. Then suitable sensor types and locations are selected for each control strategy and results are obtained taking into account stochastic disturbances.
- In [8], an assessment of a railway wheelset in control engineering terms was presented. It addresses a linearised dynamic model and some simulation results for straight and curved track; it also gives an interpretation of the fundamental stability problem based upon the control system stability analysis, and suggests theoretical possibilities for active control laws.

### 1.3 Paper contributions

Based on the idea in [2,7,8], here the authors present preliminary research results on the $H_\infty$/LPV active wheelset control system with the aim of improving the wheelset stability. Hence the following contributions are brought:

- We propose an LPV wheelset system by considering the forward velocity, the longitudinal and lateral creep coefficients as the three varying parameters. The two exogenous disturbances used include the curvature and the cant angle. The control input includes the lateral force and yaw torque which are controlled by the active controller.

- We use the grid-based LPV approach to synthesize the $H_\infty$/LPV controller self-scheduled by the forward velocity, the longitudinal and lateral creep coefficients. The aim of the controller is to reduce the lateral displacement and yaw angle of the wheelset. Simulation results show that the proposed controller ensures the above targets in the considered frequency domain up to 100 rad/s.

The paper is organised as follows: Section 2 presents a single active wheelset LPV model. Section 3 develops the $H_\infty$/LPV control synthesis for an active wheelset system to improve stability. Section 4 presents some simulation results in the frequency domain. Finally, some conclusions are drawn in section 5.

## 2. WHEELSET MODELLING

A single wheelset model shown in Figure 1 is considered for the robust LPV control design. It has a solid axle with linear wheel profiles, therefore the model has 2 degrees of freedom (DOF) [7,8]. There are four actuators which can be used for this model, with two actuators to create the lateral force ($F_y$) and two actuators for the yaw torque ($T_\psi$). The parameters and variables of the wheelset model are detailed in Table 1. The motion differential equations are formalized as follows:

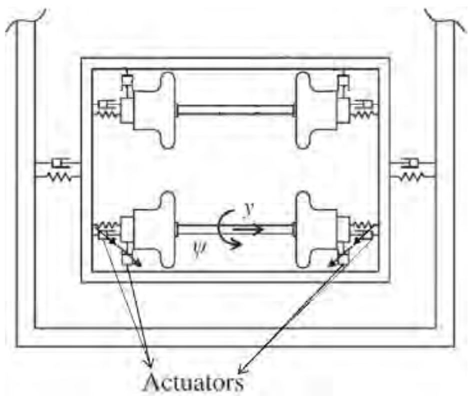


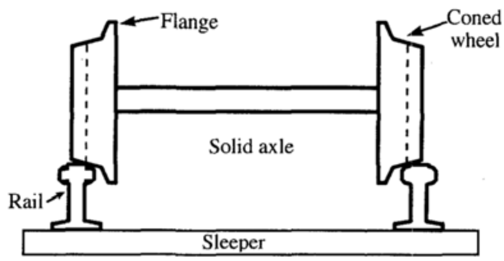


Fig. 1 A single wheelset model [1,8].

$$\begin{cases} \ddot{y} = -\dfrac{2f_{22}}{mv}\dot{y} + \dfrac{2f_{22}}{m}\psi + \dfrac{F_y}{m} + \dfrac{v^2}{R_0} - g\theta \\ \ddot{\psi} = -\dfrac{2f_{11}l\lambda}{Ir_0}y - \dfrac{2f_{11}l^2}{Iv}\dot{\psi} + \dfrac{T_\psi}{I} + \dfrac{2f_{11}l^2}{IR_0} \end{cases} \tag{1}$$

The set of differential equations of motion (1) can be rewritten in the LPV state-space representation with the three varying parameters $\rho=[\rho_1, \rho_2, \rho_3]$ ($\rho_1= v$, $\rho_2= f_{11}$, $\rho_3= f_{22}$) as follows:

$$\dot{x} = A(\rho).x + B_1(\rho).w + B_2(\rho).u \tag{2}$$

with the state vector $x = \left[ \dot{y} \ y \ \dot{\psi} \ \psi \right]^T$, the exogenous disturbance includes the curvature and the cant angle $w = \left[ \frac{1}{R_o} \ \theta \right]^T$, the control input includes the lateral force and the yaw torque $u = \left[ F_y \ T_\psi \right]^T$.

Table 1: Variables and Parameters of the single wheelset model [2,8].

| Symbols | Description | Value | Unit |
|---|---|---|---|
| $m$ | Wheelset mass | 1250 | kg |
| $v$ | Forward velocity | - | km/h |
| $l$ | Half gauge | 0.75 | m |
| $I$ | Wheelset yaw inertia | 700 | $kgm^2$ |
| $r_0$ | Nominal wheel radius | 0.5 | m |
| $R_0$ | Curve radius | - | m |
| $\theta$ | Track cant angle | - | rad |
| $\lambda$ | Conicity | 0.15 | - |
| $f_{11}$ | Longitudinal creep coefficient | $10^7$ | N |
| $f_{22}$ | Lateral creep coefficient | $10^7$ | N |
| $y$ | Lateral displacement | - | m |
| $\psi$ | Yaw angle | - | rad |

# 3. H∞/LPV CONTROL DESIGN FOR ACTIVE WHEELSET SYSTEM

## 3.1. LPV control for the active wheelset system

One of the key factors in railway operations (especially at high speeds) is running stability which is particularly important for safety and ride comfort. Therefore, the controller should first of all stabilise the wheelset motion. In order to satisfy the above mentioned design requirements, it is not necessary to control all the states of the system. A global sensitivity analysis on the wheel/rail contact properties w.r.t. the wheelset dynamics proved that the contact properties such as creeps, contact forces, and contact patch dimensions are mostly sensitive w.r.t. the wheelset lateral and yaw motions. The lateral wheelset motion should be below some limit (8mm in most of the cases) to avoid a flange contact. On the other hand, the wheelset yaw motion can significantly affect the contact forces. In order to describe the control objective, the model (2) has a partitioned representation in the following way:

$$\begin{bmatrix} \dot{x}(t) \\ z(t) \\ y(t) \end{bmatrix} = \begin{bmatrix} A(\rho) & B_1(\rho) & B_2(\rho) \\ C_1(\rho) & D_{11}(\rho) & D_{12}(\rho) \\ C_2(\rho) & D_{21}(\rho) & D_{22}(\rho) \end{bmatrix} \begin{bmatrix} x(t) \\ w(t) \\ u(t) \end{bmatrix} \tag{3}$$

where $z(t) = \left[ y, \psi, T_\psi, F_y \right]^T$ is the performance output vector and $y(t) = \left[ \ddot{y}, \dot{\psi} \right]^T$ the measured output vector.

The bounds ($\overline{\upsilon}$, $\underline{\upsilon}$) of the varying parameters are taken into account. The control goal is to minimize the induced $L_2$ norm of the closed-loop LPV system $\sum_{CL}(\rho)$ = $LFT(G(\rho),K(\rho))$, with zero initial conditions, which is given by:

$$\left\|\Sigma_{CL}(\rho)\right\|_{2\to 2} = \sup_{\substack{\rho\in P \\ \overline{v}\le\dot{\rho}\le\underline{v}}} \sup_{\substack{w\in L_2 \\ \|w\|_2\neq 0}} \frac{\|z\|_2}{\|w\|_2} \tag{4}$$

If $\sum_{CL}(\rho)$ is quadratically stable, this quantity is finite. The quadratic stability can be extended to the parameter dependent stability, which is the generalization of the quadratic stability concept [9], [10].

### 3.2. H∞/LPV control synthesis

In this section, the forward velocity, the longitudinal and lateral creep coefficients are considered as the three varying parameters ($\rho=[\rho_1, \rho_2, \rho_3]$, $\rho_1= v$, $\rho_2= f_{11}$, $\rho_3= f_{22}$). The forward velocity can be measured directly by sensors, whereas the two creep coefficients vary a lot as the train moves.

#### 3.2.1. H∞/LPV control design

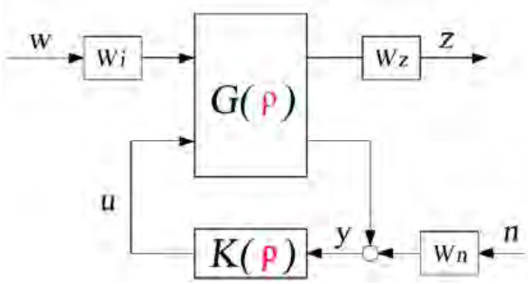


Fig. 2 Closed-loop interconnection structure with LPV active controller.

Figure 2 shows the control scheme for the $H_\infty$/LPV control design. It includes the feedback structure of the nominal model $G(\rho)$, the controller $K(\rho)$, the weighting functions and the performance objectives. In this diagram, $u$ is the control input, $y$ the measured output, $n$ the noise measurement, $z$ the performance output and $w$ the disturbance signal.

The main objective of the active system is to reduce the lateral displacement and yaw angle. Furthermore, the lateral force and yaw torque should be kept as small as possible in order to avoid the saturation of the actuators. Therefore the weighting functions are chosen as given in Table 2.

The LPV controller $K(\rho)$ in Figure 2 is defined as:

$$\begin{bmatrix} \dot{x}_c(t) \\ u(t) \end{bmatrix} = \begin{bmatrix} A_c(\rho) & B_c(\rho) \\ C_c(\rho) & D_c(\rho) \end{bmatrix} \begin{bmatrix} x_c(t) \\ y(t) \end{bmatrix} \tag{5}$$

The closed-loop system $\sum_{CL}(\rho)= LFT(G(\rho),K(\rho))$ can be derived from the generalized plant $G(\rho)$ (3) and the controller $K(\rho)$ (5) as follows:

$$\begin{bmatrix} \dot{\xi}(t) \\ z(t) \end{bmatrix} = \begin{bmatrix} \mathbf{A}(\rho) & \mathbf{B}(\rho) \\ \mathbf{C}(\rho) & \mathbf{D}(\rho) \end{bmatrix} \begin{bmatrix} \xi(t) \\ w(t) \end{bmatrix} \tag{6}$$

Where

$$\begin{cases} \mathbf{A} = \begin{bmatrix} A(\rho) + B_2(\rho)D_c(\rho)C_2(\rho) & B_2(\rho)C_c(\rho) \\ B_c(\rho)C_2(\rho) & A_c(\rho) \end{bmatrix} \\ \mathbf{B} = \begin{bmatrix} B_1(\rho) + B_2(\rho)D_c(\rho)D_{21}(\rho) \\ B_c(\rho)D_{21}(\rho) \end{bmatrix} \\ \mathbf{C} = \left[ C_1(\rho) + D_{12}(\rho)D_c(\rho)C_2(\rho)D_{12}(\rho)C_c(\rho) \right] \\ \mathbf{D} = D_{11}(\rho) + D_{12}(\rho)D_c(\rho)D_{21}(\rho) \end{cases} \tag{7}$$

with $\xi(t) = \left[ x^T(t),\ x_c^T(t) \right]^T$.

The quadratic LPV γ-performance problem is to compute the parameter-varying control matrices $A_c(\rho)$, $B_c(\rho)$, $C_c(\rho)$, $D_c(\rho)$ in such a way that the resulting closed-loop system is quadratically stable and the induced $L_2$ norm from $w(t)$ to $z(t)$ is less than γ. The existence of a controller that solves the quadratic LPV γ-performance problem can be expressed as the feasibility of a set of linear matrix inequalities (LMIs), which can be solved numerically [9-11].

Table 2: The weighting functions of the closed-loop structure [1].

| Weighting function | Description | Value |
|---|---|---|
| $W_z$ | Weighting functions for the performance output | $diag\left[W_{zy}, W_{zpsi}, W_{zFy}, W_{zTpsi}\right]$ |
| $W_{zy}$ | Weighting function for the lateral displacement | $100\frac{40s^2+60s+100}{1s^2+200s+100}$ |
| $W_{zpsi}$ | Weighting function for the yaw angle | $100\frac{10s^2+20s+1}{1s^2+200s+100}$ |
| $W_{zFy}$ | Weighting function for the lateral force | 5e-8 |
| $W_{zTpsi}$ | Weighting function for the yaw torque | 5e-8 |
| $W_i$ | Weighting functions for the disturbance signals | $diag\left[W_{i1}, W_{i2}\right]$ |
| $W_{i1}$ | Weighting function for the curvature | 0.5 |
| $W_{i2}$ | Weighting function for the cant angle | 0.5 |
| $W_n$ | Weighting functions for the noise measurement | $diag\left[0.01, 0.01\right]$ |

### 3.2.2. Solution for the H∞/LPV control

Several approaches can be used to design an LPV controller, based on the LPV model (3): Linear Fractional Transformations (LFT) [12,13], Polytopic solution [14,15], Linearizations on a gridded domain (grid-based LPV) [16]. The grid-based LPV approach is interesting since it does not require any special dependence on the parameter vector. This method is used in this paper together with the LPVTools™ [17] to synthesize the H∞/LPV controller.

For the interconnection structure shown in Figure 2, the $H_\infty$ controllers are synthesized for 10 values of the forward velocity in a range of $\rho_1 = v = [50\text{-}130]$ km/h, 50 values of the longitudinal creep coefficient in a range of $\rho_2 = f_{11} = [5\text{-}10]$ MN, 50 values of the lateral creep coefficient in a range of $\rho_3 = f_{22} = [5\text{-}10]$ MN. The spacing of the grid points is based upon how well the $H_\infty$ point designs perform for the plant around each design point. The grid points and the LPV controller synthesis using LPVTools$^{TM}$ are expressed by the following commands:

*v = pgrid('rho1',linspace(50/3.6,300/3.6,10));*
*f11 = pgrid('rho2',linspace(5e6,10e6,50));*
*f22 = pgrid('rho3',linspace(5e6,10e6,50));*
*[Klpv,normlpv] = lpvsyn(H,nmeas,ncont).*

At all of the grid points, the proposed weighting functions are applied to the entire grid parameter space and the effect of the scheduling parameter is ignored. In the $H_\infty$ control design, the $\gamma$ iteration results in an optimal $\gamma$ value and an optimal controller. However, if the weighting functions were changed, another optimal $\gamma$ and another optimal controller would be obtained.

## 4. SIMULATION RESULTS ANALYSIS

The parameters of the wheelset model are detailed in Table 1. In this section we will evaluate the effectiveness of the $H_\infty$/LPV active wheelset control system in the frequency domain for the three cases:

- **First case:** the forward velocity ($\rho_1 = v$) varies from 50 km/h to 300 km/h with 10 grid points. The longitudinal and lateral creep coefficients ($\rho_2 = f_{11}$, $\rho_3 = f_{22}$) are kept at the nominal value of 10 MN.
- **Second case:** the longitudinal creep coefficient ($\rho_2 = f_{11}$) varies from 5 MN to 10 MN with 50 grid points. The lateral creep coefficient ($\rho_3 = f_{22}$) is kept at the nominal value of 10 MN and the forward velocity ($\rho_1 = v$) is considered at 20 m/s.
- **Third case:** the lateral creep coefficient ($\rho_3 = f_{22}$) varies from 5 MN to 10 MN with 50 grid points. The longitudinal creep coefficient ($\rho_2 = f_{11}$) is kept at the nominal value of 10 MN and the forward velocity ($\rho_1 = v$) is considered at 20 m/s.

For all these cases, the $H_\infty$/LPV active wheelset control system is denoted in red-solid and the “no control” in blue-dashed lines. In the following Figures, we show the transfer function magnitude from the exogenous disturbances of the curvature ($\frac{1}{R_o}$) and cant angle ($\theta$) to the lateral displacement ($y$) and yaw angle ($\psi$).

### 4.1. First case: $\rho_1 = v = [50\text{-}300]$ km/h, $\rho_2 = \rho_3 = f_{11} = f_{22} = 10$ MN.

In this section, the authors consider the varying parameter of the forward velocity $\rho_1 = v$ from *50 km/h* to *300 km/h* with 10 grid points. Figure 3 shows that in the case of the “no control” system, when the forward velocity changes, the transfer function of the variables changes a lot, so the application of LPV control with the forward velocity as a varying parameter is very necessary. We can also see that the $H_\infty$/LPV active wheelset control system reduces significantly the magnitude of the above variables in most frequency ranges. It shows that the active system can generate a roll stability, when compared with the “no control” system.

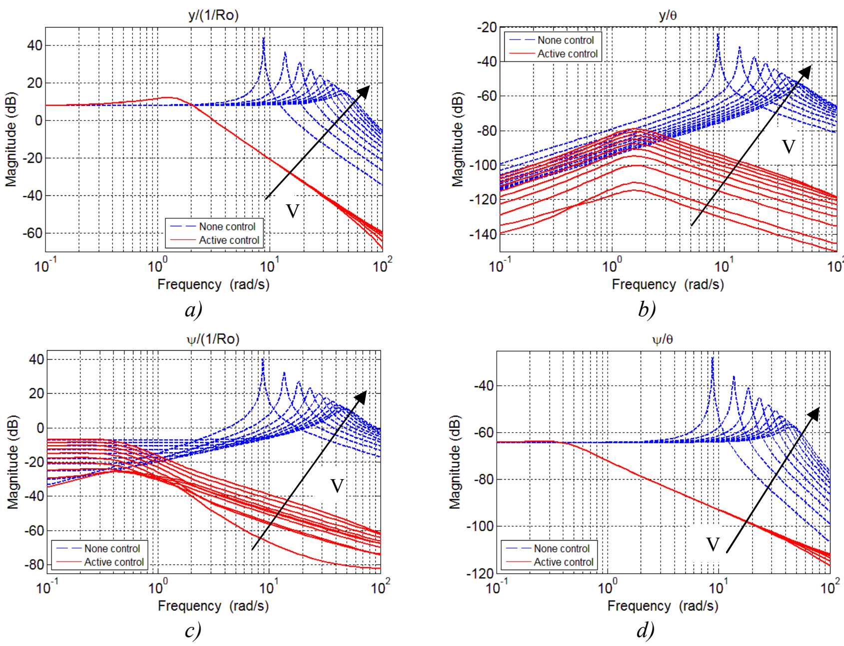


Fig 3 **First case**: transfer function magnitude of (a) $\frac{y}{\frac{1}{R_0}}$, (b) $\frac{y}{\theta}$, (c) $\frac{\psi}{\frac{1}{R_0}}$, (d) $\frac{\psi}{\theta}$

## 4.2. Second case: $\rho_2 = f_{11} = [5\text{-}10]$ MN, $\rho_3 = f_{22} = 10$ MN, $\rho_1 = v = 20$ m/s.

In this section we consider that the longitudinal creep coefficient ($\rho_2 = f_{11}$) varies from 5 MN to 10 MN. Figure 4 shows that, although the longitudinal creep coefficient varies from 5 to 10 MN, the transfer function magnitude of the variables varies negligibly. The results show that, when this coefficient varies over a wider range (eg, 0.1-100 MN), the transfer function magnitude of the variables vary greatly. In the process of moving the train, due to the different characteristics between the rail and the wheel, as well as the weather conditions and the material, it is difficult to accurately determine the value of this coefficient. Therefore, considering this coefficient as a varying parameter is still meaningful in practice. We also see that the $H_\infty$/LPV active wheelset control system achieves the goal to reduce the lateral displacement, yaw angle in most of the frequency ranges of interest.

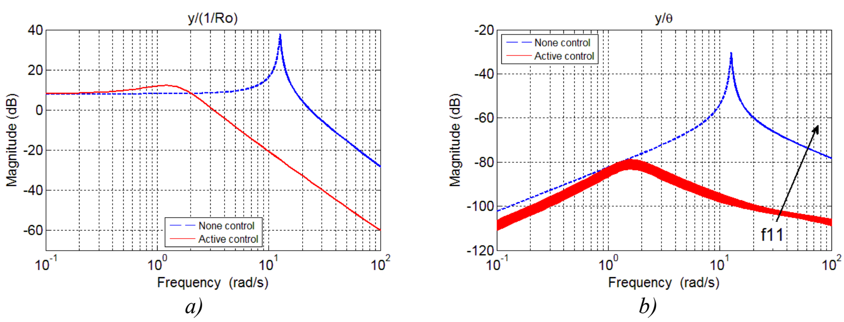

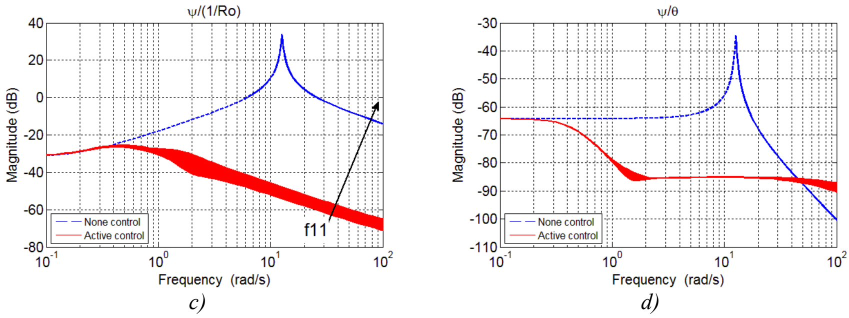


Fig 4 Second case: transfer function magnitude of (a) $\frac{y}{\frac{1}{R_0}}$, (b) $\frac{y}{\theta}$, (c) $\frac{\psi}{\frac{1}{R_0}}$, (d) $\frac{\psi}{\theta}$

### 4.3. Third case: $\rho_3 = f_{22} = [5\text{-}10]$ MN, $\rho_2 = f_{11} = 10$ MN, $\rho_1 = v = 20$ m/s.

In this section we consider that the lateral creep coefficient ($\rho_3 = f_{22}$) varies from 5 MN to 10 MN. Figure 5 shows that the transfer function magnitude of the lateral displacement does not change too much when the coefficient changes. However, the yaw angle is sensitive to the variations of this coefficient. So it is a good idea to consider this coefficient as a varying parameter. As with the two cases considered above, the H∞/LPV active wheelset control system can reduce the transfer function magnitude of the variables, thereby enhancing the stability of the wheelset.

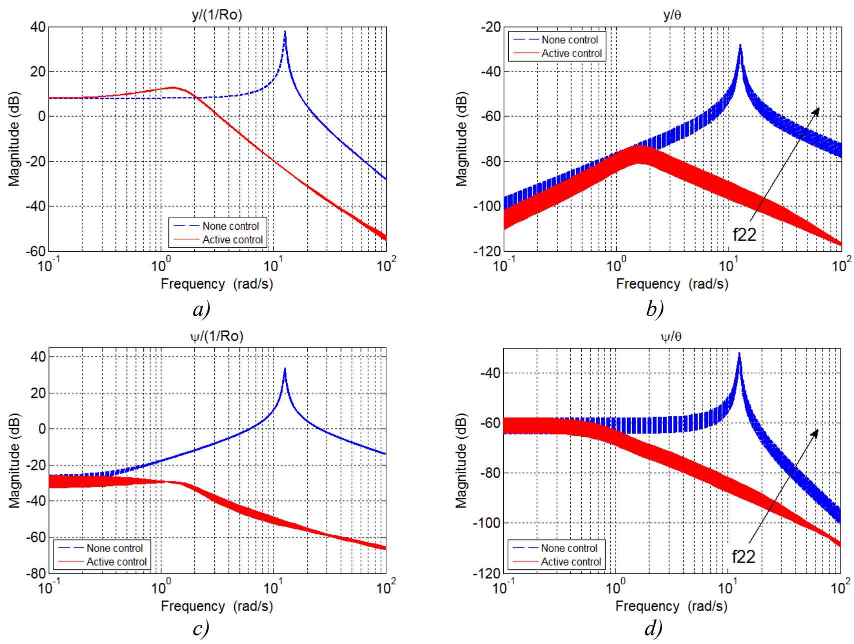


Fig. 5 Third case: transfer function magnitude of (a) $\frac{y}{\frac{1}{R_0}}$, (b) $\frac{y}{\theta}$, (c) $\frac{\psi}{\frac{1}{R_0}}$, (d) $\frac{\psi}{\theta}$

## 5. CONCLUSIONS

In this paper, we propose an LPV wheelset system by considering the three varying parameters: the forward velocity, the longitudinal and lateral creep coefficients. The grid-based LPV approach is used to synthesize the $H_\infty$/LPV controller which is self-scheduled by the three above varying parameters. The aim of the controller is to reduce the lateral displacement and yaw angle of the wheelset. Simulation results in the frequency domain show that the controller achieves the improvement of the wheelset stability in the desired frequency range.

In the future, the application of the $H_\infty$/LPV control to a more complete train model is essential. Furthermore, combining the dynamic model of the actuators will ensure that the research is more realistic and practical.

### Acknowledgements

The authors acknowledge the support of the project "Intelligent and autonomous vehicles for improving transport and road safety in Vietnam" from the French Embassy in Vietnam.

## 6. REFERENCES

[1] **Bideleh, S.M.M. - Mei, T. X. – Berbyuk V.:** Robust control and actuator dynamics compensation for railway vehicles. Vehicle System Dynamics 54(12), 2016, p.1762-1784.

[2] **Goodall, R. M. – Li, H.:** Solid Axle and Independently-Rotating Railway Wheelsets - A Control Engineering Assessment of Stability. Vehicle System Dynamics 33, 2000, p.57-67.

[3] **Wickens, A.H**. Dynamics of actively guided vehicles. Vehicle System Dynamics 20(3), 1991, p.219-242.

[4] **Zong, L. H. – Gong, X. L. – Xuan, S. H. – Guo, C. Y.**: Semi-active $H_\infty$ control of high-speed railway vehicle suspension with magnetorheological dampers. Vehicle System Dynamics 51(5), 2013, p.600-626.

[5] **Matamoros-Sanchez, A. Z. - Goodall, R. M.:** Novel mechatronic solutions incorporating inerters for railway vehicle vertical secondary suspensions. Vehicle System Dynamics 53(2), 2015, p.113-136.

[6] **Mousavi-Bideleh, S. M. – Berbyuk, V.:** Multiobjective optimisation of bogie suspension to boost speed on curves. Vehicle System Dynamics 54(1), 2016, p.58-85.

[7] **Perez, J. - Busturia, J.M. - Goodall. R. M.:** Control strategies for active steering of bogie-based railway vehicles. IFAC Mechatronic Systems, Darmstadt, Germany, 2000.

[8] **Li, H. - Goodall, R. M.:** Modelling and analysis of a railway wheelset for active control. International Conference on Control UKACC, September 1998.

[9] **Gaspar, P. - Bokor, J. – Szaszi, I.:** Reconfigurable control structure to prevent the rollover of heavy vehicles. Control Engineering Practice 13(6), 2005, p.699-711.

[10] **Wu, F.:** A generalized LPV system analysis and control synthesis framework. International Journal of Control 74(7), 2001, p.745-759.

[11] **Wu, F. - Yang, X. H. - Packard, A. - Becker, G.:** Induced $L_2$-norm control for LPV systems with bounded parameter variation rates. International Journal of Robust and Nonlinear Control 6 (9-10), 1996, p.983-998.
[12] **Packard, A.:** Gain scheduling via linear fractional transformations. Systems and Control Letters 22(2), 1994, p.79-92.
[13] **Apkarian, P. – Gahinet, P.:** A convex characterization of gain scheduled $H_\infty$ controllers. IEEE Transactions on Automatic Control 40(5), 1995, p.853-864.
[14] **Scherer, C. - Gahinet, P. – Chilali, M.:** Multiobjective outputfeedback control via LMI optimization, IEEE Transactions on Automatic Control 42(7), 1997, p.896-911.
[15] **Gahinet, P. - Apkarian, P. – Chilali, M:** Affine parameter-dependent Lyapunov functions and real parametric uncertainty. IEEE Transactions on Automatic Control 41(3), 1996, p.436-442.
[16] **Wu**, **F.:** Control of linear parameter varying systems, Ph.D. thesis, University of California at Berkeley, USA (1995).
[17] **Hjartarson, A. - Seiler, P. - Packard, A.:** LPVtools: A toolbox for modeling, analysis, and synthesis of parameter varying control systems. in: First IFAC Workshop on Linear Parameter Varying Systems, France, 2015.

# EVALUATION OF TRAJECTORIES FOR AUTOMATED ROAD VEHICLES IN SENSE OF DYNAMICAL FEASIBILITY

**Ferenc HEGEDÜS [1] and Tamás BÉCSI [2]**

[1] Robert Bosch Hungary

[2] Department of Control for Transportation and Vehicle Systems

Faculty of Transportation Engineering and Vehicle Engineering
Budapest University of Technology and Economics

*Received: November 5, 2018*

## ABSTRACT

The automation of road transportation is one of the most important fields of research for today’s vehicle industry. One of the key aspects for automated driving is the planning of safe, dynamically feasible, comfortable and customizable trajectories. Over the last decade, numerous different methods have been developed to solve the motion planning problem. However, many of these methods deal with only a very simplified – if any - model of vehicle dynamics. On one hand, the formulation of the trajectory planning problem in case of geometric, graph search or sampling based algorithms makes the consideration of the dynamic equations of vehicle motion very difficult. On the other hand, nonlinear optimization based algorithms can deal with even complex models of nonholonomic vehicle dynamics, but this goes at the expense of computational requirements, which endangers real-time applicability. This paper presents a method which is capable of the evaluation of trajectories planned by an arbitrary motion planning algorithm in sense of dynamical feasibility. A metrics is developed to qualify the trajectories in terms of their traceability for the vehicle under given working conditions. Based on the defined metrics, a threshold is developed to decide about the applicability of the trajectory. It is shown that the presented method is computationally much less demanding as an optimization-based motion planning algorithm, and can still be used to verify that the vehicle can drive on the planned trajectory even if the dynamics was not considered at the time of planning at all. The performance of the algorithm is examined with the help of computer simulations, and includes the consideration of real-time applicability. At the end of the paper, conclusions are summarized and possible future research directions are taken into account related to the presented topic.

*Keywords:* highly automated driving, motion planning, dynamical feasibility, road vehicle trajectory

## 1. INTRODUCTION

Highly automated and autonomous driving is one of the most important research fields of today’s vehicle industry and related academic institutions. Many different approaches have been developed recently to solve the motion planning problem for wheeled vehicles, all having advantages and drawbacks as well. One of the most important requirements against the planned trajectories is dynamical feasibility: the vehicle must be able to track the desired motion. Geometric approaches compose the path of the vehicle from geometric curves as clothoids, circular arcs and splines [1]. They are often used in simple low-dynamic scenarios e.g. automatic parking [2]. Although these algorithms are computationally cheap, the ability to consider the nonholonomic dynamics of the vehicle is limited to the usage of maximal kinematic acceleration constraints [3]. Graph search based methods discretize or randomly sample the configuration space (space of possible states) of the vehicle to build a graph of safely reachable and unoccupied states [4]. The shortest connection defined by a suitably chosen metric is then searched along the graph through heuristics [5]. The formulation of these methods makes it easy to deal with collision avoidance, but vehicle dynamics models are again hard to consider. Nonlinear optimization based motion planning methods enable the usage of almost arbitrary vehicle models [6]. They are proven to be able to generate dynamically feasible trajectories even in case of high-dynamic scenarios, but this comes at a price of high computational requirements which often make real-time applications impossible [7]. Present work proposes a method to decide about the dynamical feasibility of a trajectory planned by an arbitrary motion planning method. The paper is organized as follows. Section 0 describes a precise model of vehicle dynamics that is used for feasibility analysis. In Section 0, a simple trajectory generation algorithm is presented which is used to generate the motions to inspect, and tracking control is synthetized to drive the vehicle model along these trajectories. Section 0 contains the feasibility analysis with the help of computer simulation, and Section 0 summarizes the results and conclusion remarks.

## 2. MODEL OF VEHICLE DYNAMICS

In order to be able to judge the dynamical feasibility of the trajectories, a precise nonlinear vehicle model is applied. The planar single track model including a dynamic wheel slip model (Fig. 1) enables to balance between performance and computation time. Except for scenarios when the road-tire contact properties are different at the two sides of the vehicle, there is no significant loss of accuracy compared to a more complicated twin-track model. The vehicle is controlled by a total driving $M_d$ and braking $M_b$ torque and a steering angle at the front wheel$\delta$.

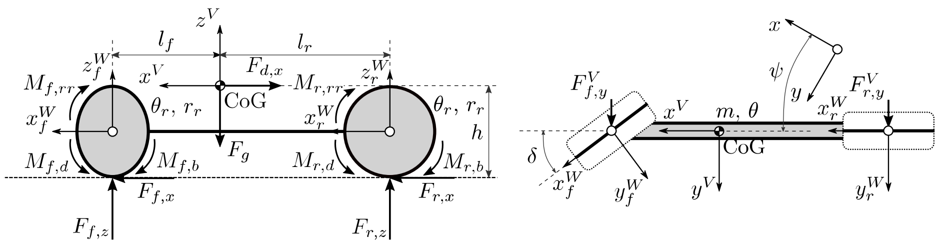


Fig. 1 Planar single track - vehicle model

In the following subsections 0 and 0 the following notations are used. Derivatives by time are noted with dot $(\dot{\_})$. Superscripts $V$ and $W$ are used for the dynamical quantities in the vehicle's coordinate system $\{x^V, y^V, z^V\}$ and in the wheels' coordinate systems $\{x_f^W, y_f^W, z_f^W\}$ and $\{x_r^W, y_r^W, z_r^W\}$ respectively. The transformations between these coordinate systems will not be described due size limitation, but it is important to mention that the steering angle input is influencing the dynamics of the vehicle through the coordinate transformation equations.

### 2.1 Wheel dynamics

In the single track model, the two wheel-pairs of the front and rear axles are reduced to a single front and rear wheel which approximately halves the computational requirements. The wheels only have one degree of freedom: they can rotate $\phi_f$ and $\phi_r$ around their rotation axes. In the following the equations are similar for the front and rear wheels thus only the ones for the front wheel will be presented.

In the present work, a dynamic slip model is used instead of static equations that have singularity at zero velocity. The equations of the slip model yield:

$$\dot{s}_{f,x} = \frac{1}{l_{f,x}}\left(r_f\dot{\phi}_f - \dot{x}_f^W - |\dot{x}_f^W| s_{f,x}\right), \tag{1}$$

$$\dot{s}_{f,y} = \frac{1}{l_{f,y}}(-\dot{y}_f^W - |\dot{x}_f^W| s_{f,y}),$$

where $l_{f,x}$ and $l_{f,y}$ are slip dependent relaxation length of the tyre, $r_f$ is the wheel radius, as well as $\dot{x}_f^W$ and $\dot{y}_f^W$ are the longitudinal and lateral velocities of the wheel. The longitudinal relaxation length can be evaluated as:

$$l_{f,x} = \max\left(l_{f,x,0}\left[1 - \frac{B_{f,x}C_{f,x}}{3}|s_{f,x}|\right], l_{f,x,min}\right) \tag{2}$$

where $l_{f,x,0}$ is the value at standstill and $l_{f,x,min}$ is the value at wheel spin or wheel lock. Eq. (2) is similar to the lateral direction with the substitution of subscript $x$ with $y$. The damping of dynamic longitudinal slip variable is necessary in case of low velocities to maintain the numerical stability of the solution [8]:

$$\tilde{s}_{f,x} = s_{f_x} + \frac{k_{f,x}}{B_{f,x}C_{f,x}\mu_f F_{f,z}^W}(r_f\dot{\phi}_f - \dot{x}_f^W), \tilde{s}_{f,y} = s_{f,y}, \tag{3}$$

where $s_{f_x}$ is the undamped value of longitudinal slip, and $k_{f,x}$ is a velotiy dependent damping factor.

The longitudinal and lateral tire forces are well known to be dependent on slip. A widely used equation to this relation is the *Magic Formula* which is calculated as:

$$\tilde{F}_{f,x}^W = \mu_f F_{f,z}^W \sin\{C_{f,x}\arctan(B_{f,x}\tilde{s}_{f,x} - E_{f,x}[B_{f,x}\tilde{s}_{f,x} - \arctan(B_{f,x}\tilde{s}_{f,x})])\}, \tag{4}$$

where $\mu_f$ is the coefficient of friction between road and tire, $C_{f,x}$, $B_{f,x}$, and $E_{f,x}$ are parameters of the *Magic Formula* and $\tilde{s}_{f,x}$ is the damped longitudinal wheel slip. Eq. (4) is similar to the lateral direction with the substitution of subscript $x$ with $y$. The superposition of longitudinal and lateral wheel slips must be considered to calculate the true acting forces transferred between the road and the tires:

$$F_{f,x}^W = \operatorname{sgn}(\tilde{s}_{f,x})\sqrt{\frac{\left(\tilde{F}_{f,x}^W\tilde{F}_{f,y}^W\right)^2}{\left(\tilde{F}_{f,y}^W\right)^2 + \left(\frac{\tilde{s}_{f,y}}{\tilde{s}_{f,x}}\tilde{F}_{f,x}^W\right)^2}}, F_{f,y}^W = \operatorname{sgn}(\tilde{s}_{f,y})\sqrt{\frac{\left(\tilde{F}_{f,x}^W\tilde{F}_{f,y}^W\right)^2}{\left(\tilde{F}_{f,x}^W\right)^2 + \left(\frac{\tilde{s}_{f,x}}{\tilde{s}_{f,y}}\tilde{F}_{f,y}^W\right)^2}}. \tag{5}$$

The total driving and braking torque are ideally distributed to the front $M_{f,d}$ $M_{f,b}$ and rear $M_{r,d}$ $M_{r,b}$ wheels, which means that the londitudinal slip values are kept equally. According to Newton's second law for rotation the equation of motion of the wheel yields:

$$\ddot{\phi}_f = \frac{1}{\theta_f}(M_{f,d} - r_f F_{f,x}^W - M_{f,b} - M_{f,rr}), \tag{6}$$

where $M_{f,rr}$ is the rolling resistance torque, calculated according to the standard SAE J2452.

### 2.2 Chassis dynamics

The vehicle chassis is considered as a rigid body that can move longitudinally $x$ and lateraly $y$ and rotate $\psi$ around its vertical axis (yaw movement). The wheels are rigidly connected. Besides the tire forces described in Eq. (5) the vehicle chassis is subject to aerodynamic drag forces evaluated as:

$$F_{d,x}^{V} = \frac{1}{2} c_D A_f \rho_A \dot{x}^V \sqrt{\dot{x}^V + \dot{y}^V},$$
$$F_{d,y}^{V} = \frac{1}{2} c_D A_f \rho_A \dot{y}^V \sqrt{\dot{x}^V + \dot{y}^V}, \quad (7)$$

where $c_D$ is the drag coefficient and $A_f$ is the frontal area of the vehicle, and $\rho_A$ is the mass density of air. According to Newton's second law for translation and rotation, the equations of motion of the chassis expressed in the inertial coordinate system of the ground yield:

$$\ddot{x} = \frac{1}{m}\left(F_{f,x} + F_{r,x} + F_{d,x}\right), \quad (8)$$

$$\ddot{y} = \frac{1}{m}\left(F_{f,y} + F_{r,y} + F_{d,y}\right), \quad (9)$$

$$\ddot{\psi} = \frac{1}{\theta}\left(l_f F_{f,y}^{V} - l_r F_{r,y}^{V}\right), \quad (10)$$

where $m$ is the total mass and $\theta$ is the moment of inertia of the vehicle around its vertical axis, as well as $l_f$ and $l_r$ are the horizontal distances between the center of gravity and the front and rear wheel centers respectively.

## 3. MOTION PLANNER AND TRACKING CONTROL

For the feasibility analysis, motions are generated by a relatively simple geometric trajectory planner, in which the longitudinal and lateral characteristics of the motion are handled independently. The vehicle is then driven on the planned trajectory by two separate controllers, one maintaining the desired longitudinal velocity and the other tracking the desired yaw rate.

### 3.1 Quintic polynomial trajectory planner

During motion planning, our primary goal is that the vehicle reaches a prescribed end state, the point we are aiming to go to. In the simplest case, the final position and orientation of the vehicle is specified, and the path of the vehicle must lead to this end state:

$$X_f = [x_f \quad y_f \quad \psi_f]. \quad (11)$$

The lateral position of the vehicle is calculated as a quintic (5th grade) polynomial function of the longitudinal position:

$$y(x) = p_1 x^5 + p_2 x^4 + p_3 x^3 + p_4 x^2 + p_5 x + p_6, \quad (12)$$

where $p_1, p_2 \dots p_6$ are the parameters of the polynomial that must be calculated to evaluate the complete path. To be able to do so, the substitution, derivative, and second derivative values of the path equation Eq. (12) are considered at initial and final longitudinal positions as follows:

$$\begin{bmatrix} x_i^5 & x_i^4 & x_i^3 & x_i^2 & x_i & 1 \\ x_f^5 & x_f^4 & x_f^3 & x_f^2 & x_f & 1 \\ 5x_i^4 & 4x_i^3 & 3x_i^2 & 2x_i & 1 & 0 \\ 5x_f^4 & 4x_f^3 & 3x_f^2 & 2x_f & 1 & 0 \\ 20x_i^3 & 12x_i^2 & 6x_i & 2 & 0 & 0 \\ 20x_f^3 & 12x_f^2 & 6x_f & 2 & 0 & 0 \end{bmatrix} \begin{bmatrix} p_1 \\ p_2 \\ p_3 \\ p_4 \\ p_5 \\ p_6 \end{bmatrix} = \begin{bmatrix} y_i \\ y_f \\ y_i' \\ y_f' \\ y_i'' \\ y_f'' \end{bmatrix}, T_X p = Y. \tag{13}$$

Initial position $x_i$, $y_i$ and heading $y_i'$ values can always be kept zero as the resulting path can be easily transformed later if necessary. The second derivative values $y_i''$ and $y_f''$ are also chosen as zero to maintain smoothness of subsequent pathes. The remaining constraints are provided in the prescribed end state vector Eq. (11) considering that $y_f' = \tan(\psi_f)$. To calculate the coefficients of the polynomial path that leads to $X_f$, the linear equation system Eq. (13) must be solved after substituting the initial and final constraints:

$$p(X_f) = T_X^{-1}(X_f)Y(X_f). \tag{14}$$

The curvature of the resulting path $y(x)$ can be calculated as:

$$\kappa(x) = \frac{y''(x)}{(1 + y'(x)^2\ )^{3/2}}. \tag{15}$$

The longitudinal characteristics of the trajectory are defined by assigning a piecewise linear velocity profile as function of time $v_{ref}(t)$ which also serves as a reference for the longitudinal control. The reference yaw rate function required for the lateral control is calculated by $r_{ref}(t) = v_{ref}(t)\kappa(t)$.

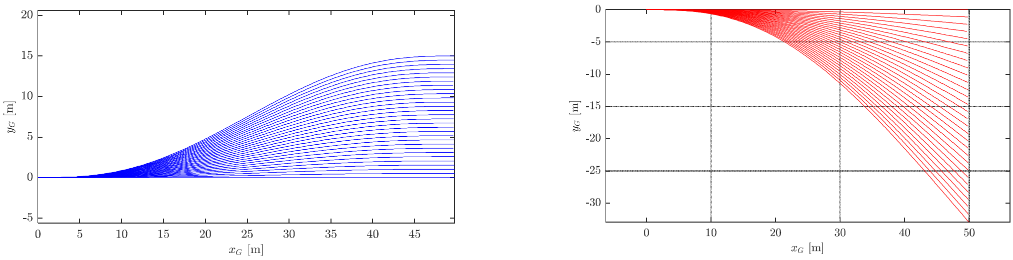


Fig. 2 Test trajectories

For the feasibility analysis, test trajectories were planned by the algorithm described in this section shown in Fig. 2. There are 30 lane-change like (left, blue) and 30 lane-keeping like (right, red) trajectories, each both with a constant velocity of $20\ \mathrm{m/s}$ and a deceleration from $20\ \mathrm{m/s}$ to $10\ \mathrm{m/s}$.

### 3.2 Trajectory tracking control

To track the longitudinal velocity profile of the generated trajectory, a PID controller is used to provide sufficient driving or braking torque. The controller was planned based on an LTI (Linear Time Invariant) transfer function model of longitudinal dynamics which yields:

$$G_V(s) = \frac{V(s)}{M(s)} = \frac{1}{r_f m \cdot s + r(c_{rr} m g + c_d)} \tag{16}$$

where $c_{rr}$ is the linear rolling resistance and $c_d$ is the linear aerodynamic drag coefficient, as well as $g$ is the gravitational acceleration. The gain constants of the controller are $K_p = 2000$ and $K_i = 16.28$.

As lateral control, an LQR (Linear Quadratic Regulator) servo controller is applied to generate the necessary steering angle input to track the planned path. To synthetize the state feedback, an LPV (Linear Parameter Varying) model of lateral vehicle dynamics was used with the following state equation:

$$\begin{bmatrix} \ddot{y}^V \\ \ddot{\psi} \end{bmatrix} = -\begin{bmatrix} \frac{g(c_f l_r + c_r l_f)}{v(l_f + l_r)} & v + \frac{g l_f l_r (c_f - c_r)}{v(l_f + l_r)} \\ \frac{m g l_f l_r (c_f - c_r)}{\theta v (l_f + l_r)} & \frac{m g l_f l_r (c_f l_f + c_r l_r)}{\theta v (l_f + l_r)} \end{bmatrix} \begin{bmatrix} \dot{y}^V \\ \dot{\psi} \end{bmatrix} + \begin{bmatrix} \frac{g c_f l_r}{(l_f + l_r)} \\ \frac{m g c_f l_f l_r}{J(l_f + l_r)} \end{bmatrix} \delta_f \tag{17}$$

where $c_f$ and $c_r$ are front and rear cornering stiffnesses (initial slope of the curve defined by Eq. (4)), and $v$ is the time-varying longitudinal velocity of the vehicle. The feedback gain of vehicle state $[\dot{y}^V \quad \dot{\psi}]^T$ is $[0.0001 \quad -0.0839]^T$ and the gain for the integral of tracking error is 1.

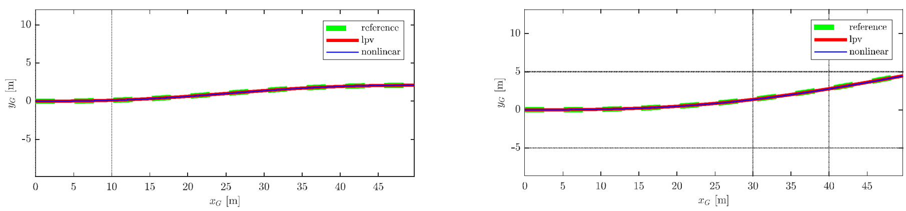


Fig. 3 Trajectory tracking

Reference motion tracking is shown in Fig. 3 in case of a lane-change like (left) and a curved lane-keeping like (right) trajectory.

## 4. SIMULATION RESULTS

This section contains the feasibility analysis of the sample trajectories. The figures Fig. 4 - Fig. 6 contain the maximal vehicle accelerations (left subfigure) and maximal wheel slips (right subfigure) as function of the maximal kinematic acceleration along the trajectory. In both subfigures, the results are on the left for the lane-change like (Fig. 2 left, blue) trajectories and on the right for the lane-keeping like (Fig. 2 right, red) trajectories.

### 4.1 Feasibility analysis

In Fig. 4 simulation results are shown in case of a mid-size passenger car with front wheel drive. It can be seen that the LPV model provides almost the same accelerations as kinematic calculations, and the nonlinear model starts to deviate from its beginning from $a_{geom}^{max} \approx 5\ \mathrm{m/s^2}$. Similarly, maximal slip values of the nonlinear model start to deviate from the LPV model the same kinematic acceleration value.

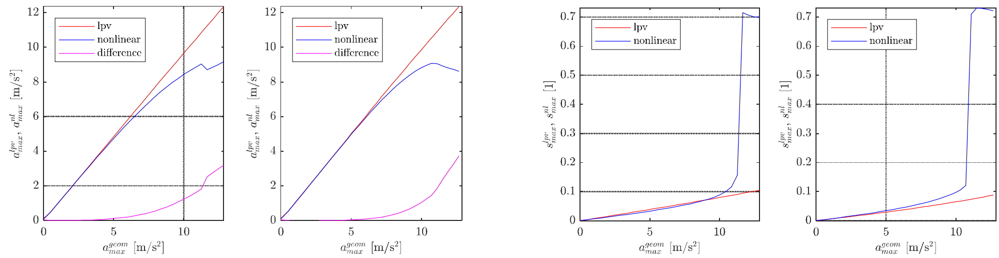


Fig. 4 Maximal acceleration (left) and slip (right) values

The total loss of stability is very conspicuous; there is a definite brake in the maximal slip curve. Although the edge of the dynamically feasible zone is not at a certain kinematic acceleration value as it also depends from the shape of the path ($a_{geom}^{max} \approx 11.17\ \mathrm{m/s^2}$ for the lane-change like and $a_{geom}^{max} \approx 10.78\ \mathrm{m/s^2}$ for the lane-keeping like trajectories), it is yet at a certain maximal slip value $s_{nl}^{max} \approx 0.12$ of the nonlinear model.

### 4.2 Effect of varying vehicle speed

Fig. 5 shows the analysis in case of the decelerating trajectories. There is no total loss of stability although the kinematic accelerations are reaching even $a_{geom}^{max} \approx 12.05\ \mathrm{m/s^2}$. The definite break in the maximal slip curve would occur in case of trajectories with even higher lateral offset as the presented ones have.

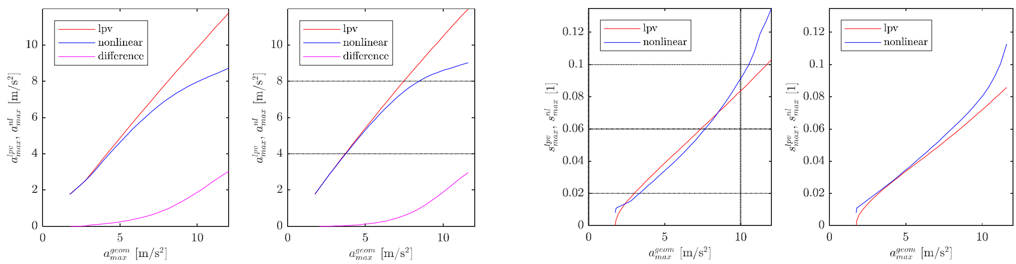


Fig. 5 Maximal acceleration (left) and slip (right) values in case of deceleration

### 4.3 Effect of tire-road friction

The effects of low tire-road friction coefficient are shown in Fig. 6. The same maximal slip value $s_{nl}^{max} \approx 0.12$ of the nonlinear model is again showing the edge of the feasible region.

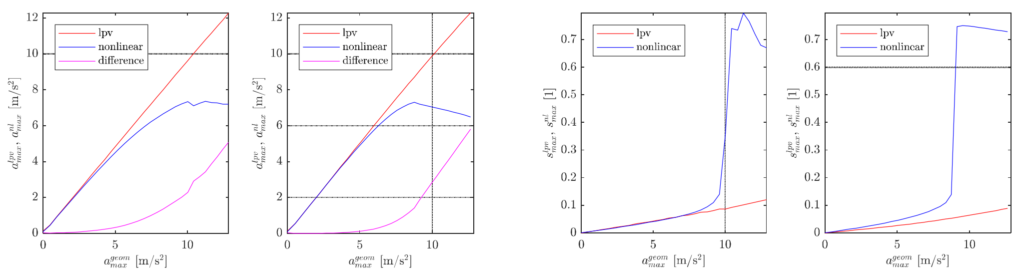


Fig. 6 Maximal acceleration (left) and slip (right) values in case of low friction

However the loss of stability happens at much lower kinematic accelerations ($a_{geom}^{max} \approx 9.23\ \mathrm{m/s^2}$ for the lane-change like and $a_{geom}^{max} \approx 8.86\ \mathrm{m/s^2}$ for the lane-keeping like trajectories).

## 5. CONCLUDING REMARKS

On the basis of our theoretical investigations and numerical simulations, the following conclusions can be drawn. On one hand, commonly applied maximal kinematic acceleration threshold is suitable for feasibility check if kept low enough, but it does not necessarily corresponds to the real edge of dynamically feasible zone and can thus lead to conservative results. It is important to mention that the road - tire friction has naturally a substantial effect on the maximal acceleration threshold to be applied. On the other hand, a threshold applied to the maximal combined slip value of the nonlinear model when driving along the trajectory can show exactly the limits of the dynamically feasible region. Because of this, with the prediction of the vehicle's motion through the simulation of the presented nonlinear model and tracking controllers, the feasibility of an arbitrary trajectory given as way coordinates with time stamps can be checked.
The presented results are not yet verified with real-life measurement, which would of course be inevitable to use it in real operating conditions. As tire-road friction coefficient and wheel slip values have a substantial effect, it would be an interesting research field to provide a method to estimate these in an accurate manner.

## 6. REFERENCES

[1] **Li,X. - Sun, Z. - He, Z. - Zhu, Q. - Liu, D.:** A practical trajectory planning framework for autonomous ground vehicles driving in urban environments, in 2015 IEEE Intelligent Vehicles Symposium (IV), June, 2015, p.1160–1166.

[2] **Vorobieva, H. - Minoiu-Enache, N. - Glaser, S. - Mammar, S.:** Geometric continuous-curvature path planning for automatic parallel parking, in 2013 10th IEEE International Conference on Networking, Sensing and Control (ICNSC), April, 2013, p.418–423.

[3] **Minh, V. T. - Pumwa, J.:** Feasible path planning for autonomous vehicles," Mathematical Problems in Engineering, vol. 2014, 2014.

[4] **Palmieri, L. - Koenig, S. - Arras, K. O.:** Rrt-based non-holonomic motion planning using any-angle path biasing, in 2016 IEEE International Conference on Robotics and Automation (ICRA). IEEE, 2016, p.2775–2781.

[5] **Gammell, J. D. - Srinivasa, S. S. - Barfoot, T. D.:** Batch informed trees (bit*): Sampling-based optimal planning via the heuristically guided search of implicit random geometric graphs, in 2015 IEEE International Conference on Robotics and Automation (ICRA). IEEE, 2015, p.3067–3074.

[6] **Singh, S. - Majumdar, A. - Slotine, J. J. - Pavone, M.:** Robust onlinemotion planning via contraction theory and convex optimization, in 2017 IEEE International Conference on Robotics and Automation (ICRA). IEEE, 2017, p.5883–5890.

[7] **Hegedüs, F. - Bécsi, T. - Aradi, Sz.**: Dynamically feasible trajectory planning for road vehicles in terms of sensitivity and robustness, 20th EURO Working Group on Transportation Meeting, EWGT 2017, 4-6 September 2017 Budapest, Hungary, Transportation Research Procedia, vol. 27, 2017, p.799 – 807.

[8] **Pacejka, H. B.:** Chapter 8 - Applications of transient tire models, in Tire and Vehicle Dynamics (Third Edition), 3rd ed.,(Ed.by Prof. H. B. Pacejka) Butterworth-Heinemann, Oxford, 2012, p.355–401.

# INTRODUCTION, IDENTIFICATION AND CONTROL OF A NEW FUEL METERING SYSTEM ON A MICRO TURBOJET ENGINE

**Károly BENEDA and Arnold J. NAGY**

Budapest University of Technology and Economics
Faculty of Transportation Engineering and Vehicle Engineering
Department of Aeronautics, Naval Architecture and Railway Vehicles
H1111 Budapest, Műegyetem rkp. 3.
kbeneda@vrht.bme.hu
*+36-1-463-1992, +36-1-463-3980*

*Received: November 5, 2018*

## ABSTRACT

Gas turbine engines are widely used throughout industry and transportation, so their investigation is always necessary. Micro turbojet engines can have an other application, they can serve as test bench for various researches as well. The main goal of the present paper is to describe a complex development work on a micro turbojet engine test bench regarding the improvement of the fuel metering system. The paper details the steps of the work from the complete redesign of the fuel metering system including selection of metering valve and differential pressure regulator. The authors describe the identification of the new system, and a new electronic device has been developed to ensure the transient behaviour acquisition through a specified frequency domain. After ensuring the reaction of the system is satisfactory, the authors have created a special programme of the control electronics. This special mode of operation can create sine wave output around a selected nominal operating point with predetermined amplitude, and the frequency of the output changes automatically from 0.1Hz through 10Hz slowly. The complete measurement takes approx. one minute, and as the fuel input alternates at this changing frequency, the gas turbine engine will exhibit similar fluctuations, too. This allows the identification of the transfer function, with the fuel metering valve control voltage as input variable and the rotor speed of the engine as the output. The last step of this investigation was to establish a discrete time control that responds on the throttle lever movements and maintains a constant rotating speed using a PID control method.

*Keywords*: PID control, Fuel flow control, System identification, Output Error model, micro gas turbine, turbojet engine

## 1. INTRODUCTION

Gas turbines are widely used as power plants of aircraft [1]. A special branch is the micro turbojet, which is a small-scale, simple unit [2], basically equivalent in buildup to the early developments in gas turbine history [3]. They cannot offer so high overall efficiency like turbofan engines [4], therefore the field of their application is rather limited. However, they still have an importance due to their simplicity and high power density when considering them as auxiliary power plant for sailplanes [5], main propulsion unit of the emerging unmanned aerial vehicles [6] including military drones [7], as well as laboratory equipment, where the above mentioned benefits can be utilized for both research and education at universities [8,9].

Despite their simple buildup and operational principle, they still offer several ways for investigation to improve their operation or even production. There are articles, which represent deeper insight into the working processes of the turbines, and these simulations allow a better design for newly developed types, as it is stated in e.g. [10]. This is extremely true when one takes into account numerical simulations or inverse design of turbomachinery [11], or even combustion chamber with its complex operational conditions [12,13]. There are many researches that focus on extending the operating range of such engines by enhancing stability [14] or just simply understand the principle behind various unstable phenomena [15]. Another important, emerging technology is additive manufacturing [16], which allows either better utilization of conventional parts [17,18] or makes it possible to design more complex [19] or more resistant components [20], even with significant mass reduction [21], which is a key factor in aviation industry.

TKT-1 micro turbojet engine is used as a versatile test bench for both educational and research purposes [22]. Its original fuel control system served for more than ten years, but it evidently showed anomalies. As part of the development, with the aim to make it similar to modern dual-channel FADEC jet engines in functionality and versatility [23], the authors decided to redesign the formerly applied solution of fuel supply that closely relates with the primary goal of any turbine propulsion unit, the generation of thrust. Thrust force is the most significant parameter in case of aircraft jet engines so its appropriate controllability is essential during the development of a gas turbine. The former buildup of the fuel metering system was unable to utterly fulfil the requirements which are standed toward modern FADEC jet engines so the redesign of it was necessary.

## 2. BUILDUP OF THE FUEL METERING SYSTEM

### 2.1 Former installation

The Type 924 fuel-oil control unit (FCU) of the TS-21, originally used the pressure of the compressor discharge (CDP) to manipulate the fuel flow. In practice this meant that the unit has been connected to the CDP section with a sense line through which the air was transferred to the Bypass Flow Metering Valve (BFMV).

In that case the fuel flow control process was the following: as the air pressure increased on the surface of the BFMV, it reduced the cross-section area of the bypass flow, which resulted the flow transfer in the bypass lines to fall and due to the positive displacement pump in the FCU, at the same time the transfer in the main flow increased, so more fuel was supplied to the combustion chamber.

To be able to control the thurst force of the turbojet engine – via RPM or other dependent parameters –, a proportional valve had been applied between the BFMV and the CDP discharge port, which released as much amount of air from the control pressure which was required to achieve a desired RPM level. This construction had several drawbacks:

- Due to the compressibility of air – as the CDP increases, the air density also grows – the control characteristic of the proportional valve was not linear.
- The control characteristic depended from the ambient air parameters as: pressure, temperature, humidity.
- The control behavior was reversed in contrast of conventional systems, i.e. control command output had to be increased to result in a reducing rotor speed.

### 2.2 Modified design of the fuel metering system

In order to provide a simpler and more deterministic control of rotating speed, the previously described controlling method was completely abandoned. After studying the fuel control solutions applied in modern aircraft the decision was to manipulate the fuel flow directly with an electrohydraulic valve built into the main fuel flow as a series-connected proportional orifice. During the modification process the air releasing proportional valve was removed and the BFMV (which is part of FCU 924) was deactivated, the electrohydraulic valve and a parallel differential pressure regulator valve were installed. The system schematic sketch is shown in Figure 1.

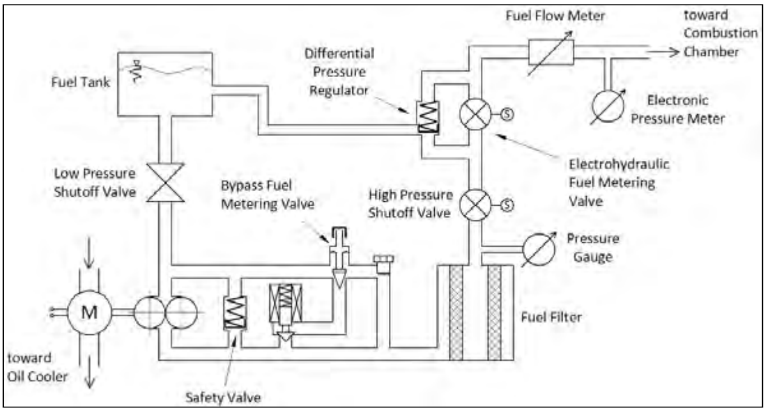


Fig. 1 Modified fuel control system schematic view

The reason behind the application of the differential pressure regulator is that if only the fuel metering valve would have been applied the control process would depend on more than one parameters. The fluid dynamic law of continuity (1) and the stationary Bernoulli equation (2) explain that statement.

$$\dot{m} = \rho \cdot c \cdot A \tag{1}$$

$$\frac{c^2}{2} + U + \frac{p}{\rho} = const. \tag{2}$$

If we assume that the density and potential of the flow do not change between its two dedicated points, then the static pressure difference will be proportional with the alteration of the fluid velocity. As a consequence, if the flow rate is to be changed, it would be impossible to execute it proportionally with the changing of the streamtube cross-sectional area, because at the same time the fluid velocity also varies.

Therefore to simplify the flow rate function to single parametric, the static pressure difference between upstream and downstream of the fuel metering valve has to be regulated to a constant value, that is what the differentional pressure regulator provides by recirculating the redundant amount of fuel to the fuel tank. In this case the flow rate only depends on the fuel metering valve's free cross-section area, so these two equipment attributes will represent linear behavior between each other. The most valuable advantages of this design against the former one are the following:

- Fluids are incompressible, so the system does not have delay which relates to this attribute.
- The single parametric flow rate function and the linear behavior simplify to create an appropriate control characteristic.
- The control is straight, larger command value means larger fuel supply.

To create an appropriate PID controller for the TKT-1 the static and dynamic characteristics of the modified fuel metering system had to be measured. In the beginning of the test stages only “cold tests” have been performed and only after the verification of results the tests with fully operating engine have been started.

## 2.3 Measurement of static characteristics

In order to be ensured about the metering valve linear behavior and about that it can provide a sufficient flow rate domain, in the first step of the test the flow rate has been measured at different control input signals from 0 to 10 V with manual adjustment. In the early stages of the experiment the maximum fuel flow rate we could achieve was approx. 60 l/h, which is significantly lower than the original 90 l/h. After incorporating some further modifications in the fuel metering system and tuning the metering valve this value was extended up to 70 l/h which was determined as the maximum throughput of the particular metering valve. This is less than the originally demanded, but still can be enough to run the engine up to 80% rotating speed, which is still suitable for a short period until further development can be carried out.
Figure 2 incorporates two main halves: the throughput versus control input signal characteristic (left figure) and the operating engine’s rotor speed diagram with different throttle lever (input signals) settings (right figure).
The static characteristics (Fig. 2 left side) have been taken with a fuel manifold supplying the liquid into a container through removed fuel manifold and nozzles rather than into the real combustion chamber, so it did not require the engine to be run, but still allowed the same back pressure as the original buildup.

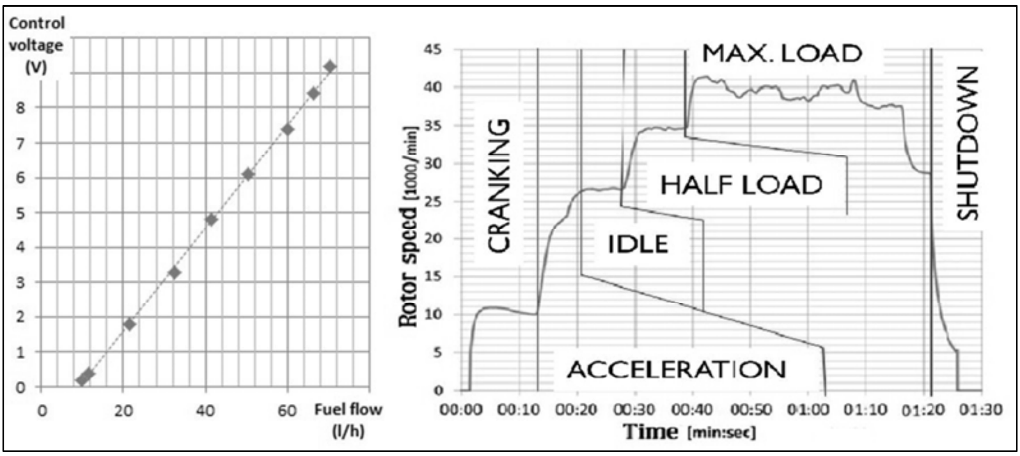


Fig. 2 Throughput-input signal (left) and rotor speed vs. time open-loop test run (right)

The live test with the gas turbine has been carried out with an open loop control of the fuel supply. This can be evaluated in Fig. 2 right side, i.e. after initial cranking such a flow has been commanded, which corresponded to the idle conditions, in turn the gas turbine accelerated to idle, then the fuel flow has been increased to an intermediate level, etc. There was no active feedback control to maintain a specified operating mode, that is the reason why during maximum load the rotating speed began to fluctuate. The engine maximum operating speed is 50500rpm, that means, the valve significantly reduces the useful operating range to 80% of the nominal speed. Despite the limitations, it can be seen that the fuel supply was stable and satisfies the requirements for the basis of an automatic control system.

## 3. SYSTEM IDENTIFICATION

### 3.1 Applied devices

The system identification required relatively fast measurement (approx. 1kSample/s per channel) so a high performance DAQ device has been applied for the virtually simultaneous data acquisition. This device was an NI USB-6218 operated by a custom written LabVIEW software. The measured parameters – data channels – were the following:

- Metering valve control signal [V] – this was chosen as input of control system
- Metering valve up- and downstream pressures [bar]
- Fuel flow rate [l/h]
- Exhaust gas temperature [°C]
- Engine rotor speed [1/min, Hz] – this parameter represents system output

To control the fuel metering valve the previously used microcontroller of the TKT-1 FADEC (MC9S08DZ60) has been substituted with an *mbed* LPC1768 prototype board. The necessity of the improvement was that the new MCU has a 32-bit architecture CPU with 100MHz clock speed which means far more computing capacity than the formerly applied one, that made it possible to execute the identification process with higher precision, and on the other hand it allows to improve the TKT-1 FADEC system by extending its tasks. The LPC1768 microcontroller analog output only can provide 3.3V signal so a level shifting circuit with an optocoupler has also been applied to decouple and amplify the metering valve input signal to 10V, which is the required control voltage range.

### 3.2 Dynamic characteristic measurement of the jet engine

For dynamic behavior measurement and to determine the transfer function of the gas turbine engine a "special mode" has been implemented in the software of the *mbed* LPC1768, which generates sine wave on the analog output with manually adjustable amplitude – selected between 0.1 and 0.5V – and automatically changing frequency from 0.1 to 10Hz around a nominal operating point. After entering special mode, the system maintains the last memorized value of amplitude. The nominal operating point selection also was made manually, basically we used the same open-loop control, what has been introduced above and an example of operation has been given in Fig. 2.
After numerous tests the one which has been performed around 4.5V input voltage seemed the most relevant because this contained the least noise. The result of this measurement is represented in Figure 3. This operating mode corresponded to a rotor speed around 38.600RPM (76% of nominal), with a fluctuation of ±800RPM, around 1.5%, which can be considered to be small enough to allow neglection of nonlinearities of the plant. As it can be evidently seen in Fig. 3, the gas turbine can react on increasing frequency excitation with a reducing amplitude.

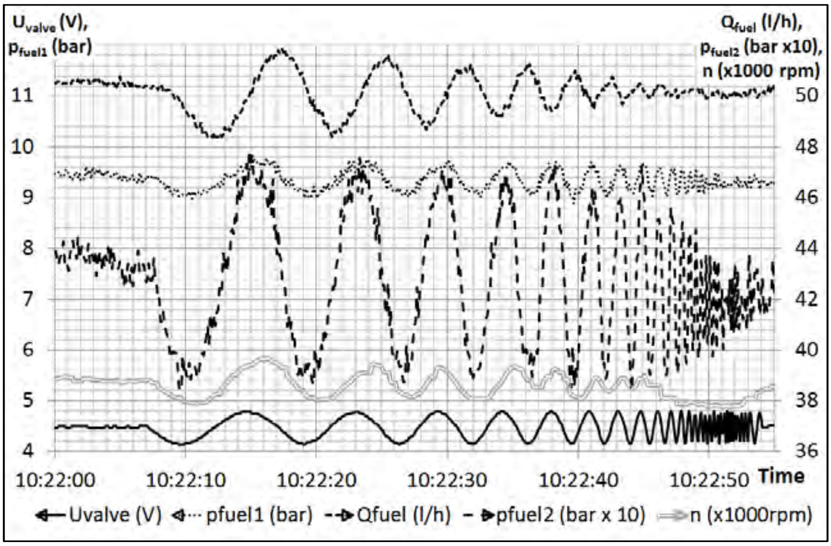


Fig. 3 Dynamic behavior of the system during test period

This measurement contains enough details about the dynamic behavior of the complete system. As the input of the plant has been chosen to be represented by the electrical control signal given to the proportional valve and the output of the system is the rotor speed of the engine, and the amplitude of the sine wave was not more than 2% we can assume that the inherently nonlinear gas turbine remained in a narrow neighborhood of the selected operating point, hence a linear identification method can be applied to extract the approximate system model to perform control design as a further step.

### 3.3 Identification method

Because the measurement contains noise and disturbance, which have unfavorable effects in the identification process, to find the best matching transfer function with the system's supposed real one, the authors have been applied three different linear identification models from MATLAB identification tools through the investigation [24]:

- *Output-Error model*: Does not use any parameters to modelling the disturbance characteristics, it only describes system dynamics.
- *ARMAX model*: The model is able to describe disturbance dynamics, useful when disturbance is represented in the whole process.
- *Box-Jenkins model*: Completely modelling disturbance separately from the system characteristic.

The comparison of the results for the Output-Error model is shown in Figure 4. All the three candidate models have performed at nearly the same level, so they could not be distinguished on a single plot. Left side of the figure indicates time series of identification data, right half represents resulting Bode plots of the modeled systems.

After analyzing the diagrams of Fig. 4, the Output-Error model seemed to be ideal choice in the aspect of performance, so this one has been chosen for the further investigation, however, one interesting anomaly we have to describe first.

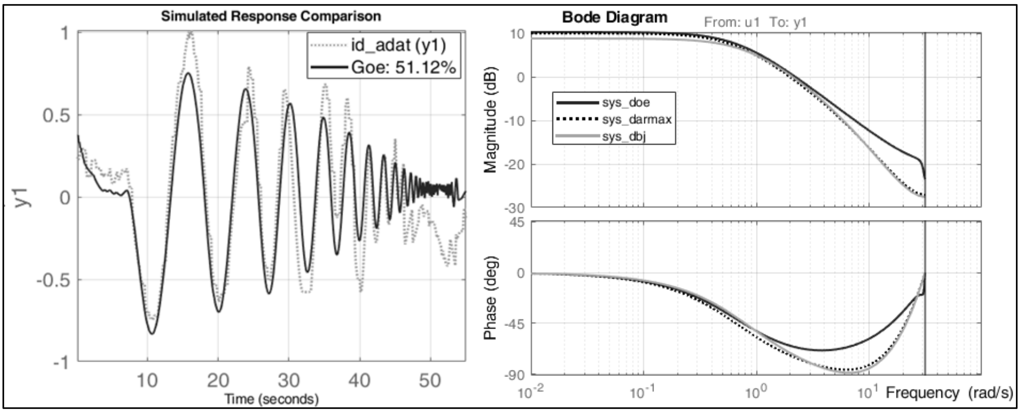


Fig. 4 Time (left) and frequency response (right) of discrete approximations

The Bode-diagram phase plot of Fig. 4 shows unexpected behavior at higher frequencies due to noise. In practice gas turbines do not tend to respond to frequencies over 10Hz. To eliminate this pseudo-behavior the transfer function had to be modified. The system has been transferred into continuous time for the truncation. During modification the second- and first order parts in the numerator of the original transfer function (3) were eliminated and only the zero-order part was kept as indicated in (4). The result of the truncation is represented on Figure 5, which demonstrates that the application of the simplification could eliminate the effects of the noise and creates a more realistic frequency response.

$$G(s) = \frac{0.06691s^2+28.96s+552.4}{s^2+237.8s+168.6} \tag{3}$$

$$G_{res}(s) = \frac{552.4}{s^2+237.8s+168.6} \tag{4}$$

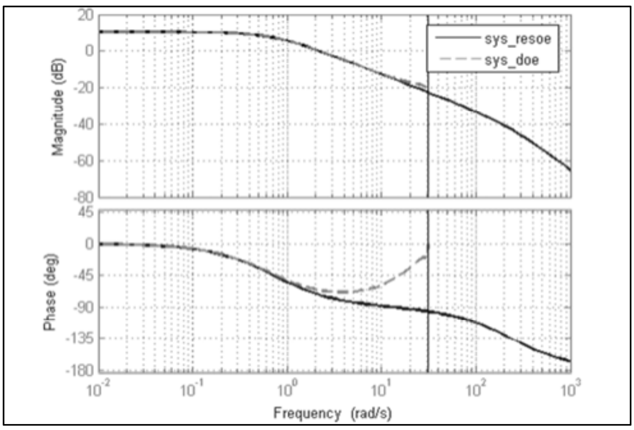


Fig. 5 Bode plot of the original (sys_doe) and truncated (sys_resoe) system (4)

## 4. CONTROLLER DESIGN

After all the relevant characteristics had been determined during the identification process the controller could been designed. The controlling process in and MCU is based on sampling method, so the transfer function must been converted back to discrete time (5).

$$G_{res}(z) = \frac{0.2157z+0.009189}{z^2-0.9313z+4.712\cdot10^{-11}} \tag{5}$$

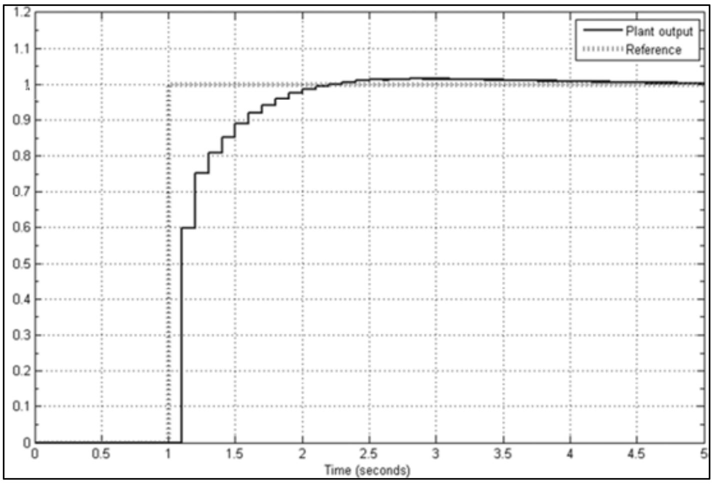


Fig. 6: Reference signal and plant output comparison of the controller

The design of the discrete time PID controller was executed in MATLAB Simulink using its dedicated tool for tuning controller parameters. The characteristic of the optimized controller shown on Figure 6. The values of the most significant properties of the PID controller are the following:

- Rise time: 0.5s
- Settling time: 1.0s
- Overshoot: 1.49%
- Gain margin: 9.85dB (at 31.4rad/s)
- Phase margin: 90° (at 5.31rad/s)

After the controller setting was done, the applicated stability tests confirmed the closed loop system stability, so the controller design found successful completed.

## 5. CONCLUSION

Summarizing the main steps the new fuel metering system has been implemented in the TKT-1 turbojet engine. Initial "cold tests" have been performed for the proportional valve characteristic measurement. In the next phase with operating gas turbine live test cases have been carried out for data collection to achieve sufficient amount of data to determine the transfer function. The discrete time identification of the system has been completed by comparing different (Output-error, ARMAX and Box-Jenkins) models. After selected the model which shown the best performance it was used for designing the discrete time PID controller. The stability tests confirmed the closed loop system stability so as a result the redesign of the fuel metering system has been successfully.

Some further actions are recommended to be managed in the future. The first and most important is that to implement the PID controller into the system to realize the closed loop rotor speed control in practice. On the other hand the applied *mbed* LPC1768 microcontroller is able to extend the FADEC functions of the TKT-1 so several additional sequences e.g. startup control could be defined.

## 6. REFERENCES


[1] **McIsaac, B. - Langton, R.**: Gas Turbine Propulsion Systems. Wiley & Sons, Chichester, UK, 2011. p.328, ISBN: 978-0-470-06563-1

[2] **Savka, J. - Főző, L. - Andoga, R. - Nikolas Ivanics**: Is it Possible to Use the Experimental Identification Based on the Transition Characteristics for Micro Turbo Compressor Engines? In: 2018 XIII International Scientific Conference - New Trends in Aviation Development (NTAD), pp. 114-117. doi: 10.1109/ NTAD.2018.8551655

[3] **Giampaolo, T.**: Gas turbine handbook: principles and practices. 3rd Ed., Fairmont Press, Lilburn, USA, 2006, p. 437, ISBN 0-88173-515-9

[4] **El-Sayed, A. F.**: Fundamentals of Aircraft and Rocket Propulsion. Springer, London, 2016, p.1010, ISBN 978-1-4471-6794-5.

[5] **Katolicky, Z. – Bušov, B. – Bartlová, M.:** Turbojet Engine Innovation and TRIZ. In: Proceedings of the 16th International Conference on Mechatronics – Mechatronika 2014, p.16-23, doi: 10.1109/MECHATRONIKA.2014.7018230

[6] **Cwojdziński, L. – Adamski, M.**: Power Units and Power Supply Systems in UAV. Aviation, ISSN 1648-7788, Vol. 18(1), p.1-8, doi: 10.3846/ 16487788. 2014. 865938

[7] **Dutczak, J.:** Micro turbine engines for drones propulsion. In: 2016 IOP Conf. Ser.: Mater. Sci. Eng. **148** 012063, doi: 0.1088/1757-899X/148/1/012063

[8] **Jombo, G. - Pecinka, J. – Sampath, S. – Mba, D.:** Influence of Fouling on Compressor Dynamics: Experimental and Modeling Approach. J. Eng. Gas Turbines Power 140(3), p.7, doi: 10.1115/1.4037913.

[9] **Nyulászi, L. – Andoga, R. - Butka, P. - Főző, L. - Kovacs, R. – Moravec, T.:** Fault Detection and Isolation of an Aircraft Turbojet Engine Using a Multi-Sensor Network and Multiple Model Approach. Acta Polytechnica Hungarica, Vol. 15(2), 2018, p.189-209, doi: 10.12700/APH.15.1.2018.2.10

[10] **Broatch, A. - Galindo, J. - Navarro, R. - García-Tíscar, J.:** Methodology for experimental validation of a CFD model for predicting noise generation in centrifugal compressors. International Journal of Heat and Fluid Flow, Vol. 50 (2014), p.134-144, doi: 10.1016/j.ijheatfluidflow.2014.06.006

[11] **Zare, F. – Veress, Á.:** Novel Application of Inverse Design Method by Means of Redesigning Compressor Stator Vanes in a Research Jet Engine. Proceedings of the 15th MINI Conference on Vehicle System Dynamics, Identification and Anomalies: VSDIA 2016, (Ed. Prof. I. Zobory), Budapest, 2017, p.261-280.

[12] **Calabria, R. - Chiariello, F. - Massoli, P. – Reale, F.:** Numerical study of a micro gas turbine fed by liquid fuels: potentialities and critical issues. In: Energy Procedia 81 (2015) p.1131 – 1142, doi: 10.1016/j.egypro.2015.12.138

[13] **Graça, M. - Duarte, A. – Coelho, P.J. – Costa, M.:** Numerical simulation of a reversed flow small-scale combustor. Fuel Processing Technology, Vol. 107 (2013), p.126-137, doi: 10.1016/j.fuproc.2012.06.028

[14] **Pescini, E. - DeGiorgi, M.G. - Suma, A. - Francioso, L. - Ficarella, A.:** Separation control by a microfabricated SDBD plasma actuator for small engine turbine applications: influence of the excitation waveform. Aerospace Science and Technology, Vol. 76 (2018), p.442-454, doi: 10.1016/j.ast.2018.01.019

[15] **Brun, K. – Simons, S. – Kurz, R.:** The Impact of Reciprocating Compressor Pulsations on the Surge Margin of Centrifugal Compressors. Journal of Engineering for Gas Turbines and Power, Vol. 139 (2017), p.15, doi: 10.1115/ 1.4035822

[16] **Beneda, K. – Veress, Á.:** Virtual Prototyping and Additive Manufacturing of a Vaned Diffuser for a Research Jet Engine. In: 2018 XIII International Scientific Conference - New Trends in Aviation Development (NTAD), pp. 19-24, doi: 10.1109/NTAD.2018.8551628

[17] **Min, Z. – Parbat, S.N. – Yang, L. – Kang, B. – Chyu, M.K.:** Fabrication and Characterization of Additive Manufactured Nickel-Based Oxide Dispersion Strengthened Coating Layer for High-Temperature Application. Journal of Engineering for Gas Turbines and Power, Vol. 140 (2018), p.7, doi: 10.1115/ 1.4038351

[18] **Ramakrishnan, A. – Dinda, G.P.:** Direct laser metal deposition of Inconel 738. Materials Science and Engineering: A. Vol. 740–741, 7 January 2019, p.1-13, doi: 10.1016/j.msea.2018.10.020

[19] **Kirsch, K.L. – Thole, K.A.:** Numerical Optimization, Characterization, and Experimental Investigation of Additively Manufactured Communicating Microchannels. Journal of Turbomachinery, Vol. 140, No. 11, 2018, p.11, doi: 10.1115/ 1.4041494

[20] **Fayaz, G. – Kazemzadeh, S.:** Towards additive manufacturing of compressor impellers: 3D modeling of multilayer laser solid freeform fabrication of nickel alloy 625 powder mixed with nano-CeO2 on AISI 4140. Additive Manufacturing, Vol. 20 (2018), p.182-188, doi: 10.1016/j.addma.2018.02.001

[21] **Dubrovskaya, A. - Dongauzer, K. - Faskhutdinov, R.:** The design of lightweight gas turbine engine parts using topology optimization. In: MATEC Web of Conferences Vol. 129 (2017), doi: 10.1051/matecconf/201712901067

[22] **Pásztor, E. - Beneda, K.:** The first ten years of TKT-1 micro gas turbine for research and education. (In Hungarian, A TKT-1 kisméretű, oktatási és kutatási célú gázturbinás sugárhajtómű első tíz éve). Repüléstudományi Közlemények, HU ISSN 1789-770X, 2015/3, p.117-132.

[23] **Beneda, K.:** Development of a modular FADEC for small scale turbojet engine. In: 2016 IEEE 14th International Symposium on Applied Machine Intelligence and Informatics (SAMI), p.51-56, doi: 10.1109/SAMI.2016.7422981

[24] **Ljung, L.:** System Identification: Theory for the user. Prentice-Hall, Upper Saddle River, New Jersey, 1999, p. 609.

# SLOPE OPTIMISATION (SLOOP): TAILOR-MADE OPTIMISATION FOR ROAD LONGITUDINAL PROFILE ECODESIGN CONSIDERING THE DYNAMICS OF VEHICLES

**Pierre-Olivier VANDANJON, Emmanuel VINOT and Taha EL ALMI**

Ifsttar, Ame-Ease, Route de Bouaye,
F-44341 Bouguenais, France

*Received: November 5, 2018*

## ABSTRACT

The current transport system is not sustainable because of its high consumption of finite resources (mainly oil) and its impact on the environment (air quality, global warming, etc.). The design phase of the transport infrastructure has to be reconsidered in order to take into account these environmental burdens. Very recently, a methodology called Sloop (Slope Optimization) has been proposed to optimize the road longitudinal profile according to either an energy consumption or a Global Warming Potential (GWP) criterion calculated for construction and use phases. However, this optimization requires a high computation effort. It is a severe limitation to deploy this application to significant road project. The purpose of this paper is to propose a tailor-made optimization process which improves significantly this methodology. For the construction phase assessment, the methodology is based on a model of earthworks which computes the differences of geometry between the natural terrain and the road longitudinal profile. The use phase is assessed by simulating the traffic. Traffic simulations are based on vehicle dynamic models validated with real experiments. Starting from an initial longitudinal profile proposed by road designers, our algorithm finds a better profile in terms of Energy or GWP. The degrees of freedom of the optimization problem are mainly the road slopes and secondly the radii of the circles which connect them. The main constrain is the connection of the profile with the existing road. The optimization is complex due to the important number of degrees of freedom and the computation cost of the use phase assessment. It is the reason why, we developed a specific algorithm based on the Sequential Quadratic Programming Method (SQP) with suited computations of the linear approximation.

*Keywords: Energy, GWP, Road, Optimization, Dynamic Model, SQP*

## 1. INTRODUCTION

Our current transportation system is not sustainable. According to the report for the Organization for Economic Cooperation and Development (OECD), GHG emissions from transportation should increase by 60% between 2015 and 2050 [2]. During this same period (2010-2050), in order to maintain the global warming below 1.5˚, experts from the Intergovernmental Panel on Climate Change (IPPC) advise keeping the GHG emissions from transportation constant [4].

New transportation projects have to take into account this burden by assessing the environmental impacts of road infrastructure within Life Cycle Assessment (LCA) framework. An LCA analysis considers several steps in the life of road infrastructure: planning/design, construction, maintenance, operations and end- of-life. Ecodesign of transportation projects takes into account these different steps. We developed a methodology in order to optimize the longitudinal profile of road project called sloop for slope optimization within this ecodesign framework [6].

The optimization criteria are selected from among classical life-cycle environ- mental impact indicators. This study has focused on primary energy consumption and global warming potential (GWP. The degrees of freedom of this optimization process consist of the longitudinal road profile. With respect to the environmental impact assessment, two life cycle phases are taken into account: construction and operations. The maintenance phase is considered to be the same regardless of the longitudinal road profile. Firstly, the computation of the cost of one longitudinal profile is described. The construction phase is primarily assessed by examining the earthworks, which are estimated by computing geometric variations between the natural terrain and the longitudinal profile. The pavement layers are assumed to be the same for each profile. The operations phase is assessed by simulating traffic over a ten-year period. The traffic's simulation is carried out with vehicle dynamic models associated with engine models. The optimization process based on a classical algorithm is then described. This algorithm is adapted to our specific problem.

## 2. ASSESSMENT OF A LONGITUDINAL PROFILE

This section exhibits the equation of a road longitudinal profile and its assessment. This assessment is divided in two parts: construction and operation assessment.

### 2.1 road longitudinal profile

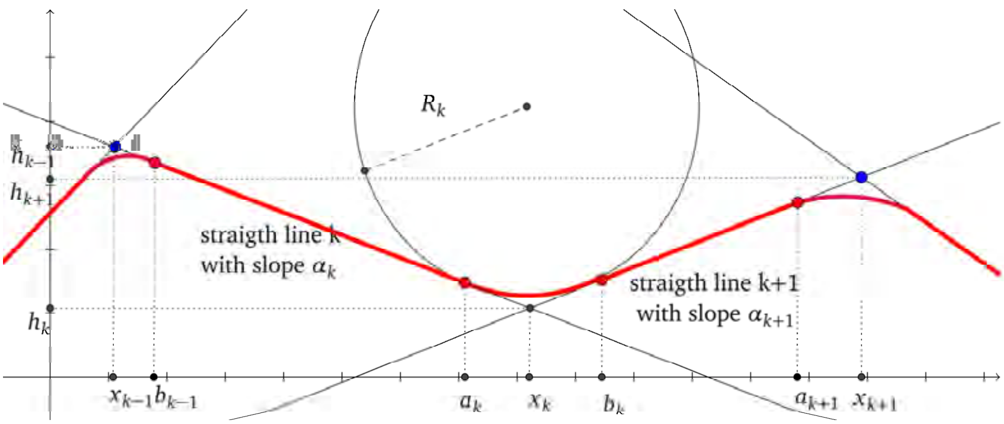


Fig. 1 Longitudinal profile (in red) modeled as a sequence of straight lines linked by circular arcs

The longitudinal profile Ps is parameterized as illustrated in Figure 1 and described by the following set of typical equations for road draftsmen:

$$\begin{aligned} \mathrm{Ps}(x) &= \alpha_k(x - x_k) + h_k \text{ if } b_{k-1} \le x < a_k \\ \mathrm{Ps}(x) &= C_{x_k,h_k,\alpha_k,R_k,x_{k+1},h_{k+1},\alpha_{k+1}}(x) \text{ if } a_k \le x < b_k \\ \mathrm{Ps}(x) &= -\alpha_{k+1}(x_{k+1} - x) + h_{k+1} \text{ if } b_k \le x < a_{k+1} \end{aligned} \tag{1}$$

$\alpha_k$ is the longitudinal slope of the straight line $k$, $x_k$, $h_k$ are the abscissa and altitude of the point of the intersection of straight line $k$ and straight line $k + 1$. $b_{k-1}$ and $a_k$ are internal variables output from the computation of the circle linking this straight line $k$ to the next straight line.

$C_{xk}$, $h_k$, $\alpha_k$, $R_k$, $x_{k+1}$, $h_{k+1}$, $\alpha_{k+1}(x)$ is the equation of the circle, with radius $R_k$ , that links straight line $k$ to straight line $k + 1$. This circle is tangent to straight line $k$ at the point with abscissa $a_k$ and is tangent to the straight line $k + 1$ at the point with abscissa $b_k$. With these equations, the derivative of Ps($x$) is continuous which is a mandatory condition for simulating vehicle dynamical models. Also, circular arcs are often used by road designers to "smooth" the profile. For this purpose, large radii ($R_k$ > 10, 000 m) are chosen, thus implying that the circular arcs cannot be neglected in the longitudinal profile model.

The boundary conditions, i.e. the connection with the existing road, are managed by setting: $x_0 = x_b$, $\alpha_0 = \alpha_b$, $P_s(x_0) = P_{sb}$, $x_n = x_e$, $\alpha_{n+1} = \alpha_e$, $x_n = x_e$, $P_s(x_n) = P_{se}$. $\alpha_b$ is the longitudinal slope of the existing road before $x_b$, which is the beginning of the studied profile, $\alpha_e$ is the longitudinal slope of the existing road after $x_e$, which is the end of the studied profile.

The degrees of freedom in this parameterization are: $x_k$ , $\alpha_k$ , $R_k$ , with $k$ varying from 1 to $n - 1$ and $R_0$, $R_n$, $\alpha_n$.

The other variables can be obtained from the degrees of freedom. $h_k$ is computed in knowing $x_{k-1}$, $x_k$ and $\alpha_k$. $a_k$, $b_k$ are computed in knowing the equation of circle $C(x_k, h_k, \alpha_k, R_k, x_{k+1}, h_{k+1}, \alpha_{k+1})$.

### 2.2 Construction

Starting from this longitudinal profile, a 3D model of the road sub-grade, which supports the pavement layers, is computed. The comparison between this reference profile and the natural soil requires an accurate assessment of earthmoving. Various longitudinal profiles therefore lead to significant differences in earthmoving quantities. At the same time, these longitudinal road profiles do not imply significant changes in the pavement layer size because their widths and lengths mainly depend on traffic levels. Consequently, road pavement layers have not been formalized in the optimization process. Earthworks can be broken down into the following operations: raw material extraction, transportation and deposit as fill (in the case of reuse) or storage as final deposit [1]. Any assessment of earthmoving quantities must therefore include an estimate of the fuel consumed by earthworks equipment (bulldozer, scraper, dump truck) during each task. Soil treatment needs to be quantified as well. These aspects are incorporated into the evaluation of energy consumption and GHG (GreenHouse Gazes emissions for the optimization process. To achieve this goal, earth movements are estimated from volume differences between the natural ground level and the current longitudinal profile (this computation will be detailed in the next section). The energy consumption and GHG emissions assessment is performed using the software ECORCE M, which features an extensive database pertaining to earthworks equipment [3].

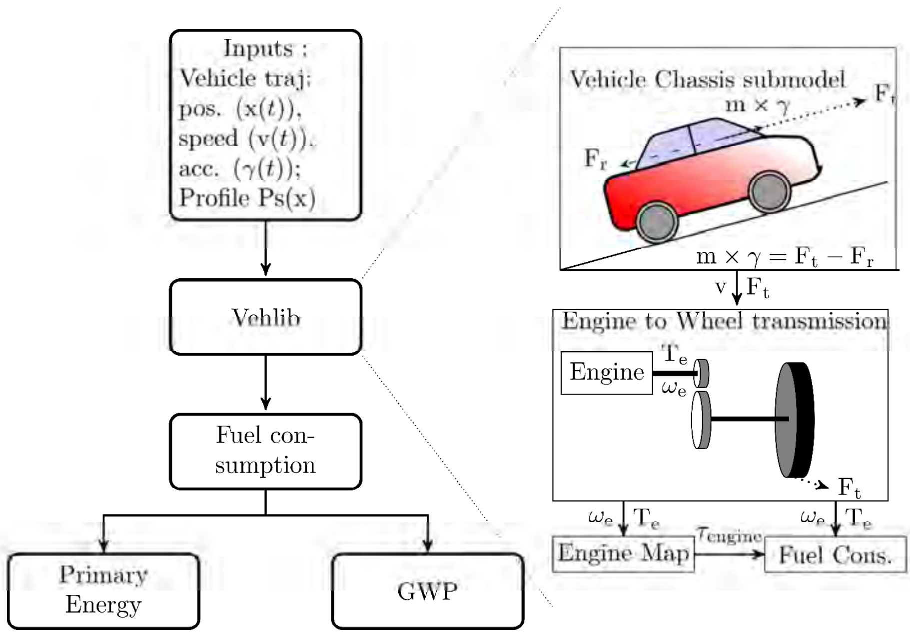


Fig. 2 Fuel consumption computation

Operation assessment is based on Traffic simulation. Traffic is modeled using different classes of vehicles from passenger cars to heavy vehicles. The vehicle sub-classes can also be defined by engine type. For passenger cars, both diesel and gasoline engines are considered, whereas for all other categories, only diesel engines are assumed. For each class, a vehicle model has been parameterized to be representative of the average fuel consumption of the entire fleet. The vehicle speed is either the maximum legal speed or the maximum achievable speed, which means that vehicle speed actually depends on slope. For example, the truck speed may lie below the legal speed when traveling uphill and at the legal speed on downhill stretches, in using the engine brake and/or brake.

It was decided in this study to use a customized model called VEHLIB [7], which is a Matlab/Simulink library developed at Ifsttar/LTE (Environment and Transportation Laboratory) to simulate all types of vehicles (from cars to articulated vehicles) and power-train architectures (from conventional to complex hybrid power-trains). It uses a modular cybernetic approach that allows for an easy exchange of vehicle components. According to this model, the vehicle is thus considered as a set of sub-systems. Modeling the vehicle therefore entails modeling its various units and the interactions taking place between them. The VEHLIB model is mainly composed of the engine, clutch, gear-box, final gear and vehicle chassis sub-model. The vehicle chassis model comprises an aerodynamic model and a rolling resistance model. The fundamental dynamic principle is solved in order to proceed upstream from wheel effort to engine solicitation.

Figure 2 displays the general principles of the fuel consumption computation. Starting from the trajectory of the vehicle and the longitudinal profile, Vehlib simulates the vehicle. One simulation output is the fuel consumption. Direct calculations yield the primary energy consumption and the CO2 emissions which is converted in GWP.

$$\mathrm{m} \times \gamma = \mathrm{F_t} - \mathrm{F_r} \tag{2}$$

Firstly, Newton's second law is applied to a vehicle described as a single degree of freedom model (see the car on Figure 2) in order to compute the tractive force Ft developed by the wheels:

where m is the vehicle's mass and γ is its acceleration. $F_r$ is the running resistance

$$\mathrm{F_r} = \frac{1}{2}\rho S C_x \mathrm{v}^2 + \mathrm{m}g(C_{rr0} + C_{rr1}\mathrm{v}) + \mathrm{m}g\sin(\alpha_r) \tag{3}$$

Where ρ is the air density, $S$ is the front vehicle area, $C_x$ is the drag forces coefficient, $C_{rr0}$ et $C_{rr1}$ are the tires rolling resistance coefficients, g is the acceleration of gravity and $\alpha_r$ is the angle of the slope in radian. This quantity varies according to the profile.

As illustrated by the gears on Figure 2, knowing Ft and v, the engine torque and angular speed ($T_e$ and $\omega_e$) are then computed. We exhibit the equations only for the engine torque, equations for the angular speed are symmetric. Knowing $F_t$, the torque $T_w$ to be applied to the wheel is then:

$$T_w = \mathrm{F_t} \times R_w \tag{4}$$

where $R_w$ is the wheel radius. Going upstream to the engine shaft considering the

$$\mathrm{T_e} = T_w \frac{k_{fg}.k_{gb}}{\eta_{fg}.\eta_{gb}} \qquad if\ T_w > 0 \tag{5}$$

different gear ratios, the engine torque $T_e$ is then:

*where* $k_{fg}$ and $\eta_{fg}$ are the gear ratio and efficiency of the final gear, $k_{gb}$ and $\eta_{gb}$ are the gear ratio and efficiency of the gear box. Fuel consumption is then calculated using specific fuel consumption maps. VEHLIB has been validated with experimental data. The fuel consumption is then transformed in GWP ($CO_2$ emissions) or primary energy.

## 3. OPTIMIZATION

The previous section displays the methodology to assess the cost in GWP or Energy of a road longitudinal profile. In this section, we present how to find an optimal profile which minimizes one of both criteria. The mathematical formulation is the following.

$$\begin{gathered} \underset{x_k,\alpha_k,\, R_k,\, k=1\ldots n-1\; R_0\; R_n\; \alpha_n}{\text{minimize}} \quad \mathrm{J(Ps)} \\ \text{subject to } \mathrm{Ps}(\mathrm{x}_o) = \mathrm{Ps}_o,\ \mathrm{Ps}(\mathrm{x}_f) = \mathrm{Ps}_f \\ \alpha_{min} \leq \alpha_k \leq \alpha_{max}\ \alpha_k \neq \alpha_{k+1}\ x_{min} \leq x_k \leq x_{max}\ R_{min} \leq R_k \leq R_{max} \end{gathered} \tag{6}$$

Where $J(P_s)$ is the cost of the longitudinal profile Ps according to the previous section. The optimization problem (6) is a finite dimensional non-linear optimization with linear inequalities and two non-linear equalities. A classical algorithm to solve this type of optimization is the sequential quadratic programming (SQP, see [5] for a complete description).

### 3.1 SQP algorithm

SQP is an iterative algorithm starting from the initial profile designed by draftsmen:

$$\mathrm{Ps}_{k+1} = \mathrm{Ps}_k + d_k \quad , \quad \forall k \in \mathbb{N} \tag{7}$$

with $d_k$ is the descent step and is computing:

- by calculating $p_k$, solutions of the *Karush Kuhn Tucker* (KKT) conditions of the quadratic optimization with linear equality constrains approximating the non-linear optimization (6);
- by reducing the length of $p_k$, $d_k = \mu p_k$ with $0 < \mu \leq 1$ taking into account:
  - the activation of non-active linear inequalities;
  - the quadratic approximation of the Lagrangian;
  - the linear approximation of the non-linear equality constrains.

In our specific study, the non-linear equality constrains of the optimization problem (6) are a sequence of straight lines and circle arcs. It means these constrains are quadratic equality constrains. In the following, we exploit this property for the second non-linear equality. The procedure is the same for the first constrain.

### 3.2 tailored SQP algorithm

The linear approximation of the second constrain (see Eq. 6) is

$$\mu \nabla \mathrm{Ps}(\mathrm{x}_{kf}) p_k = \mathrm{Ps}_f - \mathrm{Ps}(\mathrm{x}_{kf}) \tag{8}$$

Our objective is to find µ in order to get:

$$|\mathrm{Ps}(\mathrm{x}_{k+1f}) - \mathrm{Ps}_f| < \mathtt{tol} \tag{9}$$

where tol is the tolerance. It yields

$$|\mathrm{Ps}(\mathrm{x}_{kf}) + \mu \nabla \mathrm{Ps}(\mathrm{x}_{kf}) p_k + \frac{1}{2}\mu^2 p_k^t (\mathrm{Hess\,Ps}(\mathrm{x}_{kf})) p_k - \mathrm{Ps}_f| < \mathtt{tol} \tag{10}$$

If this last inequality is not true if μ = 1, it means that μ has to be reduced. Supposing that the +tol is exceeded, μ is then the solution of the second grade equation:

$$\mathrm{Ps}(\mathrm{x}_{kf}) + \mu\nabla\mathrm{Ps}(\mathrm{x}_{kf})p_k + \frac{1}{2}\mu^2 p_k^t(\mathrm{Hess\,Ps}(\mathrm{x}_{kf}))p_k - \mathrm{Ps}_f - \mathtt{tol} = 0 \qquad (11)$$

The calculation is straightforward. The equation is symmetric if it is −tol which is exceeded.

### 3.3 Results

This methodology was then applied to a real case study: the considered road section is a 4.75 km long 2x2 lane road in the French national road network. The number of degrees of freedom is 18. There are two non-linear equalities constrains and more than 40 linear inequality constrains. Results of the optimization process yield a 6 % savings of the global primary energy compared to the initial profile. A 8 % savings on GWP is also obtained.

## 4. CONCLUSION

Sloop is a methodology which optimizes road longitudinal profile according to GWP or energy consumption criteria. It is solved with sequential quadratic programming which is an iterative algorithm. At each step, a quadratic optimization problem is solved. The length of the descent step depends on the approximation of the non linear constrains. We exploit a specific property of this constrain in order to calculate exactly this length. The next step is to improve the computation burden of the quadratic approximation of the cost function.

## 5. REFERENCES

[1] **Capony, A. – Muresan, B. – Dauvergne, M. – Auriol, J. C. – Ferber, V. – Jullien, A.:** Jan. 2013. Monitoring and environmental modelling of earthwork impacts: A road construction case study. Resources, Conservation and Recycling 74, pp.124–133.

[2] ITF, 2017. ITF Transport Outlook 2017. Tech. rep., ITF, ISBN: 978-92-82- 10799-7.

[3] **Jullien, A. – Dauvergne, M. – Proust, C. :** 2015. Road LCA: the dedicated ECORCE tool and database. International Journal of Life Cycle Assessment 20, 655–670.

[4] **Meyer, L. – Brinkman, S. – van Kesteren, L. – Leprince-Ringuet, N. - van Boxmeer, F.:** 2014. IPCC, 2014: Climate Change 2014: Synthesis Report. Contribution of Working Groups I, II and III to the Fifth Assessment Report of the Intergovernmental Panel on Climate Change, 3–87.

[5] **Nocedal, J. – Wright, S.,** 2006. Numerical Optimization, 2nd Edition. Springer Series in Operations Research and Financial Engineering. Springer-Verlag, New York.

[6] **Vandanjon, P.-O. – Vinot, E. – Cerezo,V. – Coiret, A. – D uvergne,**M.: Publication in Progress. Longitudinal profile optimization for roads, within an eco-design framework. Transportation Research Part D: Transport and Environment.

[7] V**inot, E. - Scordia, J. - Trigui, R. - Jeanneret, B. - Badin, F.:** 2008. Model simulation, validation and case study of the 2004 ths of toyota prius. International Journal of Vehicle Systems Modelling and Testing 3 (3), 139–167.

## SESSION FOR DYNAMICS, IDENTIFICATION AND ANOMALIES OF RAILWAY VEHICLES

**ZOLLER, V.** (Hungary)
Analysis of the Track/Vehicle Interaction with Regard to the Coupling with the Subgrade Dynamics ........ 85

**CHUDZIKIEWICZ, A. – STELMACH, A.** (Poland)
Evaluation of the Process of Placing in Service of a Rail Vehicle with Regard to Safety of Transport Operation ........ 91

**JAKUSHEV, A. – HOMONETS, I.** (Russia)
Impact of Residual Stresses on the Railcar Wheel Strength........ 93

**ALBON, A.** (France)
On Wheel Profile Optimization by Generic Algorithm........ 101

**SZABÓ A. – ZOBORY, I.** (Hungary)
Vertical Dynamical Loading Conditions of Driven Wheel-Set........ 109

**ZOBORY, I. – NAGY, D.** (Hungary)
Creep Control in Brake Operation to Avoid Wheel Sliding and Flattening........ 121

**NÉMETH, I.** (Hungary)
How to Avoid Dynamical Instability in Disc-Brake System by Using Additional Linear Damping ........ 131

**KRÉMER, M.** (Hungary)
Knorr-Bremse Results in Adhesion Management and Participating in PINTA Project ........ 143

**LIN, S. – SUDA, J.** (Japan)
Vehicle Condition Monitor System Considering Vehicle and Track Maintenance........ 151

**ALFI, S. – BRUNI, S. – FU, B.** (Italy + China)
Condition Monitoring and Fault Detection of Suspension Components in Freight Wagons Using Acceleration Measurements ........ 157

**CSIBA, J.** (Hungary)
Numerical Analysis of the Failures, Reliabilities and Availabilities Concerning a Given Family of Railway Carriages under Different Operation and Maintenance Circumstances ........ 165

**ZÁBORI, Z. – ZOBORY, I.** (Hungary)
Track Qualification Method by Using System Dynamics Based Parameter Identification ........ 173

**MALATINSZKY, S.** (Hungary)
Conformity Assessment of Modernised Locomotive Bogie and Body Connection ........ 187

**DI GIALLEONARDO, E. – BIONDA, S. – BRAGHIN, F. – SOMASCHINI, C.** (Italy)
Design of Experiment Approaches for the Calibration of Instrumented Wheel-Set ........ 193

**SOMASCHINI, C. – D I GIALLEONARDO, E. – COLLINA, A. – BOCCIOLONE, M.** (Italy)
Algorithm Development to Classify the Deterioration of Insulated Rail Joints by Means of on Board Measurements ........ 201

**CARNEVALE, M – COLLINA, A. – ZUIN, A.** (Italy)
A Rolling Stock Based System for Pantograph and Catenary Condition Monitoring: Validation through Numerical Simulations on Rigid Catenary ............. 209

**SZŐKE, D. – ZOBORY, I.** (Hungary)
Investigation into the Structure of the Railway Track/Vehicle Connection .............. 219

# ANALYSIS OF THE TRACK/VEHICLE INTERACTION WITH REGARD TO THE COUPLING WITH THE SUBGRADE DYNAMICS

**Vilmos ZOLLER**

S. Rejtő Faculty, Óbuda University,
Doberdó út 6, H-1034 Budapest, Hungary

*Received: November 5, 2018*

## ABSTRACT

We investigate the effect of various generalizations of the concept of a beam supported by viscoelastic subgrades. The beam is subjected to the action of moving loads. In the paper the closed-form analytical solutions obtained in earlier papers of the author and I. ZOBORY for the cases of BERNOULLI–EULER beams on WINKLER foundations are generalized to the case of more complicated beam/foundation systems. The generalizations of the track/vehicle system are connected with the appearence of the thermal expansion effect in the beam, and that of the PASTERNAK term in the supporting system. These two effects together result in a wave-like propagation in the system. We analyze the appearance of critical speeds avoiding the continuous motion of the system under such generalized circumstances.

*Keywords*: track/vehicle system, beam, thermal explosion, Pasternak foundation

## 1. INTRODUCTION

We investigate here the simple boundary value problem with a moving, damped oscillatory load excitation acting at points $x = vt$ of form

$$EI\,\partial_x^4 u + \rho A\,\partial_t^2 u + k\partial_t u = F_0 e^{wt}\delta(x - vt)\,,$$
$$\lim_{x\to\pm\infty} u(t,x) = \lim_{t\to\pm\infty} u(t,x) = 0$$

on an infinite BERNOULLI–EULER beam of parameters $EI$ and $\rho A$, laying on a WINKLER foundation of viscoelastic stiffness and damping parameters $s$ and $k$, and subjected to the action of a moving load, where the motion of the beam is fixed at infinities, or, more generally, the problem

$$EI\,\partial_x^4 u + \rho A\,\partial_t^2 u - G\partial_x^2 + k\partial_t u = F_0 e^{wt}\delta(x - vt)\,,$$
$$\lim_{x\to\pm\infty} u(t,x) = \lim_{t\to\pm\infty} u(t,x) = 0\,.$$

Here $u(t,x)$ stands for the vertical displacement of the beam and $\delta$ denotes DIRAC's unit impulse distribution. The extra term in the middle can represent either the effect of thermal expansion (more characteristic in case of rods/short beams) built in to the first part of the left-hand side of the differential equation, representing the beam operator, or the effect of a PASTERNAK-type foundation built in to the second part, representing the differential operator governing the subgrade, cf. [4], or both of them.

In the second equation above parameter

$$G = G(T) = G_{\mathrm{th}} + G_{\mathrm{P}}$$

stands for the superposition of the thermal expansion coeffiecient depending on the actual value of temperature $T$, likely different from the one acting during the welding of the rails, and the reduced shear modulus corresponding to the PASTERNAK foundation, respectively.

## 2. SOLUTION TO THE PROBLEM

One can look, in a standard way, for the solution to the general problem in the form

$$u(t,x) = \mathrm{e}^{wt} U(\xi),$$

where

$$\xi := x - vt$$

stands for the relative displacement of the moving load.

This way we obtain ODE boundary problem

$$EI\, U^{\mathrm{IV}} + (\rho A\, v^2 - G)U'' - v(k + 2\rho A v)U' + (s + kw + \rho A v^2)U = F_0 \delta$$

under boundary conditions

$$\lim_{\xi \to \pm\infty} U(\xi) = 0$$

with characteristic polynomial

$$P(\lambda) = EI\lambda^4 (\rho A v^2 - G)\lambda^2 - v(k + 2\rho A w)\lambda + (s + kw + \rho A v^2)\,.$$

The unique solution of form

$$U(\xi) = F_0 \mathrm{e}^{wt} \sum_{i=1}^{4} \sigma_i / P'(\lambda_i) \mathrm{e}^{\lambda_i \xi} \mathrm{H}(\sigma_i \xi)$$

can be obtained if and only if the characteristic roots are *well-positioned*, i.e. there are exactly two characteristic roots of polynomial $P$ both in the left and in the right complex halfplanes, cf. [2], [5-6].

Here for the sign $\sigma_i = \operatorname{sgn} \operatorname{Re} \lambda_i$ is satisfied, $P'$ stands for the derivative of polynomial $P$, while H denotes HEAVISIDE's unit jump function.

## 3. VERTICAL DISPLACEMENT UNDER THE LOAD

In numerical computations we shall use our usual data for railway beams

$$\mathrm{EI} = 6 \cdot 10^6 \text{ Nm}^2, \quad \rho A = 60 \text{ kg/m}.$$

The thermal expansion coefficient is $G_{\mathrm{th}} = 8 \cdot 10^5$ N by the data from Hungarian State Railways, while the reduced shear modulus of the PASTERNAK foundation is given by $G_{\mathrm{P}}$= 666 875 N, cf. [1].
The stiffness of the foundation is $s = 1.5 \cdot 10^7$ Pa, its damping is $k = 4.6 \cdot 10^4$ Ns/m$^2$, while the weight of the load is $F_0 = 6 \cdot 10^7$ N.
The maximal vertical displacement of the beam is of form

$$\max u(t,x) = u(t, x - vt) = U(0) = F_0 (1/P'(\lambda_1) + 1/P'(\lambda_2))$$

achieved under load $F_0$.

0) In the case G = 0 of the WINKLER foundation without thermal expansion we have $U(0) = -1.78$ mm.

1) If we take the thermal effect into consideration on a WINKLER foundation, then one has $U(0) = -1.74$ mm, and the relative effect of the thermal term is of 2%.

2) In the case of the non-heated PASTERNAK foundation of parameter $G_P$ we have $U(0) = -1.75$ mm, and the relative effect of the thermal shear modulus is of 1.7%.

3) In the case of the superposition of the two effects with an increased value $3G_P$ of the shear modulus results already $U(0) = -1.66$ mm, and a relative effect of 6.7% in.

## 4. CRITICAL SPEEDS

The supremum of the speeds $|v|$, where a (unique) continuous solution still exists (i.e. the characteristic roots are still well-positioned) is called the *critical speed* of the system. Exceeding of the critical speed can lead to the damage of the track or to rail breaking.
With the help of of the generalized ROUTH–HURWITZ criterion one can prove, that critical speeds, preventing the continuous motion of the system can appear only if, while increasing the speed, a characteristic root moves through the imaginary axis, i.e. the characteristic polynomial has an imaginary root.
It implies, that the complex excitation $w$ (awakening inside the system) satisfies

$$k + 2\rho A \,\mathrm{Re} w = 0,$$

and, in the case $\mathrm{Im}(w) = 0$ the critical speed $c$ can be reckoned by formula

$$(\rho A\, c^2 - G)^2 = 4EI\, s + k^2 /(\rho A).$$

The existence of the solution of the previous chapters can be guaranteed if the speed of the load is under the critical one.
In the undamped case of a non-heated beam on a Winkler foundation one has critical speed

$$c = (4EI(\rho A)^{-2})^{1/4},$$

cf. [3].

In the case $G \neq 0$ and $k = 0$ one has simple dependence

$$\rho A\, c^2 = G + 2(EI\, s)^{1/2}.$$

One can see in Fig.1, that a 'realistic' critical speed can occur only in case $G_{th} < 0$, i.e. when the beam is refrigerated.

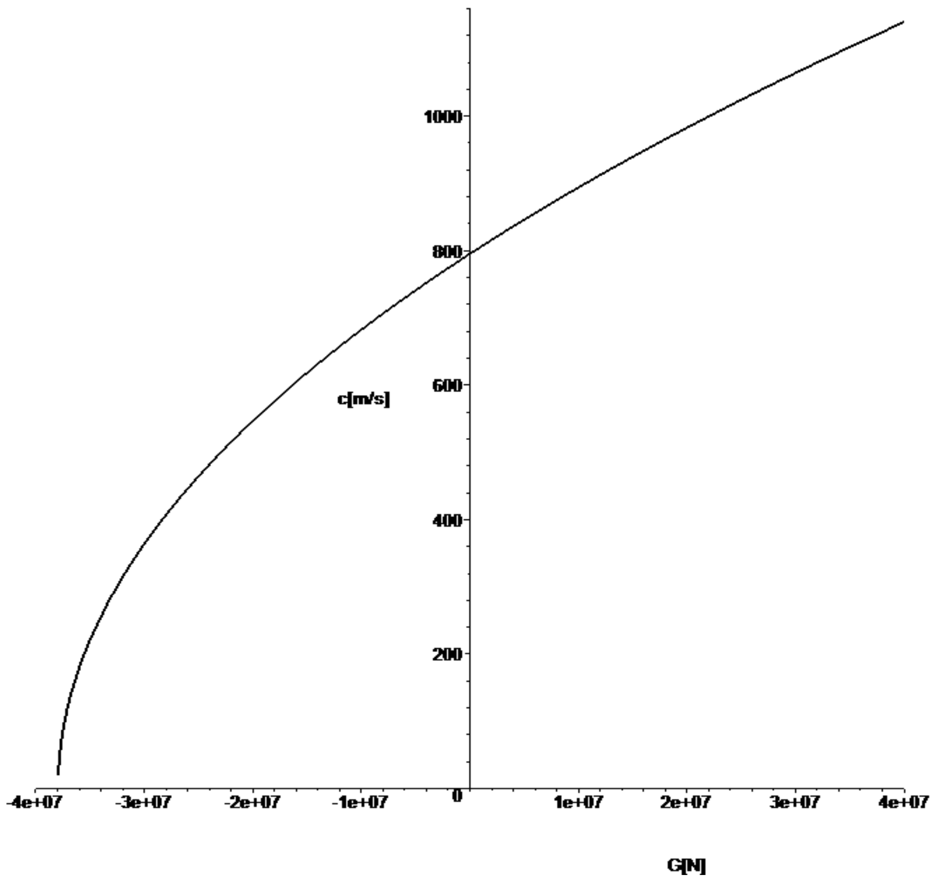


Fig.1 Dependence of the critical speed on the thermal/Pasternak coefficient $G$

Another interesting 'critical' speed appears in connection with the speed of the wave propagation awakening in the system, caused by the thermal and/or the PASTERNAK effects.

The left-hand side of the governing equation of the motion can be transformed into form

$$EI\,\partial_x^4 u + \rho A\,(\partial_t^2 - v_0^2\,\partial_x^2)\,u + k\,\partial_t u + s\,u$$

where wave operator

$$\Box_{v_0} := \partial_t^2 - v_0^2\,\partial_x^2$$

appears in the middle with $v_0^2 = G/(\rho A)$ for the speed constant of wave propagation in case $G > 0$.

## 5. CONCLUDING REMARKS

In the paper we generalized results of [6] to the case of BERNOULLI–EULER beams subjected to thermal expansion and laying on a PASTERNAK foundation.

Further possibilities of development can be:
Building in more general beam models, e.g. the TIMOSHENKO beam operator

$$B_{v_1,v_2} := \Box_{v_1} \Box_{v_2} = (\partial_t^2 - v_1^2\, \partial_x^2)\,(\partial_t^2 - v_2^2\, \partial_x^2),$$

and/or using more general (viscoelastically coupled discrete / continuous) supporting systems.

## 6. ACKNOWLEDGEMENTS

The author thanks Professor GYÖRGY SZEIDL and Mr RAMI BENKREIF for calling his attention to the middle term in the differential equation.

## 7. REFERENCES

[1] **Cao, C.Y., Zhong Y.**: Dynamic response of a beam on a Pasternak foundation and under a moving load. *J. Chonqing Univ.* **7**(4), 2008, p.311-316.

[2] **De Pater, A.D.**: Inleidend onderzoek naar het dynamisch gedrag van spoorstaven, Thesis: Waltman, Delft, 1948.

[3] **Fortin, J.P.**: Dynamic track deformation. *French Railway Rev.* **1**, 1983, p.3-12.

[4] **Pasternak, P.L.**: Fundamentals of a new method of analyzing structures on an elastic foundation by means of two foundation constants (in Russian): GIZ literatury po stroitel'stvu i arkhitekture: Moscow, 1954.

[5] **Zoller, V. - Zobory, I.**: Relations between the motion-responses caused by fixed and moving loads acting on discretely supported strings and beams. Anile, M., Capasso, V., Greco, A. (eds) Progress in Industrial Mathematics at ECMI 2000, *Mathematics in Industry* **1**: Springer/Berlin. 2002, p.657-661.

[6] **Zoller, V. - Zobory, I. - Zibolen, E.**: Theoretical investigations into the dynamical properties of railway tracks using a continuous beam model on elastic foundation. *Periodica Polytechnica, Ser. Transp. Eng.* **22** (1), 1994, p.35-54.

# EVALUATION OF THE PROCESS OF PLACING IN SERVICE OF A RAIL VEHICLE WITH REGARD TO SAFETY OF TRANSPORT OPERATION

**Andrzej CHUDZIKIEWICZ and Anna STELMACH**

Warsaw University of Technology
Pl-00-662 Warszawa, Koszykowa 75
ach1@wt.pw.edu.pl, ast@wt.pw.edu.pl
Phone: +48 22 2347964

*Received: November 5, 2018*

## ABSTRACT

Authorizing the placing in service of a rail vehicle, which is called in Polish regulations *permitting a vehicle type to operation*, is meant as a procedure carried out by appropriate authorities in order to hand over a rail vehicle to be operated with accordance to its purpose. A condition for permitting vehicle types to be operated is to obtain a certificate of placing in service for the first piece of the vehicles.

Before obtaining the certificate of placing in service of a type, the piece of vehicles of a given type is subjected to technical tests, which are performed by an organizational unit authorized for that. One of the elements of these tests is the line test, i.e. tests realized along railway lines, which are aimed, among other things, at the following:

a) evaluating dynamic properties of a traction vehicle,
b) checking strength of the main elements, in particular, fatigue strength of buggy frames.

Relevant order of the Minister of Infrastructure [1] determines the range of tests of a vehicle, which must be performed in this case. The tests are realized on tracks of QN1, QN2 and QN3 class, accepting, according to the EN 14363 standard [2], a percentage share of tracks of the aforementioned classes as follows:

– 50% share of track of class ≤ QN1
– 40% share of track of class > QN2 ≤ QN2
– 10% share of track of class > QN3

where: QN1 – track *of a very good maintenance condition,* QN2 – track *of a good maintenance condition,* QN3 – track *of a bad maintenance condition*

However, it must be pointed out that there exist in Poland also tracks *of a very bad maintenance condition*, which are not taken into account during the tests, i.e. a vehicle is not tested on such tracks, assuming that the tested vehicle will not be operated on such tracks or will be operated within a small range only.

Meanwhile, the operation practice shows that the share of tracks of a bad and very bad maintenance condition may exceed even 50% of operation. Example of this kind of a track is shown on Figure 1. Of course, in such cases, limit values of vertical and horizontal accelerations acting upon particular elements of the vehicle, including the buggy frame, are obviously exceeded; at the same time, the assumed unlimited durability of the mechanical structure is decreased. At the same time, it results in increasing a risk of a failure of basic subassemblies of a rail vehicle, and thus decreasing safety level of railway transport, as a consequence.

A problem of placing in service of rail vehicles will be discussed as well as conditions of their operation, taking into account the safety of running in railway traffic under Polish conditions. A railway event being a result of operating a vehicle on tracks of a bad maintenance condition will be discussed as an example.
*Keywords*: rail vehicles, safety, authorization for placing in service.

Fig. 1 Example of the track QN3 class

## REFERENCES

[1] Order of the Minister of Infrastructure, dated 12th of October 2005, on the range of tests required for certifying the placing in service of building types and device types designed for running the railway traffic and types of railway vehicles (in Polish).

[2] PN-EN 14363:2005 Standard. Railway System – Tests of dynamic properties of rail vehicles prior to placing in service – Test of running properties and stationary tests (in Polish).

# THE EFFECT OF RESIDUAL STRESSES ON THE RAILCAR WHEEL STRENGTH

**Aleksei IAKUSHEV and Iulia HOMONETS**

Emperor Alexander I Petersburg State Transport University
Saint Petersburg, Russia

*Received: November 5, 2018*

## *ABSTRACT*

The results of the experimental studies of the initial residual stress in the railway car wheel are presented in this paper. The fatigue strength of the railway car wheel considering the effect of the residual stress is evaluated.

*Keywords:* initial residual stress, strength, railway car wheel, fatigue crack, service life

## 1. INTRODUCTION

The wheel in the bogie of railway passenger and freight cars is a critical load-bearing part, which should withstand both vertical and lateral dynamic forces caused by a moving train. There have been cases of railway car derailment due to breaks in the wheel disk-to-rim transition zone (Fig. 1). According to the statistical data, 2 freight car wheels with a circumferential fatigue crack up to 250 mm long in the wheel disk-to-rim transition zone were recorded in Russia in 2013; 4 wheels with fatigue cracks were recorded in 2014, and 3 wheels – in 2015. Bench-run tests to investigate the effect of cyclic vertical loads on the railcar wheel showed that the wheel fatigue breaks occur in the disk-to-rim transition zone.

Fig. 1 Freight car derailment caused by a wheel disc fracture

The reasons for premature railway wheel breaks can be uneven wheel rolling on the rolling surface, chipping or flaking, and initial residual tensile stress formed during the hardening of the wheel rim in the manufacturing process [3-5]. It is worth noting that the existing standard methods for calculating the fatigue strength of the wheel due to the loads induced on the wheel in operation do not account for the initial residual stress [1, 2]. Therefore, it is of vital importance to take into consideration the effect of the initial residual stress on the fatigue strength of the wheels at the design stage.

## 2. DEFINITION OF THE PROBLEM

The problem is to determine the level of axial residual stresses in the wheel disc-to-rim transition zone using the tensometry method and consider these stresses in the fatigue strength calculations.

## 3. EXPERIMENTS

The following types of railway wheels (Fig.2) in as-manufactured state are subjected to tests:

- type N 1, solid-rolled wheel with a flat cone disk, 957 mm running tread diameter, compliant with GOST 10791-2011, grade 2 steel;
- type N 2, solid-rolled wheel with a flat cone disk, 957 mm running tread diameter, compliant with GOST 10791-2011, grade T steel;
- type N 3, solid-rolled wheel with a curvilinear disk, 920 mm running tread diameter, BA004 or BA005 type;
- type N 4, solid-rolled wheel with a curvilinear disk, 920 mm running tread diameter, BA318 / 319 type;
- type N 5, solid-rolled wheel with a flat disc, 920 mm running tread diameter, designed for the Desiro RUS Lastochka electric train.

The number of tested wheels: one item of each wheel type was tested.

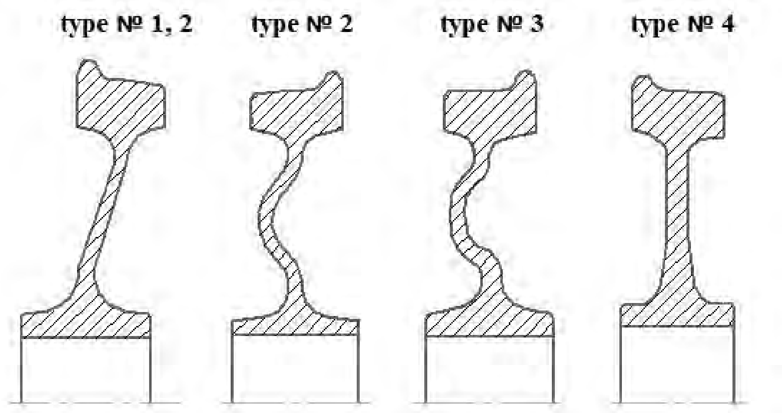


Fig. 2 Test wheels

The axial residual stresses in the disk-to-rim transition zone of the test wheels are determined by the tensometry method in compliance with DIN EN 13262: 2011-06 Standards “Railway applications - Wheelsets and Bogies - Wheels - Product Requirements” (Germany) and GOST R 54093-2010 “Railway Rolling Stock Wheels. Methods for Determining Residual Stresses” (Russia). According to DIN EN 13262: 2011-06 and GOST R 54093-2010, the method for determining residual stresses is based on cutting operations that lead to the sequential release of residual stresses in the wheel.

Variations in residual stresses are evaluated on the surface contour after each cut by measuring local tensions on the inner and outer sides of the wheel with a tensometre.

The tensile strength inside the disk and the rim is derived from a linear extrapolation of the tension evaluated on the surface (according to DIN EN 13262: 2011-06) as well as from the diagrams of the distribution of residual stresses over the wheel cut section (GOST R 54093-2010) . Positioning of strain gauges (tensoresistors) on the wheel is shown in Figure 3. A diagram of phased cutting of the wheel with simultaneous measurement of deformations in the resulting new surface of the wheel is shown in Figure 4.

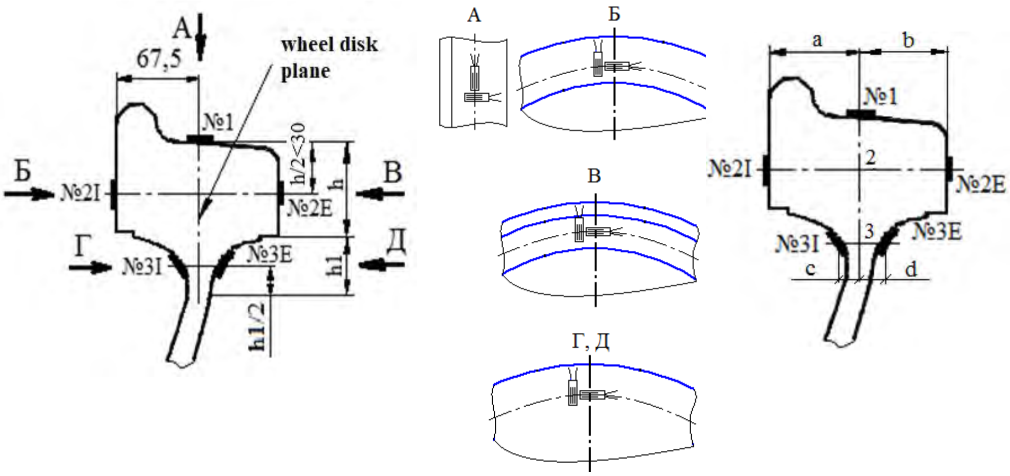


Fig. 3 Diagram of positioning strain gauges (tensoresistors) on the wheel

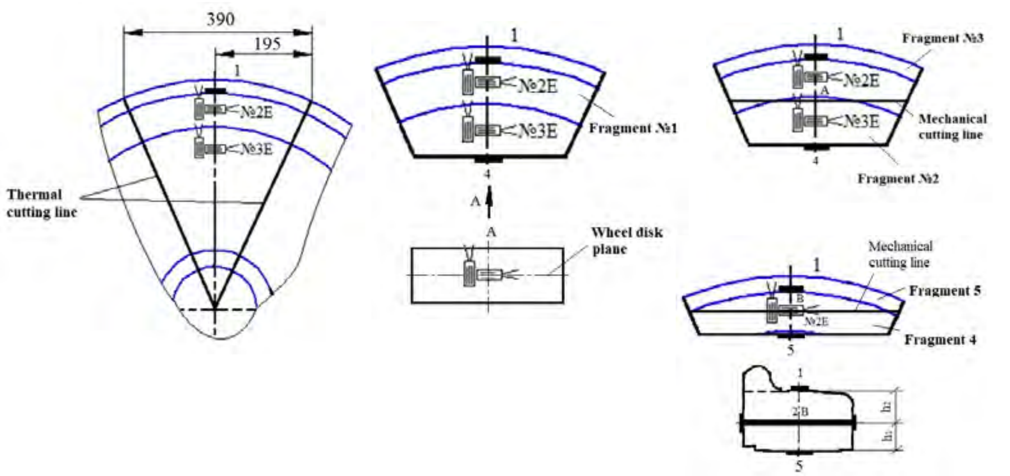


Fig. 4 Diagram of phased cutting of the wheel

Axial stresses in three gauges blocks 1, 2I, 2E, 3I, 3E after cutting out each fragment are calculated by the formula:

$$\sigma_i^{axi} = \frac{E}{1-\mu^2}\left(\varepsilon_i^{axi} + \mu\varepsilon_i^{cir}\right), \quad (1)$$

where E=2.1x10$^5$ MPa is elasticity modulus of wheel steel; μ=0,28 is the Poisson ratio; $\varepsilon_i^{axi}$ is relative axial (radial) deformation; $\varepsilon_i^{cir}$ is relative circumferential deformation; $i$ is the number of the gauge block.

Since the axial deformations in the gauge blocks 2I, 2E, 3I and 3E are determined for the inner (I – internal) and outer (E - external) surfaces of the rim and the rim part of the wheel, the average axial deformations at points 2 and 3 after cutting fragment №1, given the plane of the wheel, are calculated by the formulas:

$$\sigma_2^{axi} = \frac{a}{a+b}\sigma_{2I}^{axi} + \frac{b}{a+b}\sigma_{2E}^{axi}, \quad (2)$$

$$\sigma_3^{axi} = \frac{c}{c+d}\sigma_{3I}^{axi} + \frac{d}{c+d}\sigma_{3E}^{axi}, \quad (3)$$

where a, b, c, d is a distance between the gauge block position and the plane of the wheel (Fig. 3).

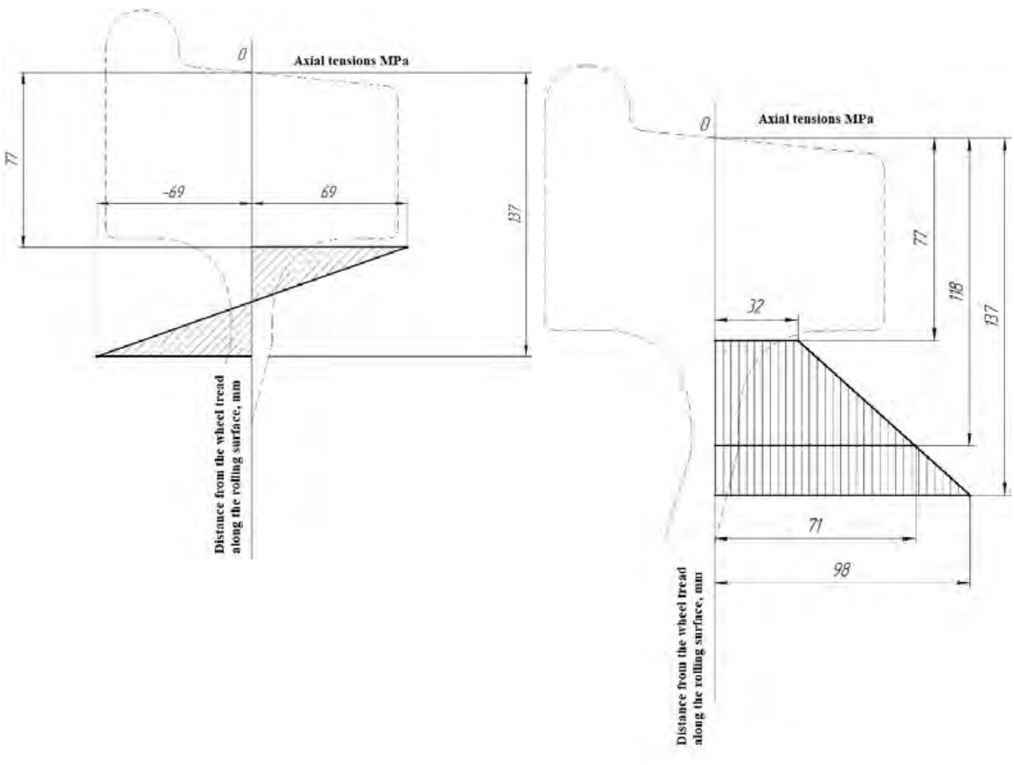


Fig. 5 Diagrams of the distribution of residual axial stresses in a type 1 wheel (left) and type2 wheel (right)

The residual axial stresses in the wheel disk-to-the rim transition zone were calculated by constructing intermediate diagrams after three cuttings. The resulting diagrams of the residual axial stress distribution in the tested wheels are shown in Figures 5 and 6. Figures 5 and 6 illustrate that the initial residual axial stresses (tensile stresses) are present in all types of the wheels in the disk-to-rim transition zone in a range of 41 MPa – 98 MPa.

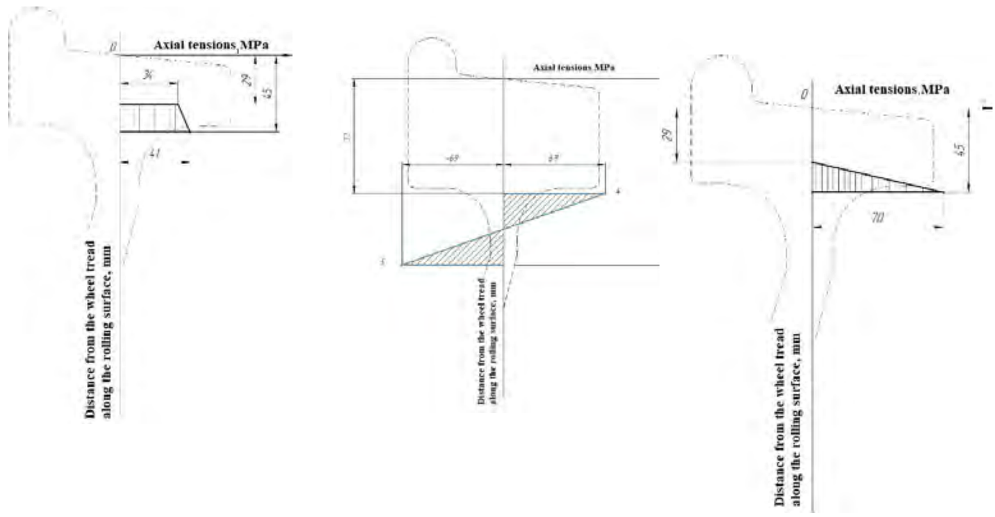


Fig. 6 Diagrams of the distribution of residual axial stresses in type 3, 4 and 5 wheels (from left to right)

The wheel rim residual stress measurements using Ultrasonic (UST) and tensometry methods and their compliance with the standards regulations are compared and presented in Table 1. Sixty percent convergence of the results are due to different measurement evaluation criteria and different algorithms used for the recorded data recalculations. Therefore, the authors rely on the destructive method results.

Table 1 The wheel-rim residual stress measurements by the tensometry method and UST

| Type of wheel | Statement of Compliance With Standards | | | | Convergence of results after UST and tensometry |
|---|---|---|---|---|---|
| | GOST R 54093-2010 (tensometry) | RD 32.144-2000 (UST) | DIN EN 13262:2011-06 | | |
| | | | tensometry | UST | |
| 1 | yes | no | - | - | no |
| 2 | no | no | - | - | *yes* |
| 3 | - | - | no | no | *yes* |
| 4 (continuous cast billet) | - | - | no | yes | no |
| 5 | - | - | no | no | *yes* |

## 4. FATIGUE STRENGTH CALCULATIONS

The fatigue strength values are experimentally obtained for a cone-disc wheel with an axial load of 23.5 tf considering the residual stresses, with the experiment conducted according to [1]. The experimental tests imply the application of a vertical load *P* in the rolling plane and a transverse load *Q* perpendicular to it, fixed in the centre of the wheel [1]. The experimental area is the disk-to-rim transition zone. The fatigue strength factor of the wheel for the experimental area is calculated by the formula:

$$n = \frac{\bar{\sigma}_k^a}{\sigma_{аэ}} \geq [2{,}0], \tag{4}$$

where $\bar{\sigma}_k^a$ is the mean fatigue strength of the disk in the experimental area with variable loading during $10^8$ cycles tests; $\sigma_{аэ}$ is the calculated magnitude of the steady loading of the wheel based on $10^8$ cycles, the effect of which, in terms of damage accumulation, is equivalent to the actual non-steady operational mode for the design service life of the wheel.

The mean fatigue strength in terms of the magnitude taken the decreasing coefficient of 0.75 is calculated by the formula:

$$\bar{\sigma}_k^a = 0{,}75(\bar{\sigma}_k^{max} - \bar{\sigma}_k), \tag{5}$$

where $\bar{\sigma}_k^{max} = 0{,}5\sigma_в = 0{,}5 \cdot 910 = 455$ MPa is the maximal stress of the fatigue strength cycle of grade 2 steel in compliance with GOST 10791-2011, which depends on fatigue strength $\sigma_в$;

$\bar{\sigma}_k = \frac{\bar{\sigma}_k^{max} + \bar{\sigma}_k^{min}}{2} = 250$ MPa is the mean stress of the fatigue strength cycle of grade 2 steel with an asymmetry coefficient r = 0.1. From formula (5), $\bar{\sigma}_k^a = 154$ MPa.

The estimated value of magnitude $\sigma_{аэ}$ is calculated by the expression:

$$\sigma_{аэ} = \sqrt[m]{\frac{N_c}{N_0} \cdot \frac{0{,}5}{1+k_n} \cdot \frac{1}{n} \sum_{i=1}^{n} \sum_{j=1}^{12} \frac{\lambda_j}{\sqrt{2\pi} S_{\sigma_{ij}}} \int_{\sigma_{min}}^{\sigma_{max}} \sigma^m e^{-\frac{(\sigma - \bar{\sigma}_{ij})^2}{2S_{\sigma_{ij}}^2}} d\sigma}, \tag{6}$$

where m = 9 is the fatigue curve exponent of the wheel; $N_0=10^8$ is a base number of cycles; $N_c=30 \cdot 10^8$ is a total number of vertical load cycles for the design service life of the wheel; $s_{min}$ , $s_{max}$ are the minimum and maximum values of the stress magnitude in the experimental zone; j is number of a load block; i is a serial number of various calculated thicknesses of the rim; $k_п$ is the coefficient of the empty mileage of the car; n = 5 is a number of wheels with various rim thicknesses after machining; $\lambda_j$ is the run ratio of the wheel without defects, a flat wheel, and the wheel with uneven rolling in the total mileage of the wheel, respectively, $\lambda_1=0{,}838$; $\lambda_2=0{,}150$; $\lambda_3=0{,}012$;

$\bar{\sigma}_{ij} = \sigma \bar{P}_j \left(1 + 0{,}683 \frac{\bar{Q}_j}{\bar{P}_j}\right)$ is the mean value of stress in a block;

$S_{\sigma_{ij}} = \sigma S_{P_j}\left(1 + 0{,}683\frac{S_{Q_j}}{S_{P_j}}\right)$ is the mean-square deviation in a block.

The mean square deviations calculated by [1] are: $S_{P_1}$=26,5 кN for a wheel without defects; $S_{P_2}$=21,2 кN for a flat wheel; $S_{P_3}$=62,7 кN; $S_Q$=14,2 кN.

According to [1], the vertical loads P and transverse loads Q acting in operation were calculated and grouped in blocks, given the conditions of the wheel (without defects, flat wheel, and uneven rolling), the run ratio of the wheel in each of the three conditions during the service life, and the car condition ( see Table 2). Table 2 shows the mean Mises stresses calculated using SolidWorks / Simulation and the formulas mentioned above.

Table 2 Mises stresses in the experimental area of type 1 wheel appearing during the service life

| Load block number j | Condition of the car | Actual loading, кН | Run ratio λ | The mean Mises stress $\bar{\sigma}$ in the computational area while machining, MPa | | | | |
|---|---|---|---|---|---|---|---|---|
| | | | | n=0 | n=1 | n=2 | n=3 | n=4 |
| 1 | Loaded | $\bar{P}_1$=142,8 | 0,2514 | 45 | 50 | 55 | 57 | 60 |
| 2 | | $\bar{P}_2$=196,9 | 0,045 | 55 | 60 | 65 | 72 | 77 |
| 3 | | $\bar{P}_3$=273,8 | 0,0036 | 75 | 85 | 90 | 100 | 110 |
| 4 | Empty | $\bar{P}_1$=37,3 | 0,1676 | 10 | 11 | 12 | 15 | 16 |
| 5 | | $\bar{P}_2$=51,4 | 0,03 | 15 | 18 | 19 | 21 | 22 |
| 6 | | $\bar{P}_3$=182,7 | 0,0024 | 50 | 55 | 60 | 70 | 75 |
| 7 | Loaded | $\bar{P}_1$=142,8 Q=21,7 | 0,2514 | 48 | 53 | 60 | 64 | 69 |
| 8 | | $\bar{P}_2$=196,9 Q=21,7 | 0,045 | 60 | 70 | 78 | 82 | 92 |
| 9 | | $\bar{P}_3$=273,8 Q=21,7 | 0,0036 | 80 | 90 | 100 | 110 | 120 |
| 10 | Empty | $\bar{P}_1$=37,3 Q=5,67 | 0,1676 | 10 | 12 | 15 | 17 | 18 |
| 11 | | $\bar{P}_2$=51,4 Q=5,67 | 0,03 | 15 | 19 | 21 | 22 | 24 |
| 12 | | $\bar{P}_3$=182,7 Q=5,67 | 0,0024 | 55 | 60 | 67 | 73 | 76 |
| Note: $\bar{P}_1$ is for the wheel without running surface defects; $\bar{P}_2$ is for a flat wheel; $\bar{P}_3$ is for the wheel with uneven rolling | | | | | | | | |

Using the data of Table 2 and formulas (4) - (6), the fatigue strength factor of a type 1 wheel in the disc-to-rim transition area is n = 2.05, which exceeds the permissible value n = 2.0 [1]. With axial residual stresses in a type 1 wheel as-manufactured, the wheel fatigue strength factor is reduced to $n_r$ = 1.2, which may cause its breakage from excessive operational loads. The effect of the wheel machining during service life on the residual stress changes in the near-rim area has not been studied. The fatigue

strength values for a type 4 wheel are similar to those of type 1. For type 2 and 5wheels, n = 1.7 and $n_r$ = 1.0. For a type 3 wheel, n = 2,3 and $n_r$ = 1,5.
The described method of calculating the fatigue strength factor is valid only for the disk-to-rim transition area [1]. To correctly calculate the fatigue strength factors for wheels with a curvilinear disc, other algorithms are to be used as this kind of wheels has different stress zones effected by vertical and transverse loads, and their maximum axial residual stress zones are different, too.

## 5. CONCLUDING REMARKS

Since wheel failures caused by fatigue cracks in the zone of the disc-to-rim transition area occur before the end of the service life, account must be taken of the residual stresses when calculating the wheel strength under dynamic loads.

## 6. REFERENCES

[1] Regulatory standards for calculation and design of the 1520 mm gauge wagons of the Ministry of Railways (non-self-propelled). GosNIIV-VNIIZhT: 1996, 319 p.
[2] **Yakushev, A.V. - Arkhipova, A. E. - Getmanets, R. M. et al.**: The calculations of the Safety Factor of a Cone-Disc Wheel Set by Means of Mathcad - Internet magazine "Naukovedenie" Issue 5 (24), September - October 2014, p.1-11.
[3] **Ivanov, I. A. – Kononov, D. P. – Urushev, S. V. – Yakushev, A. V.:** Residual Stresses in Solid-Rolled Wheels after Hardening - Izvestiya PGUPS, 2016/3 p.337-343.
[4] **Kerentcev, D. E. – Ponomarev, Ju. K.:** The influence of residual technological stress and service heat loads on the strength of railway wheels – VESTNIK of Samara University, Aerospace and Mechanical Engineering, T.14, №3, P.2, 2015, p.336-344.
[5] **Kuhlman, C. – Sehitoglu, H. – Gallagher, M.:** The Significance of material properties on stresses developed during quenching of railroad wheels – Proceedings of the 1988 Joint ASME/IEEE Railroad Conference, The American Society of Mechanical Engineers, New York.

# ON WHEEL PROFILE OPTIMIZATION BY GENETIC ALGORITHM

**Adrien ALBON**

ALSTOM
F-17440 Aytré, France

*Received: November 5, 2018*

## ABSTRACT

Decrease the wear of the wheel by profile optimization while maintaining a correct dynamic behavior could be difficult. This document purposes a methodology to optimize the wheel profile in the same time than other dynamics parameters are maintained.

*Keywords:* railway wheel-profile, genetic optimization, wear

## 1. INTRODUCTION & OBJECTIVE

To design a wheel profile is generally a difficult task, mainly concerning the equivalent conicity impact and evolution aspects. Indeed, a same value of this parameter could lead to opposite effects for curving ability or lateral stability/comfort:

- vehicle stability: high conicity is more likely to give rise to wheelset or bogie hunting instability,
- curving behavior: high conicity gives more steering of the wheelset in curves,
- Vehicle ride : high conicity makes the wheelset more susceptible to lateral track geometry.

In addition, a small difference on the wheel profile could lead to a strong difference on the dynamic behavior of the tram. The drawings here-after are an illustration to show how the wheel profile can influence the dynamic behavior of the tramway. Two different wheels have been implemented on the same dynamic model of tram. Wear number on curve and trainset stability on alignment have been compared.

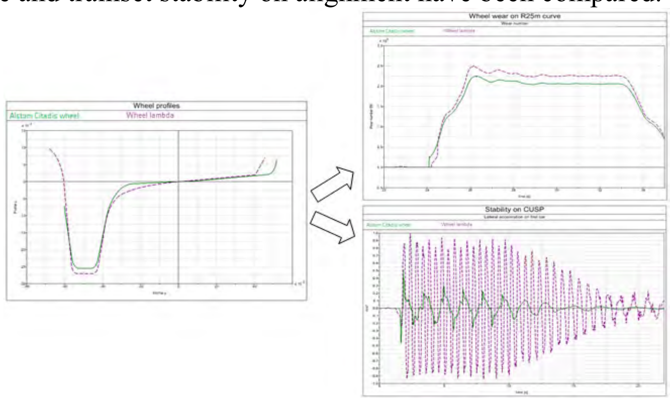


Fig. 1 Influence of the wheel profile dynamic behavior

The hard work is to choose the best compromise regarding the network and the product.

However, 90% of the Citadis® trams use the same wheel profile whereas network could be very different in term of:

- Distribution of percentage of curves and percentage of alignment
- Rail profile
- Rail quality
- Rail gauge
- Track quality

This standard wheel is a compromise which induces a quite good dynamic behavior in most of the cases but not the best one for each specific network.
The objective of this paper is to describe a methodology which allows designing a specific optimized wheel profile for each network taking into account the environment of the tram in order to optimize its dynamic behavior, especially the wear of the wheel.

## 2. GENETIC ALGORITHM APPLIED TO THE WHEEL OPTIMIZATION

### 2.1 Concept of genetic algorithm

The wheel optimization is based on the genetic algorithm (GA) method. A GA is a metaheuristic inspired by the process of natural selection. GA are commonly used to generate high-quality solutions to optimization and search problems by relying on bio-inspired operators such as mutation, crossover and selection. The principle is to create a population of individuals which will evolve by itself regarding a specific problematic. GA are well adapted when the problem has huge range of possible solution and when there are several criteria to optimize.
The different steps of the algorithm are indicated on the following flow chart.

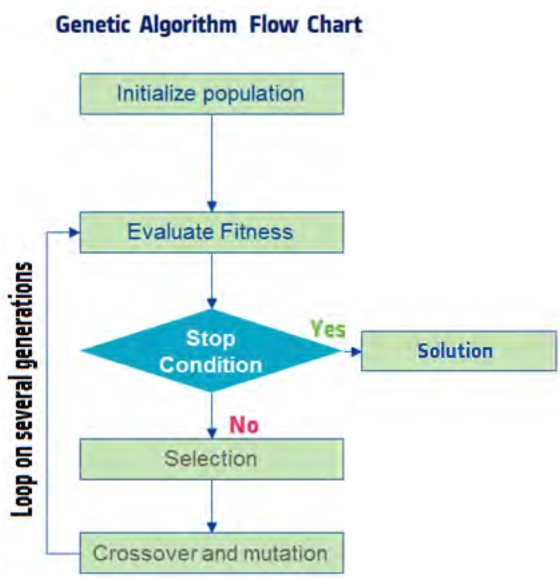


Fig. 2 Genetic algorithm flow chart

### 2.2 Steps of the genetic algorithm

Terminology

Before to start, it is important to define some specific key words:

| Terms | Generic definition | Application to wheel optimization |
|---|---|---|
| Population | Set of individuals | Set of dynamics models of tram |
| Individual | Set of chromosomes | Dynamic model of trams. All models are similar exept for the wheel profiles. |
| Chromosome | Set of genes | Wheel profile. The wheel profile is defined by a set of geometrical parameters |
| Gene | Set of allels | 1 geometrical parameter of the wheel profile |
| Allel | Expression of gene | Value for a geometrical parameter |

Initialisation of the population

It consists on the generation of an initial population composed by random individuals. By random means that the value of each parameter (gene), which acts on the problem, is defined randomly inside a defined search area.

**<u>Application to wheel optimisation</u>** :

The population is composed by dynamics models which are all similar in terms of masses, suspensions and environment where they evolve. However, each model has its own wheel profile. Indeed, at the first generation, the program assign random wheels to each model. Therefore, the wheel profiles have been defined by geometrical parameters such as radius, angles, lengths or slopes. These geometrical parameters, indicated on the following drawing, are allocated from A to N letters.

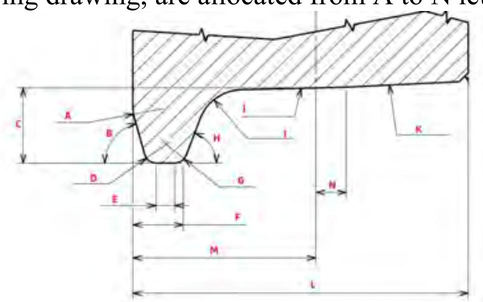


Fig. 3 Geometrical parameters for the wheel profile

Next, they are set with random values which are chosen inside a range area, previously fixed by the user. In addition, the user has the possibility to define some constraints on the wheel profile like the range areas for Sd, Sh, qR values and for the equivalent conicity.

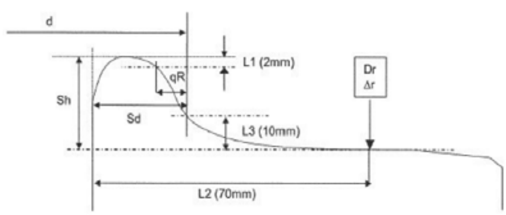


Fig. 4: Geometrical constraints for the wheel profiles

It is important to note that for performance reasons of the GA, the values of geometrical parameters for each wheel profile are converted into the binary sytem. The following table represents an example of chain of bits for different wheel profiles.

| | A | B | C | D | E | F | G | H | I | J | K | L | M | N |
|---|---|---|---|---|---|---|---|---|---|---|---|---|---|---|
| Wheel profile for tram 1 | 0 1 0 1 0 0 0 0 | 0 0 1 1 1 1 1 1 | 0 0 0 0 1 0 1 0 | 1 0 1 1 0 1 0 1 | 0 0 0 1 1 0 0 0 | 0 1 1 0 0 1 1 1 | 0 1 1 0 1 1 1 0 | 0 0 1 0 1 0 1 0 | 1 0 0 1 0 1 0 1 | 1 1 1 0 1 1 0 1 | 0 1 1 1 0 1 1 1 | 1 1 0 0 1 1 0 1 | 1 1 0 1 1 0 0 1 | 0 0 1 1 0 0 1 0 |
| Wheel profile for tram 2 | 0 1 0 0 0 1 1 1 | 1 0 0 1 1 0 1 1 | 0 0 0 1 1 0 0 1 | 0 1 0 0 1 0 0 1 | 1 1 1 1 0 1 0 1 | 1 0 1 1 1 1 1 0 | 0 1 1 0 1 0 1 1 | 1 1 0 1 1 1 1 0 | 1 1 1 1 0 1 1 0 | 0 1 0 0 1 0 1 0 | 0 0 1 1 1 0 1 0 | 1 1 1 0 0 1 0 0 | 0 1 1 1 0 0 1 1 | 1 1 1 0 0 0 1 1 |
| .. | | | | | | | | | | | | | | |
| Wheel profile for tram N | 0 0 1 1 1 1 1 1 | 1 0 1 1 0 1 1 1 | 1 1 1 1 0 0 1 1 | 0 1 0 0 0 1 0 0 | 1 0 1 0 0 1 0 1 | 0 0 0 0 1 1 1 1 | 0 1 0 0 0 1 1 0 | 0 1 0 1 1 0 1 0 | 0 0 0 1 0 0 1 1 | 0 0 1 0 1 1 1 1 | 0 0 1 0 1 1 0 1 | 0 1 1 0 1 1 0 0 | 1 0 1 0 0 0 1 1 | 0 1 0 1 0 1 0 0 |

Fig. 5: Example of wheel profile definition for a generation

**Selection**

It consists on the evaluation of each individual regarding the problem to solve. The idea of selection phase is to select the fittest individuals and let them pass their best genes to the next generation.

As a first step, a fitness function has to be defined in order to assign a quotation to each individual related to its capacity to fit to the environment.

Next, a selection has to be made for detecting the most fitted individuals and to pass them to the next generation. Different methods of selection exist but the most common is the wheel selection. This method distributes all individuals on a wheel where the fittest make up greater portions. Thus, they have more chance to be selected.

| | Quotation (/1) | Chance to be selected |
|---|---|---|
| Individual 1 | 0.9 | 28.1% |
| Individual 2 | 0.5 | 15.6% |
| Individual 3 | 0.1 | 3.1% |
| Individual 4 | 0.6 | 18.8% |
| Individual 5 | 0.8 | 25.0% |
| Individual 6 | 0.3 | 9.4% |

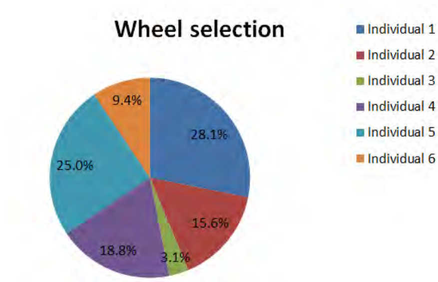


Fig. 6 Illustration for the wheel selection

**Application to wheel optimisation** :

The dynamic behaviour of each model is evaluated with a dynamic software (Simpack). The complete tram model is built (duplicated for each individual) and the different wheel profiles are put on each model. Next, the objective is to define the environment where will be assessed the different model depending on the criteria we decide to optimize. In our case, the optimisation concerns different aspects :

- On a R25m curve radius at the velocity of 18km/h :
    - The wear number (N) of the external wheel of the front wheelset:

$$N = |T_x \cdot v_x| + |T_y \cdot v_y| + |M_z \cdot \varphi_z| \ , \tag{1}$$

    - The average of the wear number from all wheels of the train (Na),
    - The derailment criterion for all wheels (Y/Q),
    - Lateral forces fro the wheelsets to the rail (SY).
- On alignment with a lateral defect at maximum speed. The objective is to check how the tram absorbs the accelerations after the collision with the defect. Therefore, the maximum lateral accelerations on the cars (AQ) between 10 seconds after the defect and 30 seconds after the defect are taken into account.

Indeed, the train has to be efficient both on curve and on alignment. Consequently, the assessment of an individual will be a combination of the here-above criteria. The fitness function is the following:

$$f_i = \frac{\left( \frac{N_i}{N_{\max}} + \frac{Na_i}{Na_{\max}} + \frac{Y/Q_i}{Y/Q_{\max}} + \frac{AQ_i}{AQ_{\max}} + \right)}{Nb_{criteria}},$$

where: $X_i$ is the value of the criterion for the current individual
$X_{max}$ is defined by the user as the worst value for the criterion
$Nb_{criteria}$ is the number of criteria which are considered (4 in our case)

**Crossover**

The crossover phase consists on sharing information (genes) between the fittest individuals. Two parents, selected during the previous phase, combine their genetic information in order to generate new offspring. New solutions are generated from an existing solution, analogous to the crossover that happens during sexual reproduction in biology.

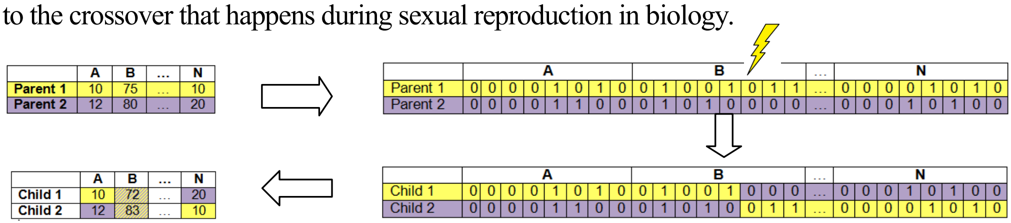


Fig. 7 Example of crossover application

**Mutation**

Mutation is used to maintain genetic diversity from one generation of a population of chromosomes to the next. Mutation alters one or more gene values in a chromosome from its initial state. The probability of mutation should be set low in order to avoid transforming the search into a primitive random search.

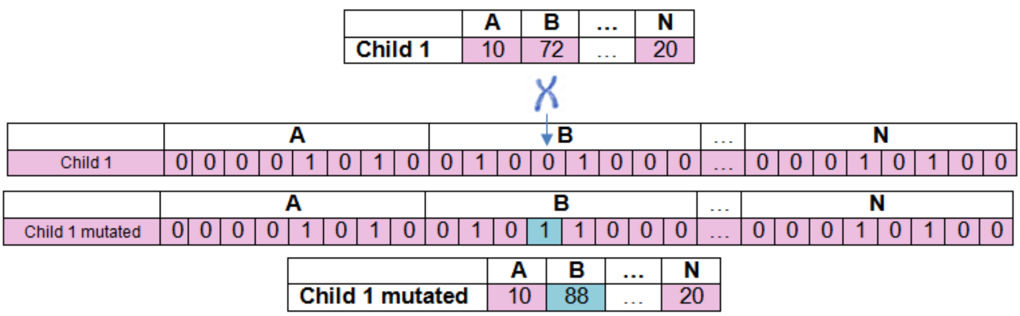


Fig. 8 Example of mutation application

## 3. OPTIMIZATION OF CITADIS® WHEEL PROFILE

### 3.1 Hypothesis of calculation

**Model**

The wheel profile optimisation is led on the new generation of Citadis® equipped with 3 Arpege bogies. The simulation model is a 30m length.

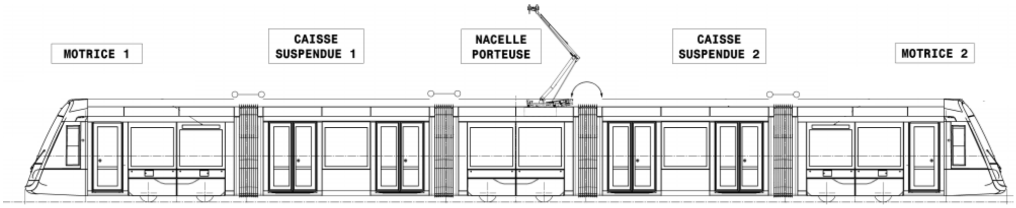


Fig. 9 Diagram of the model used for optimization

**Track**

The track is an alignment 400m followed by a R25m curve radius of 35m length. The tram is running at 70 km/h and met a the lateral defect at the beginning of the alignment. 30s after the defect, the tramway will decrease its velocity to 18km/h in order to pass the curve.

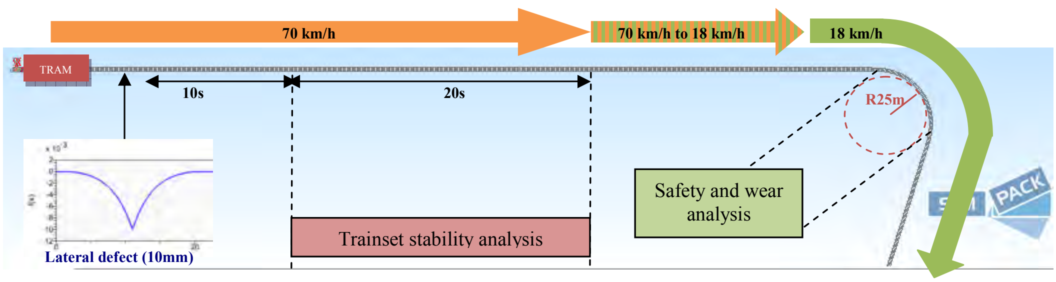


Fig. 10/a Track used for wheel profile optimization

The rail profile considered for this optimization is Ri54G2.

Genetic algorithm parameters

| | |
|---|---|
| Size of population | 100 |
| Number of generations | 10 |
| Crossover rate | 80% |
| Mutation rate | 3% |

## 3.2 Results of the optimization

The here-under plot (Fig.10/b) shows the fitness assessements for each individual over 10 generations. The quotations are contained between 0 and 1 (0 is the worst individual). The green dotted line represents the quotation for the B05 wheel profile (which is the reference profile used on the majority of the Citadis® fleet). We can observe that at the first generation, several found wheel profiles are already better than the reference. At the 6$^{th}$ generation, the program builds a better profile by combination of the parameters from the other fittest wheels. This phenomenon is reproduced at the 10$^{th}$ generation where the quotation of 0.755 is reached.

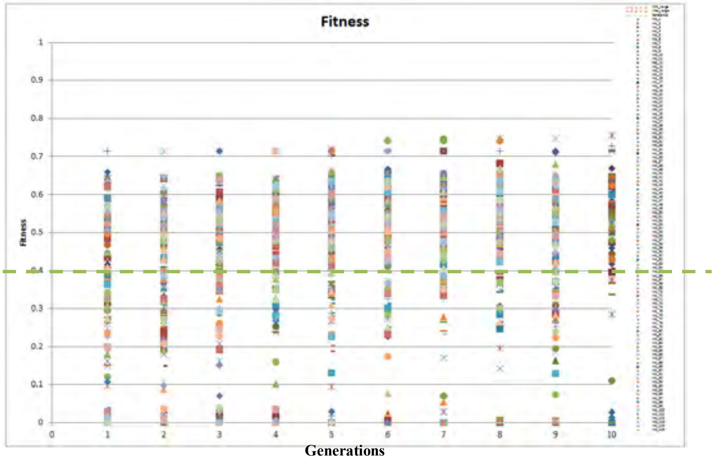


Fig. 10/b  Track used for wheel profile optimization

### 3.3 Best solution from GA vs reference wheel

The following drawing compares the reference wheel profile to the best solution found by the program.

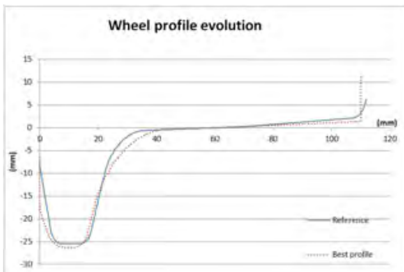


| Regerence profile | Best solution |
|---|---|
| 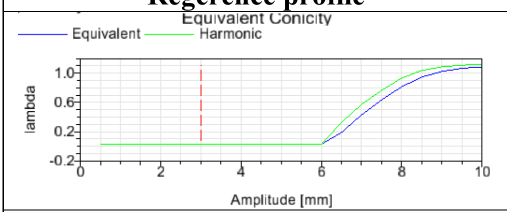 | 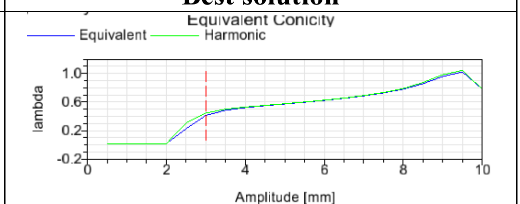 |
| 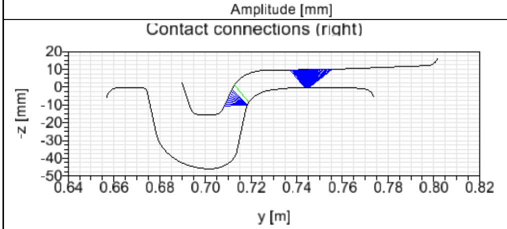 | 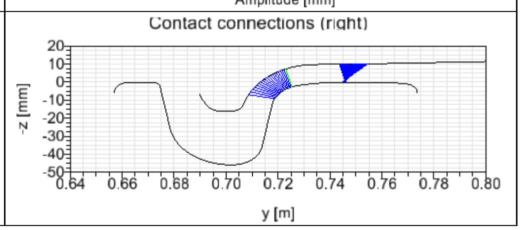 |



It can observed that the equivalent conicity of the best solution is quite higher than the reference at +/-3mm. We can also observe a better distribution of the contact points, in particular on the flange transition area.

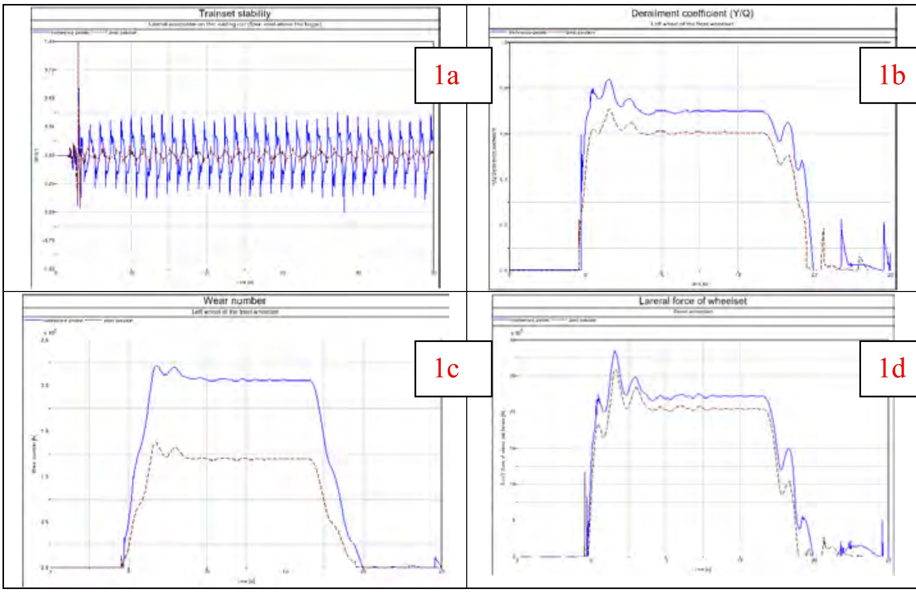


Fig. 11 Optimization results

On, the different plots here-above, we can observe that all criteria checked by the optimization program have been improved:

- **1a**: the lateral acceleration measured after the defect collision have been decreased by 75% on the floor of the leading car (from 0.35m/s² to 0.09m/s²)
- **1b**: the Y/Q coefficient with the best solution has been decreased by 15% (0.84 to 0.71)
- **1c**: the wear number has been decreased by 38% (from 2227 to 1376)
- **1d**: the lateral forces from the wheelset to the rail have been decreased by 9% (from 28519N to 25961N)

## 4. CONCLUDING REMARKS

In conclusion, the preliminary optimization, done only on 100 individuals over 10 generations gave interesting results. The dynamic behaviour, obtained with the found wheel profile, has been improved for all considered criteria, in particular the wear number. The tool seems to be able to build adapted wheel for any specific network by changing environment or models. The next step are the following :

- To integer other criteria in the assessment such as bogie stability or comfort
- To integer other constraints such as track quality in the environment
- To test the wheel profile found by the opitmization in real condition and to confirm this conclusion.

## 5. REFERENCES

[1] **EN14363**: Railway applications – Testing and Simulation for the acceptance of running characteristics of railway vehicles – Runnin Behaviour and stationary tests, 2016.

[2] **EN14811**: Railway applications – Tracks – Special purpose rail – Grooved and associated construction, January 2010

[3] **UIC519**: Method for determining the equivalent conicity

# VERTICAL DYNAMICAL LOADING CONDITIONS OF DRIVEN WHEEL-SETS

**András SZABÓ and István ZOBORY**

Department of Aeronautics, Naval Architecture and Railway Vehicles
Faculty of Transportation Engineering and Vehicle Engineering
Budapest University of Technology and Economics
H-1521 Budapest, Hungary

*Received: November 5, 2018*

## ABSTRACT

In the paper a model-based identification procedure will be introduced which has been elaborated at the Department of Railway Vehicles and Vehicle System Analysis of the BME. The goal was to assess the vertical dynamic forces acting in the wheel-rail contact, which forces – due to a hypotheses - could be able to the drive forward the crack process of experienced on the wheel-tyre of the electro-locomotive type V43. The estimation of the vertical wheel-rail contact forces starts with the measuring of the axle-box vertical acceleration. Using dynamical simulation model the connection between the axle-box accelerations and the vertical wheel-rail forces is determined, and on the basis of this correlation the real vertical wheel-rail contact forces attacking the tyre can be estimated from the measured vertical axle-box accelerations. The statistical evaluation of the vertical forces is carried out for the sake of determining the role/effect of the dynamic vertical wheel/rail contact forces on the experienced occurrence of wheel-tyre cracks.

*Keywords:* model-based identification, dynamical simulation, acceleration measurements.

## 1. INTRODUCTION

In the operation of the electro-locomotive type V43 (see in Fig 1.) wheel-tyre cracks have been found by the maintenance personals. The BME was asked for doing research work in order to recognize and identify the possible causes of this safety relevant phenomenon. The cracks were always originated in the identification letters and figures on the side-planes of the tyre, which identification signs were made still in the course of producing the tyres (hopefully) in glowing state including certain notches. The notch type surface disturbance could be in itself a cause of emerging cracks, depending on the actual geometry (e.g. sharp groove bottoms) of the notch. At the same time the up-keeper firm initiated an investigation into the range of the dynamic vertical wheel/rail forces occurring due to the excitation effect of the track irregularities (unevennesses) [1].

The direct measurement of the vertical wheel/rail contact forces is very problematic, thus an indirect way has been followed. Basically there were two branches of the examinations. On the one hand, field tests were carried out to get full-scale information on the accelerations occurring on the un-sprung points of the bogie side-frame just over the axle-boxes when the locomotive runs at the maximum permitted speed in the course of scheduled Inter-City train operation. In this way it was possible to assess the dynamical responses in the locomotive in form of vertical acceleration processes caused by the excitation effects coming from the vertical interaction with track of given quality. On the other hand the vertical and pitching dynamical model of the electro-locomotive under examination has been elaborated. The model dynamical parameters were known, thus it was possible to carry out simulations by unified form track unevenness excitations, for determining the vertical axle-box acceleration processes and the dynamic vertical wheel/rail contact force processes [2],[3]. In this way it was possible, to evaluate the functional relationship between the axle-box accelerations and the wheel/rail contact forces. On the basis of the so generated relationship, it was possible to process the really measured vertical axle-box accelerations, if they can be caused so high vertical wheel/rail forces that can initiate to drive the cracks from the mentioned notches coming from the identification numbers and letters on the side planes of the tyre.


Fig. 1 The electro-loco type V43

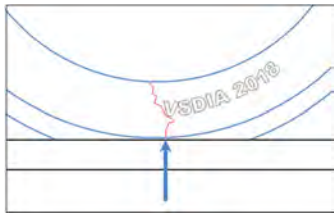


Fig. 2 The crack appearing on tyre

## 2. VERTICAL WHEEL-SET FORCE ESTIMATION BASED UPON VERTICAL ACCELERATION MEASUREMENTS AND SIMULATION BY THE VERTICAL AND PITCHING DYNAMICAL MODEL OF THE LOCOMOTIVE

### 2.1 The axle-box acceleration measuring system

For the measuring of the vertical acceleration of the wheels the accelerometers were mounted on the un-sprung axle-connecting side-beam of the locomotive bogie over the axle-boxes. The position of the accelerometers on the bogie side-beam can be seen in Fig. 3. The little adapter, which gave easy possibility of installing the accelerometers is shown in Fig. 4.


Fig. 3 Places of the accelerometers to be mounted on the bogie frame.

Fig. 4 The accelerometer type SETRA and the adapter.

The scheme of the measuring system is shown in Fig 5. The power source for supplying both the Laptop PC and the data collector type SPIDER 8 was the accumulator of the locomotive. The four SETRA-type accelerometers were connected to the SPIDER-type data collector and the data collector passed on the measured signals to the computer. The sampling frequency of the acceleration measurements was 1200 Hz.

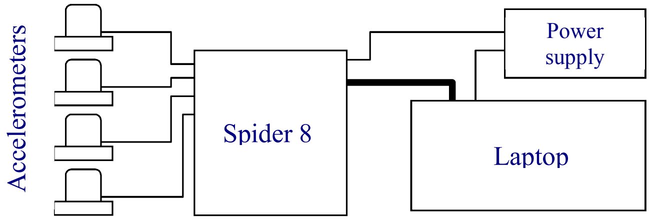


Fig. 5 The measuring system

### 2.2 Determination of the travelling velocity

The computation of the travelling velocity was based on the info contained by the vertical acceleration signals measured over the axle boxes of the bogie. The axle-base $l$ of the bogie was known as it is indicated in Fig 6. The measured peaks in the vertical acceleration caused by the track irregularities appear both at the front and rear axles of the bogie. The distance measured with time between the emergence of the characteristic (almost congruent) acceleration peaks in the acceleration signals taken from the front wheel and from the rear wheel is designated by $\tau$ is inversely proportional to the loco's velocity $v$, thus, after rearrangement: $v = l / \tau$ (see Fig. 7).

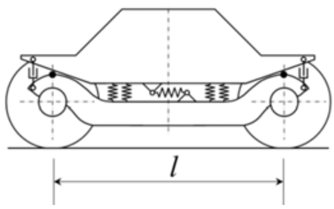


Fig. 6 Axle-distance of the bogie

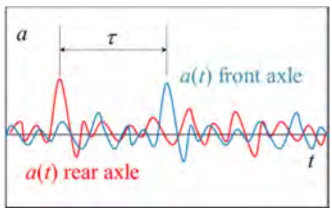


Fig. 7 Signal for computation of the travelling velocity

## 3. EVALUATION OF THE ACCELERATION MEASUREMENT RESULTS CONCERNING THE 11 TRACK SECTIONS ASSIGNED

Continuous acceleration measurements were realized during the normal (scheduled) operation of the „Round IC" from Budapest to Budapest via Debrecen. The maximum velocity of the V43 loco was 100-120 km/h. The trip was divided 11 track sections, and the numbering of these sections is shown in the Table 1.

| Numbering of the track sections: | | | | | |
|---|---|---|---|---|---|
| 1 | Budapest Keleti Pu. – Füzesabony | 5 | Tokaj – Nyíregyháza | 9 | Püspökladány – Szolnok |
| 2 | Füzesabony – Miskolc Tiszai Pu. | 6 | Nyíregyháza – Debrecen | 10 | Szolnok - Cegléd |
| 3 | Miskolc Tiszai Pu. – Szerencs | 7 | Debrecen – Hajdúszoboszló | 11 | Cegléd – Budapest Nyugati Pu. |
| 4 | Szerencs – Tokaj | 8 | Hajdúszoboszló - Püspökladány | | |

Table 1 The track sections of the „Round IC".

Between the adjacent track-sections covered there were short stops, when there was enough time to save the measured raw data, taken by using a sampling frequency 1200 Hz. During of the measuring process the track quality was also subjectively noticed and manually recorded.

The measuring results and the statistical evaluations of them for each track section can be seen in Fig. 8 below. In the sub-figures the speed-timing diagrams, the vertical axle-box acceleration vs. time diagrams of the four locomotive axles (in a common plot), and the relative frequency histograms of the vertical axle-box accelerations (in separate plots for the four axle) are shown. In the little tables there are the main statistical values: maxima, minima and dispersions. In the least (12th) box the summarization of these numerical statistical values is given.

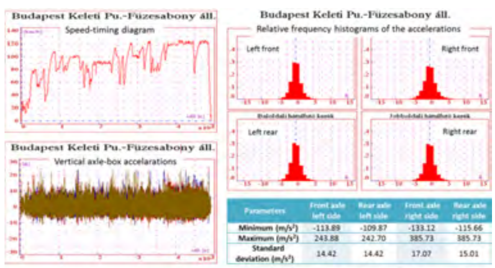

Measured results, Track section: No.1

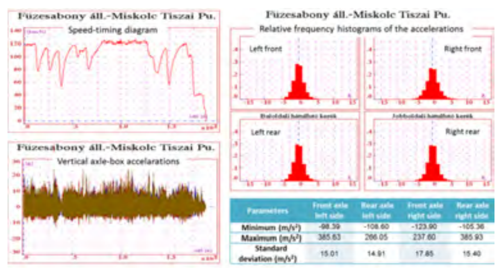

Measured results, Track section: No.2

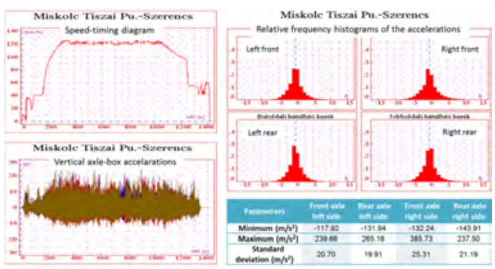

Measured results, Track section: No.3

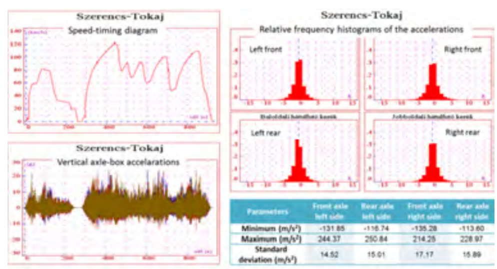

Measured results, Track section: No.4

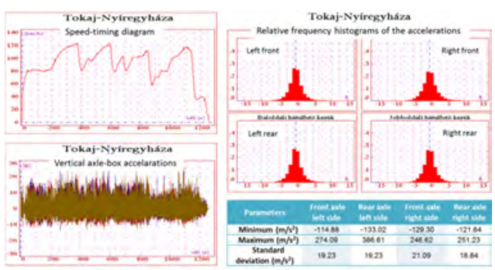

Measured results, Track section: No.5

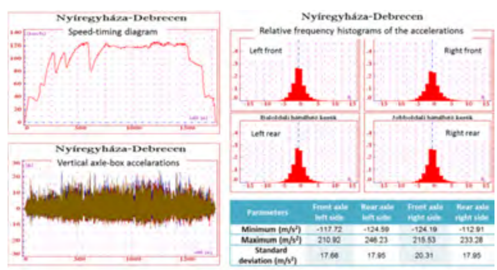

Measured results, Track section: No.6

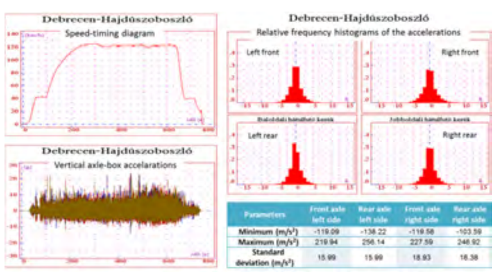

Measured results, Track section: No.7

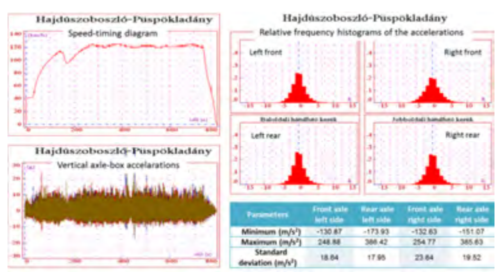

Measured results, Track section: No.8

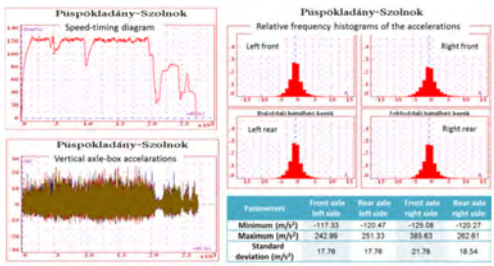


Measured results, Track section: No.9

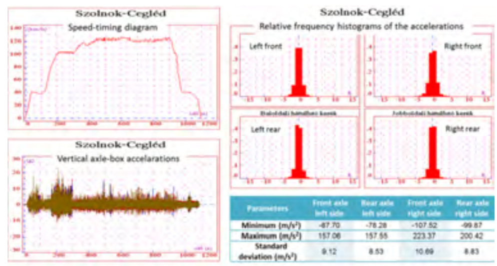


Measured results, Track section: No.10

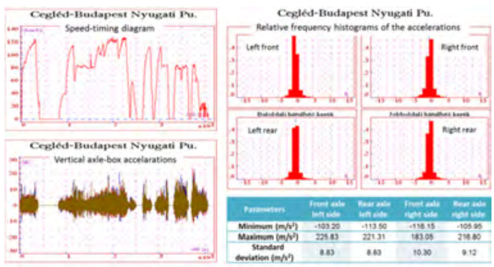


Measured results, Track section: No.11

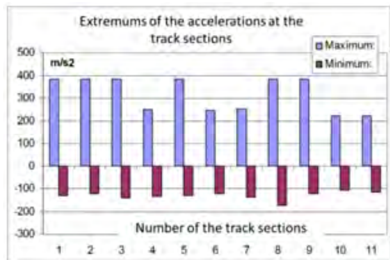


Statistics of the measured results

Fig. 8 Evaluation of the measurement results.

It can be seen in the diagrams, that where the vertical axle-box acceleration has lower maximum value and the relative frequency histogram of the vertical acceleration covers a narrower band, there the track quality is higher. The illustrated maximum and minimum values of the vertical axle-boxes accelerations represent the most disadvantageous dynamical interaction between the rails of the considered 11 track sections and the loco of type V43.

## 4. DYNAMICAL SIMULATION MODEL FOR DETERMINING THE WHEEL-SET FORCES BASED UPON ARTIFICIAL SHOCK-LIKE EXCTITATIONS

To determine the maximum vertical force arising in the wheel-rail contact it is necessary to know the relationship between the measured axle-box vertical accelerations and the force in the question. Since the relationship in question depends on all the inertial, stiffness and dissipative features of the vehicle-track system, it is necessary to use a complex vehicle/track simulation model to determine the required characteristics. The elaborated complex vehicle/track dynamical model is shown in Fig 9.

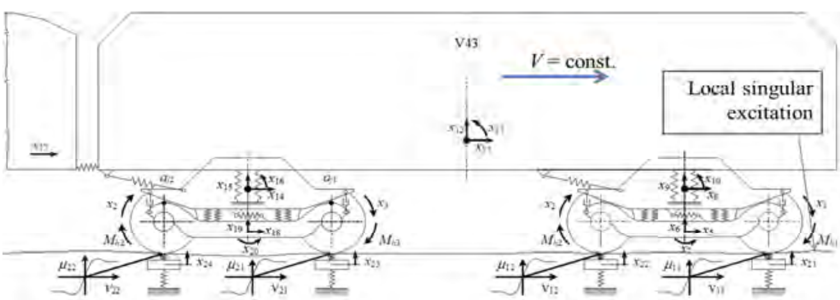


Fig. 9 The combined dynamical model of electro-loco V43 and the track

This vertical in-plane dynamical model is of 18 degrees of freedom for the vehicle and further 4 degrees of freedom for describing the motion of track under the wheel-sets. The main question is the peaks of the vertical wheel-rail contact forces, which are mainly generated when the loco moving over the local track irregularity.

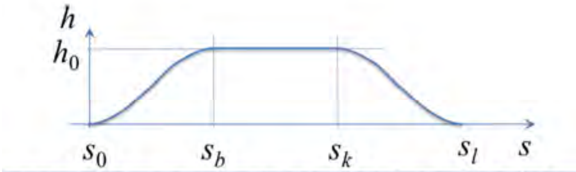


| $h_0$ (mm) | 0.75 | 1.5 | 2.0 | 2.6 | 3.0 | 3.5 | 4.0 | 4.5 |
|---|---|---|---|---|---|---|---|---|

Fig. 10 The local singular excitation profile.

As it is described above, the applied singular excitation function $h(s)$ depends on the longitudinal track coordinate $s$ and there are three adjacent intervals on axis $s$. The three intervals are as follows: $[s_0,s_b]$ where $h(s)$ is increasing, $[s_b,s_k]$ over which h = $h_0$, and $[s_k,s_l]$ over which $h(s)$ is decreasing down to zero. Over the three intervals the function $h(s)$ is determined by the following relationships:

$$[s_0, s_b]: h = h_0 \left(1 - \cos\left(\pi \frac{s-s_0}{s_b-s_0}\right)/2\right) \tag{1}$$

$$[s_b, s_k]: h = h_0 \tag{2}$$

$$[s_k, s_l]: h = h_0 \left(1 + \cos\left(\pi \frac{s-s_k}{s_l-s_k}\right)/2\right) \tag{3}$$

The lengths of the above intervals are as follows: $s_b-s_0$=300 $mm$, $s_k-s_b$=50 $mm$, $s_l-s_k$=300 $mm$. To prepare the simulation the first step is to build up the motion equations of the examined nonlinear vehicle-track system in form of a set of ordinary differential equations. Let $\mathbf{x}$ be the vector of the *free coordinates*, so the *motion state vector* $\mathbf{Y}$ is composed by the following definition:

$$\mathbf{Y} = \begin{bmatrix} \dot{\mathbf{x}} \\ \mathbf{x} \end{bmatrix} \tag{4}$$

Based on this motion state vector the nonlinear differential equation-system of the dynamical model gets the following form:

$$\dot{\mathbf{Y}} = \mathbf{A}\mathbf{Y} + \mathbf{F}(t, \mathbf{Y}), \tag{5}$$

where the $\dot{\mathbf{Y}}$ derivative defines the so called *direction-field*, $\mathbf{A}$ is the matrix of the linear part of the differential equation-system while $\mathbf{F}(t,\mathbf{Y})$ represents the nonlinear part and contains also the outer time dependent excitation acting on the system in normal operation, travelling along the track at a constant velocity $v$. For getting a unique solution, it is necessary yet to prescribe the initial condition vector $\mathbf{Y}_0$ belonging to the initial time instant $t_0$ of the simulation:

$$\mathbf{Y_0} = \mathbf{Y}(t_0). \tag{6}$$

The computer program was elaborated direct for the sake of the above dynamical investigations in MATLAB environment.

## 5. DETERMINATION OF THE CORRELATIVE CONNECTION BETWEEN THE SIMULATED MAXIMUM VERTICAL WHEEL-SET FORCES AND THE MAXIMUM VERTICAL WHEEL-SET ACCELERATIONS

The results of the dynamical simulations are shown in Figure-sets 11 and 12 below. In the set of figures the vertical axle-box accelerations are shown as function of the time, during the time period when the loco is running over the above introduced artificial local excitation. In Figure-set 11 the diagrams belong to travelling speed 100 km/h, while in Figure-set 12 the results belong to travelling speed 120 km/h.

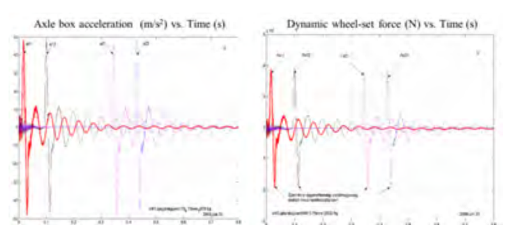

Simulations results: $V = 100$ km/h, $h_0 = 0.75$ mm

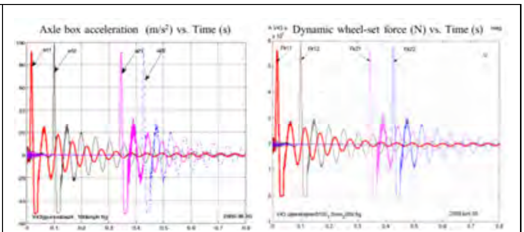

Simulations results: $V = 100$ km/h, $h_0 = 1.5$ mm

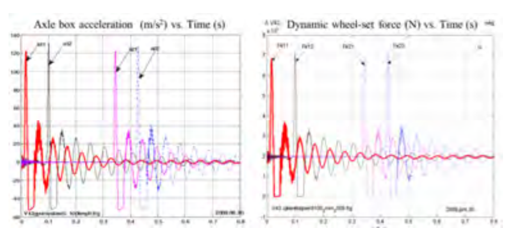

Simulations results: $V = 100$ km/h, $h_0 = 2.0$ mm

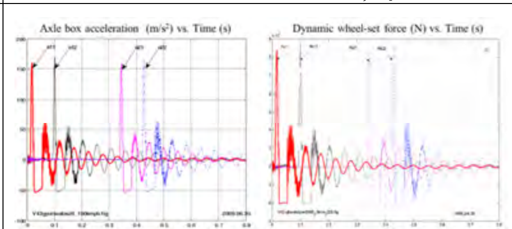

Simulations results: $V = 100$ km/h, $h_0 = 2.6$ mm

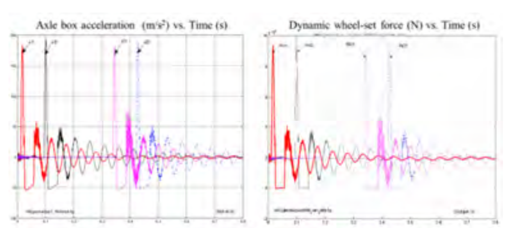

Simulations results: $V = 100$ km/h, $h_0 = 3.0$ mm

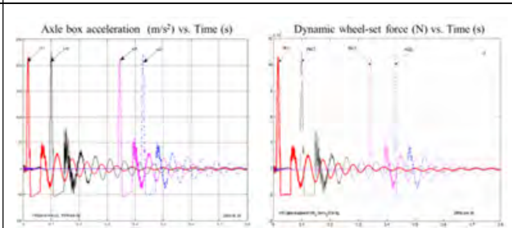

Simulations results: $V = 100$ km/h, $h_0 = 3.5$ mm

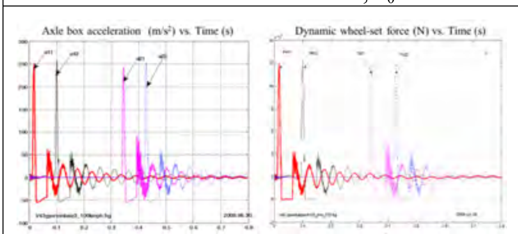

Simulations results: $V = 100$ km/h, $h_0 = 4.0$ mm

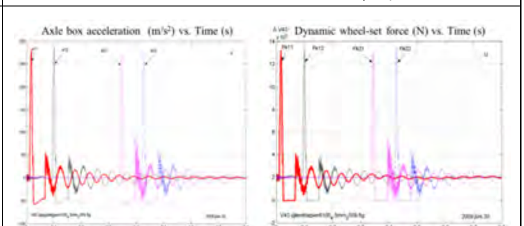

Simulations results: $V = 100$ km/h, $h_0 = 4.5$ mm

Figure-set 11 Vertical axle-box acceleration and wheel/wheelset force variations with time. Simulation results for travelling speed 100 km/h

In the Figure-set one can observe an *asymmetry* in the shape of the acceleration vs. time functions when the loco-wheels are vertically moving upwards (lifting, $dh/ds > 0$) to the medium located constant level ($dh/ds = 0$) or moving downwards (descant, $dh/ds < 0$)

from the medium located constant level of the local excitation function $h(s)$. The acceleration peaks belonging to lifting are (in absolute value) always greater than the peaks of belonging the motion phase of descants.

In the cases of higher speeds $v$ or higher excitation levels $h_0$ it sometimes occurs that the wheel tread vertically leaves the railhead (separation is from some microns to maximum *1* mm) for some instants. The mentioned phenomenon in itself cannot cause derailment, because the time span of the separation is very-very little (much more less than the hight of the flange) and of short duration. Thus there is not enough lifting off and time for the occurrence of derailment.

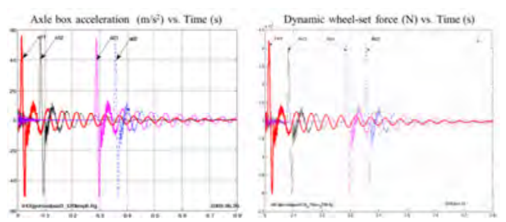

Simulations results: $V$ = 120 km/h, $h_0$ = 0.75 mm

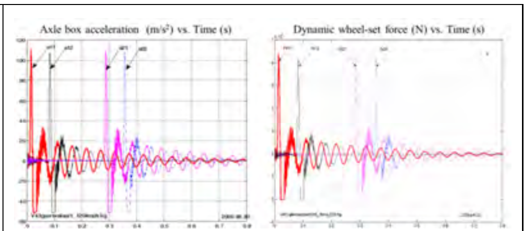

Simulations results: $V$ = 120 km/h, $h_0$ = 1.5 mm

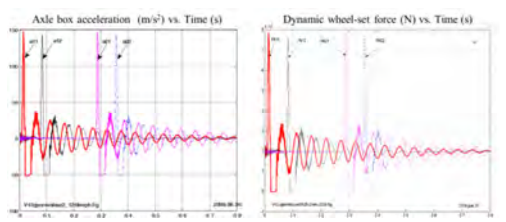

Simulations results: $V$ = 120 km/h, $h_0$ = 2.0 mm

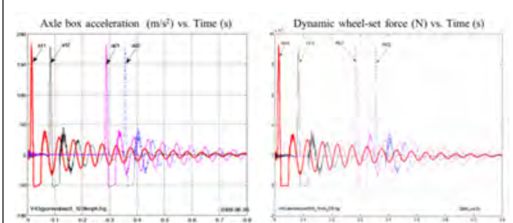

Simulations results: $V$ = 120 km/h, $h_0$ = 2.6 mm

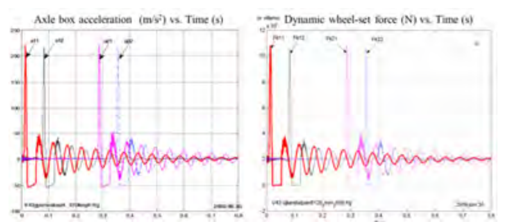

Simulations results: $V$ = 120 km/h, $h_0$ = 3.0 mm

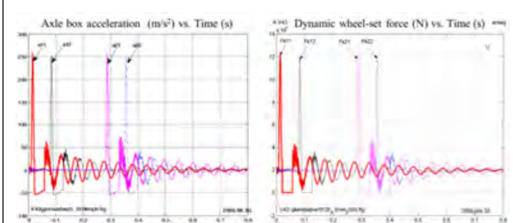

Simulations results: $V$ = 120 km/h, $h_0$ = 3.5 mm

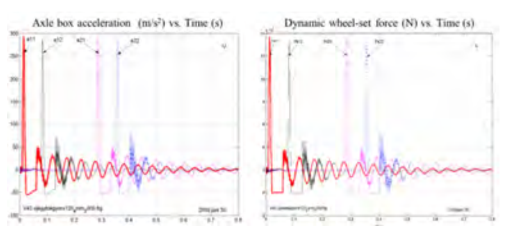

Simulations results: $V$ = 120 km/h, $h_0$ = 4.0 mm

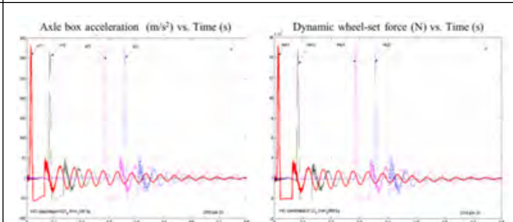

Simulations results: $V$ = 120 km/h, $h_0$ = 4.5 mm

Figure-set 12 Vertical axle-box acceleration and wheel/wheelset force variations with time. Simulation results for travelling speed 120 km/h

## 6. DISCUSSION OF THE OCCURRENCE PROBABILITY OF THE MAXIMUM VERTICAL WHEEL-LOAD LEVELS IN LOCOMOTIVE OPERATION ON THE MEASURED TRACK SECTIONS

The simulation results contain the vertical axle-box acceleration peak values and also the peak values of the wheel-rail vertical connection forces belonging to each other. On the basis of these results the relationship between the maximum vertical wheel-set forces and the maximum axle box accelerations was evaluated. In Fig. 13 in the left upper corner the mentioned relationship is shown for the case of 120 km/h travelling speed, while in the right upper corner the relationship in question can be seen for the case of 100 km/h travelling speed. In the left bottom corner the diagrams are represented in a common co-ordinate system. Since the two diagrams are almost congruent with each other, it was reasonable to evaluate the relationship by a common regression line fitting on the united point set in the sense of least squares. In the right bottom corner this common regression line is shown. In the last mentioned figure the range belonging to the measured maximum acceleration amplitude is also visualized.

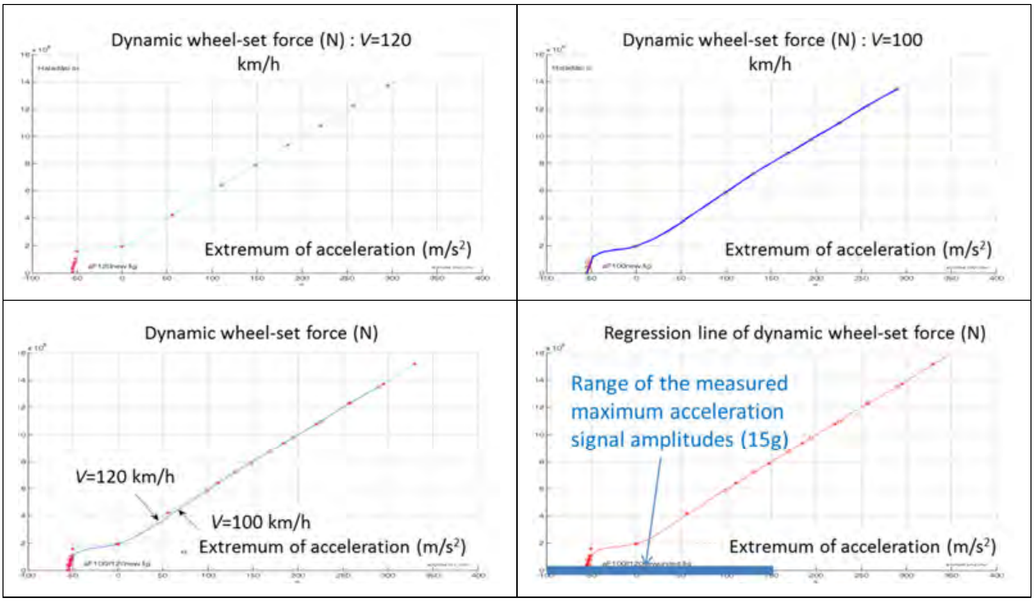


Fig. 13 Relationship between the peak values of the vertical wheel-set forces and the maximum axle box accelerations

Taking into consideration the maximum and minimum values of the dynamical wheel forces and using the *Hertz*-method the maximum values of the contact pressure over the contact patch are computed, and the maximum of tensile stress at the border of the contact ellipse is also determined. These results are shown in Fig. 14.

Taking into the consideration the dynamical contact tensions caused by the dynamical wheel forces the high level of the Hertz-type vertical compressive stresses (practically as the stress-state of the hydrostatic pressure without shearing) do not mean the critical condition for evolving wheel cracks. The yielding limit of the material of the wheel-tyre is in the interval of 460...600 MPa. Likewise, the $\sigma = 0{,}133\ \sigma_H$ tensile stress caused by the dynamical wheel forces is not a sufficient driving effect for the occurrence of tangential cracks, because as it can be seen in Fig. 14 it does not emerge such excitation level, from which the resulting stress exceeds the yielding limit. In short: the maximum of the tangential stresses remain under the yielding limit. It is also known that in the case of dynamically applied loads one can reckon with 1,3...1,5 times increase in yielding limit in comparison with the static case.

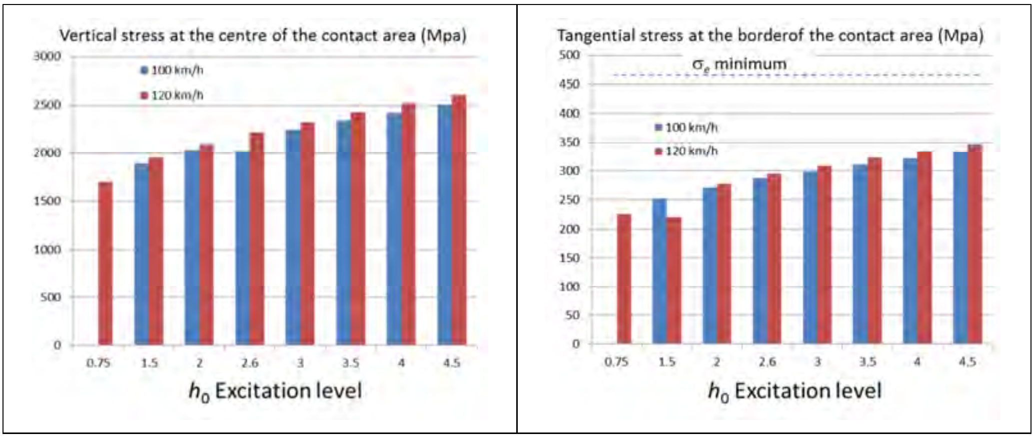


Fig. 14 Results of the stress-analysis.

Based on the above, it can be stated that *the dynamical wheel forces cannot be the reason of the damage to the running surface of the wheel*. Because moving away from the running surface in radial direction at a depth of 7...10 mm inward the tangential components of the tensile stress vanished, so these do not play an essential role in driving the cracks started from the marks bashed into the wheel-tyre.

## Track acceleration extrema

The statistical processing of the results of acceleration measurements pointed out, that the maximum of acceleration peak values during operation are under the level 15 g at a probability 99.998%. Very rarely there are higher acceleration peaks (maximum 40 g), but the time intervals of belonging to these peaks are extremely short. According to this fact, taking into consideration that the geometrical probability of overlapping of the potential position of the crack appearance and the occurrence of acceleration peak values of 15 g ...40 g is less than 0.01 the combined probability is very small, equal to $2 \cdot 10^{-7}$.
Number of acceleration peak occurrences on different track sections is shown in Table 2. Extrema of acceleration qualify the tracks.

| No | Track section | km | 15-20 g | 20-25 g | 25-30 g | ≥30g | Evaluation |
|---|---|---|---|---|---|---|---|
| 1. | Bp.Keleti Pu.–Füzesabony | 125 | 35 | 14 | 4 | 2 | - |
| 2. | Füzesabony–Miskolc Ti.Pu. | 57 | 38 | 4 | 1 | 3 | Bad track at speed limit |
| 3. | Miskolc Ti.Pu. - Szerencs | 38 | 80 | 14 | 4 | 1 | Bad track |
| 4. | Szerencs - Tokaj | 18 | 35 | 10 | 2 | 0 | - |
| 5. | Tokaj - Nyíregyháza | 32 | 90 | 12 | 5 | 1 | Bad tracIk |
| 6. | Nyíregyháza - Debrecen | 49 | 38 | 13 | 1 | 0 | In some places bad track |
| 7. | Debrecen - Hajdúszoboszló | 20 | 21 | 7 | 1 | 0 | - |
| 8. | Hajdúszoboszló – Püspökl. | 34 | 29 | 2 | 1 | 3 | - |
| 9. | Püspökladány - Szolnok | 77 | 75 | 18 | 3 | 1 | Bad track |
| 10. | Szolnok - Cegléd | 27 | 6 | 1 | 0 | 0 | Very good track |
| 11. | Cegléd – Bp.Nyugati Pu. | 73 | 13 | 4 | 0 | 0 | Good track |
| | Total distance covered (km) | 540 | Σ 460 | Σ 99 | Σ 22 | Σ 11 | ΣΣ 592 |

Table 2 Number of acceleration peak occurrences on different track sections.

## 7. CONCLUDING REMARKS

Based on the measurement results concerning the vertical axle-box accelerations realized on different track sections and the results of the dynamical simulation carried out the following statements can be made:

- The geometrical probability *p* that the critical section (the location of the ID number, made in glowing state of the wheel-tyre) of the wheel periphery comes into contact with the rail-head is small: $p<0.01$.
- The probability of that case that the contact point falls in the critical section and at the same time the acceleration is between values 15g and 40g is extremely small: $q \approx 2 \cdot 10^{-7}$.
- Furthermore at vertical axle-box acceleration 40g the dynamical stresses are under the dynamical yielding stress limit 598…780 MPa of the wheel-tyre material.
- The Hertz-type horizontal compressive stresses in the centre point of the contact cannot be the reason of emerging crack at the wheel-tread.
- The tangential tensile stresses emerging at the border of the contact area cannot be a reason of emerging crack of the wheel-tread.
- The reason occurring crack in the tyre is rather the anomaly of stress carrying capacity at the bottom of the groove (the groove of the ID marks of the tyre-side), which is established during the non-proper process of the applied warm-technologies of the tyre manufacturing.

## 8. REFERENCES

[1] **Zobory, I. – Szabó, A. – Kovács, K. – Iványi, Z.:** Investigation into the Dynamic Forces Acting on the Wheels of the Locos V43 Running on the Track Sections of Different Technical Conditions. Final research report for the MÁV Co. BME, VJT, Budapest, 2009. (p.71). (in Hungarian)

[2] **Zobory, I. – Szabó, A. – Kovács, K.:** Investigation into the Operation Load Collectives of Bogie-Frames and other Load Bearing Components. Proceedings of the 7th International Conference on Railway Bogies and Running Gears (BOGIE ’07), (Ed. by Prof. I. Zobory). BME Department of Railway Vehicles, Budapest, 2009, p.333-350.

[3] **Zobory, I. – Szabó, A.:** Vehicle Dynamics and Drive Technique**.** Technical University Lecture Notes. Tipotex, Budapest, 2006. (In Hungarian)

# CREEP CONTROL IN BRAKE OPERATION TO AVOID WHEEL SLIDING AND WHEEL FLATTENING

**István ZOBORY[1] and Dezső NAGY[2]**

Budapest University of Technology and Economics,
[1] Faculty of Transportation Engineering and Vehicle Engineering,
[2] Faculty of Electric Engineering and Informatics
H-1111 Budapest, Műegyetem rkp. 3. Hungary

*Received: 7 November, 2018*

## ABSTRACT

A creep control procedure to avoid macroscopic sliding at the rail/wheel contact due to excessive braking torque application is elaborated. Macroscopic sliding can lead to wheel flattening and to a considerable decrease in the force that can be transmitted from the rail to the wheel, in short: the braking force is also decreased. In this study, the model presented at VSDIA 2016 is extended. Firstly, the vertical springing and damping connections of the rigid bodies in the vehicle model are included, and excitation by vertical track irregularities is introduced into the dynamical system through linearized (Hertzean) vertical contact spring/damper elements. The second innovation is modelling of the measurement disturbences allways present in the measured feedback signals determining the controlled friction torque. Longitudinal creep is controlled, i.e. the creep is held in the close neighbourhood of a prescribed creepage-value. The control system ensures that in the presence of disturbances, the braking torques acting on the wheel-sets vary such that the time function of the creepage at each wheel always returns to the prescribed value, i.e. the resultant control process is asymptotically stable.

*Keywords*: feed-back control, creepage, rolling contact, vehicle dynamics, track excitation, simulation, noisy measurement, optimum gain

## 1. INTRODUCTION

When developing braking systems it is important to improve the anti-skid devices to avoid macroscopic wheel sliding under poor adhesion conditions. In most approaches it is crucial to have information on the creep-dependent *force connection coefficient* (*fcc*) defined by the ratio: $\mu = F_t/F_n$ , i.e. *the ratio of the tangential $F_t$ and normal $F_n$ forces acting upon the wheel/rail contact surface* either in a deterministic or a stochastic scheme. In our approach the magnitude of the braking torque is determined from the measured longitudinal acceleration and velocity and the measured angular acceleration and angular velocity of the wheels, to control the torque acting upon the wheel. The measured values of the relative displacement and speed of the wheel and the bogie-frame are also needed. The method using the principle of „*Inverse Dynamics*” *does not need* the *fcc* function, but is able to ensure *stable return* to the pre-scribed creepage in the presence of disturbing effects. This method is called a *„creep control”* procedure, and it was introduced in our VSDIA 2016 paper for a four-axle locomotive/train model. In this study the former dynamical model has been extended by including the *track excitation* and the *vertical and pitching vibration responses of the wheels, bogies and the loco superstructure*. Furthermore all measured quantities determining the controlled variable have been disturbed by measurement noise processes.

## 2. CREEP-CONTROL

The longitudinal creepage arising during rolling contact is in a variable stochastic relationship with the force transmitting *fcc* property of the rolling wheel. If a small and constant creepage can be maintained during braking, it can be anticipated that the macroscopic sliding and the wheel flattening can be avoided. The principle of „Inverse Dynamics" will be introduced, in the course of which a stable linear creep-control system is achieved. *The method does not require the explicit knowledge of the fcc.* First an elementary system of 3 DoF will be treated by creep-control, then the method will be applied for all the four braked wheel-sets of a *vertically sprung* locomotive pulling a non-braked train. The extended dynamical system is *excited by the controlled braking force and by vertical track irregularities*. The motion equations of the excited dynamical system will be numerically solved in the time domain to show the stability of the control process under the effect of the *track excitation and measurement noise.*

## 3. SIMPLIFIED ELEMENTARY MODEL

Dynamical model of a braked wheel-set with its longitudinally guided elastic/dissipative connection to a mass representing the bogie is shown in Fig. 1. The equations of motion are:

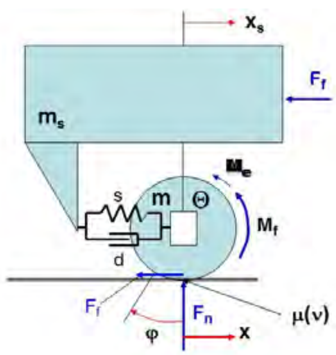


Fig. 1 Elementary model of the braked wheel-set

1. Wheel-set rotation:

$$\theta\ddot{\varphi} = -F_n\mu(\nu)R - M_e(\dot{\varphi}) - M_f(t)$$

2. Wheel-set translation:

$$m\ddot{x} = F_n\mu(\nu) + s(x_s - x) + d(\dot{x}_s - \dot{x})$$

3. Bogie translation:

$$m_s\ddot{x}_s = -s(x_s - x) - d(\dot{x}_s - \dot{x}) - C\dot{x}_s^2$$

In explicit form:

$$\ddot{\varphi} = \frac{1}{\theta}(-F_n\mu(\nu)R - M_e(\dot{\varphi}) - M_f(t))$$

$$\ddot{x} = \frac{1}{m}(F_n\mu(\nu) + s(x_s - x) + d(\dot{x}_s - \dot{x}))$$

$$\ddot{x}_s = \frac{1}{m_s}(-s(x_s - x) - d(\dot{x}_s - \dot{x}) - C\dot{x}_s^2)$$

For non-zero velocities ( $\dot{x} \neq 0$ ) the *longitudinal creepage* ν is defined as follows:

$$\nu = \frac{R\omega - \dot{x}}{\dot{x}} .$$

The *force connection coefficient* (*fcc*) is defined as the ratio of the wheel-tread creep-force $F_f < 0$ when braking, and the wheel load $F_n > 0$:

$$\mu = \frac{F_f}{F_n} .$$

In accordance with the theory and experience, the force connection coefficient μ is *creep-dependent* and when braking, the sign of $\mu$ is negative:



$\theta\ddot{\varphi}$

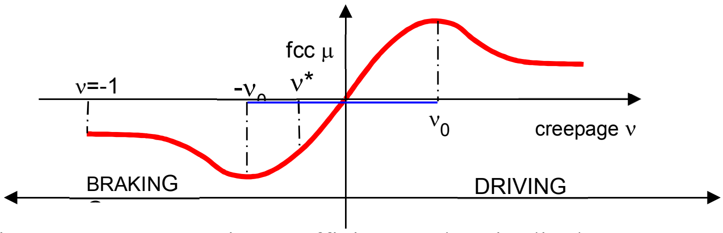


Fig. 2 Force connection coefficient vs. longitudinal creepage

As it can be seen the maximum tractive effect can be exerted at $\nu_0$, whilst the maximum braking effect can be exerted at $-\nu_0$. The creepage span $[-\nu_0, \nu_0]$ is called the interval of *micro sliding* on the wheel/rail contact spot. Our aim is to maintain the prescribed creepage $\nu^* < 0$ by the *creep control process*.

## 2. CREEP-CONTROL

### 2.1 Introductory remarks

The longitudinal creepage arising in the course of rolling contact is *in a variable stochastic relationship* with the force transmitting property *ffc* of the rolling wheel. If a small and constant creepage can be maintained during braking, then it can be anticipated that macroscopic sliding and wheel flattening can be avoided. The principle of „Inverse Dynamics" will be introduced, in the course of which an always stable linear creep-control system is achieved, and the method does not require the explicit knowledge of the *ffc*. First, an elementary system of 3 DoF will be treated by creep-control, then the method will be applied for all the four braked wheel-sets of a vertically sprung locomotive, pulling a non-braked train. The extended dynamical system is excited by the controlled braking force and by vertical track irregularities. The motion equations of the excited dynamical system will be solved numerically in the time domain to show the stability of the control process under track excitation and in the continuous presence of measurement noise in the feed-backs.

The objective of the creep-control is to maintain the prescribed *constant creepage value* $\nu^*$ during stop braking, thus the task is to determine the appropriate variation with time of the braking torque $M_f(t)$ to be exerted.

In order of determine the appropriate $M_f(t)$ function, consider first the *deviation* $\Delta\nu(t)$ of the actual creepage $\nu(t)$ from the prescribed $\nu^*$ value, in formula: $\Delta\nu(t) = \nu(t) - \nu^*$.

To achieve the control objective, consider the derivative of *creep deviation* function $\Delta\nu(t)$ with respect to time, taking into consideration, that $\nu^*$ is constant, thus:

$$\frac{d}{dt}\Delta\nu(t) = \dot{\nu}(t) = \frac{d}{dt}\left(\frac{R\dot{\varphi} - \dot{x}}{\dot{x}}\right) = \frac{(R\ddot{\varphi} - \ddot{x})\dot{x} - (R\dot{\varphi} - \dot{x})\ddot{x}}{\dot{x}^2} = \frac{R\ddot{\varphi}}{\dot{x}} - \frac{R\dot{\varphi}}{\dot{x}^2}\ddot{x}$$

From motion equation No 2, written for the wheel's longitudinal translation, the *longitudinal force* $F_f$ arising on the wheel/rail contact area (the braking force) when braking torque $M_b(t)$ is applied on the wheel can easily be expressed:

$$F_f = F_n\mu(v) = m\ddot{x} - s(x_s - x) - d(\dot{x}_s - \dot{x})$$

From the last equation it can be seen that knowing $\ddot{x}, \dot{x}, x, \dot{x}_s\ and\ x_s$ the braking force can be determined *without knowing the explicit value of the creep dependent fcc function* $\mu(\nu)$. In other words it turns out that the *value of the fcc is reflected in the motion characterising quantities of the system*, thus it is *not necessary to get direct information on the fcc* to realise the control process if the motion state characteristic quantities $\ddot{x}, \dot{x}, \dot{\varphi}, \dot{x}_s - \dot{x}\ and\ x_s - x$ can continuously be measured. It is a direct consequence of the above that in equation No 1 for the rotatory motion of the wheel, *fcc* can be eliminated by substituting the known motion state characteristic values. The first step is to express the angular acceleration of the wheel in form:

$$\ddot{\varphi} = \frac{1}{\Theta}\left[\left(-m\ddot{x} + s(x_s - x) + d(\dot{x}_s - \dot{x})\right)R - M_e(\varphi) - M_f(t)\right].$$

If one substitutes the above expression for the angular acceleration into the formula for the creep-derivative, then one can vary the braking torque $M_f(t)$ with time to ensure stable control of the longitudinal creepage, by which stability of the prescribed creepage $\nu^*$ can also be maintained in the case when other disturbances temporarily force the longitudinal creepage to deviate from the prescribed (commanded) value $\nu^*$. The creep-derivative deduced above now takes the following form [2]:

$$\frac{d\nu}{dt} = \frac{R\ddot{\varphi}}{\dot{x}} - \frac{R\dot{\varphi}}{\dot{x}^2}\ddot{x} = \frac{R}{\Theta\dot{x}}\left[\left(-m\ddot{x} + s(x_s - x) + d(\dot{x}_s - \dot{x})\right)R - M_e(\varphi) - M_f(t)\right] - \frac{R\dot{\varphi}}{\dot{x}^2}\ddot{x}.$$

With some imagination it can be recognised that if the braking torque has the variation with time

$$M_f(t) = \frac{\dot{x}\theta K}{R}\Delta v - M_e(\dot{\varphi}) - \left(R + \frac{\theta\dot{\varphi}}{m\dot{x}}\right)\ddot{x} + sR(x_s - x) + d(\dot{x}_s - \dot{x}),$$

then the whole right hand side part of the expression for the creep-derivative takes the following very simple and useful form [2]:

$$\frac{d\Delta\nu(t)}{dt} \equiv -K\Delta\nu(t) \text{ or } \frac{d\Delta\nu(t)}{dt} + K\Delta\nu(t) \equiv 0, for\ any\ t \in I.$$

Here $I$ stands for the time interval of the analysis. Since the initial value problem of the resulting first order ordinary differential equation can always be solved for any initial value being not too far from the origin, and the solution is always stable, the appropriate brake torque variation $M_f(t)$ based on the time dependent and measured motion state characteristics $\ddot{x}, \dot{x}, \dot{\varphi}, \dot{x}_s - \dot{x}\ and\ x_s - x$ the intended stopping brake process with constant deceleration can be successfully realised. The logical flow-chart of the control process for a single wheel-set (One of the four braked wheel-sets) is plotted in Fig. 3.

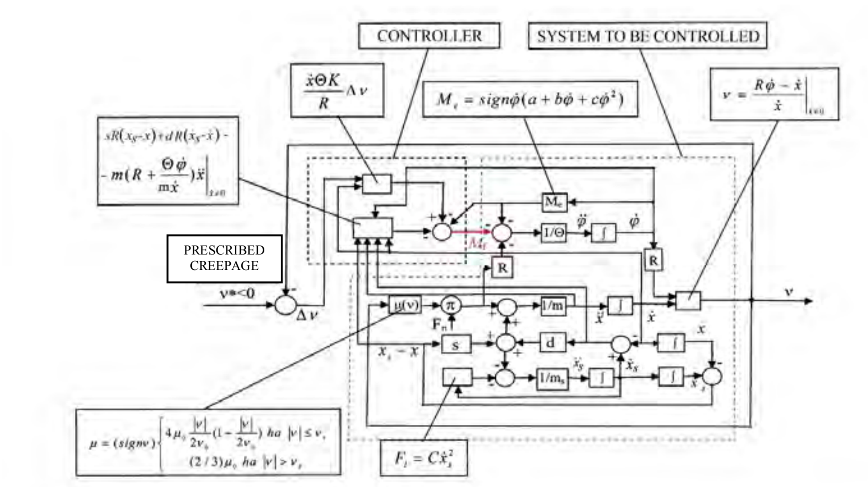


Fig. 3 Flow-chart of the control process for a single wheel-set

## 3. SYSTEM MODEL FOR THE TRAIN CONTROL ANALYSES

### 3.1 The original model version for longitudinal dynamics

The original vehicle system model, which only models the longitudinal dynamics [2] is shown in Fig. 4. The total number of degrees of freedom of the model is 11+1=12.

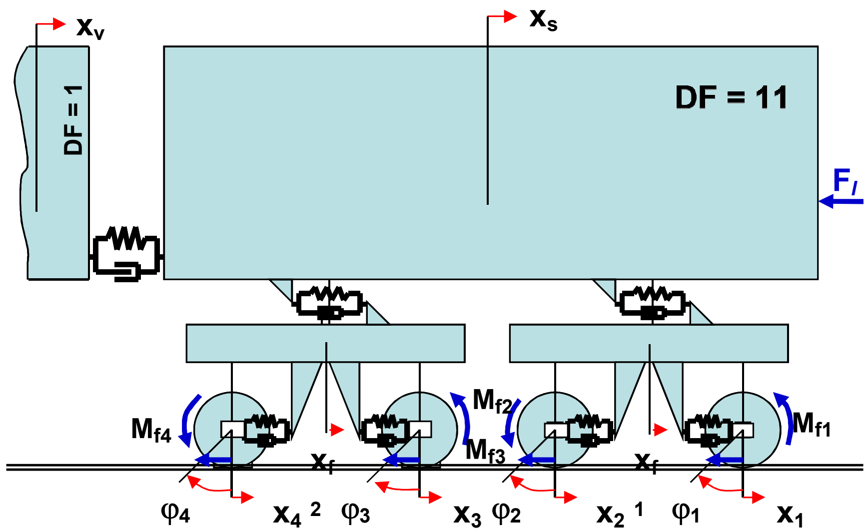


Fig. 4 The original vehicle system model for longitudinal dynamics

### 3.1 The extended model for longitudinal, vertical and pitching dynamics

The extended model is shown in Fig. 5. There are two characteristic changes in this extended model, namely the vertical linear elastic and dissipative *Hertzean*-contact at the wheel/rail contact spots, and the vertical linear elastic and dissipative primary suspensions, which connect the axle boxes and the bogie frames, as well as the vertical linear elastic and dissipative secondary suspension elements which connect the bogies and the locomotive-body. Thus, the number of the free coordinates – degrees of freedom of the system – has increased from the original version. DoF = 21+1 = 22.

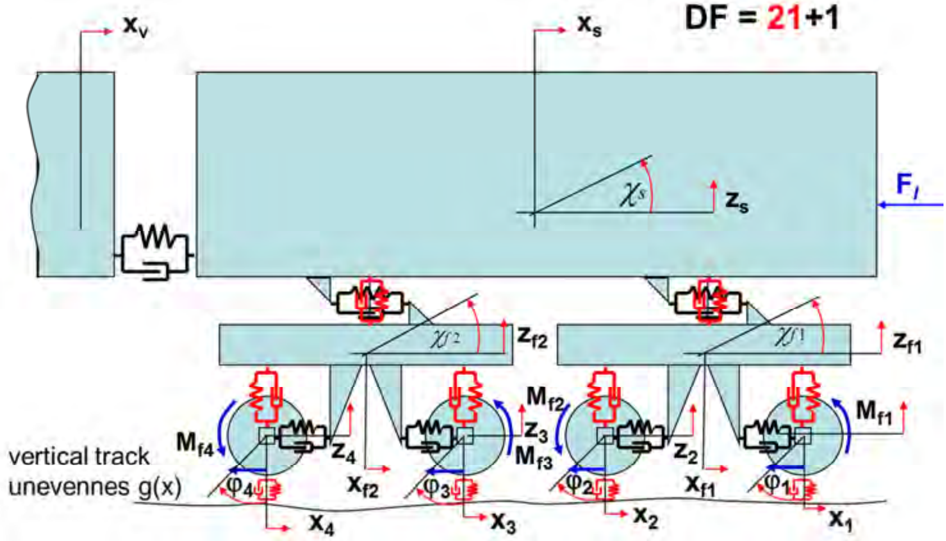


Fig. 5 The extended model to be controlled for constant creepage at the wheel/rail contact while braking of the train at a prescribed constant deceleration and in the presence of disturbances due to the track unevenness

### 3.3 Disturbances of the control process due to track excitation of the system

It is obvious that due to the elastic and dissipative suspension elements both the bogies and the locomotive-body as rigid bodies can undergo both vertical and pitching motions (vibrations) in the vertical plane. The vertical motion of the wheel-sets and the vertical and pitching motion of the bogies and the locomotive-body are excited by the rail surface irregularities at the wheel/rail contact spots in the course of the motion of the train system. The effect of the geometric irregularity excitation is given by the rail profile function $g(x)$. The lower point of the *Hertzea*n spring/damper elements at the wheel/rail contact spots follow the track profile during the whole braking process. It is a consequence of the track unevenness excitation that the vertical wheel supporting forces transmitted by the *Hertzean* elements will vary in the course of the braking process, which obviously also *disturbs* the rotating motion of the wheel-sets and gives *perturbations* to the control process. All the same, each wheel-set of the locomotive is controlled by its own braking moment exertion $M_{fi}(t)$, i=1,2,3,4 determined by applying the same control process shown in Fig. 3. The prescribed (commanded) creepage $\nu^*$ is the same for all the four wheel-sets.

### 3. Disturbances of the control process due to measurement noise in the feedbacks

In this study we intended to also get information on the system behaviour in the presence of disturbances in the measured quantities which are fed back to the controller when generating the controlled brake torque. To this end all the fed back components to be realized by measurements in the real control system should be loaded with a certain disturbing signal. As a first approach to the problem, small amplitude, constant frequency sinewave signals were added to all the feedback signals at the input side of the controller. More exactly, the amplitudes of the disturbances were selected as x% of the time dependent values in the feedback loops, with values of 2,5% and 5% selected. The frequency of the sinewave disturbing signal was $f = 7$ *Hz*, with *phase angles* of random values from the interval [-π,π]. Some results of the simulated time functions of the decisive importance for the control system will be shown in diagrams in Chapter 5.

## 4. THE SYSTEM EQUATIONS

The strongly non-linear, *implicit* set of the system equations, which take into consideration the non-linearities of the wheel/rail contacts (the non-linear *fcc*), the journal friction torques, the air drag and the fedback motion state dependent braking torques can be formulated for the unknown motion state vector $\boldsymbol{x}(t)$ as follows:

$$\boldsymbol{F}(\dot{\boldsymbol{x}}(t), \boldsymbol{x}(t)) \equiv 0, for\ any\ t \in I,$$

where in accordance with Fig. 5, the *44*-dimension motion state vector $\boldsymbol{x}$ has the following co-ordinates:

$$\boldsymbol{x} = [\dot{x}_{k1}, \dot{x}_{k2}, \dot{x}_{k3}, \dot{x}_{k4}, \dot{x}_{f1}, \dot{x}_{f2}, \dot{x}_{s}, \dot{x}_{v}, \dot{z}_{k1}, \dot{z}_{k2}, \dot{z}_{k3}, \dot{z}_{k4}, \dot{z}_{f1}, \dot{z}_{f2}, \dot{z}_{s}, \dot{\varphi}_{k1}, \dot{\varphi}_{k2}, \dot{\varphi}_{k3}, \dot{\varphi}_{k4}, \dot{\chi}_{f1}, \dot{\chi}_{f2}, \dot{\chi}_{s}, x_{k1}, x_{k2}, x_{k3}, x_{k4}, x_{f1}, x_{f2}, x_{s}, x_{v}, z_{k1}, z_{k2}, z_{k3}, z_{k4}, z_{f1}, z_{f2}, z_{s}, \varphi_{k1}, \varphi_{k2}, \varphi_{k3}, \varphi_{k4}, \chi_{f1}, \chi_{f2}, \chi_{s}] \in R^{44}$$

For a prescribed initial time instant $t_0$ the state vector should take a prescribed vector value: $\boldsymbol{x}(t_0) = \boldsymbol{x}_0 \in R^{44}$. The initial-value problem formulated was solved numerically. The actual structure of function $\boldsymbol{F}$ is determined by the motion equations written for *22* motion forms, and also contains the feedback rules, formulated above in the form of the motion-state dependent braking torques. The relative difficulty of treating this initial value-problem for the implicit differential equation system is avoided by an *approximation method.* The motion state dependent braking torque input to the set of motion equations at time instant $t_i$ is computed by using the motion state values for the previous time instant $t_{i-1}$ of the simulation. For small time steps in the simulation this approximation proved to be valid. Thus, the numerical solution procedure works in a *two tact operation mode*:

1. Computation of $\boldsymbol{M}_f$ at $t_{i-1}$, designated by $\boldsymbol{M}_f(t_{i-1})$,
2. Computation of all the accelerations at $t_i$ using $\boldsymbol{M}_f(t_{i-1})$ **.**

## 5. SIMULATION RESULTS

The differential equation system of the train model consisting of 22 free co-ordinates was solved numerically by using the approximation. The train runs on vertically periodic rail surfaces of 6 m wavelength and 1mm amplitude. The creep-controlled *stop braking process* was analysed with an initial velocity of $v_0$ = 30 km/h. The mass of the loco was 80 t and that of the trailer vehicle was 25 t. Only the loco was braked. The intended train deceleration was $a_v$ = -1 m/s$^2$. The *prescribed creepage* computed based on this deceleration was ν*= -0.0026. The simulation program was written in MATLAB.

### 5.1 The controlled braking torques applied on the wheel-sets

The controlled braking torques acting on the four wheel-sets for the stop braking process for gain factor K = 10000 are shown in Fig. 6.

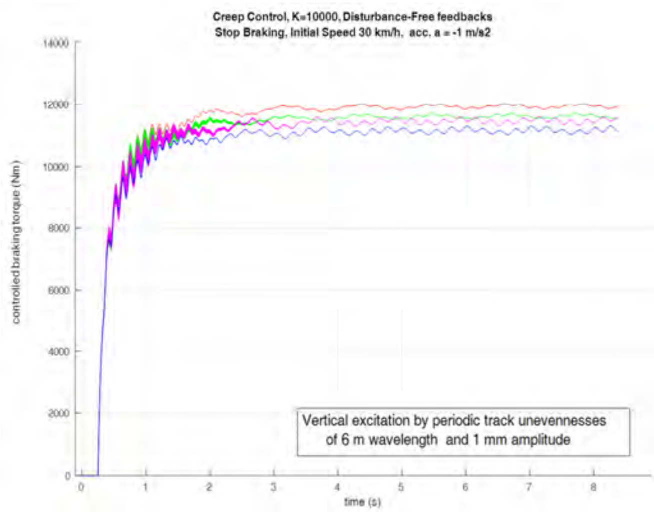


Fig. 6 The controlled braking torques vs. time
applied on the wheel-sets in case of gain factor K = 10000

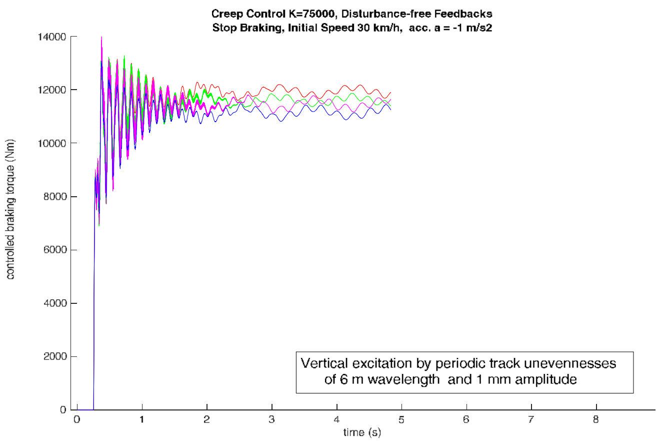


Fig. 7 The controlled braking torques vs. time to be applied
on the wheel-sets, at gain factor K = 75000

The controlled braking torques acting on the four wheel-sets for gain factor K = 75000 are shown in Fig. 7. The increased gain factor is disadvantageous, because the harmonic content in the transition interval shows higher amplitudes.

In Fig. 8 the controlled creepages vs. time functions are shown in case of gain factor K = 10000. In Fig. 9 the controlled creepages vs. time function is plotted for the case of gain factor K=75000. It is clear that in this case the control target achieved faster, which is in accordance with the expectations.

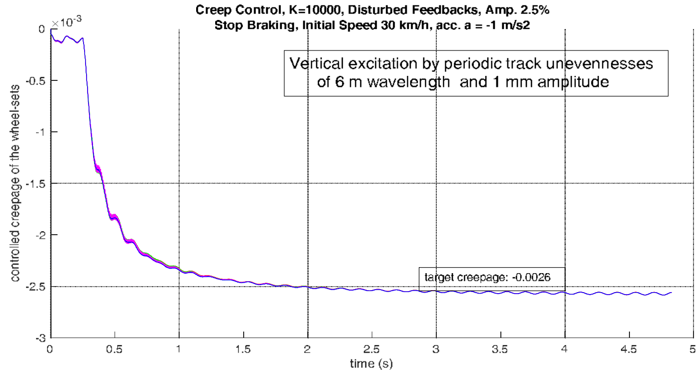


Fig. 8 The controlled creepages vs. time in case of gain factor K = 10000

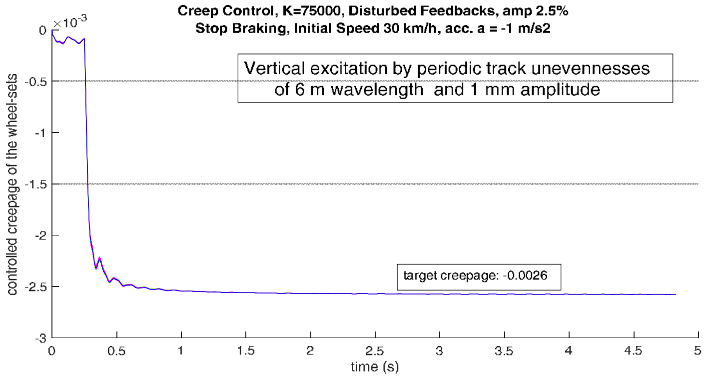


Fig. 9 The controlled creepages vs. time in case of gain factor K = 75000

Figs. 10 and 11 show the case when parallel to the track excitation the feed-backs were sinusoidally disturbed by 5% amplitudes of the actual motion signals which the controlled brake torques depend on.

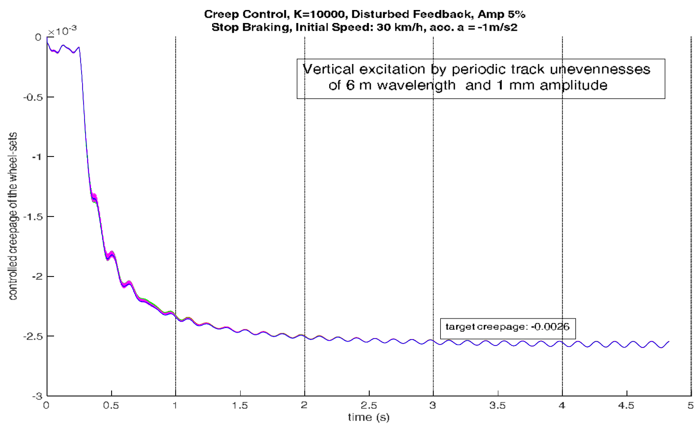


Fig. 10 The controlled creepages, K=10000
with *disturbed feed-backs* were sinusoidal inaccuracy functions
with frequency 7 Hz and amplitude, 5 % of the actual accurate values

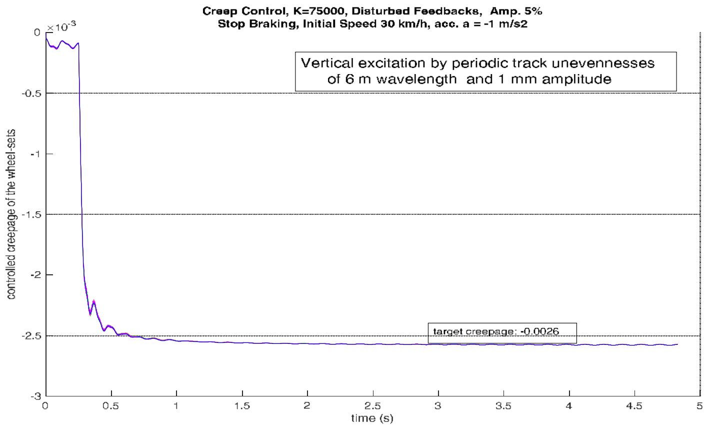


Fig. 11 The controlled creepages, K=75000
with disturbed feed-backs were sinusoidal inaccuracy functions
with frequency 7 Hz and amplitude, 5 % of the actual accurate values

## 6. CONCLUSIONS

The following conclusions can be drawn from the investigations described above:

- Creep-control based on the principle of „inverse dynamics" gives a stable solution for the stop-braking with constant deceleration, and provides steps towards the development of a *novel antiskid-device*.
- The dynamical model with the Hertzian springs and dampers also works reliably on tracks loaded with vertical irregularities, thus the vertical and pitching vibrations excited by track irregularities don't hinder the operation of the creep control system
- The parameter sensitivity analysis for the gain factor K showed that smooth operation needs lower values, while the fast reaction requires higher values. A medium solution K=50000 could balance the contradictory demands,
- The parameter sensitivity analysis for measurement errors and noise showed that even if all the five feedbacks in the control processes are loaded by a sinusoidal signal error of 5% amplitude in the instantaneous signal levels the control system did not lose its stability,
- The development of system models for braking torque applied both electrically and by friction is the target of further research.
- The sensor system to be used in a real control system also needs detailed research.

## 7. REFERENCES

[1] **Ariyur, K.B. – Krstič, M.:** Real-Time Optimization by Extremum Seeking Control. Wiley&Sons, Inc. New-York, 2003.

[2] **Zobory, I. – Nagy, D.:** Dynamical Analysis of a Special Anti-Skid-System for Railway Cars and Traction Units. Proceedings of the 15th MINI Conference on Vehicle System Dynamics, Identification and Anomalies (VSDIA 2016). (Ed. by Prof. I. Zobory). BME ITS non-profit ZRt. Budapest, 2017. p.149-162. ISBN: 978-963-313-266-1

[3] **Gáspár, P. – Szabó, Z. – Bokor, J.:** An Estimation Method For The Wheel-Rail Friction Coefficient. Proceedings of the 10th MINI Conference on Vehicle System Dynamics, Identification and Anomalies (VSDIA 2006). (Ed. by Prof. I. Zobory). BME, Department of Railway Vehicles, Budapest, 2007, p.237-244. ISBN: 9789634209683

# HOW TO AVOID DYNAMICAL INSTABILITY IN DISC-BRAKE SYSTEMS BY USING ADDITIONAL LINEAR DAMPING

**István NÉMETH**

Department of Aeronautics, Naval Architecture and Railway Vehicles
Faculty of Transportation and Vehicle Engineering
Budapest University of Technology and Economics
H-1111 Budapest, Műegyetem rkp. 3. Hungary

*Received: November 6, 2018*

## ABSTRACT

In this article simplistic mechanical models of the disc brake system are set up by considering only a few degree of freedom of the system, but incorporating non-linear effects such as the friction characteristics between brake pad and disc. Disc brake vibrations generate structural vibrations, as well as air-born noise and thereby affect ride comfort of passengers, as well as wear and durability of the brake components, and not least have a contribution to the noise emission of the vehicle. From this follows, that it is essential to avoid or more realistically at least attenuate railway brake noise and vibration. Many publications demonstrate that the vibration and noise of frictional brake systems is basically a self-induced vibration, which can be described as an un-stability of the equilibrium state of the system. The instability of the system is generally explained by the falling characteristic of the friction coefficient vs sliding velocity however it is also known that self-induced mechanical vibrations can occur even with constant coefficient of friction. Experiments and everyday observations show that sometimes disc brake vibration of in service vehicles appear and disappear seemingly in a random way during operation, therefore the phenomenon must be more complex and nonlinear. The approach of this investigation is to keep the model degree of freedom small, but reproduce some nonlinear effects, in order to gain better understanding of the emergence of disc brake vibration, and develop strategies for its avoidance. The influence of the brake console stiffness and damping, and as an option, the application of additional linear damping is examined e.g. by the analysis of limit-cycle oscillations.

*Keywords: disc-brake, vibration, damping, stability*

## 1. INTRODUCTION

From point of view of the environmental pollution the railway sector is better positioned, than many other transport modes, except when it comes to the question of noise emission. Noise emission of railways is getting a basic issue, which cannot be dismissed any more, because concerns about noise quite often build up an obstacle for railway development projects, especially in dense populated urban regions. The sources of railway noise are more or less well known: machine noise, rolling noise and aerodynamic noise, however their mitigation is not trivial at all. Braking noise is naturally classified as machine noise, which have a dominating contribution to the entire railway noise emission in the lower velocity range, generally below 50 km/h vehicle velocity. Some braking noise is probably unavoidable, but its level shall be reduced as far as possible.

## 2. THE OBJECT OF THE INVESTIGATION

The Hungarian railway manufacturer Ganz Motor Kft. (earlier Ganz Hunslet Zrt.) has developed a family of railway bogies called GH-250, which is a well-established long standing and not least silent bogie series [1]. This examination focuses on an earlier development stage subtype of the bogie family, which represents a now days outdated subversion.

The bogie has two a level suspension: the primary suspension is a duplex steel coil spring, while the secondary suspension consists of coil springs and rubber sandwich springs stacked above each other. Vertical primary and secondary hydraulic dampers are built in as well. The wheelset guidance is realised by rigid wheelset link, which is connected to the bogie frame by rubber bushings. The bogie is equipped with a disc-brake system containing two brake-discs on each wheelset-axle, see Fig. 1 and 2.

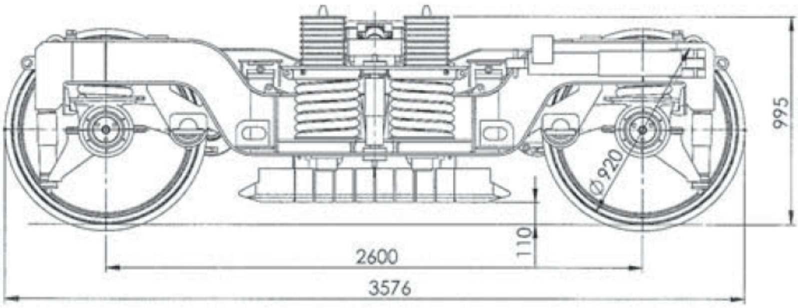


Fig. 1 Side elevation of the bogie under investigation

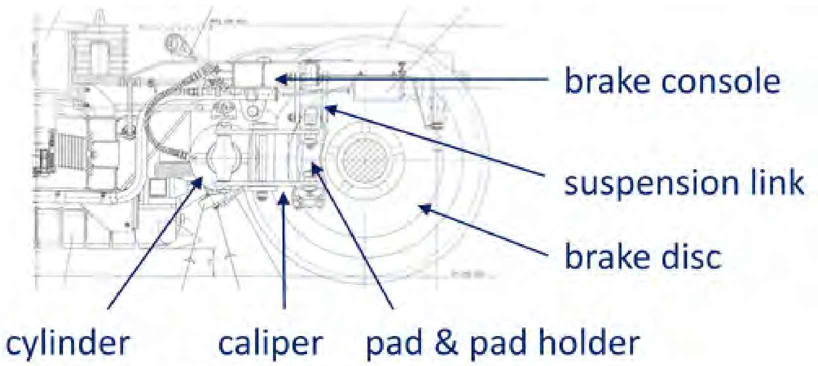


Fig. 2 Disc brake-unit components

The brake pad is of type Becorit 918, having an organic material. The measured data of the brake pad friction coefficient are taken from the research report by *Zobory* [2]. A nonlinear, sliding velocity-dependent friction model has been fitted to the measured values based on to the following $\mu(v_s)$ friction coefficient vs sliding velocity function:

$$\mu(v_s) = \mu_s + \frac{\mu_s - \mu_{k\infty}}{1 + \lambda|v_s|}$$

where the parameters are: $\mu_s$ static friction coefficient, $\mu_{k\infty}$ kinetic friction coefficient, and $\lambda$ is a parameter influencing the initial slope. The friction coefficient characteristics and its derivative by the $v_s$ sliding velocity are plotted in Fig. 3.

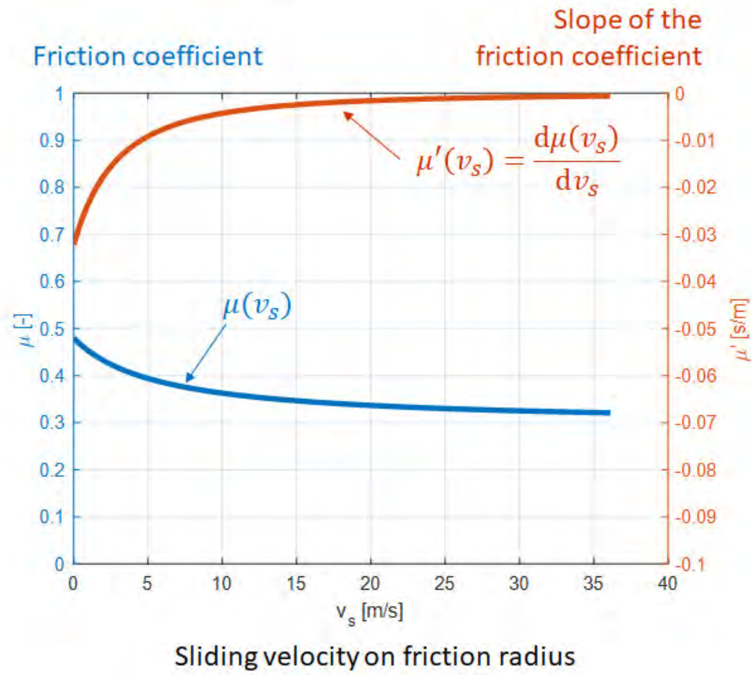


Fig. 3. Friction characteristics of the brake pad

## 3. METHOD OF INVESTIGATION

Simplistic lumped parameter dynamical models of the disc brake system were set up by considering only a few degrees of freedom of the system, but incorporating non-linear effects such as the friction characteristics between brake pad and disc.
Several researchers adopted for the description of the brake vibration the so called "stick-slip model", which can be found in mechanics textbooks as well.

### 3.1 One degree of freedom – stick-slip model

The stick-slip phenomena is an active research field in tribology, in development of cutting machines, but also in the precision control of actuators, see e.g. [3]. This basic model consists of a linear spring of stiffness $s$, a linear damper of damping coefficient $d$, a single rigid body of mass $m$, and a frictional contact pair between the rigid body (brake pad) and an other body (here the brake-disc) moving at constant circumferential velocity $v_d$. The non-linear tangential friction force is denoted by $F_f(v_s)$ see Fig. 4. The well-known differential equation of the system motion reads as

$$m\ddot{z} = -sz - d\dot{z} + F_f(v_s)\,,$$

where the sliding velocity can be expressed as $v_s = v_d - \dot{z}$. In the equilibrium state $\ddot{z} = \dot{z} = 0$, therefore the equilibrium position is $z_0 = \frac{F_f(v_d)}{s}$. By introducing a new variable $q = z - z_0$, which measures the displacement relative to the equilibrium position, we get to a new non-linear ordinary differential equation:

$$\ddot{q} = -\frac{d}{m}\dot{q} - \frac{1}{m}F_f(v_s) - \frac{s}{m}q = \mathcal{F}(q, \dot{q})$$

The characteristic surface $\mathcal{F}(q, \dot{q})$ in the non-linear differential equation can be expanded into *Taylor*-series at the stationary point. After neglecting the second and higher order terms, the $\mathcal{F}(q, \dot{q})$ surface is actually replaced by its tangent plane in close proximity of the stationary point. If the new linearized model appears to be stable, then this stability holds for the original non-linear model as well, according to *Poincaré*'s axiom on this matter. Of course this is only valid until the system does not move far away from the stationary point, and do not reach some strong non-linearity, i.e. in our particular case until $\dot{q} < v_d$ or practically, rather $\dot{q} \ll v_d$, which means that the validity of the linearized model vanishes at least when sticking occurs.

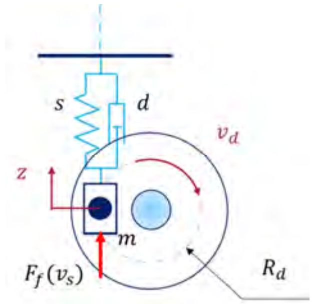


Fig. 4. Stick-slip model

Thus, the linearized differential equation can be written as follows:

$$m\ddot{q} + \underbrace{\left(d + \left.\frac{\mathrm{d}F_f(v_s)}{\mathrm{d}v_s}\right|_{v_s=v_d}\right)}_{\eta}\dot{q} + sq = 0\,,$$

where the term designated by $\eta$ represents the resultant linearized damping of the system, containing damping effect due to the slope of the friction force as well. The latter slope can take also negative value. The condition of the dynamical stability of the system at equilibrium can be formulated in terms of the damping ratio:

$$D = \frac{\eta}{\eta_{cr}} = \frac{\eta}{2\sqrt{sm}} = \frac{\eta}{2m\omega_0} > 0\,, \tag{1}$$

where $\eta_{cr}$ is the critical damping and $\omega_0$ is the eigen angular frequency of the undamped dynamical system. The stability criterion can be expressed in several equivalent ways:

$$D > 0\text{, or }\ \eta > 0\text{, or furthermore}$$

$$d > d_{limit} = -\left.\frac{\mathrm{d}F_f(v_s)}{\mathrm{d}v_s}\right|_{v_s=v_d} = -2\,F_n\left.\frac{\mathrm{d}\mu(v_s)}{\mathrm{d}v_s}\right|_{v_s=v_d} = -2\,p_c A_c(\eta_b/i)\,\mu'(v_d), \tag{2}$$

where the normal force $F_n = 2p_c A_c k\eta_b$, is expressed as a product of the brake cylinder pressure $p_c$, the brake piston surface $A_c$, the arm-ratio $i$ and efficiency of $\eta_b$ of the brake caliper.

Phase portrait for different damping ratios are given in Fig. 5. In case of the bogie under investigation the nominal normal force was $F_n = 15.6\ kN$, thus for the minimal necessary damping we get the value $d_{limit} = 1\ kNs/m$.

Some preliminary conclusions can be drawn from this model:

- The stability of undamped systems ($d = 0$) only depends on friction coefficient characteristics $\mu(v_s)$ of the brake pad material, provided that the normal force is constant,
- By applying sufficiently high damping ($d > d_{limit}$), the friction induced self-excited (auto-excited) vibrations could be eliminated,
- The smaller the normal force, the lower is the necessary damping $d_{limit}$.

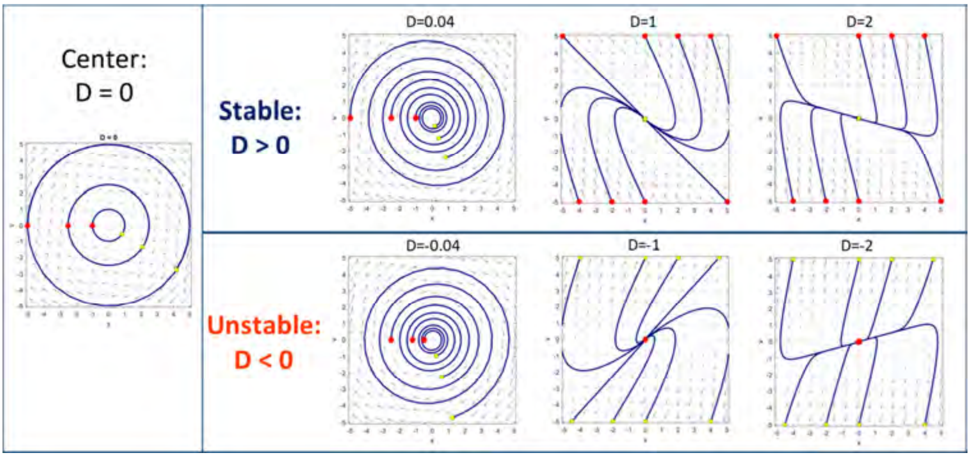


Fig. 5 Phase portraits of the linearized system: red dots = starting points, yellow squares = end points of the trajectories

### 3.2 Model for bogie frame pitch motion – 1 dof

In this modell we consider only one degree of freedom, namely the pitch motion $\theta_f$ of the bogie frame. Moment of inertia $J_f$ of the bogie frame and the mass of the brake unit $m_b$ including the brake suspension link are summed up into the mass $m_1$ in the equivalent single degree of freedom model, see Fig. 6. Primary and secondary springs and dampers are also concentrated into one spring and one damper, with coefficients $s_1$ and $d_1$ respectively, see also Fig. 11 for geometrical notations. The pitching motion equation of the bogie reads as

$$(J_f + 4m_b)\,\ddot{\theta}_f = -4a^2 s_p \theta_f - 4a^2 d_p \dot{\theta}_f - 4c^2 \underbrace{\frac{s_{s1} \cdot s_{s2}}{s_{s1} + s_{s2}}}_{= s_s} - \underbrace{2 \cdot \emptyset \cdot d_s \dot{\theta}_f}_{= \emptyset} + 4bF_f(v_s).$$

Introducing the relationship $z = b\,\theta_f$ and dividing the previous equation by $4b$, we can write the motion equation for the reduced system representing a quarter bogie:

$$\underbrace{\left(\frac{J_f}{4b^2} + m_b\right)}_{m_1} \ddot{z} = -\underbrace{\left(\left(\frac{a}{b}\right)^2 s_p + \left(\frac{c}{b}\right)^2 s_s\right)}_{s_1} z - \underbrace{\left(\frac{a}{b}\right)^2 d_p}_{d_1} \dot{z} + F_f(v_s)$$

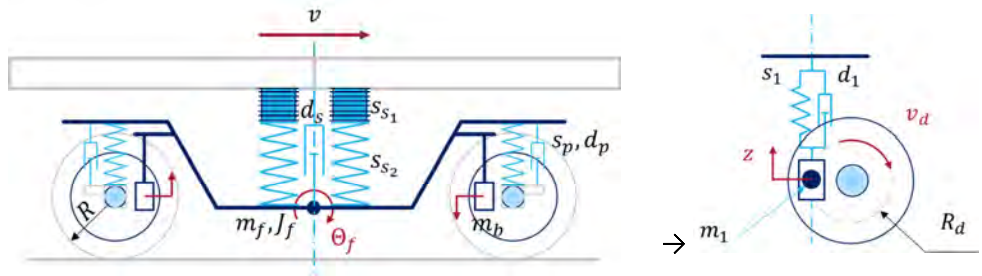


Fig. 6. Simplified model for bogie frame pitch motion

The undamped eigenfrequency of the model is $f_1 = 8.5\,Hz$, and for the equivalent damping we take at least $d_1 = 5\frac{kNs}{m} > d_{limit} = 1\frac{kNs}{m}$. By rearangeing eq. 2, a disc velocity dependent cylinder pressure $p_c(v_d)$ can be expressed as

$$p_c(v_d) < p_{c,limit}(v_d) = -\frac{d}{2\,A_c k \eta_b \mu'(v_d)},$$

where the $p_{c,limit}(v_d)$ curve separates the stable and unstable regions. Fig. 7. shows that the system is stable in the entire operational cylinder pressure range, i.e. below the horizontal line at ca. 3.8 bar.

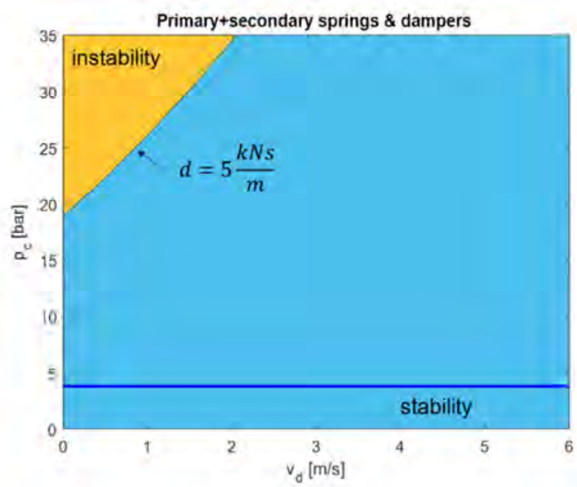


Fig. 7. Stability map cylinder pressure vs. disc circumferential velocity

The results suggest the conclusion that the source of the vibration phenomena is not the pitch motion of the bogie frame.

### 3.3 Model with elastic brake console and suspension link – 1 dof

In this modell we consider only one degree of freedom, namely the vertical motion of the brake unit reduced to the center of the brake pad. Mass of the brake unit $m_b$ including the brake suspension link are summed up into the mass $m_2$ in the equivalent single degree of freedom model, see Fig. 8. Stiffness $s_2$ and damping $d_2$ of the equivalent model are calculated from the elastic and dissipative properties of the brake console and the suspension link, while the rigid bogie frame is fixed in this case [4, 5].

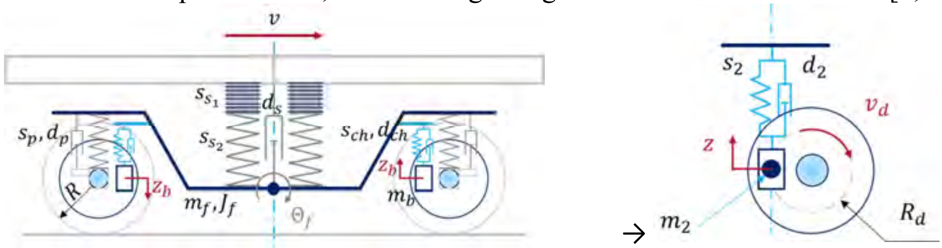


Fig. 8 Simplified model for brake unit vertical vibration

The model parameters are as follows: $m_2 = 108.3\,kg$, $s_2 = 60\frac{kN}{mm}$, $f_2 = 118\,Hz$. The eigenfrequency of the brake console itself is $f_c = 213.5\,Hz$, and the damping ratio of the steel brake console is set to $D = 0.3\%$, thus the equivalent damping is $d_2 = 0.27\frac{kNs}{m} < d_{limit} = 1\frac{kNs}{m}$, [3]. The stability map of cylinder pressure vs. disc circumferential velocity can determined in a similar way as in the previous section, however, the result is quite different, see Fig. 9. It can be seen in this figure, that there is a stable and an unstable region in the operational range, i.e. are below the horizontal line at 3.8 bar. Under a critical disc circumferential velocity of 5.2 *m/s*, i.e. under a critical vehicle speed of ca. 38 *km/h* the system is unstable at constant cylinder pressure of $p_c = 3.8\,bar$.

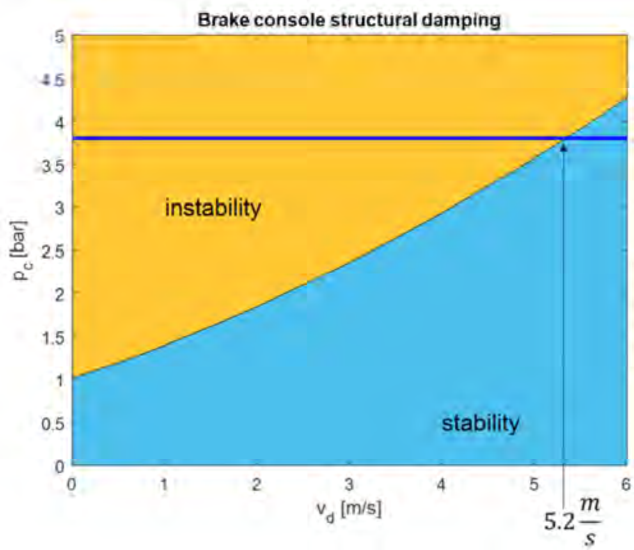


Fig. 9 Stability map cylinder pressure vs. disc circumferential velocity

It is a common practice to reduce the cylinder pressure at lower speed to account for the higher friction coefficient available, besides, locomotive drivers usually release the brake just before stopping in order to avoid longitudinal jerk. Based on these, one could come to the idiea to control the cylinder pressure in a way, that keeps the braking force constant: $F_f = -2\, A_c k \eta_b p_c(v_d)\mu(v_d)$ = const. It is a reasonable method from point of view of the stopping distance, but not enough to ensure the stability of the brake system. Fig. 10. shows that below ca. 30 *km/h* vehicle speed the cylinder pressure is in the unstable region, because it is abowe the $p_{c,limit}$ curve. In order to ensure stability one should control the cylinder pressure to a value, which complies with $p_c(v_d) < p_{c,limit}(v_d) = -\frac{d}{2\, A_c k \eta_b \mu'(v_d)}$. Decreasing the cylinder preassure, of course, could result in a – to some extent – increased stopping distance, which must be regarded as well.

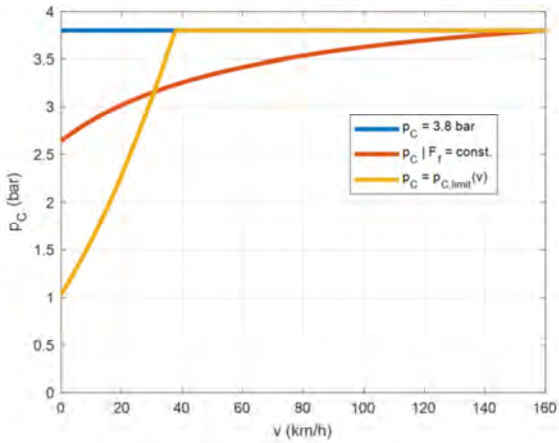


Fig. 10 Control strategies for the cylinder pressure

*Remark:* The damping capability of the brake console can be increased theoretically in two ways:

1. Apply high damping materials for the brake console, e.g. a layerd composite structure.
2. Keep steel as the base material of the console, but increase the critical damping, i.e. construct a heavier and stiffer brake console, see eq. 1.

### 3.4 Two degree of freedom model

Now we combine the previous two models into a 2-dof model to account for bogie pitch motion $\theta_f$ and brake unit vertical motion $z_b$ too. The following assumptions are adopted:

- No slip in the wheel-rail contact
- No vertical excitation from the rail
- Constant vehicle velocity
- Symmetric structure
- Sliding velocities are always positive, equal in magnitude, and have opposite directions at the two wheelsets.

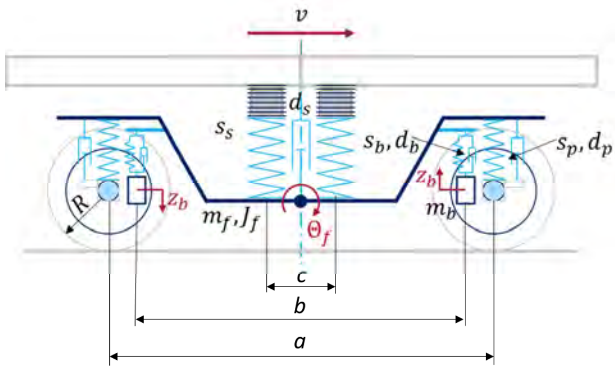


Fig. 11 Bogie model with two degrees of freedom

The motion state vector of the model is set up as $x = \left[\theta_f, z_b, \dot{\theta}_f, \dot{z}_b\right]^T \in \mathbb{R}^4$ and the ODE system of the model is $\dot{x} = f(x,t) = f(x)$, i.e. the system is autonomous.
The model can be linearized in a similar way as it is described in section 3.1, which implies the assumption that no sticking of the brake pad occurs. The equilibrium state is determined by solving the $0 = f(x_0)$ system of equations for vector $x_0$. Then system of motion equations is linearized at the equilibrium state $x_0$, which results in the system matrix $A = \left.\frac{\mathrm{d}f(x)}{\mathrm{d}x}\right|_{x=x_0}$. Finally, the stability condition for the linearized system can be stated as $\Re\{\mathrm{eig}(A)\} < 0$, which means that the system is stable only if the real part of the eigenvalue of the system matrix $A$ is negative.
In the subsequent part of this section the results of a parameter study are presented, where the equivalent brake unit mass is plotted against the vehicle velocity, while one single parameter is varied in three stages and all other parameters are kept constant, see Figures 11–15.

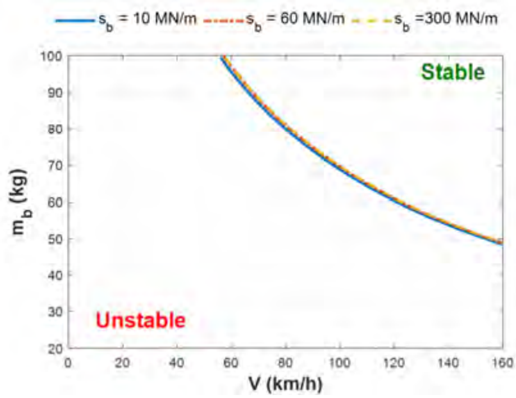


Fig. 11. Parameter study on brake unit suspension stiffness

This method is motivated by the experience, on the one hand that we usually want to know the critical vehicle velocity, below which unstable behaviour of the brake system can emerge. On the other hand the determination of the equivalent mass of the brake unit is very difficult, because of the complexity of the mechanism, because of rubber parts applied in the suspension of the brake unit, and generally due to lack of information.

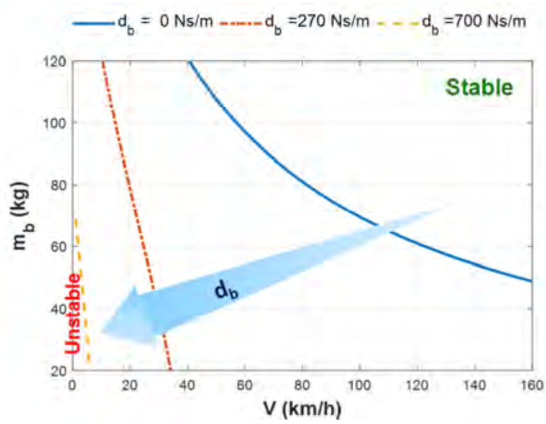


Fig. 12  Parameter study on brake unit suspension damping

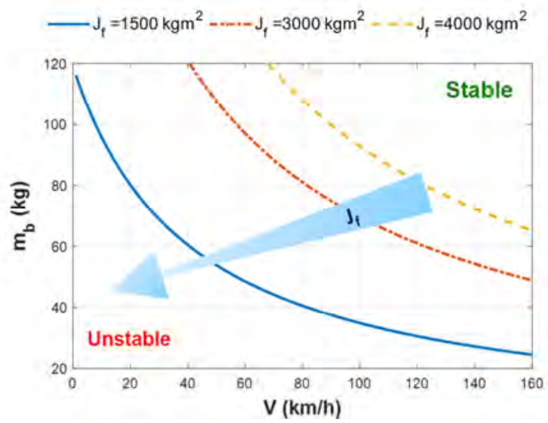


Fig. 13. Parameter study on bogie frame moment of inertia

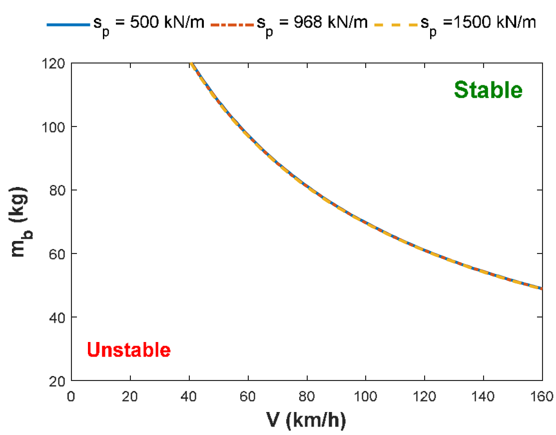


Fig. 14  Parameter study on primary stiffness

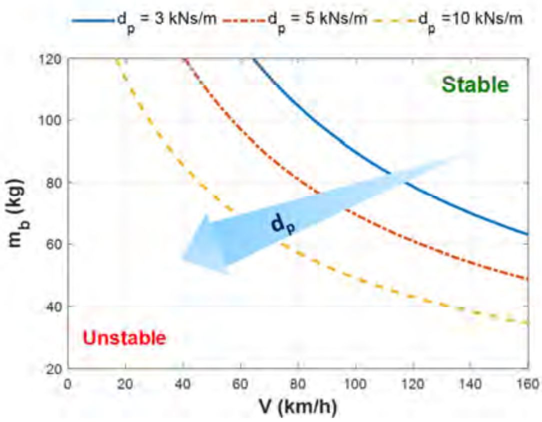


Fig. 15 Parameter study on primary damping

## 4. CONCLUDING REMARKS

Based on the models analysed in this study some short guidelines regarding the design parameters of disc brake systems can be given, with the aim of increasing the stability region of the system:

- *Signed* slope of friction coefficient function, i.e. derivative of the friction coefficient by the sliding velocity shall be increased: $\mu'(v_s) \uparrow$
- Brake cylinder pressure shall be lower than the velocity dependent limiting value, which mainly depends on the friction coefficient characteristics, as far as it is acceptable from point of view of the braking distance: $p_C \downarrow \leq p_{C,limit}$
- Equivalent brake unit mass shall be increased, but of course there are other design objectives as well: $m_b \uparrow$
- Brake unit suspension stiffness (i.e. brake console and brake pad suspension link): Obviously, the suspension stiffness itself has no direct effect on the stability, however the damping coefficient was constant in the parameter study, which is not the case in reality, compare Fig. 11. with the remark at the end of section 3.3.
- Brake unit suspension damping shall be increased above the limiting value determined by the slope of the friction coefficient function, see Fig. 12: $d_b \uparrow > d_{limit}$
- Bogie frame inertia shall be decreased, see Fig. 13: $J_f \downarrow$
- Primary stiffness $s_p$ has no direct effect on stability, see Fig. 14.
- Primary damping shall be increased, see Fig. 15: $d_p \uparrow$

Further investigation, experiments and sensitivity analysis are necessary to evaluate other non-linear effects, such as deterioration of components for example due to wear, joint gaps and aging of rubber parts.

## 5. ACKNOWLEDGEMENT

The author thanks to the Ganz Motor Kft. for providing important technical data and experience for this investigation. The investigation was carried out by using Matlab®, available under academic licence at the Budapest University of Technology and Economics.

## 6. REFERENCES

[1] **Süveges, L.**: Development of railway bogies at GANZ, with special emphases on bogie family type GH250, Vasútgépészet, Issue 4, 2017, p. 38 – 44. (In Hungarian)

[2] **Zobory, I.**: Investigation into the vibration phenomena of the disc-brake system of a railway bogie, Research Report, Technical University of Budapest, Faculty of Transportation Engineering, Department of Railway Vehicles, Budapest, 1997. (in Hungarian)

[3] **Gao, Ch. et al.**: Fundamentals of stick-slip, Wear, 1993, vol. 162-164, p.1139–1149.

[4] **Zobory, I. - Békefi, E. - Anka, L.**: On self-excited vibrations in disc-braked running gears, Proceedings of the 6th VSDIA (Ed. by Prof. I. Zobory), BME Department of Railway Vehicles, Budapest Hungary, 1998. p.83-92.

[5] **Németh, I. - Zobory, I.**: Identification of Structural Damping in Railway Disc Brake Suspension Systems, Proceedings of the 7th VSDIA (Ed. by Prof. I. Zobory), BME Department of Railway Vehicles, Budapest, 2000. p.303-314.

# KNORR-BREMSE RESULTS IN ADHESION MANAGEMENT AND PARTICIPATING IN PINTA PROJECT

**Miklós KRÉMER**

Knorr-Bremse Railway Vehicle Systems Hungaria Ltd.
H-1238 Budapest Helsinki út. 105., Hungary

*Received: November 6, 2018*

## ABSTRACT

Knorr-Bremse Brake Systems Hungaria Ltd. has constantly evolving results for ensuring to keep the stopping distance also in case of low adhesion conditions. It is self-evident that Knorr-Bremse is participating in PINTA Project, and in some topics also as project leading actor, i.e.: in WP7 with respect of adhesion database creation. This paper summarizes the advanced solutions of Knorr-Bremse to the railway transport demands and the goals of Pinta1

*Keywords*: adhesion, brake system

## 1. INTRODUCTION

In railway train operation it is a general goal to generate hard and sure deceleration. The timetable is the basic regulator of train operation (visualized timetables are speed-timing Train Diagram variants) reduction in journey time (red) causes more cycles, with the same fleet. Hard acceleration and braking deceleration is contributing to reduction in journey time. The limits of journey time reduction are: the maximum permitted speed for the infrastructure/vehicle components, the acceleration and the deceleration capability.

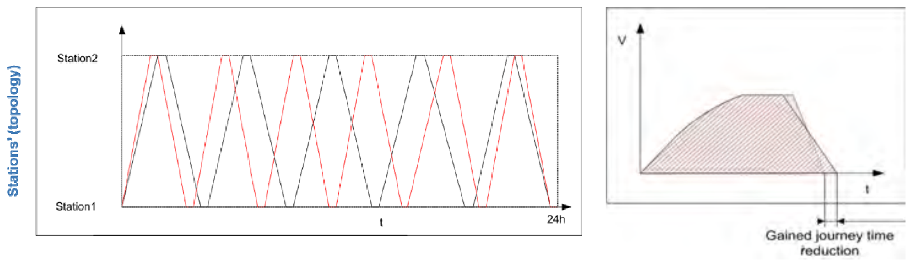


Fig. 1 One more train turning=capacity increase

## 2. DRY TRACK CASE ALSO FOR TRAIN ACCEPTANCE

The deceleration curves begin to be normative. Deceleration curves concern on „Dry" track + safety margin

The dry friction braking case focuses on the brake pad and disc system, in the following sense:

- Force actuation process is to be considered
- Heat dissipation process is to be considered
- Following the wear process is necessary
- The kinematics of train running is to be analysed

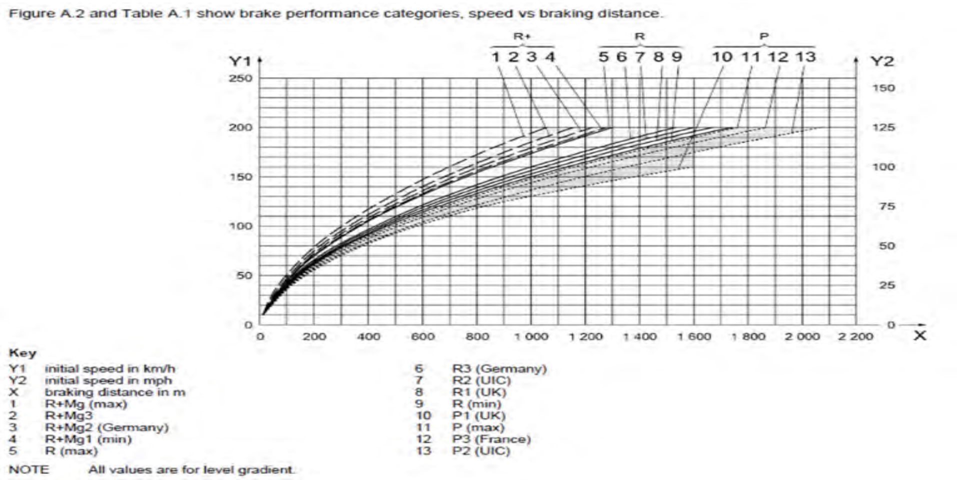


Fig. 2 The 'dry braking curves' and categorization on multiple units [6]

## 2. ACTUAL NORMATIVE LIMITS AND METHODS TRYING TO HANDLE THE ADHESION'S UNCERTAINTY

In the wheel/rail connection the adhesion coefficient utilization is limited during braking in a value of 0.15 (this belongs to a deceleration ~1.5m/s$^2$ (if WSP exists))

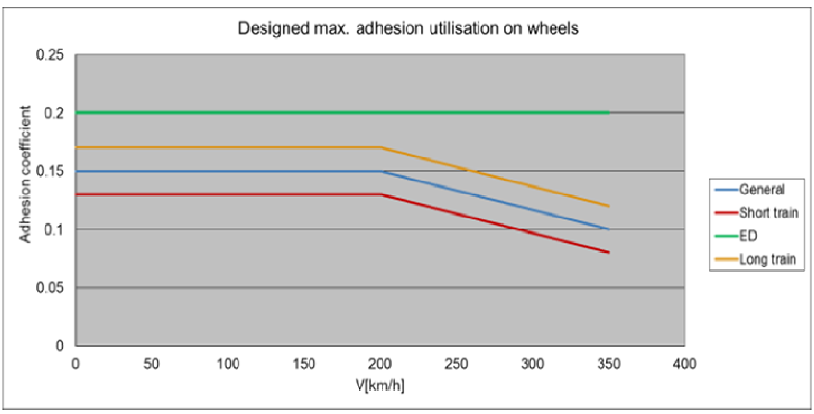


Fig. 3 Prescription on vehicle brake system design – adhesion utilization limits

Status quo: In some lands autumn also the 0.15 adhesion is not guaranteed – autumn time tables cause less capacity or more trainset demand.
Documents dealing with realistic stopping distance increase limits within low adhesion cases:

- UICB126_RP48_2016
- UIC_B126_DT414_2006
- UIC_B126_DT414_2006
- EBI curves

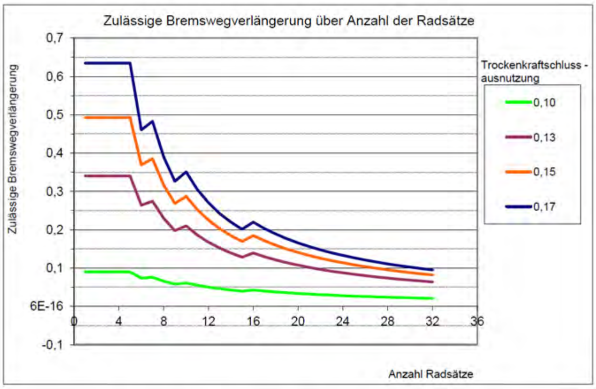


Abb. 2: Zulässige Bremswegverlängerung über Anzahl der Radsätze

Fig. 4 Stopping distance extension limitation in case of low adhesion [2]

If we intend to accept higher adhesion utilization via brake design, more actions are needed to limit the stopping distance increase in case of low adhesion. The train length dependency shows that a wheel-set ahead increases adhesion behind.

## 3. ACTUAL ACTION SOLUTIONS OF KNORR-BREMSE TO REACH THE TARGETS

### 4.1 Train Braking

Knorr-Bremse is dealing with complete brake systems included all main and accessory elements

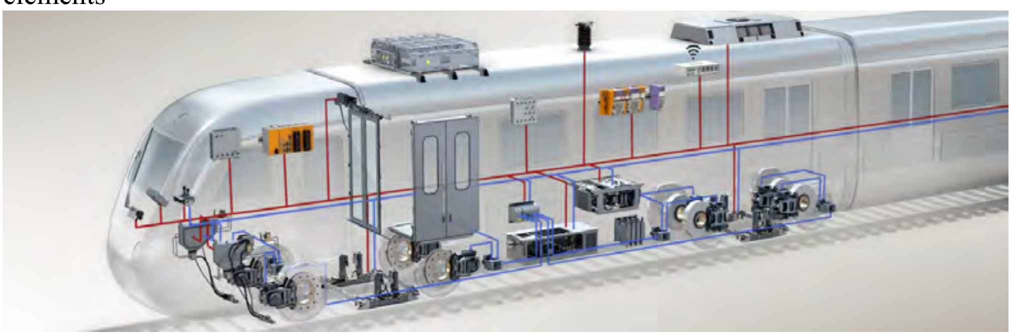

Fig. 5 Complete brake systems delivered by Knorr-Bremse

- Automatic action of the electronic Wheel Slide Protection (WSP) system
- Manual or automatic sanding
- If fitted with Eddy current brakes they decelerate undisturbed, controlled
- If fitted with Magnetic track brakes they produce extra decelerating force and Intensively cleans the leaves afterwards!

3.1 Automatic action of the electronic Wheel Slide Protection (WSP) system. Also a braking wheelset with optimized WSP control increases adhesion.

- Mechanical units MW, MWX from 1970'th
- Mikro-processor WSP "MGS1" from 1981 (8bit)

- Mikroprocessor WSP "MGS2" from 1997 (16bit)
- Mikroprocessor WSP "MGS3" for recognition and adaption to adhesion types

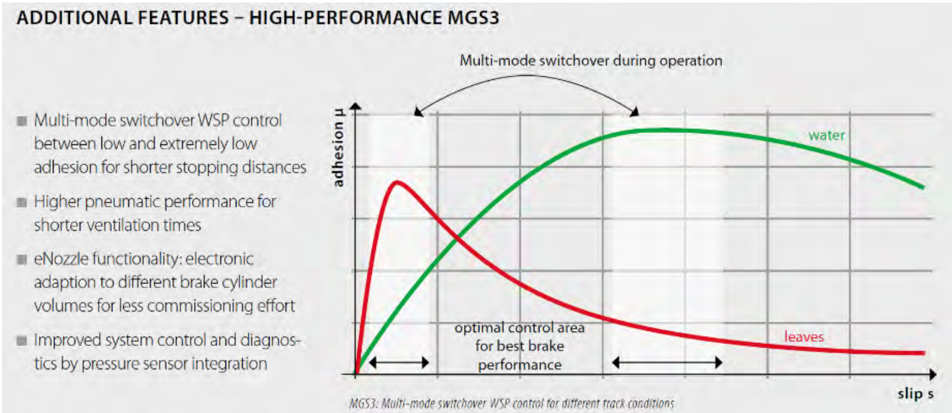


Fig. 6 Working regions of the new adaptive Wheel Slide Protection device

### 4.2 Further devices

Some further devices should be used to keep stopping distance within very low adhesion (i.e.: leaves) [10]

Very low adhesion is defined different and stopping distance extension limit is not given. UIC541-05 says adhesion "very low" if initial adhesion is less than 0.03 in, but UIC B 126 DT414 says initial adhesion is less than 0.06. The task of manufacturer to use further devices i.e.: magnetic track brake and sanding device to keep stopping distance also in these cases.

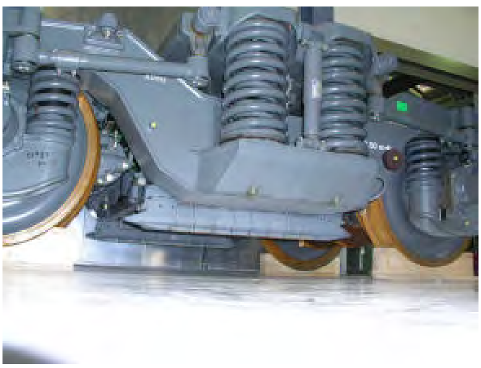

Magnetic track brake

Sanding device

Fig. 7 Devices to upgrade adhesion of advantageous circumstances

### 4.3 Improvement possibilities

Knorr-Bremse is also dealing with adhesion research, focusing on improvement possibilities. The roller rig in München, the sanding efficiency test rig in Mödling, and the Wheel slide protection device (WSP) test rig in Budapest and their engineering teams are participating in product development and also basic research.

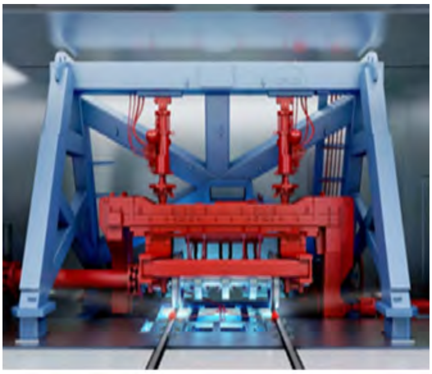

Roller rig for single wheelset (real adhesion)

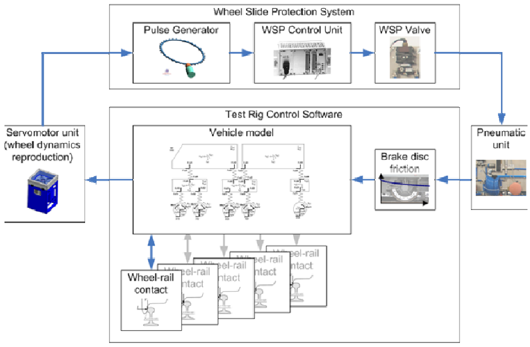


WSP HIL test rig for whole vehicle (modelled adhesion)

Fig. 8 Test devices of Knorr-Bremse supporting WSP development

## 5. PINTA WP7 ADHESION DETECTION AND LOW ADHESION MANAGEMENT [12]

Knorr-Bremse is participating in PINTA project, financed by EU, with Alstom, Bombardier, CAF, DB, Faiveley, Siemens and SNCF under grant agreement No. 730668

The companies used to have their adhesion catalogue on approaching different real conditions for WSP device development.

Adhesion data based on the Siemens Vectron test. ATLAS test rig (Knorr-Bremse) – used for generation of adhesion curves.


Fig. 9 Tests on Velim test track: controlled slip tests of locos

Adhesion data and conditions were measurement. The data were processed, and adhesion functions created for different slip, speed and also time and position dependency. The goal is harmonization and easier validation of WSP test rigs. The main feature is using correct adhesion model. Vehicle models that takes dynamic axle loads have been also negotiated (Fig. 10).

Wheel LCC aspects are concentrating on avoiding the wheel flat by now. Statuesque of EN15595 and UIC541-05, concerning on wheel slide protection systems prohibits deep slip in higher speed range or block of wheels.

| | |
|---|---|
| 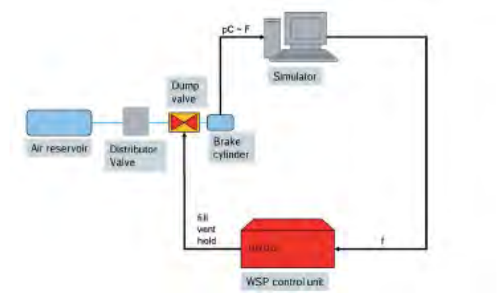 | 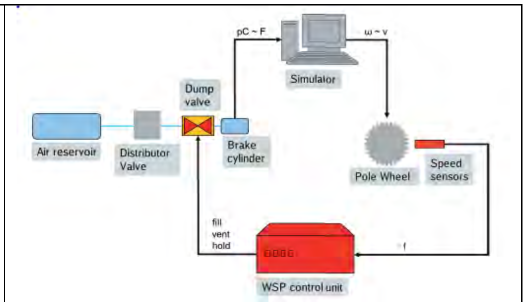 |
| Dump valve and control unit as HIL tested | All WSP dev. elements HIL tested |




Fig. 10 WSP device test rigs of different HIL (Hardware in the loop) coverage [13]. Both contain adhesion models

Generated documents:

- Multiple deliverables as well as the Adhesion Catalogue containing performance requirements for adhesion recovery systems
- and a proposal for normative changes focusing on sanding.

## 4. CONCLUDING REMARKS

- Knorr-Bremse is a market leading brake system supplier, containing the whole range of equipment
- Railway should be a renewed disruptive technology against long distance and urban road transport –"Shift to rail"
- Real „extremely low adhesion" has to be defined.
- Stopping distance extension limit should be defined also in case of „extremely low adhesion" .
- Clear demand to infrastructure managers i.e.: adhesion mapping, determined use of adhesion modifier
- PINTA goal is: harmonization and easier validation of WSP test rigs of different owners. Testing and accepting a WSP system on different test rigs can assure the determination of realistic adhesion improvement.
- The PINTA project is continuing PINTA2

## 4. REFERENCES


[1] UIC_544-1

[2] UICB_126_RP48_2016

[3] UIC_B126_DT414_2006

[3] TSI_Loc&Pas

[4] ERA_ERTMS_040026

[5] DINEN16207_2014_11_EN

[6] EN16185-1_2015

[7] EN15734-1

[8] **Sábitz, L. – Kolonits, F. - Zobory, I.:** On Rolling Contact Fatigue in Railheads: Analysis of Head Check Evolution, Proceedings of the 14th International Conference on Civil, Structural and Environmental Engineering Computing. 236 p.

[9] PINTA working documents

[10] KB, training material Track brakes

[11] prEN15313

[12] Knorr-Bremse poster on Innotrans

[13] UIC 541-05

# VEHICLE CONDITION MONITOR SYSTEM CONSIDERING VEHICLE AND TRACK MAINTEANANCE

**Shihpin LIN and Yoshihiro SUDA**

Institute of Industrial Science, the University of Tokyo.
4-6-1, komaba, Meguro-ku, TOKYO,153-8505, Japan

*Received: November 5, 2018*

## ABSTRACT

On-track condition monitoring system is installed to monitor the wheel load and lateral force of railway vehicle. An early detection system of railway vehicle abnormality utilizing the on-track condition monitoring system, which was established as a countermeasure for the derailment accidents caused by wheel load unbalance, is under construction. Data variation from the system becomes an obstacle in constructing the early detection system of railway vehicle abnormality. In this paper, a method to support detection of railway vehicle abnormality, to add vehicle inspection information and track inspection information inside big data processing is introduced.

*Keywords:* railway, vehicle, track, condition monitor system, machine learning, mainteanance information.

## 1. INTRODUCTION

Japan's railway system are recognized worldwide for its safe, timely and reliable operation. This reputation has been achieved mainly through the accurate execution of maintenance plans by railway operators. However, this type of system is not 100% full proof and some components may fail during operation of the railway vehicle. Components that unpredictably fail during operation poses a threat to the safety of the on board passengers. Failure of some components during operation often goes un-noticed until the next maintenance is scheduled which may result in unfavorable operating conditions. One of research about anomaly condition monitoring system with twist component was approached by Ohbayashi who studied in railway condition during failure of supported components, axle spring and air spring, on the railway vehicle (Ohbayashi et al.). Experiment of those conditions were set up and observed on test curve track in 2011.Then this research was followed by Kimoto in 2015. Railway condition, both normal and abnormal condition, were simulated in several criteria imitated from the experiment by using multi body dynamics software SIMPACK. However, simulation cannot cover all condition in the real world. The abnormal condition threshold derived from the simulation could not applied successfully due to variations in actual data from on-track condition monitoring system (Kimoto et al.). Adaptation to variations in actual vehicle data is necessary to detect the abnormal condition of vehicle at an early stage.

## 2. DATA OF VEHICLE RUNNING RECORDS WITH INSPECTION RECORD

### 2.1 Data of vehicle running record

The three-year running record data from on-track condition monitoring system of the commercial line was verified as a sample in order to see the actual condition of variation. The sample data includes time series data of two train sets from four sensor positions. Figure 1 shows the overview of running record shown. Two train sets are using different type bogie. Every train set has ten car bodies and twenty bogies. Each bogie, each car body were monitored individually by their running record. Details of four sensor points are shown in figure 2.

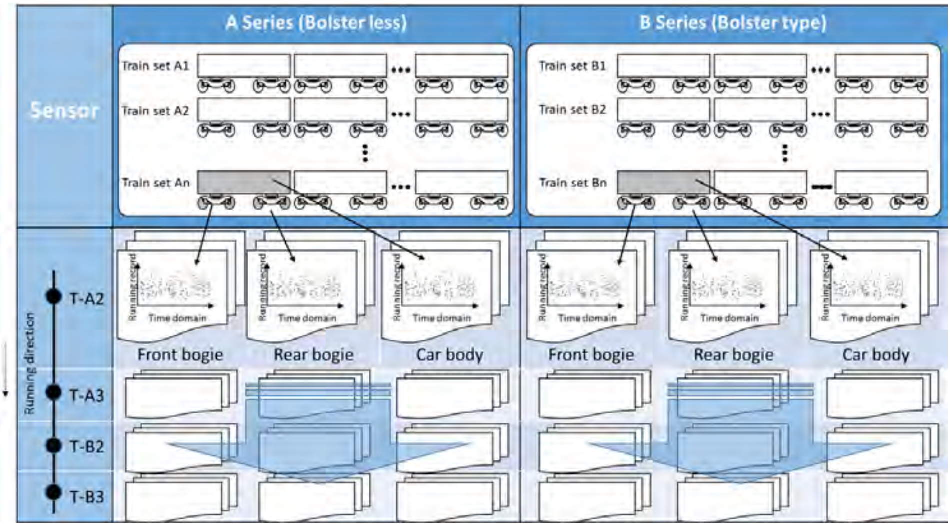


Fig. 1 Overview of running record from on-track condition monitoring system, 240 sheets in total.

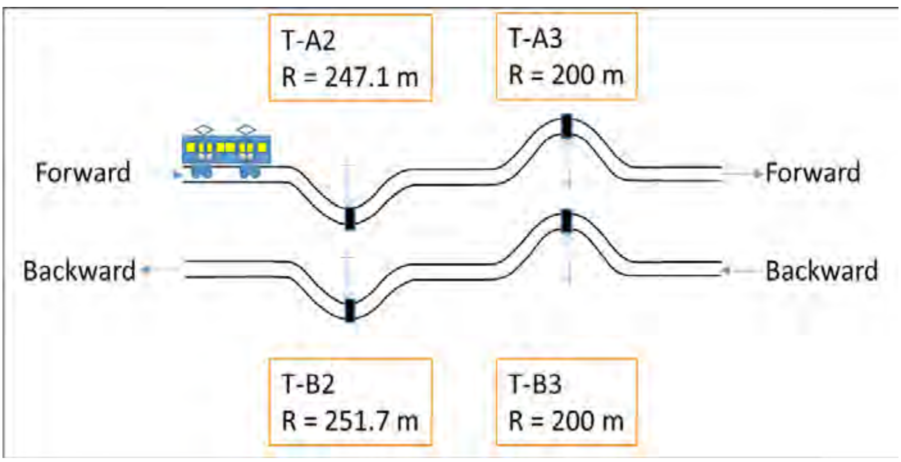


Fig. 2 Curve radius details of four sensor points on the commercial line.

## 2.2 Twist component of bogie and car body

Previous research have shown the twist component composed of wheel load is effective as an indicator of vehicle condition. Bogie twist component and car body twist component showed effect of unbalance condition of bogie and car body respectively.

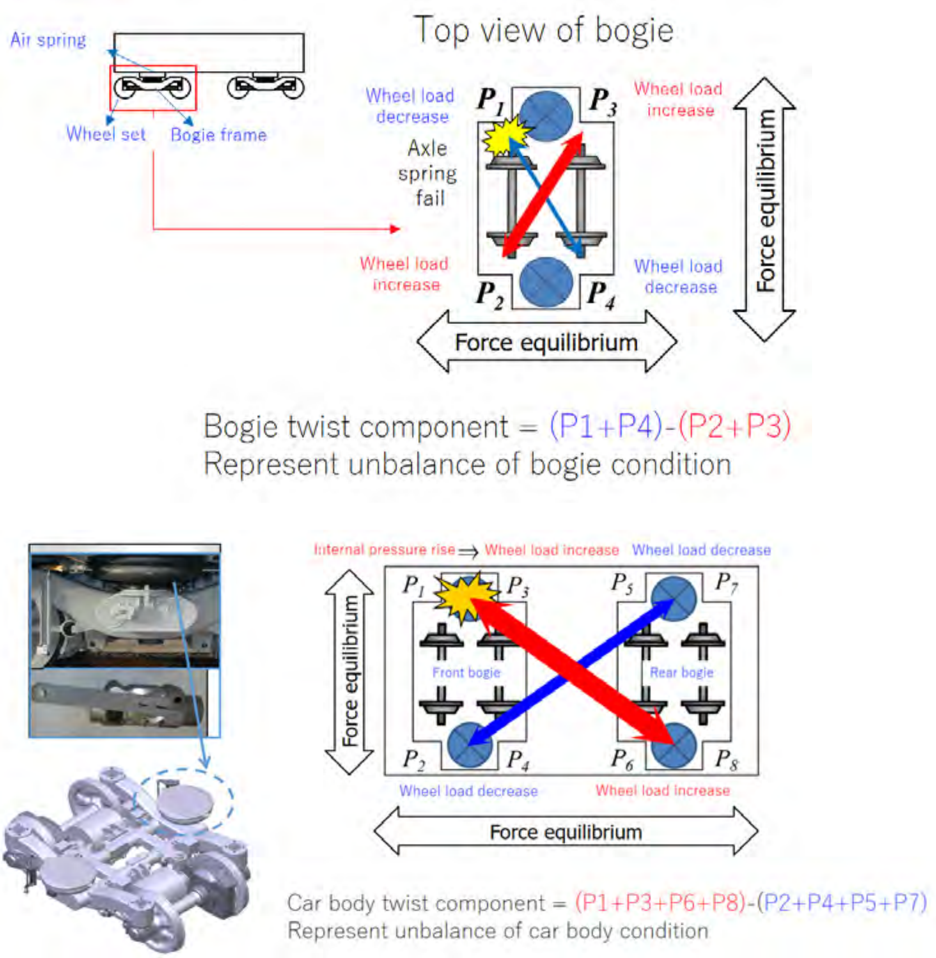


Fig. 4 Car body twist component

## 2.3 Data of vehicle running record overwritten with inspection record

One of abnormal detection concept work with data distribution of running record. If the data from a vehicle showed abnormal at all sensors point, this behavior is supposed to be abnormal of vehicle. On the other hand, if the data from all vehicles showed abnormal at one sensor point, this is supposed to be abnormal of railway track. However, the data of each vehicle, each sensor point, they have their inspection separately. Abnormal detection concept and inspection data should work together to detect correctly. We found that one of the reason is normal condition itself has fluctuated obviously after inspection activity such as wheel renewal, wheel surface re-profiling and rail head grinding. Changing of contact surface parameter, gradient and coefficient of friction, effected to wheel load and lateral force.

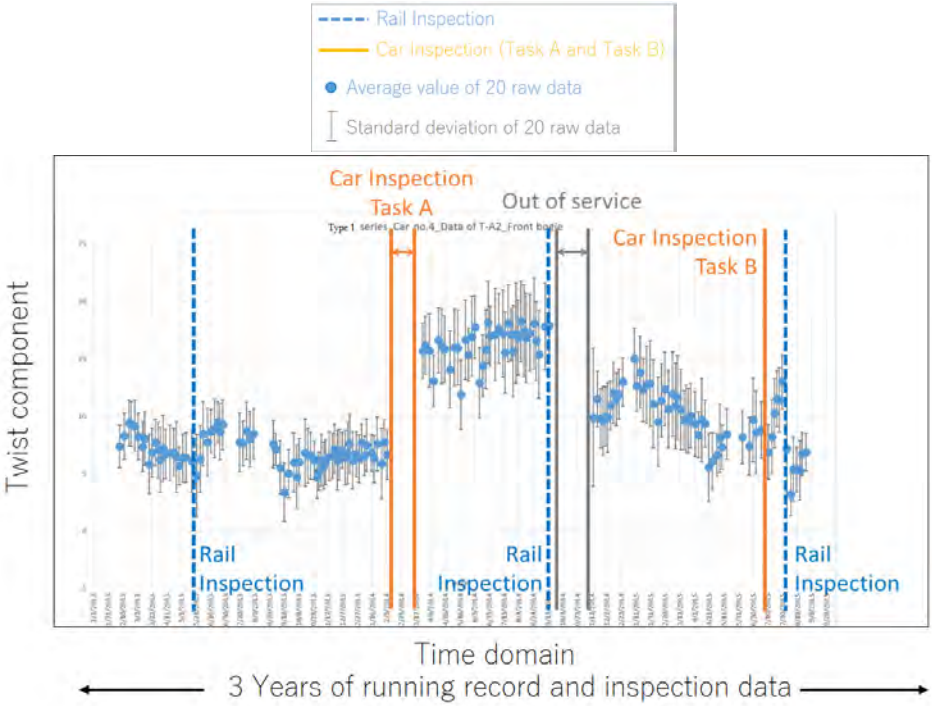


Fig. 5 An example of vehicle running record data overwritten with inspection record at front bogie.

## 3. CLASSIFICATION OF RAILWAY CONDITION CONCERNING WITH INSPECTION

### 3.1 Algorithm of abnormal detection by inspection data

The algorithm of abnormal detection by inspection data shown as figure 9. According to preceding section, running record was jumped after inspection activity.

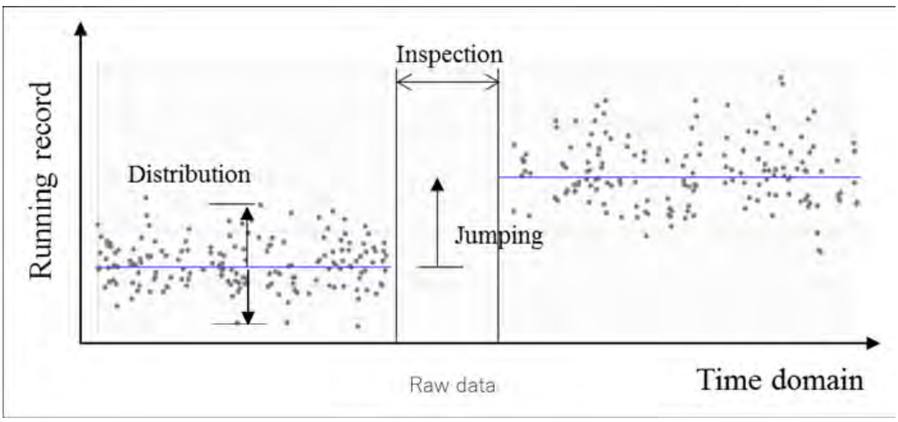


Fig. 6 Sample of data distribution and jumping data by inspection activity

In order to detect abnormal, jumping data must be confirmed in advance. This research concerned making algorithm of data pattern recognition.

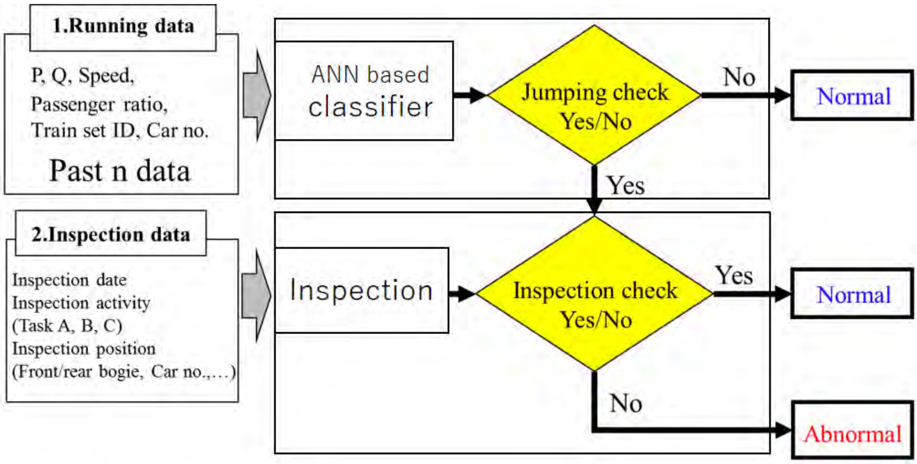


Fig. 7 Algorithm of abnormal detection by inspection data.

### 3.2 Making of Classifier

Observation of running record in time domain was known that something happen in timeline. Car inspection and rail inspection were recorded at fluctuating position in figure 10. This research is focusing on impact of car inspection (task A) to railway condition. In this research, artificial neural network ANN was chosen to make pattern recognition algorithm. Railway condition represented by twist component. Bogie twist component and car body twist component showed effect of unbalance condition of bogie and car body respectively. Twist component 20 data in time domain each before and after was set up in input layer. The data pattern that included inspection activities came from car no.2 to car no.9 (16 bogies). Moreover, the data pattern without inspection were selected from difference time at the same number. Half of total pattern were used to train ANN for making classifier. The rest of them were used to test the classifier.

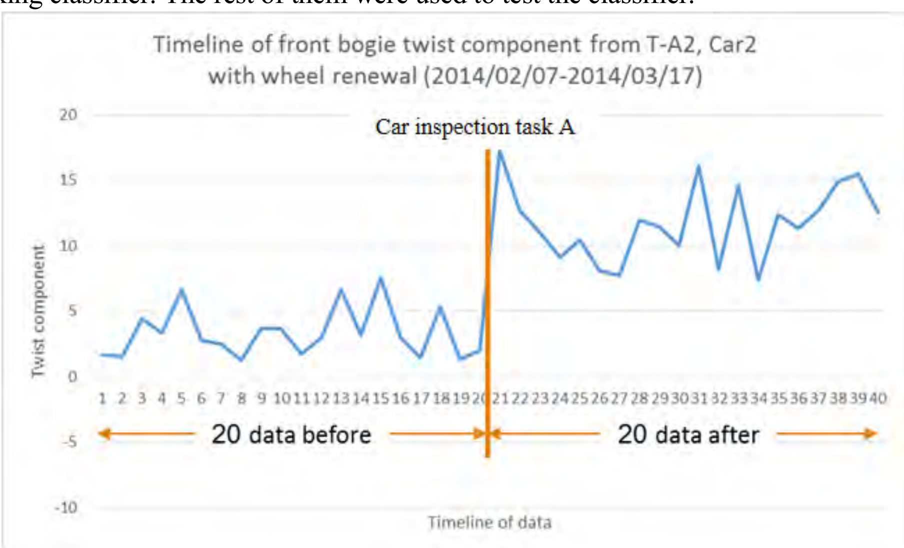


Fig. 8 Fluctuation of running record after inspection.

### 3.3 Result of pattern recognition

The result presented 100% classification of inspection pattern and normal pattern at sensor position TA-2 and TA3. In order to avoid over fitting, the algorithm was validated by dummy data regarding to limitation of information and the result also showed 100% classification. As TB - 2 and TB 3 are not 100%, tuning of classifiers should be further done.

TAb. 1 Result of pattern recognition.

| Sensor | Classified as | Accuracy |
|---|---|---|
| T-A2 | Jumping pattern | 100 % |
| | No jumping pattern | 100 % |
| T-A3 | Jumping pattern | 100 % |
| | No jumping pattern | 100 % |
| T-B2 | Jumping pattern | 85.71 % |
| | No jumping pattern | 88.89 % |
| T-B3 | Jumping pattern | 71.43 % |
| | No jumping pattern | 100 % |

## 4. CONCLUSION

An Artificial Neural Network based classifier using inspection information of railway vehicle and track used for big data analysis in early detection system of railway vehicle abnormality is proposed. Construction of an early detection system of railway vehicle abnormality using the on-track condition monitoring system has been carried out. The on-track condition monitoring system was established as a result of train derailment due to weight unbalance. In order to adapt to the variation of master data from on-track condition monitoring system, inspection information on vehicles and track was added. As a result of analyzing the data for 3 years, it was clarified that when the vehicle inspection and the track inspection were carried out, the twist component value of the car body and bogie changed. For big data processing, a classifier based on ANN was created with inspection information of vehicle and track as reference information, and its performance evaluation was performed. From the performance evaluation results, it was confirmed that the classifier can judge whether inspection was executed or not.

## 5. REFERENCES

[1] **Ohbayashi, H. et al.**: Study on the Fault Detection of Railway Vehicle using On-Track Monitoring System, Proceedings on J-Rail 2011, Tokyo, 2011, p.13-15.

# CONDITION MONITORING AND FAULT DETECTION OF SUSPENSION COMPONENTS IN FREIGHT WAGONS USING ACCELERATION MEASUREMENTS

**Stefano ALFI, Bin FU and Stefano BRUNI**

Department of Mechanical Engineering, Politecnico di Milano
Via La Masa 1, 20156 Milano, Italy
e-mail stefano.alfi@.polimi.it
ph. +39 02 2399 8495

*Received: November 9, 2018*

## ABSTRACT

Condition-based maintenance is seen as a major means to improve the business case for railway freight operators, and to improve the reliability and availability of freight trains. This paper reports on investigations performed aimed at developing methods for the condition monitoring of suspension components of Y25 bogies for freight wagons, enabling the implementation of CBM strategies for the wagon.

*Keywords*: Rail vehicle dynamics, monitoring of suspension components, freight wagons.

## 1. INTRODUCTION

Implementing condition-based maintenance (CBM) strategies for the railway running gear is a key priority for railway operators as it offers the opportunity of significantly reducing the total life cycle costs for railway vehicles, at the same time increasing safety, reliability and availability of operation. Particularly for railway freight vehicles, CBM can be a key factor to increase their attractivity compared to competing transportation means, thereby contributing to a shift of freight traffic from roads and air to the rail. This paper reports on investigations performed within project INNOWAG, funded by Shift2Rail, aimed at developing methods for the condition monitoring of suspension components of Y25 bogies for freight wagons.

In the work, the dynamic behaviour of a freight vehicle equipped with two Y25 bogies with suspensions in healthy and faulty conditions is simulated by means of a fully non-linear multi-body model and the results obtained are used as "virtual" measurements to be processed by the diagnostic algorithms. In this way, it is possible to assess the effectiveness of the algorithms in detecting different types and levels of faults in the suspensions. Given the highly non-linear behaviour of the suspension in the Y25 bogie, the use of data-driven fault detection methods is preferred compared to model-based ones and the work focusses on the analysis of the cross-correlation of bounce, pitch and roll accelerations of the bogie frame, derived from vertical acceleration signals measured at three different locations in the bogie frame.

## 2. SIMULATION OF DIFFERENT SUSPENSION FAULT MODES USING MULTI-BODY MODELS

A multi-body model of a wagon with faulty primary suspension was developed using software ADTreS, which is POLIMI's in-house software for the simulation of railway vehicle dynamics [1]. ADTreS is the Italian acronym for "dynamic analysis of train-track interaction".

The model of the wagon is based on the use of rigid bodies to represent the wagon body, two bogie frames and four wheelsets. The primary suspensions and the connection of the bogies to the wagon body are represented by means of non-linear springs and dry friction dampers. Wheel/rail contact forces are considered using a fully non-linear wheel/rail contact module taking into account the actual shape of the wheel and rail profiles and the non-linear creepage-creep force relationship. More details on the modelling of railway vehicles in this software are provided in reference [1].

Two main types of fault were modelled in this work, see Fig. **1**:

- Type A: failure of one coil spring in one primary suspension;
- Type B: failure of the dry friction damper in one primary suspension.

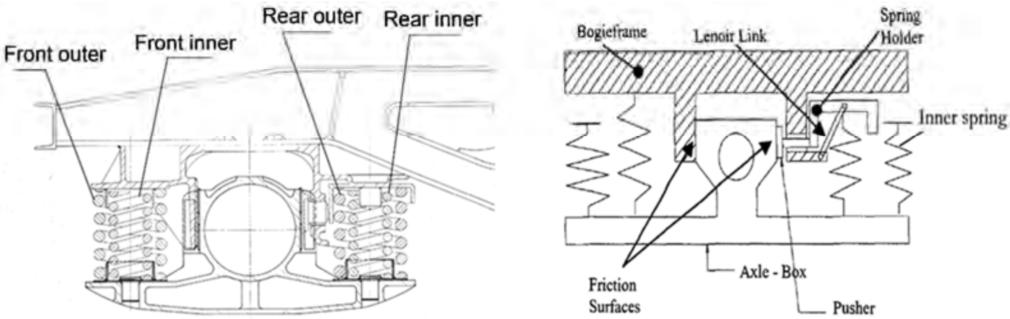


Fig. 1 The primary suspension of the Y25 bogie (left) and a functional scheme of the suspension (right)

## 2.1 Modelling of fault type A

The failure of one coil spring in the primary suspension is modelled as a change in the vertical stiffness of the spring element connecting the axle box to the bogie frame in one corner of the bogie. Given that the change in stiffness implies a re-distribution of the static forces transmitted by the coil springs, the threshold force at which sliding takes place in the friction element is also affected.

The changes in the parameters of the suspension are different depending on whether the failure takes place in the “front outer”, “front inner”, “rear outer” or “rear inner” coil spring, see Fig. **1** left. The parameters of the suspension also depend on the axle load. In this work, two extreme conditions are considered: the vehicle in full-load condition (carbody mass 80.60t) and in tare condition (carbody mass 6.86t).

Table 1 shows the values of the stiffness ($K_z$) and sliding force ($F_s$) parameters for the vehicle in full-load condition when the fault takes place at each one of the coil springs shown in Fig. **1** and for different types of fault, i.e.:

- broken spring, the stiffness of the single spring is set to 0;
- spring stiffness reduced to 50%;
- spring stiffness increased to 150%;
- spring stiffness increased to 200%;

Fault cases consisting of an increased value of spring stiffness are intended to represent failure modes leading to an improper increase of the suspension stiffness, e.g. the spring or slider getting stuck to some extent.

| | 0% (broken) | 50% | 150% | 200% |
|---|---|---|---|---|
| Front outer | $K_z$=2.06MN/m $F_s$ = 22.33kN | $K_z$=2.31 MN/m $F_s$ = 19.10kN | $K_z$=2.81 MN/m $F_s$ = 14.38kN | $K_z$=3.06 MN/m $F_s$ = 12.60kN |
| Front inner | $K_z$=1.78 MN/m $F_s$ =21.65kN | $K_z$=2.17 MN/m $F_s$ = 18.62kN | $K_z$=2.95 MN/m $F_s$ =14.96kN | $K_z$= 3.34 MN/m $F_s$ =13.77kN |
| Rear outer | $K_z$=2.06 MN/m $F_s$ = 10.69kN | $K_z$=2.31 MN/m $F_s$ = 13.92kN | $K_z$=2.81MN/m $F_s$ = 18.64kN | $K_z$=3.06 MN/m $F_s$ = 20.42kN |
| Rear inner | $K_z$=1.78MN/m $F_s$ = 11.37kN | $K_z$=2.17 MN/m $F_s$ = 14.40kN | $K_z$=2.95 MN/m $F_s$ = 18.06kN | $K_z$=3.34 MN/m $F_s$ = 19.25kN |

Table 1 - Parameters of the primary suspension for different Type A faults for the full-load condition (values in healthy condition are $K_z$ = 2.56 MN/m and $F_s$ = 16.51 kN).

Table 2 shows the values of the stiffness ($K_z$) and sliding force ($F_s$) parameters for the vehicle in tare condition for the same types of fault considered in Table 1. As shown in Fig. **1**, the inner springs are mounted with a gap between the top of the spring and the bogie frame and enter in contact with the bogie frame only when the vertical load on the suspension exceeds a threshold and compresses the outer spring sufficiently. In tare condition, the load on the suspension is too low and the two inner springs do not make contact with the bogie frame and therefore do not contribute to the total stiffness of the suspension. In this condition, the presence of a fault in the inner springs does not affect the behaviour of the vehicle and therefore cannot be detected.

| | 0% (broken) | 50% | 150% | 200% |
|---|---|---|---|---|
| Front outer | $\boldsymbol{K_z} = 0.50\ MN/m$ $\boldsymbol{F_s} = 4.23\ kN$ | $K_z = 0.75\ MN/m$ $F_s = 2.82\ kN$ | $K_z = 1.25\ MN/m$ $F_s = 1.69\ kN$ | $K_z = 1.50\ MN/m$ $F_s = 1.41\ kN$ |
| Rear outer | $\boldsymbol{K_z} = 0.50MN/m$ $\boldsymbol{F_s} = 0.\ kN$ | $K_z = 0.75\ MN/m$ $F_s = 1.41kN$ | $K_z = 1.25MN/m$ $F_s = 2.54\ kN$ | $K_z = 1.50\ MN/m$ $F_s = 2.82\ kN$ |

Table 2 - Parameters of the primary suspension for different Type A faults for the tare condition (values in the healthy condition are $K_z$ = 1.0 MN/m and $F_s$ = 2.12 kN).

## 2.2 Modelling of fault type B

The failure of the dry friction damper in one corner of the bogie is modelled as a change in the threshold force $F_s$ at which sliding takes place in the friction element, with no effect on the stiffness of the suspension. Table 3 shows the values of the $F_s$

parameter for different types of fault, with friction ranging from 50% to 150% of the nominal value.

| - Full load (Car-body mass: 80.60t) | | | | |
|---|---|---|---|---|
| | **50%** | **75%** | **125%** | **150%** |
| **Threshold force $F_s$** | $F_S = 11.6\ kN$ | $F_S = 16.74kN$ | $F_S = 27.91kN$ | $F_S = 33.49kN$ |
| **Tare load (Car-body mass: 6.86t)** | | | | |
| **Threshold force $F_s$** | $F_S = 1.06\ kN$ | $F_S = 1.59kN$ | $F_S = 2.65kN$ | $F_S = 3.18kN$ |

Table 3 – Values of the maximum sliding force for different Type B faults and for the wagon in full-load and tare condition (values in the healthy condition are 22.33 kN in full-load condition and 2.12 kN in tare load condition).

## 3. FAULT DETECTION ALGORITHM

Considering the relatively low economic value of one freight wagon, fault detection has to be based on a simple algorithm, requiring a simple measuring and data processing system. Considering different methods proposed in the scientific literature (see [2] for a recent review of the State-of-Art), the use of cross-correlation between acceleration signals measured at different locations in the bogie frame [3] appears as the best suited fault detection method in terms of achieving a good compromise between the measuring / processing effort required and the performance in terms of accuracy and reliability of fault detection.

The principle of the method is that the modes of vibration of a bogie with healthy suspensions are symmetric, due to uniform behaviour of the primary suspensions at the four corners of the bogie. Therefore, if the vibration of the body is excited by uncorrelated random irregularity from the left and right rails, the correlation between different components of bogie frame acceleration, e.g. bounce vs. roll or pitch vs. roll will be low. When a failure occurs at one corner, the symmetry of the modes of vibration is perturbed, resulting in a coupling of bounce, roll and pitch components of motion which can be detected from an increase of the cross-correlation between the acceleration signals for these components of bogie vibration.

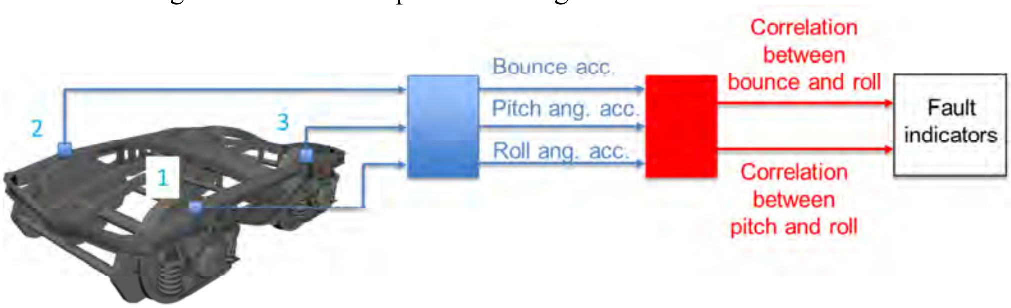


Fig. 2 Schematic representation of the signal processing technique for the detection of faults in the primary suspensions

A schematic representation of the method is shown in Fig. **2**. Three mono-axial accelerometers (numbered from 1 to 3 in the figure) are mounted at three corners of the bogie frame, to measure the vertical acceleration of the bogie frame over the axle-boxes.

The vertical acceleration signals are converted into the bounce, pitch and roll acceleration components for the bogie frame ($a_B$, $a_P$ and $a_R$ respectively) according to the kinematics of a rigid body:

$$a_B = \frac{a_2 + a_3}{2},$$

$$a_P = \frac{a_1 - a_3}{2l},$$

$$a_R = \frac{a_1 - a_2}{2b}.$$

where $2l$ is the bogie wheelbase and $2b$ is the axle box gauge. Finally, the cross-correlation between bounce and roll acceleration $C_{BR}$ and between pitch and roll acceleration $C_{PR}$ are evaluated:

$$C_{BR}(\tau) = \frac{1}{T}\int_{-\frac{T}{2}}^{\frac{T}{2}} a_B(t) a_R(t-\tau) dt\,,$$

$$C_{PR}(\tau) = \frac{1}{T}\int_{-\frac{T}{2}}^{\frac{T}{2}} a_P(t) a_R(t-\tau) dt\,.$$

To diagnose faults in the suspensions, four fault indicators are computed.

The first two indicators are based on the standard deviation of the cross-correlation between the acceleration signals while the other two indicators are based on the instantaneous value of the cross-correlation between pitch and roll at zero-time delay.

- Indicator 1: Standard deviation of the cross-correlation between bounce and roll accelerations for time delay $-10\text{ s} \leq \tau \leq +10\text{ s}$;
- Indicator 2: Standard deviation of the cross-correlation between pitch and roll accelerations for time delay $-10\text{ s} \leq \tau \leq +10\text{ s}$.
- Indicator 3: Value at time delay $\tau=0$ of the cross-correlation between pitch and roll accelerations low pass filtered at 10 Hz;
- Indicator 4: Value at time delay $\tau=0$ of the cross-correlation between pitch and roll accelerations without low pass filter.

## 4. RESULTS OF NUMERICAL EXPERIMENTS

Numerical experiments were run to consider fault types A and B for full load and tare load condition of the wagon. The results are described below for the different cases considered.

Fig. 3 shows the value of the four fault indicators for different degrees of severity of a fault of type A occurring in the rear outer spring of the primary suspension, when the vehicle is in the full-load condition. It is confirmed that all four indicators have a minimum absolute value when the suspension is in the nominal condition (stiffness is

100% of the nominal value) whilst the absolute values of all indicators increase when a deviation of the spring stiffness is applied in the numerical experiment, either decreasing or increasing the stiffness parameter. In principle, all 4 indicators appear suitable for the detection of the fault considered, but indicators 2 and 4 show more clearly the presence of a fault.
Similar numerical experiments were performed considering a fault happening in the rear inner, front outer and front inner springs of the primary suspensions, leading to the same conclusions as in the case presented below. The results of these additional cases are not shown for the sake of brevity but are considered in a summary table (Table 4) reported at the end of this section.

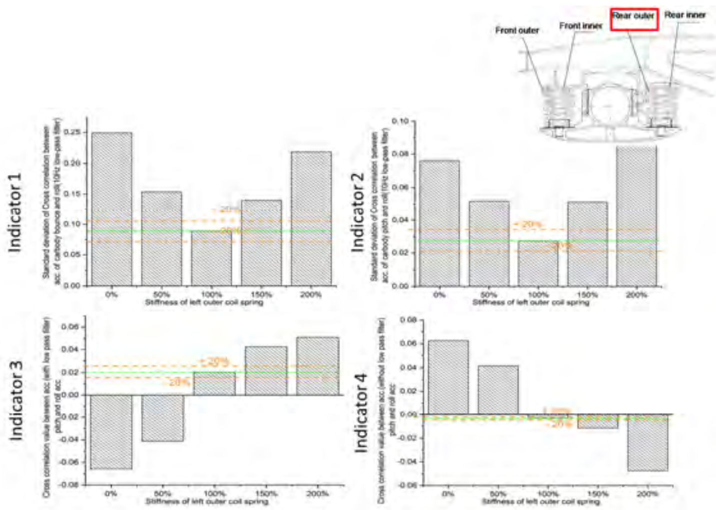


Fig. 3 Fault indicators 1 to 4 for a fault in the rear outer coil spring (type A) and vehicle in full load condition

Fig. **4** shows the value of the four fault indicators for different degrees of severity of a type A fault occurring in the rear outer spring of the primary suspension, when the vehicle is in the tare load condition. In this case, the indication is less clear than in the case of the full load condition, probably because the effect of spring fault on the dry friction damper is lower. The only indicator that shows a clear trend with the change of stiffness in the faulty spring is Indicator 3. Similar results are obtained when the fault is simulated in the front outer spring, again with the wagon in the tare load condition.
Fig. **5** shows the value of the four fault indicators for a fault occurring in the friction element of the primary suspension (fault type B), with the vehicle in the full load condition. In this case, a clear indication of the fault is obtained from all indicators except indicator 3. When the same fault type is considered for the vehicle in tare condition (not shown due to space restrictions) the only indicator that provides a clear trend with the occurrence of the fault is Indicator 3.

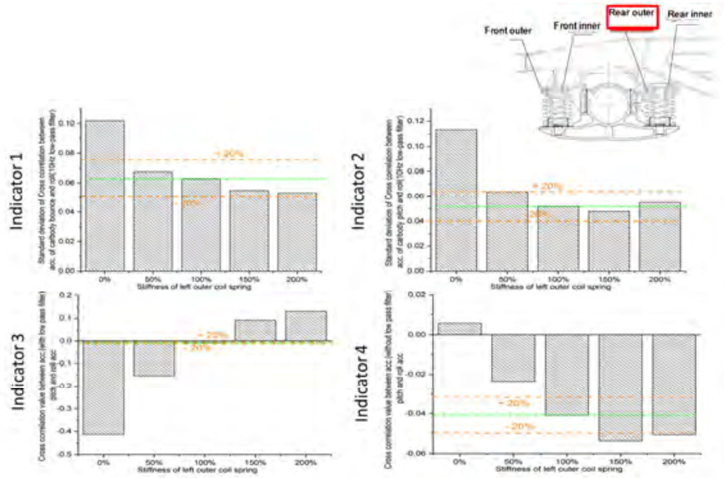


Fig. 4 Fault indicators 1 to 4 for a fault in the rear outer coil spring (type A) and vehicle in tare condition

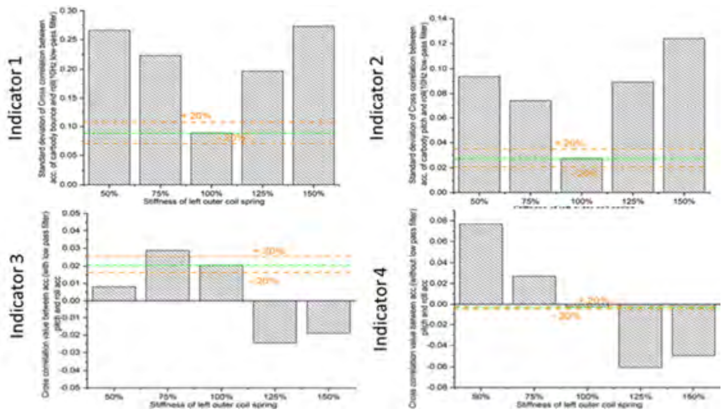


Fig. 5 Fault indicators 1 to 4 for a fault in the dry friction element (type B) and vehicle in full load condition

| | | | Indicator1 | Indicator2 | Indicator3 | Indicator4 |
|---|---|---|---|---|---|---|
| Fault Case A: coil springs | Full load | Front outer | ✓ | ✓ | ✓ | ✓ |
| | | Front inner | X | ✓ | ✓ | ✓ |
| | | Rear outer | ✓ | ✓ | ✓ | ✓ |
| | | Rear inner | ✓ | ✓ | ✓ | ✓ |
| | Tare load | Front outer | X | X | ✓ | X |
| | | Rear inner | X | X | ✓ | X |
| Fault Case B: Friction components | Full load | \ | ✓ | ✓ | X | ✓ |
| | Tare load | \ | X | X | ✓ | X |

Table 4– Summary of the results of numerical experiments for identification of faults in primary suspensions.

A summary of results from numerical experiments performed to assess the proposed method is provided in Table 4, with symbols "✓" and "✗"denoting respectively successful and non-successful identification of the fault. It is confirmed by the results shown in the table that faults in suspensions components are more easily detectable when the vehicle is in full-load condition.

## 5. CONCLUSIONS

In this paper, a method to detect faults in the suspension of a freight wagon with Y25 bogie is proposed, based on the examination of the cross-correlation of bounce, pitch and roll vibration. The method is assessed based on numerical experiments performed using a multi-body model of the wagon. It is shown that different fault indicators can be defined that could prospectively allow the detection of faults in coil springs and friction dampers.

Future extension of this work is foreseen, particularly to identify and classify faults based on the use of suitable outlier detection / artificial intelligence methods. Furthermore, the application of the method to measurements from on-track tests is envisaged.

## 6. ACKNOWLEDGEMENTS

The work presented in this paper has received funding from the Shift2Rail Joint Undertaking under the European Union's Horizon 2020 research and innovation programme under grant agreement no. 730863 – INNOWAG. The contents of this publication only reflect the authors' view and the Joint Undertaking is not responsible for any use that may be made of the information contained in this paper.

## 7. REFERENCES

[1] **Di Gialleonardo, E. – Braghin, F. – Bruni S.:** The influence of track modelling options on the simulation of rail vehicle dynamics. Journal of Sound and Vibration, vol. 331, 2012, p.4246-4258.

[2] **Li, C. – Luo, S. Cole, C. – Spiryagin, M.:** An overview: modern techniques for railway vehicle on-board health monitoring systems. Vehicle System Dynamics, vol. 55(7), 2017, p.1045-1070.

[3] **Mei, T. X. – Ding, X. J.**: Condition monitoring of rail vehicle suspensions based on changes in system dynamic interactions. Vehicle System Dynamics, vol. 47(9), 2009, p.1167-1181.

# NUMERICAL ANALYSIS OF THE FAILURES, RELIABILITIES AND AVAILABILITIES CONCERNING A GIVEN FAMILY OF RAILWAY CARRIAGES UNDER DIFFERENT OPERATION AND MAINTENANCE CIRCUMSTANCES

**József CSIBA**

BME ITS Non-Profit Co.
H-1111 Budapest,
Műegyetem rkp. 3

*Received: 6 November, 2018*

## ABSTRACT

The group of the most important key performance indicators of the operation and maintenance of railway vehicles as passenger carriages is composed by the availability, the failure rate and further failure occurrence characteristics. Concerning the vehicles the main structural subsystems and also the elements belonging to the latter after appropriate numerical description are naturally well represented by the elements of this group of indicators. In the present investigation the object of the examination are such vehicles which compose a vehicle family. However this family consists of four types, in this way the basic manifold gets layered. The types mentioned were constructed on the basis of same principles and the reliable constructional units and technical subsystems (bogie, draw- and buffer gear, brake gear, car-body, air-conditioning equipment, energy supplying equipment, heating equipment, etc.) are identical. The vehicles operated and are operating under different operation and maintenance conditions. The objective of the investigation is to make treated numerically the elements, as well as to point out the anomalies of the above mentioned indicator performance group of the passenger carriages type Z2 designed on the basis of identical principles and were "born" under identical circumstances. The evaluation of the indicators gives an opportunity to point out the influence of the different operation and maintenance conditions, furthermore to judge about certain management decisions, as well as the appropriate decision preparations and professional decision-makings, respectively.

*Keywords:* vehicle, passenger carriage, subsystem, key performance indicator, availability, failure, failure rate.

## 1. INTRODUCTION

A very valuable and useful information package is given to the operators, repairers, manufacturers, designers, vehicle owners and a lot of different experts by the continuous collection, comparative investigation and evolution with time of maintenance data of different type of railway vehicles.

This presentation shows the results of depot, service shop maintenance activities of a railway carriage family type Z2 for international and internal traffic.

The results of the maintenance activities can be characterized by the failure frequency, the type of the failure, the reliability and availability of the all vehicles of the vehicle family or different types of it.

The investigations were expanded for two service shops the first of them is responsible for vehicles in international traffic, while the task of other one is the maintenance of vehicles for domestic traffic.

The maintenance systems are controlled by the NRA's and RIC's regulations.

Two steps of the maintenance objects can be distinguished: service shop and workshop.

The carriage family are composed by the same technical subsystem, thus inter alia car bodies, bogies, WC – equipment, seats, lighting equipment, air conditioning equipment, energy supply, brake system, draw equipment, doors, buffers etc.

## 2. VEHICLES AND THEIR TASKS, BOGIES

The carriage family, which is under the scope of investigation, was partly constructed and built in Germany. The word "party" is justified because there are bogie types GH 250-2 and GH 250-3 under the vehicles which types have been constructed and manufactured in Hungary. The design of the bogie construction was born in the *Ganz – Hunslet Factory*, that's why the identification capitals GH are used. The figures 250 sign the permitted speed. The different bogie variants are signed by numbers 2 and 3. The bogies were manufactured also at the *Ganz–Hunslet Factory*.

The carriage family consists of seated carriages and restaurant–buffet ones. The seated carriages are open first and open second vehicles. The open first vehicles can run in international traffic, a certain part of the open second vehicles can run only in internal traffic, and the complementary part of the open second vehicles can run in both types of traffic. The restaurant–buffet carriages are suitable for international traffic, but sometimes they run also in internal InterCity trains

The permitted speed of all vehicles in the carriage family is 160 km/h. Each seated coach is of open type. The carriages suitable for international traffic have been equipped by air-condition equipment, while in the ones for internal traffic air – intercoolers have been mounted. The vehicles of Class Z2 were built between years 1994 and 1995. The main data of the vehicles of the carriage family are contained in Table 1. The type-wise numbers of the 69 vehicles to be investigated, as well as the names of their maintenance are introduced in Table 2.

| MAIN DATA OF THE CARRIAGE FAMILY | | | | |
|---|---|---|---|---|
| CLASS | Apmz | Bpmz | Bpm | WRbumz |
| 1 | 2 | 3 | 4 | 5 |
| SERIES NUMBER | 10-71 | 20-71 | 20-70 | 88-71 |
| MANUFACTURER | Waggonbau Bautzen GmbH | Waggonbau Bautzen GmbH | Waggonbau Bautzen GmbH | Waggonbau Ammendorf GmbH |
| YEAR | 1994-1995 | 1995 | 1994-1995 | 1995 |
| TYP | Open First | Open Second | Open Second | Restaurant Buffet Second |
| TRAFFIC | International | International | Internal | International |

Table 1 Main Data of the carriage family

**Stock & depots**

| | 10-71 | 20-71 | 20-70 | 88-71 |
|---|---|---|---|---|
| Su | 1 | 24 | 2 | 10 |
| Sm | 8 | 0 | 24 | 0 |

Table 2 Data of the stock and depots

Mileages (km/day)

| | 2015 | 2016 | 2017 |
|---|---|---|---|
| 10-71 | 298,13 | 497,77 | 490,37 |
| 20-70 | 292,44 | 355,92 | 369,00 |
| 20-71 | 238,86 | 458,48 | 436,19 |
| 88-71 | 273,85 | 309,94 | 294,26 |

Table 3 Data of mileages

The available data of mileage give an opportunity for a more detailed investigation into the maintenance and failure data. The daily mileage data between years 2015-2017 are summarized in Table 3. Considering the data, it can be fixed, that the mileage of the seated vehicles age higher in the last two years than it was in 2015, and the mileage of the carriages running also in international traffic, are also greater than the mileage of the carriages operating only in internal traffic.

## 3. MAINTENANCE DATA

The vehicles of the carriage family were constructed and built on the basis of same principles. The maintenance of the carriages is carried out by two, workshops. The data received about the maintenance and repair activities done in these two shops, gives an opportunity to compare their works, too. Both workshops perform the service works of lower level, furthermore trouble-shooting and curing of failures, which do not require extensive human and technical conditions are performed in these maintenance shops. One of the workshops (Su) is the technical basis of carriages for international traffic, whilst the other one (Sm) is assigned for vehicles running in internal traffic. Over pointing out the weak-spots of the vehicles, there opens a possibility for comparing the results of the working-activities realized in the workshops. The numbers of the vehicle type allocation in the maintenance service shops are contained in the above mentioned table.

The maintenance works, control activities, repairs of different level of the vehicles are performed in depots and workshops. A whole system is composed from these two bases. Data arisen between two entrances of the vehicles into the same workshops are investigated up to now. It means that depot or service shop data are in the center of this investigation.

Data are originated from the years between 2010 and 2017. All of these data in connection with are traffic safety-critical elements, groups of elements and subsystems of the vehicles. On the basis of the above mentioned, the investigation was actually extended for the next units of the carriage family:

- bogie,
- wheelset,
- buffer,
- draw equipment,
- wheel slide protection (WSP).

## 4. COMPARATIVE INVESTIGATION

An absolute exact wide-spread evaluation can be practicable by the by the comparative investigation on the available comprehensive maintenance data basis. The aim is only to show the opportunities, some short example in connection with a few traffic security parts of the chosen bogies.

The mileages of vehicles are not too high and they spread strongly.

The reliability of the wheelsets can be acceptable if the number of wheelset changes is low; it means: the maintenance plan is reasonable or the mileage is too low between two maintenances in workshop.
The assigned life-times of the brake pads and brake blocks are too high and they spread on wide scale. Not total set is changed mostly. It can be a reason of surplus vehicle dwelling in depots. Vehicle lack can cause an undesirable anomaly in the availability of carriages.
During 8 years concerning the number 69 carriages number 8510 maintenance events were registered. This data-set is contained by Table 4 and Fig 1.

**Maintenance events & traffic sequrity**

| | 2010 | 2011 | 2012 | 2013 | 2014 | 2015 | 2016 | 2017 | |
|---|---|---|---|---|---|---|---|---|---|
| 10-71_0 | 74 | 56 | 50 | 46 | 54 | 81 | 67 | 238 | 666 |
| 20-70_0 | 205 | 150 | 212 | 118 | 153 | 307 | 176 | 501 | 1822 |
| 20-71_0 | 307 | 236 | 259 | 369 | 471 | 726 | 548 | 1231 | 4147 |
| 88-71_0 | 213 | 91 | 162 | 130 | 278 | 266 | 240 | 495 | 1875 |
| Σ | 799 | 533 | 683 | 663 | 956 | 1380 | 1031 | 2465 | 8510 |

Table 4 Daily mileage of the different carriage types year by year

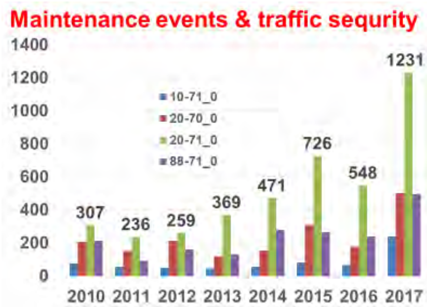


Fig. 1 Data of the maintenance events (by carriage types and annually)

The above mentioned number 8510 events covers number 1,25 monthly number of events. Considering the completey carrige-stock this number can be qualified as a little one.
Regarding these four carriage types, the number of the maintenance events concerning the safety critical vehicle structural elements, groups of elements and subsystems grew multi-folded during this time period. This growth was quadruple in connection with carriage class 20–71. (The determination of this growth could be the object of an extra investigation. It the course of such an extra investigation, parallel to the examination of the variation in event occurring numbers, it is proposed to examine also the number of the actual failures, the availability and maintenance key performance indicators and also the variation in costs.
The number of the maintenance events of the bogies can be seen in the Table 5 and Fig 2.

| | 2010 | 2011 | 2012 | 2013 | 2014 | 2015 | 2016 | 2017 | Σ |
|---|---|---|---|---|---|---|---|---|---|
| Bogie | | | | | | | | | |
| 10-71_0 | 2 | 4 | 2 | 2 | | 2 | | 6 | 18 |
| 20-70_0 | 5 | 5 | 11 | 2 | 3 | 2 | 3 | 3 | 34 |
| 20-71_0 | 25 | 18 | 15 | 24 | 9 | 34 | 14 | 95 | 234 |
| 88-71_0 | 14 | 1 | 13 | 7 | 9 | 8 | 2 | 35 | 89 |
| Σ | 46 | 28 | 41 | 35 | 21 | 46 | 19 | 139 | 375 |

Table 5 Data of the maintenance events of the bogies

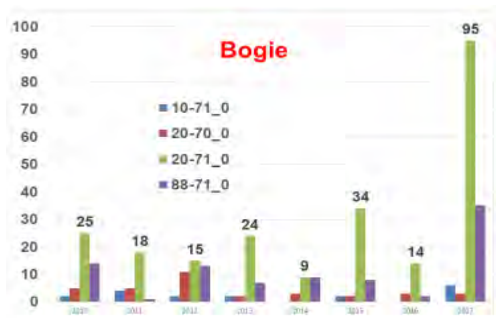


Fig. 2 The number of the maintenance events of the bogies

| | 2010 | 2011 | 2012 | 2013 | 2014 | 2015 | 2016 | 2017 | Σ |
|---|---|---|---|---|---|---|---|---|---|
| Wheelset | | | | | | | | | |
| 10-71_0 | 14 | 6 | 6 | 2 | 2 | 8 | 13 | 17 | 68 |
| 20-70_0 | 39 | 29 | 22 | 13 | 11 | 46 | 28 | 41 | 229 |
| 20-71_0 | 19 | 19 | 83 | 115 | 87 | 162 | 160 | 110 | 755 |
| 88-71_0 | 22 | 6 | 55 | 31 | 82 | 58 | 92 | 50 | 396 |
| Σ | 94 | 60 | 166 | 161 | 182 | 274 | 293 | 218 | 1448 |

Table 6 Data of wheelset maintenance activity


Fig. 3 The number of maintanence events of wheel-sets

The number of the maintenance events of the bogies can be seen in the Table 5 and Fig. 2. The number of break-pad changing and the events of wheelsets connected to the maintenance operations of bogies are quantified in Table 6 and Fig 3, as well as in Table 7 and Fig 4.

| Number of changed brake pads | 2010 | 2011 | 2012 | 2013 | 2014 | 2015 | 2016 | 2017 | Σ |
|---|---|---|---|---|---|---|---|---|---|
| 10-71_0 | 561 | 482 | 372 | 320 | 392 | 380 | 152 | 538 | 3197 |
| 20-70_0 | 1277 | 829 | 1178 | 656 | 952 | 1234 | 682 | 1347 | 8155 |
| 20-71_0 | 1525 | 642 | 262 | 441 | 708 | 692 | 434 | 911 | 5615 |
| 88-71_0 | 1281 | 342 | 489 | 390 | 227 | 198 | 134 | 195 | 3256 |
| Σ | 4644 | 2295 | 2301 | 1807 | 2279 | 2504 | 1402 | 2991 | 20223 |

Table 7 Data of the changed brake pads in different carriages types during

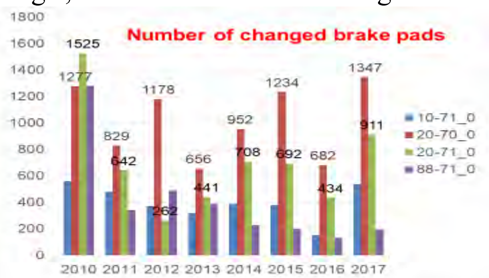


Fig. 4 The greatest numbers of the changes brake pads

The question can arise, why the number of brake pad changings at the open second carriages running in internal traffic since 2011 are significantly higher than is this type of carriages operating in international traffic. (Of course it is to be taken into consideration that in principle the distances covered between two stops by the vehicles running only in internal traffic are shorter than the distances without brake operation in the international traffic) The quantification of the maintenance works of buffers, as events is contained in the Table 8.

**Buffer**

| | 2010 | 2011 | 2012 | 2013 | 2014 | 2015 | 2016 | 2017 | |
|---|---|---|---|---|---|---|---|---|---|
| Buffer change | | | | | | | | 6 | 6 |
| 20-71_0 | | | | | | | | 6 | 6 |
| Fixing of buffer | 4 | | | 45 | 117 | 181 | 179 | 85 | 611 |
| 10-71_0 | | | | | | | 12 | 4 | 16 |
| 20-70_0 | | | | 1 | 5 | 7 | 9 | | 22 |
| 20-71_0 | 2 | | | 35 | 71 | 113 | 109 | 62 | 392 |
| 88-71_0 | 2 | | | 9 | 41 | 61 | 49 | 19 | 181 |
| Assembly of buffer | 19 | 19 | 17 | 7 | 21 | 10 | 28 | 20 | 141 |
| 10-71_0 | 4 | | | 2 | 6 | 2 | 2 | 2 | 18 |
| 20-70_0 | 1 | | | | 2 | 3 | 3 | 4 | 13 |
| 20-71_0 | 12 | 12 | 8 | 2 | 7 | 1 | 7 | 7 | 56 |
| 88-71_0 | 2 | 7 | 9 | 3 | 6 | 4 | 16 | 7 | 54 |
| Adjustment of buffer height | | | | 2 | | | | | 2 |
| 20-70_0 | | | | 1 | | | | | 1 |
| 20-71_0 | | | | 1 | | | | | 1 |

Table 8 The number of the different maintenance operations concerning the buffers

The data in question contain also the changings of buffers, the mountings of the bolted joints and the high-adjustments.
The maintenance data of draw-gears and those of anti-skid-devices (WSP ~ Wheel Slip Protection) having great importance from the point of view of traffic safety can be found in Tables 9 and 10, as well as in Fig 5. A further extra investigation should be suggested because of the important dispersion in the data concerning the failure events of the WSP.

Draw equipment

| Draw equipment | 2010 | 2011 | 2012 | 2013 | 2014 | 2015 | 2016 | 2017 |
|---|---|---|---|---|---|---|---|---|
| 10-71_0 | 1 | 1 | | | | 20 | 16 | 33 |
| 20-70_0 | 18 | | 8 | | 5 | 89 | 24 | 54 |
| 20-71_0 | 23 | 28 | 17 | 35 | 81 | 141 | 101 | 90 |
| 88-71_0 | 13 | 5 | 23 | 10 | 37 | 69 | 38 | 43 |
| Σ | 55 | 34 | 48 | 45 | 123 | 319 | 179 | 220 |

Table 9 Data of the maintenance events of the draw gear

| Wheel – slide protection | 2010 | 2011 | 2012 | 2015 | 2016 | 2017 |
|---|---|---|---|---|---|---|
| 10-71_0 | | | | | | 30 |
| 20-70_0 | 5 | | 1 | | 1 | 68 |
| 20-71_0 | 2 | 5 | | 7 | 10 | 195 |
| 88-71_0 | | | | | | 82 |
| Σ | 7 | 5 | 1 | 7 | 11 | 375 |

Table 10 Data of the WSP maintenance events

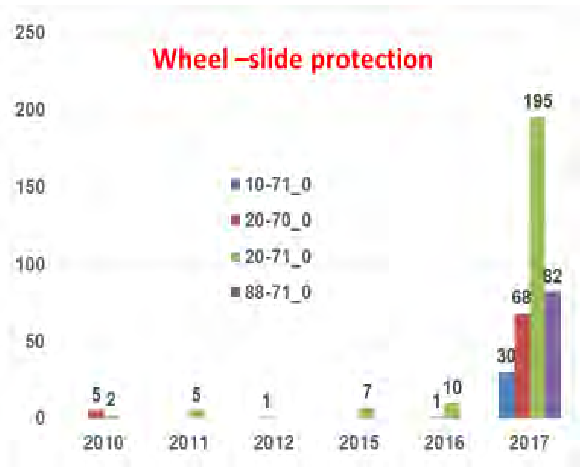


Fig. 5 The number of the maintenance events of the WSP equipment

## 5. FURTHER TASKS AND PROPOSALS

The above data-set concerning the failure events inducing maintenance and repair activities gives an unambiguous opportunity for the determining the weak points of the vehicle family, their vehicle sub-sets and the bogies belonging to the vehicles of the sub-sets mentioned. Knowing the data there is an opportunity to qualify the activity of the workshops carrying out the maintenance works. This qualification can be directly realized based on the data of the tables and their comparison by different views. A more advantageous analysis can be based on the so called key performance indicators extracted them from the data.

After having composed the key performance indicators, the targets can be fixed as future activities:

- identification of weak points of vehicle and bogie constructions,
- *exact analysis* of failure causes,
- *cost and time analysis* considering the failure events,
- systematic collection of the mileage of the vehicles,
- giving rise a common database of the depot and workshop maintenance activities,
- systematic evaluation of the available data.

## 6. REFERENCES

[1] **Csiba, J. – Malatinszky, S. – Murárik, L. – Németh, A.– Tárczi, T. – Vozáry, Gy. – Zákonyi, Gy.:** Vehichle Album. Passenger Carriages, EMUs and DMUs. MÁV Zrt. Kommunikációs Igazgatóság, Budapest, 2009,p.360. (in Hungarian)

[2] **Kovács, L.** (Editor in Chief): The History of The Hungarian Railways 1846 – 2000. Hungarian State Railways Co., Budapest, 2000. p. 529.

[2] **Mezei, I.** (Editor in Chief): The Construction, Equipment and Operation of Railway Carriages and Wagons. MÁV – START Co., Budapest, 2013. p. 415. (in Hungarian)

# TRACK QUALIFICATION METHOD USING SYSTEM DYNAMICS BASED PARAMETER IDENTIFICATION PROCEDURE

**Zoltán ZÁBORI** and **István ZOBORY**

Group of Railway Vehicles and Vehicle System Analysis
Faculty of Transportation Engineering and Vehicle Engineering
Budapest University of Technology and Economics
H-1521 Budapest, Hungary

*Received: November 7, 2018*

## ABSTRACT

A Track Qualifying Vehicle using a system dynamics based measurement evaluation method has been developed at the Department of Railway Vehicles at the Budapest University of Technology and Economics (BME) . The measured vertical and the lateral accelerations of the measuring wheelset-carrier-frame contain higher frequency components due to the vibrations of the elastic vehicle components. This paper presents a simulation based identification procedure for determining the inhomogeneities in the vertical track stiffness along the track. The necessary smoothing of the measured acceleration signals is also dealt with. The measuring wheelset together with its close environment is modelled as a lateral in-plane dynamical system supported by the right- and left rails where the rails are modelled as an Euler-Bernoulli beam supported by non-homogeneous Winkler foundation subjected to moving time dependent load. Time-domain technique is applied by using the *Galerkin* method to find the numerical solution of the governing partial differential equation describing the vertical the rail motion. The dynamical system model of the complete measuring system consists of discrete and continuous sub-systems. The *Galerkin* method enables the discrete-continuous system to be managed in a unified way. The effect of foundation parameters such as, stiffness and damping modulus on dynamic deflection and bending moment responses were also investigated for the case of a moving measuring wheel-set of constant load at constant speed. The parameter identification has been traced back to the minimisation in *Sobolyev*-norm of the deviation of the measured and simulated accelerations on the measuring frame over the axle boxes of the measuring wheel-set. Numerical results obtained from the study are presented and discussed. The method described contributes to the reliable estimation of the inhomogeneity in the ballast stiffness and damping parameters along the track, thus the necessary track maintenance actions can be reliably planned.

Keywords: Railway track qualification, system dynamics, parameter identification, *Sobolyev*-norm

## 1. INTRODUCTION

A railway track qualifying vehicle using a system dynamics based measurement evaluation method was developed at the BME over the last decade.

- The measured signals of the vertical and the *lateral accelerations* of the measuring wheelset-carrier-frame *contain* higher frequency *disturbance components* due to the vibrations of the elastic vehicle components [1]
- This paper presents a simulation based identification procedure for determining the variations of the vertical track stiffness under the rails along the track [4]. The necessary smoothing of the measured acceleration signals is also dealt with. The right- and left rails are modelled as *Euler-Bernoulli beams* supported by a *non-homogeneous Winkler foundation* subjected to a moving, time dependent load. Time-domain technique is applied by using *Galerkin*'s method for finding the numerical solution of the governing set of partial differential equations [7].
- The dynamical system consists of *discrete and continuous sub-systems*. The *Galerkin* method makes it possible to manage the discrete-continuous system as a *unified finite dimensional system*.

- The effects of longitudinal variation in the vertical stiffness and damping of the track foundation on the dynamic deflection and bending moment responses were also investigated for the case of loads moving at constant speed. Numerical results obtained from the study are presented and discussed [4].
- The method described contributes to the reliable prediction of the inhomogeneity in the underlying stiffness and damping parameters along the track.

## 2. DYNAMICAL MODEL OF THE MEASURING SYSTEM

In Fig. 1 the independently supported measuring wheelset and measuring frame can be seen. Air springs connected to the chassis of the vehicle apply a constant force [5] on the measuring wheelset.

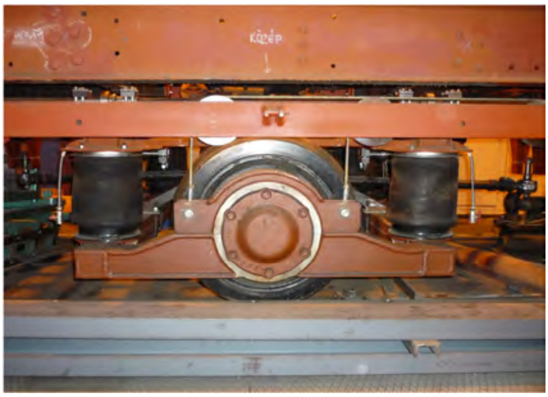

Fig. 1 The measuring wheel-set with the compressed air operated actuators

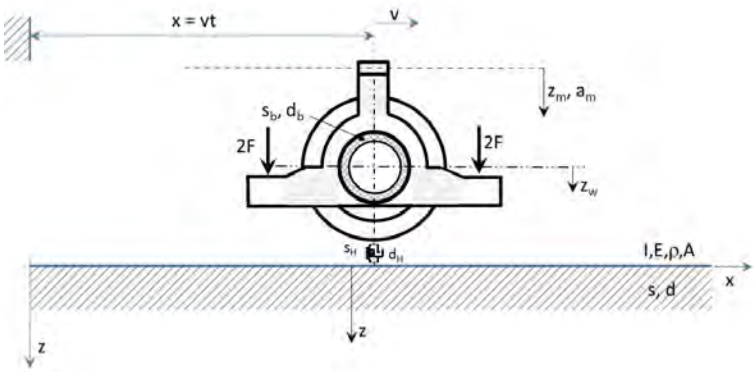


Fig. 2 Side elevation of the vertical dynamical model of the measuring wheel-set and the measuring frame connected with it

Figure 2 presents the side elevation of the vertical dynamical model of the measuring wheel-set. The vertical accelerations of the measuring frame are measured at two points at lateral distance *a* from each other in which the *inhomogeneity of the variation in vertical stiffness of the elastic half planes under the rails are reflected when running along the track at a constant velocity v* [1], [4].

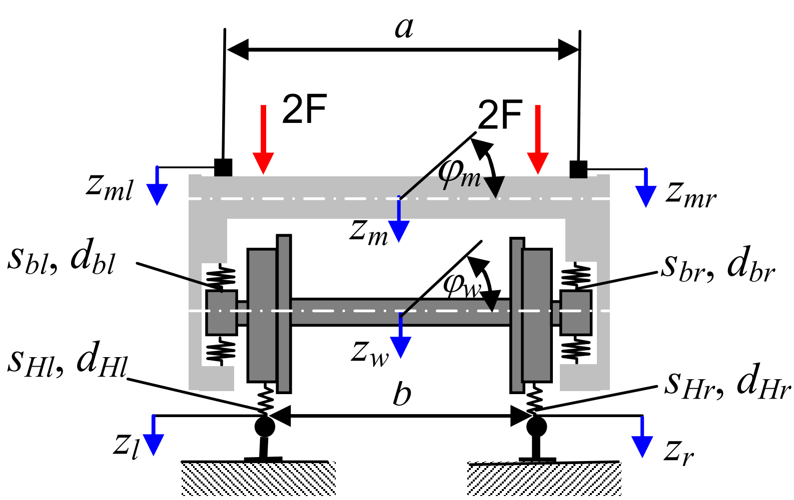


Fig. 3 Front elevation of the vertical dynamical model of the measuring wheel-set and the measuring frame

The motion equations of the measuring wheel-set and the measuring frame take the form of a system of ordinary second order differential equations, as follows:

$$\ddot{z}_w(t) = F_w(z_w(t), \dot{z}_w(t), \varphi_w(t), \dot{\varphi}_w(t), z_m(t), \dot{z}_m(t), \varphi_m(t), \dot{\varphi}_m(t), z_r(x,t), \frac{d}{dt} z_r(x,t), z_l(x,t), \frac{d}{dt} z_l(x,t))$$
$$\ddot{z}_m(t) = F_m(z_w(t), \dot{z}_w(t), \varphi_w(t), \dot{\varphi}_w(t), z_m(t), \dot{z}_m(t), \varphi_m(t), \dot{\varphi}_m(t))$$
$$\ddot{\varphi}_w(t) = G_w(z_w(t), \dot{z}_w(t), \varphi_w(t), \dot{\varphi}_w(t), z_m(t), \dot{z}_m(t), \varphi_m(t), \dot{\varphi}_m(t), z_r(x,t), \frac{d}{dt} z_r(x,t), z_l(x,t), \frac{d}{dt} z_l(x,t))$$
$$\ddot{\varphi}_m(t) = G_m(z_w(t), \dot{z}_w(t), \varphi_w(t), \dot{\varphi}_w(t), z_m(t), \dot{z}_m(t), \varphi_m(t), \dot{\varphi}_m(t))$$

The vertical motion equations of the rails as prismatic beams supported by Winkler-foundations have been extended by also taking into consideration the existing dynamical interaction with the measuring wheel-set, using linearized *Hertzian* springs and dampers to give the elastic/dissipative connection between the rails and the wheel-treads The extended motion equation of the right hand side reads [2], [6], [8]:

$$IE\frac{\partial^4 z_r(x,t)}{\partial x^4} + \rho A\frac{\partial^2 z_r(x,t)}{\partial t^2} + d_r\frac{\partial z_r(x,t)}{\partial t} + s_r(x) z_r(x,t) =$$
$$= \delta(x - vt)\left[s_{Hr}(z_w(t) - (b/2)\varphi_w(t)) - z_r(x,t)) + d_{Hr}(\dot{z}_w(t) - (b/2)\dot{\varphi}_w(t) - \frac{d}{dt}(z_r(x,t))\right]$$

Similarly, the motion equation of the left hand side rail takes the following form:

$$IE\frac{\partial^4 z_l(x,t)}{\partial x^4} + \rho A\frac{\partial^2 z_l(x,t)}{\partial t^2} + d_r\frac{\partial z_l(x,t)}{\partial t} + s_r(x) z_l(x,t) =$$
$$= \delta(x - vt)\left[s_{Hl}(z_w(t) + (b/2)\varphi_w(t)) - z_l(x,t)) + d_{Hl}(\dot{z}_w(t) + (b/2)\dot{\varphi}_w(t) - \frac{d}{dt}(z_l(x,t))\right],$$

where for the solution functions the following boundary conditions must be fulfilled:

$$\lim_{n\to\pm\infty} z_r(x,t) = 0 \;\; és \;\; \lim_{n\to\pm\infty} z_l(x,t) = 0\,.$$

## 3. THE MAIN PROBLEM TO BE SOLVED

Let's suppose that the measuring system has an operator $\boldsymbol{J}$, which transfers the *unknown vertical track stiffness function* $\boldsymbol{s}(x)$ via the whole signal transfer properties of the track and the measuring system into the measured acceleration $\boldsymbol{a}_{\mathrm{m}}(x)$ of the rubber sprung measuring frame over the axle boxes of the measuring wheel-set. In formula [3], [4]:

$$\boldsymbol{a}_m(x) = \boldsymbol{J}\boldsymbol{s}(x).$$

The task is to identify the unknown vertical track stiffness function $\boldsymbol{s}(x)$ in form of a finite parameter approximating function structure designated by $\boldsymbol{s}_a(x,\boldsymbol{p})$ which can ensure an appropriate framework for explaining the measured acceleration response straight over the axle box of the measuring wheel-set by appropriate (in a given sense optimum) selection of parameter vector $\boldsymbol{p}$. If the structure of the $\boldsymbol{p}$ parameter vector dependent stiffness function $\boldsymbol{s}_a(x,\boldsymbol{p})$ were *exactly correct*, such that $\boldsymbol{s}(x) = \boldsymbol{s}_a(x,\boldsymbol{p})$, then the measured acceleration function $\boldsymbol{a}_m(x)$ would result as the effect of system operator $\boldsymbol{J}$ on the assumed "exact" stiffness function $\boldsymbol{s}_a(x,\boldsymbol{p})$, in formula:

$$\boldsymbol{a}_m(x) = \boldsymbol{J}\,\boldsymbol{s}_a(x,\boldsymbol{p}).$$

Unfortunately, the signal transfer properties realised by the measuring system operator $\boldsymbol{J}$ are unknown. The authors therefore built up a detailed, combined hybrid dynamical model of the railway track and the loaded measuring wheel-set, embedded into a vertically loaded measuring frame through a linearly elastic and dissipative connection with the axle boxes of the measuring wheel-set. This hybrid dynamical model of the track/measuring wheel-set and measuring frame system model appears as a hybrid differential equation system, consisting of the two *Euler-Bernoulli* beams (modelling the rails) continuously supported by the right and left stiffness functions $s_{\mathrm{r}}(x,\boldsymbol{p})$ and $s_{\mathrm{l}}(x,\boldsymbol{p})$, and a finite dimensional lumped parameter dynamical sub-system, modelling the vertical and rolling motions of the measuring wheel-set and the measuring frame. It is useful to treat the above two track stiffness inhomogeneity functions together by the vector $\boldsymbol{s}_a(x,\boldsymbol{p}) = [s_{\mathrm{r}}(x,\boldsymbol{p}), s_{\mathrm{l}}(x,\boldsymbol{p})]^{\mathrm{T}}$. Furthermore, it is to be emphasized, that the vertical force between the rail-heads and the wheel-treads is transferred by *Hertzian* springs and dampers, i.e. the linearized version of the *Hertzian* contact law, around the static mean wheel-load values. Accelerometers are mounted on the measuring frame (connected to the axle boxes with rubber springs) just over the centres of the right and left axle-boxes of the measuring wheel-set.

If the hybrid dynamical system depicted above is considered, then one can characterise the signal transfer from the parameter dependent approximating vector valued stiffness function $\boldsymbol{s}_a(x,\boldsymbol{p})$ into the vector valued numerical simulation generated acceleration function by the symbolic mapping

$$\boldsymbol{a}_s(x,\boldsymbol{p}) = \boldsymbol{J}_m\,\boldsymbol{s}_a(x,\boldsymbol{p}),$$

where operator $\boldsymbol{J}_m$ stands for the combined simulation procedure, carried out by solving the *hybrid differential equation system* of the track/measuring system, taking into consideration the longitudinal motion of the wheel-set/measuring frame system of speed $v$ along the track.

In the course of the practical simulation procedure it is convenient to include the *parameter dependent* track stiffness inhomogeneity functions from which the track irregularity function can be composed in the form of a linear combination using shift, contraction or dilatation and multiplier transformations on a properly normalised *Gaussian bell-curve* shown in Fig 4. This function can be called a *basic* function for generating the parameter dependent track stiffness inhomogeneity function components (right and left) [3].

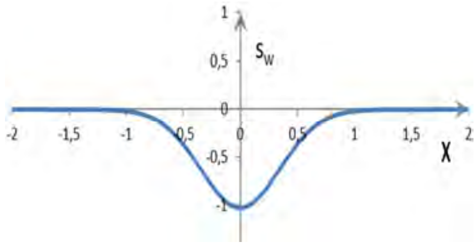


Fig. 4 Basic function for generating track stiffness inhomogeneity function

The functional relationship for the introduced basic function mentioned, is as follows [4]:

$$s_w(x) = -\exp\left\{-\frac{(3x)^2}{2}\right\}.$$

The vertical stiffness inhomogeneity functions under the two rails are composed by using the sum (linear combination) of appropriately transformed versions above basic function in form:

$$s_r(x) \approx s_{ra}(x) = \overline{s}_{ra} + \sum_{i=1}^{n} b_{ri} \cdot s_w(e_{ri} \cdot (x - c_{ri}))$$

$$s_l(x) \approx s_{la}(x) = \overline{s}_{la} + \sum_{i=1}^{n} b_{li} \cdot s_w(e_{li} \cdot (x - c_{li}))$$

The constants entered the formulas are included in four characteristic multidimensional vectors as follows:

$\overline{\boldsymbol{s}} = [\overline{s}_{ra}, \overline{s}_{la}]^T$ mean stiffness vector

$\mathbf{b} = [\mathbf{b}_r, \mathbf{b}_l]^{\mathrm{T}} = [b_{r1},\ b_{r2}, \ldots, b_{rn}, b_{l1}, b_{l2}, \ldots, b_{ln}]^{\mathrm{T}}$ multiplication coefficient vector

$\mathbf{c} = [\mathbf{c}_r, \mathbf{c}_l]^{\mathrm{T}} = [c_{r1},\ c_{r2}, \ldots, c_{rn}, c_{l1}, c_{l2}, \ldots, c_{ln}]^{\mathrm{T}}$ shift constant vector

$\mathbf{e} = [\mathbf{e}_r, \mathbf{e}_l]^{\mathrm{T}} = [e_{r1},\ e_{r2}, \ldots, e_{rn}, e_{l1}, e_{l2}, \ldots, e_{ln}]^{\mathrm{T}}$ dilatation factor vector

In accordance with the formerly used designations, the parameter vector of the vector valued stiffness inhomogeneity approximating function $\boldsymbol{s}_a(x, \boldsymbol{p})$ gets a detailed meaning, using the unified parameter vector $\boldsymbol{p} = [\overline{\boldsymbol{s}}, \boldsymbol{b}, \boldsymbol{c}, \boldsymbol{e}]^T$. The approximating vector valued track stiffness representing inhomogeneity function takes the following detailed form:

$$\boldsymbol{s}_a(x,\boldsymbol{p}) = \boldsymbol{s}_a(x,[\overline{\boldsymbol{S}},\boldsymbol{b},\boldsymbol{c},\boldsymbol{e}]^T) = \begin{bmatrix} s_{ra}(x,[\overline{\boldsymbol{S}},\boldsymbol{b},\boldsymbol{c},\boldsymbol{e}]^T) \\ s_{la}(x,[\overline{\boldsymbol{S}},\boldsymbol{b},\boldsymbol{c},\boldsymbol{e}]^T) \end{bmatrix}.$$

The above vector valued assembly of the multivariable track stiffness describing functions
ensures the optimum fitting of the simulated vertical acceleration functions $\boldsymbol{a}_s(x,\boldsymbol{p})$ to the measured $\boldsymbol{a}_m(x,\boldsymbol{p})$accelerating functions. The approximate model-based operator $\boldsymbol{J}_m$ will now be used to represent operator $\boldsymbol{J}$. The former consists of the pair of fourth order linear partial differential equations representing the track, while the measuring system being in connection with the track system through the *Hertzian* spring/damper elements modelling the vertical contact of the track/wheel-set is described by a set of ordinary differential equations constructed for the vertical and rolling motion characterisation of the measuring wheel-set and the measuring frame.
The set of fourth order partial differential equations of variable coefficients describing the motion of the track is solved numerically by using *Galerkin's* approximation method, which seeks for the solution in form of the following expressions [7]:

$$z_r(\xi,t) = \sum_{j=0}^{n} \varphi_j(\xi)T_{rj}(t) \ , \ z_l(\xi,t) = \sum_{j=0}^{n} \varphi_j(\xi)T_{lj}(t).$$

Here variable $\xi$ is in relation with the original position co-ordinate $x$ as follows:

$$\xi = x - vt \ .$$

In the sum, functions $\varphi_j(\xi)$; $j$ = 0,1,2,…,n are orthonormal, at least $n$-times continuously differentiable functions over the whole real line. This system of basic functions satisfy the prescribed boundary conditions with respect to their behaviour at limit transition$\xi\rightarrow\pm\infty$. The latter steps described meant that the examination transformed into a moving reference frame. The assumed solution function should be substituted into the two partial differential equations. If the function pair $z_r(\xi,t)$ and $z_l(\xi,t)$ were exact solutions to the set of equations, the two sides of the differential equations would be identically equal for every pair $(\xi,t)$. In this case one must multiply the both sides of the equations in the sense of scalar product by any function $\varphi_j(\xi)$; $j$ = 0,1,2,…,n and the balance of the equations would not change. Due to the orthonormal property [9] of the basic function used, it turns out that the resultant products at both sides depend only on the time t. This time dependence comes from the functions $T_{rj}(t)$ and $T_{lj}(t)$ and their first and second time derivatives. Omitting the details, one can get two sets of variable coefficient linear inhomogeneous ordinary differential equation systems for determining the unknown functions $T_{rj}(t)$ and $T_{lj}(t)$; $j$ = 0,1,2,…,n. It is practical to include vector valued time functions formed from the unknown time dependent functions, which leads to the two set of ordinary differential equations below:

$$\mathbf{A}_r\underline{\ddot{T}_r}(t) + \mathbf{B}_r\underline{\dot{T}_r}(t) + \mathbf{C}_r(t)\underline{T_r}(t) = \underline{F_r} \ ,$$
$$\mathbf{A}_l\underline{\ddot{T}_l}(t) + \mathbf{B}_l\underline{\dot{T}_l}(t) + \mathbf{C}_l(t)\underline{T_l}(t) = \underline{F_l} \ ,$$

where the vector valued forces at the right hand side can be expressed by the following formulae:

$$\underline{F_r} = \left[ s_{Hr}\left(\left(z_w(t) - \left(\frac{b}{2}\right)\varphi_w(t)\right) - \underline{\varphi}(0)\cdot \underline{T_r}(t)\right) + d_{Hr}\left(\left(\dot{z}_w(t) - \left(\frac{b}{2}\right)\dot{\varphi}_w(t)\right) - \left(\underline{\varphi}'(0)\cdot v\cdot \underline{T_r}(t) + \underline{\varphi}(0)\cdot \underline{\dot{T}_r}(t)\right)\right)\right] \cdot \underline{\varphi}(0)$$

$$\underline{F_l} = \left[ s_{Hl}\left(\left(z_w(t) + \left(\frac{b}{2}\right)\varphi_w(t)\right) - \underline{\varphi}(0)\cdot \underline{T_l}(t)\right) + d_{Hl}\left(\left(\dot{z}_w(t) + \left(\frac{b}{2}\right)\dot{\varphi}_w(t)\right) - \left(\underline{\varphi}'(0)\cdot v\cdot \underline{T_l}(t) + \underline{\varphi}(0)\cdot \underline{\dot{T}_l}(t)\right)\right)\right] \cdot \underline{\varphi}(0)$$

Here designation

$$\underline{\varphi}(0) = [\varphi_0(0), \varphi_1(0), \dots, \varphi_n(0)\,]^T$$

has been introduced, which represents a constant $n+1$ dimensional vector, containing the substitution values of the basic functions at $\xi = 0$, in other form at $x=vt$.
It is to be mentioned, that the vector character of $\underline{F_r}(t)$ and $\underline{F_l}(t)$ originates from the vector character of $\underline{\varphi}(0)$, in other words the coefficients in bracket are identical time functions in any row of vectors $\underline{F_r}(t)$ and $\underline{F_l}(t)$,respectively.
The above mentioned identical time dependence of the expressions in bracket can be introduced in the following forms by using appropriate rearrangements:

$$F_r(t) = s_{Hr}\left(\left(z_w(t) - \left(\tfrac{b}{2}\right)\varphi_w(t)\right) - \underline{\varphi}(0)\cdot \underline{T_r}(t)\right) + d_{Hr}\left(\left(\dot{z}_w(t) - \left(\tfrac{b}{2}\right)\dot{\varphi}_w(t)\right) - \left(\underline{v\cdot\varphi'}(0)\cdot T_r(t) + \underline{\varphi}(0)\cdot \underline{\dot{T}_r}(t)\right)\right)$$
$$= s_{Hr}\left(\left(z_w(t) - \left(\tfrac{b}{2}\right)\varphi_w(t)\right)\right) + d_{Hr}\left(\left(\dot{z}_w(t) - \left(\tfrac{b}{2}\right)\dot{\varphi}_w(t)\right)\right) - s_{Hr}\cdot \underline{\varphi}(0)\cdot \underline{T}_r(t) - d_{Hr}\left(v\cdot \underline{\varphi}'(0)\cdot \underline{T}_r(t) + \underline{\varphi}(0)\cdot \underline{\dot{T}}_r(t)\right)$$

and

$$F_l(t) = s_{Hl}\left(\left(z_w(t) + \left(\tfrac{b}{2}\right)\varphi_w(t)\right) - \underline{\varphi}(0)\cdot \underline{T_l}(t)\right) + d_{Hl}\left(\left(\dot{z}_w(t) + \left(\tfrac{b}{2}\right)\dot{\varphi}_w(t)\right) - \left(v\cdot\underline{\varphi}'(0)\cdot \underline{T_l}(t) + \underline{\varphi}(0)\cdot \underline{\dot{T}_l}(t)\right)\right)$$
$$= s_{Hl}\left(\left(z_w(t) + \left(\tfrac{b}{2}\right)\varphi_w(t)\right)\right) + d_{Hl}\left(\left(\dot{z}_w(t) + \left(\tfrac{b}{2}\right)\dot{\varphi}_w(t)\right)\right) - s_{Hl}\underline{\varphi}(0)\cdot \underline{T_l}(t) - d_{Hl}\left(v\cdot \underline{\varphi}'(0)\cdot \underline{T_l}(t) + \underline{\varphi}(0)\cdot \underline{\dot{T}_l}(t)\right)$$

After recognising that the third and fourth members in the above final expressions for $F_r(t)$ and $F_l(t)$ depend on the components of vectors· $\underline{T_r}(t)$ and $\underline{\dot{T}_r}(t)$, and vectors· $\underline{T_l}(t)$ and $\underline{\dot{T}_l}(t)$, it becomes clear that after appropriate rearrangements the following two second order ordinary set of differential equations are yielded:

$$\mathbf{A}'_r\underline{\ddot{T}_r}(t) + \mathbf{B}'_r\underline{\dot{T}_r}(t) + \mathbf{C}'_r(t)\underline{T_r}(t) = \left[s_{Hr}\left(z_w(t) - \left(\tfrac{b}{2}\right)\varphi_w(t)\right) + d_{Hr}\left(\dot{z}_w(t) - \left(\tfrac{b}{2}\right)\dot{\varphi}_w(t)\right)\right]\cdot\underline{\varphi}(0),$$
$$\mathbf{A}''_l\underline{\ddot{T}_l}(t) + \mathbf{B}''_l\underline{\dot{T}_l}(t) + \mathbf{C}''_l(t)\underline{T_l}(t) = \left[s_{Hl}\left(z_w(t) + \left(\tfrac{b}{2}\right)\varphi_w(t)\right) + d_{Hl}\left(\dot{z}_w(t) + \left(\tfrac{b}{2}\right)\dot{\varphi}_w(t)\right)\right]\cdot\underline{\varphi}(0).$$

In the two new sets of differential equations the coefficient matrices are different from, thus the following matrix-triples are deduced:

$$\mathbf{A}'_r, \mathbf{B}'_r, \mathbf{C}'_r(t)\ , \mathbf{A}''_l, \mathbf{B}''_l, \mathbf{C}''_l(t).$$

At this point of the discussion one should take into consideration that the measuring frame is in elastic and dissipative connection with the wheel-set and is loaded by constant, vertical pneumatic forces $F$ applied at four symmetrically located points on the measuring frame.
Due to the above, the introduction of further motion equations is necessary, namely for the vertical motions and rolling motions of the measuring wheel-set and the measuring frame. Knowing the magnitudes of the time dependent vertical wheel/rail contact forces $F_r(t)$ and $F_l(t)$ transmitted onto the wheel-set by the *Hertzian* springs

and dampers treated above, the following two linear sets of second order ordinary differential-equations are yielded:

$$m_w\ddot{z}_w(t) = -F_r - F_l + s_{br}\left[\left(z_m(t) - \left(\frac{a}{2}\right)\varphi_m(t)\right) - \left(z_w(t) - \left(\frac{a}{2}\right)\varphi_w(t)\right)\right] + d_{br}\left[\left(\dot{z}_m(t) - \left(\frac{a}{2}\right)\dot{\varphi}_m(t)\right) - \left(\dot{z}_w(t) - \left(\frac{a}{2}\right)\dot{\varphi}_w(t)\right)\right] + s_{bl}\left[\left(z_m(t) + \left(\frac{a}{2}\right)\varphi_m(t)\right) - \left(z_w(t) + \left(\frac{a}{2}\right)\varphi_w(t)\right)\right] + d_{bl}\left[\left(\dot{z}_m(t) + \left(\frac{a}{2}\right)\dot{\varphi}_m(t)\right) - \left(\dot{z}_w(t) + \left(\frac{a}{2}\right)\dot{\varphi}_w(t)\right)\right];$$

$$m_m\ddot{z}_m(t) = 2F - s_{br}\left[\left(z_m(t) - \left(\frac{a}{2}\right)\varphi_m(t)\right) - \left(z_w(t) - \left(\frac{a}{2}\right)\varphi_w(t)\right)\right] - d_{br}\left[\left(\dot{z}_m(t) - \left(\frac{a}{2}\right)\dot{\varphi}_m(t)\right) - \left(\dot{z}_w(t) - \left(\frac{a}{2}\right)\dot{\varphi}_w(t)\right)\right] - s_{bl}\left[\left(z_m(t) + \left(\frac{a}{2}\right)\varphi_m(t)\right) - \left(z_w(t) + \left(\frac{a}{2}\right)\varphi_w(t)\right)\right] - d_{bl}\left[\left(\dot{z}_m(t) + \left(\frac{a}{2}\right)\dot{\varphi}_m(t)\right) - \left(\dot{z}_w(t) + \left(\frac{a}{2}\right)\dot{\varphi}_w(t)\right)\right];$$

Similarly, for the rolling motion of the measuring wheel-set and the measuring frame the following two linear sets of second order ordinary differential-equations are in force:

$$\begin{aligned}\Theta_w\ddot{\varphi}_w(t) = {} & F_r(t)\left(\frac{b}{2}\right) - F_l(t)\left(\frac{b}{2}\right) + s_{br}\left(\left(z_m(t) - \left(\frac{a}{2}\right)\varphi_m(t)\right) - \left(z_w(t) - \left(\frac{a}{2}\right)\varphi_w(t)\right)\right)\left(\frac{a}{2}\right) \\ & + d_{br}\left(\left(\dot{z}_m(t) - \left(\frac{a}{2}\right)\dot{\varphi}_m(t)\right) - \left(\dot{z}_w(t) - \left(\frac{a}{2}\right)\dot{\varphi}_w(t)\right)\right)\left(\frac{a}{2}\right)s_{bl}\left(\left(z_m(t) + \left(\frac{a}{2}\right)\varphi_m(t)\right)\right. \\ & \left. - \left(z_w(t) + \left(\frac{a}{2}\right)\varphi_w(t)\right)\right)\left(\frac{a}{2}\right) - d_{bl}\left(\left(\dot{z}_m(t) + \left(\frac{a}{2}\right)\dot{\varphi}_m(t)\right) - \left(\dot{z}_w(t) + \left(\frac{a}{2}\right)\dot{\varphi}_w(t)\right)\right)\left(\frac{a}{2}\right)\end{aligned}$$

$$\begin{aligned}\Theta_m\ddot{\varphi}_m(t) = {} & -s_{br}\left(\left(z_m(t) - \left(\frac{a}{2}\right)\varphi_m(t)\right) - \left(z_w(t) - \left(\frac{a}{2}\right)\varphi_w(t)\right)\right)\left(\frac{a}{2}\right) \\ & - d_{br}\left(\left(\dot{z}_m(t) - \left(\frac{a}{2}\right)\dot{\varphi}_m(t)\right) - \left(\dot{z}_w(t) - \left(\frac{a}{2}\right)\dot{\varphi}_w(t)\right)\right)\left(\frac{a}{2}\right) \\ & + s_{bl}\left(\left(z_m(t) + \left(\frac{a}{2}\right)\varphi_m(t)\right) - \left(z_w(t) + \left(\frac{a}{2}\right)\varphi_w(t)\right)\right)\left(\frac{a}{2}\right) \\ & + d_{bl}\left(\left(\dot{z}_m(t) + \left(\frac{a}{2}\right)\dot{\varphi}_m(t)\right) - \left(\dot{z}_w(t) + \left(\frac{a}{2}\right)\dot{\varphi}_w(t)\right)\right)\left(\frac{a}{2}\right)\end{aligned}$$

The above set of second order differential equations with respect to the unknown function vector of dimension $2n+6$:

$$\underline{Z}(t) = [\underline{T}_r(t), \underline{T}_l(t), z_w(t), z_m(t), \varphi_w(t), \varphi_m(t)]^T$$

can be written into the following concise form:

$$\mathbf{M}\ddot{\underline{Z}}(t) + \mathbf{D}\dot{\underline{Z}}(t) + \mathbf{S}(t)\underline{Z}(t) = \underline{0},$$

with given initial time $t_0$ and initial conditions $\underline{Z}(t_0) = \underline{Z}_0$ and $\underline{\dot{Z}}(t_0) = \underline{\dot{Z}}_0$ ordered to the former. For the numerical solution it is reasonable to introduce a state-vector in form $\underline{X}(t) = [\underline{\dot{Z}}(t),\underline{Z}(t)]^T$, in other words the treatment is continued in the framework of the state-space method. In the end a first order linear homogeneous *variable coefficient* set of ordinary differential equations is yielded, more exactly an initial value problem of the following form:

$$\underline{\dot{X}}(t) = \mathbf{A}(t,\mathbf{p})\,\underline{X}(t)$$
$$\underline{X}(t_0) = \underline{X}_0$$

At this point, the proper selection of the components of the initial value vector $\underline{X}_0$ arises. On the one hand the time dependent factor functions $\underline{T}_r(t)$ and $\underline{T}_l(t)$ in the *Galerkin* approximation of the vertical profile $z_r(\xi,t,\mathbf{p})$ and $z_l(\xi,t,\mathbf{p})$ of the right and left rails at time $t_0$ can be determined with the $\xi$-dependent orthonormal shape-function system used in the *Galerkin* approximation. In other words the shapes of the rails are considered under the static-load from the measuring wheel-set through the right and left *Hertzian* springs. For the sake of convenient treatment the initial time derivatives of time dependent factor functions $\underline{T}_r(t)$ and $\underline{T}_l(t)$ at $t_0$ can be taken as zero vectors. On the other hand initial displacements $z_w(t_0)$, $z_m(t_0)$, and angular displacements $\varphi_w(t_0)$, $\varphi_m(t_0)$ of the measuring wheel-set and the measuring frame can be determined by taking into account the static equilibrium under gravity, the static constant load acting on the measuring frame and the rail reaction forces. As for the initial time derivatives at $t_0$ of functions $z_w(t_0)$, $z_m(t_0)$, and angular displacements $\varphi_w(t_0)$, $\varphi_m(t_0)$ can be considered to be approximately zero.

With the application of the initial condition $\underline{X}_0$ the initial value problem formulated for the unknown vector function $\underline{X}(t)$ can be solved numerically by using a proper ODE code, and in this way the vector-valued solution manifold $\underline{X}(t,\underline{X}_0,\mathbf{p})$ becomes principally known for any parameter vector $\mathbf{p}$.

Knowing vector function manifold $\underline{X}(t,\underline{X}_0,\mathbf{p})$, the vertical shape of the right and left rails $z_r(\xi,t,\mathbf{p})$ and $z_l(\xi,t,\mathbf{p})$ can be determined by the linear combination of the *Galerkin* approximation since the orthonormal shape function system is known per definition. In our problem treatment the rail shape functions mentioned are interesting characteristics, but our attention is directed primarily to the variation of the supporting stiffness with track arc length under the right and left rails, which stiffness functions depend upon the parameter vector $\mathbf{p}$. The question is the determination of such a parameter vector $\mathbf{p}^*$ the coordinates of which ensure such linear combinations of the basic stiffness shape function in Fig. 4 for the right and left stiffness functions that they lead such simulated vertical acceleration vector $\boldsymbol{a}_s = \boldsymbol{a}_s(x,\mathbf{p}^*)$ for the measuring frame points over the axle-boxes of the measuring wheel-set, that the differences from the measured acceleration vector $\boldsymbol{a}_m(x)$ with respect to the *Sobolyev*-norm of second order should be *minimum* by using the objective function $\Psi(\boldsymbol{p})$ to be specified given in the following section.

### 3.2 Identification of the track stiffness inhomogeneities

The simulation backed identification method is based on minimising the second order *Sobolyev* norm of the deviation between the measured accelerations on the measuring frame over the axle boxes and the numerically generated parametrised response functions of the complex track and measuring system model, the response functions of which are also determined on the measuring frame over the axle-boxes of the measuring wheel-set. In accordance with the above, the functional to be minimalized is formulated by the integral expression below:

$$\Psi(\boldsymbol{p}) = \Psi(\bar{s}, \mathbf{b}, \mathbf{e}, \mathbf{c}) =$$

$$\int_X \left\{ \left| \boldsymbol{J}_m \begin{bmatrix} \bar{s}_{ra} + \sum_{j=1}^{n} b_{rj} \cdot s_w\left(e_{rj}(x - c_{rj})\right) \\ \bar{s}_{la} + \sum_{j=1}^{n} b_{lj} \cdot s_w\left(e_{lj}(x - c_{lj})\right) \end{bmatrix} - \boldsymbol{a}_m(x) \right|^2 + \left| \frac{d}{dx} \boldsymbol{J}_m \begin{bmatrix} \bar{s}_{ra} + \sum_{j=1}^{n} b_{rj} \cdot s_w(e_{rj}(x - c_{rj})) \\ \bar{s}_{la} + \sum_{j=1}^{n} b_{lj} \cdot s_w(e_{llj}(xc_{lj})) \end{bmatrix} - \frac{d}{dx} \boldsymbol{a}_m(x) \right|^2 \right\} dx$$

$$= min!$$

As it is obvious, operator $\boldsymbol{J}_{\mathrm{m}}$ *is a mapping* from the parametrized set of the possible rail supporting stiffness irregularity functions $\{\boldsymbol{s}_a(x, \boldsymbol{p})\}$ into the set $\{\boldsymbol{a}_s(x, \boldsymbol{p})\}$of the *simulated acceleration functions* valid of the measuring frame over the axle boxes of the measuring wheel-set. In the integral expression, the square of the absolute values of the deviations in the parameter vector-dependent *simulated accelerations* $\{\boldsymbol{a}_s(x, \boldsymbol{p})\}$ and *acceleration derivatives* $\frac{d}{dx}[\boldsymbol{a}_s(x, \boldsymbol{p})]$ (*jerk*) from the measured (real) $\boldsymbol{a}_m(x)$ and $\frac{d}{dx}\boldsymbol{a}_m(x)$ acceleration jerk characteristics emerges. The action-parameters of the minimization of the integral expression are included into a parameter vector $\mathbf{p} \in \{\mathbf{p}\}$.Here $\{\mathbf{p}\}=\{[\,\overline{s}\,, \mathbf{b}\,, \mathbf{e}\,, \mathbf{c}\,]^{\mathrm{T}}\} \subset R^{6n+2}$ is the set of *6n+2* dimensions of the possible parameters determining the two rail supporting stiffness functions $s_{\mathrm{r}}(x)$ and $s_{\mathrm{l}}(x)$.

It is to be emphasized that by introducing the second order *Sobolyev*-norm, the *quadratic deviation* between the measured and simulated vertical *measuring frame accelerations and vertical jerks* over the axle boxes are included in the evaluating functional $\Psi(\mathbf{p})$. Thus, by minimising $\Psi(\mathbf{p})$ the possibly high conformity in the shape of the simulated and measured measuring frame acceleration functions over the measuring wheel-set axle boxes can be ensured.

### 3.3 Numerical minimization of $\Psi(\mathbf{p})$

The numerical minimization of the integral expression generated $\mathbf{p}$–dependent objective function $\Psi(\mathbf{p})$ is carried out by the gradient-method formulated by the sequence $\{\mathbf{p}_{\mathrm{k}}\}$ of the approximating parameter vectors below:

$$\mathbf{p}_{k+1} = \mathbf{p}_k - \frac{\mathbf{grad}\,\psi(\mathbf{p}_k)}{|\mathbf{grad}\,\psi(\mathbf{p}_k)|} \cdot \tau\,,$$

where $\tau$ is a non-negative small scalar increment, $k$ is the number of iteration steps. The minimizing process can be started by selecting a proper initial vector $\mathbf{p}_0$, and the numerical process comes to an end if the difference in absolute value between two neighbouring steps remains under a sufficiently small bound $\varepsilon$, formulating the accuracy demand:

$$|\Psi(\mathbf{p}_{\mathrm{k+1}}) - \Psi(\mathbf{p}_{\mathrm{k}})| < \varepsilon\,.$$

In the course of the numerical procedure, the co-ordinate-wise entering partial derivatives of the gradient vector of the objective function $\Psi(\mathbf{p})$ are approximated by the natural difference quotients taken by applying small increments in the co-ordinates of parameter vector $\mathbf{p}$.

## 4. NUMERICAL RESULTS

To test the applicability of the developed identification method we set out from a known pair of simple artificial track stiffness inhomogeneity functions which had one wavelet term on both sides of the track. We carried out the dynamical simulation of the motion process of the track-measuring wheelset-measuring frame system when the wheelset passes through the known track stiffness inhomogeneities. The acceleration functions received at the positions of the acceleration transducers placed on the carrier frame above the axle-boxes, as well as their versions smoothed by known method for both sides of the track are stored in appropriate files.

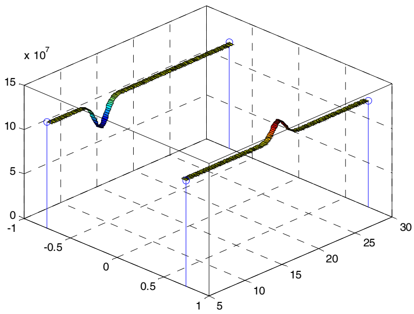

Fig.5 Track stiffness inhomogeneity on the right and left side rail

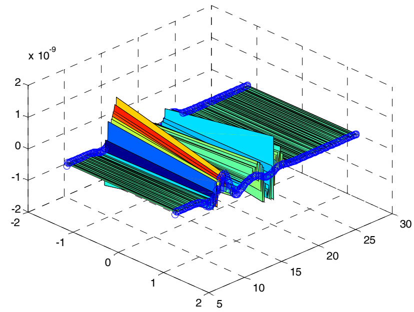

Fig.6 The smoothed and simulated acceleration of the measuring frame over the right and left side axle-box computed by the dynamical model

Fig. 5 represents the track stiffness inhomogeneity at the left and right side rails, while Fig. 6 shows the acceleration of the in-space model, and the thick lines show the smoothed curve of the vertical acceleration on the measuring frame over the axle-boxes of the measuring wheel-set.

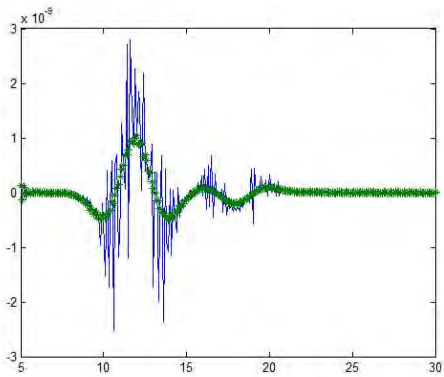

Fig.7 The simulated and smoothed acceleration of the left rail

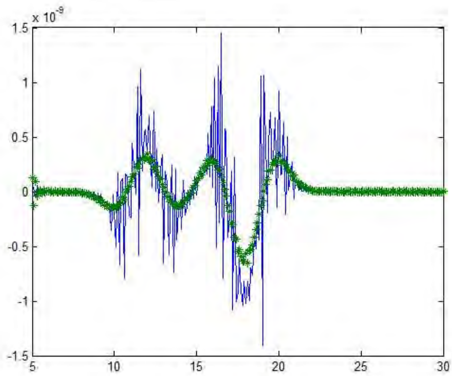

Fig.8 The simulated and smoothed acceleration of the right rail

Fig. 7 and Fig. 8 show the side-view of the simulated and smoothed accelerations. By using the described gradient method, the optimum estimations of the parameter **p**, as well as the identified track stiffness functions have been determined. In Fig. 9 and 10 the initial and the identified track stiffness functions are shown in common diagrams. The deviation between the real and the identified functions is less than the margin of error.

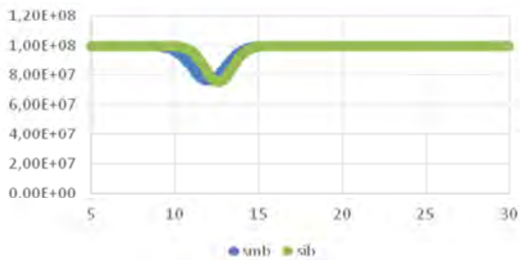


Fig. 9 Original (input) track stiffness inhomogeneity and the identified stiffness inhomogeneity along the left rail

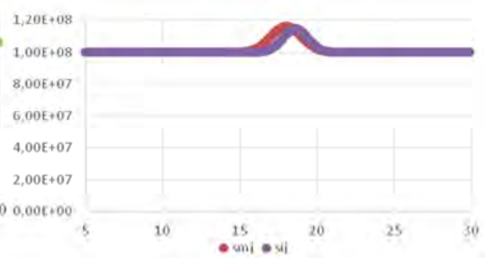


Fig.10 Original (input) track stiffness inhomogeneity and the identified stiffness inhomogeneity along the right rail

## 5. CONCLUDING REMARKS

- A simulation procedure has been elaborated for the determination of the elastic and dissipative supporting parameters present under the rails along the track by applying acceleration signals measured on the carrier-frame over the two axle boxes of the measuring wheel-set [1], [5].
- The variation in the elastic- and dissipative parameters of the track are included in the model, containing homogeneous beams representing the rails supported on inhomogeneous *Winkler*-foundation [2], [6]. The beams (the rails) are loaded by the moving measuring wheelset, which is connected to the carrier-frame of the measuring wheel-set receiving practically constant vertical load from four pneumatic actuators [3].
- The dynamical behaviour of the measuring wheel-set and the carrier-frame is described by a set of ordinary differential equations which is joint to the variable coefficient partial differential equation system describing the motion of the rails via the contact springs (*Hertzian*-springs) modelling the elastic and dissipative vertical wheel/rail connection [4].
- The received hybrid differential equation system can be solved by a numerical approximation method so that the manifold of the unknown motion state describing length-dependence are obtained by applying *Galerkin's* method [7], [8]. Each numerical solution has a given parameter vector specifying the track supporting stiffness and damping inhomogeneity functions assumed to be in force in the simulation step. Using this set of numerical solutions of the rail motion characteristics, the parameters of the unknown track supporting stiffness and damping functions can be approximated by applying the minimizing procedure for the sequence of differences in *Sobolyev*-norm of second order between the measured signals and the simulated approximations.
- The minimizing procedure is implemented by a version of the gradient method, where the partial derivatives of the objective function with respect to the coordinates of the parameter vector have been taken into account [3], [4].
- Further research is necessary to refine the identification method for in-space models and to take into account the statistical characteristics of the measurement errors, as well.
- It is of great practical importance in track qualification to develop considerably

faster numerical procedures for full scale (on line) applications.

## 6. REFERENCES

[1] **Destek, M.**: Investigation of the Interaction of Track/Vehicle System in Approach of System Theory. Közlekedéstudományi Szemle, Budapest, 1974. No. 6, p.271-276. (In Hungarian)

[2] **Zobory, I. - Zoller, V. - Zábori, Z.**: Time Domain Analysis of a Railway Vehicle Running on a Discretely Supported Continuous Rail Model at a Constant Velocity, Z. angew. Math. Mech. 76, S4 (1996), p.169-172.

[3] **Zobory, I. - Zábori, Z.**:Track Qualification Method and Its Realisation Based on System Dynamics, Proceedings of the 5th Mini Conferenceon Vehicle System Dynamics, Identification and Anomalies, VSDIA 1996, (Ed. by Prof. I. Zobory). BME Department of RailwayVehicles, Budapest, 1997, p.173-181.

[4] **Zobory, I. – Békefi, E. - Zábori, Z.**: Simulation Backed Identification of Vertical Track Stiffness Functions by Using Wavelets, Proceedings of the 6th Mini Conferenceon Vehicle System Dynamics, Identification and Anomalies, VSDIA 1998, (Ed. by Prof. I. Zobory). BME Department of RailwayVehicles, Budapest, 1998, p.151-159.(ISBN: 963 420 6352)

[5] **Zobory, I.**:A vasúti pálya-jármű rendszer dinamikája - mérése- minősítése. In: Futástechnikai Konferencia. Konferencia helye, ideje: Harkányfürdő, Magyarország, 2007.07.27-2007.07.29. Proceedings of the Conference on Running Technique. p.1-12. (In Hungarian)

[6] **Zoller, V. –Zobory, I.**: On the Dynamics of the RailwayTrack/Vehicle System in the Presence of Inhomogeneous Rail Supporting Parameters. Proceedings of the 10th Mini ConferenceonVehicle System Dynamics, Identification and Anomalies VSDIA 2006. (Ed. by Prof. I. Zobory). BME Department of RailwayVehicles, Budapest, 2007, p.117-122. (ISBN: 9789634209683)

[7] **Kisilowski, J. - Sowinski, B.**: Problems of Simulating Vehicle Motion by Mathematical Models. In: *Advanced Railway Vehicle System Dynamics*, (Ed. by Prof. J.Kisilowski and Prof. K. Knothe), Wydawnictwa Naukowo-Techniczne, Warsaw, 1991, p.93-139.

[8] **Zábori, Z.**: Analysis of the in Plane Model of a Railway Track Measuring Car. Studies in the Sphere of Topics of Railway Vehicles and Vehicle System Analysis. *Remembrance-Book for the 70th Birth Day of Prof.Dr. István Zobory*. Öt Évszak Kft. Budapest, 2014. (In Hungarian)

[9] https://hu.wikipedia.org/wiki/Hermite-polinomok

# CONFORMITY ASSESSMENT OF A MODERNISED LOCOMOTIVE BOGIE AND BODY CONNECTION

**Sándor MALATINSZKY**

KTI Institute for Transportation Sciences Non-Profit Ltd.
H-1119 Than Károly út 3-5, Budapest

*Received: November 12, 2008.*

## ABSTRACT

Having finished the long-lasting tests on prototype MÁV electric locomotives No. V63,001-002, the serial production of the Class started, in 1981. The first units of the Class were delivered with type UFC bogies designed by the manufacturer Ganz-MÁVAG Company. Even though, this types of bogies were running also under the fastest Hungarian Diesel locomotive of MÁV No. M63,002, which had the Hungarian locomotive speed record 180 km/h, the customer MÁV decided to continue putting into service the heavy electric locos of C'0 C'0 wheel arrangement with Krupp licence bogies. Only seven units of Class V63 locomotives were delivered with Ganz-MÁVAG type UFC bogies. Some of them survived the past decades in operation and the MÁV-START Co. – the owner of the locomotives – decided to modernise their bogie-locomotive body connection, based on the good experiences gained by the similar modification of Class V43 electric locos. Aims of the modernisation were the improvement of riding quality and the noise reduction in the driver's cab taking into consideration the working conditions of the locomotive staff. This kind of modification requires licencing and new Type Approval. The precondition of granting the new Type Approval is the conformity assessment of the modification according to the requirements of related Technical Specifications (TSIs). The MÁV-START Co. announces a tender for the conformity assessment of the modified locomotives. KTI Institute for Transportation Sciences Non-Profit Ltd. – as the accredited Notified Body – started the conformity assessment process with Design Review and Quality Management Approval according to the chosen assessment modules in July 2017. The necessary riding quality and noise test runs were planned in September 2018 when the modification of the first locomotive would be finished. The lecture presents the conformity assessment of a railway rolling stock subsystem on the example of modernisation of an old electric locomotive when only the modification related parts should be certificated. It contains the process, including the experiments of the Design Review, the Quality Management Approval and the applied test methods, which led to the certification of the modified bogie and body connection of the locomotives

*Keywords: conformity assessment, vehicle dynamics, health and safety at workplace*

## 1. INTRODUCTION

The story began in 2017, when KTI, as a Notified Body signed a contract for the conformity assessment of a modernised bogie and body connection of an old type electric locomotive. The aims of the modernisation were the improvement of riding quality and the noise reduction in the driver's cab taking into consideration the working conditions of the locomotive staff. This kind of modification requires licencing and new Type Approval according to the European Union's present legal system, which is defined in the Directive 2008/57/EC of the European Parliament and of the Council of 17 June 2008 on the interoperability of rail system within the Community.

Some facts, which are worth to know about these locomotives. The UFC type three axle bogies were designed for heavy duty diesel-electric and electric locomotives of 20 t axle load up to 160 km/h speed in the late 1960s. The special features of this type were the axle load equaliser system and the pendular body suspension, according to the technical requirement of the era.

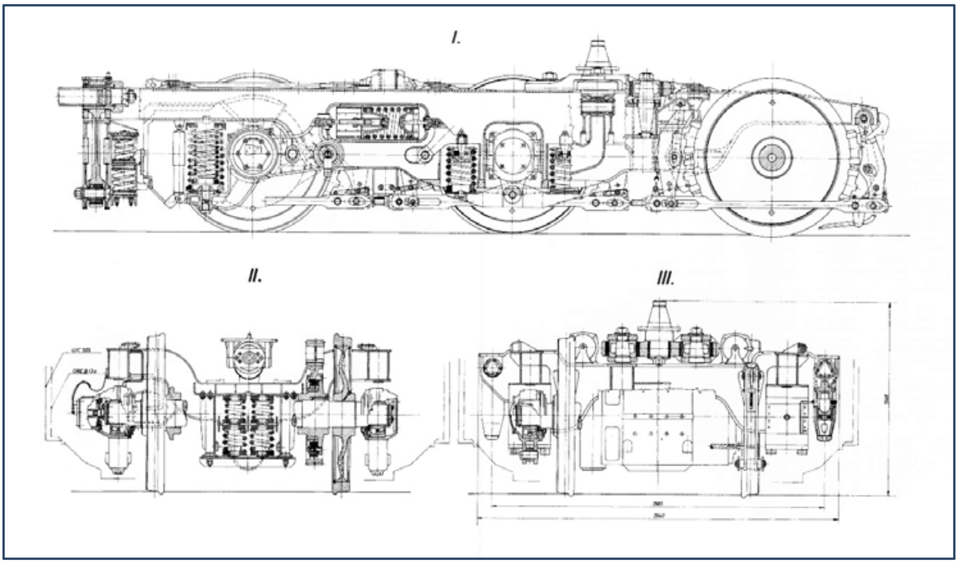


Fig. 1 UFC type bogie of MÁV Class M63 diesel electric locomotives

The bogies were manufactured by the Ganz-MÁVAG works in Budapest between 1970 and 1981 for MÁV Class M63.diesel electric and Class V63 electric locomotives. These DVM10 and VM15 factory type locomotives were the most powerful traction units designed and built in Hungary for heavy freight and express passenger services. These locomotives keep also the not official speed records in their category.

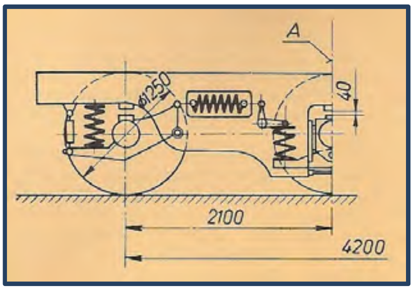


Fig. 2 The axle load equaliser system of the UFC type bogies

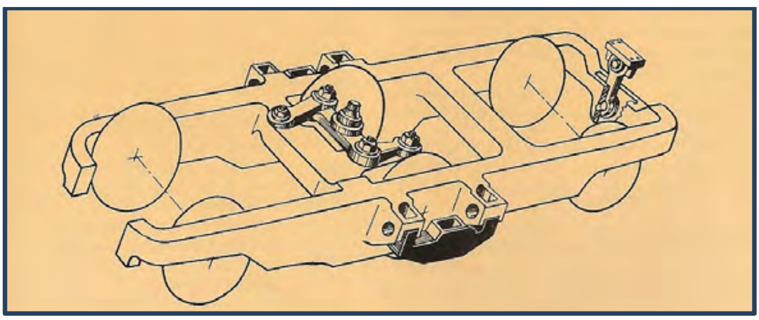

Fig. 3 The pendular body suspension system

Some of the Class V63 electric locomotives survived the past decades in operation and the MÁV-START Co. – the owner of the locomotives – decided to modernise their bogie-locomotive body connection, based on the good experiences gained by the similar modification of Class V43 electric locos, to improve the working conditions of the locomotive staff.

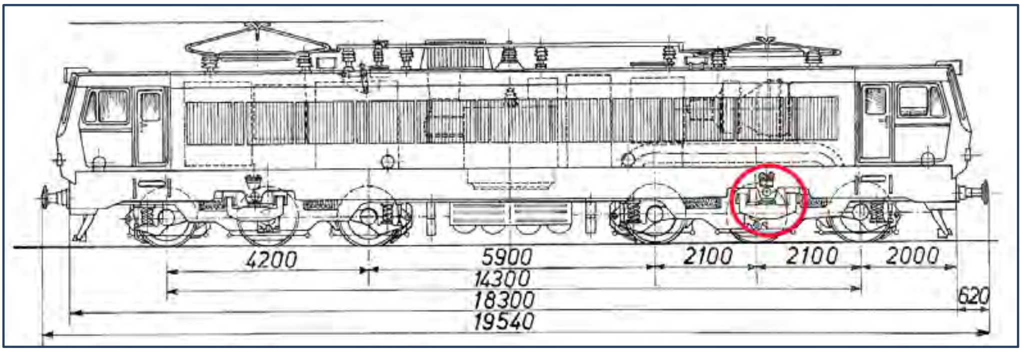


Fig. 4 MÁV Class V63 electric locomotive equipped with bogies type UFC

The precondition of granting the new Type Approval is the conformity assessment of the modification according to the requirements of related Technical Specifications (TSIs).

The Notified Bodies are responsible for the conformity assessment of the subsystems of the European railway system on the bases of the Community rules, and the Designated Bodies for the conformity assessment according to the national rules. There is an intersection, a common territory where the national rules override the European requirements in case of open questions, special cases and derogations.

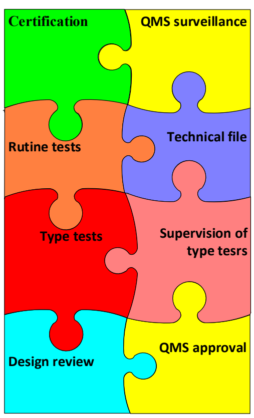


Fig. 5 Conformity assessment of the rolling stock subsystem

The related TSIs prescribe the applicable conformity assessment modules and module combinations. The 2010/713/EU: Commission Decision of 9 November 2010 on modules for the procedures for assessment of conformity, suitability for use and EC verification to be used in the TSIs.

Although the conformity assessment process is often confused with only certification or testing, it is a puzzle of a quite long procedure which contains the design review, quality management approval and surveillance, type testing or supervision of type tests, supervision of production, preparation of technical documentation and at the end the certification comes, like the peak of the iceberg. It needs skilled experts and proper staff for the justification.

## 2. THE LEGAL FRAMEWORKS

One of the most important requirements for conformity assessment is that the subsystems shall comply with the TSIs in force at the time of their placing in service, upgrading or renewal. The Directives 2008/57/EC and 2016/797/EU – as the highest level of European legislation – contain the definition and the list of the subsystems, including rolling stock. Subsystems means the result of the division of the rail system, as shown in Annex II of the Directives:

(a) structural areas:
- infrastructure,
- energy,
- control-command and signalling,
- rolling stock;

(b) functional areas:
- traffic operation and management,
- maintenance,
- telematics applications for passenger and freight services.

In case of putting into service of the new rolling stock the requirements are well defined, but in case of upgrading or renewal of an existing rolling stock the way, the method for the conformity assessment must be fined. Upgrading means any major modification work on a subsystem or part of the subsystem which improves its overall performance. Renewal means any major substitution work on a subsystem or part subsystem which does not change the overall performance of the subsystem
The Technical Specifications for Interoperability, the TSIs represents the next level of the legal framework under the directives. Their status is also law, such as the directives. The Member States shall use the following principles as the basis for determining the application of the LOC&PAS TSI - Commission Regulation No 1302/2014/EU of 18 November 2014 concerning a technical specification for interoperability relating to the 'rolling stock – locomotives and passenger rolling stock' subsystem of the rail system in the European Union - in case of upgrade:

(1) Parts and basic parameters of the subsystem that have not been affected by the upgrading works are exempt from conformity assessment against the provisions of this TSI.

(2) A new assessment against the requirements of this TSI is only needed for the basic parameters which have their performance influenced by the modification(s).

As we go downwards, the next level is of the Commission Recommendations. The essence of the Commission Recommendations 2011/217/EU is that the Member State will decide whether the extent of the works means a new authorisation for putting into service. In the case of a new authorisation, the MS decide to what extent the TSIs need to be applied to the project.
Annex VII of Directive 2008/57/EC contains the rolling stock characteristics to be checked in case of non-TSI conform vehicles:

- vehicle dynamics,
- vehicle superstructure,
- draw and buffer gear,
- bogie and running gear,
- wheel set/wheel set bearing,
- brake equipment,
- technical systems requiring monitoring; e.g. compressed air system,
- front/side windows,
- doors,
- devices for passing,
- control systems (software),
- drinking water and wastewater systems,
- environmental protection,
- fire protection,
- health and safety in the workplace,

Vehicle dynamics, health and safety in the workplace are in the list of the rolling stock characteristics. The drivers' cab is a workplace for the drivers and for the locomotive staff.

The dynamic behaviour of the rolling stock influences running safety and affects the fulfilment of essential requirements safety and technical compatibility. Running of the vehicle shall be safe and shall produce an acceptable level of track loading when operated within the limits defined by the combinations of speed and cant deficiency under the reference conditions set out in the LOC&PAS TSI 1302/2014/EU. This shall be assessed by verifying that the specified limit values are respected.
The TSI describes also the documentation requested by the Directive 2008/57/EC titled Technical file, which contains the test report of running dynamic behaviour, including the test track quality recording and the track loading parameters including possible limitations of use if testing of the vehicle.
Commission Regulation No 1304/2014/EU of 26 November 2014 on the technical specification for interoperability relating to the subsystem 'rolling stock — noise also contains also essential requirement related to the basic parameters. of railway vehicles. These are:

- Limits for stationary noise
- Limits for starting noise
- Limits for pass-by noise
- Limits for driver's cab interior noise

In this case only the driver's cab interior noise tests provide assessable values to evaluate, since he modification does not make any influence on the stationary, the starting and the pass-by noise.
When during the upgrade it is not economically feasible to fulfil the TSI requirement, the upgrade could be accepted if it is evident that a basic parameter is improved in the direction of the TSI defined performance. Therefore, simplified tests are planned to compare the riding quality and the driver's cab interior noise by testing an original type locomotive waiting for the modification and a modified one.


Fig. 6 One of the electric locomotives waiting for the modernisation

## 8. CONCLUDING REMARKS

KTI started the conformity assessment process with the design review and quality management approval according to the chosen SB+SD module combination in July 2017.
The riding dynamic behaviour and noise test runs were planned in September 2018 after that the modification of the first locomotive would be finished. Unfortunately, the program has delayed, and the tests were postponed later than the Conference VSDIA 2018 would begin.

## 9. REFERENCES

[1] **Falk, A. – Pál, J. – Villányi, Gy.:** 100 éves a mozdonygyártás (The 100 Years Old Locomotive Manufacture) Ganz MÁVAG Közlemények, 44. szám (No44),(In Hungarian).
[2] Directive 2008/57/EC of the European Parliament and of the Council of 17 June 2008 on the interoperability of rail system within the Community
[3] Directive 2016/797 of the European Parliament and of the Council of 11 May 2016 on the interoperability of rail system within the European Union
[4] Commission Regulation No 1302/2014/EU of 18 November 2014 concerning a technical specification for interoperability relating to the 'rolling stock - locomotives and passenger rolling stock' subsystem of the rail system in the European Union
[5] Commission Regulation No 1304/2014/EU of 26 November 2014 on the technical specification for interoperability relating to the subsystem 'rolling stock - noise'
[6] 2010/713/EU: Commission Decision of 9 November 2010 on modules for the procedures for assessment of conformity, suitability for use and EC verification to be used in the technical specifications for interoperability adopted under Directive 2008/57/EC of the European Parliament and of the Council
[7] 2011/217/EU: Commission Recommendation of 29 March 2011 on the authorisation for the placing in service of structural subsystems and vehicles under Directive 2008/57/EC of the European Parliament and of the Council Text with EEA relevance

# DESIGN OF EXPERIMENT APPROACHES FOR THE CALIBRATION OF INSTRUMENTED WHEELSET

**Egidio DI GIALLEONARDO, Stefano BIONDA, Francesco BRAGHIN and Claudio SOMASCHINI**

Department of Mechanical Engineering
Politecnico di Milano
Via La Masa 1, I-20156, Milan, Italy

*Received: November 9, 2018*

## ABSTRACT

The presented work aims at showing how design of experiments concepts can be applied for the calibration of instrumented wheelsets thus significantly reducing time and costs. In this work, a model is used to relate the strains measured on the instrumented wheelset to the contact forces applied on the wheels. Then, through the model, the optimal set of calibration tests is determined using different optimality criteria. The accuracy of the estimated forces, which are calculated applying the calibration experiments obtained through optimality criteria, is presented and critically analyzed. It is shown that the accuracy of the estimated forces converges for a given number of elements used in the candidate set in case optimal design of experiments are used. It can be concluded that it is possible to reach effective calibration results with less tests using optimal experiment designs.

*Keywords:* design of experiments, instrumented wheelset, wheel-rail contact forces.

## 1. INTRODUCTION

Train in-line tests are mandatory to meet security and quality requirements according to the standard EN 14363 [1]. During in-line tests, wheel-rail contact forces have to be estimated in order to understand the vehicle's behaviour and thus to evaluate the vehicle's stability and to assess its running safety. In order to obtain reliable force estimations, the calibration of the instrumented wheelset has to be done experimentally.

The calibration of an instrumented wheelset relates wheel-rail contact forces with the strains measured on specific sections on the wheels/axle. Thus, during in-line tests, by measuring the strains on the same wheelset it is possible to estimate the forces applied on wheelset itself. However, finding the relation between strains and forces may require numerous laboratory tests. Design of experiments (or DoE), is used to reduce the total time that is spent on the tests as well as to improve the accuracy of the estimated forces. DoE aims at setting up an effective and efficient test plan by implementing an optimality criterion based on a model. The applicability of different optimality approaches are investigated and verified for the calibration of instrumented wheelsets.

## 2. CALIBRATION OF THE INSTRUMENTED WHEELSET

In order to correctly define the test plan, it is necessary to analyse the contact forces applied on the wheelset: in general, having three contact force components on each wheel, i.e. the vertical, the lateral and the longitudinal components, six forces must be estimated. In the case of non braked or driven wheelsets, it is assumed (for the longitudinal dynamic equilibrium) that the longitudinal contact forces acting on each wheel have the same magnitude but opposite directions; thus, in this case, only five forces have to be estimated. Without loss of generality, let's do this assumption for the following. Having five contact force components to estimate, at least five independent

strain measurements are needed. Previous works on this topic have highlighted the influence of the contact point position. Thus, at least two additional independent measurements are required [2, 3].
The relation between contact forces applied on the wheelset and strains at given positions on the wheelset can be expressed by equation 1:

$$\varepsilon = [S]F \tag{1}$$

where $\varepsilon$ is a vector containing the strains and has a dimensions of at least 7×1, $F$ contains the contact force components and has dimensions of 5×1 and $[S]$ is the sensitivity matrix and has a dimensions of at least 7×5.
As shown in Fig. 1, the calibration process is an inverse problem in which, using the output responses and knowning the input excitations, a model is defined [4].

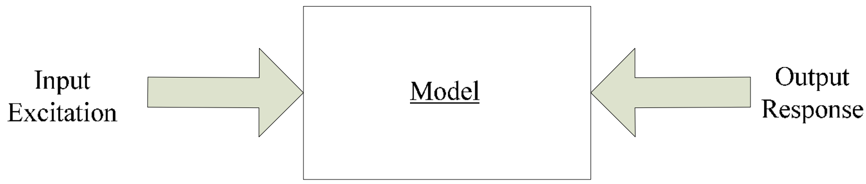


Fig. 1 Inverse problem.

$$F = [A]\varepsilon \tag{2}$$

Once the model is known, i.e. the calibration matrix $[A]$ has been determined, contact forces can be estimated based on measured strains. The calibration matrix is found by using the least squares approach ([5], [6]):

$$[A] = [F][\varepsilon]^T([\varepsilon][\varepsilon]^T)^{-1} \tag{3}$$

where $[F]$ denotes the force matrix having dimensions of n×5, with n being the number of experiments. Similarly, $[\varepsilon]$ is the strain matrix having dimensions of n×b, with b indicating the number of signals that have been used. The term $[\varepsilon]^T([\varepsilon][\varepsilon]^T)^{-1}$ is the Moore-Penrose pseudo-inverse of strain matrix, also known as $[\varepsilon]^*$.

| **Factor** | **Symbol** | **Levels** |
|---|---|---|
| *Vertical Force[kN] (Left)* | Q1 | 55, 70, 85, 100 |
| *Vertical Force[kN] (Right)* | Q2 | 55, 70, 85, 100 |
| *Lateral Force[kN] (Left)* | Y1 | -40, -20, -10, 0, 10 |
| *Lateral Force[kN] (Right)* | Y2 | -40, -20, -10, 0, 10 |
| *Longitudinal Force[kN]* | X | -15, -7.5, 0, 7.5, 15 |
| *Relative Lateral Wheel-Rail Position [-]* | - | Left wheel flanging, Centered, Right wheel flanging |

Table 1 Factors of the experiment and their levels.

Experiments for the calibration of the wheelsets are generally done according to design loads defined by the manufacturer. In the specific case considered in this paper, the test plan included 471 tests, with forces levels and relative lateral position of the wheelset with respect to the rails shown in Table 1. It should be noted that the number of tests should be much higher but not all combinations of force levels and relative lateral positions are feasible. Thus, constrains have been introduced:

- constraint 1: $|Y_1| < Q_1\mu$
- constraint 2: $|Y_2| < Q_2\mu$
- constraint 3: $-40$ kN $\leq Y_1 < Q_1\mu$
- constraint 4: $-40$ kN $\leq Y_2 < Q_2\mu$
- constraint 5: $Q_1 + Q_2 > 150$ kN

$\mu$ being the friction coefficient between wheel and rail (assumed to be equal to 0.36).

| **Position** | **Const. 1** | **Const. 2** | **Const. 3** | **Const. 4** | **Const. 5** |
|---|---|---|---|---|---|
| *Left Flanging* | | √ | √ | | √ |
| *Centered* | √ | √ | | | √ |
| *Right Flanging* | √ | | | √ | √ |

Table 2 Application of constraints for different relative wheel-rail lateral positions.

Table 2 shows for which relative wheel-rail lateral positions constrains are active. For example, for left flanging conditions, the lateral force $Y_1$, applied to the left wheel should be within the interval of constraint 3 while the lateral force $Y_2$, applied to the right wheel should be smaller than the friction force generated by the vertical force (constraint 2).

## 3. OPTIMISED DESIGN OF EXPERIMENT APPROACHES AND THEIR APPLICATION

In order to design the experiments, a full factorial design that investigates all possible working conditions can be adopted: if k is the number of factors (in our case the contact force components and the relative wheel-rail lateral position) each one having two levels, the full factorial design requires to have $2^k$ elements in candidate set, i.e. $2^k$ test conditions. Moreover, one should know the mathematical relation between the factors and the responses (in our case the strains). In general, this relation, called characteristic equation, can be nonlinear:

$$y = \beta_0 + \beta_1 x_1 + \beta_2 x_2 + \beta_3 x_1 x_2 + \epsilon \quad (4)$$

$x_i$ being the factors and $y$ being the response.

Based on the characteristic equation, the design matrix X, having size equal to n × p (where n is the number of experiments of the candidate set and p is the number of coefficients $\beta_i$ of the characteristic equation), can be defined.

As the number of factors and/or the levels of factors increase, the full factorial design needs too many experiments to be done. In case all experiments foreseen by the full factorial design cannot be carried out, a subset of the candidate set has to be selected.

To be able to determine the best combination of experiments for optimal design matrix, two intermediate-step matrices named information matrix and dispersion matrix should be determined. The information matrix is equal to $(X^T X)$ (i.e. the transpose of design matrix cross-multiplied by the design matrix itself) while the dispersion matrix is the inverse of information matrix, $(X^T X)^{-1}$ [7]. The dispersion matrix is used for determining the best set of coefficients via least square estimate as shown in equation (5):

$$\hat{\beta} = (X^T X)^{-1} X^T y \tag{5}$$

The optimal design matrix, denoted by $X^*$, may be determined using one of the known criteria, i.e. D-optimality, A-optimality, V-optimality and G-optimality. In the following D-optimality and V-optimality criteria are briefly described and applied to the wheel-rail contact force estimation problem.

D-optimality was allegedly the first alphabetically named criterion [8] and it is a simple criterion due to the easiness of calculation. As Ozol-Goldfrey [9] describe, the bigger the value of the determinant of the information matrix, the better the estimation of the model's parameters[1]:

$$|X^{*T} X^*| = max(|X^T X|) \tag{6}$$

It is worth mentioning that, for second order models, there is no upper limit for D-optimal designs since an increase in the number of elements of the candidate set will always lead to an increase in the determinant of the information matrix.

V-optimality, instead, is a criterion that requires high computational cost but is frequently used due to its higher accuracy. It is based on the minimization of the average scaled prediction variance (SPV), a measure of the success of estimating the response at any point (experiment) in the design space [10]. Let vector $\chi_i$ be a generic experiment. Its variance is equal to:

$$d(\chi_i) = \chi_i^T * (X^T X)^{-1} * \chi_i \tag{7}$$

The optimal set of experiments is determined by the lowest average variance:

$$\frac{1}{n}\sum_{i=1}^{n} \chi_i^T * (X^{*T} X^*)^{-1} * \chi_i = min\left(\frac{1}{n}\sum_{i=1}^{n} \chi_i^T * (X^T X)^{-1} * \chi_i\right) \tag{8}$$

Considering the problem of the contact force estimation, some preliminary considerations are needed in order to define the problem in a suitable form for DoE approaches. Since the absolute angular position of the axle, and thus of the plane of the strain measurements, is not known precisely (unless one introduces additional sensors such as encoders), the resultant stain at each measuring section is considered. Since the two strain gauge bridges, at each i[th] measuring section, are phase shifted by 90 degrees one with respect to each other, the resultant stain is equal to:

$$\varepsilon_i = \sqrt{\varepsilon_{i0}^2 + \varepsilon_{i90}^2} \tag{9}$$

This resultant strain is also equal to the resultant of the strains in the (absolute) vertical and horizontal planes:

[1] It is assumed that the determinant of the information matrix is inversely proportional to the square of the volume of the confidence region for the regression coefficients.

$$\varepsilon_i^2 = \varepsilon_{i0}^2 + \varepsilon_{i90}^2 = \varepsilon_{ih}^2 + \varepsilon_{iv}^2 \tag{10}$$

Bending moments in the horizontal plane are generated only by the longitudinal force components applied to the wheels. Thus, the strain in the horizontal plane is (linearly) proportional to longitudinal forces. Remembering that, for a wheelset that is not driven nor braked, the longitudinal forces on the two wheels are equal in magnitude (and opposite in direction) we can write:

$$\varepsilon_{ih} = b_{i1}X_1 + b_{i2}X_2 \cong b_{i3}X_1 \tag{11}$$

Note that the proportionality coefficients are a function of the considered section.
Bending moments in the vertical plane, instead, are affected by lateral and vertical force components as well as by the lateral position of the wheel-rail contact point as described in [2]. The lateral position of the wheel-rail contact point $\Delta y$ is associated to a vertical displacement $\Delta z$ of the contact point due to the conicity of the wheels. Both displacements determine a bending moment in the vertical plane of the axle. However, the contribution of the vertical displacement $\Delta z$ is negligible with respect to the one of the lateral displacement $\Delta y$. Moreover, it is assumed that the lateral displacement $\Delta y$ is equal for the two wheels (rigid wheelset). Note that the exact lateral displacement $\Delta y$ is not easily measurable, even during calibration tests. Thus, the lateral position of contact point is approximated by a discrete variable $d_A$. If the wheelset is in centered position, $d_A$ is set equal to 0. In left wheel flanging conditions, $d_A$ is set equal to 1 and in right wheel flanging conditions, $d_A$ is set equal to -1. Summing up, the strain in the vertical plane can be expressed through the following (nonlinear) equation:

$$\begin{aligned}\varepsilon_{iv} = a_{i1} + a_{i2}Q_1 + a_{i3}Q_2 + a_{i4}Y_1 + a_{i5}Y_2 \\ + a_{i6}Q_1 d_A + a_{i7}Q_2 d_A\end{aligned} \tag{12}$$

Again, note that the proportionality coefficients are a function of the considered section.
Recalling equation (10), the resultant strain at the i$^{th}$ section is equal to:

$$\begin{aligned}&\varepsilon_i^2 = \beta_{i1} + \beta_{i2}Q_1^2 + \beta_{i3}Q_1Q_2 + \beta_{i4}Q_1Y_1 + \\ &\beta_{i5}Q_1Y_2 + +\beta_{i6}Q_2^2 + \ldots\end{aligned} \tag{13}$$

In general, one can write:

$$\varepsilon_i^2 = f(Q_1, Q_2, Y_1, Y_2, X_1, d_A) \tag{14}$$

It is now possible to define the problem in a suitable form for DoE approaches:

$$\varepsilon^2 = [X]\beta \tag{15}$$

## 4. RESULTS

As explained before, the more elements used in the candidate set, the better D-optimal design. In order to assess how close the design matrix is to the optimal one, the so-called called D-Optimal value can be computed. A similar measure can also be defined for V-optimality criterion. In Fig. 2, V-optimal and D-optimal values for increasing size of the candidate set are shown. It can be seen that the V-optimal value converges to a minimum at increasing number of tests used in candidate set while the D-optimal value does not reach a maximum. This is in agreement with the fact that, for second order models, the determinant of the information matrix is continuously increasing with the number of experiments.

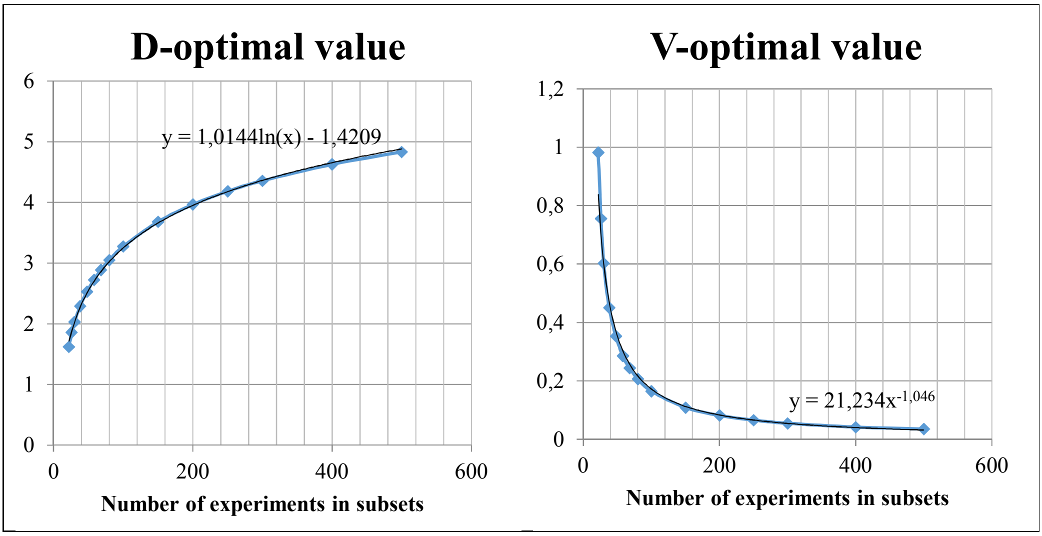


Fig. 2 D-optimal (left) and V-optimal (right) values as a function of the number of experiments.

The assessment of the effectiveness of the proposed methods can also be done by evaluating the calibration results by comparing the optimal test subset (selected among the 471 tests with the previously mentioned optimality criteria) with randomly selected calibration tests. It is worth mentioning that, due to the selection constraints, there is a possibility of not finding the optimal test subset with the optimality criteria. The algorithm selecting the optimal subsets from the 471 experiments divides the difference between the target value of the criterion and the achieved value by the level of each factor (i.e. the contact force components and the relative wheel-rail lateral position). In this way, the effect of the different factor amplitudes is normalized and the tests having the least difference between the target and achieved values are selected.

In figure 3 the effectiveness of the proposed methods is shown in terms of the standard deviation of the estimation error on a vertical (Q2) and a lateral (Y2) force component considering different test subsets:

- random selection;
- D-optimal test subset;
- V-optimal test subset.

For the random selection both the average (blue), the maximum (red) and the minimum (orange) standard deviation of the estimation error is reported. It can be seen that, even with a reduced number of tests selected using D-optimal and V-optimal designs, the standard deviation of the estimation error is very close to the minimum achievable one. The differences between the results obtained using D-optimal and V-optimal test plans are really small so there is no reason to prefer one approach with respect to the other.

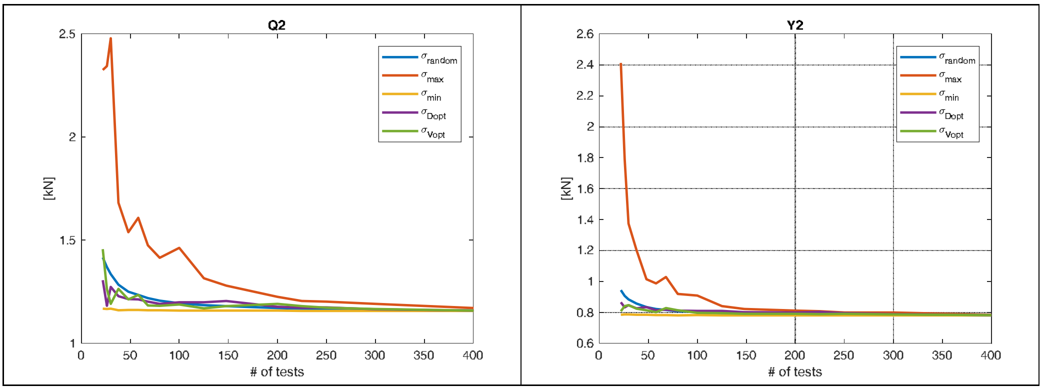


Fig. 3 Standard deviation of the estimation error for the vertical force Q2 (left) and lateral force Y2 (right) considering different test plans.

## 5. CONCLUDING REMARKS

In the work optimal DoE approaches are presented and are applied to the calibration of an instrumented wheelset. The full test plan of calibration experiments consists of 471 tests. The aim of applying DoE approaches is to decrease the number of required tests. A physical model of the system under analysis has to be developed in order to identify the factors influencing the resultant strains on the axle and, thus, to identify a design matrix. Several candidate test subsets having different number of elements are found with optimal designs and their effectiveness is assessed through comparison with randomly selected experiments in terms of standard deviations of the difference between the estimated and measured forces. It is shown that the optimal design guarantees a standard deviation that is in general smaller than the average standard deviation of randomly selected tests. Moreover, the standard deviation found through optimal designs has a converging trend with increasing number of elements. This means that, above a certain number of elements in the subset, the accuracy of the force estimations does not improve further. Thus, much less than 471 tests could be used to effectively calibrate and instrumented wheelset.

## 6. REFERENCES

[1] **EN14363.** “Railway applications - Testing for the acceptance of running characteristics of railway vehicles - Testing of running behaviour and stationary tests.” 2005.

[2] **Bionda, S. - Braghin, F. - Cazzulani, G. - Di Gialleonardo, E.:** “Evaluation of the metrological characteristics of an instrumented wheelset for the measurement of wheel-rail contact forces.” Proceedings of the 13th MINI Conference on Vehicle System Dynamics, Identification and Anomalies (VSDIA 2012) (Ed. by Prof. I. Zobory), BME, Department of Railway Vehicles and Vehicle System Analysis, Budapest, 2012, p.131–140.

[3] **Cazzulani, G. - Di Gialleonardo, E. - Bionda, S. - Bassetti, M. - Crosio, P. - Braghin, F.:** "A new approach for the evaluation and the improvement of the metrological characteristics of an instrumented wheelset for the measure of wheel-rail contact forces." Proceedings of the Institution of Mechanical Engineers, Part F: Journal of Rail and Rapid Transit 231, 4, 2017, p.381–393.

[4] **Uhl, T.:** "The inverse identification problem and its technical application." Archive of Applied Mechanics 77, 5, 2006, p.325–337.

[5] **Braghin, F. - Bruni, S. - Cervello, S. - Cigada, A. - Resta, F.:** "A New Method for the Measure of Wheel-Rail Contact Forces." 6th International Conference on Contact Mechanics and Wear of Rail/Wheel Systems, 2003, p.313–319.

[6] **Diana, G. - Resta, F. - Braghin, F. - Bocciolone, M. - Di Gialleonardo, E. - Crosio, P:** "Metodologia di calibrazione di sale dinamometriche per la misura delle forze di contatto tra ruota e rotaia." Ingegneria Ferroviaria 12, No. 1, 2012, p. 9-21.

[7] **de Aguiar, P.F. - Bourguignon, B. - Khots, M. S. - Massart, D. L. - Phan-Than-Luu, R.:** "D-optimal Designs". Chemometrics and Intelligent Laboratory Systems 30, 2, 1995, p.199-210.

[8] **Kiefer, J.:** "On the Nonrandomized Optimality and Randomized Nonoptimality of Symmetrical Designs". Annals of Mathematical Statistics, 1958, p.675-699.

[9] **Ozol-Goldfrey, A.:** "Understanding Scaled Prediction Variance Using Graphical Methods for Model Robustness, Measurement Error and Generalized Linear Models for Response Surface Designs." PhD Thesis Virginia Polytechnic Institute and State University, 2004.

[10] **Box, G. E. - Hunter, J. S.:** "Multi- factor Experimental Designs for Exploring Response Surfaces." Annals of Mathematical Statistics, 1957, p.195-241.

[11] **Triefenbach, F.:** "Design of Experiments: The D-Optimal Approach and Its Implementation As a Computer Algorithm." BSc Thesis Umea University, South Westphalia University of Applied Sciences, 2008.

# ALGORITHM DEVELOPMENT TO CLASSIFY THE DETERIORATION OF INSULATED RAIL JOINTS BY MEANS OF ONBOARD MEASUREMENTS

**Claudio SOMASCHINI, Egidio DI GIALLEONARDO, Andrea COLLINA and Marco BOCCIOLONE**

Department of Mechanical Engineering
Politecnico di Milano
20156, Milan, Italy

*Received: November 12, 2008*

## ABSTRACT

Insulated rail joints are fundamental components of some railway lines due to their role in the signalling systems. On the other hand, being highly stressed components, their monitoring is a fundamental activity to guarantee the safety of running trains. Currently, the monitoring of these elements is carried out directly by trained personnel. It follows that the control of a railway line takes long time and there are no objective parameters that guarantee the health condition of a joint. Considering this context, this work shows the preliminary results of the analysis of experimental data through an algorithm developed to detect and classify the glued insulated rail joints by means of accelerometers placed on two wheelsets of a train.

*Keywords:* Insulated rail joints, axle box acceleration, health condition monitoring.

## 1. INTRODUCTION

The monitoring of insulated rail joints (IRJ) is a very important activity to ensure the safety of the railways. IRJ, on the one hand, are fundamental components for some types of the signalling systems (as they are the essential components of the automatic block signalling system) while, on the other hand, being discontinuities of the rail, they are high stressed elements [1][2]. The low bending stiffness of joint bars compared with that of a common rail section [5] results in the generation of impact forces which could lead to a fast deterioration of the IRJs that often suffer from problems such as rail head damage due to wear, bolt looseness, joint-bar and rail fracture resulting from fatigue and ballast deterioration [3][4][6].
To date, the monitoring of these elements is carried out directly by trained personnel who walks the railway line, analyses the dynamic behaviour of the joints during the passages of trains and, in the event of anomalies, performs specific checks such as ultrasound analysis to guarantee the absence of cracks. It follows that the analysis of an entire railway line takes long time and, by their nature, the results are often subjective.
Since the deterioration of a suspended joint depends mainly on the loads arising from the passages of trains, following other researches on this topic [8] an algorithm of identification and classification of joints is developed relying on the dynamic response of the wheelset at the passage of a joint. In this way, it is possible to quickly analyse all the joints of a railway line using a single measurement setup placed on board of a train.
In this work, first of all, the diagram and the steps of the algorithm of analysis of the experimental data are shown. Subsequently, some examples of obtained results are reported checking the quality of the analysis by changing parameters such as train speed and rail irregularity. Finally, the results obtained from the measurements of

accelerometers placed on two consecutive wheelset of a train are compared with those deriving from the standard trackside analysis.
These results show the effectiveness of this procedure and indicate that, at least, a first selection of the most damaged joints could be carried out by means of on-board measurements.

## 2. JOINT IDENTIFICATION

### 2.1 Exper*imenta*l setup

The measurements were conducted using a two-axles service vehicle. Eight accelerometers were mounted on the four axle-boxes of the two axles in order to have a redundancy of the data. Both lateral and vertical accelerations were measured. The sampling frequency was set to 2000 Hz and an anti-aliasing filter at 900 Hz was used.
The tests were carried out on a commuter line of approximately 60 km, measuring both the tracks and repeating the measurement twice.

Fig. 1 Position of the accelerometers above the axle-box

### 2.1 Algorithm

Usually, the positions of the IRJs should be known while, in our case, we had to identify their positions since the provided positioning was not accurate.
In order to recognise the IRJ positions through the accelerations we developed an algorithm based on these main steps:

- The accelerations are acquired at 2000 Hz;
- The Kurtosis is evaluated on the raw data (without any kind of filter) for each vertical acceleration using a moving window of 20 m;
- The two Kurtosis of the same side are multiplied;
- IRJ are identified through a threshold value;
- The peaks due to the passing over railway switches are excluded.

Since the Kurtosis is able to measure the tailedness of the probability distribution of the data, with this analysis the dynamic peaks due to discontinuities in the rail are highlighted. Subsequently, multiplying the Kurtosis values of the two accelerometers of the same side, the acceleration peaks due to IRJ are emphasized with respect to the possible defects of the geometry like short pitch rail corrugation. Finally, excluding the peaks resulting from the passages over railway switches, the IRJ are identified as a function of the position along the line.

## 3. PRELIMINARY RESULTS

### 3.1 Position identification

An example of the data acquired in a test run is reported in in Fig. 2a, where the data acquired by the two vertical accelerometers of the left side are superimposed. Globally, the level of vertical acceleration measured by the sensors is similar and this consideration confirms the possibility of identifying the singular points on the line by correlating the acceleration measurements of the same side.

In the same section, the algorithm was applied to identify the positions of the IRJs and, knowing the position of the switches along the line, it was possible to exclude them by associating these singularities only to the presence of a joint.

The results are shown in Fig. 2b, where the vertical continuous lines indicate the joints reported as "deteriorated" by the infrastructure manager, while the blue stars point the IRJs identified by the algorithm. The dashed lines represent the joints described as in good health condition.

As it can be seen from the figure, the algorithm was able to identify all the joints pointed out by the infrastructure manager. Furthermore, also the joint placed at km 33.2 is highlighted while the two joints at km 33.35 and 33.95 were excluded from the analysis since they correspond to two switches that are positioned in the sections indicated by the orange circles. The only joint that was not identified by this analysis is the one at the km 33.55. On the other hand, this joint is characterized by a very low acceleration value indicating an excellent health condition.

Another important result of the algorithm is that it is able to highlight the presence of IRJs independently from the speed of the train. As can be seen in Fig. 2c, in the selected section the speed is very variable and despite this, the analysis highlight both joints travelled at 40 km/h both joints travelled at less than 10 km/h. Furthermore, as can be seen in Fig. 3, the identification is not affected by the high noise due to short pitch rail corrugation highlighted in the figure with red circles (while the orange circle represents also in this case the presence of a switch).

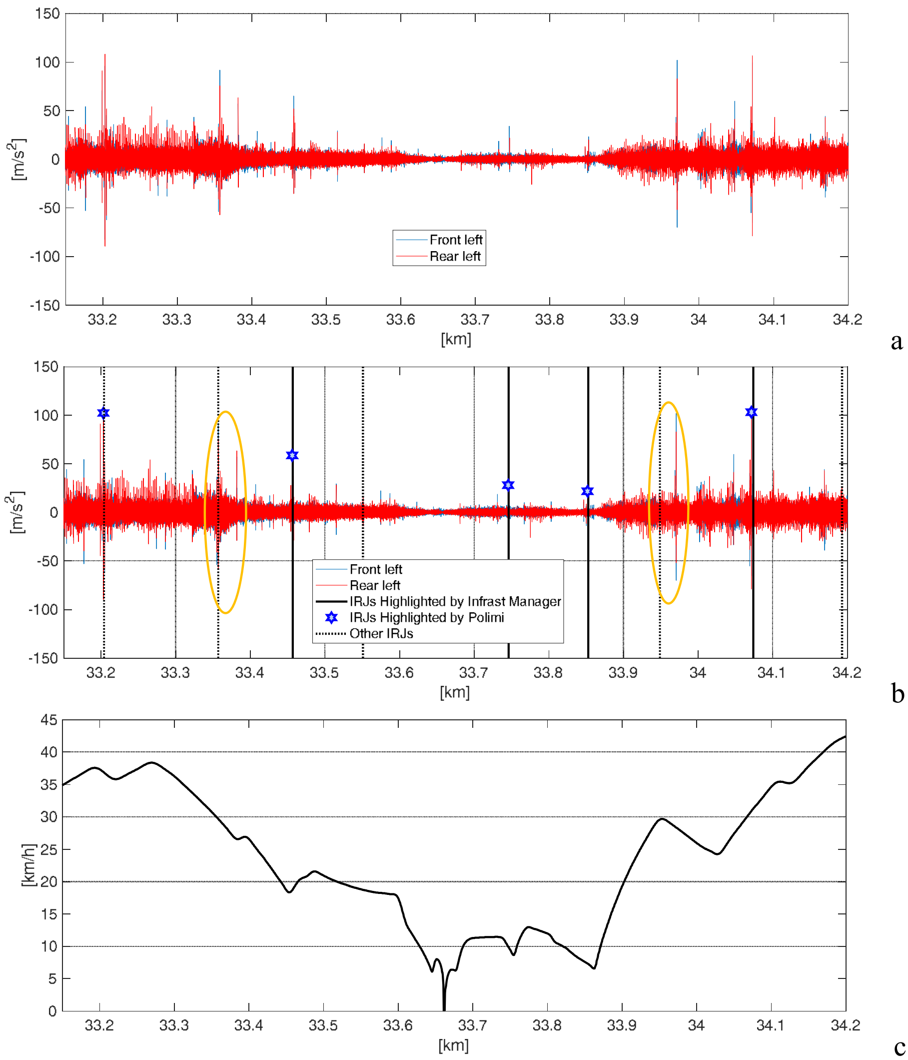


Fig. 2 Example of the accelerations measured on the left axle boxes (a), results of the algorithm of identification (b) and train speed profile in the analysed section.

### 3.2 Repeatability

To confirm the repeatability of the identification, it is possible to compare the results of the measurements carried out in two different days on the same line. An example of the identification of the left IRJs is proposed in Fig. 4 considering a section of 2.5 km. The number of joints reported is almost identical, while the actual acceleration values are slightly different depending on the travelling speed. This result prove that the identification of the joints is robust although a method should be defined to correct the absolute value considering the speed of the train.

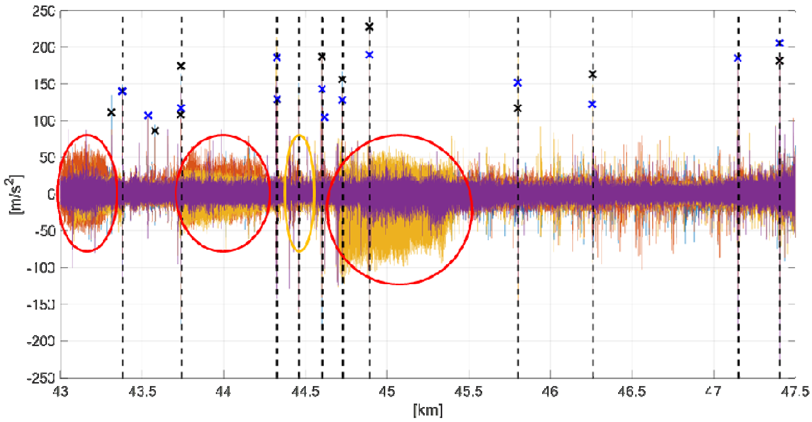


Fig. 3 Identification results in correspondence of high noise due to short pitch rail corrugation.

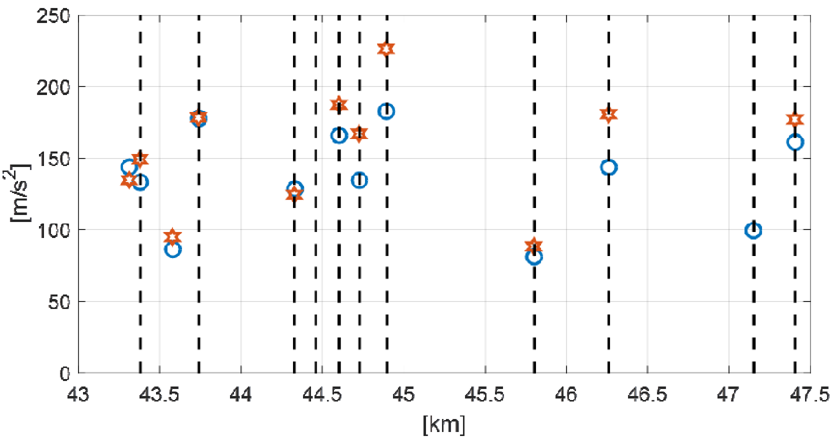


Fig. 4 Comparison of the joints identified in two runs of two different days represented by stars and circles.

## 4. FUTURE DEVELOPMENTS

The work presented in this paper is in a phase of development and, at the moment, we are looking at whether it is possible to identify a "signature" in the time history of the accelerations at the passage of the train over a IRJ. The idea is to identify a characteristic trend due to the passage over a joint and then to extrapolate from the overall acceleration only the information due to anomalies in the joint.

Fig. 5 shows a diagram of how this idea could be developed considering the measurements carried out on a new experimental train where, on both bogies of a car, eight vertical accelerometers were positioned both on the axle boxes and on the chassis of the bogies near the primary suspensions. In all the graphs, the accelerations measured on the bogies are reported in the upper part while in the lower part those measured on the axle boxes are presented.

The analysis process could be:

- a - the joint is identified and the accelerations measured crossing it are extracted;
- b - the measurements of different accelerometers are compared;
- c - the average behaviour (red line) and variations with respect to it (orange line) are extracted;
- d - from the comparison between average trends in many different runs, a sort of "signature" of the response to the joint is obtained, while from the variations with respect to the "signature" damages to the joint are identified.

For simplicity, the procedure has been shown in the time domain, but it is possible to carry out a similar analysis also in the frequency domain. At the moment, both the approaches are under investigation considering also intermediate algorithms as the analysis by means of the wavelet transform [7].

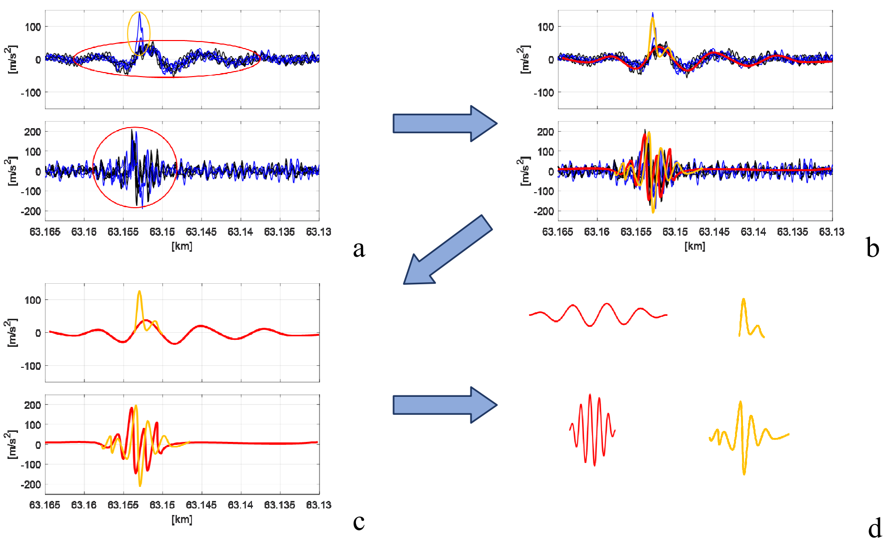


Fig. 5 Diagram of the procedure to extract a signature and of an index of the defect of the IRJ from the behaviour of the accelerations measured on the bogies (upper graphs) and on the axle boxes (lower graphs).

## 5. CONCLUDING REMARKS

The preliminary results showed in this work prove that the approach used is promising and, although it is in an initial phase, it is able to detect IRJs.

Considering the presented analyses, the following conclusions can be drawn:

- accelerometers placed onboard are able to identify insulated joints;
- the algorithm developed proved to be robust independently from the speed of the train;

- the use of the Kurtosis ensure that the results are not affected by the high noise due to rail irregularity.

The results show the effectiveness of the procedure and indicate that at least a first selection of the most damaged joints could be carried out by means of onboard measurements.

The work is progressing and at the moment the main objectives to be achieved are:

- a formulation should be defined to correct the absolute value of the acceleration considering the speed of the train;
- the analysis of the behaviour of the acceleration in correspondence of the joints could be deepened considering many different passages;
- typical "signature" of the defect could be found but it is necessary to investigate whether it is possible to identify this signature in the time domain or in the frequency domain.

## 6. REFERENCES

[1] **Askarinejad, H. – Dhanasekar, M. – Cole, C.:** Assessing the effects of track input on the response of insulated rail joints using field experiments. Proceedings of the Institution of Mechanical Engineers, Part F: Journal of Rail and Rapid Transit, 227(2), 2013, p.176-187. doi:10.1177/0954409712458496.

[2] **Chen, Y. C. – Kuang, J. H.:** Contact stress variations near the insulated rail joints. Proceedings of the Institution of Mechanical Engineers, Part F: Journal of Rail and Rapid Transit, 216(4), 2002, p.265-274. doi:10.1243/095440902321029217.

[3] **Kabo, E. – Nielsen, J. C. O. – Ekberg, A.:** Prediction of dynamic train–track interaction and subsequent material deterioration in the presence of insulated rail joints, Vehicle System Dynamics, 44:supl, 2006, p.718-729, DOI: 10.1080/00423110600885715

[4] **Himebaugh, A. K. – Plaut, R. H. – Dillard, D. A.:** Finite element analysis of bonded insulated rail joints. International Journal of Adhesion and Adhesives, 28(3), 2008, p.142-150. doi:10.1016/j.ijadhadh.2007.09.003

[5] **Kerr, A. D. – Cox, J. E.:** Analysis and tests of bonded insulated rail joints subjected to vertical wheel loads. International Journal of Mechanical Sciences, 41(10), 1999, p.1253-1272. doi:10.1016/S0020-7403(98)00042-3.

[6] **Mandal, N. K.:** On the low cycle fatigue failure of insulated rail joints (IRJs). Engineering Failure Analysis, 40, 2014, p.58-74. doi:10.1016/j.engfailanal. 2014. 02.006.

[7] **Molodova, M. – Li, Z. – Núñez, A. – Dollevoet, R.:** Validation of a finite element model for axle box acceleration at squats in the high frequency range. Computers and Structures, 141, 2014, p.84-93. doi:10.1016/j.compstruc. 2014.05. 005

[8] **Molodova, M. – Oregui, M. – Núñez, A. – Li, Z. – Dollevoet, R.:** Health condition monitoring of insulated joints based on axle box acceleration measurements. Engineering Structures, 123, 2016, p.225-235. doi:10.1016/j.eng struct. 2016.05.018.

# A ROLLING STOCK-BASED SYSTEM FOR CATENARY CONDITION MONITORING: VALIDATION THROUGH NUMERICAL SIMULATIONS ON A RIGID CATENARY

**M. CARNEVALE, A. COLLINA and A. ZUIN**

Department of Mechanical Engineering, Politecnico di Milano
Via La Masa 1, 20184 Milano, Italy
e-mail marco.carnevale@mecc.polimi.it
phone: +39 02 2399 8247

*Received: November 9, 2018*

## ABSTRACT

Condition monitoring of rolling stock and infrastructure is becoming a key requirement for railway companies throughout the world, which are making a significant effort to equip commercial trains with diagnostic systems, to gather data daily instead of periodically as currently allowed by special-purpose diagnostic trains. This paper is part of a long-term work in which a diagnostic system, previously proposed by the authors, is being developed in cooperation with rolling-stock manufacturers, train operating companies and the Italian infrastructure manager. The system is able to monitor the pantograph and the overhead contact line through authomatic data acquisition and post processing in a wayside server, and should help shifting maintenance operations from time-based to condition based approaches. As a further application, the paper is focused on the detection of defects in a rigid overhead contact line. Numerical simulations of a healthy and a defective line are carried out to address the problem of signature definition for the identification of the defects.

*Keywords:* pantograph, rigid overhead contact line, diagnostics.

## 1. INTRODUCTION

Automatic condition monitoring is becoming a key requirement for railway companies worldwide, and diagnostic systems are being tested all around the world. They are based on sensors placed on-board train or directly on the infrastructure, as well as on image processing systems for automatic recognition of patterns. The entire diagnostic system is composed of several basic steps:

- measurement of significant parameters, by means of sensors, to gather data related to the status of the investigated elements/subsystem;
- localisation of the considered elements/subsystems along the network;
- data processing to extract meaningful indexes, to compress the amount of data still retaining the relevant information. Data processing can be on-board or off-board;
- creation of a database to be used for off-line analysis. This is achieved by transmitting the data set (or indexes) from the processing unit to a central server;
- database analytics, to perform data fusion from different sources and data fusion with other sources, especially the outcomes of the inspection trains, required by standards.

The present paper deals with the first step of the entire process of diagnostics. It is focused on the extraction of signatures or patterns of defects in the overhead contact line, to be obtained from the processing of accelerations measured on the collector strips of the pantograph.

In the last years a measurement set-up and processing unit for condition monitoring of pantograph and overhead contact line was developed ([1], [2], [3]), both for high-speed

trains, and conventional rail network. The system is based on the measurement of pantograph collector accelerations through fibre optic sensors. Raw data are processed in real time on-board train to obtain indexes, computed by pantograph control units, related to pantograph damages or to distributed or localised defects of the contact line. The actual position of the train along the line is calculated by an algorithm run in an auxiliary board of the DIS (Driver Information System), relying on map-matching of GPS data and odometry. The data are subsequently transferred to a wayside server, where they can be analysed and compared for trend analysis. Thanks to the data gathered daily from commercial trains, the system should help shifting the pantograph inspections from time-based to condition-based approaches, and it will also allow the early detection of incipient defects in the overhead contact line, allowing a more frequent delivery of information on the status of the overhead line.
Previous works by the authors dealt with the pantograph operating under a standard wire catenary but, since in the last decade the attention of operators and manufactures has also turned to the so called rigid catenary system, the present paper focuses on this type of overhead contact line. Rigid catenary (also named conductor rail) is composed of a series aluminium extruded bars from 10 m to 12 m long, bolted together to form a continuous long beam discretely supported. Although traditionally confined to lower speed range (lower than 120 km/h maximum), application for moderately higher speed (say up to 160 km/h) or proposals for high speed application (in the range 200÷250 km/h) can be found. This is the case of long tunnels, part of a medium to high speed network, where the rigid catenary is gaining interest thanks to its reduced dimensions and lower maintenance requirements. The higher structural strength is another important property, relevant for risk assessment. The drawbacks of the rigid catenary are its singular points that require particular attention, like the connection with the standard catenary wire (if any) and the insulating sections, and the fact that a pantograph in contact with a rigid catenary system is more sensitive to local geometrical defects. Consequently, their impact on the quality of current collection is generally higher compared to the case of a standard wire catenary.
Following a similar approach adopted in previous works ([2], [3], [4]), in this paper numerical simulations of the dynamical interaction between the pantograph and the rigid catenary are performed through the software PCaDA [5], and then used to extract indexes from the simulated collector acceleration, treated as the real measured raw data. The analysis is performed by simulating two local defects with increasing intensity, and by analysing the trend of processed RMS levels from the undamaged reference condition to the fully damaged condition. It is demonstrated that the presence and the intensity of defects can be detected by comparing the data with those of a reference operational condition.

## 2. ARCHITECTURE OF THE DIAGNOSTIC SYSTEM

The proposed pantograph diagnostic system is based on the measurement of collector accelerations. The costs of a system for a diagnostic application must be contained to allow the applicability on commercial trains, so the measuring set-up proposed is simplified by using only two accelerometers for the entire pan-head [2]. The two sensors are placed in a crossed configuration (Fig. **1**), so that when the contact point moves laterally due to contact line stagger, a defect in the contact line impacting on the pan-head is significantly detected by at least one of the two sensors [2].

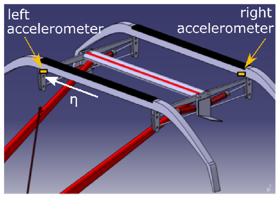


Fig. 1 System layout: positioning of accelerometers on the pan-head

Accelerometers allow to deal with a relatively large frequency range (up to 200 Hz), so that also the deformable modes of vibration of the collector are included in the analysis, and a higher increase in the signal power is achieved when the pantograph impacts a defect in the overhead contact line.

## 3. PANTOGRAPH MODELLING

The pantograph is modelled through lumped masses, representing the equivalent mass of the articulated frame and the masses of the collectors as rigid bodies, and through deformable collectors modelled with a modal superposition approach [5],[6]. Table 1a reports the parameters of the lumped masses model, Table 1b the modal properties of the first three flexural mode of the collector, identified in [6]. The mass of each collector $m_c$ is pertinent to the rigid vertical mode, with amplitude equal to one in the vertical direction. The terms $k_c$ and $c_c$ in Table 1a represent the total stiffness and damping values of a single collector, sum of the two suspension springs located on the left and right side. The generalized forces applied from the left and right springs on each collector are evaluated, for each mode of vibration, through the corresponding shape functions.

(a)

| | | | |
|---|---|---|---|
| Articulated frame | $m_f = 13.2$ [kg] | $k_f = 60$ [N/m] | $c_f = 90$ [Ns/m] |
| Single collector | $m_c = 4.2$ [kg] | $k_c = 1356$ [N/m] | $c_c = 30$ [Ns/m] |

(b)

| | Modal mass* | Non-dimensional damping h |
|---|---|---|
| Mode No.1 (freq. 60.1 Hz) | 0.182 [kg] | 0.0066 |
| Mode No.2 (freq. 76.9 Hz) | 0.135 [kg] | 0.0060 |
| Mode No.3 (freq. 136 Hz) | 0.160 [kg] | 0.0052 |

Table 1: Data for Pantograph model. (a) Rigid model parameters. (b) Deformable modes parameters. ∗Modal mass values are relevant to the mode shape amplitudes normalized as in [6]

Fig. **2** shows the collector mode shapes [6], with a detail, in Fig. **2**b, of the normalized shape functions in the range actually interesting the contact strips (i.e. ±0.4 m from the centre of the collector).

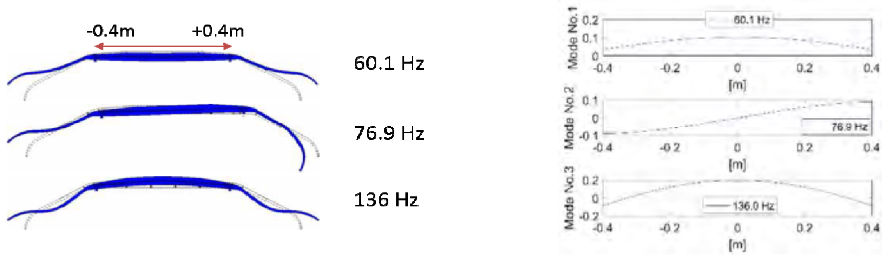


(a) (b)

Fig. 2 Collector mode shapes. (a) Finite element modelling [6].
(b) Normalized mode shape in the contact strip length.

In Fig. **2**a, it is possible to observe that the maximum displacements are localized in the lateral horns. Consequently, the maximum normalized displacement in Fig. **2**b is rather low, and equal to 0.2. The nodes of the mode shapes are out of the contact strip range for mode No. 1, whereas in the case of the antisymmetric mode No. 2 there is a node in the middle of the collector, and for mode shape No.3 there are two nodes at a distance of 0.33 m from the centre of the collector.

The accelerations generated by a contact line defect at the location of the sensors on each collector (i.e. $\eta$ in Fig. **1**) are evaluated through modal superposition, based on the acceleration values of the vertical rigid motion $z_r$, of the modal coordinates $q_i$, and of the corresponding mode shape values $\Phi_i(\eta)$.

$$\ddot{z}(t,\eta) = \ddot{z}_r(t) + \sum_{i=1}^{3} \Phi_i(\eta)\, \ddot{q}_i(t).$$

## 2. RIGID CATENARY AND DEFECT MODELLING

The main singularities of a rigid catenary system [7], which may evolve in defective hot spots, are sections overlaps, expansion joints [8], fixed-points, rigid-flexible transitions, section insulators and bolted joints connecting adjacent conductor rails. In the numerical model adopted [5], Eulero-Bernulli beams are used for suspension arms and for the overhead conductor rails, the latter having stiffness and mass properties of the section composed of the conductor rail and the clipped-in contact wire. Two kinds of singularities are specifically modelled: bolted joint and section insulators (schemes in Fig. **3**). At the locations of bolted joints, the section properties of the beam are modified to consider also the mass and the stiffness properties of the splice. Section insulators are modelled in detail by considering the properties of the insulating fibre glass beam, and by modelling all the lateral auxiliary swords driving the pantograph contact along the insulated section, numbered from 1 to 6 in Fig. **6**b. As in the case of flexible catenaries, overhead line geometrical irregularities are introduced in the rigid catenary model, which allows considering the difference between nominal design and actual installation, and ultimately getting contact force results comparable to experimental measures. The following irregularities are therefore considered in all the simulations, including the model of the healthy line assumed as reference:

- variability of span lengths: ± 0.25 m;
- variability of suspension heights: ± 0.005 m;

- straightness error of conductor rails: ± 1 ‰
- angular misalignment of conductor rails at bolted joints: ± 0.1 deg. (Fig. **3**).

The angular misalignment of adjacent conductor rails in a bolted joint is further studied as a possible defect which may evolve due to bolt loosening. Fig. **3**a shows a scheme of the component considered: the joint plate (dashed square) is 300 *mm* long, bolted to the left and right conductor rails. By admitting a design clearance of 0.5 mm in the coupling between the plate and the conductor rail, a maximum angular misalignment (2φ) equal to 0.38 degrees may occur in the two adjacent bars. Such a defect is introduced in the simulations by firstly considering an angle 2φ equal to 0.19 degrees, which is half the maximum value and almost twice the angular misalignment considered in standard irregularity (i.e. ± 0.1 degreed, as indicated in the last bullet point in the list above). As a second step, the maximum misalignment of 0.38 degrees is simulated to seek for a trend in the RMS level from the undamaged to the fully damaged condition.

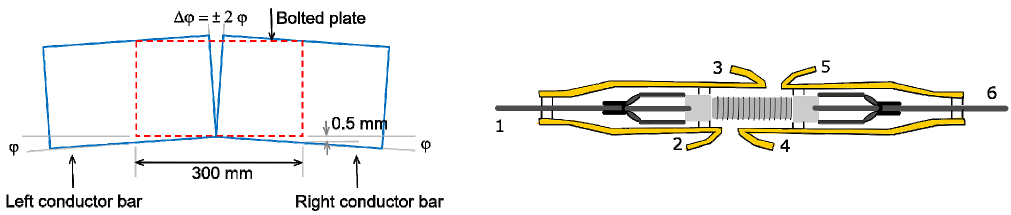


(a) (b)

Fig. 3 a) Scheme of the bolted joints of adjacent conductor rails: angular misalignment. b) sketch of an nsulating section (1 and 6 are conductor bars, from 2 to 5 auxiliary swords)

Fig. **4** reports the static deformed shapes of the rigid contact wire corresponding to the reference case and to the case with a defect at the bolted joint with position x=181.5 m (angular misalignment equal to -0.19 degrees). In Fig. **4**a the static deflection of the entire catenary is visible, with the suspension positions highlighted through red squares (spacing 8 m). The vertical dashed lines identify the section close to the defective joints, which is enlarged in Fig. **4**b. It is possible to observe a variation of the deformed shape, due to the presence of the defective joint.

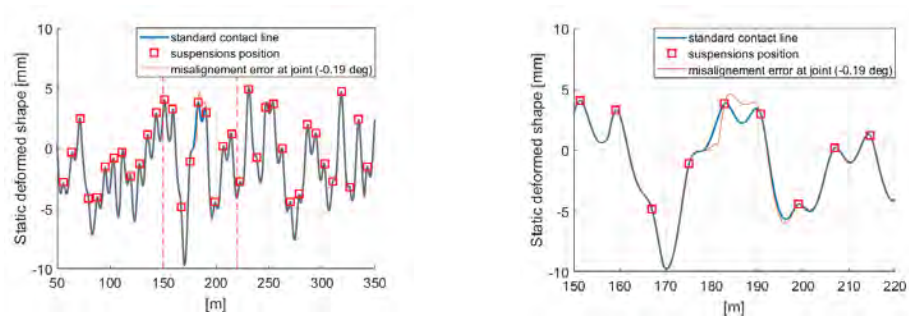


(a) (b)

Fig. 4 Static deformed shapes of the rigid contact wire. Standard and defective cases. (a) Catenary length considered for the analysis. (b) Enlargement close to the defective joint.

The stagger **value of** the contact line at the position of the simulated defect is equal to 24.6 mm, which means that the contact point on the collectors is close to the node of the second mode of vibration represented in Fig. **2**b.
A second defect is simulated in a section insulator, by generating a misalignment between the contact wires that the pantograph encounters when exiting the insulated section. Two anchor points of the swords numbered with 4 and 5 in Fig. **3**b are lowered respectively of 1 mm and 2 mm, generating an additional inclination of each sword equal to 0.06% and 0.15%.

## 3. SIMULATION RESULTS AND DEFECT IDENTIFICATION

Fig. **5** reports the contact force results of the simulations carried out at 160 km/h with the reference and the defective bolted joint, for the two frequency ranges equal to 0-20 Hz (Fig. **5**a) and to 0-150 Hz (Fig. **5**b). At the location of the defect (i.e. x=181.5 m), a perturbation of the contact force is visible in the signal corresponding to the 0-20 Hz range, but the contact force peak does not exceed normal peak values. On the contrary, an outstanding contact force peak is observed in the 0-150 Hz range.

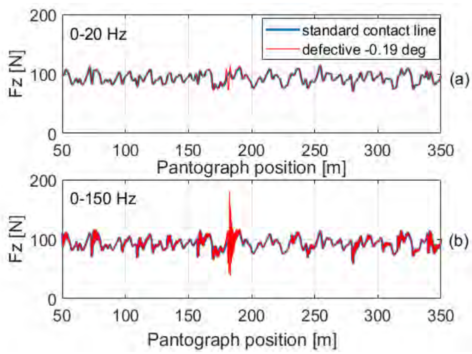


Fig. 5 Contact force numerical results. (a) 0-20 Hz range. (b) 0-150 Hz range

This peak could not be observed in a standard contact force measurement system, due to its limitation to 20 Hz (as required by the EN50317 standard), and this is one of the reasons why researchers are trying to extend the contact force measuring range above 20 Hz. However, with the current techniques, the contact force is not measurable over this frequency, especially on commercial trains, so that the measurement of accelerations [2] or collector strains [8] is being proposed for the purposes of condition monitoring.
Fig. **6** shows the accelerations of the leading collector and the corresponding RMS evaluated over a short time window with width T=0.2 s, and 90% overlap between subsequent windows [2].

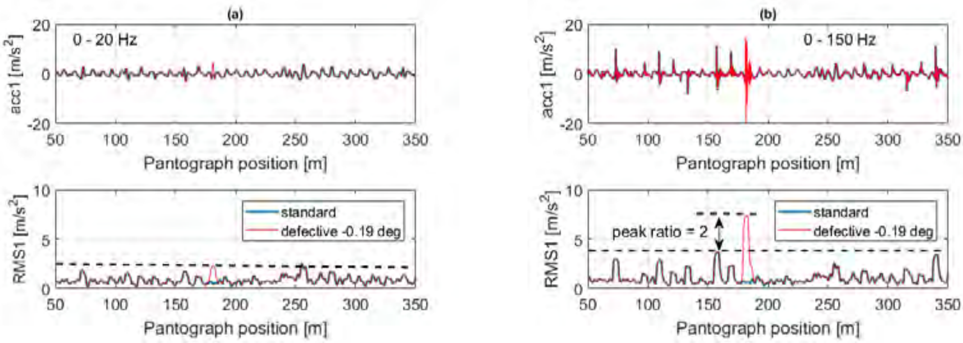


Fig. 6  Acceleration and RMS analysis. Bolted joint. (a) 0-20 Hz. (b) 0-150 Hz

The top figures report the raw signals, the bottom ones the corresponding RMS. The data in Fig. **6**a correspond to the frequency range 0-20 Hz, those in Fig. **6**b to the range 0-150 Hz. The acceleration RMS in the 0-20 Hz range shows a peak at the location of the bolted joint defect, which cannot be easily distinguished from common RMS variability. On the contrary, the RMS of acceleration in the 0-150 Hz extended range can identify the defect, with an RMS peak which is twice the highest peak of the background level. The extension of the measuring range up to 150 Hz, and the inclusion in the analysis of the frequencies related to the collector flexural modes, are therefore essential to strengthen the identification of the defect.

(a) (b)

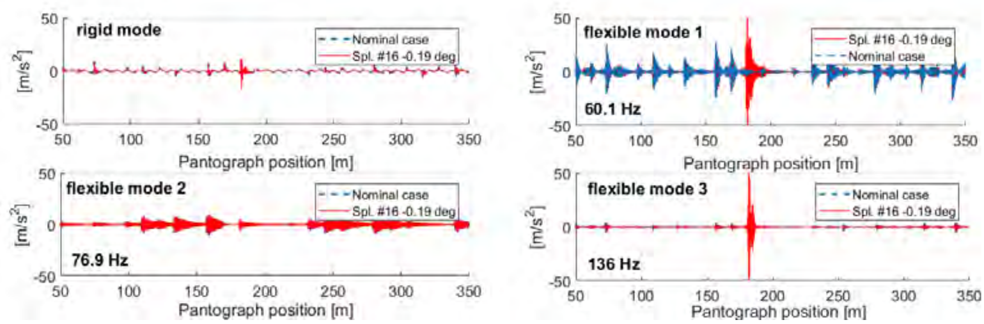


(c) (d)

Fig. 7  Accelerations of leading collector degrees of freedom. (a) Rigid vertical mode. (b) First flexural mode (symmetric). (c) Second flexural mode (antisymmetric). (d) Third flexural mode (symmetric)

When the maximum misalignment of -0.38 degrees is simulated at the bolted joint, the RMS peak further increases to 19 $m/s^2$ in the 0-150 Hz range, showing for this singularity an increasing trend in the RMS peaks from the undamaged condition to the fully damaged condition.

Fig. **7** details the contributions of each mode of vibration of the collector to the acceleration peak in Fig. **6**b.

The accelerations with the highest power content are those corresponding to the first and third flexible modes of vibration (Fig. **7**b and Fig. **7**d respectively). The second mode of vibration (Fig. **7**c) is not much excited in correspondence of the defect, due to the actual stagger value (i.e. 25 mm) making the contact point close to the node of the mode shape.
The results relative to the healthy and defective section insulators are reported in Fig. **8**, with the indication of the RMS peak ratios (damage over healthy). As in the bolted joint case, the 0-150 Hz range shows a higher peak ratio (Fig. **8**b), consequently easing the identification of the defect. A higher RMS level is obtained in the standard case of this singularity, compared to the case of the bolted joint, due to the fact that the pantograph gets in contact with a high number of contact wires when transiting under the section insulator.

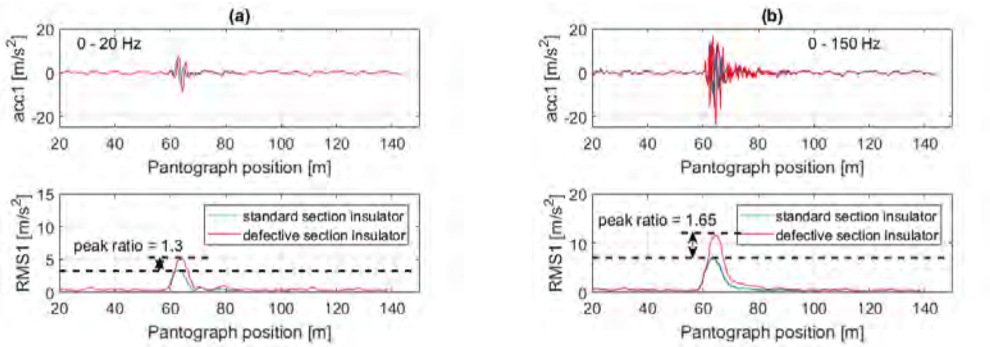


Fig. 8  Acceleration and RMS analysis. Section insulator. (a) 0-20 Hz. (b) 0-150 Hz

Nevertheless, the presence of the defect further increases the RMS peaks, and the defect can be identified by comparison with the reference case. This implies that the data analysis in the wayside server should not be simply done by setting a threshold value for the RMS along the entire line, but carrying out a preliminary mapping of the line to set a reference value for each singularity, which can only be feasible if the data are automatically correlated to their actual position.

## 8. CONCLUDING REMARKS

The paper investigated two kinds of defects in a rigid overhead contact line, by means of numerical simulations, finding a procedure to extract a meaningful index from collectors' accelerations. The simulated defects are a misalignment in the bolted joint connecting two adjacent conductor rails, and a lack of parallelism in the swords of a section insulator. The RMS analysis in the 0-150 Hz allows a more robust identification of the defects, whereas the RMS peaks in the 0-20 Hz range can hardly be distinguished from the background RMS variability. The inclusion in the analysis of the frequencies related to the collector flexural modes is therefore essential to strengthen the identification of the defects.

## 9. REFERENCES


[1] **Carnevale, M. - Collina, A. - Frattolillo, G. - Del Gobbo, G. - Marinis, D. - Menci, M. - Ramieri, A.**: The innovative JRC15 3kVDC pantograph [Il pantografo innovativo JRC15 a 3kVcc] Ingegneria Ferroviaria, 2017.j 72 (11), p. 827-863.

[2] **Carnevale, M. - Collina, A.**: Processing of collector acceleration data for condition-based monitoring of overhead lines. (2016) Proceedings of the Institution of Mechanical Engineers, Part F: Journal of Rail and Rapid Transit, 230 (2), p. 472-485. DOI: 10.1177/0954409714545637.

[3] **Carnevale, M. - Collina, A. - Palmiotto, M.**: Condition monitoring of railway overhead lines: correlation between geometrical parameters and performance parameters. Proceedings of the First World Congress on Condition Monitoring, London 13-16 June 2017.

[4] **Carnevale, M. - Collina, A.**: Pantograph and catenary condition-based monitoring through pan-head acceleration. Proceedings of 13th MINI Conference on Vehicle System Dynamics, Identification and Anomalies, VSDIA 2012 (Ed. by Prof. I. Zobory), BME Department of Railway Vehicles and Vehicle System Analysis, Budapest, 2013, p.229-236.

[5] **Collina, A. - Bruni, S. - Facchinetti, A. - Zuin, A.** PCaDA statement of methods (2015) Vehicle System Dynamics, 53 (3), pp. 347-356. DOI: 10.1080/ 00423114. 2014.959027

[6] **Collina, A. - Lo Conte, A. - Carnevale, M.**: Effect of collector deformable modes in pantograph-catenary dynamic interaction (2009). Proceedings of the Institution of Mechanical Engineers, Part F: Journal of Rail and Rapid Transit, 223 (1), pp. 1-14. DOI: 10.1243/09544097JRRT212

[7] **Vera, C. - Suarez, B. - Paulin, J. - Rodríguez, P.:** Simulation model for the study of overhead rail current collector systems dynamics, focused on the design of a new conductor rail (2006). Vehicle System Dynamics, 44:8, 595-614, DOI: 10.1080/ 00423110500165499

[8] **Tan, M. - Zhou, N. - Wang, J. - Zou, D. - Zhang, W. - Mei, G.**: A real-time impact detection and diagnosis system of catenary using measured strains by fibre Bragg grating sensors (2018) Vehicle System Dynamics. Article in Press. DOI: 10.1080/00423114.2018.1556396

# INVESTIGATION INTO THE STRUCTURE OF THE RAILWAY TRACK/VEHICLE CONNECTION

**Dezső SZŐKE and István ZOBORY**

Budapest University of Technology and Economics,
Faculty of Transportation Engineering and Vehicle Engineering
H-1111 Budapest, Műegyetem Rkp. 3, Hungary

*Received: November 7, 2018*

## ABSTRACT

In certain cases the railway track having almost failure-free track geometry can however be non-proper for carrying normal railway traffic. The stiffness and the damping (the dynamical stiffness) of the stone bed – which is apparently constant – can change significantly along the track (due to stone-bed loosening, eventual hardening, etc.), thus the qualification of the elastic rail/stone bed system should take into consideration the different axle load levels up to the maximum permitted axle-load, as well as the different speed limits up to the maximum permitted speed. This qualification, this track failure recognition can be supported by an appropriate track measuring vehicle which makes it possible to evaluate the dynamical stiffness variations along the track from the time dependent vertical motion signals measured on the vehicle by using parameter identification procedure [1]. This paper deals with the structure examination of the vehicle (the vehicle with the measuring wheel-set) and the track system based on static and dynamical models. The paper looks for those necessary and sufficient model structures with the help of which the dynamical stiffness of the railway track can efficiently and reliably be approximated and estimated.

*Keywords*: railway track modelling, rail models, elastic beam, discretisation, lumped parameter model, modal structure, vibration modes

## 1. INTRODUCTION

The invisible *vertical stiffness and damping* of the stone-bed of the permanent way can significantly vary along the track-length (stone-bed loosening, stiffening, etc.), thus the track subsystem consisting of elastic rails, sleepers and stone-bed can only be successfully qualified when the track is loaded by a constant vertical force through an appropriate measuring wheel-set.. This qualification, this track-stiffness and damping state identification is supported by the appropriate track measuring vehicle, which makes it possible to measure the vertical accelerations of the bogie-frame close to the axle-boxes of a measuring wheel-set, and from these time varying measured vertical accelerations conclusions can be drawn concerning the track-length dependent variations in the dynamical parameters of the railway track. This study deals with the *structure analysis and parameter-sensitivity examination* of the elements of the system measuring vehicle/track . Our method seeks for those necessary, but at the same time sufficient model structures, by the help of which, the dynamical stiffness of the railway track can efficiently and reliably be approximated and estimated.

## 2. THE SUB-SYSTEMS OF THE „VEHICLE/RAILWAY TRACK" SYSTEM

### 2.1 Sub-systems of the railway track/vehicle system

The vertical contact force means the connection between the railway vehicle and the track. Along the action line of this vertical connection force the vehicle/track system can be divided into sub-systems: the time dependent (inner) vertical force which depends also on the vehicle motion state exerts time-parallel excitation effect on the track and through the wheel-set also the vehicle receives excitation, thus the sub-systems possess dynamic features. The vertical connection force is basically the static wheel-set force, to which time dependent dynamic force is added which depends also

on the motion (vibration) state of the vehicle, the travelling speed and the track irregularities (unevennesses).
In case of investigations into the structure of the railway track/vehicle connection it seems to be reasonable – especially in case of track of good quality and in case of low motion speeds – to examine the connection of the massless but elastic so called static (S) sub-systems and in the reality dynamic (D) mass possessing sub-systems. From among the 4 connection-pairs (see Fig. 1), here now the connection of the statically loaded measuring wheel-set (represented by a constant force) and the different track structures is analysed (sub-systems S-S and S-D).

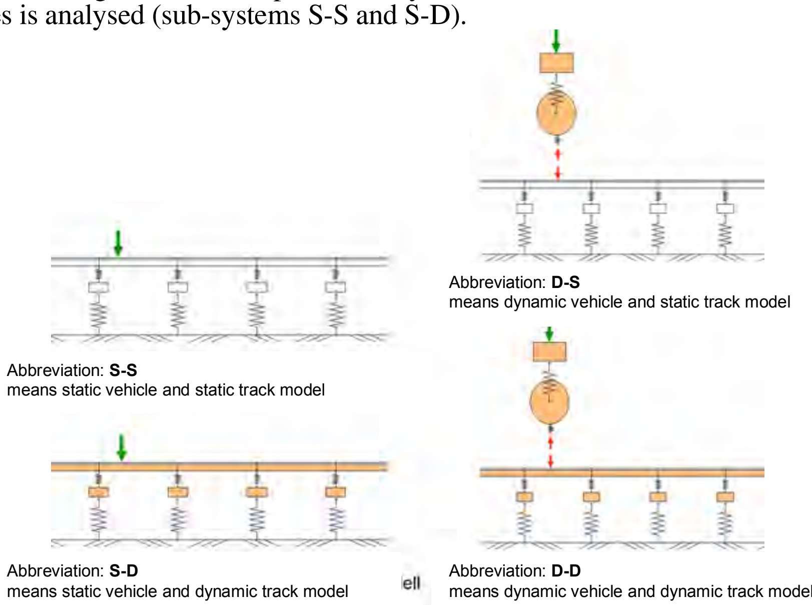


Fig. 1 Possible connection structures of the sub-systems vehicle and tracks

## 2.2 Mechanical model of the track

The elastic stone-bed practically continuously supports the rail-beam which can be considered to be infinite long, thus the track can be described by a homogeneous *Winkler*-supported beam (continuum model). The track irregularities come basically from the variation in supporting stiffness of the stone-bed, which is complemented with the variation in damping, eventually also in mass distribution of the stone-bed. In case of irregularity-less track the effect of the moving static load causes a constant deformed shape, which is traversing the track at a constant speed, the moving deformed shape is independent of the mass characteristics of the track.
In the reality, however, the sleepers represent considerable mass concentration (in an equidistant tact). On the other hand, the rail-beam considered to be homogeneous is supported only sleeper by sleeper, therefore only local supports carry the rail (in case of standard railway tracks) and a similar local tforce-transfer character appears concerning down to the stone bed. The mentioned deficiencies can be eliminated by using discretized track model, see Fig. 2. It is to be noted, that in case of irregularity-less track as an effect of the moving static load in the spatial coordinate slowly changing deformed railshape-wave can move along the static track. All the same, taking into account the masses of the track (dynamic model) one can expect evolution of position, time and vehicle-speed dependent vibrations, being in coherence with the steady state.

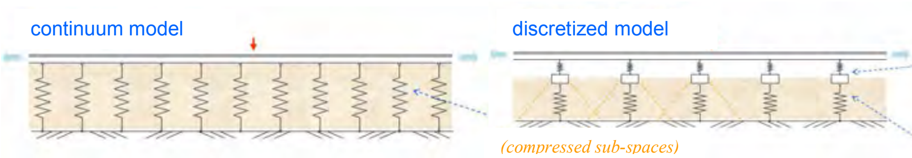


Fig. 2 Models of the railway track

In the discretized model of the track the infinite long continuum beam representing the rail loads the sleepers elastically (Fig. 3), and the latter load the elastic track-bed (characterised by an appropriate sequence of replacing springs). The stiffness characteristics of a specified rail section is described by the stiffness matrix of the 4-degree of freedom finite element of the elastic beam, in accordance with the rail material, rail cross-section and element-length. The mass characteristics of the rail-section are mass points attached to the end points of the beam element (lumped masses), thus the dynamical behaviour of a rail-beam element is described by the vertical displacements of their ends. The angular displacement co-ordinates can easily be computed from the two displacement time function mentioned. The sleepers are modelled by discrete mass points.

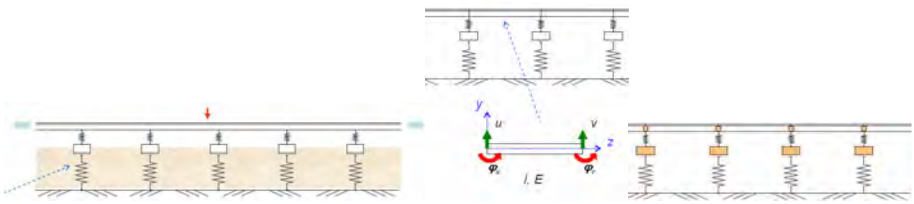

Fig. 3 The discretized model of the railway track

Between the rail and the sleeper there is a pre-stressed rubber pad. There was a shortage in information about the real stiffness, so this latter stiffness was included in the stiffness of that spring element that describes the stiffness of the stone bed. This procedure means that the displacement of the rail over the sleeper has been taken to be equal to the displacement of the sleeper (merging of displacements, Fig. 4). This merging is error-free in the case of the formerly introduced relation S-S for the track-vehicle connection. Nevertheless, for track models having mass characteristics, the latter merged model carries change also in structural sense in the investigation into the sub-system pair S-D. The merged model in Fig. 4 has the advantage, that it is not necessary to solve further additional differential equations for determ-ining the motion of the sleepers. (The applicability of the mentioned structure change in case of track modelling should be checked in the following.)

The railway track – the permanent way – is practically infinite long. Due to experiences the rail-beam and the whole track takes the wheel-load only on a finite track length. For the dynamical investigation into the question it is necessary and at the same time also sufficient to selectio a finite track length. The so called "*stiffness length*" belonging to the nominal static load of the track is a (measurable) track characteristics [2].

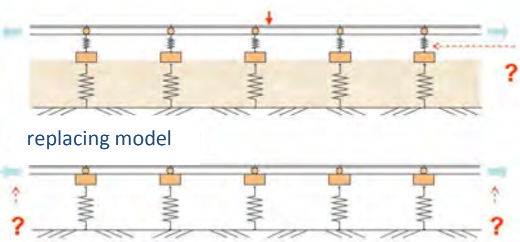


Fig. 4 Simplified (replacing) model of the railway track

The track constructor and track maintenance people in part carry out the control and quali-fication of the vertical stiffness properties of the track by using the concept of "*stiffness length*", [2]. The latter per definition is the distance measured from the action line of the vertical load, up to those points on the rail where the vertical deformation function of the rail first changes its sign.

If the double value of this "stiffness length" is considered to be the minimal track-length, then the vertical deflection at the end of the section is about 1% of the maximum vertical deformation at the action line of the loading force (Fig. 5). It is a natural question if the latter percentage value remains valid also in case of time dependent wheel-load and varying track-bed characteristics, resp. the question arises, how the effect of the neglected (principally of infinite length) track parts can be described, or eventually the latter effect is negligible. (The exact survey of the last topic requires further research activities.)

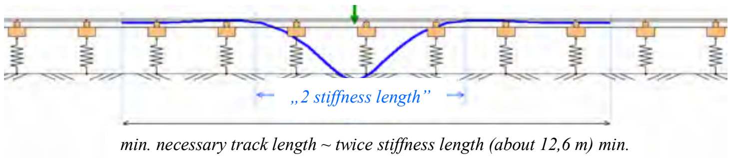


Fig. 5 Assigning of the track section of finite length

## 2.3 Modelling of the excitation

The static vertical connection force moves between two sleepers, in such a way that the force effect can be modelled as to two *dinams* acting on both ends of the beam element (S-S). In the case of the dynamical track model (S-D) the close neighbourhood of the force application point is refined and the rail-beam elements are of varying lengths (10, 20, 30 further on 60 cm span). In such a way the dynamics of the track model can be described by reasonable number (35) of displacement functions, when a 12.6 m long track section is examined (Fig. 6).

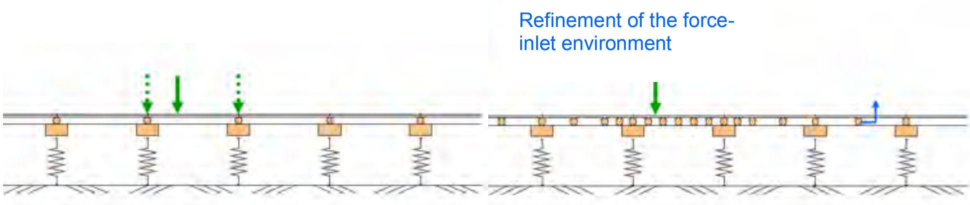


Fig. 6 Refined model in the close neighbourhood of the force application point with modelling also the excitation

## 2.4 Connection of the sub-systems (S-S)

On the one hand, this examination gives basic information about the static properties of the jointed system, and about the stiffness properties and numerical behaviour of the track sub-system through solving the static equation, on the other. In Fig. 7 the deformation surface of the rail can be seen over the 12.6 m track-length, whereas the force moves over the length span [6, 6.6] (2 degree of freedom elements of varying length, the load appears in the form of distributed forces). Virtually, a curve section resulted by the bending deformation proceeds along the track with a deepest point depending on the position of the loading force.

However, if the settlement of the wheel-tread – as the force application locus – is examined between two sleepers, i.e. the moving *effect-plot* is determined, the additional elastic deformation of the rail over the support-span can be well observed, the value of which can be characterized by about 3‰ degree of irregularity (see Fig. 7). By the latter our former conjecture has been proved, furthermore we can conclude with higher safety concerning the case of the vehicle-track connection of type S-D, in the case of moving static wheel load (S) the track of non-zero mass (D), the rail of the track undergoes to vibrations depending on the speed of the vehicle (moving, position-dependent, steady state).

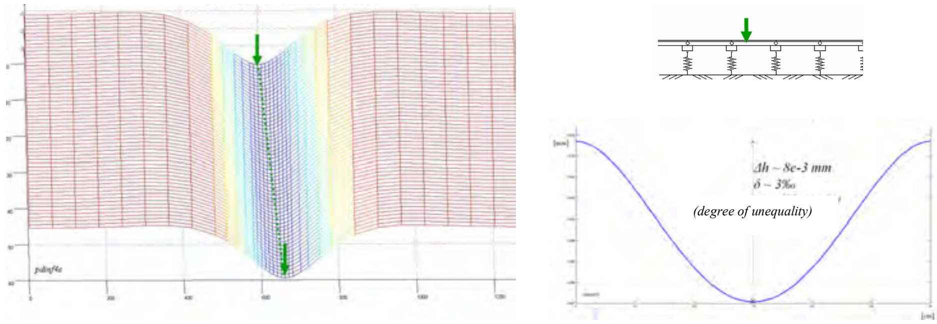


Fig. 7 Static deformation surface of the rail and the moving *effect-plot* of the force application between two sleepers

## 3. DYNAMICAL ANALYSIS OF THE RAILWAY TRACK LOADED BY STATIC FORCE

The track model containing mass-characteristics should be loaded by constant moving forces in accordance with the controlled static load caused by the measuring vehicle, i.e. the connection of S-D type sub-systems is analysed based on the solution of the differential equation. A direct numerical solution however does not lead to result (un-stable solution), because the system consists of elements of highly different stiffnesses. (The numerical inaccuracy has been observed already in case of the static equations.) Components with frequency content emerge practically only as static components in the response function. (Due to the static equilibrium the mentioned components are not negligible.) The question is, which components should be described by dynamical equation. From among the dominant modal parameters of the track practically it is enough to examine only the symmetric components (see Fig. 8). Namely the anti-metric components play less role in the response function of the system, because they are less (or almost not) excited (the node-point of the vibration plot is in the close neighbourhood of the excitation input). The eigenfrequency of the vibration component of lowest frequency is over 40 Hz, whilst the dynamics of the vibration components over 150 Hz are neglected. (The latter approximation is valid for the anti-metric components, as well.)

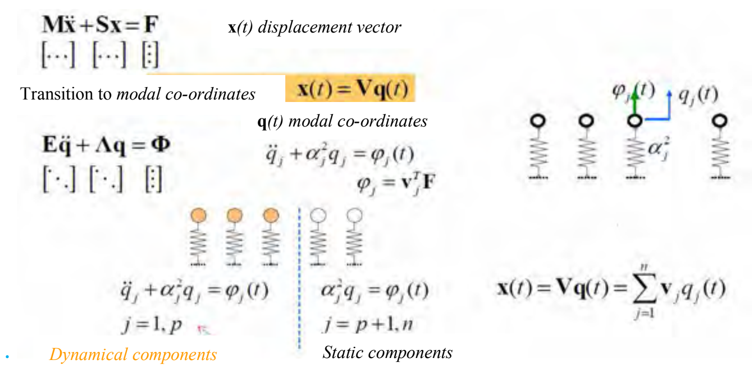


Fig. 8 Dominant, symmetric modal components of the track shape

These thoughts can emerge when investigating the specific influence of the dynamical components. We may assume that practically under the static load deformed wave is moving under the vehicle's wheel-set in accordance with the speed of the vehicle, thus the basic frequency of the parametric excitation is $f_{0,carrying} = v/L$ [(m/s)/m=1/s=Hz]. Taking into account the real parameters valid for the case of the track measuring vehicle BME PM 001 (v=100 km/h, stiffness-length L~6 m), the excitation function, namely the basic frequency of the appearance of the track unevennesses $f_{0v,Max}$ is under about 4.5~5 Hz (Fig. 9). However this means, that the frequency of excitation at all modal components to be taken into consideration in the track model, is under the 1/10 part of the eigen-frequency.

In the case of vibration components of higher frequency this ratio is even less. Thus, in those displacement components which belong to the latter components the dynamical influence is practically (and even increasingly) negligible, and is appearing only as static signal component in the displacement of the track sub-system. Based on the aforesaid, the response components in question can approximately be computed by using the static equations and overall so, the time dependent response of the track can be determined by means of a numerically stable DAE solution.

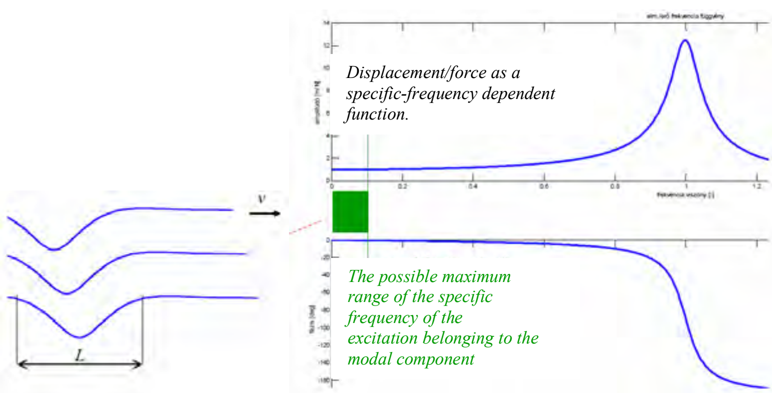


Fig. 9 Displacement response of the modal component due to the propagation of the track-wave

The numerical procedure has been tested by an artificial moving load process: the wheel is moving to and fro between two adjacent sleepers at a constant speed v=10 m/s (shuttling).

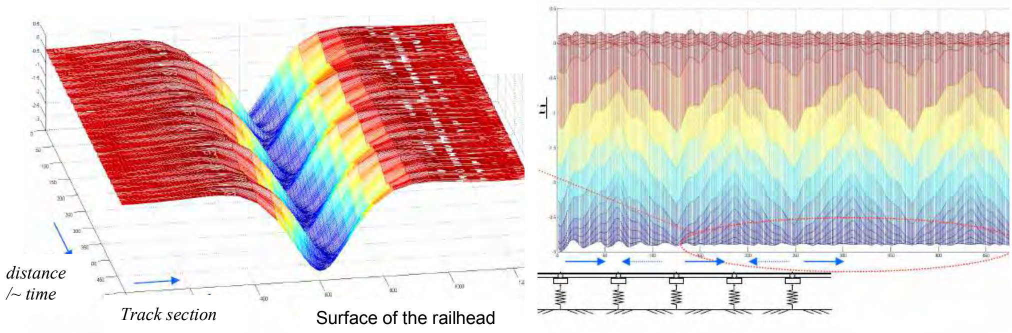


Fig. 10 Morphosis of the track surface at the shuttle motion between the sleeper-pair (v=10 m/s)

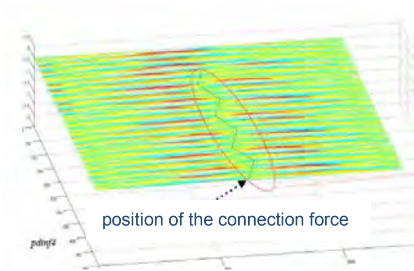


Fig. 11 **Morphosis of** the relative track surface in the case of shuttle motion (to and fro motion) between the adjacent sleepr-pair (v= 10 m/s)

The load moves within a finite track length, so the applicability of the simulation-purpose model can be tested (structure and parameters, numerical method), since the motion characteristic at a time point $t + dt$ can uniquely be computed knowing the value of the motion characteristic at time $t$, (see Fig. 10). In the course of the shuttle motion practically after twice covering (at v=10 m/s) the distance between the adjacent sleepers evolves the motion belonging to the steady state motion, which is depending on position, time and travelling speed. The time dependent track surface proves in a graphical way, that the system response is stable, thus the elaborated track model is proper for further applications (at other track length, speed, numerical integration step-length, as well).

The response functions belonging to the above shuttle motion were determined for the track model containing only stiffnesses (massless model), using exclusively the static equations. (Comparative examination of the S-S and S-D track-vehicle structures). The deviations of the two track surfaces evolved under the same loading process is visualized in Fig. 11. The scale is identical to that of applied in Fig. 10. It can be ascertained that in steady state the rail motions are practically independent of the model structure, especially in the close neighbourhood of the moving wheel-tread.

## 4. APPLICABILITY OF THE FINTE TACK SECTION MODEL IN CASE OF TRANSLATORY MOTION OF THE VEHICLE

By having built up such a condensed model, which can describe the track-vehicle connection in a stable way, it has already become possible to examine such a track section of finite length over which the measuring wheel-set moves between two sleepers, only. Nevertheless, in case of real vehicle motion, this finite track length describing model structure touches (and then leaves) a newer track section (between two newer sleepers) of unknown properties in the simulation procedure (section-wise shifting). In this case the influence of the track parts being out of the domain moving in accordance with the vehicle motion there emerges as an unknown boundary condition in the system model to be actually examined.

The problem arises due to the fact that the rail motions are unknown prior to the considered finite track section (the window), thus also both the displacement and the velocity of the entering new sleeper are unknown. For giving estimation, approximate description concerning the unknown motion charac-

teristics, in principle there would be a demand for introducing such an additional member, which describes the influence of the track section of infinite length being out of the window. If it would be possible to compose such a structure, even its parameters, the in the future to be recognized and measured system (track-bed) parameters would be sure unknown. Maximum the averaged parameter values, belonging to the homogeneous track could be taken into account in the above mentioned way.
It seems to be a more realistic solution, if the conditions accepted for the static case are extended: the motion (deformation and velocity) of the track section (entering edge) beeing out of the window can with good approximation be negligible. More exactly, only for the motion of the entering sleeper point is supposed the standstill (both the displacement and the velocity are zero). But by such a method also a parametric excitation is generated in the course of simulation. The influence of this mentioned excitation should be treated (see Fig. 12).
One can characterize the shift-backed track surface (Fig. 13) generated by the wheel (wheel-load) moving at 20 m/s constant speed along a homogeneous track: after covering a distance of 3 sleeper-distance evolves the motion belonging to the steady state, witch motion is position, time and travelling speed dependent. This structural result was expectable on the basis of our conjecture formulated with the treatment of the properties of sub-systems of type S-S. (With the visualization the deformed track surface segments are 60 cm-wise “pushed back”.)
The elaborated simulation-based track model can be applied also for the examination of the connection of type S-D sub-systems (track length, local shift, speed, numerical integration). Using sectional *windowing*, when the unknown motion state of the entering new sleeper point is replaced by the *still-stand state* of the former, an (unknown) parametric excitation is generated with the simulation (which excitation does not exist in the reality).

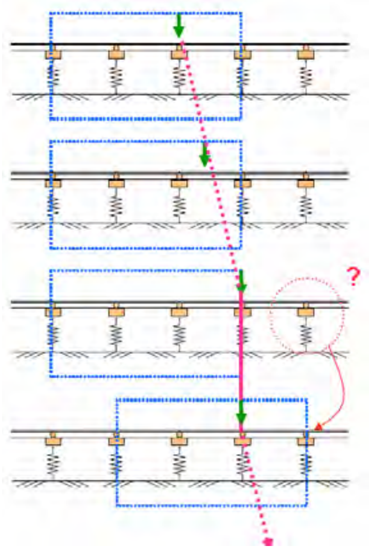

Fig. 12 Process of the section-wise varying model structure changing

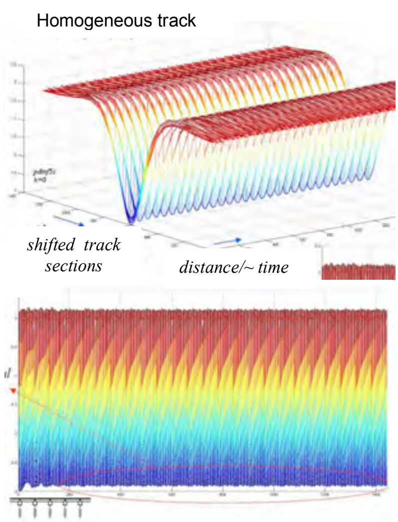


Fig. 13 Morphosis of the push-generated track surface (travelling speed: v=20 m/s)

The influence of this latter excitation does practically not appear in the dynamical behaviour of the system. As a matter of fact, only those system properties and responses remain in force which are in accordance with the steady state, we would like to examine.

The applicability and goodness of the numerical analysis is proved, if its results are compared with the results concerning the structure S-S. (Comparative examination of the vehicle-track structures S-S and S-D.) The deviation between the two shift-backed track surfaces with respect to the static surface is visualized in Fig. 14. It can be stated that in steady state the rail motions are practically independent of the track model structure, especially in the close neighbourhood of the wheel-tread, up to v=20 m/s travelling speed. To tell the truths, the applicability of the simulation method elaborated for the dynamical analysis of the track can be read out from the comparative diagram of the wheel-tread motions (motions at the excitation point, in Fig. 15 for v=20 m/s, and for structures S-S and S-D). After having evolved the steady state, a periodic motion appears under the wheel moving between two adjacent sleepers, as a function of position and time, which motion carries the modal vibration components, characteristic for the track. The time and position dependent deflections between the sleepers are larger in the system possessing mass (S-D), as in the massless track model (S-S) containing spring-elements, only. In case of a static model the deflection at the wheel-tread is only position dependent.

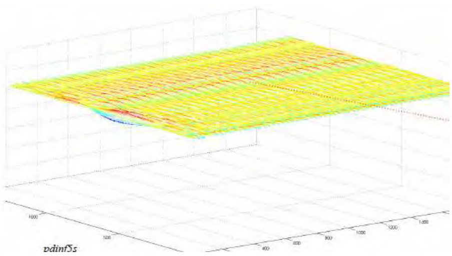


Fig. 14 Morphosis of the shift-backed relative track surface (wheel travelling speed: v=20 m/s)

With increasing travelling speeds the deviation caused by the different structures changes in a characteristic way, its measure increases (see Figs 16, 17, 18). The measure of the mentioned deviation is significant (3…4 times greater) in comparison with the unevenness of the static model, but considering the absolute deformations, deflections, these values are still almost negligible. Thus the measuring wheel-set is dwelling practically at a constant vertical position independent from its horizontal motion. (In our example, this vertical position is about -2.88 mm. The figure represent the functions in a range of [-3, 0] in mm, but the sub-range [-3,-2.5] in mm has also been blown up.)

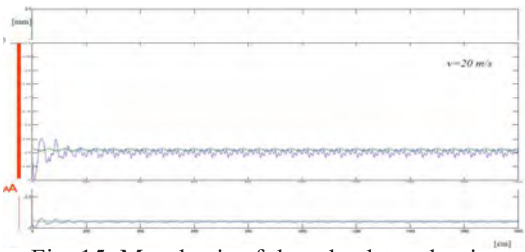


Fig. 15 Morphosis of the wheel-tread point displacements on homogeneous track, in case of sub-system structures S-S and S-D

## 5. EXAMINATIONS WITH TEST TRACK

The applicability of the connection model elaborated for homogeneous track and the reliability of the numerical procedure will be visualized for the case of track irregularities (variation in stone-bed stiffness) caused by disturbances realized by typical test signals. The layout of the test track is as follows: a straight track of length of 18 m is taken, the track stiffness under the sleepers are nominally homogeneous, but for the sake of generating parametric disturbance, 50% decrease in stone-bed stiffness is allowed over a section of length of 1.8 m (as designated in the figure, a length among 4 sleepers). The measuring wheel-set of constant static load runs along the test-track at a constant travelling speed. For different travelling speeds and for different connection structures (S-S and S-D) the absolute and relative beam displacements at the wheel-tread are shown in Figs. 16, 17 and 18. On the basis of the results received for the examined speed range the following statements can be presented:

- on a homogeneous track section the steady state is achieved after about 0.1 s duration, independent of the travelling speed (the solver algorithm starts from the static position as initial condition);
- in case of travelling on a homogeneous track the unequal vertical motion (vibration) among the sleepers is moderately increasing with the dynamical track model and in the majority the latter results in greater deflections compared with the values computed by the static model;
- but the measure of the mentioned differences can almost be neglected, thus with the longitudinal travelling motion of the measuring wheel-set the track unevenness function (signal form) practically identical with the static deformation of the track passes along (traverses) the railway track;

· on the track section loaded by local stiffness deviation (decrease in stiffness) the deflection of the wheel tread point significantly increases (from 2.8 mm to about 4.5 mm), practically independent from the track model structure (structures S-S and S-D);
· when passing along the sections loaded by stiffness deviation the difference between the results received for the two structures (the results for structures S-S and S-D) one can observe the uneven motion form between the sleepers, which deviates only in a little measure from the signal form experienced on the homogeneous (irregularity-free) track sections;
· on the track sections loaded by local stiffness deviation the track deflection under the wheel-tread significantly increases (from 2.8 mm to about 4..5 mm) practically independent from the track, which all the same deviates only in a little measure from the signal form experienced on the homogeneous (irregularity-free ) signal forms structure versions S-S and S-D;
· also when passing through the sections loaded by stiffness irregularity on the deviation functions (characterising the difference between structures S-S and S-D) one can observe the uneven motion between the sleepers, which deviates only in a little measure from the signal form experienced on the homogeneous (irregularity-free) track section;
· thus, independent from the value of the stone-bed stiffness (irregularity loaded vs. irregularity-free track) practically the same behaviour can be observed, independent from structure of the track model;
· in this way the measuring wheel-set returning to the irregularity free track section obviously the same wheel-tread motion forms, what it did before the disturbing irregularity;

All these means that the static track model describes practically the same track surface in the examined speed range and stone-bed stiffness range than the one generated by the dynamic model. Thus, by solving the static equations one can already get estimation, prediction about the state of the railway track.

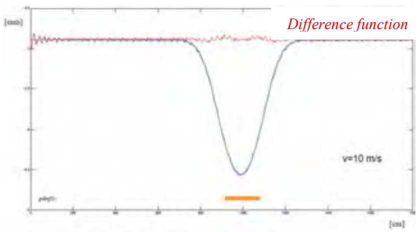


Figs 16-18 Motion of the wheel-tread point along the test-track in case of S-S and S-D sub-system structures (absolute displacements and deviation function, v=10 m/s)

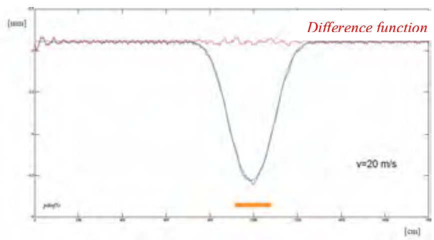


Fig. 17 Absolute displacements and deviation function along the test track, v=20 m/s

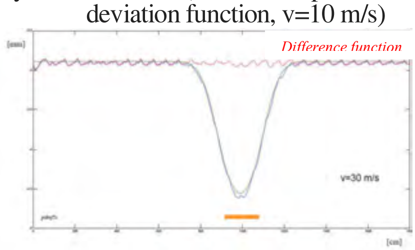


Fig. 17 Absolute displacements and deviation function along the test track, v=30 m/s

## 6. CONCLUSIONS

In this paper the discretized model of the railway track has been elaborated, which can be proper for the examination of the non-homogeneous track with changing parame-ters. It has been pointed out, that the static track model generates practically the same track surface (by solving static equations) over the whole examined speed range, as the dynamical model

## 6. REFERENCES

[1] **Zábori, Z. – Zobory, I.:** Track Qualification Method Using System Dynamics Based Parameter Identification Procedure. Proceedings of the 16th MINI Confe-rence on Vehicle system Dynamics, Identification and Anomalies (Ed. by Prof. I. Zobory). BME ITS nonprofit Co. Budapest, 2020. p.173-186. (In this Volume)

[2] **Megyeri, J.:** Vasútépítéstan. Közdok. Budapest, 1991.(In Hungarian)

## SESSION FOR DYNAMICS, IDENTIFICATION AND ANOMALIES OF ROAD VEHICLES

**COSTA, L. – PERRIN, CH. – DUBOIS-LOUNIS, M. – SERRE, T. – M'SIRDI, N.K.** (France)
Modelling of the Two-Wheeler Dynamic Behaviour for Emergency Situations Analyses ........ 231

**KOKREHEL, Cs. – NÉMETH, H.** (Hungary)
Wheel-brake Design for Heavy Duty Electric Vehicles ........ 239

**SZŰCS, G. – BÁRI, G.** (Hungary)
Tire Data Analysis Method for Finding Grip-Optimal Slip and Camber Values ........ 247

**WIDNER, A. – BÁRI, G.** (Hungary)
Investigating the Effects of Roll Centre Height, during Transient Vehicle Manoeuvres ........ 255

**ERŐSDI, Z. – BÁRI, G.** (Hungary)
Yaw Rate Control for Enhancing Vehicle Steering Behaviour ........ 261

**BÁRDOS, Á. - NÉMETH, H.** (Hungary)
Diesel Engine Cylinder-Charge Composition Control with HpEGr and Exhaust Throttling ........ 269

**NAKANO, K. – SEKI, M. – KAIZUKA, T. – ZHENG, R. – SAKURA, T. – MAKI, T.** (Japan)
Design of Haptic Steering Guidance Controller Considering Look-ahead Distance ........ 277

**LENGYEL, H. – SZALAY, ZS.** (Hungary)
Potential Weak Points of Environment Sensors in Autonomous Vehicles ........ 285

**SIMON, T. S. – MELEGH, G – SZALAY, ZS.** (Hungary)
Automated Vehicles' Accidents – Uber Self-Driving Vehicle Accident ........ 293

**NYERGES, Á. – TIHANYI, V.** (Hungary)
Environment Sensing and Parking Place Detection for Automated Vehicles ........ 303

**ARADI, SZ. – TARI, B. – BÉCSI, T. – GÁSPÁR, P.** (Hungary)
Reinforcement Learning Based Racing Car Control ........ 313

**KONCZ, A.** (Hungary)
Failure Mode and Effect Analysis Types in the Automotive Industry ........ 321

# MODELLING OF THE POWERED TWO-WHEELER DYNAMIC BEHAVIOUR FOR EMERGENCY SITUATIONS ANALYSIS

**Laura COSTA[a&b], Christophe PERRIN[a], Maxime DUBOIS-LOUNIS[a], Thierry SERRE[a] and Nacer K. M'SIRDI[b]**

[a] IFSTTAR LMA
304, chemin de la Croix Blanche F-13300 Salon de Provence, France
[b] Aix-Marseille University LSIS UMR CNRS 7296
Avenue Escadrille Normandie Niemen F-13000 Marseille,France

*Received: November 5, 2018*

## ABSTRACT

This paper deals with a numerical modelling of the Powered Two-Wheelers (PTW) dynamic in order to simulate its behaviour during emergency situations. Firstly, a multibody model of a Honda VFR has been developed. It consists of six bodies and eleven degrees of freedom and takes into account the specificities to simulate hard braking, avoidance and slalom manoeuvres. In parallel, a motorcycle was instrumented to conduct a series of emergency manoeuvres in order to validate the model. The experimental tests have been compared to the simulated model and results give good correlations showing that the model is well adapted to simulate emergency situations.

*Keywords:* Power Two Wheeler, motorcycle dynamics, experimental tests, numerical modelling, multibody simulation

## 1. INTRODUCTION

In France, users of PTW are less than 2% of traffic but, in the accidents, represent 43% of serious injuries and 23% of killed [1]. One of the different issues can be explained by a problem of the manoeuvrability dynamic capacity of this kind of vehicle for emergency situation. In the field of kinematic accident reconstruction, more or less complex PTW dynamic behaviour models are used to define levels of speed or acceleration achieved by these vehicles. They allow in particular to reconstruct the accident in its different phases of approach, emergency, impact and post-collision. Understanding the dynamic behaviour of these vehicles is difficult during the pre-crash phase because the dynamics of PTW is more complicated than cars and less studied so far [2].

Several PTW dynamic behaviour models have been developed. In 2001 Sharp and Limebeer [3] developed a model with 8 bodies and 13 degrees of freedom dedicated to study the stability and control analysis. The automated model building platform used is AutoSim. This code was used to generate a variety of linear and nonlinear models in symbolic form. In 2004 Sharp, Evangelou and Limebeer [4] improved the previous model. The modifications concerned tyre/road contact geometry, tire properties, monoshock rear suspension mechanism, steering control, parameter values describing a contemporary high performance machine and rider . The new model is used for steady turning, stability, design parameter sensitivity and response to road forcing calculations. Cossalter and Lot [5] developed also an eleven degrees of freedom, non-linear, multi-body dynamic model of a motorcycle with 6 bodies. The originality of the model is that it is implemented with a tire model which takes into account the geometric shape of tires and the elastic deformation of tire carcasses. In 2012, Nasser and M'Sirdi [6] developed a model with 5 bodies and 11 degrees of freedom. The main

objective is to identify the dynamic parameters and evaluate the couplings between the different sub model blocs of the whole studied system.
These models have varying degrees of complexity in terms of mechanical representation of the physical phenomena and validity. These models are mainly developed to study the dynamic and the stability of the vehicle. In addition, these models are not dedicated for the purpose of emergency manoeuvre.
The objective of this work is to make a numerical model able to represent the dynamic behaviour of a PTW during emergency manoeuvre. In contrary to other multi body models developed to study the stability in steady-state turning for example, this model has to be able to simulate slalom or avoidance manoeuvre and braking.

## 2. MATERIALS AND METHODS

### 2.1 Modelling of the motorcycle

The modelling is based on the multibody mechanical theory [7]. The model developed here is composed of 6 bodies and 11 degrees of freedom (DoF) as shown on Fig. 1. Characterization of suspensions as well as pneumatics force and torque are included respectively in the connections of body concerned. The model has two inputs: the torque applied by the driver on the handlebars and the braking/traction forces. The driver's body is anchored to the frame. Simulation is driven with the scientific software Matlab Simulink/SimMechanics.
Since this software supports only the forces and torque as input, it was necessary to transform the expected (or requested or desired) speed in a positive or negative force applied on the front and rear wheel. A control force proportional to the difference between the setpoint target speed and the speed of the main frame is applied using the equation:

$$F = k.\Delta_V \tag{1}$$

With $F$ the traction force applied on the motorcycle, $k$ a constant gain and $\Delta_V$ the difference between the desired and actual speed.
If the speed of the motorcycle is less important than the desired speed, the force applied is positive otherwise negative.

Concerning the tires, the model of Pacejka adapted for motorcycle which accepted large camber angle is used [8]. The university of Delft proposed a module for Matlab Simulink/SimMechanics which was implemented in the global model [9].

The position of the center of gravity, the mass and the inertias of each body comes from the results of an extensive literature review and measurement on the motorcycle [10],[4],[11].

The proposed model takes into account technical and geometrical specificities of the vehicle. These values have been measured on the Honda VFR.

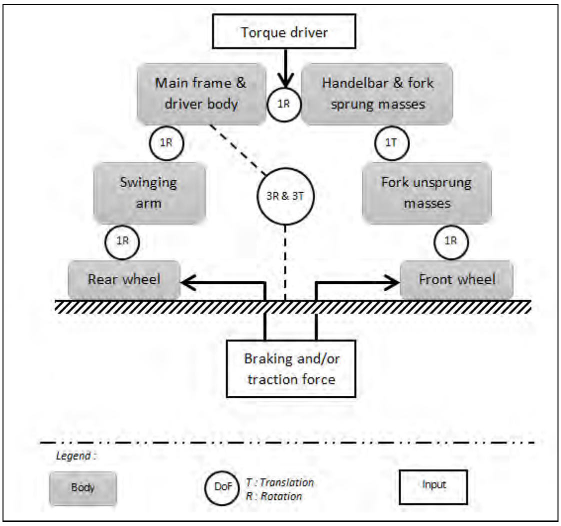


Fig. 1 Multibody model architecture

### 2.2 Experimental tests and motorcycle instrumentation

The best way to validate a model is to compare results from numerical simulations with data acquired during experimental tests. So, a motorcycle Honda VFR 800 was instrumented in order to achieve experimental tests. The motorcycle is equipped with several sensors to obtain the majority of information needed for the study of the dynamic behaviour of a motorcycle and external forces applied by the driver. All the sensors are listed below :

-The roll angle is determined by using two laser rangefinders on both sides of the motorcycle.

-The speed is measured via Hall Effect sensors which are mounted on each wheel. The installed sensors are the same as those that fit the motorcycle ABS system.

-The braking information is double, an On/Off sensor is wired directly on the brake light but information on the braking intensity was missing, so pressure sensors were integrated into the braking system.

-The roll, yaw and pitch rate, accelerations estimation and GPS position (1Hz) are measured with an Inertial Measurement System (IMU).

-The quantification of suspension travel is doing with laser rangefinders.

-The throttle opening is measured with a potentiometer placed on the throttle.

-The context is given by a camera placed on the front of the motorcycle.

-The torque applied by the driver on the handlebar and the steering angle are measured with a sensor placed between the handlebar and the steering system.

In all, more than 25 channels are recorded.

The experimental trials are conducted on a closed track and the motorcycle is ridden by an experimented but non-professional driver.

Three kinds of tests were performed: braking, avoidance and slaloms manoeuvres. Each of these tests is conducted at various speed and performed three times. No ISO standard specifying the layout of specific driving situations exists in literature that is

why the chosen layout for slalom or avoidance manoeuvre are those defined in the new motorcycle driving test in Europe[12] as show on
Fig. 2. Braking are made at different speed by operating the front or the rear brake or both.

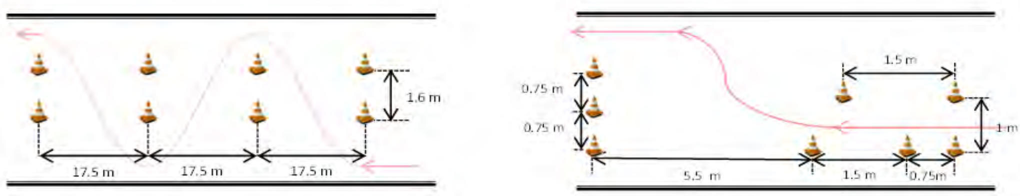


Fig. 2 Slalom and avoidance layout

A total of 69 tests was conducted and distributed as follows: 18 avoidances (on the left and right, at 30 km/h, 40 km/h and maximum speed of about 45 km/h), 18 slaloms (entrance on the left and right, at different speeds 30 km/h, 40 km/h and maximum speed of about 50 km/h) and 33 braking (front brake, rear brake, combined braking, engine braking). More than 1700 data acquired were collected and processed.

## 3. RESULTS

To validate the model in lateral dynamic, roll and steering angles as well as trajectories of the simulation are compared to results obtain by experimental tests for slalom and avoidance at 30, 40 and 50 km/h on right and left (36 simulations). For braking, comparison between speeds and accelerations acquired and simulated is done to validate in longitudinal dynamic, at 30, 50, 70 and 90 km/h with only rear or front or both brake (33 simulations). Results presented here concern speed at 30 and 50 km/h for slalom and avoidance and 30 and 90 km/h with rear and front brake for braking.

### 3.1 Avoidance manoeuvres

As shown on Fig. 3 at the speed of 30 km/h and 50 km/h the model is able to reproduce the avoidance recorded during experimental test. The two trajectories are compying with the route between the cones. During experimental test it was noticed that for an avoidance at 50 km/h the trajectory is more direct while at 30km/h because the driver had enough time to avoid the cone.
As shown on Fig. 4 the model had a better answer at high speed than at lower speed. At 30 km/h, the entry in the avoidance is similar with data acquired than with data simulated, but in the second part, in exiting, a difference can be noticed. At 50 km/h, the model gives a response in accordance with experimental test. A slight delay can be reported on the results of the simulation with respect to those from the acquisition. For an avoidance at 30km/h, the maximum steering angle acquired is 5° (6° simulated). The maximum steering angle observed during the counter steering phases is about 2°. It can be noticed that the exit of the avoidance is more stressing than the entry. The maximum roll angle acquired is approximately 20° (22° simulated). On the contrary to steering angle, there is no difference between the two phases of the avoidance concerning the roll angle.

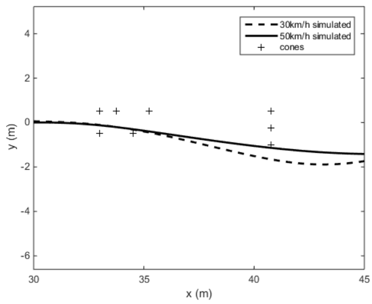


Fig. 3 Avoidance trajectories

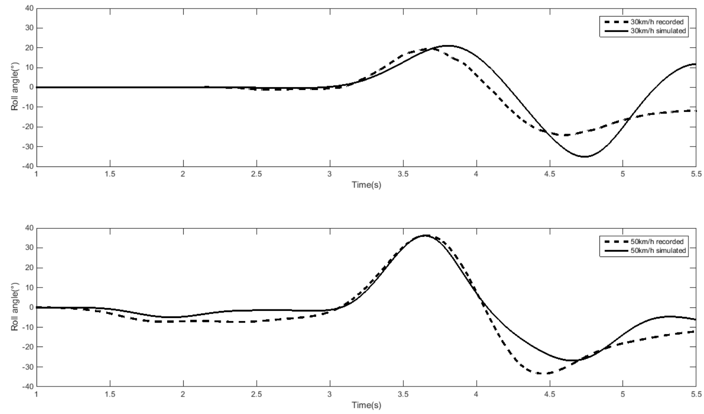


(a)

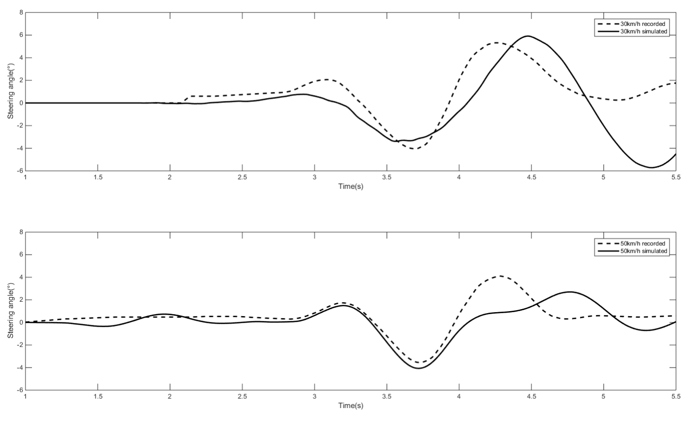


(b)

Fig. 4 Roll angle (a) and steering angle (b) for avoidance at 30 and 50 km/h.

For an avoidance at 50 km/h, the maximum steering angle acquired is 3° (4° simulated). Concerning the roll angle acquired and simulated, at 50 km/h, the maximum is 37° and the entry is more stressing that the exit. This can be explain by the fact that the driver is constrained in entry by the layout but not in exit.

### 3.2 Slalom manoeuvres

Figure 5 shows the simulated trajectories during a slalom at the two speed 30km/h and 50km/h. At the speed of 30 km/h the driver had time to browse the slalom that is why the trajectory is more fluid than at 50 km/h. However at the two speeds the model is able to describe a slalom between cones.

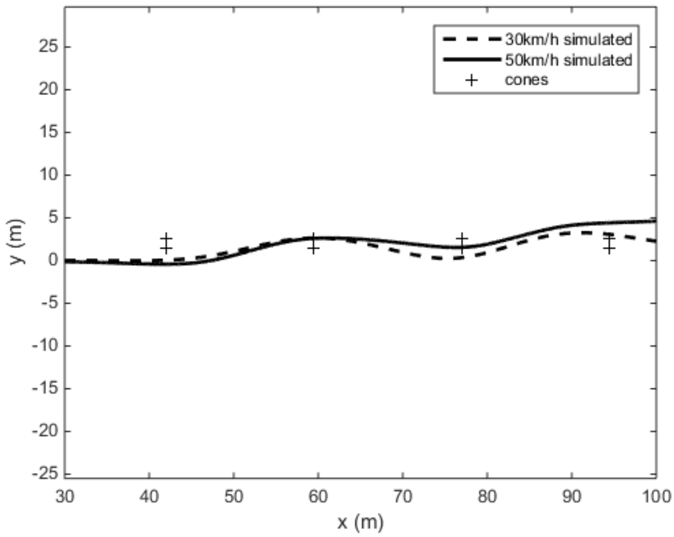


Fig. 5 Slalom trajectories.

Fig. 6 gives the roll angle and the steering angle for slalom at 30km/h and 50 km/h obtained with the model and compared with the experimental acquisition. At 30 km/h or 50 km/h the bigger difference is at the exit of the slalom. The roll angle changes are more brutal at 50 km/h. Indeed, the increasing of the speed decrease the time necessary to react. For a slalom at 30 km/h, the maximum steering angle acquired is 5° (6° simulated). The passage of the last cone is more stressing than the others. It can be explained by the fact that the driver accumulates the constraints of each change of phases. Concerning the roll angle, the maximum value acquired is 20° (22° simulated). The last skirt is less stressing, like the first, because they are not complete.

For a slalom at 50 km/h, the maximum steering angle acquired is 6° (4° simulated). Each phases of the slalom is as much stressing as the others. Concerning the roll angle, the maximum value acquired is 30° (32° simulated). The passages of the first and the last cones are less stressing because the driver is not constrained in entry or in exit.

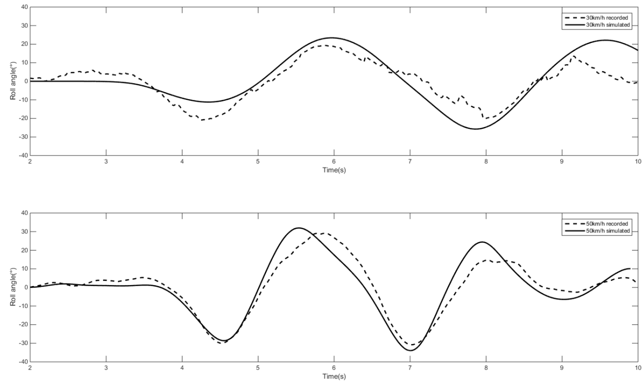


(a)

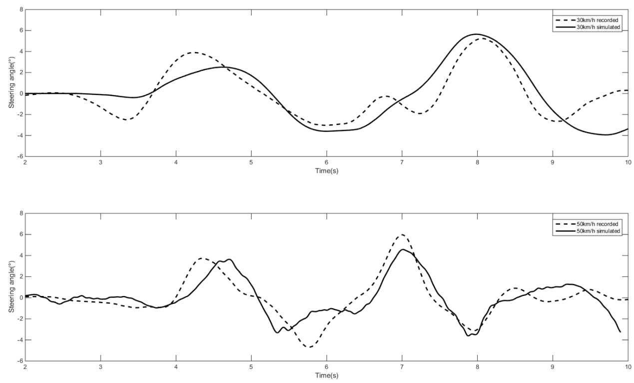


(b)

Fig. 6 Roll angle (a) and steering angle (b) for slalom at 30 and 50 km/h.

### 3.3 Braking

Concerning the braking (**Hiba! A hivatkozási forrás nem található.**), according to experimental test, it has been observed that at the speed of 30 km/h the distance necessary to stop the motorcycle is about 4.3 meters and the mean deceleration is 7.8 m/s². At the speed of 50 km/h the braking distance is nearly tripled and is about 11.4 meters for a deceleration of 7.7 m/s². At the speed of 70 km/h the distance necessary to stop the motorcycle is 18.6 meters and the deceleration is 7.4 m/s². Finally at the speed of 90 km/h, the braking distance is 24.6 meters and the deceleration is 6.5 m/s².

## 4. CONCLUDING REMARKS

A multi body model which can simulate emergency driving situations have been developed and compared with experimental tests. Globally, the multi body model have dynamical responses in accordance with the real acquisition both in longitudinal and in transversal solicitations. For slalom and avoidance the model is valid between 30 and 50 km/h, and for braking between 30 and 90 km/h. These ranges of speed match the

majority of cases that can be encountered on the road. Indeed, previous study have shown that accident occur at an average speed of 37 km/h [13].
Some improvement can be made on the model, especially in consideration of the driver. A driver model should be developed to take better into account his movement on the motorcycle. But in order to develop a driver model, additional sensors should be install on the instrumented motorcycle to record the roll torque applied by the body of the driver in addition of the steering torque on the handlebar.
Future work will concern the application of the numerical model to real accidents reconstructions involving PTW. Based on parametric studies, the objective is to determine the most probable accident configuration from inputs driver variations. Particular attention will be paid to PTW loss of control since they appear as situations more complex to understand.

## 5. REFERENCES


[1] **Observatoire national interministériel de la sécurité routière**, "L'accidentalité routière en 2014." La documentation Française.

[2] **Obenski, K. S. - Hill, P. F. - Shapiro, E. S. - Debes,J. C.:** Motorcycle Accident Reconstruction and Litigation. 1994.

[3] **Sharp, R. S. - Limebeer, D. J.:** "A motorcycle model for stability and control analysis," Multibody Syst. Dyn., Vol. 6, No. 2, 2001, p.123–142.

[4] **Sharp, R. S. - Evangelou, S. and Limebeer, D. J.:** "Advances in the modelling of motorcycle dynamics," Multibody Syst. Dyn., Vol. 12, No. 3, 2004, p.251–283.

[5] **Cossalter, V. - Lot, R.:** "A Motorcycle Multi-Body Model for Real Time Simulations Based on the Natural Coordinates Approach," Veh. Syst. Dyn., Vol. 37, No. 6, 2002, p.423–447.

[6] **Nasser, H. - M'Sirdi, N. K.:** "Decoupled model for motorcycle and identification of dynamic parameters," in 2012 IEEE/ASME International Conference on Mechatronics and Embedded Systems and Applications (MESA), 2012, p.142–147.

[7] **Shabana,A.:** Dynamics of Multibody Systems. Cambridge University Press, 2003.

[8] **Pacejka**, **H.:** Tire and Vehicle Dynamics. Elsevier, 2005.

[9] "Delft-Tyre - MF-tyre/MF-Swift," TASS International, 07-Jan-2013. [Online]. Available:https://www.tassinternational.com/delft-tyre-mf-tyremf-swift. [Accessed: 28-Nov-2016].

[10] **Versteden**, **W. D.:** "Improving a tyre model for motorcycle simulations," TU Eindhoven. Rep. DCT, vol. 2005.

[11] **Evangelou**, **S.:** "Control and Stability Analysis of Two-wheeled Road Vehicles," University of London, 2004.

[12] Arrêté du 10 janvier 2013 modifiant l'arrêté du 23 avril 2012 fixant les modalités pratiques de l'examen du permis de conduire des catégories A1, A2 et A. .

[13] **Serre, T. - Masson, C. - Perrin, C. - Martin, J.L. - Moskal, A. - Llari,M.:** "The motorcyclist impact against a light vehicle: Epidemiological, accidentological and biomechanic analysis," Accid. Anal. Prev., Vol. 49, Nov. 2012, p.223–228.

# WHEELBRAKE DESIGN FOR HEAVY DUTY ELECTRIC VEHICLES

**Csaba KOKREHEL and Huba NÉMETH**

Knorr-Bremse R&D Center Budapest
H-1119 Budapest, Major u. 69., Hungary
csaba.kokrehel@knorr-bremse.com, Phone: +36 1 382 9434.
huba.nemeth@knorr-bremse.com,

*Received: November 7, 2018.*

## ABSTRACT

Developments of heavy duty commercial vehicle powertrains resulted in the appereance of electric buses and trucks, which are expected to become widespread on the roads in the upcoming years. Main drivers for electrification are reduction of emissions and operational costs. The high power electric system for vehicle propulsion enables the introduction of multiple electrified auxiliaury systems on such vehicles. Since the traction battery is the sole source of onboard energy the powertrain and the auxiliaury systems are in competition, consequently auxiliaury systems are more directly impacting the achievable range. Therefore low consumption and high efficiency auxiliauruies are more important than before. It drives the fully electric solutions for vehicle actuation systems like braking, steering, and also for auxiliary systems as door handling, heating, air conditioning, etc. For some consumers e.g. the air suspension the compressed air system might be still required onboard, but long term a significant reduction of compressed air system coverage is assumed for electric commercial vehicles. Electric propulsion gives the possibility to combine brake systems and traction engines in case of braking resulting in the so called brake blending. During the vehicle's lifetime majority of the brakings are realized in 10 - 15 % of the maximal deceleration range, which can be well covered by the traction motors. Due to the brake blending with traction motors the service brake actuators are rarely involved into the braking, or just used to stop the vehicle in near-zero speed levels resulting in significantly reduced brake pad wear. The reduced actuation number and activation level of the friction brakes is the main driver of reconsidering the brake design, focusing on possible weight and packaging reductions. Major dimensioning principles derived from vehicle dynamics and legal requirements for an electromechanic wheelend sub-systems are included and discussed in the paper. To support mechanical design process and estimate dynamical behaviour of the brake, a simulation model has been set up. The results in terms of energy consumption and system performance are evaluated in the paper.

*Keywords:* electric vehicle, wheel brake, electric actuation, brake blending

## 1. INTRODUCTION

Environmental issues of local air pollution and global warming raised technlogical changes in the automotive sector to transit powertrains from internal combustion engines towards electrified tractions. In this trend commercial vehicles are no exception.

The electrification of commercial vehicles is expected first in segments were the daily operation range can be achieved with the available battery technologies. These applications are vehicles operated in the proximity of urban areas, such as distribution trucks and city buses (see Fig.1). Here is anyway the highest pressure from society and politics to achieve zero local emissions. Moreover reduced system complexity and maintenance is also a further driver.

For both of these applications are still a challenge to reduce battery cost and weight, however the charging infrastructure should be no problem, since these vehicles can be charged at the local depot of the operators.

All electricfied powertrain technologies are based on the same core components of electric traction engines, power and control electrics and a certain size of traction battery.

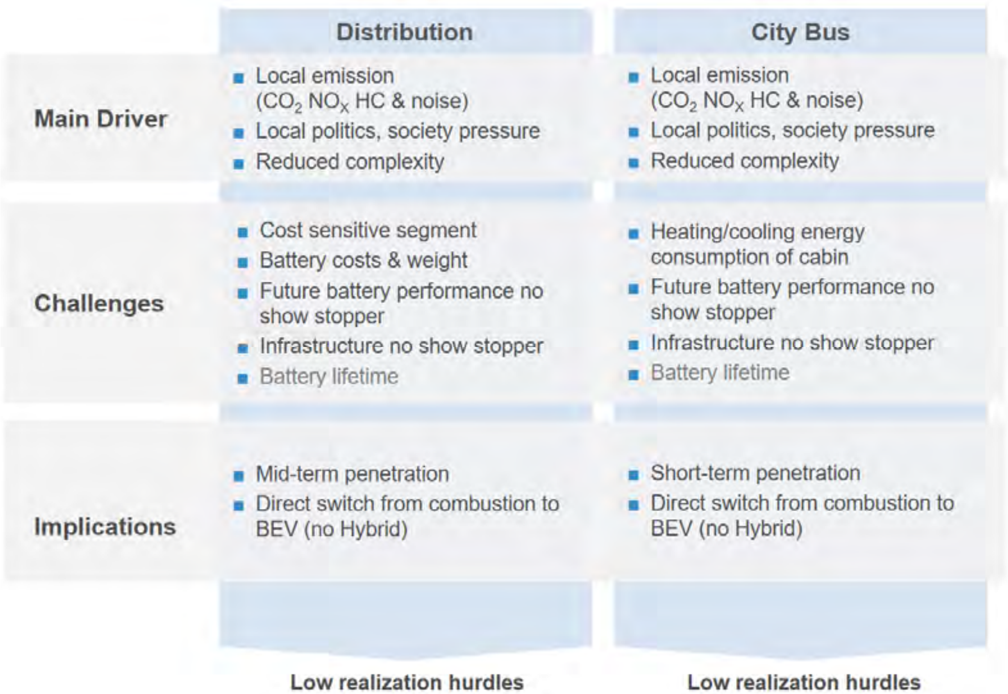


Fig. 1 Commercial vehicle electricfications in urban applications

Since the sole primary energy available onboard is already in electric form and used for both the traction and auxiliauries therefore there is a competition for this energy to attain a certain operation range. In conventional commercial vehicles auxiliaury system consumption can contribute up to 8-15% from the total fuel consumption, however in such cases there was no big cost impact to compensate the range reduction with an increased size fuel reservoir. In electric vehicles this situation changes significantly since the majority of the vehicle cost is the traction battery. Consequently the efficiency of auxiliauries has a major importance. In this process the electricifcation of friction wheel brakes is a potential answer, which is the scope of this paper.

## 2. WHEEL BRAKES FOR ELECTRIC VEHICLES

The friction brake design can be potentially influenced by two major factors on electric vehicles: the one is how the wheel brake contribution changes due to the electric traction, and the other is by electrifying the brake actuation.

### 2.1 Impact by electric powertrain

Electric power trains are targeting to improve energy utilization by recuperating the maximum amount of kinetic energy where possible. The torque capabilities of electric tractions engines can cover approximately up to 20% of the maximal deceleration requirements at fully laden vehicles. On the other hand most braking maneuvers are in the range of comfort brakings with 10-15% of the maximal deceleration capacity of wheel brakes. Therefore a majority of real life braking manuvers can be well covered by recuperating with the traction engine and only at near zero speeds levels the friction brake needs to be launched, where losses of e-motors are too high. The consequence of this behavior is a significant reduction of brake wear, therefore there are some options to consider this effect in the wheel brake design (see left side of Fig.2.).

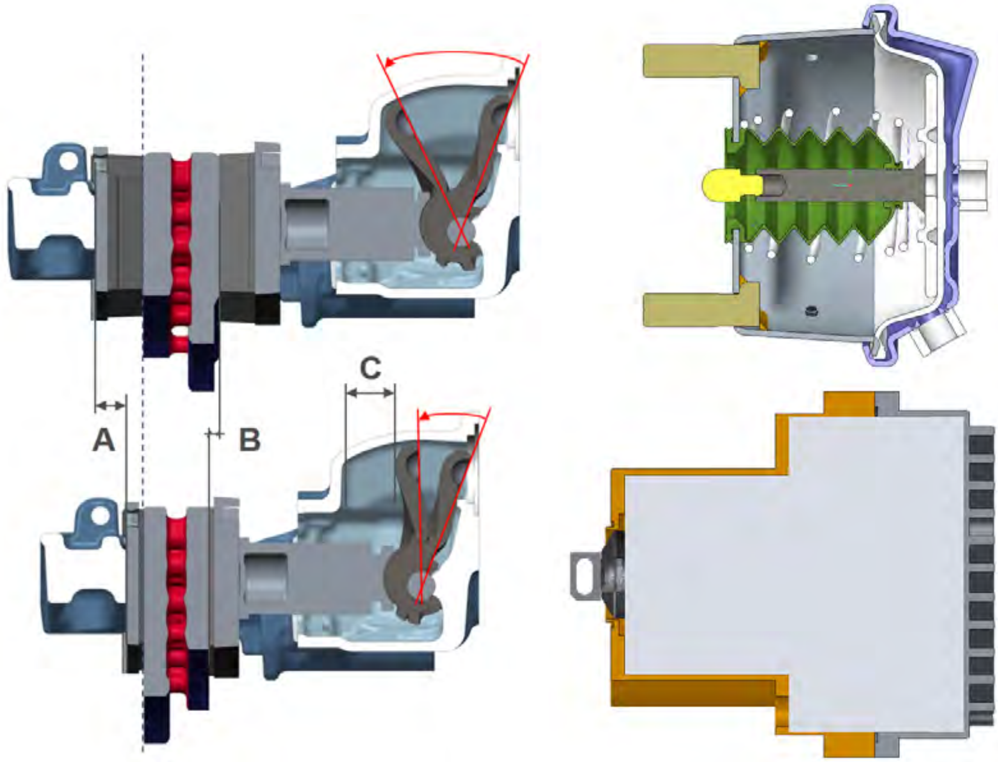


Fig. 2 Impacts of electric powertrain (left) and electic actuation (right) to the wheel brake

On one hand this effect enables a reduction of the direct wear material on the brake pad (A) and the disc rotor (B). Both of these contribute in increasing the overall stiffness of the brake caliper requiring shorter effective stroke for the brake actuation (C).

## 2.2 Impact by electrified actuation

In the past wide research activities were spent on electro-machnic brakes, which used the so called self-amplified brake mechanics to reduce actuator power demands [1-9]. Since electric vehicles have no such shortage of onboard electric power, therefore the complex brake mecahnics can be avoided, while the power consumption can be still superior to the pneumatic counterparts. The electrificiation of the brake actuation should target the same actuator interface to the caliper like the pneumatic brake chambers and should fit into the same installation envelope (see right side of Fig.2.). Contrary to electro-pneumatic brakes, which use external pressure modulator to the brake actuators, the control and power electronics for electrified brakes can be better integrated into the actuator therefore the overall number of brake components can be reduced. Since the brake pads are moved by a translational movement a conversion is required from a rotational electric actuation motor. A spindle transmission option is considered throughout this paper.

## 3. BRAKE REQUIREMENTS

The wheel brake requirements can be derived from the vehicle dynamic in terms of maximum axle load and deceleration requirements. Here we distinguish between medium duty- and heavy duty commercial vehicles (see Fig. 3). The brake torque difference between the two applications translates directly into the actuator force and actuation power requirements.

| | Medium duty (Usually applied for R17.5 – R19.5" wheels) | Heavy duty (Usually applied for R22.5" wheels) |
|---|---|---|
| Brake torque, M (Nm) | 19.000 | 30.000 |
| Disc effective radius, R (mm) | 140 | 170 |
| Pad friction coefficient, μ (-) | **0.25 – 0.5** | **0.25 – 0.5** |
| Caliper lever ratio | **15.6 (~)** | **16.9 (~)** |
| **Actuator nominal force F (N)** | 18.000 | 23.000 |
| **Motor peak power P (W)** | ~ 3300 | ~ 4200 |

Fig. 3 Basic wheel brake requirements for electric commercial vehicles

## 4. SYSTEM MODEL DESCRIPTION

In order to investigate the behaviour of electromechanic brakes a simplified dynamic model has been set up (see Fig. 4). The models includes a single balance volume, represented by the inertia $\theta_m$ of the brake actuator. This rotating enertia is effected by the electro-magnetic torque $T_e$ of the e-motor. The e-motor is driving a spindle converting the rotational motion to translation with a pitch of $h$. The spindle is connected to a lever mechanism which realizes a transmission towards the brake pad. The brake caliper is represented with its total stiffness of $s_0$.

The state equition for the wheel brake model is written in the following form:

$$\begin{bmatrix} \dot{\varphi}_a \\ \dot{\omega}_a \end{bmatrix} = \begin{bmatrix} f_1(\mathbf{x}) \\ f_2(\mathbf{x}) \end{bmatrix} + \begin{bmatrix} g_1 \\ g_2 \end{bmatrix} T_e . \tag{1}$$

The coordinate functions from the conservation of motion is given as:

$$f_1(\mathbf{x}) = \omega_a , \tag{2}$$

$$f_2(\mathbf{x},\mathbf{d}) = \frac{k_0\omega_a + s_0(\delta - h\varphi_a)}{\theta_m}, \tag{3}$$

$$g_1 = 0, \tag{4}$$

$$g_2 = \frac{1}{\theta_m}, \tag{5}$$

where $k_0$ represents the total viscous losses of the actuator and $\delta$ the air gap between the brake pad and the brake rotor.

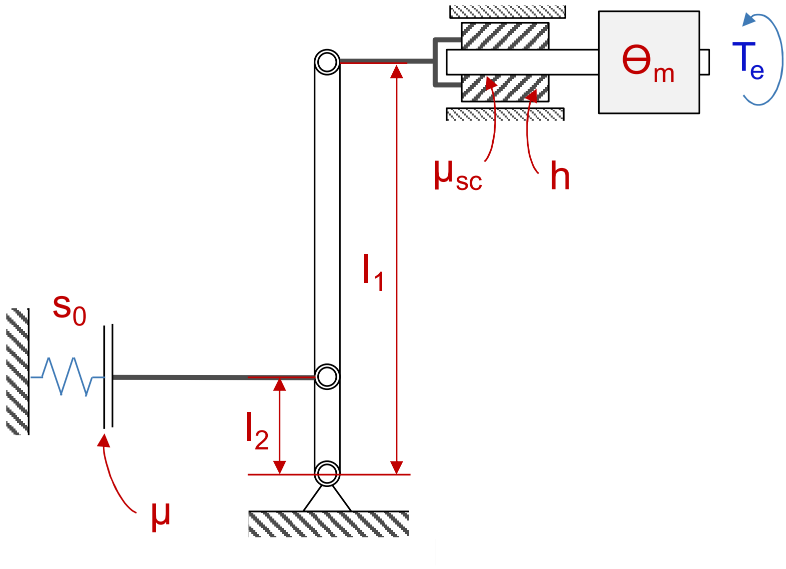


Fig. 4 Model of the electro-machnanic brake

The wheel brake model has been embedded into a longitudinal vehicle model, a brake actuation control loop and driver model to able to carry out predefined drive cycles.

The electric power supply for the wheel brake was included in a form of a simple voltage source so that the current drawn by the actuators can be accounted.

## 5. DRIVE CYCLE

The above simulation model has been extensively evaluated using different vehicle applications and their corresponding drive cycles. Here a city bus application is presented. For this application the widly used Ulm city bus cycle has been applied, which is based on a real bus drive cycle in a dense city traffic and corresponding intensive dynamics. Fig.5 shows a portion of test cycle with the vehicle speed and the rated brake torque levels. Note that in the bus stops a door brake function of the service brake has been applied with 30% rated brake level. The total cycle duration was 90 minutes.

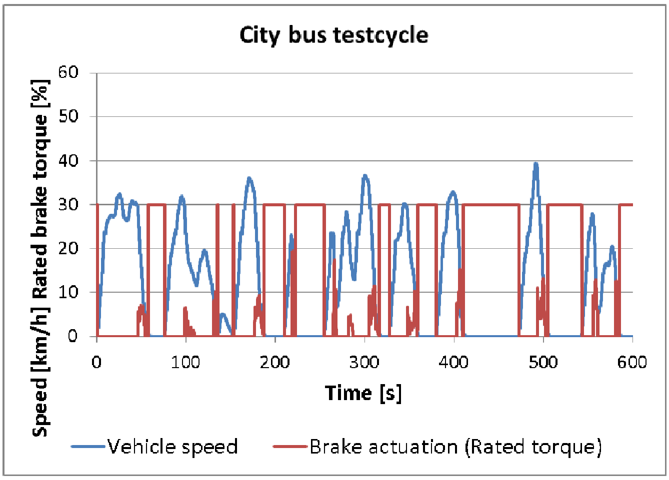


Fig. 5 City bus drive cycle

## 6. SIMULATION RESULTS

An example of the simulation results is given in Fig.6. for a city bus operation with the vehicle speed profile (top diagram), the current drawn from the battery and the corresponding power consumption (middle diagram) and the integrated energy consumption of the brake actuation (bottom chart).

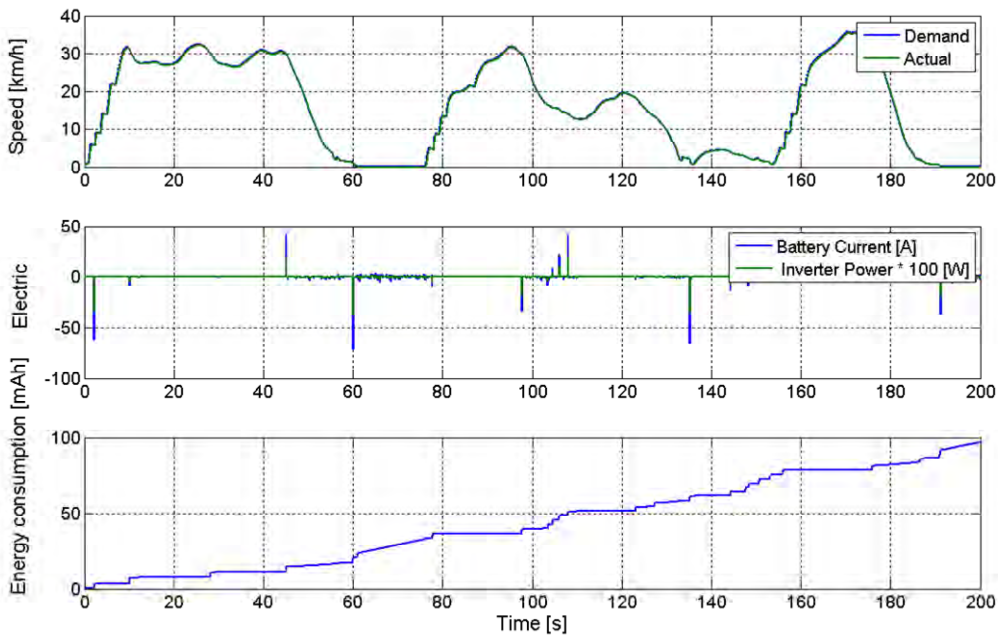


Fig. 6 City bus drive cycle results of an electric wheel brake

The simulation results showed the following main characteristics. The average brake loads are on the 10-15% range of the rated level in majority of all drive cycles during the movement of the vehicle. The door brake application for bus operation with 30% rated brake level contributes significantly to the brake load spectrum and represents the peak load for such applications.

The wheel brake peak current consumptions are generated mostly form the dynamic application of the brake and less from the static load of the brake force. This is present in short time, high current peaks, however their energy consumption contributions are not high by its short duration. On the other hand there are significant recuperation current peaks form the wheel brake actuators alos coming from the brake actuator dynamics with up to 50% of the peak currents. The average power consumption per wheel brake is approx. 100 W in a city drive cycle. The energy consumed per wheel brake in a city cycle was in the range of 10-15 Wh per wheel per hour operation time.

## 8. CONCLUSIONS

This paper focused to the wheel brake investigations for electric commercial vehicles. It is expected that electric vehicles gain a significant share in the road vehicle population in the future in order to reach zero local emissions and reduced operation costs. Commercial vehicles are not an exception in this tendency, especially distribution vehicles and city buses may benefit of this process.

It was concluded that wheel brake design is impacted by two main factors for electric commercial vehicles: (1) by the electric powertrain itself, which takes over a significant share from the brake torque of the wheel brakes for recuperation, resulting in reduced wear and more compact brake design as a consequence, and (2) by the electrification of the brake actuation, which is a more effective means of the actuation than state-of-the-art pneumatics.

For the updated electrified wheel brake simulation models have been used to investigate its behaviour on different vehicle drive cycles. The simulation results confirmed the expected reduction in electric energy consumption compared to compressed air counterparts and revealed its characteristic behaviour.

## 9. REFERENCES

[1] **Balogh, L. - Németh H.**: Development of self-energized mechanisms for brake systems; A JÖVŐ JÁRMŰVE: JÁRMŰIPARI INNOVÁCIÓ 2010: (FISITA edition), 2010, p.49-54.

[2] **Balogh, L. – Stréli, T. – Németh, H. – Palkovics, L.:** Control of Self-amplifying Brake Mechanism; Proceedings of the 10th MINI Conference on Vehicle System Dynamics, Identification and Anomalies. VSDIA 2006 (Ed. by Prof. I. Zobory) BME Department of Railway Vehicles, Budapest, 2007, p.537-548.

[3] **Balogh, L. – Németh, H. – Frank, P. – Széll, P.:** Electromechanical brake application for commercial vehicles; In: 11th EAEC Congress. Budapest, Hunagary, 2007.05.30-2007.06.01.

[4] **Balogh, L. – Stréli, T. – Németh, H. – Palkovics, L.**: Design Anomalies of Electro-Mechanic Brake Systems; In: FISITA, World Automotive Congress. Yokohama, Japan, 2006.10.22-2006.10.27.

[5] **Balogh, L. – Stréli, T. – Németh, H. – Palkovics, L.**: Modelling and simulating of self-energising brake system; Vehicle Ssystem Dynamics Vol.44. 2006, p.368-377.
[6] **Stréli, T. – Balogh, L. – Németh, H. – Stépán, G. – Palkovics, L.:** Dynamics of a Self-Amplifying Brake Mechanism; Proceedings of the 9th MINI Conference on Vehicle System Dynamics, Identification and Anomalies: VSDIA 2004. (Ed. by Prof. I. Zobory), BME Department of Railway Vehicles, Budapest, 2005, p.291-296.
[7] **Stréli, T. – Balogh, L. – Németh, H. – Palkovics, L.:** Nonlinear dynamic analysis and control of self-amplifying brakes; In: Conference on Advanced Vehicle Control 06 (AVEC'06). Taipei, Taivan, 2006.08.20-2006.08.24., p.115-120.
[8] **Stréli, T. – Balogh, L. – Németh, H. – Palkovics, L.:** Nonlinear dynamic analysis and control of self-amplifying brakes; International Symposium on Advanced Vehicle Control, Review of Automotive Engineering Vehicle System Dynamics, Taipei, Taiwan (2006)
[9] **Balogh, L. – Stréli, T. – Németh, H. – Palkovics, L.:** Modelling and simulating of self-energising brake system; In: 19th Symposium of International Association of Vehicle System Dynamics (IAVSD 2005). Milan, Italy, 2005.08.29-2005.09.02.

# TIRE DATA ANALYSIS METHOD FOR FINDING GRIP-OPTIMAL SLIP AND CAMBER VALUES

**Gergely SZŰCS and Gergely BÁRI**

Department of Vehicle Technology
John von Neumann University
H-6000, Kecskemét, Izsáki út 10. Hungary

*Received: November 5, 2018*

## ABSTRACT

This paper shows a method for improving grip with the choice of optimal tire data. Tires are important parts of cars, because these parts transfer forces from the contact patch, so tires can greatly affect grip. Vehicle behaviour at the grip limit is really important for avoiding collisions. Vehicle suspensions are usually designed with wide range of requirements in the field of comfort, price, safety, dynamic properties, and maximising tire grip is only one aspect of these. When grip limit behaviour gets more attention, suspension kinematic design should be based mainly on tire behaviour. In these cases, understanding "what the tire want"; from the suspension has key importance. For this we have to plot diagrams and tables to show which conditions are preferred by tires to maximize forces on the contact patch. First, the main tire parameters which have the biggest effect on grip are identified. After that a method is shown for choosing the tire with the best fitting properties for given requirements. We show how to compare tires effectively, and why a tire can perform better than an other in a given situation. We have to look at the tires for many parameters for different directions. Longitudinal and lateral characteristics are the most important, but it is important to know the combined characteristics too. These properties are assigned with weighed scores, and the best tire is chosen according to scores. During a suspension design process, after choosing the best tire, the next step is usually to understand, what is the maximum resultant force that the tire can create. In this work we create a mapping, that maps normal force and the desired direction of the combined force to the slip, and camber values that corresponds to the maximum combined force in the desired direction. As a result a tool is shown, that can be used with simulation environments to make possible better evaluation of a given suspension.

*Keywords:* tire, griplimit, suspension design, optimal camber

## 1. INTRODUCTION

The car contacts on four places with the ground, where tires produce forces which control the car. So tire is the most important part of the suspension from view of grip. Moreover if we want to simulate vehicle motion [4] we have to have tire models based on measurements [5].

In this paper our goal is to show how can we chose the best tire in view of grip and how can we get information to design suspension to tire. It is hard task, because in most cases there is no any information about tire we want to use. If we have information from tires it is easier, but we have to know what we want from tires. Which parameters are the most important to know, and which parameters we have to look at to choose the best of available tires.

We can get information about tires by measuring vehicle motion [6], but the best way to know tires by testing them in laboratory [5] and fitting model to measurements [7].

## 2. CHOOSING THE BEST TIRE

Tire choice is the first important part of suspension design. In this chapter we want to show how to choose the best tire according to measurement [5]. There was 2 type of measurement. The first type was "Cornering": In this measurement slip angle was swept, while slip ratio was kept at zero and lateral forces were measured. The second type was “Combined”: In this measurement slip ratio was swept, with different slip angles while longitudinal and lateral forces were measured too. In our example we show 3 available chosen tires: *TireA*, *TireB* and *TireC*. The graphs are plotted by MATLAB.

### 2.1 Longitudinal - and lateral force (Fx & Fy)

The first viewpoint of 3 tires are the longitudinal force vs. slip ratio ($F_x$ - *SR*) and lateral force vs. slip angles ($F_y$ - *SA*) graphs. [1]

First of all, to compare these graphs we have to look that the 3 measurement were at the same circumstances, such as the same normal forces, pressures, temperatures, cambers and velocities. It is important because the $F_x$ and $F_y$ forces are mainly functions of these parameters too.

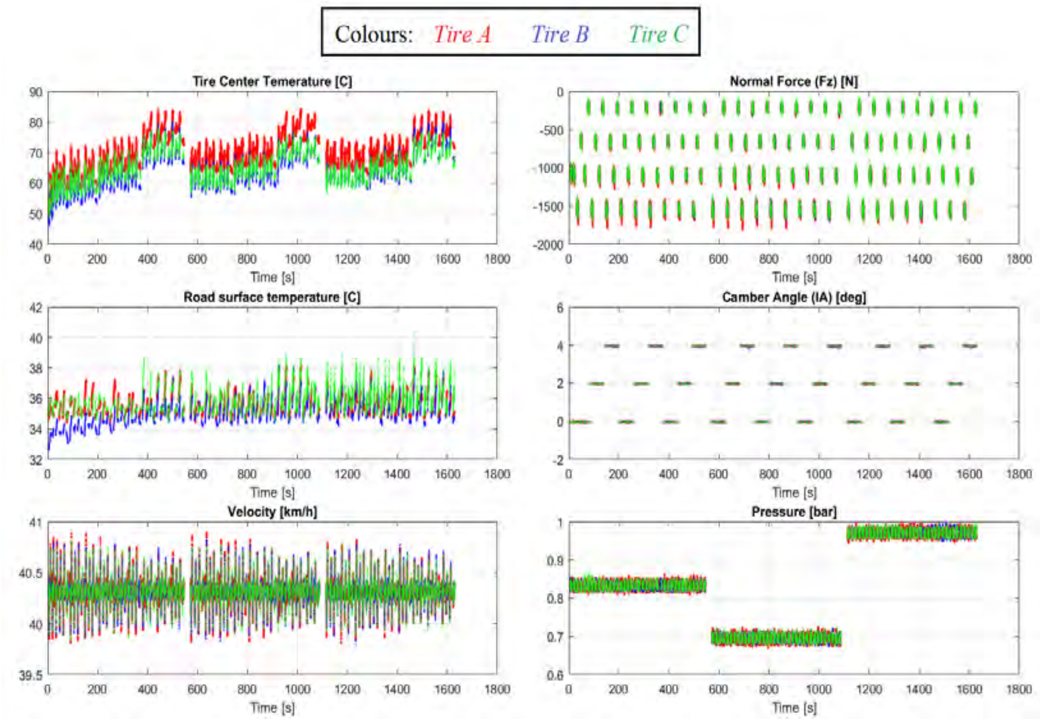


Fig. 1 The circumstances of the measurement

As it can be seen in *figure 1* in our example the pressures, velocities, cambers, normal forces and road surface temperatures were the same. Tire temperature were quite the same, but you can see a few degrees of Celsius. It can be the speciality of each tires. According to *figure 1 TireA* is warming up better during measurement.

Looking at $F_x$ – *SR* graphs in *figure 2*, we can see *TireA* is the best for acceleration at high normal forces (higher maximum peak), but at lower normal forces *TireC* is the best. In view of braking *TireC* looks too the best of three tires.

Friction graphs at the right side of *figure 2*. can be useful if the normal forces were different during measurement.

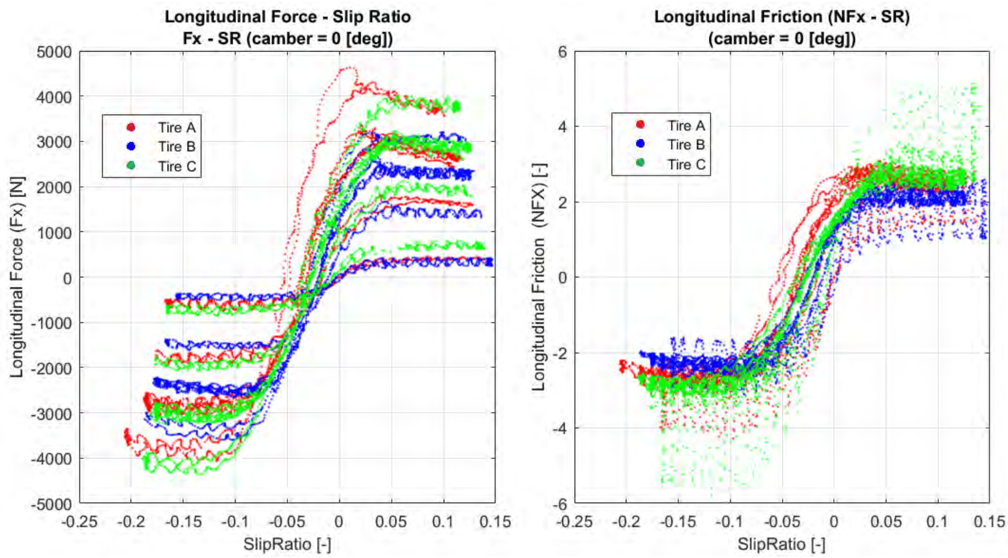


Fig. 2 The Fx-SR and Longitudinal friction-SR graphs

This graph is almost the same, because it plots $F_x / F_z$ instead of $F_x$, so the effect of different $F_z$ normal forces can be disappeared.
To decide which one we want to choose, take a look at statistic results in *table 1*.

| 'Tire ID' | 'Tire A' | | | | 'Tire B' | | | | 'Tire C' | | | |
|---|---|---|---|---|---|---|---|---|---|---|---|---|
| 'Normal Force (Fz) [N]' | 205 | 655 | 1087 | 1541 | 204 | 667 | 1090 | 1540 | 203 | 666 | 1093 | 1544 |
| 'MAX Fx (Traction) [N]' | 514 | 1829 | 3359 | 4629 | 491 | 1663 | 2640 | 3233 | 823 | 2118 | 3219 | 3994 |
| 'MAX Fx (Brake) [N]' | -735 | -1928 | -3068 | -4062 | -534 | -1614 | -2655 | -3596 | -864 | -2069 | -3245 | -4352 |
| 'MAX mu_x [-]' | 4.28 | 3.16 | 3.08 | 2.92 | 3.18 | 2.62 | 2.54 | 2.42 | 5.98 | 3.43 | 3.11 | 2.94 |
| 'Avg. mu_x [-]' | 1.86 | 1.87 | 2.02 | 1.87 | 1.59 | 1.61 | 1.66 | 1.52 | 2.70 | 2.00 | 1.92 | 1.74 |
| Points relative to Tire A | | | | | | | | | | | | |
| 'MAX Fx (Traction) [N]' | 100 | 100 | 100 | 100 | 95 | 91 | 79 | 70 | 160 | 116 | 96 | 86 |
| 'MAX Fx (Brake) [N]' | 100 | 100 | 100 | 100 | 73 | 84 | 87 | 89 | 118 | 107 | 106 | 107 |
| 'MAX mu_x [-]' | 100 | 100 | 100 | 100 | 74 | 83 | 82 | 83 | 140 | 109 | 101 | 101 |
| 'Avg. mu_x [-]' | 100 | 100 | 100 | 100 | 86 | 86 | 82 | 81 | 145 | 107 | 95 | 93 |
| AVERAGE | 100 | | | | 83 | | | | 112 | | | |

Table 1 Summarize of longitudinal grip

Table 1 is containing forces and friction coefficient (maximum and average values) at different normal forces. Below these numbers calculated points can be seen, relative to *TireA* numbers, so *TireA* number is 100%. Summarize the points, in view of longitudinal grip *TireC* seems to be the best choice.
Let's take a look at *figure 3*. On the one hand, in view of lateral forces *TireC* seems to be better at high normal forces, but at lower normal forces *TireA* has more grip.
In view of lateral grip *TireC* is the best. On the other hand, according to *figure 3 TireC* has higher cornering stiffness. [1][3] It means that, it can produce higher lateral forces at low slip angles, so rolling resistance is lower during turns. Moreover it has the least load sensitivity [1], which is advantage in case of weight transfer.

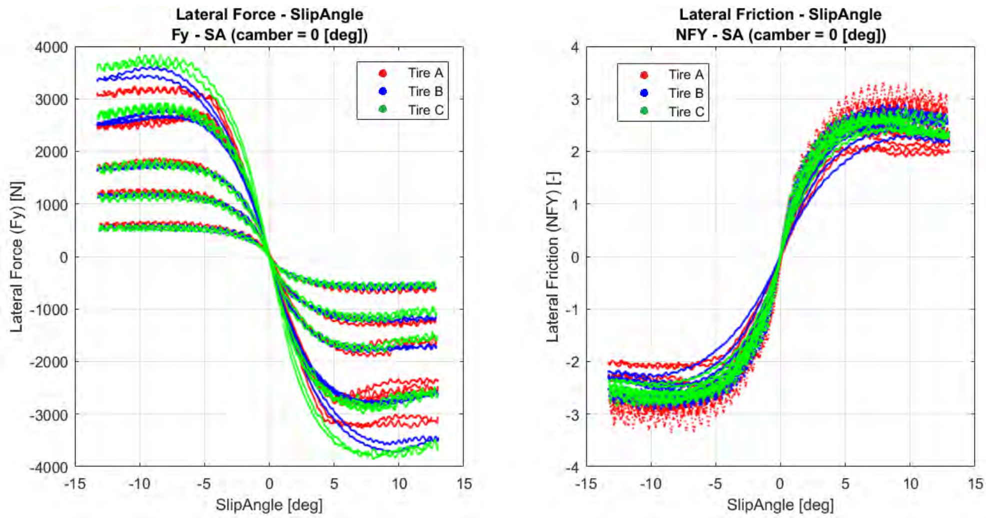


Fig. 3  The Fy-SA and Lateral friction-SA graphs

Table 2 summarizes the lateral grip of three tires.

| 'Tire ID' | | 'Tire A' | | | | | 'Tire B' | | | | | 'Tire C' | | | | |
|---|---|---|---|---|---|---|---|---|---|---|---|---|---|---|---|---|
| COMBINED | 'Normal Force (Fz) [N]' | 205 | 655 | 1087 | 1541 | | 204 | 667 | 1090 | 1540 | | 203 | 666 | 1093 | 1544 | |
| | 'MAX Fy [N]' | 469 | 1551 | 2474 | 3196 | | 509 | 1404 | 2285 | 2915 | | 694 | 1677 | 2539 | 3385 | |
| | 'MAX mu_y [-]' | 2.86 | 2.47 | 2.38 | 2.15 | | 3.12 | 2.22 | 2.19 | 1.96 | | 5.03 | 2.72 | 2.47 | 2.29 | |
| | 'Avg. mu_y [-]' | 1.00 | 1.08 | 0.74 | 0.88 | | 0.88 | 0.93 | 0.78 | 0.85 | | 1.44 | 1.17 | 0.90 | 1.01 | |
| CORNERING | 'Normal Force (Fz) [N]' | 209 | 438 | 668 | 1107 | 1559 | 208 | 444 | 662 | 1101 | 1551 | 209 | 434 | 665 | 1104 | 1550 |
| | 'MAX Fy [N]' | 747 | 1387 | 1945 | 2881 | 3492 | 664 | 1279 | 1861 | 2855 | 3724 | 670 | 1300 | 1890 | 3034 | 4015 |
| | 'MAX mu_y [-]' | 3.67 | 3.15 | 2.93 | 2.65 | 2.29 | 3.08 | 2.92 | 2.81 | 2.63 | 2.44 | 3.06 | 2.89 | 2.83 | 2.68 | 2.57 |
| | 'Avg. mu_y [-]' | 2.61 | 2.45 | 2.31 | 1.98 | 1.67 | 2.43 | 2.37 | 2.18 | 2.05 | 1.77 | 2.38 | 2.31 | 2.24 | 2.09 | 1.95 |
| Points relative to Tire A | | | | | | | | | | | | | | | | |
| COMBINED | 'MAX Fy [N]' | 100 | 100 | 100 | 100 | | 109 | 91 | 92 | 91 | | 148 | 108 | 103 | 106 | |
| | 'MAX mu_y [-]' | 100 | 100 | 100 | 100 | | 109 | 90 | 92 | 91 | | 176 | 110 | 104 | 107 | |
| | 'Avg. mu_y [-]' | 100 | 100 | 100 | 100 | | 87 | 86 | 105 | 97 | | 143 | 108 | 122 | 116 | |
| CORNERING | 'MAX Fy [N]' | 100 | 100 | 100 | 100 | 100 | 89 | 92 | 96 | 99 | 107 | 90 | 94 | 97 | 105 | 115 |
| | 'MAX mu_y [-]' | 100 | 100 | 100 | 100 | 100 | 84 | 93 | 96 | 99 | 107 | 83 | 92 | 97 | 101 | 112 |
| | 'Avg. mu_y [-]' | 100 | 100 | 100 | 100 | 100 | 93 | 97 | 95 | 103 | 106 | 91 | 94 | 97 | 105 | 117 |
| AVERAGE | | 100 | | | | | 96 | | | | | 109 | | | | |

Table 2  Summarized values of lateral grip

## 2.2 Friction Circle

The next viewpoint is longitudinal force vs. lateral force (*Fx - Fy*) graph, which is known as friction circle. [1]
It shows us the tire limit in every direction of acceleration, such as during braking and cornering at the same time.
Looking at *figure 4* we can see quasi circles. The radius of circles (at left) are the resultant force wich the tire can produce. Resultant force ($F_{res}$) is the vectorsum of $F_x$ and $F_y$ forces. Four circles means the measurement was on 4 different normal forces. As you can see according to angle ($\beta$ on *figure 4*) of $F_{res}$, there are angles, where *TireC* has higher $F_{res}$, and at other angles *TireA* has more $F_{res}$.
In table 3 we summarized the average of $F_{res}$ forces between beta angles and calculateed relative point to *TireA*, with  result is *TireC* is the best in view of friction ellipse, too.

So summarize the results of *table 1-3* we can say if we had to chose the best tire, we would chose *TireC.*

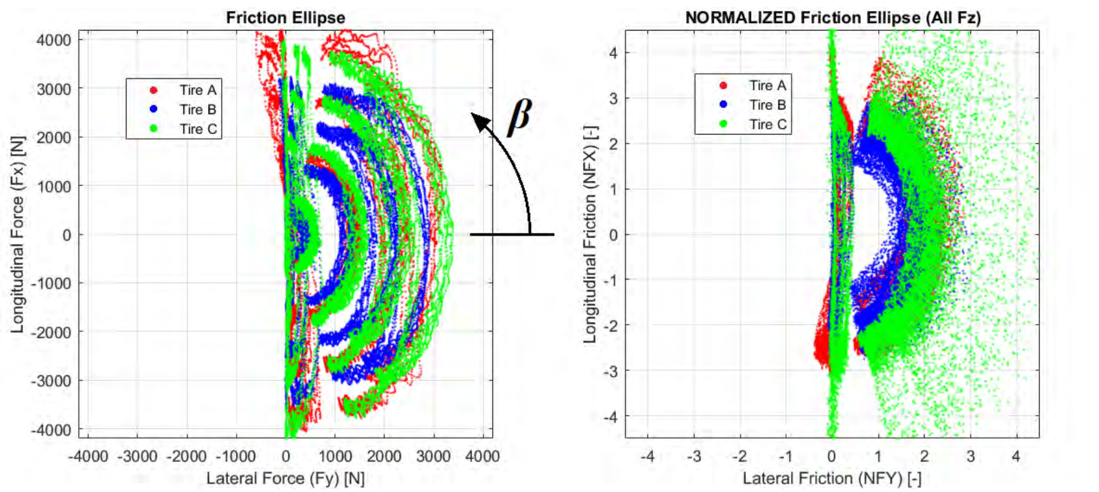


Fig. 4 The Friction Ellipse

| FRICTION ELLIPSE. Avg. F_res | Tire A | | | | Tire B | | | | Tire C | | | |
|---|---|---|---|---|---|---|---|---|---|---|---|---|
| 'Normal Force (Fz) [N]' | 205 | 655 | 1087 | 1541 | 204 | 667 | 1090 | 1540 | 203 | 666 | 1093 | 1544 |
| 'Beta = 60-90 [deg]' | 380 | 1527 | 2582 | 3627 | 344 | 1309 | 2089 | 2823 | 634 | 1720 | 2581 | 3372 |
| 'Beta = 30-60 [deg]' | 384 | 1499 | 2505 | 3416 | 380 | 1393 | 2282 | 2946 | 651 | 1708 | 2515 | 3353 |
| 'Beta = 0-30 [deg]' | 383 | 1383 | 2267 | 2932 | 387 | 1285 | 2060 | 2557 | 586 | 1525 | 2289 | 2998 |
| 'Beta = (-30)-0 [deg]' | 428 | 1415 | 2168 | 2837 | 407 | 1276 | 2028 | 2694 | 600 | 1517 | 2250 | 3029 |
| 'Beta = (-60)-(-30) [deg]' | 517 | 1609 | 2515 | 3349 | 447 | 1429 | 2308 | 3065 | 659 | 1688 | 2525 | 3447 |
| 'Beta = (-90)-(-60) [deg]' | 544 | 1644 | 2599 | 3497 | 419 | 1374 | 2229 | 3044 | 661 | 1722 | 2671 | 3623 |
| Points relative to Tire A | | | | | | | | | | | | |
| 'Beta = 60-90 [deg]' | 100 | 100 | 100 | 100 | 90 | 86 | 81 | 78 | 167 | 113 | 100 | 93 |
| 'Beta = 30-60 [deg]' | 100 | 100 | 100 | 100 | 99 | 93 | 91 | 86 | 170 | 114 | 100 | 98 |
| 'Beta = 0-30 [deg]' | 100 | 100 | 100 | 100 | 101 | 93 | 91 | 87 | 153 | 110 | 101 | 102 |
| 'Beta = (-30)-0 [deg]' | 100 | 100 | 100 | 100 | 95 | 90 | 94 | 95 | 140 | 107 | 104 | 107 |
| 'Beta = (-60)-(-30) [deg]' | 100 | 100 | 100 | 100 | 87 | 89 | 92 | 92 | 127 | 105 | 100 | 103 |
| 'Beta = (-90)-(-60) [deg]' | 100 | 100 | 100 | 100 | 77 | 84 | 86 | 87 | 122 | 105 | 103 | 104 |
| AVERAGE | 100 | | | | 89 | | | | 114 | | | |

Table 3 Summarize average $F_{res}$ values

## 3. FITTING TIRE MODEL TO MEASUREMENT

To analyze tires for more information it is better if we fit tire model to measured points. With it we can get informations on every normal forces, cambers, slip angles, not only that interval where the tire were measured. To fit tire model we used optimum tire softvare from Optimum G [7].

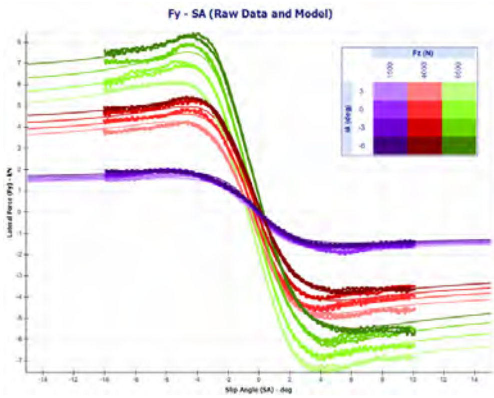


Fig. 5 Fitting tire model to measurements [7]

## 4. GETTING MORE INFORMATION FROM TIRE TO DESIGN SUSPENSION

To design suspension kinematic we have to know which camber and slip angle is the optimal value at different normal forces to get the highest available grip from tire. The problem is that this values are changing by $\beta$ angle (on *figure 6*) in friction ellipse. To get this information we investigated a tire and we wrote a script in MATLAB to make tables and plots to show optimal camber, slip angle and slip ratio values in case of we want maximum resultant force.

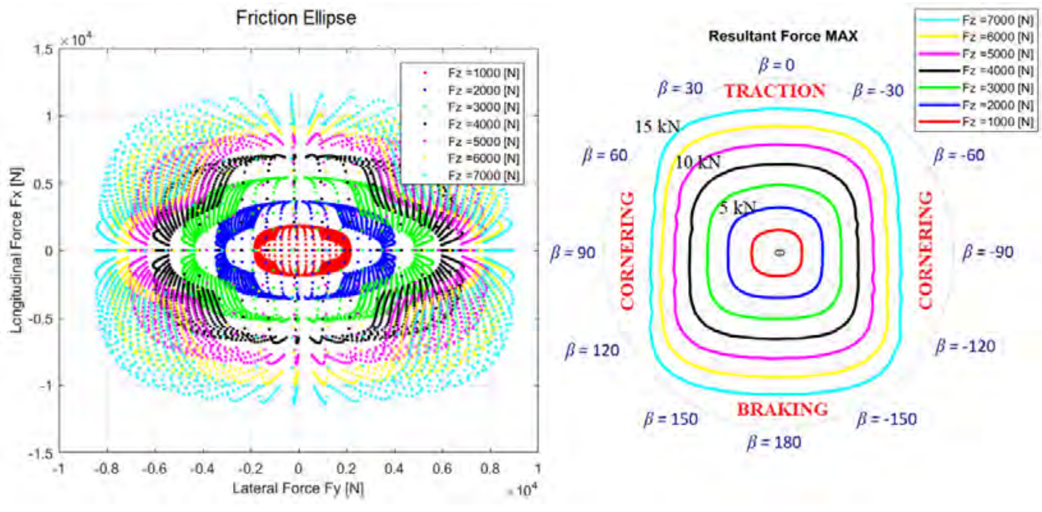


Fig. 6 Friction ellipse and maximum resultant force at function of beta angle

We found the maximum $F_{res}$ value for each beta angles at diferent normal forces of 1-7 kN, which can be seen at right of *figure 6* and top-left of *figure 7*. After it, we get the camber, slip angle and slip ratio values which belong to the maximum $F_{res}$.

Figure 7 contains a lot of information from the tire. At first we can see, in case of longitudnail traction ($\beta$ = 0) the optimal slip ratio is 0.12 - 0.125 in low normal forces (1-3 kN), but if we have more normal load on tire the optimal slip ratio is less (0.06-0.09). In case of braking ($\beta$ = 180), the tendency is the same, the optimum slip ratio is changing between (-0.07) – (-0.12) by increasing normal force. These information can be useful if we want to design ABS or ESP systems.

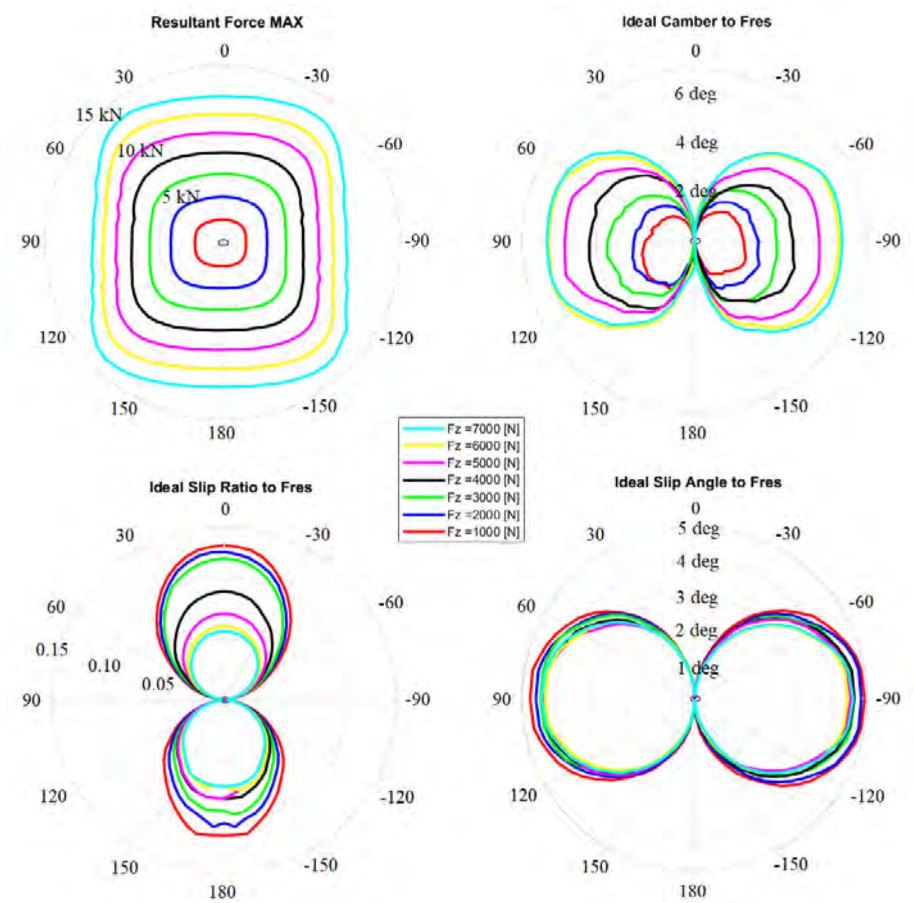


Fig. 7 Ideal camber, slip ratio and slip angle values of tire if we want maximum grip

At second, in case of cornering ($\beta$ = 90 & -90), optimal slip ratio (4.5-5 degrees) can be useful information if we design steering system, mainly for ackerman parameters. If we know how much camber gain we need, we will have easier task during designing suspension kinematic. As you can see at top - right of *figure 7* optimal camber is changing depending on we are accelerating or cornering or both of them. The optimal camber is zero if we are braking or accelerating in straight direction, but at mid turns we need more camber. If the lateral weight transfer is so high and our outer tire normal load is about 6-7 kN, we will need more camber (6 degrees).

## 5. CONCLUSION

With these information we can get the optimum values of slip and camber values for suspension. At *table 4* we can see an example, how can we use the diagrams in *figure 7*.

| Colours: | | |
|---|---|---|
| | FL | FR |
| | RL | RR |

| Braking + Cornering | | |
|---|---|---|
| Weight | 1400 | [kg] |
| Weight distr. Front | 60 | [%] |
| Long. Acc | -0.6 | [G] |
| Lat. Acc. | 0.6 | [G] |
| Wheelbase | 2700 | [mm] |
| Track | 1900 | [mm] |
| Height of CoG | 500 | [mm] |

| Braking + Cornering | |
|---|---|
| Longitudinal Weight Transfer [N] | -1526 |
| Lateral Weight Transfer [N] | 2169 |
| Angle of Acceleration (Beta) [deg] | 135 |

| STATIC Fz [N] | | DYNAMIC Fz [N] | |
|---|---|---|---|
| 4120 | 4120 | 3799 | 5967 |
| 2747 | 2747 | 900 | 3068 |

| Optimum for max grip | | | | | |
|---|---|---|---|---|---|
| Camber [deg] | | Slip Angle [deg] | | Slip Ratio [-] | |
| 3.6 | 5.0 | 3.1 | 3.0 | 0.055 | 0.048 |
| 2.2 | 3.0 | 3.3 | 3.1 | 0.072 | 0.060 |

| Cornering | | |
|---|---|---|
| Weight | 1400 | [kg] |
| Weight distr. Front | 60 | [%] |
| Long. Acc | 0 | [G] |
| Lat. Acc. | 0.8 | [G] |
| Wheelbase | 2700 | [mm] |
| Track | 1900 | [mm] |
| Height of CoG | 500 | [mm] |

| Cornering | |
|---|---|
| Longitudinal Weight Transfer [N] | 0 |
| Lateral Weight Transfer [N] | 2891 |
| Angle of Acceleration (Beta) [deg] | 90 |

| STATIC Fz [N] | | DYNAMIC Fz [N] | |
|---|---|---|---|
| 4120 | 4120 | 2675 | 5566 |
| 2747 | 2747 | 1301 | 4192 |

| Optimum for max grip | | | | | |
|---|---|---|---|---|---|
| Camber [deg] | | Slip Angle [deg] | | Slip Ratio [-] | |
| 3.5 | 5.7 | 4.9 | 4.7 | 0.000 | 0.000 |
| 2.1 | 4.3 | 5.5 | 4.8 | 0.000 | 0.000 |

Table 4 An example for optimum values of the suspension in two situation

We can calculate weight transfer, and normal forces on each tires in every situation. After that, according to *figure 7* datas, we can see the optimal values for tire. If we do this tables for every case, we will know all of information from tire to design the best suspension for our car.

## 6. ACKNOWLEDGMENTS

The research presented in this paper was carried out as part of the EFOP-3.6.2-16-2017-00016 project in the framework of the New Széchenyi Plan. The completion of this project is funded by the European Union and co-financed by the European Social Fund.

## 7. REFERENCES

[1] **Pacejka, H. B.:** Tyre and vehicle dynamics, Elsevier, 2002.

[2] **Milliken, W.F. and Milliken, D.L.:** Race car vehicle dynamics, Society of Automotive Engineers, Inc, U.S.A, 1995.

[3] **Vorotovic, G. S. - Rakicevic, B. B. – Mitic, S. R. and Stamenkovic, D. D.:** Determination of Cornering Stiffness through Integration of a Mathematical Model and Real Vehicle Exploitation Parameters, Faculty of Mechanical Engineering, Belgrade.

[4] **Doumiati, M. - Victorino, A. - Charara, A. – Lechner, D.:** Estimation of vehicle lateral tire-road forces: a comparison between extended and unscented Kalman filtering. ECC 09, Aug. 2009, Hungary. p.6, 2009.

[5] **Kasprzak, E. M. and Gentz, D.:** The Formula SAE Tire Test Consortium—Tire Testing and Data Handling, 2006, Society of Automotive Engineers, Inc.

[6] **Li, Li - Wang, Fei-Yue - Zhou, Qunzhi:** Integrated Longitudinal and Lateral Tire/Road Friction Modeling and Monitoring for Vehicle Motion Control. IEEE Transactions on Intelligent Transportation Systems. 7. 1 - 19. 10.1109/TITS. 2005.858624, 2006.

[7] **http://www.optimumg.com/software/optimumtire/** (accessed on Oct. 2018)

# INVESTIGATING THE EFFECTS OF ROLL CENTER HEIGHT, DURING TRANSIENT VEHICLE MANEUVERS

**Attila WIDNER and Gergely BÁRI**

Department of Vehicle Technologies
John von Neumann University
H-6000 Kecskemét, Hungary

*Received: November 5, 2018*

## ABSTRACT

The future of mobility is about autonomous vehicles, therefore the number of research on this subject are greatly increasing. There is a wide range of papers about control algorithm development and deep learning. Our aim is to investigate the grip limit behavior of the vehicles to define the so-called “safety-margin”. We consider this topic important, because to avoid collision the autonomous vehicle must be capable of rapid maneuvers. To define safety-margin a simulation environment is necessary, which must meet several different requirements. In a previous paper, we presented our requirements and selected the software. Also our validation process was introduced through two examples. This paper focuses on the first part of the validation process, which is face validation. The effects of roll-center-height were investigated in the course of transient test cases. Suspension geometry besides the kinematics (camber-gain, bump-steer,…) has a significant effect on the direction and magnitude of the forces that act on the chassis, therefore it influences load transfer, jacking force, anti-dive, anti-squat, anti-lift parameters. Effects of suspension-geometry were on the load transfer investigated in a previous paper with a steady-state skid pad test case. Furthermore, also a steady-state straight run simulation was carried out with different toe angles to investigate jacking force effect. To see, how the load transfer is building up, a transient step-steer and a “step-brake” simulation were carried out. The face validation showed reasonable values. In theoretical level the chosen software is suitable to analyze vehicle behavior in the grip limit.

*Keywords:* vehicle dynamics, roll center height

## 1. INTRODUCTION

The aim of our project is to create a framework which is suitable for the vehicle’s grip limit behaviour analysis during autonomous vehicle control algorithm development. The research has two major parts we are investigating the vehicle behaviour on the grip limit to define the so-called safety-margin. We are working on different methods that can be applied for this purpose: MRA Moment Method, Vehicle dynamics software. And we are also working on different sub-projects in connection with self-driving algorithm development, such as ideal line, Hardware in the loop tests.

For the previously mentioned purpose, a simulation environment was chosen, based on the information that we could gather. Besides others, we took into consideration the following main aspects: hardware in the loop module, sensor simulation (radar, lidar…), integration of Matlab/Simulink. To make sure that the previously chosen software is suitable for our needs a validation procedure was executed.

These vehicles do not operate in the tire saturation region close to the grip limit under normal conditions therefore this field is not commonly researched. Although, when it comes to collision avoidance it must operate in the above-mentioned region to be capable of rapid manoeuvres. In this case, it is crucial that the controller has the proper information about the movement change ability of the vehicle. As mentioned above the griplimit behaviour is not generally investigated therefore, the vehicle dynamics simulation software tend to oversimplify suspension parameters and phenomenons that has a significant effect in these cases. Also, most of the time, the team which developed the model also decides if the simulation is valid. [1] Therefore, it is important to validate the simulation environment for this research. We investigate if the parameter changes create the expected changes in vehicle behaviour.

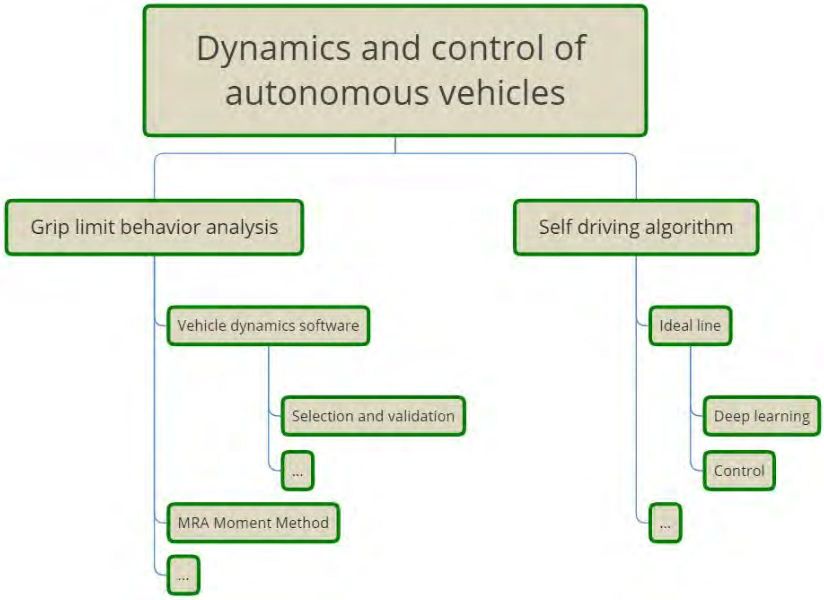


Fig. 1 Research structure

IPG Carmaker was selected for this project based on our previous work [2]
This paper introduces the next step of the validation process focusing on transient test cases. The effects of roll and pitch centre height was investigated.

## 2. PREVIOUS SIMULATION RESULTS

All simulations were carried out in IPG Carmaker with a front wheel drive passenger car, defined as an example car in Carmaker. The roll centre height and pitch centre height of the front suspension was changed by the modified inner pick-up points of the MacPherson suspension. More details in [2].
In a previous paper we investigated the effects of roll centre height in steady state test cases. A steady-state skid pad simulation was carried out to investigate the effect of roll centre on load transfer. The results showed that the higher the roll centre the larger the roll stiffness of the given axle which cause larger load transfer distribution on that axle – it is in compliance with the theory. Also, the total load transfer was higher, which is the result of the larger jacking force. The jacking force was also investigated with a straight run simulation with different toe angles, to see how does the roll centre height effect the jacking force. All expected phenomena occurred so far.

When the manoeuvrability of a vehicle is concerned it is not enough to analyse steady-state behaviour, therefore the following step of the validation process is transient simulation.

## 3.TRANSIENT MANEUVERS

Roll centre and pitch centre has an effect on the forces and torques acting on the chassis. Therefore, it influences chassis movement such as roll and pitch, and load transfer. Load transfer can be divided into suspended and non-suspended load transfer. Also, the suspended load transfer can be divided into geometric – which develops quickly, proportionally with the lateral acceleration - and elastic – which is transferred by the elastic parts of the suspension (ride springs, dampers). [3]

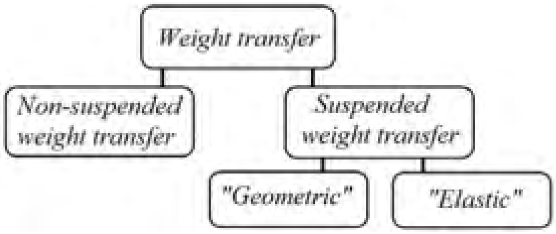


Fig. 2 Load transfer [3]

Roll and pitch centre height has an effect on geometric load transfer.

### 3.1 Step-steer simulation

To investigate the development of load transfer a transient step steer simulation was carried out. Three front suspension were analysed a basic, one with a higher and one with roll centre below the ground level.

The vehicle rides on a straight flat surface, velocity is 100 km/h. A step steer manoeuvre was executed, steering wheel angle is 30 degree which results in wheel steering angle of 1,5 to 2 degree (lower values on the outside wheels, higher on the inside, according to the Ackermann geometry). We applied small wheel steering angles to minimize the effect of king pin geometry (the effect of king-pin inclination is about 3N load transfer in this case, which is negligible). To have sufficient load transfer with low steering angles, high speed was applied.

Roll centre height has an influence on the development of load transfer. The higher the roll centre, the faster the load transfer.

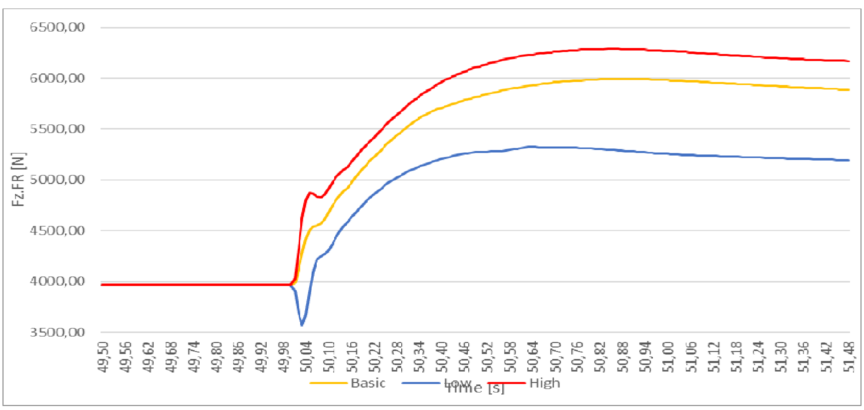


Fig. 3 Front right tire normal force

The tire normal force of the front right suspension can be seen on Figure 2. As the results show the higher the roll centre the faster the load transfer. Also, in Figure 3 you can see the derivative of Figure 1. it shows the velocity of load transfer and it underlines the above-mentioned phenomenon.

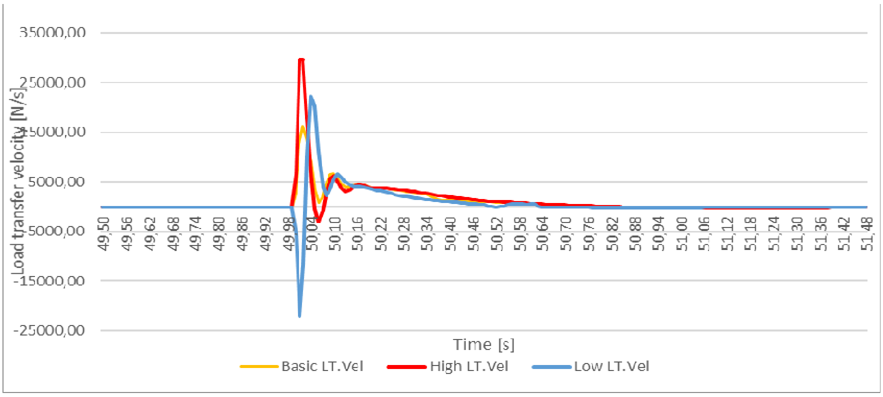


Fig. 4 Load transfer velocity

Another phenomenon can be seen on Figure 2 and Figure 3. In case of the low roll centre suspension – RC below ground level – in the initial moments the load transfer is opposite, so the normal force is increasing in the curve inner tire contact point – geometric load transfer – until the elastic load transfer develops. Also, by the different roll centre height the roll stiffness of the given suspension is changed. It is manifested by the different amount of load transfer Figure 2.

### 3.2 Step-brake simulation

When it comes to longitudinal dynamics, pitch center has similar effects as the roll center on the lateral dynamics. [4]

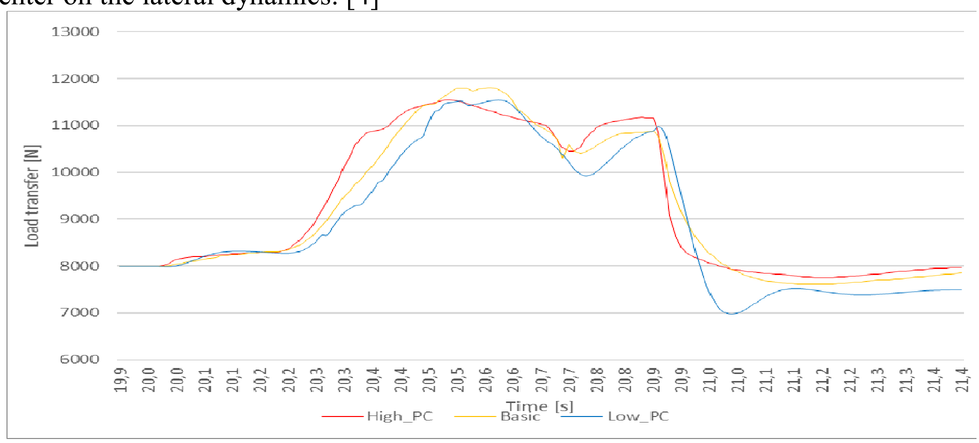


Fig. 5 Load transfer during step brake simulation

Three different pitch centre height were investigated – basic, lower and higher.

The vehicle rides with 20 km/h and then maximal brake pressure is applied. We investigated the effects of pitch centre on load transfer development.
Figure 4 shows the front axle load which is the sum of the front tire's normal force. The vehicle with the higher pitch center has a higher anti-dive value, the load transfer develops more quickly in this case, because smaller the elastic portion of the load transfer. This phenomenon is in compliance with the theory.
Pitch center has an effect on the chassis movement. The smaller the distance between pitch center and center of gravity the higher the pitch stiffness of the chassis. [4] As it can be seen on Figure 5. in case of higher pitch center, the pitch of the vehicle is smaller.

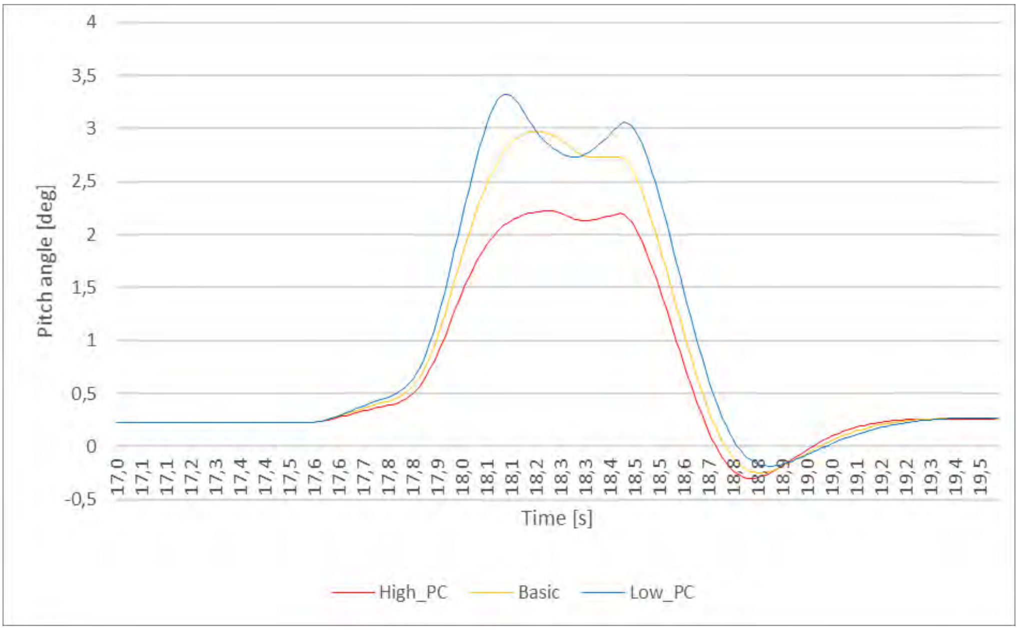


Fig. 6 Pitch angle of the vehicle body

## 4. CONCLUSION

Simulation results showed that every investigated phenomenon is in compliance with the theory, therefore there are no significant simplification. Although the investigated simulation environment seems to be suitable for our project, more investigation is necessary for example the comparison of simulation results with experimental test data.

## 5. ACKNOWLEDGMENTS

The research presented in this paper was carried out as part of the EFOP-3.6.2-16-2017-00016 project in the framework of the New Széchenyi Plan. The completion of this project is funded by the European Union and co-financed by the European Social Fund.

## 6. REFERENCES

[1] **Kutluay, E. and Winner, H.:** Validation of vehicle dynamics simulation models – a review, Vehicle System Dynamics, 2014, p.186-200.
[2] **Widner, A. – Bári, G.**: Investigating the effects of roll center height in simulation, for safety-margin research. IOP Conf. Series: Materials Science and Engineering 393 (2018)
[3] **Rouelle, C.**: Applied Vehicle Dynamics Seminar (Graz, 29. Sept.– 1. Oct.,2015)
[4] **Milliken, W.F. and Milliken, D.L**.: Race car vehicle dynamics. (Warrendale: Society of Automotive Engineers), 1995

# YAW RATE CONTROL FOR ENHANCING VEHICLE STEERING BEHAVIOR

**Zakariás ERŐSDI and Gergely BÁRI**

Department of Vehicle Technology
GAMF Faculty of Engineering and Computer Science
John von Neumann University
H-6000, Kecskemét, Izsáki út 10. Hungary

*Received: November 5, 2018*

## ABSTRACT

Vehicle steering behavior and steering response is a key aspect for vehicle safety. Therefore we can see the automotive industry to focus on stability systems such as Auto breaking system, electronic stability control and traction control. These systems are put to the test at sudden situations, when the driver makes an unexpected maneuver to avoid collision. In such situations, the car has to maintain a stable state to avoid accidents. This kind of systems can be well analyzed if we apply them on a racecar. A racedriver always tries to operate the car on it's limit. Therefore the controller can show it's benefit in everysingle curve, as it not only makes the driver more confident, but actually makes the car more agile, which can be directly observed on lap times. This paper presents a yaw rate control for enhancing a 4WD, fully electric Formula Student type car's overall performance on track. The torque vectoring strategy is realized by individually controlling each powertrain with in-wheel motors. The control itself is realized in two layers. The first layer defines the needed additional yaw moment, while the second layer distributes the torque between the motors in such way, that this additional moment is fulfilled. The first layer is examined with two different methods, a classical PID controller, and an MPC controller. The controller is tested and tuned based on simulations conducted in Carmaker/Simulink environment. The control itself is realized in Simulink, and it is applied on a vehicle model that can be tested in various situations. The main focus is on simulating sudden maneuvers, where a car without control would normally lose its stability, like slaloms, step-steering, and so on. It is deducted that the control strategy significantly improves the vehicles maneuverability. The vehicle stays stable in numerous situation when an uncontrolled car doesn't, and the overall agility of the car is increased, making the car faster on track.

*Keywords:* torque, vectoring, yaw, control, vehicle, dynamics

## 1. INTRODUCTION

An ordinary driver's, main expectation towards the car is to respond to the steering movements accurately, quickly and steadily in all circumstances, regardless of the situation. Therefore the automotive industry has been working on many different advanced driver assistance system (ADAS), to help the driver in the driving process. The most frequently used systems like ESC (electronic stability control) and ABS (anti-lock braking system) actuate the brake system in order to help out the driver in unexpected situations[1].

Another, less widespread controlling technique is TV (torque vectoring), wich helps the driver by applying different torques to the wheels[2]. Thisway, an additional yaw-moment can be generated, that helps the driver in various cases. In order to realize this, a rather complex differential has to be made[3], but with the electric cars gaining space in the automotive industry, this method could be used more often, if we just think about wheel hub motors.

In the present work, we have developed a torque vectoring technique, a yaw rate control for a 4WD, fully electric Formula Student type car, in order to increase its performance on track. In the case of a racecar, at each corner, the car is close to grip limit, so testing such a system in this kind of scenario can give us a good insight about the control's behaviour in sudden, unexpected maneuvers in case of a casual driver. The yaw rate control's purpose is to minimize the vehicle under / oversteering in any situation.

## 2. MATHEMATICAL MODEL

In order to develop a control that helps the driver in cornering, we need to analyse the steering behaviour of an uncontrolled vehicle. For this purpose a "bicycle model" or single track vehicle model is used. This model is simple enough to calculate it real time for controlling purposes, yet it gives us a good insight of the vehicle's cornering dynamics[4].

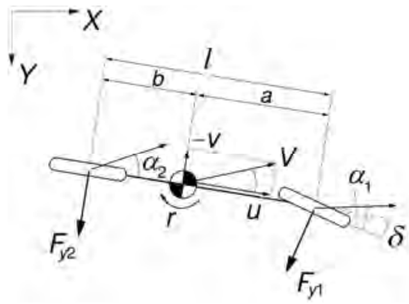


Fig. 1 Bicycle model

Equations of motion:

$$m(\dot{v} + u \cdot r) = F_{y1} + F_{y2} \tag{1}$$
$$I\dot{r} = a \cdot F_{y1} - b \cdot F_{y2} \tag{2}$$

Tire side slip angles:

$$\alpha_1 = \delta - \frac{1}{u}(v + a \cdot r),\ \alpha_2 = -\frac{1}{u}(v - b \cdot r) \tag{3}$$

Linear cornering stiffnesses:

$$F_{y1} = C_1\alpha_1,\ F_{y2} = C_2\alpha_2 \tag{4}$$

Vehicle side slip:

$$\beta = -\frac{v}{u} \tag{5}$$

After substitution and after elimination of $v$, and looking at the equation in steady state ($\ddot{r} = 0,\ \dot{r} = 0, \dot{\delta} = 0$ ) the resulting equation:

$$\frac{1}{u}\left(C_1C_2l^2 - m \cdot u^2(aC_1 - bC_2)\right)r = C_1C_2l\delta \tag{6}$$

If we assume that $\beta$ is small, the radius of a corner can be written as:

$$R = \frac{V}{r} \approx \frac{u}{r} \tag{7}$$

So the required steering angle in steady-state for a curve with a radius of R:

$$\delta = \frac{l}{R} - \frac{mV^2}{Rl}\left(\frac{a}{C_2} - \frac{b}{C_1}\right) \tag{8}$$

The lateral acceleration reads:

$$a_y = \frac{V^2}{R} \tag{9}$$

So the required steering angle can be written as:

$$\delta = \frac{l}{R} + \frac{a_y}{g}\left(\frac{mg}{l}\left(\frac{b}{C_1} - \frac{a}{C_2}\right)\right) = \frac{l}{R} + \frac{a_y}{g}\mu\,, \tag{10}$$

where $\mu$ is the understeer coefficient. This means that for a given corner with a radius of $R$, and a given steering angle, $\delta$ if the driver wants to stay on trajectory, he have to have a zero understeer coefficient, otherwise he have to decrease the velocity of the car. A zero understeer coefficient, according to this model, for an ordinary car (same tire on each wheel) can be reached if the center of gravity is in the middle of the wheelbase ($a = b$).

Unfortunately, in real life, this model has it`s limits. In transient situations, and when the vehicle side slip is high, over and understeering occurs, even in case of a well designed car.

For such situations, a yaw rate control could be useful. This control basically calculates the ideal yaw rate, that the car would have in steady state and compensates the error that the car`s actual yaw rate differs during transient situations, making the car more agile, helping the driver to reach the steady state faster.

The steady state yaw rate can be computed from the upper mentioned equations:

$$r_d = \frac{v}{(a+b)+k_{us}v^2} \cdot \delta, \tag{11}$$

where

$$k_{us} = \frac{m(bC_2 - aC_1)}{(a+b)C_1C_2}\,. \tag{12}$$

## 3. CONTROL STRATEGY

In order to achieve this desired yaw rate, we have to actuate the in-wheel motors differently. For this, a two-layer controller is proposed. The first layer calculates a desired $M_{COG}$, an additional torque that acts on the z-axis of the car, and the second layer, that distributes the torques on the wheels in such way, that this $M_{COG}$ is fulfilled.

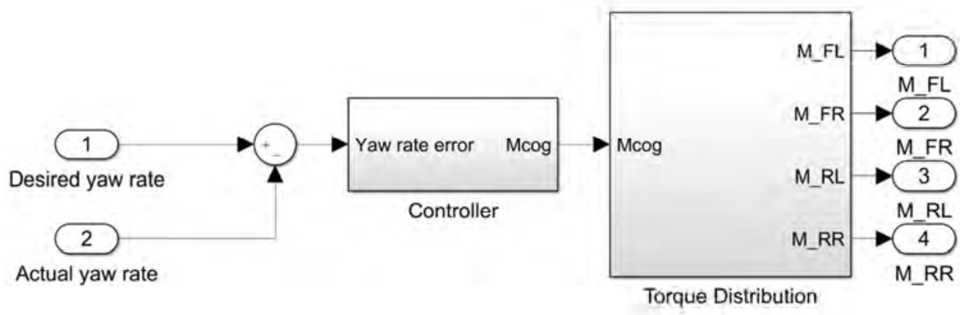


Fig. 2 Control system structure

### 3.1 Torque distribution

Many different torque distribution strategies could be developed, that fulfil this $M_{COG}$ criteria, yet the car would perform differently with each strategy. Enough if we just think of a situation, where a wheel touches a puddle. In this current work the only additional constraint that is in consideration is the normal force acting on each wheel.

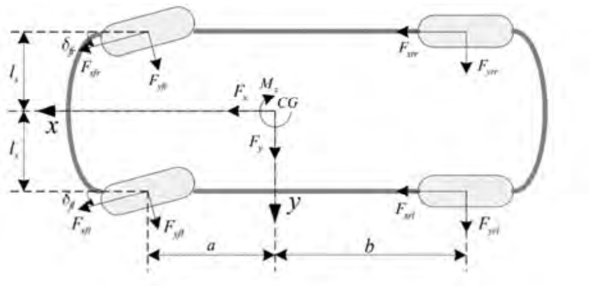


Fig. 3 Forces acting on a car

The equation of moment, acting only due to the forces on the x axis, assuming that the front and rear track of the wehhicle is the same:

$$M_z = l_s(F_{xFL} + F_{xRL} - F_{xFR} - F_{xRR}) \tag{13}$$

We neglect the forces acting in y direction, as they are not directly dependent of the wheel torque, so we can not directly actuate the $Mcog$ with them.
Now we just look at how much force we need on one side of the vehicle for a given $M_z$, and a given wheel radius, $R$:

$$R(F_R - F_L) = M_z \tag{14}$$

For a known accelerating force $F = F_R + F_L$, resulting from the acceleration pedal position, this equation modifies to:

$$R(F - F_L) - RF_L = M_z \tag{15}$$

So we can calculate the force needed for one side of the vehicle:

$$\frac{1}{2}\left(F - \frac{M_z}{R}\right) = F_L \tag{16}$$

The other side can be calculated as well. The additional distribution between the front and the rear axle is proportional with the normal force distribution of the wheels. This way we can use the tire's force capacity better, as each tire produces bigger force with bigger load. The normal force distribution with the center of gravity being in the middle of the wheelbase and with equal track lengths on front and rear axels can be calculated:

$$F_z = \frac{m \cdot g}{4} \pm m\frac{h}{2 \cdot l}a_x \pm m\frac{h}{2 \cdot t}a_y \tag{17}$$

## 4. CONTROL METHODS

For minimizing the yaw rate error, multiple control methods could be used. In the current work we have examined a classical PID controller and a more complex, MPC controller, to see how these affect the steering behaviour of the car. The controllers were tested in Carmaker/Simulink environment. Three driving scenarios were considered, a given steering angle profile with a constant acceleration pedal position, a slalom, and a skid-pad manoeuvre.

### 4.1 PID controller

With this control method, the desired additional torque results directly from the yaw rate error. The parameters were tuned in the simulation environment. The resulting parameters actually came with zero derivative term, so the transfer function between the $M_{COG}$ and the yaw rate error is the transfer function of a PI controller, that can be written as:

$$\frac{M_{COG}(z)}{r_d(z)-r(z)} = W(z) = P + I \cdot T_s \cdot \frac{1}{z-1} \tag{18}$$

$$P = 1000, \qquad I = 100, \qquad T_s = 0.005$$

A problem with this approach is that the bicycle model, and the steering behaviour is velocity dependent. So basically we would need to tune the controller for each velocity separately. A solution for this problem can be a state-space control, that recalculates the optimal control input in each state for the actual velocity.

Another problem is that the vehicle sideslip is neglected. This way, for big yaw rates, the controller would give big values of torques for one side of the vehicle, but after a certain point, vehicle side-slip can not be neglected, as the upper-mentioned ideal yaw-rate formula is only valid for small side slip values. Another constraint has to be fulfilled by the controller: keep the side slip close to zero.

### 4.2 MPC controller

Basing on the bicycle model, the space-state of the vehicle, with slip angle and yaw rate as state variables can be written as:

$$\begin{bmatrix} \dot{\beta} \\ \dot{r} \end{bmatrix} = \begin{bmatrix} \frac{-2(C_1+C_2)}{m \cdot u} & \frac{2(C_2 l_2 - C_1 l_1)}{m \cdot u^2} - 1 \\ \frac{2(C_2 l_2 - C_1 l_1)}{I} & \frac{-2(C_1 {l_1}^2 + C_2 {l_2}^2)}{I \cdot u} \end{bmatrix} \cdot \begin{bmatrix} \beta \\ r \end{bmatrix} + \begin{bmatrix} \frac{2C_1}{m \cdot u} \\ \frac{2 l_1 C_1}{I} \end{bmatrix} \cdot \delta + \begin{bmatrix} 0 \\ \frac{1}{I} \end{bmatrix} \cdot M_z \tag{19}$$

In our case, for a given $\delta$ the yaw rate error is calculated, based on this same model, so for the state-space controller, the input matrix is only $\begin{bmatrix} 0 \\ \frac{1}{I} \end{bmatrix}$, with the input being the additional $M_{COG}$ that has to be fulfilled by the torque distribution. An MPC controller can calculate the optimal $M_{COG}$ that minimizes the the yaw rate error and the vehicle side slip.

## 5. RESULTS

During the test cases the main thing that we have to look at is the yaw rate error. If the desired yaw rate is higher than the actual, means that the car is understeered, if it is smaller, then the car is oversteered. Another key aspect can be the time of a simulation, as a controlled car, with neutral steer will be more agile, resulting in better laptimes.

### 5.1 Given steering angle profile, with constant acceleration

During the first scenario, the steering input was a given profile, see, and the car was accelerating with constant 9 $\frac{m}{s^2}$. We can clearly see that an uncontrolled vehicle cannot stay on the road, the car slipps off the track, the car is heavily understeered, while in case of a controlled vehicle, the yaw rate error is significantly smaller. The PID due to neglecting the vehicle side slip, has slightly bigger error at some points, but overall both controllers can keep the car controlled during this scenario.

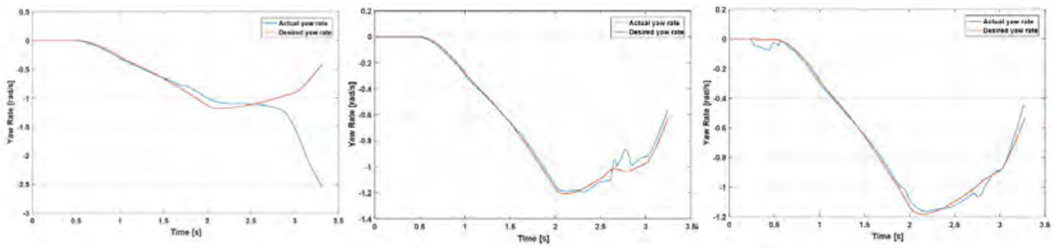


Fig. 4  Yaw rate dynamics of an uncontrolled vehicle, controlled with PID (middle) and controlled with MPC (right)

### 5.2 Slalom

Simulating a slalom can give us a good insight of how the vehicle behaves during transient situations. In each situation, the simulation wanted to reach a lateral acceleration of 18 $\frac{m}{s^2}$.

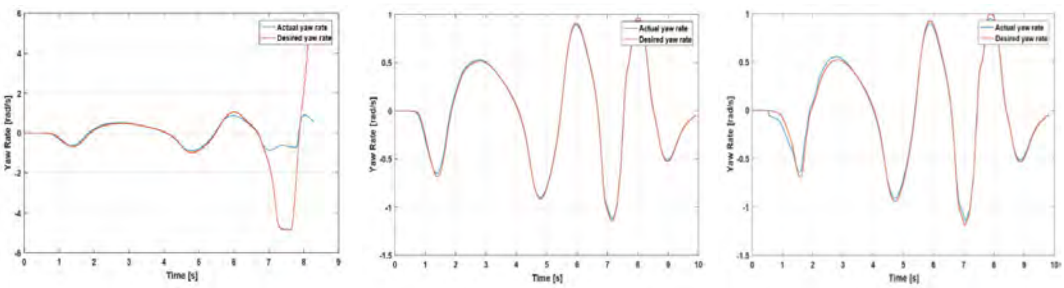


Fig. 5  Yaw rate dynamics of an uncontrolled vehicle during slalom, controlled with PID(middle) and controlled with MPC(right)

An ordinary car, without any additional help got out of control (Fig 5.), and couldn`t finish the slalom with the given constraints, while in the case of a controlled vehicle, the car stays stable, neutral steered during the whole simulation.

### 5.3 Skid-pad maneuver

During a skid-pad maneuver we can see how fast the car reaches the steady state. The simulation wanted to reach 14 $\frac{m}{s^2}$ in case of the uncontrolled vehicle and 16 $\frac{m}{s^2}$ in case of the vehicle equipped with yaw control, because an uncontrolled vehicle was`t able to keep on track with higher lateral acceleration. The car was once again heavily understeered without control.

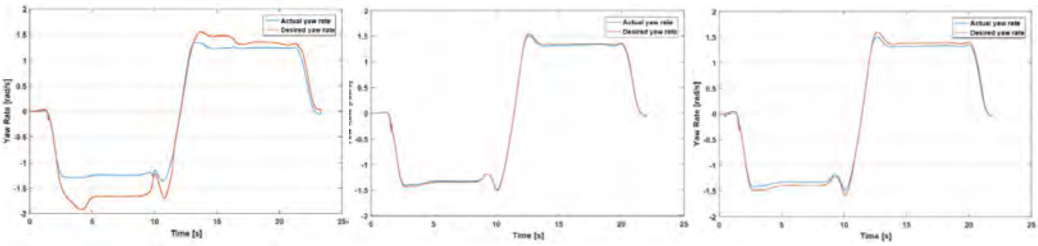

Fig. 6 Yaw rate dynamics of an uncontrolled vehicle during skid-pad, controlled with PID (middle) and controlled with MPC (right)

## 6. CONCLUDING REMARKS

On the basis of our the conducted simulations, we can say that a similar torque vectoring strategy significantly helps the driver in various situation. Using the yaw rate as a key parameter for development of such controls is a practical way to keep the vehicle neutral steered.

Regarding the control method, both PID and MPC controllers produced satisfactory results. For an actual ECU, where real-time runtime is a criteria, implementing a PID controller seems to be the choice as this method does not need that much of computational capacity, and the results did not differ vitally.

## 7. ACKNOWLEDGMENTS

The research presented in this paper was carried out as part of the EFOP-3.6.2-16-2017-00016 project in the framework of the New Széchenyi Plan. The completion of this project is funded by the European Union and co-financed by the European Social Fund.

## 8. REFERENCES

[1] **Jalali, K. – Uchida, T. – Lambert, S. – McPhee, J.:** Development of an Advanced Torque Vectoring Control System for an Electric Vehicle with In-Wheel Motors using Soft Computing Techniques. SAE International Journal of Alternative Powertrains. 2. p.261-278. 10.4271/2013-01-0698.

[2] **Gan, Yihe – Xiong, Lu – Feng, Yuan – Martinez, F.:** A Torque Vectoring Control System for Maneuverability Improvement of 4WD EV. Applied Mechanics and Materials. p.347-350. 10.2991/iccsee.2013.680.

[3] **Hirano, Y.:** Development of an Integrated Control of Front Steering and Torque Vectoring Differential Gear System Using Modelica. p.17-26. 10.3384/ecp 1713217.

[4] **Besselink, I.J.M.**: Mechanical Engineering - Dynamics & Control, Vehicle Dynamics 4L150, Eindhoven University of Technology, lecture notes, 2014

# DIESEL ENGINE CYLINDER-CHARGE COMPOSITION CONTROL WITH HP-EGR AND EXHAUST THROTTLING

**Ádám BÁRDOS[1] and Huba NÉMETH[2]**
[1] Department of Automotive Technologies
Faculty of Transportation Engineering and Vehicle Engineering
Budapest University of Technology and Economics
6 Stoczek St, building J, H-1111 Budapest, Hungary
adam.bardos@gjt.bme.hu,
Phone: +36 1 463 3914
[2] Knorr-Bremse R&D Institute Ltd.
69 Major St, H-1119 Budapest, Hungary
huba.nemeth@knorr-bremse.com,
Phone: +36 1 382 9875.

*Received: November 10, 2018*

## ABSTRACT

Current and next generation emission standards (e.g., Euro 6 and US EPA 13) include significant limitations. The most challenging for diesel engine developers are especially the reduction of particulate matter and nitrogen oxide contents of the exhaust gases. Basically, there are two possibilities to achieve this: exhaust gas aftertreatment and a decrease in raw emissions. Among several methods to handle $NO_x$ and PM emission of diesel engines (e.g., DPF, SCR, etc.) the precise control of cylinder charge composition seems to be a cost-effective solution with high dynamics and can be achieved by exhaust gas recirculation.Current EGR systems concentrate mostly on controlling EGR rates thereby ignoring the quality of the recirculated exhaust gases. The effect of the EGR is caused by the dilution of the cylinder-charge by exhaust gas components (water and carbon dioxide). However, a high EGR rate not necessarily means a high amount of water and carbon-dioxide content in the cylinder-charge because the exhaust gas of diesel engines usually contains large quantities of fresh air due to the lean mixture combustion, especially at part loads. The intake manifold oxygen concentration gives an objective measure of how diluted is the cylinder-charge namely how much is the concentration of the water damp and carbon dioxide in it. Consequently, the proposed control uses the intake gas oxygen concentration as a novel performance output. In HP-EGR systems the amount of the back-flowing exhaust gases is limited by the pressure difference on the EGR duct. In a wide region of the engine operation map, a negative average pressure ratio can occur which means no or not enough EGR mass flow for significant reduction of the $NO_x$ emission. In this paper, the authors present a novel approach to solve this problem: arbitrary EGR mass flow by using exhaust throttling. As a demonstration, a control method was developed and its performance was evaluated by engine dyno measurements. The proposed controller allows a precise intake manifold oxygen concentration adjustment with EGR valve and exhaust flap actuators while minimizing the engine pumping losses.

*Keywords:* diesel engine, emission control, EGR, exhaust throttle, LQ servo control

## 1. INTRODUCTION

Current and next generation emission standards (e.g., Euro 6 and US EPA 13) include significant limitations. The most challenging for engine developers are especially the reduction of PM and nitrogen oxide contents of the exhaust gases.

Exhaust gas recirculation is an effective tool in the limitation of the nitrogen oxides and in combustion control. However, to significantly reduce $NO_x$ emission and especially for the realization of advanced combustion processes the amount of the recirculated exhaust gases need to be adjusted in a wide range. In High-Pressure Exhaust Gas Recirculation (HP-EGR) systems the back-flowing exhaust gas mass flow rate is driven by the pressure difference between the exhaust and the intake manifold. The resulting conditions depend mainly on the turbocharger and its cooperation with the engine so the dilutent gas mass flow is limited. At a wide region of the engine map

the pressure difference is small or negative. The resulting EGR-rate is not enough for significant reduction of the NOx emission. However, emission test cycles use most frequently this part of the engine map. With the application of throttling in the engine air-path, the pressure drop on the EGR duct could be adjusted, and EGR rate could be increased. An exhaust backpressure controller with a variable geometry turbine for turbocharged Spark-ignited (SI) engines was presented in [1] for similar applications.
To be able to reach arbitrarily high EGR mass flow rates the increasing of the exhaust manifold pressure or lowering of the intake manifold pressure gives the opportunity. It can be realized by throttling at four different locations of the intake and exhaust system: upstream and downstream the compressor and upstream and downstream the turbine. However, the effect of throttling at different locations are not equal to the engine performance measures and emission such as BSFC, PM emission, etc.
Models for EGR rate increase with intake throttling are presented in [2],[3]. Preliminary investigations show in [4], that considering the maximum cylinder charge, the most advantageous placements of the throttling is downstream to the turbine. Similar advantages of exhaust side throttling in Low-Pressure Exhaust Gas Recirculation (LP-EGR) systems are shown in [5]. Based on the above results this article gives a novel proposal for the EGR rate increase through exhaust throttling.
Current EGR systems concentrate mostly on controlling EGR rates thereby ignoring the quality of the recirculated exhaust gases [6]. EGR replace or add to the fresh air amount and the recirculated $CO_2$ and water vapor will increase the heat capacity of the cylinder charge. Thanks to the dilution effect of the EGR the oxygen concentration in the cylinder charge also will decrease. More detailed explanation and investigation of the EGR effect can be found in [7].
As it was revealed in [7] the effect of the EGR is based on the dilution effect of the exhaust gas components (water and carbon dioxide) on the combustion process. However, a high EGR rate not necessarily means a high amount of water and carbon-dioxide content in the cylinder charge because the exhaust gas of the diesel engines usually contains large quantities of fresh air due to the lean mixture combustion, especially at part loads. At high lambda values, the exhaust gas contains mostly fresh air, and consequently, its oxygen concentration converges to those of the fresh air. See [8] for details. Moreover, a strong correlation can be observed between lambda, intake manifold oxygen concentration and nitrogen-oxide emission (see [9]).
Based on the above findings this work presents the novel approach of a closed-loop intake manifold oxygen concentration control with a HP-EGR valve and exhaust throttling. For this purpose an LQ servo control structure was developed based on a validated physics-based engine air-path model. As a demonstration, its performance was evaluated by engine dyno measurements.

## 2. SYSTEM DESCRIPTION AND EXPERIMANTAL SETUP

The model was validated on a common rail, medium-duty commercial vehicle, turbocharged and intercooled diesel engine. The engine was equipped with a cooled HP-EGR system. The exhaust throttle valve was installed directly downstream of the

turbine, which provides the minimum volume between the engine exhaust valves and the throttle.
The layout of the test engine is shown in Fig. 1.

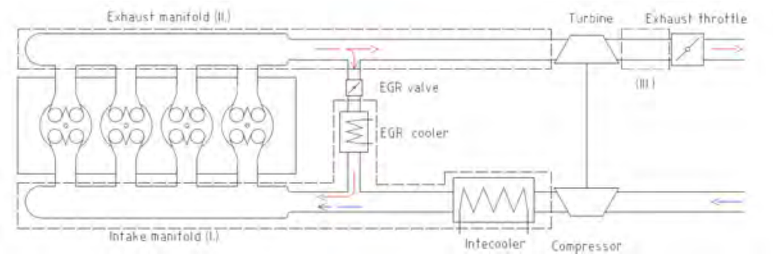


Fig. 1 Schematic drawing of the test engine

The engine was installed on an engine test bench where all the operating parameters of the engine relevant for the system model were measurable. The intake manifold oxygen concentration was measured with a UEGO sensor the signal of which was corrected due to the boost pressure change.

## 3. SYSTEM MODEL DESCRIPTION

For the controller synthesis a first-engineering principles based model was used which is briefly described below. The reader can find a detailed description in [10].
In the engine air path system three balance volumes were chosen: the intake manifold (I.), the exhaust manifold (II.) and the volume between the turbine and the exhaust throttle (III.) (each depicted by dashed lines in Fig. 1).
For the balance volume pressures, the isothermal equation was defined based on the mass conservation and the ideal gas law. The differential equation for the intake and exhaust manifold oxygen volume fractions can be derived from the definition of the intake manifold air mass fraction after manipulations. This way five differential equations were defined for the model state variables. Most theories and techniques in control system design and analysis both in linear and nonlinear control theory are based on state space models. Therefore, the nonlinear model was converted into state space form. The state vector consists of the states of the intake manifold pressure, the exhaust manifold pressure, the pressure of the volume between the turbine and the exhaust throttle and the exhaust and intake manifold oxygen concentrations. The input vector contains the EGR valve and the exhaust throttle flow areas.

$$\mathbf{x} = \begin{bmatrix} p_{im} & p_{em} & p_{to} & x_{O_2,im} & x_{O_2,em} \end{bmatrix}^T, \ \mathbf{u} = \begin{bmatrix} A_{egr} & A_{et} \end{bmatrix}^T \tag{1}$$

The sonic flow condition of the EGR valve and the exhaust throttle and the EGR checkvalve adds hybrid modes to the model. However, in order to arrive at the simplest form of the model the state space equation will be given for the nominal hybrid mode. After inserting the constitutive equations into the differential conservation balances, the state-space model can be obtained in an input-affine form.

$$\begin{bmatrix} \dot{p}_{im} \\ \dot{p}_{em} \\ \dot{p}_{to} \\ \dot{x}_{O_2,im} \\ \dot{x}_{O_2,em} \end{bmatrix} = \begin{bmatrix} f_1(\mathbf{x},\mathbf{d},r) \\ f_2(\mathbf{x},\mathbf{d},r) \\ f_3(\mathbf{x},\mathbf{d},r) \\ f_4(\mathbf{x},\mathbf{d},r) \\ f_5(\mathbf{x},\mathbf{d},r) \end{bmatrix} + \begin{bmatrix} g_{11}(\mathbf{x},\mathbf{d},r) & 0 \\ g_{21}(\mathbf{x},\mathbf{d},r) & 0 \\ 0 & g_{32}(\mathbf{x},\mathbf{d},r) \\ g_{41}(\mathbf{x},\mathbf{d},r) & 0 \\ 0 & 0 \end{bmatrix} \mathbf{u} \tag{2}$$

The performance output is the intake manifold oxygen concentration based on the modeling aim. Detailed model equations, parameter identification and validation results can be found in [10].

## 4. CONTROLLER DESIGN

LQ servo controllers were widely used successfully for numerous nonlinear control problems, see, e.g., [11, 12]. Their low computational demand makes them attractive for embedded implementation. The LQ servo controller is a full state feedback linear quadratic regulator augmented with an additional artificial integral state. Hence, it can track a reference signal. As a consequence, for the intake manifold concentration control the LQ servo control method is proposed.

The artificial state, in this case, is the error signal of the intake manifold oxygen concentration: ($e = x_{im,dem}$-$x_{im}$). The LQ servo control uses full state feedback which minimizes a quadratic cost function of the control input and states energy.

The weighting matrices **R** and **Q** are the tunable parameters of the LQ servo control with appropriate dimensions. Based on the Bryson's law a suitable initial choice was defined for the elements of the weighting matrices.

It can be clearly seen that the actuation of the exhaust throttle could increase the PMEP of the engine. Therefore, while the appropriate dilution of the cylinder charge is possible with the opening of the EGR valve only the exhaust flap needs to hold a fully opened position. The closure of the exhaust flap is only recommended when the EGR valve is saturated in its wide open position. In this context, the above control strategy can be satisfied with the separation of the MIMO system into two Single Input Single Output (SISO) systems: the first aims to track the intake manifold oxygen concentration demand with the control input of the EGR valve only with a constant fully opened exhaust flap. The other controller operates with the exhaust flap opening only with fully opened EGR valve.

Between the two controllers, the following switching logic was implemented: initially the controller with the control input of the EGR valve is actuated. If its EGR flap valve position demand is reached the 90% position, then, the switching logic actuates the other controller which operates with the exhaust throttling while holding a constant wide open EGR valve position. Switching back is occurring when the position control demand of the exhaust flap drops to 50%. Rooting from the nonlinear behavior of the system the exhaust flap valve has an only marginal effect below the 70% position.

The separated state-space models were Jacobian linearized respectively around the operation point of 1250 RPM engine speed and moderate load equilibrium point. With the above-defined weighting matrices and linear SISO state-space systems, the CARE was solved, and the controllers were synthesized in discrete time. The two controllers were implemented in MATLAB/Simulink environment with a sampling time of 1 ms. All the states were measured directly.

## 5. EXPERIMENTAL RESULTS

The implementation was made on a dSpace MicroAutoBox rapid prototyping hardware. There were two stationary measurements taken at 1000 RPM and 1250 RPM. The engine load was 100 Nm at 1000 RPM and 200 Nm at 1250 RPM. Higher loads are not typically suitable for the operation of the intake manifold oxygen concentration controller since the low level of the cylinder charge oxygen content would not allow high fuel injection or at least cause reduced air-to-fuel ratios and consequently high particulate matter emission. All the measurements start with 21 % cylinder charge oxygen concentration demand as a reference. During this initial period, the EGR valve is fully closed, and the exhaust flap is wide opened. After it, steps were performed with one percent increment down until 17% oxygen content.

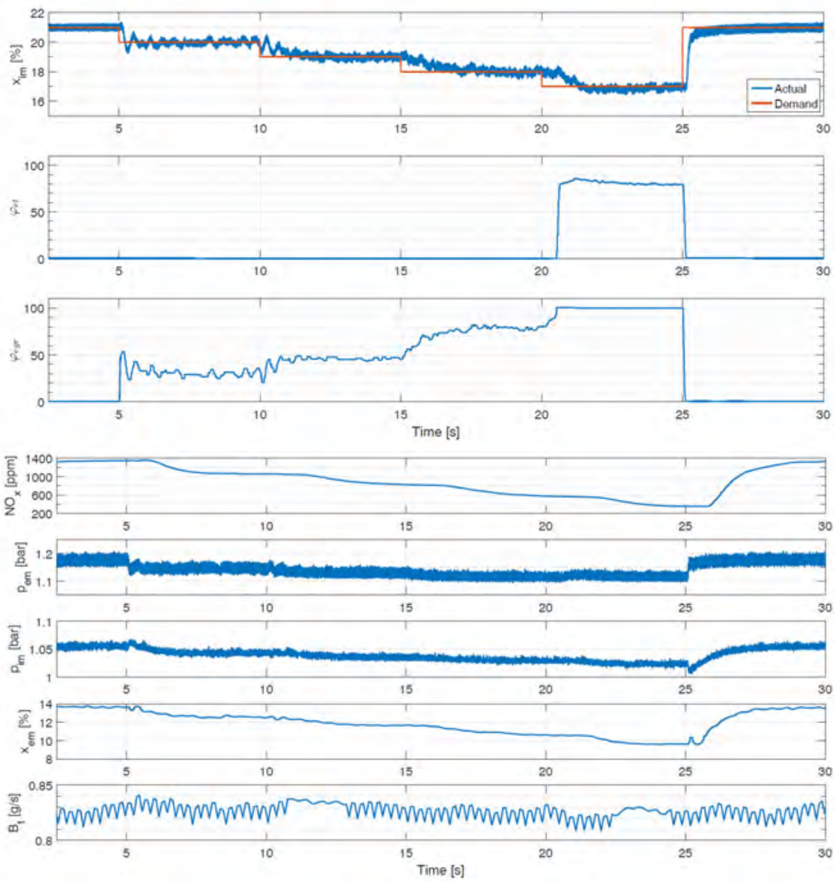


Fig. 2 Cylinder charge control at 1000RPM and 100 Nm

Fig. 2 depicts the measurement results at 1000 RPM with 100 Nm load. The first subplot shows the in-cylinder gas oxygen concentration demand and the actual measured value. The second and the third subplot shows the actual exhaust flap and EGR valve positions, respectively in percentages. As it can be seen, the 18 % oxygen concentration is achievable with the opening of the EGR valve only with the position of approx. 80 %. However, the further opening of the EGR valve makes not possible the realization of the 17 % demand, the EGR valve saturates. Switching takes place between the to above designed LQ servo controller and the closure of exhaust throttle ensure the further increase of the exhaust gas backflow.

The demand is followed accurately during the whole test case. The raw nitrogen-oxide emission decreased from about 1350 ppm to 350 ppm which means a 64 % reduction. Please note that in step from 18 % to 17 % the NOx decreased from 550 ppm to 350 ppm (approx. 37 %) thanks to the actuation of the exhaust throttle. There is no noticeable change in fuel consumption during the whole cycle. During the reference no-EGR period the engine pumping work is negative. The opening of the EGR duct equalizes the pressures between the manifold and as a consequence, the EGR reduces the engine pumping work and consequently increases the engine effective efficiency.

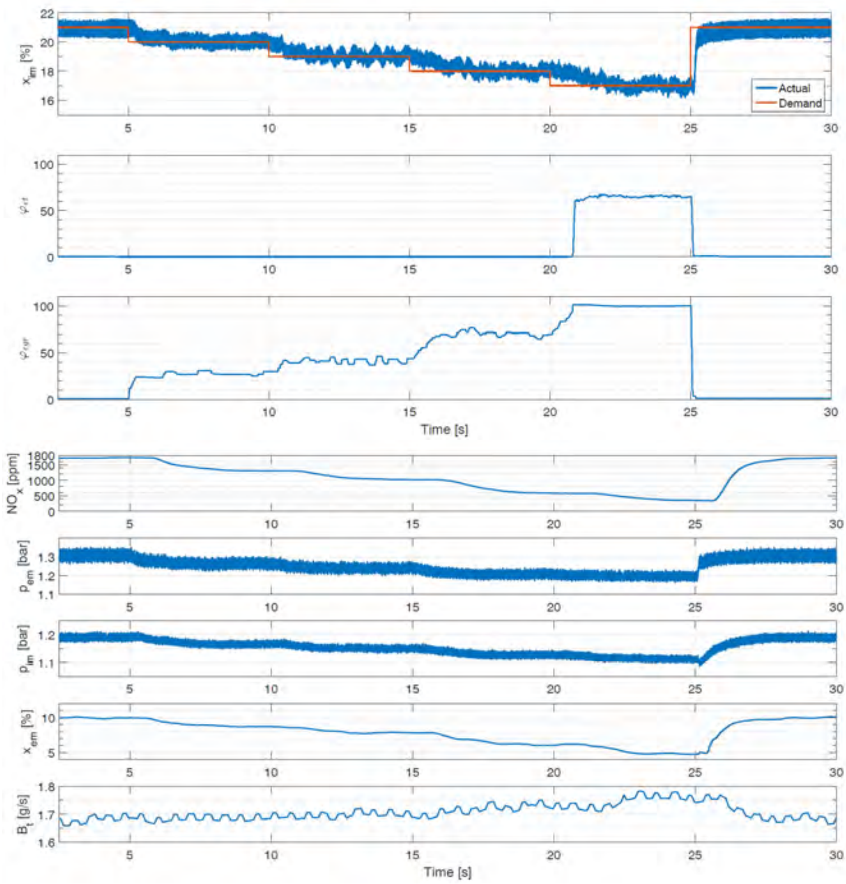


Fig. 3 Controller performance at 1250RPM and 200 Nm

Fig. 3 demonstrates the controller performance in the same step response test demand cycle but the engine speed was increased to 1250 RPM and the load to 200 Nm. It can be seen that the 18 % oxygen concentration can be achieved by opening the EGR valve only similarly to the above operation point. Although, to reach the 17 % oxygen concentration the naturally evolved differential pressure conditions between the intake and exhaust manifold are not enough. Hence, the switching to the controller with the exhaust throttle was done while the control system remained stable. Meanwhile, the EGR valve was held continuously on a fully opened position. It reveals that the actual intake manifold concentration tracks within a 0.1% range the demand. In the fourth subplot line the raw $NO_x$ emission can be seen measured by a $NO_x$ sensor. The designed control structure decreases the exhaust gas $NO_x$ concentration from the initial 1716 ppm to 346 ppm, as expected, correlating with the cylinder charge gas composition. Notably, the application of the exhaust throttling resulted in a decrease from 580 ppm to 346 ppm. At this higher load, a slight increase (from 1.69 g/s to 1.75 g/s which means 3.5 %) can be observed due to the reduction of the air-to-fuel ratio.
It reveals the recommended operating range of the proposed cylinder charge control structure: at low loads where the combustion air-to-fuel ratios are high the dilution of the cylinder charge reduces the $NO_x$ emission significantly but not affects the fuel consumption. Moreover, at a such high air-to-fuel ratio there is probably no significant PM emission occurs.

## 6. CONCLUDING REMARKS

This paper deals with the development of a cylinder charge control function. As a first step towards this aim, a novel performance output was chosen which is the intake manifold oxygen concentration. State of the art control solutions usually uses the EGR rate tracking as a target. After it, a physics-based, nonlinear, control-oriented model of the whole engine air-path was worked out as a basis for the controller design. The modeled engine setup uses an HP-EGR valve and an exhaust throttle flap, as engine air-path actuator setup. Finally, an LQ servo control structure was developed which can ensure the tracking of the intake manifold oxygen concentration demand signal. The control structure needs to minimize the pumping losses to ensure maximum engine efficiency. It can be guaranteed only if the exhaust flap starts to close after the EGR valve saturation. For this purpose, the control model was converted into two separate SISO form: one in which only the EGR valve opening is the control input and an other where the exhaust flap. In the end, the controller performance was demonstrated with engine dyno measurements in a test sequence where cylinder charge oxygen concentration was decreased in 1 % steps to 17 % and finally settled again on 21 %. From the above test results, it can be concluded that the operation of the control structure developed in this article is advantageous and hence recommended in the below 200 Nm engine load range for this particular test engine. It shows good cooperation with aftertreatment systems: at low engine loads while the exhaust gas temperature and the efficiency of the SCR catalyst is low the proposed controller can be used for emission limitation.

## 7. REFERENCES


[1] **Flärdh, O. – Martensson, J.:** "Exhaust pressure modeling and control on an SI engine with VGT." In: Control Engineering Practice 25, 2014, p.26 –35.

[2] **van Nieuwstadt, M.:** "Coordinated Control of EGR Valve and Intake Throttle for better Fuel Economy in Diesel Engines." In: SAE Technical Paper 2003-01-0362

[3] **Friedrich, I. – Liu, C. S. – Oehlerking, D.:** "Coordinated EGRrate model-based controls of turbocharged diesel engines via an intake throttle and an EGR valve." In: 2009 IEEE Vehicle Power and Propulsion Conference. Sept. 2009, p.340–347.

[4] **Bárdos, Á. – Németh, H.:** "EGR Support Investigation on a Diesel Engine." In: A Jövő Járműve 3-4 (2011), p.48–53. (In Hungarian)

[5] **Nyerges, Á. – Németh, H.:** "Low pressure intake throttle and exhaust brake support assessment on the low pressure loop exhaust gas recirculation on medium duty diesel engines." Proceedings of the 14th MINI Conference on Vehicle System Dynamics, Identification and Anomalies VSDIA 2014 (Ed. by Prof. I. Zobory). BME Knowlwdge Centre Electric and Electronic Vehicles, Budapest, 2015, p.315-324.

[6] **Isermann, R.:** Elektronisches Management motorischer Fahrzeugantriebe. Elektronik, Modellbildung, Regelung und Diagnose für Verbrennungsmotoren, Getriebe und Elektroantriebe. Vieweg+Teubner Verlag, Jan. 2010.

[7] **Ladommatos, N. – Abdelhalim, S. – Zhao, H. – Hu, Z.:** "The Dilution, Chemical, and Thermal Effects of Exhaust Gas Recirculation on Diesel Engine Emissions - Part 4: Effects of Carbon Dioxide and Water Vapour." In: SAE Technical Paper 971660 (1997). doi: 10.4271/971660

[8] **Herrmann, O. E.:** "Emissionsregelung bei Nutzfahrzeugmotoren über den Luft- und Abgaspfad." PhD thesis. RWTH Aachen, 2005

[9] **Bessai, C. – Gratzke, R.:** "Emissions Reduction Potential of Closed-Loop Intake Oxygen Control." In: IFAC Proceedings Volumes 46.21. 7th IFAC Symposium on Advances in Automotive Control, 2013, p.07 –108.

[10] **Bárdos, Á. – Németh, H.:** "Model development for intake gas composition controller design for commercial vehicle diesel engines with HP-EGR and exhaust throttling." In: Mechatronics 44.Supplement C, 2017, p.6–13.

[11] **Bauer, P. – Ritzinger, Gy. – Soumelidis, A. – Bokor, J.:** "LQ Servo control design with Kalman filter for a quadrotor UAV." In: Periodica Polytechnica 36.1-2 2008, p.9–14. doi: 10.3311/pp.tr.2008-1-2.02

[12] **Szimandl, B. – Németh, H.:** "Optimal position control of an electro-pneumatic clutch system." In: Proceedings of the 11th International Symposium on Advanced Vehicle Control (AVEC'12). Seoul, Korea, Sept., 2012, p.1 –6

# DESIGN OF HAPTIC STEERING GUIDANCE CONTROLLER CONSIDERING LOOK AHEAD DISTANCE

**Kimihiko NAKANO*, Masahiro SEKI**, Tsutomu KAIZUKA*, Rencheng ZHENG***, Toshiaki SAKURAI** and Tetsuo MAKI****

*The University of Tokyo, **Tokyo City University, ***Dalian University of Technology
* 4-6-1 Komaba, Meguro-ku, Tokyo, Japan
*knakano@iis.u-tokyo.ac.jp*knakano@iis.u-tokyo.ac.jp
Phone: +81-3-5452-6184, Fax: +81-3-5452-6644

*Received: November 5, 2018*

## ABSTRACT

The effect of the haptic steering guidance, which is a driver assist system to apply small torque to the steering wheel to induce the smooth steering, is examined through the driving simulator experiments. The three types of the guidances, which are designed on the basis of look-ahead distances for three different radiuses of curves, are tested. The results show the performance of the haptic guidance designed reffering to the longer look-ahead distance is better than those reffering to the shorter distance.

*Keywords:* automobiles, steering, driver assist system, driving simulator

## 1. INTRODUCTION

A haptic steering guidance is a driver assist system providing torque to a steering wheel to follow a target trajectory. The toque is usually smaller than that generated by a human driver, which induces smooth steering not opposing to intension of the driver[1][2]. This driver assist system is known to be effective on improving the steering performance especially in a bad weather condition like dense fog[3], a visually occluded condition [4] or when the driver feels fatigue[5].

There are two main problems to solve in this driver assist system. First one is how to decide the target tragectry. However this problem seems to be solved recently, since the technology related to automated driving has been developed. When the car travels along the same lane, the target tragectroy can be known by detecting the lane markings. Although identifying the target trajectories when changing the lanes, in merging points, or at the intersections is not easy tasks for the automated driving systems, this paper does not focuse on this point.

Second one is how to design the controller for the haptic steering guidance system. Usually the driver is assumed to steer the vehicle looking the point ahead of the vehicle called the look ahead point. Therefore it is reasonable to decide the assist torque considering the error between the look-ahead point and the target trajectory. However the position of the look-ahead distance is not always the same, which depends on the human drivers or on the road condition, for example the curvature, brightness of the environment, wetness on the surface. Then the authors build the haptic steering guidance system whose controllers are designed on the basis of different look-ahead positions and examined their performances on the driving simulater where the car travels in curves having several curvatures.

## 2. HAPTIC STEERING GUIDANCE CONTROLLER

The haptic controller is designed to reduce the lateral error and the yaw error between the look-ahead position and the target trajectory. The diagram of the look-ahead position is shown in Fig. 1. When the position of the center of the gravity of the vehicle and the yaw angle are presented by $\mathrm{G}(x_G, y_G)$ and $\theta_\mathrm{G}$, respectively. Then the position of the look-ahead point $\mathrm{P}(x_\mathrm{P}, y_\mathrm{P})$ and the yaw angle $\theta_\mathrm{P}$ are estimated using the equations shown in Eqs. (1) - (3), where $\tau$ is the estimated time to reach the look-ahead point, called preview time.

$$x_\mathrm{P} = x_\mathrm{G} + V\int_0^\tau \cos\left(\theta_G + \dot{\theta}_G t\right)\mathrm{d}t \tag{1}$$

$$y_\mathrm{P} = y_\mathrm{G} + V\int_0^\tau \sin\left(\theta_G + \dot{\theta}_G t\right)\mathrm{d}t \tag{2}$$

$$\phi_\mathrm{P} = \phi_\mathrm{G} + \int_0^\tau \dot{\theta}_G t\,\mathrm{d}t \tag{3}$$

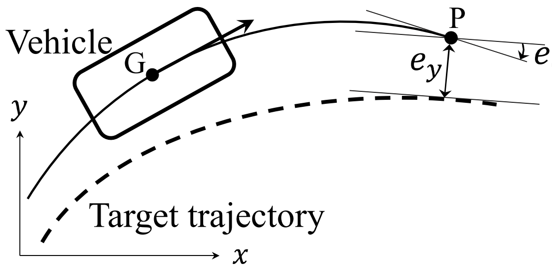


Fig. 1 Look-ahead point.

The lateral error $e_\mathrm{y}$ is the minimum distance between the target trajectory and the look-ahead distance, and $e_\theta$ is the error between the angle of the tangential line and the estimated yaw angle at the look-ahead point. The assist torque, $u$, of the haptic steering guidance is obtained based on PD control as shown in Eq. 4, where $a_1$, $a_2$, $a_3$ and $a_4$ are constants presenting the feedback gains.

$$u = a_1 e_y + a_2 \dot{e}_y + a_3 e_\theta + a_4 \dot{e}_\theta \tag{4}$$

The values of $a_1$, $a_2$, $a_3$ and $a_4$ are decided with trials-and-errors through the test rides of the driving simulator. How to obtain the optimal values is an essential problem, however it is not treated in this article.

## 3. EXPERIMENTAL SETUP

### 3.1 Subjects

Twelve healthy males were recruited to participate in the experiment. Their age range from 21 to 24 and its mean is 22.5, and all had valid Japanese driver's licenses. Each participant received monetary compensation for his involvement in the experiment. The experiment was approved by the Office for Life Science Research Ethics and Safety, the University of Tokyo.

### 3.2 Driving Simulator

The experiments were conducted using the driving simulator as shown in Fig. 2. It can simulate the six-degree-of-freedom motion with the Stewart platform and produce more than 120 degree front field of view with three projectors. In the cockpit, there are three liquid crystal displays: one at the position of the instrumentation panel displays a speedometer and a tachometer, the those at the position of the side mirrors present the rear views same as those. The motor for the electric power steering system and a torque sensor are installed at the axis of the steering wheel. In addition, three cameras and two infrared flashes for an eye tracking system, Smart Eye Pro, Smart Eye AB, Sweden, are equipped.

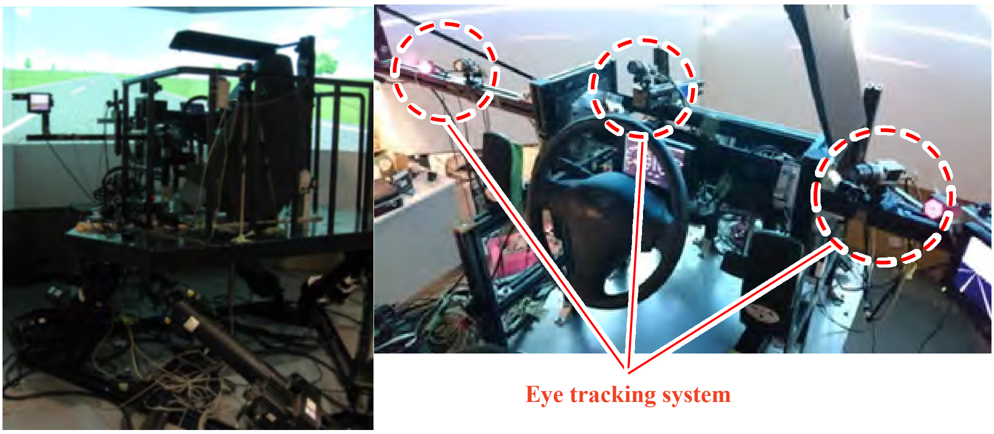


Fig. 2 Driving simulator: Left one is the general view and right one is the installed eye tracking system.

## 4. MEASUREMENT OF LOOK-AHEAD-POINT

To identify the look-ahead-point of the driver, the steady state cornerings of left and right turns in three different curvatures whose radiuses are 100m, 300m, and 1000m are tested on the driving simulator. It is a single lane road whose width is 3m and the subjects are  asked to travel along the center of the lane at the speed of 40km/h. Total experimental time for one trial is 120 seconds and gazing points are measured by Smart Eye between 30 and 90 seconds, which is unknown to the subjects. The scatter diagrams of the gazing points of one of the subjects in each condition is shown in Fig. 3. It is found the gazing points concentrate on the tangential point of the inner lane markings[6]. The look-ahead points are identified by calculating the center of the scatterd gazing points. Figure 4 presents the identified look-ahead distances, which is the distance between the look-ahead point and the vehicle positon, in each condition. For right turn, it is clear the look-ahead distance extends as the radius becomes larger, while the no clear tendency can be found in the left turn. The driver's seat of the driving simulator assume to locate in the right side of the vehicle to adjust to the left-hand traffic rule in Japan. Therefore the subject may be able to feel the width of the car in the right side better

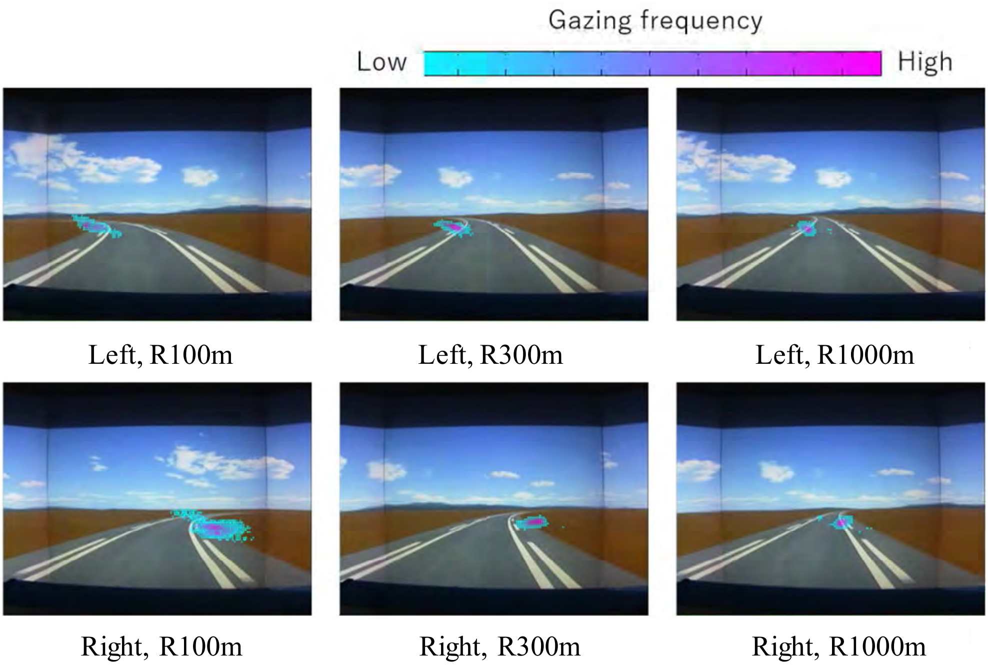


Fig. 3 Measured gazing points in steady state cornerings.

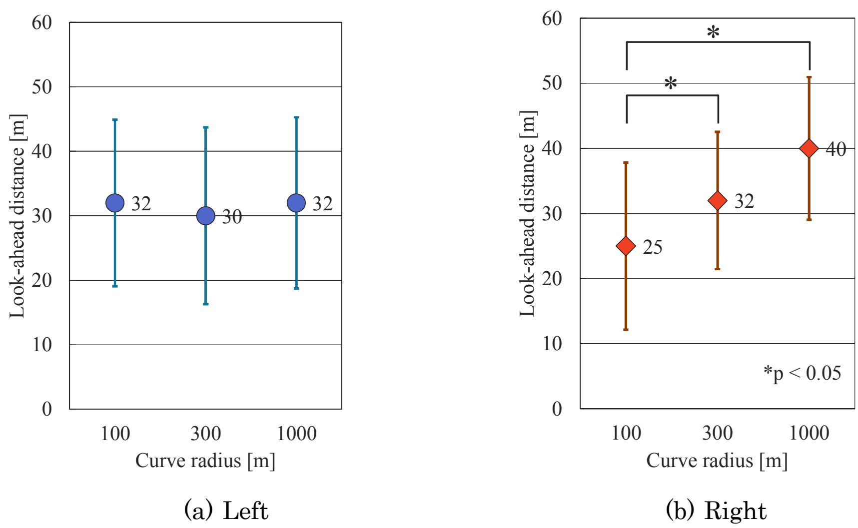


Fig. 4 Look-ahead distance for each condition: * indicates the significant difference ($p$<0.05, Bonferroni).

## 5. PERFORMANCE OF HAPTIC STEERING GUIDANCE

### 5.1 Road Scenario

The identified look-ahead distances for the radiuses 100m, 300m, and 1000m are 25m, 32m, and 40m, respectively. The preview times are derived by dividing them by the speed, 40km/h. Then the three controllers of the haptic steering guidance are designed based on the preview times for the radiuses 100m, 300m, and 1000m, which are called near, middle and far, respectively. The feedback gains of the assist torque used in the experiments, $a_1$-$a_4$, are 10.0Nm/m, 0.3 Nms/m, 10.0Nm, and 0.3Nms, respectively, which were decided with trials-and-errors. The schematic of the test road is shown in Fig. 4, which consists of straight in the first 300m, curve in the second 300m, and straight in the last 300m. The performance are evaluated in the curve section including 100m straight sections before the entrance and after the exit of the curve. The first 200m, the second 200m and the last 200m of the evaluation section are called entry, middle, and exit parts.

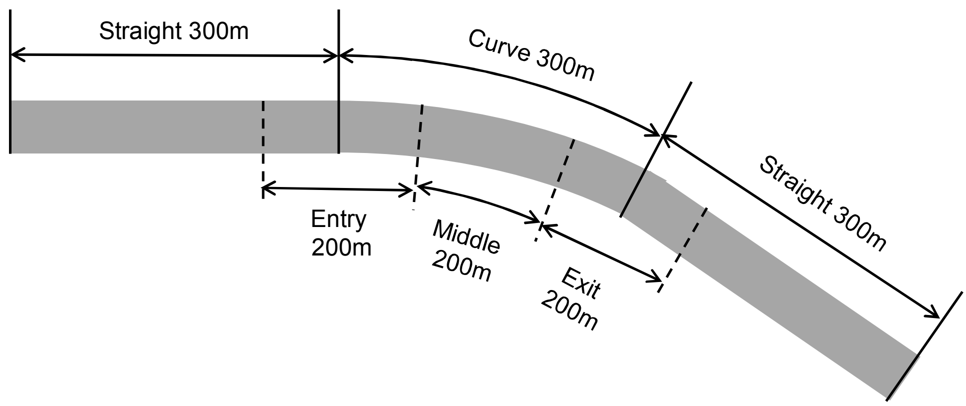


Fig. 5 Road for performance evaluation.

### 5.2 Evaluation Index

To evaluate the performance, Standard deviation of lateral position called SDLP[7] and the integral of the squared yaw acceleration, $Y_{\mathrm{n}}$, are utilized as evaluation indexes. Equation 5 represents how to obtain SDLP, where $\mu$ is mean of the lateral positions and $N$ is number of samples:

$$\mathrm{SDLP} = \sqrt{\frac{1}{N-1}\sum_{i=1}^{N}(x_i-\mu)^2}\ . \tag{5}$$

The integral of the squared yaw acceleration is given by

$$Y_n = \sum_{i=1}^{n} \dot{\gamma}^2\ . \tag{6}$$

The SDLP evaluates the steering mainly in view point of the lateral error, while $Y_{\mathrm{n}}$ assesses mainly the yaw error. Smaller value is better for both indexes

### 5.3 Results

Figure 6 shows the results: mean of SDLP and $Y_n$ for each condition, where "without" means the condition when the haptic steering guidance is not applied. It is found SDLP becomes smaller when the assist is applied in the entry and exit part of the curve whose radius is 1000m, although the effect of the haptic steering guidance is not clear in SDLP in the curve whose radiuses are 100m and 300m. In $Y_n$, the effect of the assist is clearly shown in entry and exit parts and "far" setting seem to be the best even in the curve whose radius is 300m.

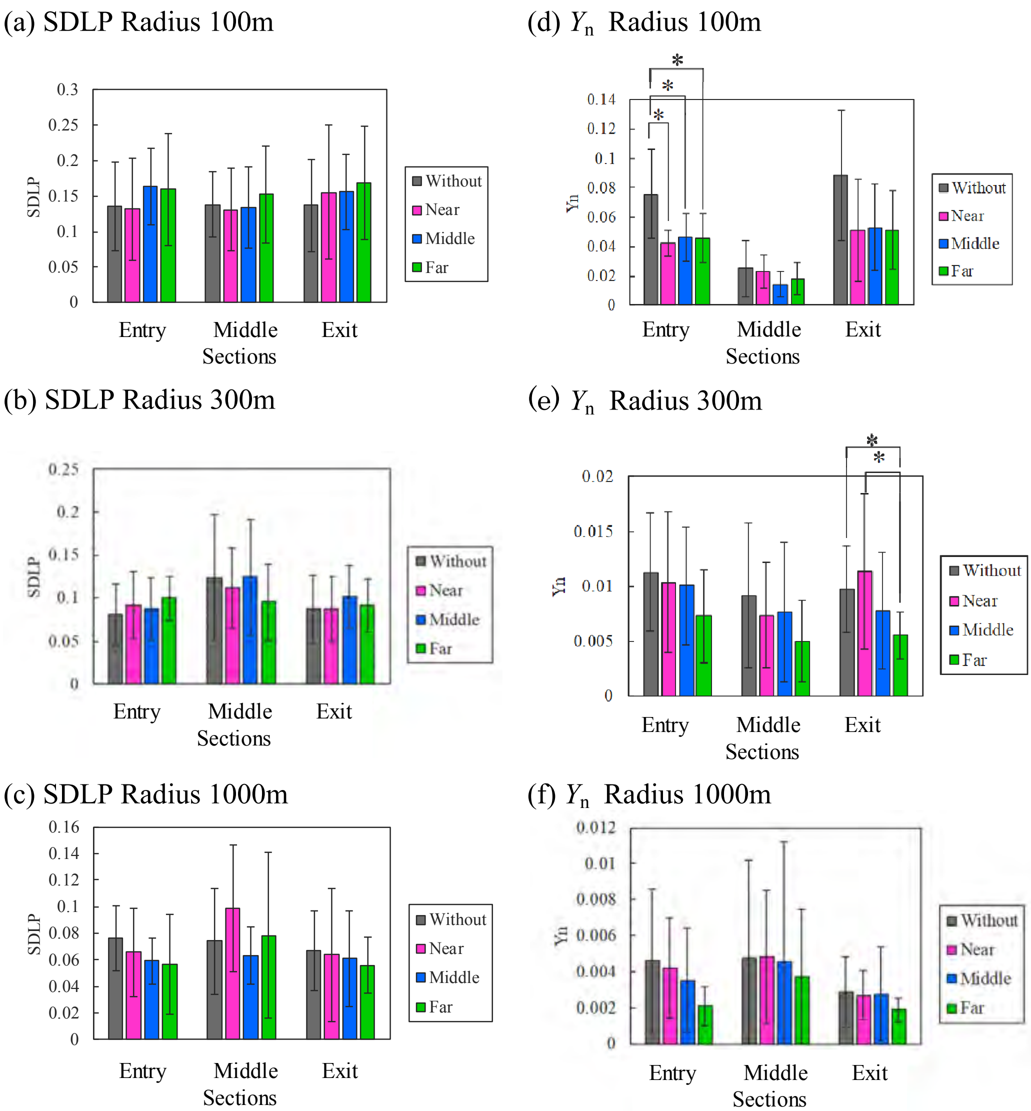


Fig. 6 SDLP and $Y_n$ in the curves whose radius is 100m, 300m and 1000m: * indicates the significant difference ($p<0.05$, Bonferroni)

Figure 7 shows the assist torques and steering angles of one of the subjects in entry and exit parts in the curve whose radius is 100m. As the assist torque is applied earlier before entering the curve when the controller is designed based on the look-ahead position for the radius 1000m, that is "far" setting, the driver has longer time to prepare for the steering maneuvour. This induces better steering performance even in the curve of the smaller radius.

(a) Assist torque in the entry part of the radius 100m curve.

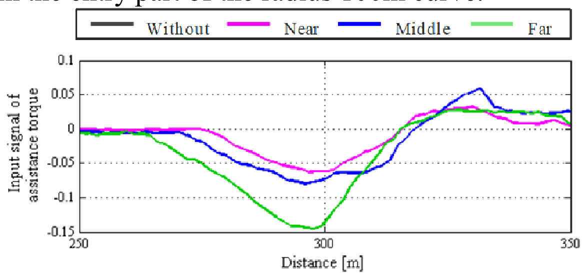


(b) Steer angle in the entry part of the radius 100m curve.

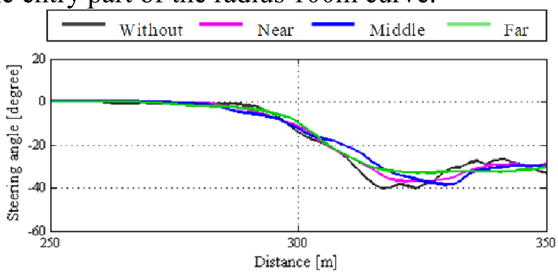


(c) Assist torque in the exit part of the radius 100m curve.

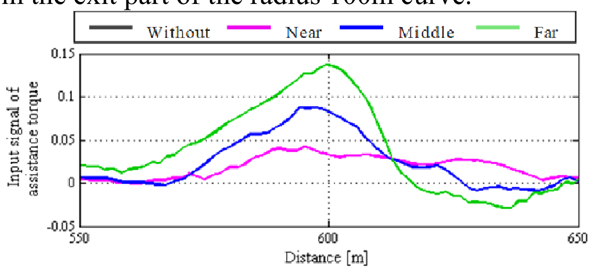


(d) Steer angle in the exit part of the radius 100m curve.

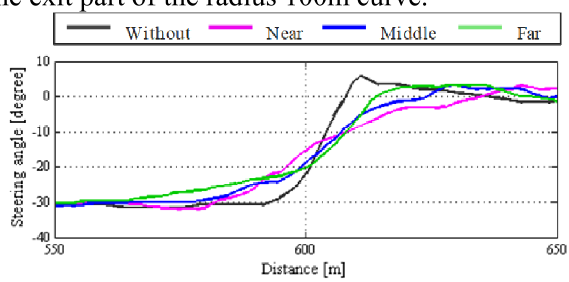


Fig. 7 Assist torque and steering angle of one of the subjects in the entry and the exit part of the radius 100m curve.

## 6. CONCLUDING REMARKS

Through the driving simulator experiments, following conclusions are obtained:

1. The look-ahead distance extends when the radius of the curvature becomes longer.
2. The haptic steering guidance designed on the basis of the look-ahead distance for the curve whose radius is 1000m is effective in the entrance or in the exit part of the curves whose radius is smaller than 1000m.
3. The haptic steering guidance based on the far look-ahead distance seems to induce the driver to prepare for the steering maneuver earlier, which causes good steering performance in the curve.

## 7. REFERENCES

[1] **Forsyth, B.A. – MacLean, K.E.**: Predictive haptic guidance: Intelligent user assistance for the control of dynamic tasks, IEEE Transactions on Visualization and Computer Graphics, **12**, 2006, p.103-113.

[2] **Mulder, M. – Abbink D.A. – Boer, E.R.:** The effect of haptic guidance on curve negotiation behavior of young, experienced drivers, IEEE International Conference on Systems, Man and Cybernetics, 2008, p.804-809.

[3] **Mars, F. – Deroo, M. – Hoc, J.M.:** Analysis of human-machine cooperation when driving with different degrees of haptic shared control, IEEE Trans. Haptics, 7, (3), 2014, p.324-333.

[4] **Wang, Z. – Zheng, R. – Kaizuka, T. – Nakano, K.:** Influence of haptic guidance on driving behaviour under degraded visual feedback conditions, 2018, IET Intelligent Transport Systems, DOI: 10.1049/iet-its.2017.0112

[5] **Wang, Z. – Zheng, R. – Kaizuka, T. – Shimono, K. – N kano, K.:** The effect of a haptic guidance steering system on fatigue-related driver behavior, IEEE Transactions on Human-Machine Systems, 47(5), 2017, p.741-748.

[6] **Land, M.F. – Lee, D.:** Where we look when we steer, Nature 369, 1994, p.742-744.

[7] **Verster, J.C. – Roth, T.:** Standard operation procedures for conducting the on-the-road driving test, and measurement of the standard deviation of lateral position (SDLP), International Journal of General Medicine, 4, 2011, p.359-371.

# POTENTIAL WEAK POINTS OF ENVIRONMENT SENSORS IN AUTONOMOUS VEHICLES

**Henrietta LENGYEL and Zsolt SZALAY**
Department of Automobiles and Vehicle Manufacturing
Faculty of Transportation Engineering and Vehicle Engineering
Budapest University of Technology and Economics
H-1111 Budapest, Stoczek utca 4-6, Hungary

*Received: November 06, 2018*

## ABSTRACT

Accurate recognition and identification of horizontal and vertical traffic signs might be problematic for autonomous vehicles. The state of the signals significantly affects the recognition potential. To be able to safely navigate an autonomous vehicle, it is necessary to have a very accurate environment recognition. But there are a lot of problems with the sensors recognitions ability. The current article therefore addresses the fusion of different sensors, which helps to detect signs and eliminate the main problems of recognition. The paper introduces a special method to enhance the recognition potential of traffic signs by cameras, RADAR and LIDAR. The method uses a special dye or marker tool that highlights traffic signals which is recognised by RADAR. Analysing and evaluating the resulting images helps finding the weaknesses and anomalies of the different sensor systems. Searching for extreme cases from real life can be helpful in creating artificial damages to signal systems that enable the development of traffic sign recognition systems. As well as looking for opportunities that help with the identification of traffic signs now and in the presence of autonomous vehicles. This article points out the boundary values and circumstances that make a traffic sign difficult to identify, which are environment, weather, and visibility conditions and various traffic situations. The study can further develop critical test environments for traffic signs, which will help to develop future autonomous vehicle systems.

*Keywords:* autonomous vehicles, environment sensors, traffic sign recognition, environment recognition

## 1. INTRODUCTION

Nowadays, more and more manufacturers and developers deal with the development of autonomous vehicles. Among its primary goals include the development of reducing accidents on public roads and reducing the pollution of the environment. Secondary goals include a built infrastructure that relates to every participant on the roads and able to communicates about traffic.

It is imperative to ensure the perfect environment recognition for safe transport. But in the used vehicles, the sensors for traffic sign recognition are often blame. The article also introduces a measurement methodology, which is also used to test a demonstration vehicle table recognition system. Nowadays it is hard but acceptable if a given road segment misrepresents traffic signs. But when an autonomous vehicle has to travel with it, adjusting speed and adhering to the rules, accuracy is imperative. Therefore, these systems have to go through considerable progress.

In order to assist in more accurate detection, we have examined several areas. These systems include testing the camera, RADAR and LIDAR for detecting the environment and identifying traffic signs within it. The article explores one by one the possibilities and the difficulty of trying out a new system in detecting traffic signs. Highlights that, if all were to be used together the sensors, how much assistance and precision would they give to the environment.

The article is still presented with the help of the traffic signs by using a LIDAR measurement. The point cloud will show what kind of image get back and how can see

the traffic signs in the pictures. Then it can be concluded that it could be used later with other sensors.
This article points the boundary values and circumstances that make a traffic sign difficult to identify, which are environment, weather, and visibility conditions based on previous experience.

## 2. TRAFFIC SIGNS AND ENVIRONMENT RECOGNITION POSSIBILITIES

At this time many sensor systems used in transport and vehicle technology. There are plenty of sensors in the nowadays used vehicles. For autonomous vehicles, however, it is even more important that they work well and harmonize, because it will be able to travel on the road A point to B. In the present the transport system is concentrate for the human drivers who have the sense (hearing, sight) what needed for the driving and do the right reaction.
The vehicle receives the information from its surroundings using built-in sensors. Each sensor can provide other help with orientation. For example the autonomous environment sensor system includes a remote RADAR, which is located on the bumper. The medium and short distance RADARs and ultrasonic sensors can map the area in front of the vehicle. The long-range RADAR detects the objects in front of the vehicle at high speed. The LIDAR Laser Scanners map medium distance objects around the vehicle. The cameras are used to recognise road markings, lines and traffic signs. The sensors used in autonomous cars are shown in Fig. 1. [1]

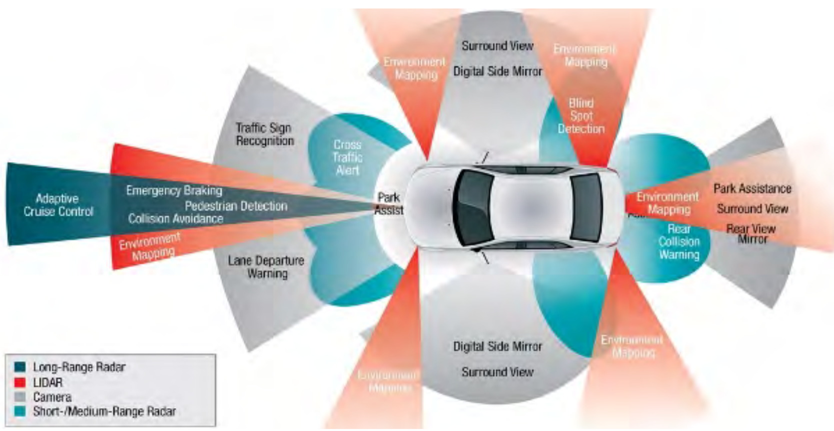


Fig. 1 Sensors on the autonomous vehicle

Sensors can help you get information about nearby, medium and distant surroundings of your vehicle. Each sensor has its own specificity, which means it can be used well depending on other environmental influences, light conditions and other weather conditions. The intensity and sharpness of the light also have a great impact on their ability to operate. The following table summarizes the used sensors and their properties and advantages. The green fields mean the sensor is able to recognize under specified conditions, the red means it is not. (Table 1.)

| | RADAR | LIDAR | Camera |
|---|---|---|---|
| Weather | + | | - |
| Light Condition | + | + | - |
| Dirt of the sensors | + | - | - |
| Speed Detection | + | - | |
| Measurement of distance | + | - | |
| Measurement range | + | | |
| Detection of Objects | + | + | |
| Detection of Pedestrian | - | | + |

Table 1 Advantages and disadvantages of RADAR, LIDAR and Camera

The sensors differ in the basic operating principles. The LIDAR works an optical beam and the RADAR uses sound wave to recognize the environment. The LIDAR cannot detect transparent objects because the light passes through them. The radar is able to do so and can tell the distance of the object from the vehicle.
It could be solved with the data collected from the sensors which can recognise the signs, environment under other environmental conditions. Using sensor fusion can be create a map with a lot of information would be provided for an autonomous vehicle that would allow it to travel.[1]

## 2. RADAR CHARACTERISTICS AND PROPERTIES

The radar base was used as a different observation tool (street observations, military targets). Radars are becoming more and more common in both military and civilian environments. There are more research in the direction that radar can be used to detect the environment. [2]
Traffic sign recognition can be done with camera and LIDAR, but radar can also be used. They are trying to detect traffic signals by radar because the radar is less affected by environmental conditions (such as day and night or summer and winter). Before it, it is necessary to identify and collect cases and markings when the traffic signals detected by the radar look good.
Most radars used on the vehicle are watching moving objects, pedestrians and vehicles. But in this case it is necessary to detect objects on the edge of the road. Other objects in the traffic sign are those that may make the conditions of recognition difficult. As in the LIDAR the radar also under certain weather conditions (fog, rain) deteriorates due to the propagation ability.

Certain research results that traffic signs can be recognised by radar. But since reflective waves are taken into account and the objects are perceived, the accuracy of recognition influenced by the position and angle of the signals on the side of the road. [3]

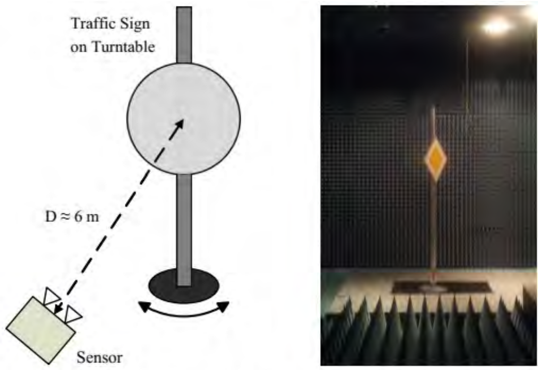


Left: Measurement Setup
Right: Sign photographed from the sensor position

Fig. 2 Measuring of traffic signs with RADAR

Other columns and outsourced objects may influence the identification of the signals. That's why it is hard to use the RADAR to recognise traffic signs, but use other sensors maybe it is more precise. [7]

## 3. LIDAR CHARACTERISTICS AND PROPERTIES

The LIDAR can use the light to map the environment. The light helps to determine the distance between the vehicle and the object. The LIDAR can map medium distance objects around the vehicle and get information about them.
With LIDAR, the recognition of static objects is easier than moving objects. Some research test the LIDAR for traffic sign recognition. If it is not possible to determine with full accuracy what board is on the edge of the street, its location can be easily recognized. [8]
The system works with the help of a mirror that rotates continuously and is able to determine the distance in 2D and to map the 3D environment. The process can be executed several times in succession which makes the 3D environment possible.
There are two methods for determining the distance for laser scanning - the first method is to measure the time between the shot beam and the reflected beam. The second method is to measure the phase shift between the received and the reflected beam. [9]
The advantage of laser scanners is their measuring range, measuring accuracy and measuring speed. But the laser scanners cannot measure the distance of transparent objects such as glasses. So sometimes it can cause anomalies in the created point cloud image.

## 4. CAMERA CHARACTERISTICS AND PROPERTIES

The camera is the device that is most commonly used to recognize traffic signs on the roads. The cameras are in the vehicles behind the windshield, so it can see the whole road.

The cameras in the vehicle can be classified in several ways. The most important of these is where it is located on the vehicle. Most of the cameras are on the front and back of the vehicle and pans the way. Tesla is an exception because it can also use lateral placement. The other option is to classify that what colours the camera sees. Black and white, monochrome and one colour of RGB and RGB. These cameras can be further grouped for mono and stereo perception. [1]
The environmental effects have a great impact on the reliability of the camera functions. But other factors also affect the accuracy of traffic sign recognition. In the camera the colours influence accuracy. For example, if using a red-sensitive camera, it can help recognise traffic signs more easily at the edge of the road. [6]
Using the camera with other sensors can be a big step forward in recognizing traffic signs. [10]

## 5. MEASUREMENT METHODOLOGY WITH LIDAR

There are several possibilities in the sensor fusion and can help to correct the inaccuracy of the cameras in the field of traffic sign recognition. Other research has so far focused on the use of LIDAR to detect these traffic signals. That's why it was created point cloud images of signals using the high-precision LIDAR available to. It was investigated what results were created about the measure.
The measurement was done in a room as a test to see what quality point clouds get from the different traffic signs. Three different types of traffic signs were used in the measurement. A "Stop! and give way", a Pedestrian crossing sign, and a 30 Speed limit sign. The pedestrian crossing point had the best reflection capability, the stop table had a basic reflection capability, while the speed limit sign wasn't equipped with any feature. The traffic signs were placed on a chair and the LIDAR was 3 meters ahead of them. The point clouds were taken at 45 degrees, the distance remained the same.
The results were as follows.

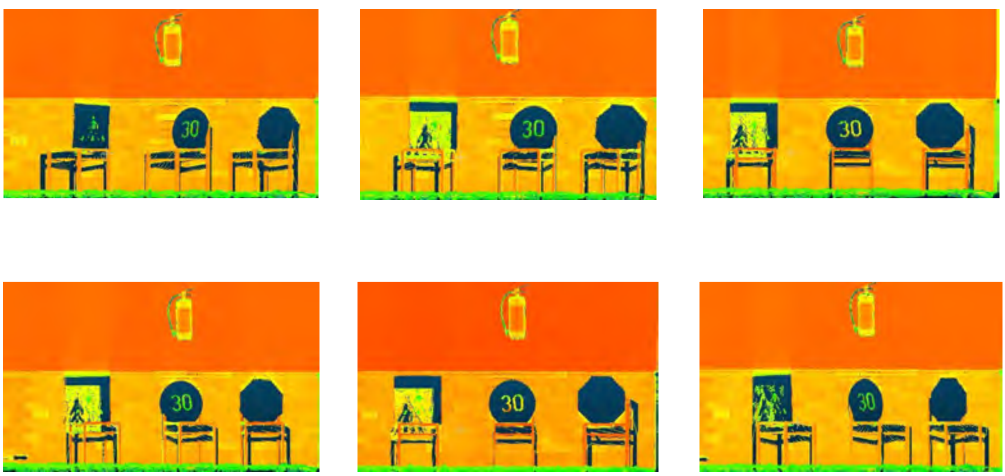


Fig. 3 Measuring of traffic signs with LIDAR

The used LIDAR was a high quality equipment, it can define a lot of points. Each signs were clearly visible, regardless of its reflective properties. However, using the MATLAB program and evaluating the received images, the reflectivity was clearly appear - occasionally even in a disturbingly high degree. [4]
On the vehicles, the LIDAR use less point to create an image, so it just can detected the location of the traffic signs. However, this also proves that if the number of points is increased, can get much more information about the signs at the near of the roads. [5]

## 5. MEASUREMENT METHODOLOGY WITH CAMERA

It would be good if the use of the sensor fusion was encouraged, so the weaknesses of the camera system were presented. Toyota CH-R hybrid was used for the measurement. The vehicle has a traffic signs recognition system detected by the camera. The measurement was done in a closed area to avoid disturbing the traffic.
It had selected 3 different speeds, which were also characteristic of the roads. It were used the 30 Speed Limit Sign for the measurement, which was hung on a vehicle. But in these cases he didn't recognize the sign at any speed. It was concluded that the background could be disturbed by recognition.
The camera only recognized the signal if it was hold it in hands at the altitudes of the prescription, because there wasn't an appropriate tool to be fitted. The measurement methodology was chosen so that we can compare it with the factors found in PreScan later. This means that although this was only a preliminary test measurement, but it will be measured and tested later with mud, cover and some tree branch later.
The results can be found in the following table.

| Traffic Signs | | Heights [m] | 10 km/h | 30 km/h | 50 km/h |
|---|---|---|---|---|---|
| Speed limits (daytime) | Temporary Sign | 0,2 | + | + | - |
| | Temporary Sign (cover) | 0,2 | | | |
| | Temporary Sign (tree) | 0,2 | | | |
| | Temporary Sign (mud) | 0,2 | | | |
| | On the road, no pedestrian | 1,2 | + | + | + |
| | On the road, no pedestrian (cover) | 1,2 | | | |
| | On the road, no pedestrian (tree) | 1,2 | | | |
| | On the road, no pedestrian (mud) | 1,2 | | | |
| | On the road, pedestrian | 2,2 | + | + | + |
| | On the road, pedestrian (cover) | 2,2 | | | |
| | On the road, pedestrian (tree) | 2,2 | | | |
| | On the road, pedestrian (mud) | 2,2 | | | |

Table 2 Measuring Speed Limit Sign with Traffic sign Recognition System

It can be seen that they had been well recognized, the vehicle had been detected sooner and showed on the dashboard the sign but just at low speeds. At higher speeds, the signal was detected and showed only after 4 meters.
The lack of the column could have disturbed the perception. However, it is absolutely necessary with these systems to detect and showed traffic signs much sooner.

## 6. CONCLUSION

The different sensors each have their weak points. The radars can detect a lot of things, but in the case of traffic signs they are difficult to use because they are able to tell their place, but they cannot provide accurate information at the present. LIDAR can be used to map the environment, and with a sufficient amount of points, they would be able to provide information about their content besides the placement of the traffic signs. In many cases, the camera recognizes it well, but it is not so accurate that give precise information about the traffic signs.

However, the weakness of each and the results of the tests and measurements have led to the conclusion that some new methods and the fusion of the sensors result in a much better result.

## 7. REFERENCES

[1] **Taraba, M. - Adamec, J. - Danko, M. - Drgona, P.:** Utilization of modern sensors in autonomous vehicles, 20th EURO Working Group on Transportation Meeting, 978-1-5386-4759-2/18/$31.00 ©2018 IEEE

[2] **Zhang, X. - Xi, X. - Li, M. - Wu, D.:** Comparison of Spread Spectrum Radar and Impulse Radar for Through-Wall Imaging Based on FDTD, 20th EURO Working Group on Transportation Meeting, EWGT 2017, 4-6 September 2017.

[3] **Werber, K. - Barjenbruch, M. - Klappstein, J. - Dickmann, J. - Waldschmidt Ch.:** How do Traffic Signs look like in Radar?, Proceedings of the 44th European Microwave Conference, 2014

[4] **Potó, V. - Somogyi, J. Á. - Lovas, T. - Barsi, Á.:** Laser scanned point clouds to support autonomous vehicles, 20th EURO Working Group on Transportation Meeting, EWGT 2017, 4-6 September 2017.

[5] **Börcs, A. - Nagy, B. - Benedek, Cs.:** Valós idejű járműdetektáció LIDAR pontfelhősorozatokon, ECCV 2014, ACCV 2014. (In Hungarian)

[6] **Huang, P. - Cheng, M. - Chen, Y. - Luo, H. - Wang, C. – Li, J.:** Traffic Sign Occlusion Detection Using, IEEE TRANSACTIONS ON INTELLIGENT TRANSPORTATION SYSTEMS, VOL. 18, NO. 9, SEPTEMBER 2017.

[7] **Krausz, N. - Lovas, T. - Barsi, Á.:** Radio Frequency Identifcation in Supporting Traffc Safety, Periodica Polytechnica 61 (4), 2017, p. 27–731.

[8] **Zhao, G. - Xiao, X. - Yuan, J. - Wah Ng, G.:** Fusion of 3D- LIDAR and camera data for scene parsing, Journal of Visual Communication and Image Representation Volume 25, Issue 1, , January 2014, p.165-183.

[9] **Asvadi, A. - Garrote, L. - Premebida, C. - Peixoto, P. - Nunes, U. J.:** Multimodal vehicle detection: fusing 3D-LIDAR and color camera data, Pattern Recognition Letters Volume 115, 1 November 2018, p.20-29.

[10] **Li, H. - Qiu, T. - Luan, S. - Song, H. - Wu, L.:** Deblurring traffic sign images based on exemplars, PLoS ONE 13(3): e0191367, 2018.

# AN ACCIDENT OF A SELF-DRIVING TEST VEHICLE: HUMAN REACTION VERSUS SELF-DRIVING SYSTEM - THE IMPORTANCE OF V2P COMMUNICATION

**Tibor Steve SIMON, Gábor MELEGH and Zsolt SZALAY**

Department of Automotive Engineering
Faculty of Transportation Engineering and Vehicle Engineering
Budapest University of Technology and Economics
H-1521 Budapest, Műegyetem rkp. 3, Hungary

*Received: November 2, 2018*

## ABSTRACT

The accident of an Uber test vehicle equipped with an intentionally partially disabled developmental self-driving system, and a driver distracted by the testing interface, on the 18th of March, 2018, in Arizona, put forward the following questions: *Could the vehicle have avoided the accident or minimalized damage if the self-driving system was fully operational? Could a fully attentive driver have noticed the pedestrian in time to avoid the accident or minimalize damages?* The use of a dual front headlights LUX analysis and simulation software like VirtualCrash and Dohladnost2 provided strong evidence that the accident could not have been fully prevented in either cases, but the collision would have been far less damaging for the pedestrian, thus, resulting in a presumably non-lethal accident in both hypothetical situations.

*Keywords:* self-driving, vehicle, accident, simulation.

## 1. INTRODUCTION

On the 18th of March, 2018, a test vehicle of UBER Technologies, Inc. fatally struck a pedestrian in Tempe, Maricopa County, Arizona. The car (a 2017 Volvo XC90) had its built-in ADASs (Advanced Driver Assistance Systems) disabled and was installed a developmental self-driving system by the testing company. The highly automated test vehicle was occupied by a 44-year-old female test vehicle operator with no passengers on board. The self-driving system was only partially enabled and the driver was preoccupied with the test system's interface in the dashboard.

Since testing the employed advanced systems and accessing their test results are both impossible, outsiders can only examine the circumstances of the accident and the mandatory policeman preliminary report. Inspecting these lends the necessary amount of data to assessing a similar, but fully operational ADAS's behavior in a similar road accident.

The present study deals with questions arising from two possible alterations of the accident situation: *Could the vehicle have avoided the accident or minimalized damage if the self-driving system was fully operational? Could a fully attentive driver have noticed the pedestrian in time to avoid the accident or minimalize damages?* In order to answer these questions, research began with a thorough review of the circumstances of the accident and the preliminary report. Relevant terms and definitions were also reviewed, along with some UN guidelines for the public use of highly and fully automated vehicles. After that, test data was acquired from the dual front light LUX analysis of a 2017 Volvo XC90 (the exact type of car involved in the studied accident), provided by the manufacturer for the duration of the present project. Then, three simulations were created, based on the original circumstances of the accident and data acquired from the analysis, employing complex simulation software (VirtualCrash and Dohladnost2 software). Finally, the proper conclusions were drawn from the results of these simulations.

## 2. THE CIRCUMSTANCES OF THE ACCIDENT

### 2.1 The test vehicle and the self-driving system

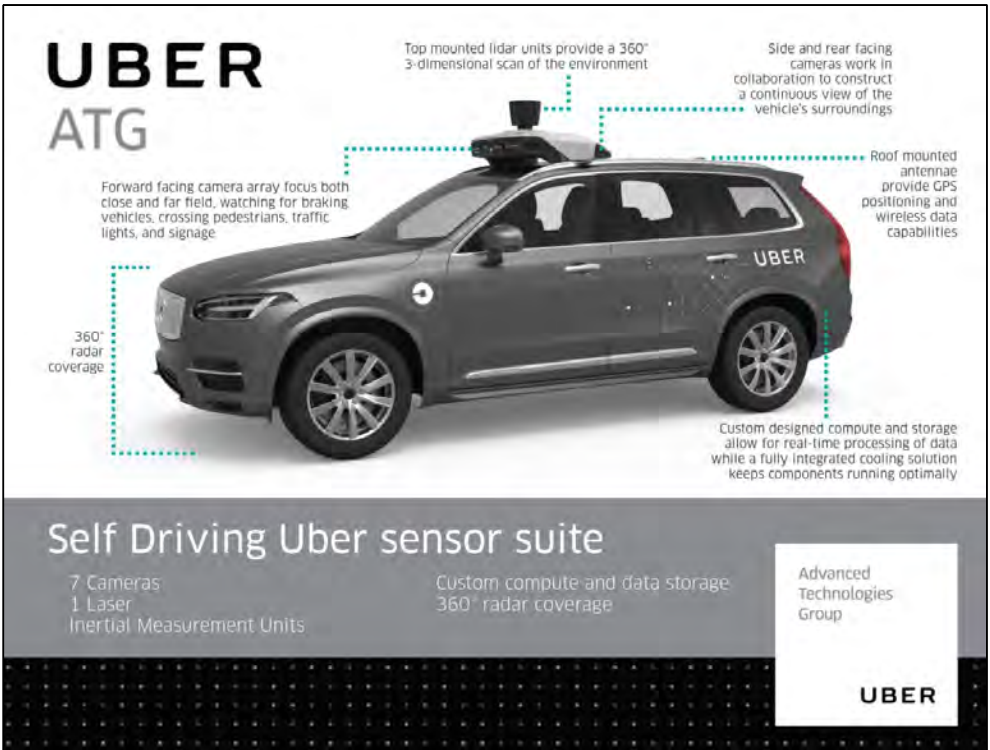


Fig. 1 Self Driving Uber Sensor Suite[1]

At the moment of the accident, the car was occupied by a 44-year-old female test vehicle operator with no passengers on board. She was doing her second round of the established test loop that night when the accident took place (9:58 p.m.). She suffered no physical harm during the incident.

The car had originally had factory built-in ADAS (City Safety system for Volvo Cars), but those were disabled for the purposes of the testing of the Uber system in question. A developmental self-driving system was installed by Uber Technologies (Fig. 1), which consisted of *"forward- and side-facing cameras, radars, LIDAR, navigation sensors, and a computing and data storage unit"*[2]. In this specific case, to the standard amount of 7 test cameras, 3 more were fixed onto parts of the car (one to the windshield, one to the rear window, and one on the dashboard, facing the driver),

[1] SDUSS
[2] NTSB PreRep.

making a total number of 10 camera angles available for investigation. An interactive self-driving system interface was also integrated into the dashboard.
Although the full system would have made the vehicle a highly automated one, the testing needed human interaction as well. During the accident, the self-driving system was operational, but many of its practical functions were intentionally disabled. It couldn't perform emergency braking or emit a warning sound in case of a detected upcoming obstacle. The automated speeding system, however, was fully operational. Thus, avoiding any accidents was the responsibility of the test driver (since the system couldn't stop or slow down the vehicle or even warn the driver), who, in this case, failed to notice the pedestrian in time. This was due to her being engaged with the aforementioned interactive self-driving system, which required the driver's attention from time to time in order to give next-to-instant feedback to perceived changes in travel conditions and the correctness of actions made by the system.

## 2.2 The environment

The accident occurred on a four-lane part of northbound Mill Avenue, with two forming left-turn lanes and two through lanes (Fig. 2). In the area of the accident, the northbound lanes are separated from the southbound lanes by a center median, which contains trees, bushes and an X-shaped brick landscaping. The four edges of this latter construction contain warning signs for pedestrians not to cross the road and use the crosswalk next to the upcoming intersection (about 360 feet or 110 meters north of the place of the accident). The speed limit at that section of the road is 45 mph (about 72 kph).

Fig. 2 The close environment of the accident.

Traffic was sparse (it was a Sunday night) and there was functional road lighting. Not all four lanes were lit sufficiently in the area of the accident, however, only the two through lanes on the right. The car was traveling in the rightmost lane.

The weather was clear with no fog ahead (according to camera footage of the accident later provided by the company and the Tempe police). There were no other external interfering circumstances apart from the limited reach of the road lighting at night.

### 2.3 The pedestrian

The victim was a 49-year-old female pedestrian who was crossing northbound Mill Avenue from left to right (eastward), walking her bicycle. She stepped off the brick landscaping in the center median onto the left-turn lanes, then she proceeded to cross all lanes.

Front camera footage shows that she didn't turn to look at incoming traffic; she only noticed the car at the moment of the impact. This was quite perplexing for investigators for a while, because the car's front headlight were turned on and working properly. The toxicology results, however, turned out to be positive for metha-mphetamine and marijuana, which seems to be the explanation for this.

The pedestrian was hit by the left front side of the vehicle. Although the driver called 911 immediately after the accident, the victim could not be saved and died as a result of the collision.


Fig. 3 Picture from the dash-cam footage provided by the police unit involved in the investigation.

## 3. RELEVANT DEFINITIONS AND UNITED NATIONS GUIDELINES

### 3.1 Relevant terms and their definitions

The seventy-seventh session of the UN's Global Forum for Road Traffic Safety[3] finalized the definition of many relevant terms in September, 2018. The following term descriptions had been agreed on:

[3] UN–77

Dynamic Control: *"carrying out all the real-time operational and tactical functions required to move the vehicle,"* including the control of lateral and longitudinal vehicle motion, monitoring and responding to the road environment, and *"planning and signaling for manoeuvers."*

Automated Driving System: *"the combination of hardware and software that can exercise dynamic control of a vehicle on a sustained basis."*

Operational design domain (ODD): *"the environmental, geographic, time-of-day, traffic, infrastructure, weather and other conditions under which an automated driving system is specifically designed to function."*

Highly Automated Vehicle: *"a vehicle equipped with an automated driving system,"* which *"operates within a specific ODD for some or all of the journey, without the need for human intervention as a fallback to ensure road safety."*

Fully Automated Vehicle: *"a vehicle equipped with an automated driving system,"* which *"operates without any ODD limitations for some or all of the journey, without the need for human intervention as a fallback to ensure road safety."*

In addition to these definitions, the different communicational directions of vehicles have to be collaborated on, with an emphasis on the vehicle's communication towards pedestrians. The collective term for these directions is vehicle-to-everything (V2X) communication. This mostly consists of vehicle-to-vehicle (V2V), vehicle-to-network (V2N), vehicle-to-infrastructure (V2I) and vehicle-to-pedestrian (V2P) communication.[4] Of course, these could be separated into further categories (e.g. vehicle-to-cyclist communication), but that' not relevant in this case. For the present study, the most pertinent term of the above list is V2P communication.

Vehicle-to-pedestrian communication includes all outwards signals that provide information to pedestrians about the intentions of the driver and foreseeable vehicular maneuvers (e.g. direction indicators), along with information about the vehicle's status (e.g. hazard warning lights).

### 3.2 UN guidelines

The UN's Inland Transport Committee[5] has formulated several recommendations for ADAS and their users. According to these, automated driving systems should prioritize safety by monitoring the vehicle and the surroundings at all times, be able to communicate and safely interact with other road users according to traffic rules, and minimize the effects of human or mechanical errors. The systems should only operate within their ODDs, signal when they are leaving these domains and deactivate safely once human interaction occurs or needs to occur.

The resolution also recommends ADAS users to follow the proper system checking procedures before and during their journeys, be ready to exercise dynamic control when it is needed, communicate with the system, and *"act lawfully at all times"*.

[4] V2X
[5] UN–77

The committee clearly emphasizes the importance of communication. The systems should be able to communicate with its surroundings (including vehicles and other types of traffic participants) and its user. It seems that the ability to communicate properly is essential for avoiding accidents. The resolution, however, doesn't define the means and methods of communication because these means and methods are currently under development.

## 4. METHODOLOGY

The practical study consisted of an examination of the lit area provided by the front headlights of an identical vehicle that was involved in the accident (dual front headlights LUX analysis), and two simulations. Both simulations aimed to determine if the accident could have been avoided or the injuries minimized under slightly different circumstances.

### 4.1 Dual front headlights LUX analysis

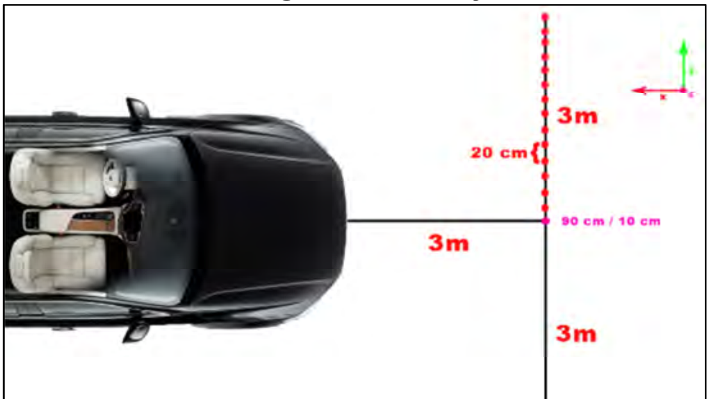


Fig. 4 LUX-measurement setup

For the analysis of the front headlights' lit area measurements, a 2017 Volvo XC90 vehicle was provided by the manu-facturer. The test vehicle was placed in a testing area where a light-measuring rod was set up as shown in Fig. 4. The testing line was placed 3 meters from the front end of the vehicle (the end of the standard effective lighting range). The testing line started from the exact middle of the car's width and spread 3 meters in both directions parallel to the front axle of the vehicle. 30 measuring spots were placed evenly along the testing line (20 centimeters between the spots, shown with red dots in Fig. 4).

There were two measuring sessions, during which one of the headlights were covered and the other was left alight (the setup was switched during the second session). In each session, LUX values were measured in nine height points along the testing line. The first line was at ground level (0 centimeters) and it was brought up by 10 centimeters after each round, ending at a height of 90 centimeters (one round means putting the LUX measuring rod in each of the 30 measuring spots along the test line).

This created two 10 x 30 sized tables of LUX data. During the first measuring, the front right headlight was covered and the front *left* headlight was measured. During the second measuring, the front left headlight was covered and the front *right* headlight was measured. Then the two tables of data were merged to determine the exact point in time when the driver could have noticed the pedestrian (and thus possibly avoid the accident or minimize damage).

## 4.2 Simulations

Three simulations were carried out with the help of the simulator program called Virtual Crash. The first simulation recreated the accident using available data from the preliminary report. The second simulation examined what would have happened if the self-driving system's braking functions weren't disabled at the time of the accident. The third simulation looked at the possibility of avoiding the accident in case the driver had payed attention to the road and hadn't been preoccupied with the test interface. As preparations for this, another computer program called Dohldnost2 was employed in order to calculate how many seconds before collision would the driver have noticed the pedestrian.

# 5. RESULTS

## 5.1 Dual front headlights LUX analysis

Data gained from the dual front headlights LUX analysis can be seen in Fig. 5. and Fig. 6. Both data tables are displayed in a manner that reflects the method of the measurement.

| [LUX] | 0 [cm] | 10 | 20 | 30 | 40 | **50** | 60 | 70 | 80 | 90 | **100** | 110 | 120 | 130 | 140 | **150** | 160 | 170 | 180 | 190 | **200** | 210 | 220 | 230 | 240 | **250** | 260 | 270 | 280 | 290 |
|---|---|---|---|---|---|---|---|---|---|---|---|---|---|---|---|---|---|---|---|---|---|---|---|---|---|---|---|---|---|---|
| 0[cm] | 30 | 54 | 60 | 50 | 51 | 53 | 46 | 61 | 54 | 58 | 65 | 63 | 70 | 45 | 42 | 40 | 35 | 25 | 14 | 9 | 6 | 4 | 2 | 1 | 1 | 0 | 0 | 0 | 0 | 0 |
| 10 | 35 | 71 | 117 | 116 | 95 | 107 | 141 | 152 | 157 | 157 | 130 | 110 | 91 | 81 | 67 | 50 | 46 | 37 | 17 | 10 | 7 | 5 | 3 | 2 | 1 | 1 | 0 | 0 | 0 | 0 |
| 20 | 130 | 162 | 232 | 287 | 271 | 280 | 350 | 410 | 395 | 340 | 300 | 240 | 195 | 210 | 182 | 120 | 55 | 40 | 21 | 15 | 13 | 9 | 5 | 2 | 1 | 0 | 0 | 0 | 0 | 0 |
| 30 | 320 | 371 | 500 | 600 | 650 | 670 | 760 | 850 | 810 | 735 | 730 | 690 | 600 | 480 | 390 | 275 | 250 | 160 | 92 | 93 | 81 | 30 | 5 | 2 | 2 | 0 | 0 | 0 | 0 | 0 |
| 40 | 630 | 770 | 960 | 1040 | 1120 | 1100 | 1300 | 1350 | 1400 | 1450 | 1490 | 1470 | 1450 | 1380 | 1140 | 850 | 970 | 525 | 350 | 260 | 200 | 154 | 61 | 14 | 2 | 1 | 0 | 0 | 0 | 0 |
| 50 | 877 | 987 | 1185 | 1340 | 1527 | 1640 | 1906 | 1925 | 2250 | 2350 | 2320 | 2260 | 2130 | 1880 | 1500 | 1070 | 670 | 420 | 307 | 216 | 132 | 57 | 10 | 0 | 0 | 0 | 0 | 0 | 0 | 0 |
| 60 | 880 | 1010 | 1300 | 1540 | 1890 | 2100 | 2720 | 3300 | 3065 | 3095 | 3095 | 3760 | 3660 | 3460 | 3010 | 2710 | 2000 | 1140 | 772 | 620 | 450 | 290 | 210 | 122 | 27 | 8 | 1 | 0 | 0 | 0 |
| 70 | 860 | 1040 | 1370 | 1650 | 1830 | 2010 | 430 | 1042 | 1260 | 400 | 515 | 915 | 495 | 279 | 1720 | 635 | 238 | 122 | 122 | 105 | 97 | 86 | 62 | 62 | 37 | 1 | 0 | 0 | 0 | 0 |
| 80 | 412 | 350 | 330 | 298 | 240 | 275 | 412 | 956 | 233 | 387 | 433 | 912 | 500 | 280 | 1720 | 650 | 240 | 125 | 120 | 100 | 90 | 80 | 61 | 61 | 47 | 15 | 0 | 0 | 0 | 0 |
| 90 | 52 | 46 | 56 | 66 | 81 | 92 | 136 | 158 | 140 | 190 | 272 | 280 | 430 | 380 | 237 | 1350 | 585 | 210 | 56 | 40 | 31 | 24 | 15 | 7 | 2 | 2 | 0 | 0 | 0 | 0 |

Fig. 5 Result table of left front headlight LUX measurement.

| [LUX] | 0 [cm] | 10 | 20 | 30 | 40 | 50 | 60 | 70 | 80 | 90 | 100 | 110 | 120 | 130 | 140 | 150 | 160 | 170 | 180 | 190 | 200 | 210 | 220 | 230 | 240 | 250 | 260 | 270 | 280 | 290 |
|---|---|---|---|---|---|---|---|---|---|---|---|---|---|---|---|---|---|---|---|---|---|---|---|---|---|---|---|---|---|---|
| 0[cm] | 0 | 0 | 0 | 0 | 1 | 1 | 2 | 4 | 5 | 8 | 11 | 20 | 33 | 33 | 35 | 41 | 50 | 60 | 60 | 56 | 60 | 65 | 81 | 65 | 63 | 51 | 45 | 45 | 32 | 25 |
| 10 | 0 | 0 | 0 | 0 | 0 | 2 | 3 | 5 | 7 | 10 | 15 | 25 | 40 | 52 | 60 | 110 | 126 | 103 | 100 | 90 | 100 | 160 | 170 | 170 | 130 | 90 | 90 | 90 | 60 | 40 |
| 20 | 0 | 0 | 0 | 0 | 0 | 2 | 5 | 8 | 14 | 24 | 25 | 26 | 39 | 70 | 162 | 200 | 230 | 220 | 240 | 250 | 300 | 375 | 397 | 410 | 330 | 260 | 260 | 242 | 200 | 170 |
| 30 | 0 | 0 | 0 | 0 | 0 | 2 | 17 | 44 | 58 | 120 | 113 | 90 | 105 | 220 | 320 | 485 | 620 | 660 | 670 | 740 | 750 | 830 | 780 | 680 | 630 | 600 | 580 | 480 | 390 | 285 |
| 40 | 0 | 0 | 0 | 0 | 1 | 5 | 18 | 61 | 145 | 192 | 257 | 322 | 520 | 720 | 990 | 1275 | 1460 | 1650 | 1670 | 1700 | 1600 | 1500 | 1350 | 1225 | 1500 | 1165 | 1100 | 920 | 740 | 580 |
| 50 | 0 | 0 | 0 | 0 | 0 | 10 | 35 | 95 | 200 | 280 | 405 | 560 | 1230 | 1780 | 2270 | 2560 | 2970 | 3380 | 3380 | 3160 | 2890 | 2600 | 2500 | 2400 | 1775 | 1520 | 1360 | 1100 | 900 | 700 |
| 60 | 0 | 0 | 0 | 0 | 2 | 22 | 52 | 131 | 270 | 357 | 485 | 777 | 1500 | 2400 | 3070 | 3440 | 4370 | 4800 | 4900 | 4620 | 4330 | 3850 | 3170 | 2600 | 2260 | 1900 | 1550 | 1175 | 860 | 410 |
| 70 | 1 | 1 | 0 | 0 | 5 | 65 | 110 | 175 | 260 | 385 | 465 | 710 | 915 | 1700 | 2530 | 4000 | 5650 | 6470 | 8970 | 7650 | 5900 | 4550 | 3220 | 2150 | 1821 | 1519 | 1242 | 1021 | 750 | 668 |
| 80 | 0 | 0 | 0 | 0 | 1 | 35 | 40 | 80 | 67 | 101 | 126 | 145 | 172 | 182 | 215 | 452 | 1440 | 2620 | 3800 | 8400 | 6000 | 3120 | 2420 | 1250 | 750 | 360 | 300 | 280 | 260 | 285 |
| 90 | 0 | 0 | 0 | 0 | 10 | 20 | 40 | 70 | 100 | 200 | 300 | 450 | 500 | 700 | 920 | 1100 | 1400 | 1700 | 2600 | 6100 | 2370 | 1678 | 1050 | 310 | 243 | 75 | 61 | 52 | 40 | 38 |

Fig. 6 Result table of right front headlight LUX measurement.

## 5.2 Simulations

Simulating the original circumstances of the accident provided the basis of comparison for the following two simulation results. Data acquired from the preliminary report made it easy to recreate the original result of the crash, as seen in Fig. 7.

The second simulation made use of the fact that UBER's system advised immediate emergency braking 1.3 seconds before collision. The system would have been able to decelerate with a rate of 6.5 m/s in case of emergency braking. The result of the simulation can be seen in Fig. 6: collision would still have occurred but with significantly less damage to the pedestrian. The car would have collided with the rear end of the bicycle only, but it wouldn't have hit the pedestrian directly. She would have been swept away for sure but that would have put her in a significantly less life threatening situation.

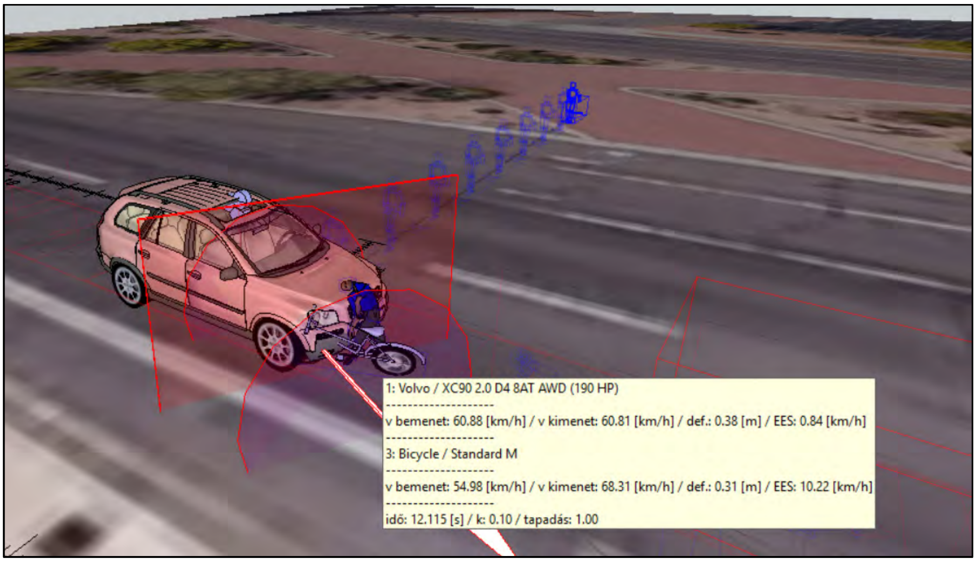


Fig. 7 First simulation’s moment of collision, reproducing the accident

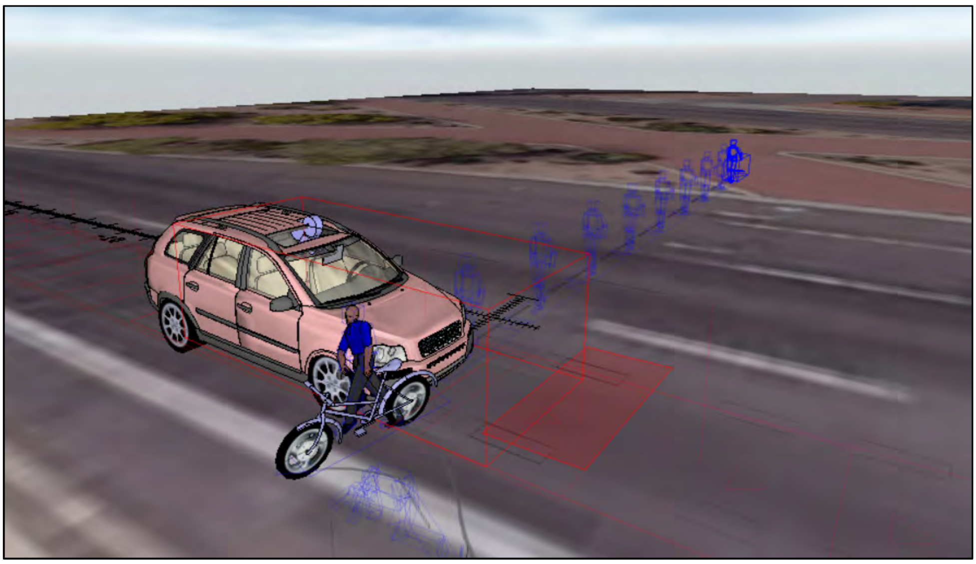

Fig. 8 Second simulation’s moment of collision

Preparations for the third simulation included importing all data gained from the dual front headlights LUX analysis into Dohldnost2. This made the simulated circumstances much more detailed with regards to light conditions. The results showed that the driver could have noticed the pedestrian 2.4 seconds before the collision. Calculating with the standard 1.0 second reaction time at night, this would have meant 1.4 seconds of quick deceleration.

Fig. 9 Dohladnost Illumination simulation

After this piece of data had been fed to the simulator program, it showed similar results as the second simulation (Fig. 8). The collision would still have happened but it would have been significantly less life-threatening.

## 6. CONCLUDING REMARKS

To sum it up, the study's aim was to find out if the accident involving a test car, with limited self-driving systems on board, could have been avoided or the damage minimalized in two, slightly different sets of circumstances. The results of simulations showed that the accident could not have been completely avoided neither by a fully enabled self-driving system (with emergency braking) nor by an attentive driver who is keeping her eyes on the road and doesn't deal with the test interface. In both hypothetical situations, however, the resulting collision would have been less damaging for the pedestrian and only result in injuries.

As both hypothetical situations still result in an accident, one might wonder if self-driving cars and their testing could be made even safer. The legislators at UNECE have already made some suggestions regarding this problem. For example, they advised creating a simple tool for V2P communication about the self-driving status of the car in the form of a headlight flasher. They also brought up the use of intelligent headlights able to aim its light at detected objects. These issues provide ample opportunities for further research within the topic of self-driving vehicles.

## 7. REFERENCES

[ [NTSB PreRep] National Transportation Safety Board (USA): *HWY18MH010 Highway Preliminary Report.* 2018.

[SDUSS] https://www.engineering.com/Hardware/ArticleID/16756/Technology-vs-Humans-Engineers-Seek-Answers-in-Ubers-Fatal-Self-Driving-Car-Accident.aspx (2018-10-26, 18:15)

[UN–77] United Nations – Economic and Social Council – Economic Commission for Europe – Inland Transport Committee – Global Forum for Road Traffic Safety, 77th session: *Revised draft resolution on the deployment of highly and fully automated vehicles in road traffic.*

ECE/TRANS/WP.1/2018/4/Rev.2
Geneva, 18–21 September 2018

[V2X] https://ofinno.com/technology/v2x/ (2018-10-26, 18:15)

# ENVIRONMENT SENSING AND PARKING PLACE DETECTION FOR AUTOMATED VEHICLES

**Ádám NYERGES and Viktor TIHANYI**

Department of Automotive Technologies
Faculty of Transportation and Vehicle Engineering
Budapest University of Technology and Economics
Stoczek utca 6, H-1111 Budapest, Hungary

*Received: November 6, 2018*

## ABSTRACT

In the last century road transport has completely changed our life, today mobility is a social need. Initially the main motivation was to make driving easier or more comfortable, but world megatrends have oriented the development towards to lower fuel consumption, higher traffic safety and reduced environmental impact. To reach these future objectives it is necessary to increase the level of automation of road vehicles. Automated vehicles will overcome today's cars in safety, efficiency, comfort, velocity and traffic density. Driving a road vehicle is a complex controlling task, substituting the human driver with software is a challenge also from the technical side. In connected and automated vehicles the control algorithm has several steps. An important step is, when the vehicle plans its own trajectory. The inputs of the trajectory planning are the purpose of the passengers and the environment of the vehicle (through the environmental perception system of the vehicle). The inputs for the trajectory planning process are the environmental protection of the vehicle, for instance the cameras, RADARs, LIDARs or the GPS. This paper presents a LIDAR based parking place detection process for automated vehicles. Our aim to realize valet parking function with the test vehicle of the University. To reach this aim maps will be given. The first one is given as a 2204 x 1294 size matrix where the roads will be defined by ones, parking areas will be defined by twos, the obstacles and the non-road zones will be defined by zeros. The second one is given in Prescan simulation environment. The map presents a smaller area of the campus of the Budapest University of Technology and Economics. The aim is to make an algorithm which can find the parking places that has a suitable size for the test. The environmental protection will be based on two 2-D LIDARs on the front corners of the test vehicle. The position of the vehicle will be measured by a DGPS system. The parking place detection will be important for further research, where the vehicle will plan the trajectory into the parking place. The research is one of the first steps to realize automated parking features in a self-drive car.

*Keywords:* connected and automated vehicles, autonomous driving, self-driving vehicles, Prescan simulation environment, LIDAR based parking place detection

## 1. INTRODUCTION

Due to the revolution of science and technology in the last few decades, vehicles have more and more automated features or systems. To make road transport safer and environmental friendlier it is necessary to increase the level of automation of road vehicles. At the end of the day, automated vehicles are going to appear in everyday transportation.

Connected and automated vehicles will be better than today's cars in efficiency, fuel consumption, and power, comfort, safety, and velocity and traffic density. Connected cars have another advantage: with intelligent traffic control systems, traffic jams can be decreased.

It is important to notice that the main motivation of the development of automated vehicles is the radical reduction of the accident number and severity, since 94% of the current traffic accidents can be traced back to the human drivers [1].

Due to the new features and in-vehicle systems, vehicle testing and validation became different as earlier. The new automated driving functions have to been tested in different traffic situations, this requirement needs new testing methods and strategies and also new testing environments. The aim is the same as earlier: to guarantee road safety with reliable operation of the systems.

In this paper the next step of the path planning process will be discussed which is related to a university research [2,3,4]. In earlier research several offline path planning algorithms were discussed.

The test vehicle can senses its environment on several ways: by the 2D LIDARs (on the front sides of the vehicle), by a RADAR (at the back of the vehicle), with an intelligent camera (behind the windscreen) and with two redundant DGPS systems. In this paper the path planning algorithm will use the LIDAR signals to recognise the obstacles.

The path planning algorithm will be done on a pre-defined map. This map is the parking area of the University which was given as a map matrix in earlier researches too [3]. In this paper the testing of the algorithm will be done in Prescan simulation environment where the signals of the LIDARs and the DGPS systems can be modelled [6].

The aim of the research is to realise valet parking function on the test vehicle in the parking area of the University. Valet parking function does not need high velocities, in this case the dynamical properties of the vehicle and the manoeuvrings can be neglected. The test vehicle can be seen in Figure 1.

Fig. 1 Photo of the test vehicle [3]

## 2. THE APPLIED MAPS

The following chapter contains the presentation of the applied map matrix. This map matrix was used in earlier researches [3], in this case this presentation is shorter, straightforward version.

The map of the pilot site was compiled based on combined survey with GNSS and terrestrial laser scanning technologies.

Terrestrial laser scanning was performed by a Faro Focus 3D 120S instrument, which has a 360° horizontal scanning and ~120 m range measurement capability. The geometrical resolution was set to 6 mm in 10 m. The raw result was a unified point cloud having x,y,z coordinates and the received laser pulse intensity.

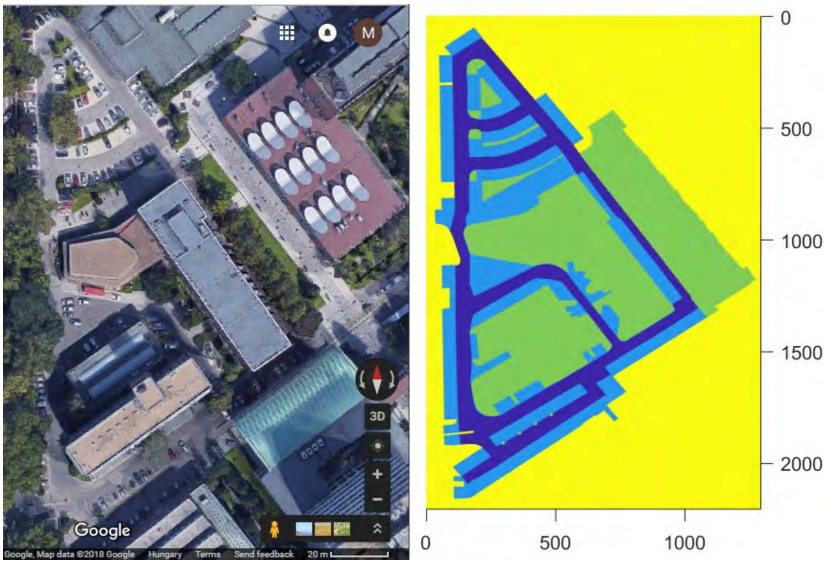


Fig. 2 The map and the map matrix of the applied territory [3]

Then the point cloud was manually reduced on the surface height and all relevant object borders were drawn in Autodesk AutoCAD environment manually. The obtained situation drawing was to be checked against topology and after accepting it, all polygons were filled by texture patterns considering that four layers are requested: (1) always available road surfaces, (2) potential parking slots, (3) surfaces not available for vehicles and (4) background (extension to minimal bounding rectangle).
The topologically correct and layer-organized drawing was imported into QGIS, where further checks were executed, then shp format was exported. The 10 cm resolution final occupancy grid was derived by an in-house developed Matlab script. The resulted raster has a size of 2204 × 1294 elements (Figure 2).

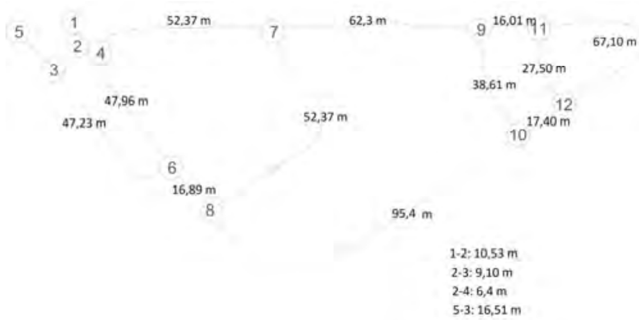


Fig. 3 The simplified directed graph [4]

The offline part of the valet parking function had two steps. At first the map of the parking area (as a road network, see Figure 3) was simplified to a directed graph. In this graph if the start and the target point are known (as additional nodes) the shortest way between the two nodes are definable, typically by Dijkstra-based algorithms [11].

## 3. THE APPLIED SIMULATION ENVIRONMENT

Due to the complexity of the systems and the stochasticity of the possible traffic situations the importance of simulation tests have been increased. There are several commercial simulation software to develop and validate functions connected and automated vehicles. For this research Prescan environment was available which was useful due to the very good connection with Matlab/Simulink [6].

Based on the map matrix the parking area was also built in Prescan. In this new map it is easy to define unexpected obstacles or other road users. In the software different vehicle models can be applied. The environmental sensing of the vehicle also can be modelled, in this case the LIDARs and the DGPS system were important for this research.

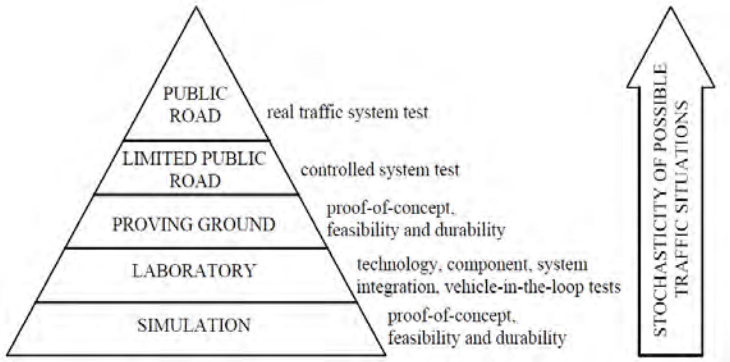


Fig. 4 The testing and validation process of connected and automated vehicles [14]

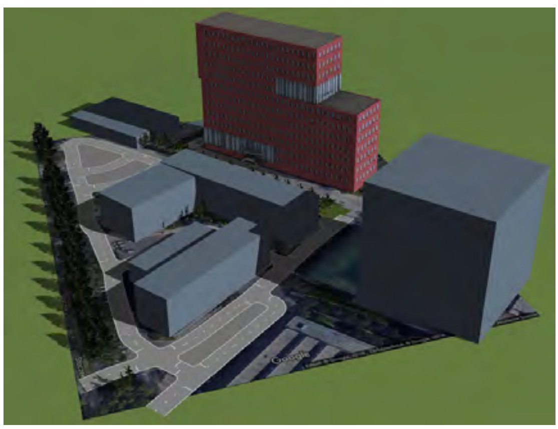

Fig. 5 The applied simulation environment [6]

The simulation environment makes possible to test the path planning algorithm without the risk of vehicle injury. Besides it also makes possible to neglect some simplifica-

tions in the algorithm (for instance the 2D perception of the LIDARs or the disturbances of environmental sensing).
The applied simulation environment can be seen in Figure 4.

## 4. LIDAR BASED ENVIRONMENT DETECTION

For the path planning method in this paper two sensors are necessary on the vehicle.
The first sensor is the DGPS system. To synchronise the map from the viewpoint of the vehicle with the global map it is necessary to know the exact position coordinates and the heading angle of the vehicle. The applied DGPS system on the vehicle has 20 millimetres and 1 degrees accuracy. With this accuracy the implemented DGPS model can be handled as an ideal position sensor in the simulation environment.
The second sensor on the vehicle are the 2D LIDARs on the front sides. The advantage of 2D measurement is the easy handling of data. The map modifier algorithm gets the LIDAR data as a vector, where the elements of the vector are the distances from the LIDAR to the obstacle in function of the angle difference from the heading angle. The disadvantage of the 2D measurement is that the LIDAR cannot sense the obstacles which are being below or above the sensed plain.
The LIDARs on the test vehicle can see for 40 meters distance and due to their localization on the vehicle they also can see the obstacles laterally from the vehicle. In front of the vehicle both LIDARs can percept the area, so on the test vehicle they can work redundantly. In this paper a simplified LIDAR model is used. There is only one LIDAR at the front of the vehicle and the angle range is just 120 degrees, de perception near the vehicle is neglected here. In further research the LIDAR model can be extended. It is not necessary to use the whole range of the LIDARs, it will enough to use only the area which is available with vehicle driving.

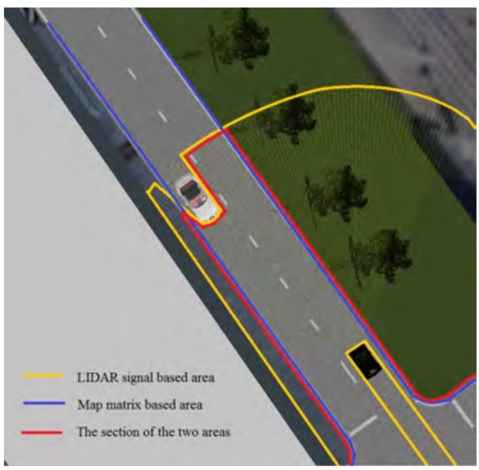


Fig. 6 Synchronization of the map and the sensed environment

In Figure 6 the LIDAR signal process can be seen where the information from the map and from the LIDAR is merged with each other.

## 5. PARKING PLACE DETECTION

In Figure 7 the measurements can be seen with the on-board LIDARs of the test vehicle. The different pictures has different sampling. Light blue represents the parking area on the map.

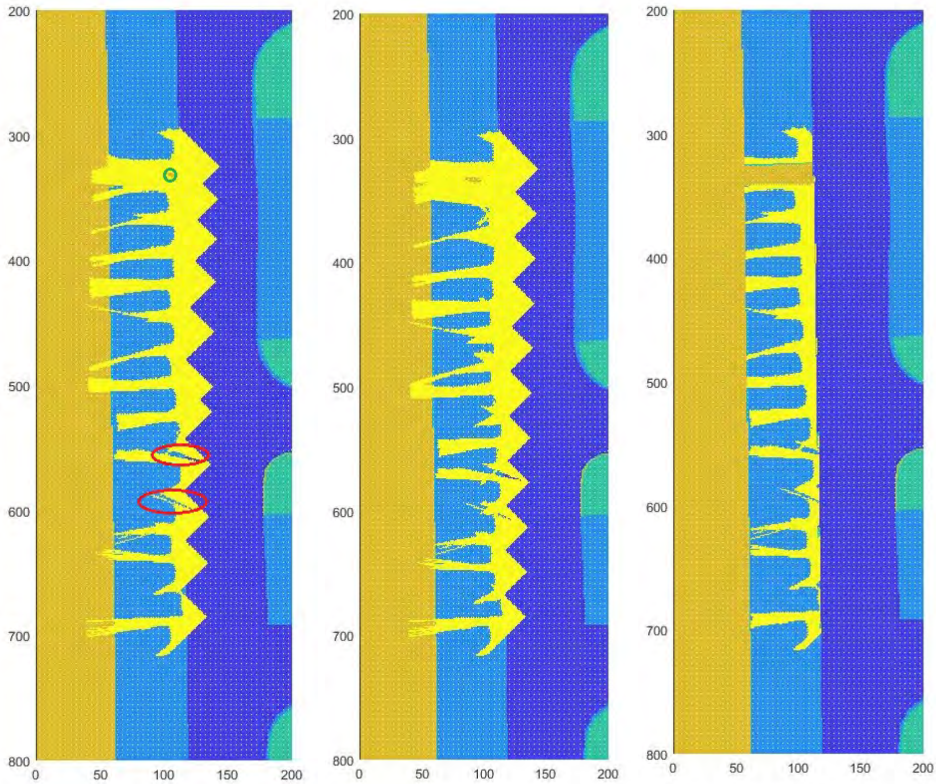


Fig. 7 Environment measurement with LIDAR in a parking area

As it can be seen the disturbances in the measurement are decrease in function of the sampling. The task of the signal processer algorithm is to find a free place which can be defined by the required distance two vehicles.
The sensed vehicles can be seen in Figure 8 with high sampling. By the boundary lines of the vehicles can be used for the map modification to realise the path planning. It is important that the vehicle only can sense a free parking place if it runs further near the parking place a bit because the LIDAR cannot sense the other sides of the vehicles. In further researches it will be also a task to handle moving obstacles in the parking places.

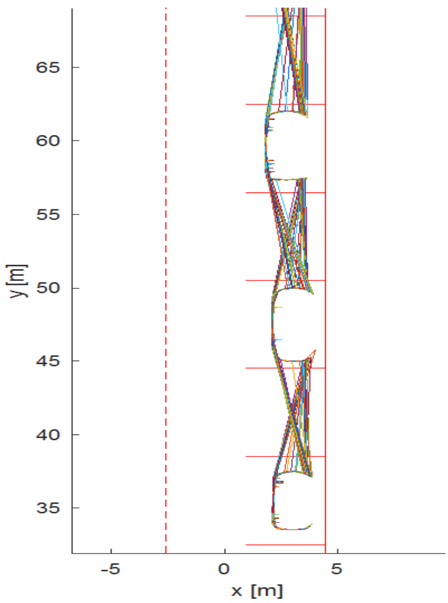


Fig. 8 Simulation of parking place perception in Prescan environment

## 6. CONCLUDING REMARKS

Connected and automated vehicles will bring disruptive changes to road transport. The main aim of the increased automatisation is the improvement of the safety of road transport. Nowadays automated vehicles can help the driver and they can do some simpler functions on their own. The development is motivated by newer and newer functions and at the end of the day automatized functions will take over the control from the human driver.

One of the functions is the valet parking function which has higher complexity. Valet parking needs also lateral and longitudinal control, it needs advanced environment perception and it needs usually a pre-defined map of the parking area.

In this paper the main steps of the valet parking function was presented. The research was done in the parking area of the University which was modelled by a matrix and in Prescan simulation environment. From previous research an offline path planning algorithm was given, this paper is an extension with the LIDAR based environment detection.

Our test vehicle has two 2D LIDARs on the front sides. If the vehicle knows where it should search a free parking place (it knows the parking areas from the pre-defined map) it can detect the availability of the parking place by the LIDARs.

In the final chapter the measurement and the simulation of the LIDAR environment sensing was presented. The next step will be signal processing of the sensed obstacles to use it in a path planner algorithm. The logics of the whole process can be seen in Figure 9.

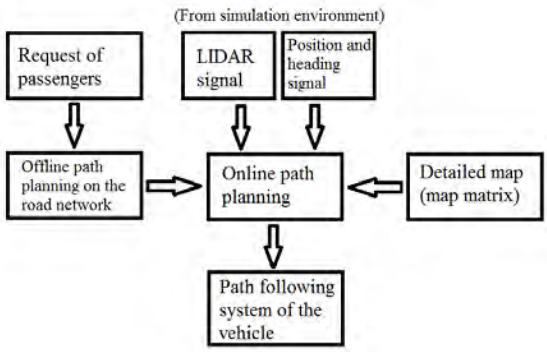


Fig. 9 Logics of the valet parking function

## 7. ACKNOWLEDGEMENT

The project has been supported by the European Union, co-financed by the European Social Fund. EFOP-3.6.2-16-2017-00002

## 8. REFERENCES

[1] ISO, "International standard road vehicles - functional safety," International Organization for Standardization, Geneva, Switzerland, ISO26262

[2] **Nyerges, Á – Tihanyi, V.**: Trajectory Planning for Autonomous Vehicles – A Basic Approach, 2nd International Conference on Vehicle and Automotive Engineering, 23-25 May. 2018, University of Miskolc (Hungary), 2018

[3] **Barsi, Á. - Nyerges, Á. – Potó, V. – Tihanyi, V.**: An Offline Path Planning Method for Autonomous Vehicles, Production Engineering Archives 19 (2018) 37-42

[4] **Barsi, Á. - Nyerges, Á. – Potó, V. - Tihanyi, V.**: Offline Path Planning for Autonomous Vehicles, 35th International Colloquium, Advanced Manufacturing and Repair Technologies in Vehicle Industry, 23-25 May., Zielona Góra – Lagow Lubuski (Poland), 2018

[5] **Barsi, Á. - Nyerges, Á. - Potó, V. - Siroki, Sz. – Tihanyi, V. – Virt, M.**: Offline path planning of automated vehicles for slow speed maneuvering IEEE 18th International Symposium on Computational Intelligence and Informatics, 21-22 November, Budapest, 2018

[6] Tass International: Prescan Manual Version 8.4.0

[7] **Gu, T. - Snider, J. – Dolan, J. – Lee, M.**: Focused trajectory planning for autonomous on-road driving. IEEE Intelligent Vehicles Symposium (IV) June 23-26, 2013, Gold Coast, (Australia), 2013

[8] **Hult, R. – Tabar, R.**: Path planning for highly automated vehicles Master's Thesis in Systems, Control and Mechatronics. Gothenburg, (Sweden), 2013

[9] **Chebly, A. - Tagne, G. – Talj, R. – Charara, A.**: Local trajectory planning and tracking for autonomous vehicle navigation using clothoid tentacles method. HAL Id: hal-01139316, 2015

[10] **Dolgov,D. - Thrun, S. – Montemerlo, M. – Diebel, J.**: Path planning for autonomous vehicles in unknown semi-structured environments. The international journal of robotics research Vol. 29, No. 5, 2010, p.485–501.

[11] **Dijkstra, E. W.**: A note on two problems in connexion with graps. Numerische Mathematik 1 (1959), p.269-271.
[12] SAE International: Taxonomy and definitions for terms related to on-road motor vehicle automated driving systems. SAE standard, nr. J3016__201401, 2014-01-16, http://standards.sae.org/j3016_20140 (Accessed 30 October 2018)
[13] **Szalay, Zs. - Nyerges, Á. - Hamar, Z. – Hesz, M.**: 'Technical specification methodology for an automotive proving ground dedicated to connected and automated vehicles. Periodica Polytechnica, Transportation Engineering, , 45(3), Budapest (Hungary), 2017, p.168-174.
[14] **Szalay, Zs.**: Structure and architecture problems of autonomous road vehicle testing and validation. Proceedings of the 15th MINI Conference on Vehicle System Dynamics, Identification and Anomalies – VSDIA 2016 (Ed. by Prof. I. Zobory). Budapest (Hungary), 2016, p.229-236.
[15] **Tettamanti, T. – Varga, I. - Zs. Szalay**: Impacts of autonomous cars from a traffic engineering perspective, Periodica Polytechnica, Transportation Engineering, Hungary, 44(4),Budapest, 2016, p.244-250,
[16] MathWorks: Graph and network algorithms toolbox: User's guide (R2015b) 2015. www.mathworks.com/help/pdf_doc/ (Accessed 30 October 2018)
[17] MathWorks: Curve fitting toolbox: User's guide (R2015b) 2015. www. mathworks. com/help/pdf_doc/ (Accessed 30 October 2018)
[18] **Bertolazzi, E. – Frego, M.**: Fast and accurate clothoid fitting, ACM Transactions on Mathematical Software, 2012
[19] **Zöldy, M.**: Legal Barriers of Utilization of Autonomous Vehicles as Part of Green Mobility Burnete, N. and Varga, B. O. (Eds.): AMMA 2018, PAE, p. 1–6, 2019 https://doi.org/10.1007/978-3-319-94409-8_29 (Accessed 30 October 2018)
[20] **Gáspár, P. – Szalay, Zs. – Aradi, Sz.**: 'Highly automated vehicle systems' BME MOGI 2014, http://www.mogi.bme.hu/TAMOP/ jarmurendszerek _iranyitasa_ angol/ index.html (Accessed 30 October 2018)
[21] **Nyerges, Á. – Szalay, Zs.**: A new approach for the testing and validation of connected and automated vehicles. Paper presented at 34th International Colloquium on Advanced Manufacturing and Repairing technologies in Vehicle Industry, 17-19 May, Visegrád (Hungary), 2017
[22] **Lengyel, H. – Szalay, Zs.**: Classification of traffic signal system anomalies for autonomous vehicles tests environment, Production Engineering archives, (19), 2018, p.43-47.
[23] **Lengyel, H. – Szalay, Zs.**: Traffic sign anomalies and their effects to the highly automated and autonomous vehicles, 35th International Colloquium on Advanced Manufacturing and Repair Technologies in Vehicle Industry, 2018
[24] **Paden, B. - Cáp, M. - Zheng Yong, S. - Yershov, D. – Frazzoli, E.**: A Survey of Motion Planning and Control Techniques for Self-driving Urban Vehicles, 2016
[25] **Bautista, D. G. - Pérez, J. – Milanes, V. - Nashashibi, F.**: A Review of Motion Planning Techniques for Automated Vehicles, IEEE Transactions on Intelligent Transportation Systems · November, 2015
[26] **Domina, Á. – Tihanyi, V.**: Comparison of path following controllers for autonomous vehicles, SAMI 2019 IEEE 17th World Symposium on Applied Machine Intelligence and Informatics, 2019

# REINFORCEMENT LEARNING BASED RACING CAR CONTROL

**Szilárd ARADI, Balázs TARI, Tamás BÉCSI and Péter GÁSPÁR**

Department of Control for Transportation and Vehicle Systems
Faculty of Transportation Engineering and Vehicle Engineering
Budapest University of Technology and Economics
H-1521 Budapest, Hungary

*Received: November 5, 2018*

## ABSTRACT

In the field of autonomous vehicle control the ideal trajectory planning problem is of great interest. In this paper, the results of a machine learning based race track control are presented. The models of the race track, the vehicle and the sensors are provided by TORCS, The Open Racing Car Simulator. The control of the vehicle is realized with a deep dense neural network. The aim of the research is to define a learning algorithm and reward system ensuring that the learning agent develops high-level driving skills from scratch without a prior knowledge. The developed system can be seen as an end-to-end black box control, though its performance is compared to other reference methods.

*Keywords:* machine learning, reinforcement learning, reward, vehicle control, TORCS

## 1. INTRODUCTION

Artificial intelligence's role in our daily life will be more and more significant over time. This is also true for the vehicle industry and transportation. Since its invention the AI has a long, rough developing path. It was forgotten for a long time because even in the recent past its high demand of computing capacity inhibited its widespread usage. But nowadays when we have more and more powerful computers the AI lives its renaissance.

At the same time due to never seen wealth and industrialization more and more vehicles are on the roads every day. More vehicles mean more complex transportation system and even more accidents. A solution could be to minimize the human factor with self-driving cars. Now Level 5 self-driving systems are the vision of the distant future. In 2018 there is only one commercial car to claim to be capable of level 3 self-driving (Audi A8).

Implementing such a high-level autonomous system is nearly impossible, or at least very hard with conventional programming and controlling tools. AI could make it easier to prepare a self-driving system for even unexpected situations. The world is moving in that direction. Tesla connects every data from their sold cars and uses them to train their own neural networks. In the near future Roborace, a formula racing series for autonomous cars will intorduce teams using AI actively.

This paper is about the work in the field of vehicle control with neural networks which is a part of the scholarship program about autonomous vehicles at the Budapest University of Technology and Economics.

In Section 2 the theoretical basis of reinforcement is introduced, Section 3 describes the simulation environment, then in Section 4 our proposed method is detailed and finally the results and the conclusion is discussed.

## 2. REINFORCEMENT LEARNING BASED VEHICLE CONTROL

### 2.1 Reinforcement Learning Introduction

In reinforcement learning (as in other areas of artificial intelligence) the learner and decision maker is called the agent. It interacts with the so-called environment, comprising everything outside the agent. These interact continually with each other, the agent selecting actions and the environment responding to these actions and presenting new situations to the agent (see Fig. 1). The terms agent, environment, and action meet the control engineers' terms controller, plant and control signals.

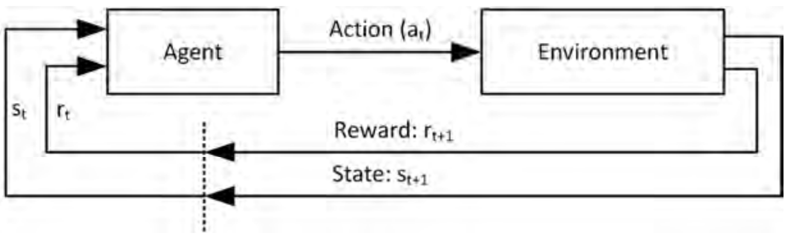


Fig. 1. Agent-environment interaction in reinforcement learning

In reinforcement learning the environment can be typically formulated as a finite-state Markov Decision Process (MDP). It is described with state $s_t$ (where $s_t \in S$ and $S$ represents the system's state space), action $a_t$ changes the environment state from $s_t$ to $s_{t+1}$ with state transition probability $P(s_t, a_t, s_{t+1})$. The agent and environment interact at each of a sequence of discrete time steps, $t = 0,1,2,3$ .... Finally, the most interesting part of reinforcement learning is the numerical reward $r_{t+1} \in R$ indicates how well agent is doing. The agent's job is to learn how can be the reward maximized, i.e. to find policy $\pi: S \to A$ that maximizes the cumulative future reward $R = r_0 + r_1 + \cdots + r_n$ exactly the discounted future reward $R = \sum_0^n \gamma^t r_t$. The discount factor $0 \leq \gamma \leq 1$ represents the uncertainty of the future, i.e. how much the future rewards depend on the actions in the past. A prediction of cumulative future reward $V_\pi(s) = E_\pi[R|S_t = s]$ is defined as the ``value'' of the state which can be used to evaluate the badness or goodness of the state and therefore to select between actions. There exists an optimal policy $\pi^*$ for which $V^{\pi^*}$ is optimal for every state.

In a finite MDP, the sets of states, actions, and rewards $(S, A, R)$ all have a finite number of elements. The Markov property of MDP requires that the probability distribution of random variables (transitions and rewards) depends on the current state and action only, and on the past actions and states.

Depending on the selected method, the RL agent may include policy function, value function and model. The latter is the agent's representation of the environment, according to its presence in the solution we can categorize RL methods as model-free or model-based solutions.

### 2.2 Deep Deterministic Policy Gradient

Deep Deterministic Policy Gradient [4] combines the policy and value based methods above, where we substitute the policy and value-based methods with neural networks. It gives us the base equation of DDPG:

$$\frac{\partial L(\theta)}{\partial \theta} = \frac{\partial\big(Q(s,a,w)\big)}{\partial \theta}$$

But in this case, because of the actor's deterministic policy the exploration is not provided. In order to simplify calculations, instead of using a stochastic policy, we simply add some noise to the prediction of the actor network.
These neural networks are often unstable in many environments, so we also need target networks, which are slowly updated, improving stability of learning.

$$\theta' = \tau\theta + (1-\tau)\theta'$$

The algorithm itself can be seen at Fig. 2.

**Algorithm 1** DDPG algorithm

Randomly initialize critic network $Q(s, a|\theta^Q)$ and actor $\mu(s|\theta^\mu)$ with weights $\theta^Q$ and $\theta^\mu$.
Initialize target network $Q'$ and $\mu'$ with weights $\theta^{Q'} \leftarrow \theta^Q$, $\theta^{\mu'} \leftarrow \theta^\mu$
Initialize replay buffer $R$
**for** episode = 1, M **do**
  Initialize a random process $\mathcal{N}$ for action exploration
  Receive initial observation state $s_1$
  **for** t = 1, T **do**
    Select action $a_t = \mu(s_t|\theta^\mu) + \mathcal{N}_t$ according to the current policy and exploration noise
    Execute action $a_t$ and observe reward $r_t$ and observe new state $s_{t+1}$
    Store transition $(s_t, a_t, r_t, s_{t+1})$ in $R$
    Sample a random minibatch of $N$ transitions $(s_i, a_i, r_i, s_{i+1})$ from $R$
    Set $y_i = r_i + \gamma Q'(s_{i+1}, \mu'(s_{i+1}|\theta^{\mu'})|\theta^{Q'})$
    Update critic by minimizing the loss: $L = \frac{1}{N}\sum_i (y_i - Q(s_i, a_i|\theta^Q))^2$
    Update the actor policy using the sampled policy gradient:

$$\nabla_{\theta^\mu} J \approx \frac{1}{N}\sum_i \nabla_a Q(s, a|\theta^Q)|_{s=s_i, a=\mu(s_i)} \nabla_{\theta^\mu}\mu(s|\theta^\mu)|_{s_i}$$

    Update the target networks:

$$\theta^{Q'} \leftarrow \tau\theta^Q + (1-\tau)\theta^{Q'}$$
$$\theta^{\mu'} \leftarrow \tau\theta^\mu + (1-\tau)\theta^{\mu'}$$

  **end for**
**end for**

Fig. 2 DDPG pseudo code

## 3. SIMULATION ENVIRONMENT

### 3.1 TORCS

The Open Racing Car Simulator (TORCS) [5] is an open source 3D car racing simulator, used as an ordinary car racing game and as a research platform. It is developed by Eric Espié, Cristopher Gouinneau and Bernhard Wymann. The simulation features a simple damage model, collisions, tire and wheel properties (springs, dampers, stiffness, etc.), aerodynamics (ground effect, spoilers, etc.) and much more.
There is an extension for TORCS, hereafter referred to as Competiton Software [6]. This software extends the original TORCS a server-client architecture (see Fig. 3.).

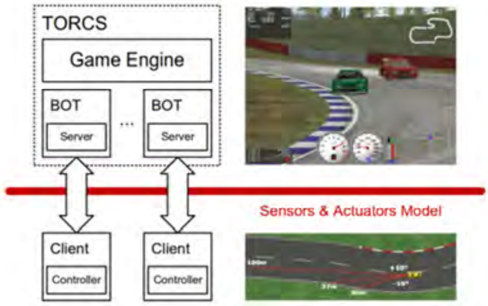


Fig. 3 TORCS server-client architecture

### 3.2 Client Environment

The client is based on Chris Edward's SnakeOil library [7]. SnakeOil is a Python library for interfacing with the Competition Software patched TORCS. Using SnakeOil writing a code for a client is very easy. It calls the function that gets the sensory data every 20 milliseconds and will eventually send the response. The initial project, which is Ben Lau's DDPG TORCS project [8] uses this library. It uses DDPG with an actor and critic networks having 300 and 600 neurons in their 2-2 hidden layers. As it could be seen later, we reduced the number of neurons in each hidden layer to 128.

The agent was trained on *'CG-Track2'* racetrack and tested on *'Street1'* and *'E-Track5'* (see Fig. 4).

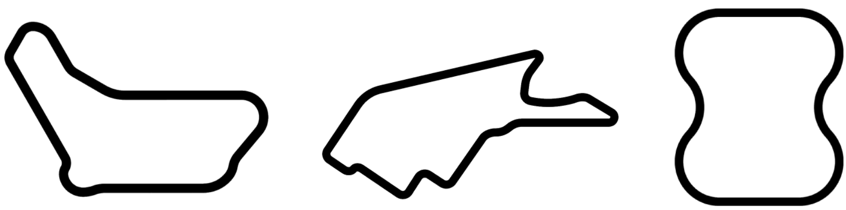

Fig. 4 From left to right: CG-Track2, Street1, E-Track5

## 4. LEARNING TO RACE

### a. Modified sensors and rewards

With the reduced numbers of hidden layer neurons, we could not reproduce the results of the original project. Our answer for this challenge was rethinking the input data and the reward system. We needed less, but more 'informative' inputs. Instead of the original, 29 sensor data, we ended up with 12. The changes were the addition of acceleration, yaw-rate and curve radius normalized between -1 and 1 and removal of Z axis speed, RPM. The curve radius was calculated from the 19 track edge range finder sensors, therefore we could also remove 18 of them. A complete list of the inputs of the neural network:

- yaw error
- lateral error
- X-axis velocity
- Y-axis velocity
- X-axis acceleration
- curve radius
- rotation speed of the four wheels
- yaw-rate
- one track edge range sensor facing forward

The modified reward system is based on the Stanley controller [8] and the kinematic bicycle model [9]. Stanley had a steering angle law

$$\delta = -\left(\psi + \arctan\left(k \cdot \frac{y}{v}\right)\right),$$

where delta is the steering angle, psi is the yaw error, y is the lateral error and k is a gain parameter. According to the bicycle model

$$\dot{\psi} = v \cdot \frac{\tan\delta}{L},$$

where L is the vehicle's wheelbase, in this case 2600 mm. After expressing delta from this equation:

$$\delta = \arctan\left(\dot{\psi} \cdot \frac{L}{v}\right)$$

we can equate this to the Stanley model's delta:

$$-\left(\psi + \arctan\left(k \cdot \frac{y}{v}\right)\right) = \arctan\left(\dot{\psi} \cdot \frac{L}{v}\right),$$

$$\psi + \arctan\left(k \cdot \frac{y}{v}\right) + \arctan\left(\dot{\psi} \cdot \frac{L}{v}\right) = 0 .$$

Hence the left side of this equation will be referred to as B. We see that the better the action, the closer the value of B to zero. We used an empirical formula to calculate a normalized reward using the value of B and the X-axis velocity of the car:

$$Reward = \tanh\left(\frac{V_x}{150}\right) \cdot \cos\sqrt{B \cdot \pi \cdot \frac{2}{3}} .$$

We needed to divide the X-axis velocity with 150 because the top speed of the car is around 300km/h, and the $\pi \cdot \frac{2}{3}$ factor to set the argument of the cosine function between $-\pi$ and $\pi$.

If the car is **out of track** or running backwards (yaw angle is greater than 180 degrees) the episode terminates, and the agent gets a reward equals to -1.

### b. Modified Negative Reward Calculation

The basic idea behind that new method is that the agent maybe never experiences negative reward right before the end of an episode, because the reward system is based on states, not on actions. In DDPG, we use future discounted reward, because the great negative reward at the end of an episode has an effect on this. But at such a complex problem like this (50 steps per second, a lot of input data, etc.) the future discounted reward is not effective enough. In some cases, there are situations when it is improper to punish the agent, but in but in another cases, it must be given a negative reward despite of it is in a very similar state. For example, driving in the edge of the track is sometimes desirable, but steering the car out of the track is a big mistake. Maybe it could be solved with an overcomplicated reward system, but instead of that, we figured out a new method, which could judge whole processes instead of just steps more effectively than discounted future reward.

A solution to this problem could be that if we did not determine the reward instantly, but after a few steps. It can be easily implemented without major changes in the code because the structure of the DDPG. The *(s, a, r, s')* transition is added to the Replay Buffer, and after that we sample a random minibatch of some transition from there, so it is possible to wait a few steps to determine the value of the reward.
We sliced every episode into small, 100 step (2 seconds) pieces. After 200 steps, the first 100 transitions with the original values of rewards are added to the Replay Buffer. From now, after every 100 steps, the next 100 steps slice is added too. At the end of every episode (in case the car crashes, etc.) there is a complete and an incomplete slice of 100 steps which are not added to the Replay Buffer. The idea of judging whole processes is implemented by applying linear interpolation on the value of rewards in the last 100 steps between the last value (-1) and the hundredth last value, as seen on the linear interpolating the value of rewards in the last 100 steps as seen on Fig. 5.

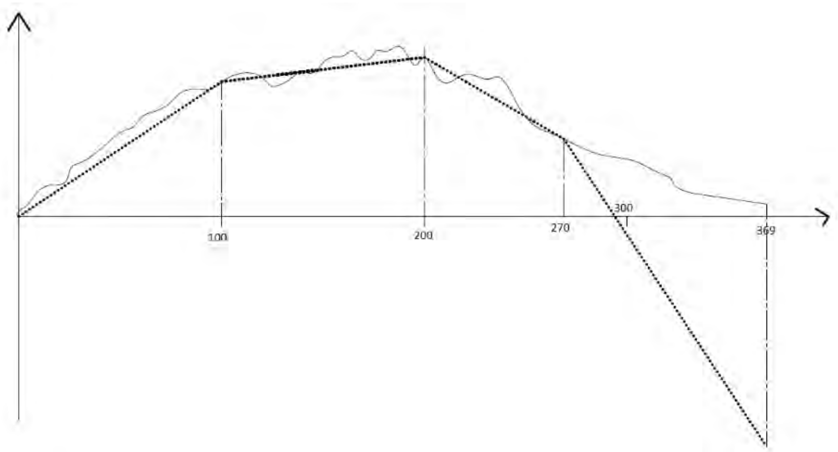


Fig. 5 New negative reward calculation

In case of this method we tried two similar reward systems. First the one that was introduced in *Modified sensors and rewards*, as seen as (11), then a slightly modified version, as setting the gain parameter $k$=0 and changing the factor under the square root to $\pi \cdot \frac{2}{2}$.

$$Reward = \tanh\left(\frac{V_x}{150}\right) \cdot \cos\sqrt{\left(\psi + \arctan\left(\dot{\psi} \cdot \frac{L}{v}\right)\right) \cdot \pi^2} \quad .$$

This calculation ignores the lateral error, so in theory it encourages the actor to find apexes. This assumption was correct. agent was trained on *'CG-Track2'* racetrack and tested on *'Street1'* and *'E-Track5'*.

## 5. RESULTS

This new method (Modified Negative Reward Calculation) was the most promising we have tried. It was the only one, where the agent learned how to brake, and could complete a whole lap on E-track5 and found the apex in left turns. It was trained for a few hundred episodes. While training, the agent has learned not to crash into walls at the very beginning of the track in just 10-15 episodes, but in 30-50 episodes it began to use the brake increasingly, causing that it stood still at the starting line. But too low speed is punishable too, like crashing the walls, so after a while the agent has learned that it should start first and only use brake before the turns. If the agent completed a lap while testing, the episode was terminated after a given number of steps during lap two. The process can be seen in Fig 6.

Fig. 6 Maximum raced distance (blue) and velocity (red) over episodes using modified negative reward calculation

## 6. CONCLUDING REMARKS

There is a great potential in automotive use of neural networks and machine learning. We saw that choosing a proper state-space and reward system can improve the training speed and the results. Sometimes this is not enough because the complexity of the problem like the control of a simulated racecar in a virtual world when in every seconds there are 50 steps. DDPG is simply ineffective with the given neural networks size and computing time available.

This new method called “Modified negative reward calculation” is an improvement in the rewarding system. The idea behind is that we should “punish” whole processes instead of just the episode's terminating step worked. It was the fastest learning method that we tried in these months, and it was the only one which used the car's brakes before entering a turn. This is the most promising algorithm of all we implemented, so in the future our research will be focus on this method.

## 7. ACKNOWLEDGEMENT

EFOP-3.6.3-VEKOP-16-2017-00001: Talent management in autonomous vehicle control technologies - The Project is supported by the Hungarian Government and co-financed by the European Social Fund

## 8. REFERENCES

[1] **van Hasselt, H. - Guez, A. - Silver, D.:** “Deep reinforcement learning with double q-learning”, *CoRR,* vol. abs/1509.060461, 2015.

[2] **Wang, Z. - de Freitas, N. - Lanctot, M.**: “Dueling network architectures for deep reinforcement learning”, *CoRR*, vol. abs/1511.06581, 2015.

[3] **Sutton, R. S. - McAllester, D. - Singh, S. – Mansour, Y.:** “Policy gradient methods for reinforcement learning with fuction approximation”, *Advances in Neural Information Processing Systems,* vol. 12, 2000, p.1057-1063,

[4] **Lillicrap, T. P. - Hunt, J. J. - Pritzel, A. - Heess, N. - Erez, T. - Tassa, Y. - Silver, D. - Wierstra, D**: “Continuous control with deep reinforcement learning”, *CoRR*, vol. abs/1509.02971, 2015.

[5] **C. G., C. D., R. C., A. S., Bernhard - Espié, E.**: “TORCS, The Open Racing Car Simulator”, http://www.torcs.org, 2014.

[6] **Loiacono, D. - Cardamone, L. - Lanzi, P. L.**: “Simulated car racing competition software manual”, vol. abs/1304.1672v2, 2013.

[7] **Edwards, C.**: “Snakeoil”, http://xed.ch/p/snakeoil

[8] **Lau, B.**: “Using keras and deep deterministic policy gradient to play TORCS”, https://yanpanlau.github.io/2016/10/11/Torcs-Keras.html

[9] **Stanley Racing Team**: “Stanley: The robot that won the DARPA Grand Challenge”, *Journal of Field Robotics*, vol. abs/1511.06581, 2015

[10] **Polack, P. - Altché, F. - D’Andréa-Novel, B. - De La Fortelle, A.**: “The kinematic bicycle model for planning feasible trajectiroes for autonomous vehicles” in *IEEE Intelligent Vehicles Symposium (IV),* 2017.

# FAILURE MODE AND EFFECT ANALYSIS TYPES IN THE AUTOMOTIVE INDUSTRY

**Annamária KONCZ**

Óbuda University
Doctoral School on Safety and Security Sciences
H-1081 Budapest, Hungary

*Received: November 5, 2018*

## ABSTRACT

Nowadays, the automotive branch gains more and more importance in industry in the EU and in Hungary as well. The automotive sector consists of a complex supply chain, as the products (vehicles) are getting more and more complex as well. Quality is the most important factor of mass production of automotive products. Failure Mode and Effect Analysis is a quality tool of the automotive industry. FMEA has a long history from the 20th century until nowadays. It was developed by the NASA for identifying risks in processes. Soon it came to light that this method can be used for the analysis of different processes as well. At the end of the 20th century, it was the most known quality tool of the automotive industry. FMEA usage is not just a possibility in the automotive sector, but it is a must according to IATF 16949:2016, the surplus criteria of the ISO 9001:2015. (The usage of the IATF 16949 standard is obligatory for car producers and their supply chain.) Even the car producer companies made as well their own requirements in the past like the AIAG (USA) and VDA (Germany). In my work, I define the VDA FMEA methodology.

*Keywords:* automotive industry, domestic automotive industry, automotive manufacturers, Failure Mode and Effect Analysis, IATF 16949:2016

## 1. INTRODUCTION

Domestic automotive industry has a long history from the end of the 19th century until nowadays, despite that our region is not obviously industrial. Nowadays, all levels of the automotive supply chain is represented in Hungary (automotive manufacturers and automotive suppliers). Hungarian automotive industry is a dynamically growing and internationally recognized sector [1]. This is mainly a result of the relocalization trend in the industry which affects the biggest automotive companies [2]. As this industry branch is significant in employment and performance it is worth to analyze. The quality of automotive products increases competitiveness. Working according to standards is the key feature of success in this sector, so in my work I present IATF 16949:2016. Failure Mode and Effect Analysis is one of the core quality tools. It's usage is even obligatory according to standards and quality handbooks of trade associations.

The paper is organized as follows: Chapter 2 introduces the present situation of automotive industry, Chapter 3 presents IATF 16949:2016, Chapter 4 defines FMEA and its different types. Finally, the study is summarized in Chapter 5.

## 2. AUTOMOTIVE INDUSTRY

In Chapter 2, the aim is to present the automotive industry of the European Union and Hungary. It is important to analyze the automotive status of the region to recognize tendencies in the region.

## 2.1 Automotive industry in the European Union

As Hungary is a member state of the European Union, I would like summerize the most important features of the EU automotive status at first.

According to statistics, the automotive industry employs approximately 12 million people in Europe:

- approximately 3 million people are employed in manufacturing area,
- approximately 4 million people are employed in sales and maintenance,
- approximately 5 million people are employed in transportation.

In addition, automotive industry accounts for 4% of the EU's industry [3].

In Table 1, the most important features of automotive are summarized.

| | |
|---|---|
| Motor vehicle production (EU28) | 19.6 million units |
| Passenger car production (EU28) | 17 million units |
| Motor vehicle registration (EU27) | 17.5 million units |
| Passenger car registration (EU27) | 15.1 million units |
| Motor vehicles in use (EU28) | 298.9 million units |
| Passenger cars in use (EU28) | 259.7 million units |
| Motorisation rate (EU28) | 587 units per 1000 inhabitants |
| Average age of vehicles (EU 25) | 11 years |
| Vehicle export (EU28) | 138.6 billion EUR |
| Vehicle import (EU28) | 48.3 billion EUR |

Table 1. Important feaures of EU automitive industry 2016-2017 [4]

According to recent data, 19.6 million motor vehicles were produced in the EU, which means 20% of global motor vehicle production. Besides, 17 million passenger cars were manufactured, which is 21% of global passenger car production. Meanwhile, 17.5 million motor vehicles and 15.1 million passeneger cars were registered in the period of 2016-2017.

Not only production is relevant, but the number of vehicles in use as well: 298.9 million motor vehicles and 259.7 million passenger cars were used in 2017. The motorisation rate was 587 units per 1000 habitants (motorisation rate was 389 in Hungary) in 2017. It is an interesting fact that the average age of the cars were 11 years. (Yearly vehicle export was 138.6 billion €, and import of 48.3 billion € [4].)

The relevance of EU automotive industry can be seen on Figure 1 as well. There will be 227 automobile assembly and production plants in the period of 2018-2019 [5].

As it can be seen on Figure 1, five automotive production plants will be located in Hungary [5]. These plants are/will be the following:

- Suzuki production plant in Esztergom (built in 1991) [6],
- Opel production plant in Szentgotthárd (built in 1991) [7],
- Audi production plant in Győr (built in 1993) [8],
- Mercedes production plant in Kecskemét (built in 2008) [9],
- BMW production plant in Debrecen (planned to be built in 2019) [10].

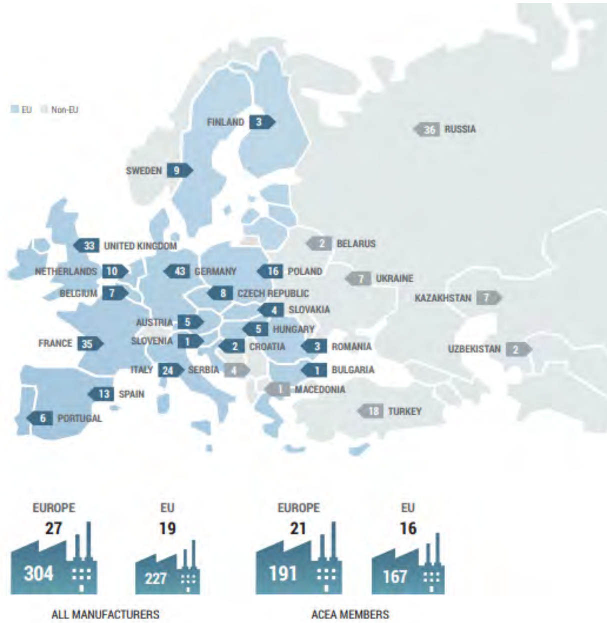


Fig.1 Automotive production plants in the European Union and in Europe (2018-2019) [5]

## 2.2 Automotive industry in Hungary

The Hungarian automotive industry consist of 5 automotive production plants (Suzuki, Opel, Audi, Mercedes, BMW) as mentioned in Chapter 2.1, and several automotive suppliers are situated in the region of automotive plants [5].

Automotive industry is an important domestic branch, although it must be pointed out that Hungary is not the leading country in this area. Amongst the Visegrád Group (V4) members (Czech Republic, Poland, Slovakia, Hungary) Hungary is at the third place in the amount of automotive production plants. According to 2015 data, 15 automotive production plants were located in Poland, 8 in the Czech Republic, 4 in Hungary and 3 in Slovakia [2]. Besides this, at the beginning of the 2010's there were more than 600 companies (suppliers) operating in this sector (in Hungary), with 15 billion EUR revenue and the employment of approximately 100.000 people [11]. These values exceeded until 2017: more than 700 companies (suppliers) are operating in the sector, with 26.1 billion EUR revenue and approximately 175.800 people employed [12]. In Table 2 the important features of automobile producers are presented.

| Company name | Number of employees | Car/engine production |
|---|---|---|
| Magyar Suzuki Corporation | 3100 | 176.705 (car) |
| Mercedes-Benz Manufacturing Hungary Ltd. | 4000 | ca. 190.000 (car) |
| Opel Szentgotthárd Ltd. (PSA) | 1251 | 486.302 (engine) |
| AUDI Hungária Ltd. | 12.307 | 105.491 (car)<br>1.965.165 (engine) |

Table 2. Production values and employment data of automotive manufacturers (2017) [12]

As it is stated in Table 2, the employment and production values of automotive manufacturers are outstanding. AUDI Hungária Ltd. itself employed 12.307 people, produced 105.491 cars and 1.965.165 engines in 2017 [12].
The TOP3 Tier 1 automotive suppliers in Hungary are: Bosch Group, Continental Group and Knorr-Bremse Group, according to Table 3. (As well it is important to see that these enterprises are subsidiaries of German companies.)

| Company name | Location (manufacturing) |
|---|---|
| Bosch Group | Hatvan, Miskolc |
| Continental Group | Budapest, Szeged, Nyíregyháza, Veszprém, Makó, Vác |
| Knorr-Bremse Group | Budapest, Kecskemét |

Table 3. TOP3 Tier 1 automotive suppliers [12]

## 3. INTRODUCTION OF IATF 16949:2016 (AUTOMOTIVE QMS STANDARD)

In this Chapter my aim is to introduce IATF 16949:2016, which is an important key to ensure the quality of automotive products. IATF 16949:2016 (1st edition) is the replacement of the ISO/TS 16949 technical specification, which is the surplus criteria of ISO 9001. IATF 16949 is an automotive QMS standard, which is obligatory in the automotive industry. ISO/TS 16949 had three editions (1st edition in 1999, 2nd edition in 2002, 3rd edition in 2009)[13]. As all ISO/TS 16949 certificates expired on 14th September 2018, it was crucial for the organisatios to switch to IATF 16949. The transition to IATF 16949 could have been done with transition audits, or later on with initial audits [14]. It is important to point out, that IATF 16949:2016 cannot be considered as a stand-alone standard, but it must be used in conjunction with ISO 9001:2015 [15].
IATF 16949:2016 standard was issued by IATF (International Automive Task Force), which is an „ad hoc" group of automotive manufacturers and trade associations. The aim this group is to provide quality products.
This goal can be reached through the following: with consensus development concerning international quality system requirement; with providing training to support requirements; with supporting formal connections of appropriate bodies; with developing policies and procedures [16].

IATF includes the following members: automotive manufacturers:BMW Group, FCA US LLC, Daimler AG, FCA Italy Spa, Ford Motor Company, General Motors Company, PSA Group, Renault, Volkswagen AG; trade associations: AIAG (*Automotive industry Action Group, United States*), ANFIA (*Associazione Nazionale Filiera Industria Automobilistica, Italian Association of the Automotive Industry, Italy*), FIEV (*Fédération des Industries des Equipements pour Véhicules, Equipment Industries Vehicle Federation, France*), SMMT (*The Society of Motor Manufacturers and Traders,United Kingdom*) and VDA QMC (*Verband der Automobilindustrie, German Association of the Automotive Industry, Germany*) [16].

In the following, I would like to summarize the most important FMEA-affected parts of IATF 16949:2016:
Product (Design) and process FMEAs have to be conducted and special approvals have to be obtained in terms of part Product Safety (Section 4.4.1.2) [15],
According to part Design and development planning, risk analysises have to be carried out and one used tool is FMEA (Section 8.3.2.1) [15],
In term of part Special Characteristics, all features have to be marked in the Risk analyises (FMEAs) [15],
According to part Design and development output, all outputs have to be verified and valideted against the input requirements (in case of FMEAs a well) (Section 8.3.5.1) [15],
According to part Manufacturing process design output, the output have to be verified against manufacturing process input requirements (FMEAs) (Section 8.3.5.2) [15],
In terms of Control Plans, the documentation has to contain the results of FMEAs, and has to be reviewed if risk analyses change (Section 8.5.1.1) [15],
According to Control of reworked product, FMEA has to be carried out on the basis of the process (Section 8.7.1.4) [15],
In terms of Control of repaired products, FMEA has to be conducted as well (Section 8.71.5) [15],
According to Monitoring and measurement of manufacturing processes, FMEA has to be implemented, and contain measurement techniques, sampling plans, acceptance criteria, records of actual measurement values, reaction plans and escalation process (Section 9.1.1.1) [15],
In terms of Identification of statistical tools, a proper verified tool has to be used in case of design risk analysis (D-FMEA) and process risk analysis (P-FMEA) (Section 9.1.1.2) [15],
According to Manufacturing process audit, the implementation of P-FMEA has to be regularly audited besides control plan (Section 9.2.2.3) [15],
In terms of Problem solving, the results have to be impemented in P-FMEA (Section 10.2.3) [15],
According to Error-proofing, the methods have to be implemented in P-FMEA (Section 10.2.4) [15],
In terms of Continual improvement, the organization has to carry out risk analysises (FMEA) (Section 10.3.1) [15],
Annex B of IATF 16949 describes the FMEA-relevant documents of trade associations (*AIAG:Potential Failure Mode and Effect Analysis, ANFIA:FMEA, VDA:Volume 4 Chapter Product and Process FMEA*). [15]
As it can be seen, FMEA is an unavoidable part of automotive quality systems.

## 4. FAILURE MODE AND EFFECT ANALYSIS IN AUTOMOTIVE INDUSTRY

Failure Mode and Effect Analysis is a method for failure cause identification. As a result of analysis, prevention actions (reduction of failure causes) and detection actions (detection of failure causes) are formed.
There are four main types of FMEA:

•System FMEA (e.g. for analysis of a whole car),
•Design (Product) FMEA (e.g. for analysis of a given product, like control systems),
•Process FMEA (e.g. for analysis of a production process, like SMT (*Surface Mounted Technology*) process,
•Service FMEA (e.g. for analysis of car repair services)[17].
Risk Priority (RPN) is the index number of FMEA. It is the multiplication of three factors:
•Severity (S): failure effect seriousness rating (rated 1-10),
•Occurrence (O): failure cause prevention rating (rated 1-10),
•Detection (D): failure cause detection rating (rated 1-10)[17].
The multiplication of S,O,D factors results in RPN, the biggest rating of it is 1000. (RPN is a value without dimension)[17].

In Chapter 3, it has been pointed out that different trade associations have guidelines (Handbooks on FMEA). These have to be followed by automotive suppliers (these are additional criteria to IATF 16949). In the following, the VDA method is presented, as Hungarian suppliers are mainly in contact with German manufacturers . (FMEA is defined in VDA Handbook 4.) [18]
According to VDA, a five-step model is implemented on FMEA creation:

1. Definition (definition of FMEA topics),
2.Analysis (identification of risks, valuation, optimization),
3.Measures (decision on measures),
4.Realization (introduction of measures,FMEA actualization and closure)
5.Communication (communication of FMEA results)[18].

In addition to standard multiplication of S ,O, D other evaluation methods are mentioned in VDA 4 Handbook as well:

• multiplication of S and O factors,
• multiplication of S and D factors,
• sum of S and O factors,
• sum of S and D factors,
• decreasing sequence of S,O,D multiplicated values,
• decreasing sequence of multiplicated S and O factors,
• decreasing sequence of multiplicated S and D factors,
• usage of risk matrix on S,O,D values [18].

In connection with development, it is important to point out that there is an ongoing VDA and AIAG process alignment, in order to simplify the status of suppliers both in contact with German and US automotive manufacturers [19].

## 5. SUMMARY

Chapter 2 pointed out the importance of automotive industry with the introduction of EU and domestic automotive status. It can be clearly seen that automotive industry is significant in both markets.

The aim of this study was to point out complexity of FMEA regulation and the introduction of FMEA types. The basic point is IATF 16949, but the "know-how" is defined in guidelines (Handbooks) of trade associations (e.g.VDA).
Further aim of the author is to analyse the main differences and similarities between VDA and AIAG FMEA methods, as it is important actual topic due to process alignment.

## 5. REFERENCES


[1] **Molnár, E.:**Egy dinamikus iparág foglalkoztatási hatásainak földrajzi aspektusai: a magyarországi autóipar esete, Területi Statisztika, 2013, 53(4), p.322–339.

[2] **Rechnitzer, J. – Hausmann, R. – Tóth, T.**: A magyar autóipar helyzete nemzetközi tükörben, Hitelintézeti Szemle, 16. évf. 1. szám, 2017. március, p.119–142.

[3] **European Commission**: Automotive industry (Internal Market,Industry, Entrepreneurship and SMEs), https://ec.europa.eu/growth/sectors/automotive_en, (Accessed: 02.11.2018)

[4] **European Automobile Manufacturers Association**: Key Figures, https://www.acea.be/statistics/tag/category/key-figures, (Accessed:02.11.2018)

[5] **European Automobile Manufacturers Association**: The automobile industry pocket guide, https://www.acea.be/uploads/publications/ ACEA_Pocket_Guide_ 2018-2019.pdf, (Accessed: 02.11.2018)

[6] **Magyar Suzuki Corporation**: A Suzuki Magyarországon, https://www.suzuki.hu/ corporate/hu/vallalat/gyar/gyar- tortenelem-2014 (Accessed:02.11.2018)

[7] **Opel Szentgotthárd Ltd**: Az Opel gyár története, https://www.opel.hu/opel-elmeny/ szentgotthardi-opel gyar/tortenetunk.html (Accessed:02.11.2018)

[8] **AUDI Hungária Ltd**:Az AUDI Hungária története, https://audi.hu/hu/a-vallalat/ az-audi-hungaria-tortenete/ (Accessed:02.11.2018)

[9] **Mercedes-Benz Manufacturing Hungary Ltd**.:Mercedes-Benz gyártörténet, https://www.gyar.mercedes-benz.hu/index.php/hu/ (Accessed:02.11.2018)

[10] **BMW Group**:Információk az új BMW gyárról, https://www.bmwgroup.jobs/hu/hu.html, (Accessed:02.11.2018)

[11] **Hungarian Investment and Trade Agency**:Automotive industry in Hungary (2011), http://investexport.brussels/documents/, (Accessed 02.11.2018)

[12] **Hungarian Investment Promotion Agency:** Automotive industry in Hungary (2017), https://hipa.hu/main#publications, (Accessed 02.11.2018)

[13] **International Automotive Task Force**: About IATF 16949:2016, https://www.iatfglobaloversight.org/iatf-169492016/about/, Accessed 02.11.2018)

[14] **International Automotive Task Force**:IATF 16949 transition update, https://www.iatfglobaloversight.org/, (Accessed 02.11.2018)

[15] **International Automotive Task Force**: IATF 16949:2016 (Automotive Quality System Standard)

[16] **International Automotive Task Force**: About IATF, https://www.iatfglobaloversight.org/about-iatf/, (Accessed 02.11.2018)

[17] **Stamatis,D.H.**: Failure Mode and Effect Analysis: FMEA from Theory to Execution, (2003), ASQ Quality Press

[18] **Szilágyi, G.– Lukács, K. – Szamosi, B. – Pokorádi, L**.:A QS 9000 és a VDA szerinti hibamód és -hatáselemzések összehasonlítása (2014), Repüléstudományi Közlemények, Volume XXVI, issue 2/2014, http://www.repulestudomany.hu/kulonszamok/2014_cikkek/2014-2-33-0115_Szilagyi_Gabor_et_al.pdf (Accessed 02.11.2018)

[19] **VDA QMC**:FMEA alignment VDA and AIAG (2018), https://vda-qmc.de (Accessed 02.11.2018)

## SESSION FOR DYNAMICS, IDENTIFICATION AND ANOMALIES OF AIRCRAFT AND SHIPS

**SZONDA, G. – VERESS, Á.** (Hungary)
CFD Analysis and Redesign of Main Landing Gear Unit on Skycruiser Sc-200 Autogyro for Drag Reduction ........ 331

**BÍRÓ, O. – SZABÓ, G.** (Hungary)
Integrating Large Remotely Piloted Vehicles into the Controlled Airspace ........ 349

**URBAN, A.X.C. – MOLNAR, I.T. - VERESS, A.** (Mexico+Hungary)
Investigation of Hybrid Propulsion Systems Applied on Small Sized Aircraft ........ 357

**BENEDA, K. – DERBEL, K.** (Hungary+Tunesia)
Identification of Single Spool Micro Turbojet Engine with Fixed Exhaust Nozzle at Multiple Operating Points for Linear Parameter Varying Control ........ 371

**HARGITAI, CS. – SIMONGÁTI, GY. – ZALACKÓ, R.** (Hungary)
Operational Profile of Inland Public Transport ........ 381

# CFD ANALYSIS AND REDESIGN OF MAIN LANDING GEAR UNIT ON SkyCruiser SC-200 AUTOGYRO FOR DRAG REDUCTION

**Gellért SZONDA and Árpád VERESS**

Department of Aeronautics, Naval Architecture and Railway Vehicles
Faculty of Transportation Engineering and Vehicle Engineering
Budapest University of Technology and Economics
H-1111 Budapest, Műegyetem rkp. 3, Hungary

*Received: November 6, 2018*

## ABSTRACT

Nowadays, flying as a sport or free time activity is becoming more and more popular due to the decreasing costs of vehicles and their operation. However, this would not be possible without using modern design techniques and processes in the industry. With the spread of simulation software, cost and time demand of research and development has dropped. In addition, as a result of ever-evolving technologies the manufacturing costs have also decreased over the past few decades. One of the main scopes of this paper is to introduce the recent activity on reducing drag of the main landing gear of the SkyCruiser SC-200 autogyro by analysing the flow conditions around it using CFD (Computational Fluid Dynamics). CFD provides realistic fluid dynamic parameters and offers wide variety of different visualisation techniques in order to get better comprehension of the evolved physical phenomena. As part of the present project, some rational simplifications was performed on the geometrical model of the baseline landing gear unit, then the drag force was determined at cruising speed and altitude. Design modifications were completed with respect to the baseline model taking the experience gained into account. With the new, aerodynamically improved model the main goal was to reduce the drag of the main landing gear system, which resulted in fuel consumption reduction and lower emission rates. Better fuel consumption increases the range and the uptime of the autogyro. Sensitivity analysis and plausibility check was completed to investigate the mesh independency and the correctness of the results. Moreover, by means of an experimental aerodynamic investigation, the flow characteristics generated by the software and the real photos about the flow pattern visualized by strips of yarns were compared with each other.

*Keywords:* autogyro, Computational Fluid Dynamics, landing gear, drag force, industrial development

## 1. INTRODUCTION TO SKYCRUISER AUTOGYRO LTD.

SkyCruiser Autogyro Ltd. was founded in October 2012 with the aim to create and develop an autogyro according to high-quality standards, which is also suitable for serial production. The company's philosophy consists in that premium quality has to be present throughout the whole lifecycle of the autogyro, starting from design through construction to operation, thus guaranteeing the costumer's satisfaction and the company deserving to be trusted. For the company, besides safety, one of the most essential aspects is to meet the personal demands of the costumers, so each autogyro manufactured by SkyCruiser is customised.

One of the company's main objectives is to promote the domestic microlight, sport flight, to which the company not only contributes with autogyro manufacturing, but also with air shows, sightseeing flights, education and attending various exhibitions. Considering the safety and low maintenance costs of the autogyros, as well as its favourable flight characteristics, the benefits of this type of aircraft can be exploited in a wide range of areas. Its versatility may represent an excellent solution and alternative for law-enforcement and military purposes, to secure government convoys and events, for observation and tracking objects, monitoring buildings, highways and railways, or even border protection. Furthermore, the potential hidden in autogyros can be used in forestry and hunting to monitor wildlife, to map and to eliminate illegal deforestation and landfills. Moreover, it can be utilised effectively also in agriculture for aerial spraying soil in order to destroy harmful insects or in populated areas for mosquito control.

SkyCruiser Autogyro Ltd. contributes to the development and growth of domestic industry, aeronautical engineering and vehicle manufacturing. Beside the inland market, it aims the foreign market also with high quality autogyros in order to achieve higher market share. The company with its continuous and innovative developments, it offers competitive solutions in comparison with other autogyro companies' products, thus guaranteeing its position in ultralight aircraft manufacturing.

Furthermore, it is important to emphasise the company's effort to cooperate with Budapest University of Technology and Economics, since SkyCruiser Autogyro Ltd. not only provides summer internships for flight and aircraft enthusiast students, but also offers a wide variety of interesting and useful diploma thesis topics. Therefore, for students it is provided the chance to use their knowledge acquired at the university in their profession, as well as having the opportunity to gain further expertise in aeronautics. The company can be characterised by open-mindedness to innovative and modern solutions, thus developments realised by student are often used in the autogyros.

## 2. SKYCRUISER SC-200 AUTOGYRO

The SkyCruiser SC-200 (Fig. *1*) is a pusher configuration, open cabin, two-seater and tandem arrangement autogyro, based on an initially designed and built gyrocopter. Even though the current model has undergone many improvements and upgrades over the past years, the SC-200 is still based on the first autogyro of the company.

Fig. 1 SkyCruiser SC-200 Autogyro

Due to the favourable properties of stainless steel, like corrosion-resistance, excellent weldability and high strength, the SC-200 is built on a welded frame made of hollow structural sections. The arrangement of the aircraft's landing gear is tricycle, the main landing gears being equipped with shock absorbers for comfortable take-off, landing and taxiing.

In addition to its favourable aerodynamic properties, the fiberglass cabin also enhances the passenger comfort. The cabin is not a load-bearing element, its function is to reduce the drag of the autogyro. Owing to the open design of the SC-200, it offers excellent visibility to the crew, while protecting them from the wind and increasing the security. In order to reduce the drag of the main landing gears, the wheels are also equipped with streamlined wheel cowlings.

The aircraft is powered by a Rotax 912 UL/A/F type, 4-cylinder, and four-strike boxer engine developed especially for ultralight aircrafts. The engines built in the SC-200 autogyros are equipped with a turbocharger kit, thus its maximum performance results in 125 hp. The engine is fitted with carbon-composite VelezProp propellers.

The lift is produced by a rotor of 8,4 m diameter Gyro-Tech carbon-composite rotor blades. The carbon fibre blades, despite their low weight, have high strength and are durable, since they withstand fatigue wear better resulting from vibrational stress, moreover the vibration damping properties of carbon fibre are favourable. For the convenience of the pilot, several systems in the SC-200 gyrocopter are electronically controlled, e.g. the actuation of the prerotator system, the trim control and rotor brake. Prior to take-off the prerotation is controlled electronically, however the procedure is mechanical.

SC-200 gyrocopter technical specifications are next:

- OWE: 290 kg
- MTOW: 560 kg
- $v_{cruise}$: 100-145 km/h
- $v_{min}$: 40 km/h
- $v_{NE}$: 160 km/h
- fuel tank capacity: 65 litres
- operating time: 3-4 hours
- average consumption: 12-16 litres/hour
- required take-off distance: 20-80 metres

## 3. COMPUTATIONAL FLUID DYNAMICS

Over the last couple of decades Computational Fluid Dynamics, or shortly CFD, has become a determining component of modern industrial design process with the sudden advancement of the CPUs' computing capacity. CFD means the numerical, mathematical-physical modelling of the fluid flow with the use of computers. There are many benefits of applying CFD, which makes it attractive in engineering practice; it can reproduce actual flow phenomena with acceptable accuracy. Furthermore significant amount of cost, time and human capacity can be saved, since "production" and "testing" in virtual space is less time- and cost consuming. In order to achieve the best results, the numerical methods used in the simulation can also be linked with optimization algorithms. Using CFD allows to perform analyses at locations or in special environments where direct measurements would not be possible (e.g. in the atmosphere

of an alien planet) or the measurement sensor would largely influence the results. Owing to the wide variety of visualization techniques it makes simpler the understanding of the physical phenomena. Although CFD was primarily developed for the aerospace and nuclear industry due to its many advantages, nowadays it is extensively used in many areas of industry to examine and solve flow problems: vehicle industry, turbomachinery design, meteorology, environmental protection, building engineering and astronomy for example. [1]
The CFD is based on the conservation laws of the physics as follows:

- Mass conservation law
- Momentum conservation law (in three directions in the Cartesian coordinate system)
- Total energy conservation law

The most common approach to make turbulence computationally tractable is the Reynolds-averaged Navier–Stokes Simulation (RANS), which solves the time-averaged Navier–Stokes equations, based on statistical averaging, introducing averaged and fluctuating parameters. The turbulence is modelled and SST (Shear Stress Transport) turbulence model was used in the present case [1], [2].

## 4. THE AIM OF THE ANALYSIS AND STRUCTURE OF THE WORK

The first goal of the simulation was to determine the drag force on the main landing gear and wheel cowling of the SkyCruiser SC-200 autogyro at cruising altitude and speed using CFX software in Ansys Workbench environment. By analysing the flow field around these domains, design modifications was proposed to reduce the drag force on the mentioned components. However, the aim of this paper was not to create the optimum shape with minimum drag, since the optimisation takes longer and time-consuming process that requires significant amount of design of experiences and more complex simulations.
The baseline model was prepared, including the cabin and the main landing gear unit as a first step of this work. Simplifications were realised on them, an initial mesh was created, the boundary conditions were imposed and then, after starting the execution, the convergence and imbalance curves and data were evaluated. The obtained results were used for mesh sensitivity analysis to determine the optimal mesh configuration.
In order to know the drag force on the cabin only for plausibility analysis, as a second step, another simulation was performed with the simplified cabin without landing gear unit. In this way, in addition to obtaining the drag force on the cabin, a plausibility test was performed. The result of the CFD simulation was compared with the outcome of analytical equation based on drag coefficient determined on similar shaped body.
Finally, geometry improvements were performed on the baseline model to make the main landing gear unit more streamliner and decrease the drag force. Following the numerical analysis, the aerodynamic results of the baseline and the improved version were compared with each other.

## 5. PREPARATION OF THE BASELINE MODEL

The flight of the autogyro involves aerodynamically complex and complicated phenomena. Not only due to the rotor and propeller, but also because of the flow around the cabin, rotor tower, landing gear, pushing rods and other parts of the aircraft. This is the reason of the simplifications realised during the preparation of the model, otherwise an overly complex model would highly increase the computational cost, the execution time and it is less likely that simulation would provide a convergent result.

Examined from co-moving coordinate system with the aircraft, the flow is slightly decelerated and deflected downwards as a result of the induced speed caused by the rotor. However, at cruising speed (120 km/h) the flow velocity is approximately one order of magnitude greater than the induced velocity of the rotor. Thus, the downward pushing effect of the rotor on the mean flow stream becomes dominant farther behind the autogyro. Taking into consideration the shading effect of the cabin and the fact that the landing gear unit is relatively far below and not behind the rotor, leads to the conclusion that the flow reaching the landing gear is only minimally disturbed by the the rotor. According to these assumptions, the effect of the rotor was ignored in the simulation.

The propulsion system (Rotax 912 turbocharged engine equipped with Velezprop propellers) produces ~280 kg of thrust. Knowing the thrust and the cruising speed of the autogyro, the induced speed of the propeller can be determined by using the momentum (or actuator disk theory). [3]

$$T = \dot{m}\, v_3 \,, \tag{1}$$

where: $T$ [N]: thrust;
$\dot{m}$ [kg/s]: air mass flow;
$v_3$ [m/s]: far wake speed.

$$\dot{m} = \rho\, R_{pr}^2\, \pi\, (c_0 + v) \,, \tag{2}$$

where: $\rho$ [kg/m$^3$]: density of the flowing medium;
$R_{pr}$ [m]: radius of the propeller;
$c_0$ [m/s]: cruise speed;
$v$ [m/s]: near induced speed.

Furthermore, based on momentum theory it is known that:

$$v_3 = 2\, v \,. \tag{3}$$

Thus, equation number (2) and (3) is substituted in equation number (1) it leads to the following equation:

$$T = 2\, v^2 \cdot \rho\, R_{pr}^2\, \pi + 2\, c_0\, v \cdot \rho\, R_{pr}^2\, \pi \,. \tag{4}$$

In case of knowing the thrust ($T = 2746.8$N), the cruising speed ($c_0 = 33.33$ m/s), the air density at cruising altitude (based on International Standard Atmosphere (ISA) at the altitude of 1000 meters above sea level: $\rho = 1.112$ kg/m$^3$) and the propeller diameter ($R = 1.778$ m), the near induced speed is: $v = 3{,}38$ m/s.

Thus, it can be deduced that near wake velocity is smaller by one order of magnitude in comparison with the undisturbed mean flow around the aircraft. Moreover, it is worth mentioning that the near induced speed is defined as the velocity right after the plane of the propeller, so in front of the propeller the effect of induced speed on the landing gear is even less significant. Based on these considerations, the model was further simplified by ignoring the effect of the propeller on the mean flow.

In comparison with the real physical model, there were additional simplifications on the model used for the simulation: the rotor tower, the horizontal and the vertical stabilizers were also ignored, since the rotor tower is above the cabin and the stabilizer surfaces are far behind the landing gear, thus they have zero or very little effect on the examined parts.

Further reductions were completed on the solid model of the landing gear itself (Fig. *2*). The hollow and surface parts were filled in and removed, thus reducing the complexity and mesh size. The smaller structural elements (connectors, screws, bolts, ball joints, the support plates of the wheel cowling and callipers) were not taken into consideration during the pre-processing for saving cell numbers and computational time. Tubes connecting to each other by structural joints were replaced with interconnecting rods. The tire and the rim were also swapped with a solid disk of the same size as the original model has. Considering that the shock absorber and the spring of the landing gear are located inside the cabin, so they are not exposed to the flow, these parts were excluded from the simplified model. The model of the wheel cowling being a surface model was transformed into a solid one.

Fig. 2 Original (without covering) (left) and the simplified (right) model of the main landing gear unit

As there are several segments on the cabin model, which have no effect on the flow around the main landing gear unit, additional simplifications was made. In order to reduce the calculation capacity demand by simplifying the mesh and the flow, the upper, open segment of the cabin was enclosed with streamlined section so the flow field inside the cabin was not simulated (Fig. *3*). The flow field is expected to be modified only above the cabin, it remains unaffected underneath. The simulation can take the effect of the cabin into consideration when generating the flow fields around the landing gear.

The updated geometry with all the mentioned rational simplifications discussed above in detail is suitable to simulate the flow accurately around that taking into consideration the effect of the cabin on the mean flow and to determine the drag force on the autogyro.

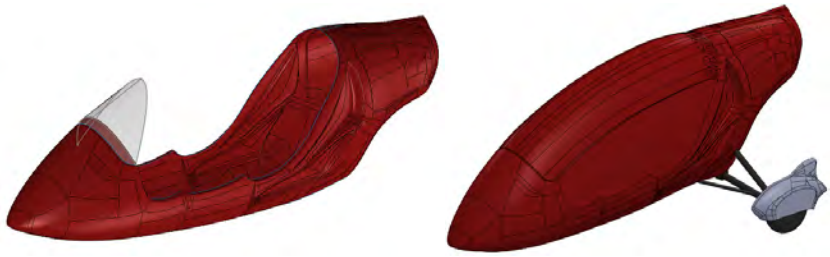

Fig. 3  Original model of the cabin (left) and the complete, simplified model used for the simulation (right)

## 6. FLOW DOMAIN PREPARATION

Large flow domain was generated around the cabin and the landing gear unit in order to minimize the propagation intensity of the disturbed flow till the outside boundaries and so to capture correctly the developed phenomena (Fig. *4*). The solid domains of the structures are inside of a sphere and a non-overlapping rectangle is around them. The reason of that composition is to have possibilities setting different angle of attack by rotating the sphere around its center in the next steps (out of the present work). Only half part of the geometry was prepared due to the symmetry in geometry, boundary and flow (e.g.: there is no rotor or propeller inside the flow domain) conditions.

Fig. 4  Flow domain

## 7. MESHING

One of the most crucial aspects of the simulation is the quality of the mesh. The software divides the flow field into small cells and uses finite volume method to

determine the parameters of the flow field. Although smaller mesh elements provide more accurate results, it can significantly increase the calculation capacity demand.
Different cell sizes were used during the mesh generation (Fig. *5*). The hemisphere was divided into smaller tetra elements due to the complexity of the cabin's geometry and the complicated flow pattern surrounding the aircraft. The rectangular cuboid domain was partitioned into larger tetra elements, since the effect of the autogyro on the mean flow is still significant in this area, but not as much as it is close to the cabin. Mesh refinement was applied on the boundary of the hemisphere and the rectangular cuboid zones to ensure the smooth transition between the cell sizes.

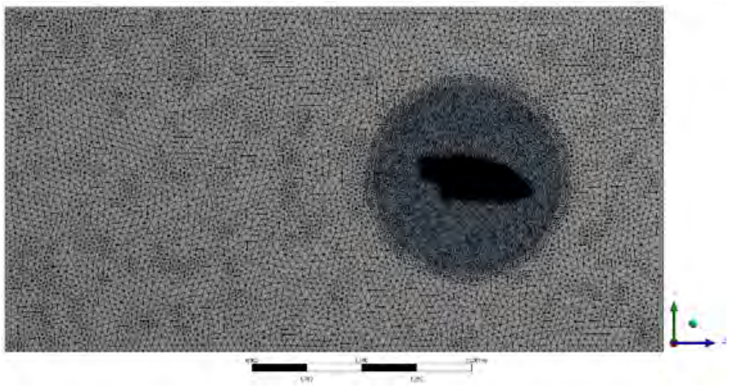

Fig. 5 Flow domain and meshing around the model

More fine mesh with prismatic elements was used close to the solid walls in order to capture correctly the phenomena developed in the boundary layer, where the flow velocity is less than the far field velocity by 1 % (Fig. *6*). [3]

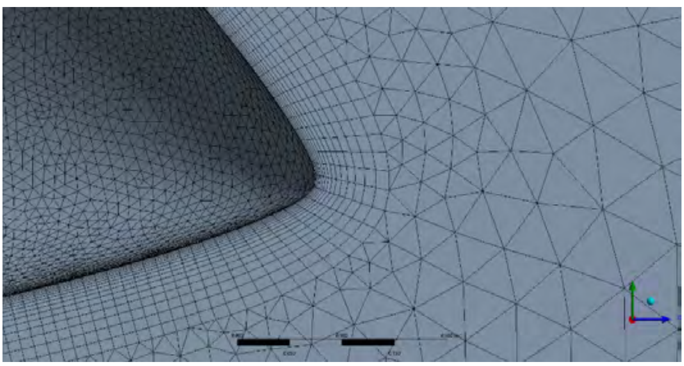

Fig. 6 Boundary layer mesh at the nose of the cabin

Wall function approach was intended to be applied for reconstructing the velocity profile in the boundary layer. The logarithmic-based wall function provides adequate and accurate results at reasonably computational capacity demands except for the separation. The value of the first cell thickness away from the wall, in the form of dimensionless distance; $y^+$ was specified to be 80, thus ensuring the fine mesh resolution in the boundary layer. The height of the first cell in the boundary layer is y =1.09 mm. The boundary layer mesh was composed of 15 cell layers and the growth ratio between the different layers was set to be 1.2.

## 8. BOUNDARY CONDITIONS

Assuming that autogyro performs a horizontal, trimmed flight in the most of the time spent in the air, the simulation was carried out in accordance with that. The boundary conditions were defined based on International Standard Atmosphere at cruising altitude of 1000 meters and speed of 120 km/h. Subsequently, the input parameters at the given conditions were the static pressure of the air (p = 89,880 Pa), the velocity of the medium (v = 33.33 m/s) and static temperature (T = 293 K).
The air as the fluid in the flow domain is defined as ideal gas with a reference pressure of 89,880 Pa. Since the Shear Stress Transport turbulence model provides accurate results for common fluid dynamics problems, this turbulence model was applied for the simulation. Furthermore, it is worth mentioning, that symmetry boundary condition was applied in the model's plane of symmetry.

## 9. MESH SENSITIVITY ANALYSIS

The resolution of the mesh should not adversely influence the accuracy of the results in case of any numerical methods use spatial discretisation. In fact, finer mesh resolution means smaller element sizes and the results are more close to reality. However, for a given geometry the decrease in cell size causes increase in the number of elements, which leads to higher computational capacity and requires more time to run the simulation. Because of the computational power and time available at present disposal for beneficial business point of view, it is important to create an optimal mesh that no longer affects significantly the results of the simulation if the mesh is further refined. [4]

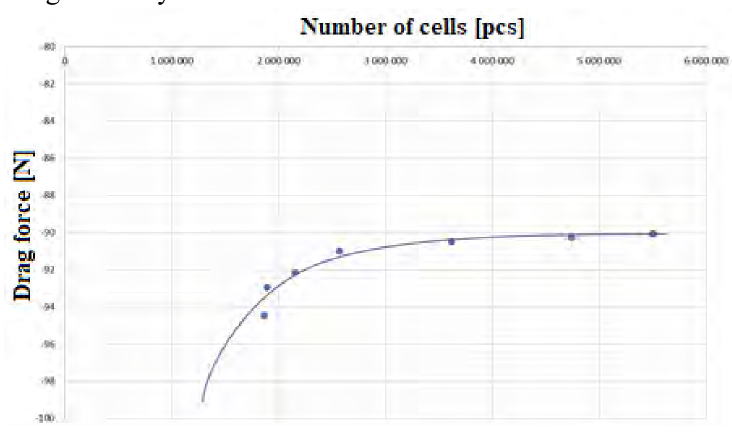


Fig. 7 Graph of the mesh sensitivity analysis

As far as the simulation and the mesh sensitivity study is concerned, the most important parameter is the aerodynamic drag on the simplified model of the SC-200. During the study, the cell sizes of the rectangular cuboid and the hemisphere (including boundary layer) were modified simultaneously, then the drag force was shown on a graph as a function of the number of elements (Fig. *7*). Concerning the results, it can be stated that the drag force converges to approximately to -90 Newton-s. The default mesh setting (3,602,410) was sufficiently dense and it provided results, which was not changed significantly in case of using finer mesh. However, the subsequent simulations were carried out with the settings used at the simulation with 4,726,321 cell numbers for the reason to obtain even more precise output.

## 10. PLAUSIBILITY CHECK OF THE RESULTS

In order to verify the credibility of the results obtained in the simulations plausibility study was performed. The investigation was based on the results of the simulation on the model without the main landing gear unit, thus the drag coefficient of the cabin was determined stand alone. After calculating the drag coefficient of the cabin, the result was compared with the drag coefficient of similar, but slightly different shaped body, where the drag coefficient was determined empirically by measurements. The shape of the cabin's simplified model can be defined as a long, streamlined body, so if its drag coefficient belongs to the same magnitude as the coefficient of a similar shaped body, the results of the simulations are plausible, and they can be utilised for later analyses.

The drag coefficient of a body can be calculated using the following formula:

$$c_D = \frac{D}{\frac{1}{2}\rho \cdot v^2 \cdot A_{hf}} \ , \tag{5}$$

where: D: drag force on the cabin, without the landing gear unit, $D = 57.505$ N (from the CFD results);

ρ: density of the air, $\rho = 1.112\ kg/m^3$;

v: flight velocity, $v = 33.33$ m/s;

$A_{hf}$: characteristic frontal area of the body, $A_{hf} = 0.693774\ m^2$.

The drag coefficient of the cabin:

$c_D = 0.1342$ .

The cabin can be considered as "a long, streamlined body", which has the following drag coefficient:

$c_D = 0.1$ [5] .

Since the drag coefficient of the cabin resulting from the simulation differs only to a minimal extent from the empirical, measurement-based drag coefficient of a similarly shaped body, it can be asserted, that the plausibility check was successful, the results of the simulation provide correct, valid information.

## 11. MODEL IMPROVEMENTS AND REDESIGN

Assuming that, the autogyro spends the most of its time in a horizontal, trimmed condition during flight, it is reasonable to design new, improved model with aiming to reduce the drag force. The new, aerodynamically improved CAD model of the main landing gear unit (Fig. *8*) was created after thoroughly and rigorous analysis of the simulation results given by the baseline model and presented in the next paragraph.

During the improvements of the initial geometry, it was essential to create an aerodynamic shape having as minimal disturbing effect as possible on the mean flow. The main landing gear unit of the SC-200 autogyro can be divided aerodynamically into three major parts as i. tubes, ii. attachment point of the main strut and the damped strut and iii. wheel including its cowling. Based on the available experiences in aerodynamics, the drag of cylindrical shaped tubes is significant. Given the form of the connection point having a rather large frontal surface, the flow cannot follow its shape causing separation. As the results of the simulation revealed, the shape of the wheel cowling is also not ideal one, since the flow is disturbed by the fin of the cowling (Figs. 15 and 16.).

To minimize the drag force on the model, the tubular components of the landing gear unit were covered by symmetric air foils (Fig. 8). The connection point of the main strut with the damped strut was also covered with a symmetric air foil, which forms an integrated part with the new wheel cowling. Several wheel streamliners of other aircrafts were analysed to create new design of the wheel cowling, having drop-shaped silhouette. The transition between the air foil shaped struts, the connection point with hub and the wheel cowling was adjusted with a large radius coverage to reduce interference drag.

Fig. 8 New, improved design of the landing gear and the wheel cowling

With the new, aerodynamically improved design the geometrical dimensions of the structural parts remained unchanged, so there is no need for separate redesign and conversion of the structural elements of the baseline model. Therefore, with minor modifications on the landing gear, after the production of cowling elements made of carbon fibre or fibreglass are ready to be installed.

However, the cost and the weight of these additives should also be investigated to determine the beneficial of the design modification in business point of you.

## 12. EVALUATION OF THE RESULTS; COMPARISON OF THE BASELINE AND IMPROVED MODEL

Useful conclusions can be drawn about the examined fluid dynamics problem after analysing and interpreting data obtained by the results of CFD simulations. New design guidelines can be established by applying the outcomes of the calculations and experiences that are going to be used for creating appropriate design versions. These design variants can be compared with each other for selecting the best alternative. However, first, parameter and evaluation criteria have to be selected to compare the results of different models with each other.

The following simulation data of the baseline and the improved model of the SC-200 autogyro was compared with each other:

- pressure distribution,
- velocity distribution and velocity vectors,
- streamlines and
- drag force

in the next subchapters.

Different planes were defined in the flow domain, on which the desired parameters were shown to obtain representative illustration of the results. The same colour scales and value ranges were used on the figures to increase the level of the transparency for comparison and evaluation.

### 12.1 Pressure distribution

Three different cutting planes were defined at main landing gear for demonstrating relative pressure measured from the atmospheric one as it has the mean contribution to drag force.

The pressure distribution around the redesigned wheel cowling is much more homogeneous and thus more favourable than it is in the baseline version especially around the stagnation point at the trailing edge (Fig *9*). The effect of the cabin on pressure distribution can also be observed slightly upwards in front of the wheel.

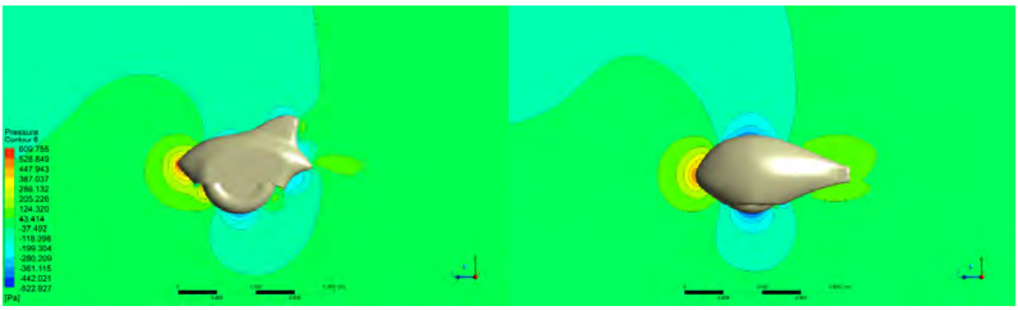

Fig 9 Pressure distribution in the vertical plane of the wheel and wheel cowling (left: baseline model, right: improved model)

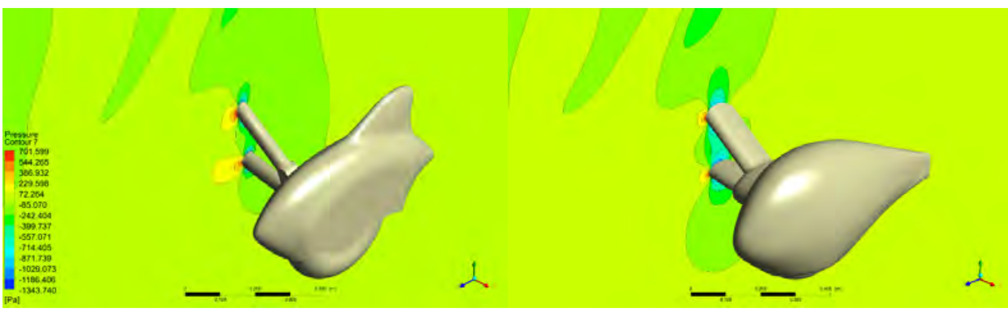

Fig. 10 Pressure distribution around the struts (left: baseline model, right: improved model)

Similar statement can be made when examining the pressure distribution around the main- and the damped struts (Fig. *10*). The pressure distribution in front of the tubes with streamliner profiles and after them is more uniform, the stagnation points has pressure distribution with less intensity, influencing areas than it is in the case of simple, cylindrical tubes.

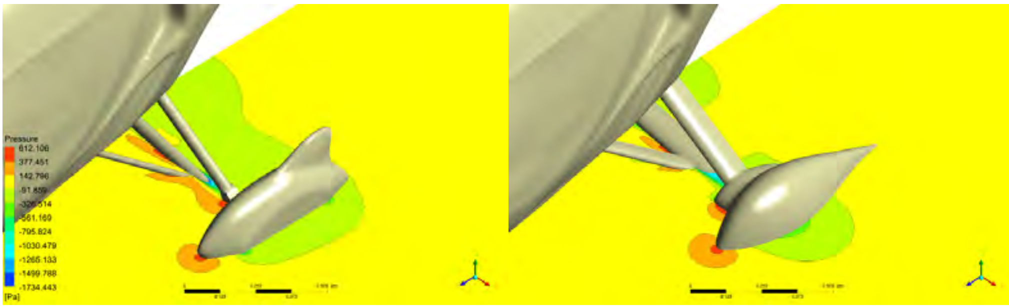

Fig. 11 Pressure distribution in a horizontal plane (left: baseline model, right: improved model)

The pressure distribution shown in the horizontal plane (Fig. *11*) reveals that in comparison with the improved model, the higher positive relative pressure before and lower negative relative pressure behind the baseline model create higher drag force.

### 12.2 Velocity distribution and velocity vectors

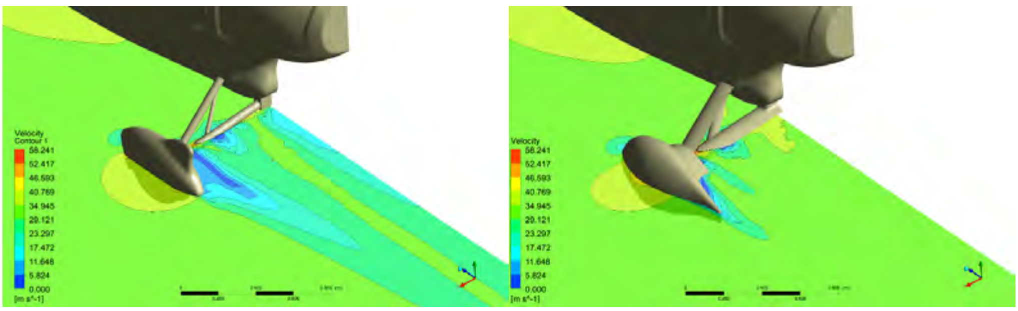

Fig. 12 Velocity distribution in the horizontal plane of the connecting point and main strut (left: baseline model, right: improved model)

The high and low velocity zones, stagnation points and flow separations can be observed in the velocity distributions. More massive flow separation can be observed behind the connection point of the baseline model in comparison with the improved design (Fig. *12*, Fig 13). The size of separation bubble can be reduced by streamlining the connection point.

The irregular flow motion due to separation has not only effect on increasing drag force, but it can reduce the efficiency of the propeller, since it is not exposed to undisturbed flow.

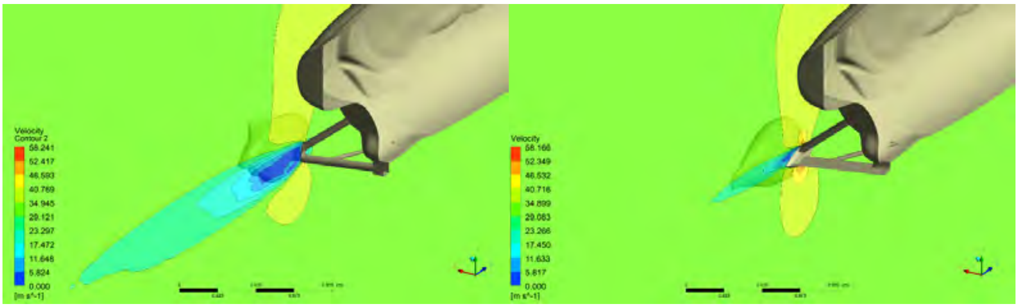

*Fig 13 Velocity distribution in the vertical plane of the connecting point (left: baseline model, right: improved model)*

In order to guarantee the expected efficiency of the propeller and maximum thrust, it is favourable to ensure homogeneous, uniform upstream flow condition with minimising flow separation and turbulent intensity.

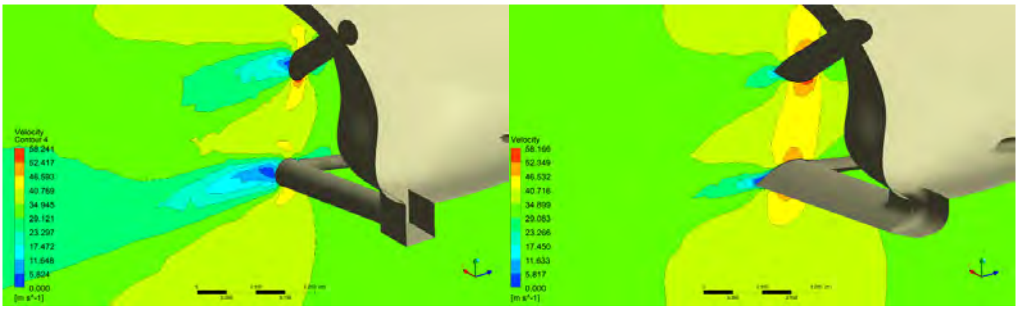

Fig. 14 Velocity distribution in the vertical plane of the tubes (left: baseline model, right: improved model)

The extent and the intensity of the flow separation zone behind the struts are also smaller in case of improved design due to the streamliner profiles in comparison with the baseline version (Fig. *14*).
The velocity vectors confirm the statements above also (Fig. *15*). The flow recirculation is observed behind the connection points of the struts and wheel cowling at initial model.

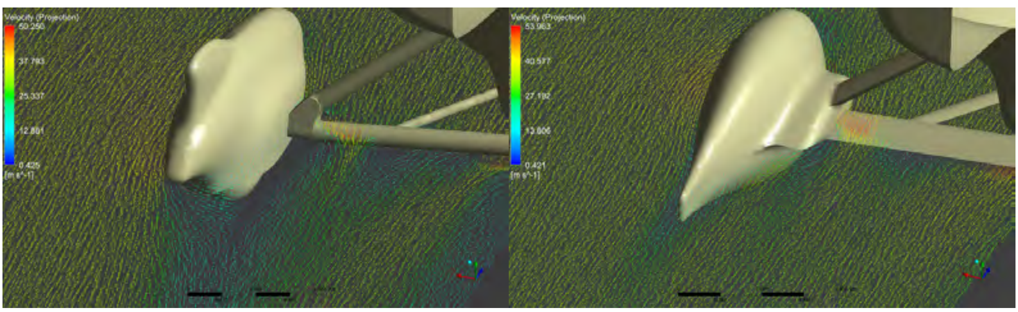

Fig. 15 Velocity vectors coloured by their magnitude in the plane of the connecting point (left: baseline model, right: improved model)

the flow is nicely distributed, homogenous and follows the shape of the landing gear unit in case of the redesigned version. as the flow separation behind the rather blunt body increases significantly the drag force and fuel consumption, the improved version has more favourable aerodynamic characteristics.

### 12.3 Streamlines

The streamlines demonstrate also flow separation behind the connection point resulting swirling flow (Fig. *16*). This is almost eliminated at the improved model. Furthermore, with the help of the streamlines, the negative, deflecting effect of the tiny fin on baseline model can also be observed, which disappears at the new design.

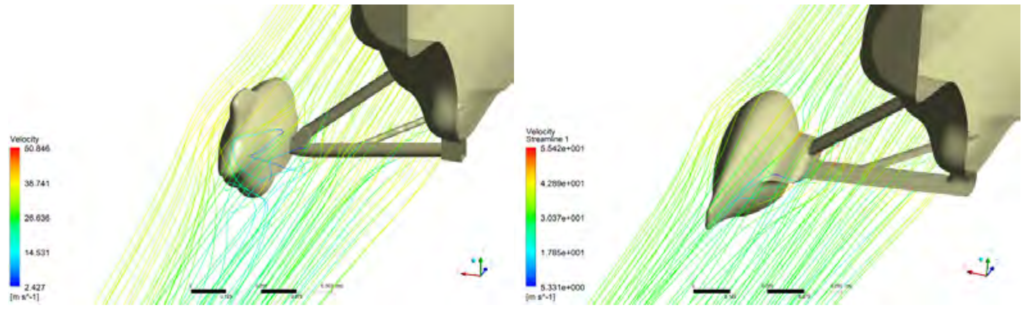


Fig. 16 Streamlines around the main landing gear and the wheel cowling (left: baseline model, right: improved model)

### 12.4 Drag force

The one of the most important parameters of the simulation results is the drag force. It is decreased significantly with the applied aerodynamic improvements. The baseline model has 90.2 N and it is 59.7 N at the improved model, which means 30.5 N drag force reduction, which corresponds to 33.8 % reduction.

These values also include the drag force of the cabin; its effect cannot be ignored due to the interference of the parts.

Finally, it can be concluded that applied design modifications as i. symmetric air foil profile around tubular components, ii. drop-shaped wheel cowling and iii. streamliner coverage at struts-hub connection were useful, the drag force was reduced significantly.

## 13. EXPERIMENTAL RESULTS FOR PLAUSIBILITY ANALYSIS

Considering the baseline configuration, experimental investigation was completed to make the flow pattern be visible close to the surface of the landing gear unit. Roughly 10 cm long strips of yarns were taped down on the outside walls of the landing gear unit (Fig. *17* and Fig. *18*). Then flight tests were completed. During the flying, the free ends of these yarns were moved in unsteady way due to the fluid structure interaction controlled mostly by the aerodynamic forces of the high speed air acting on the yarns. Thus the developments of the transient flow structure became visible. Video camera was used for recording the motion of the yarns. The possible vortices, the formation of the separations, the place of separation and the point of attachments can be investigated by this way.

The comparison of the experimental and the simulated results showed good qualitative agreement with each other. The location and the form of the separation bubbles close to the surface, behind and inner side of the wheel cowling and separations behind the struts are well visible in the Fig. *17*. They correspond to the separations observed in Figs. 12-16 left side. Although the presented experimental investigation did not give exact results, it provided good approximation for checking the correctness of the simulation results in qualitative manner. [6]

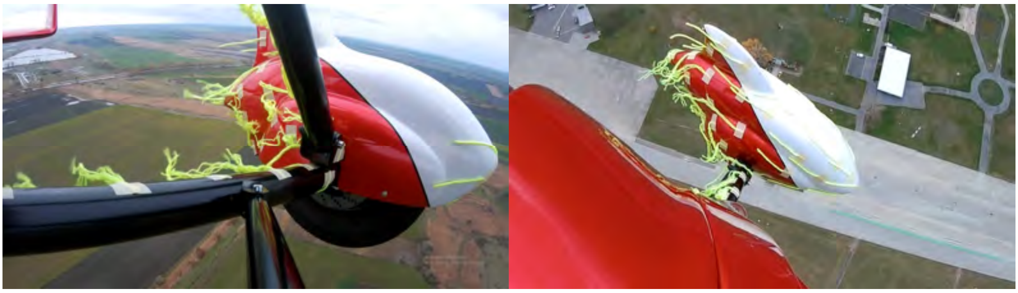

Fig. 17 Flow pattern of the baseline model during flight represented by strips of yarn

Fig. 18 State of the strips of yarn of the baseline model after the experimental test

Moreover, the intensity of turbulence can also be observed by the structure of the yarns at the end of the flight. The filaments of the yarns are rather together if they were lying in the laminar sublayer of the boundary layer, as it is show in Fig. 18 left side in a black circle for example. The filaments of the yarns are rather separated if their free end were in the turbulent log-layer or even more if they were rather out of the boundary layer in the fully turbulent and separated zones. These are also in correlation with the simulated results found in Fig. 12-16 left side.

## 14. CONCLUSIONS

CFD analysis of the baseline and aerodynamically improved version of SkyCruiser SC-200 autogyro main landing gear unit has been introduced and evaluated in the present paper with analytical and experimental plausibility check. The improvements include the applications of i. symmetric air foil profile around tubular components, ii. drop-

shaped wheel cowling and iii. streamliner coverage at struts-hub connection. The design modifications resulted in 34 % drag force reduction.
Concerning the experimental plausibility check, flight tests were performed in case of baseline model using strips of yarns. The shape of yarns during the flight and the integrity after flight in standing position were analysed and compared with the flow field resulted by the CFD simulation. The qualitative analyses showed regions with lower and higher turbulence intensities were in good agreement with each other. However, more detailed measurements and simulations are needed for validation not only at one but at more operational condition in quantitative manner to guarantee the high level confidence.

## 15. ACKNOWLEDGMENTS

This work has been supported by Hungarian national EFOP-3.6.1-16-2016-00014 project titled by „Investigation and development of the disruptive technologies for e-mobility and their integration into the engineering education”.

## 16. REFERENCES

[1] **Veress, Á.:** Bevezetés a numerikus áramlástanba (CFD), Lecture note, Budapest, (2017). URL: http://www.vrht.bme.hu/letoltes/ Tanszeki_letoltheto_anyagok/ Oktatok_anyagai/Dr.Veress_Arpad_anyagai/Oktatott_targyak/ Bevezetes_a_ numerikus_aramlastanba_CFD/CFD_v2.pdf (Downloaded: 26.04.2019). (In Hungarian)
[2] **ANSYS, Inc**.: ANSYS CFX – Solver Theory Guide. Release 15.0, 2013.
[3] **Gausz, T. :** Áramlástan (Lecture Notes on Fluid Dynamics), URL: http://www.vrht.bme.hu/ letoltes/ Tanszeki_letoltheto_anyagok/Oktatok_anyagai/ Dr.Gausz_Tamas_anyagai/ Aramlastan_teljes_jegyzet.pdf, Budapest, 2012, (Downloaded: 26.04.2019) (In Hungarian)
[4] **Róbert Dúl:** Fémszerkezet optimális tervezése áramlástani és szilárdságtani szempontok alapján (Optimal Design of Metal Structures by Means of Fluid Dynamics and Structural Mechanics), PhD dissertation, Miskolc, 2012.
[5] The Engineering ToolBox. Drag Coefficient. URL: https://www.engineering toolbox.com/drag-coefficient-d_627.html (downloaded: 20.04.2018.)
[6] **Rohács, J.:** Aerodynamics (draft). Lecture note, (2012). http://www.vrht. bme.hu /hu/hallgatoinknak/letoltesek.html (Tanszeki_letoltheto_anyagok, Oktatok_anyagai, Dr. Rohács_József_anyagai, aerodynamics_lectures) (Downloaded: 14.05.2018)

# INTEGRATING LARGE REMOTELY PILOTED VEHICLES INTO THE CONTROLLED AIRSPACE

**Oszkár BIRÓ and Géza SZABÓ**

Department of Control for Transportation and Vehicle Systems
Faculty of Transportation Engineering and Vehicle Engineering
Budapest University of Technology and Economics
H-1521 Budapest, Hungary

*Received: November 7, 2018*

## ABSTRACT

With the spread of the automation, feasibility of the autonomous vehicles turned into an emphasized research topic in the traffic industrial branches. As autonomous vehicles on the road are the subjects of such research, there are questions about the various unmanned aircrafts in aviation. However, these issues relate mainly to small vehicles, so called drones and their applicability in urban environments. The first purpose of this article is to define a category that is based on the characteristics of the current piloted cargo aircraft and later passenger aircrafts, but it is controlled by a remote pilot and at some flight stage (en-route) it also has the ability to perform various tasks autonomously. The advantages and limitations of this category (LRPV – Large Remotely Piloted Vehicle) are described, taking into account the benefits of their use in a fleet. With the introduction of this category, air traffic control issues are raised; the second chapter of this article will show a comparative analysis of aircrafts piloted normally or by remote pilots, in which the channels of communication are highlighted. The final part of this article discusses the failure modes of these communication channels, and the issues associated with the possible solutions. The formulation of these solutions includes further research options, such as the development of a new communication channel and interface between the pilots and air traffic controllers, or a new (possibly CPDLC-like) interface between the air traffic controller and the LRPV, which allows the controller to control the vehicle with limitations in possible emergency situations.

*Keywords:* air traffic control, LRPV, air traffic communication channels

## 1. INTRODUCTION

Development, implementation and integration of the autonomous vehicles are top priority issues for most of the researchers in the 21st century. Their appearance and application are no longer unknown to the industry, as this category includes metro line M4 in Budapest or the widely known Tesla vehicles. Thus, it can be seen that there are efforts in both rail and road transport, which appear in aviation as well. A number of conference articles and publications appear on unmanned aircraft, but these publications [1, 2, 3, 5] are dealing with small unmanned aircraft, called sUAS. Generally the range of sUAS usage is widening, there are already operations on agriculture, parcel delivery or even surveillance tasks. However, in this article we do not speak about fully autonomous vehicles, but we deal with remotely piloted aircraft as a transitional step between piloted and autonomous modes. We would like to examine what challenges would be faced in air traffic control if an aircraft with similar characteristics to those of commercial passenger and cargo aircraft being controlled by pilots are transferred to remotely piloted operation or later to automation. This idea is not unknown for air transportation, since in military aviation there have been operations with RPVs (Predator, Valkyrie) for long-range military missions, whether for task reconnaissance or target destruction. We based our research on this technology. In the next chapter we define the LRPV category, and describe the advantages and limitations of applying a fleet of homogenous aircraft.

The problems in air traffic control regarding the use of a fleet are discussed in chapter 3, in which we use self-made models to identify changes and possible sources of error and the possible solutions. Finally in Chapter 4 we present the recommendations and conclusions drawn for further research.

## 2. LRPV – THE NEW CATEGORY

### 2.1 Definition

The introduction stated that there are small unmanned aircraft, and there are therefore existing categories on a basis of weight, purpose or drive. However, the purpose of this article is to identify an entirely new category as a similar idea has not been published in other publications yet. The new category is called LRPV – Large Remotely Piloted Vehicle. In terms of flight characteristics, it is fully suited to today's operating aircraft such as the Boeing 747-8F. The first object of our research is to describe that if the controls of these vehicles are remote and they are able to operate autonomously en-route, then what are the advantages and limitations of applying a homogenous fleet of such airplanes. Later on, describing the challenges and innovations of their application will be researched.

### 2.2 Advantages of LRPV

When examining the advantages and limitations, we must take into consideration whether we need to list the advantages from a pilot centre point of view, or to address the financial or economic benefits of the fleet owner. If we perform the research from the point of the pilot centre, a suitable centre should be established, together with the necessary supportive infrastructure. If such a centre is established, a further issue is whether it will be established a service provider for airlines and individuals, or that an airline is establishing it for its entirely own use, or both, as a mixed solution. However, the precise conditions of the installation of a centre are not discussed in this article, it can be defined as a further research task.

For the management of a fleet with a large number of vehicles, it would be sufficient to use pilot pairs, who would simultaneously supervise several aircraft. For workload optimization and management of pair of pilots may be done in the same way like for air traffic controllers; a supervisor would be responsible for that.

The solution above (although the allocation of human resources and the associated flight optimization may be a separate research topic) is likely to ensure the operation of a large fleet compared to traditional air traffic control.

In addition to the benefits, monotonous and routine tasks could be done autonomously, to reduce staff workload and also to optimize the use of human resources. Also, it can reduce the number of staff itself, as it requires far fewer people than a conventionally piloted aircraft.

There are other economic benefits of the centralized solution, particularly when using a large fleet, such as the rotation of pilots, the transport of redeemed pilots, reserving accommodation, but further research is needed to accurately explore them. In addition to the above, potential economic and financial benefits may arise from the fact that in such a case there is no need to establish a separate pilot cabin on board (this is a significant saving in itself) and in addition, the space that is released can be used as extra cargo space for freight vehicles, or you can upload premium places for passenger transport (extra revenue).

Further research can be used to give an opinion on easier maintainability and repair processes.

### 2.2 Limitations of LRPV

Problems involving automation, such as the introduction of new technology, should be mentioned first. A new technology raises not only technical, security, but trust issues too. It is questionable whether people would be prepared to switch to automation, how much they would trust in remote or machine control. In addition, in case of a failure of the remote-pilot mode, the machine cannot be taught to resolve emergency incidents, even if it is, teaching all scenarios would take a lot of time, so we do not deal with this issue now.

In addition to the new technology and the technique available, the problem of exchanging information arises. Such questions should be answered as what platforms are needed for transmitting information, examining time criticalness, and how much information is needed to ensure safe operation. Although only a detailed analysis of the amount of data required for control can provide an accurate answer, it is evident that continuous and time-critical transmission of a large amount of data (at least from the aircraft to the pilot centre) is needed.

In the flow of large amounts of information, a possible medium (e.g. terrestrial transfer stations or satellites) for transmission of information should also be examined. For satellites, it is also needed to consider the current satellite coverage. With both technologies a problem with the loss of information at the border of the coverage zones is an issue to be solved.

Further disadvantages are the construction of pilot centre, the installation of the information medium and the operation with proper availability. Maintaining the information medium is a significant investment and can be expected to be recoverable only in the event of a large number of aircraft uses. This in turn raises the need for standardization of the information transmission interfaces (aircraft-medium, medium-pilot centre). With proper standardization, this transfer can even become a service, even in the presence of several operators. However, as the availability of information transfer is security critical, it is also necessary to regulate this area (information transfer service providers), or another solution can be the foundation of an ICAO-controlled specific service organization.

Before starting to deal with these problems, however, it is necessary to investigate the impact of the application of a fleet on the current air traffic management system.

## 3. CHANGES IN THE AIR TRAFFIC CONTROL SYSTEM

### 3.1 Model of the current air traffic control system

Fig. 1 shows the simplified, schematic model of the current air traffic control system, which is a modified and updated version of the one made in [4]. Two main parts should be highlighted. One part contains the hardware and software associated with the aircraft, which are shown on the left side of the figure and the other section contains the participants, devices of air traffic control and the between them on the right-hand side of the figure. The various navigational and surveillance tools (ILS, VOR/DME, NDB, etc.) have been added just to mention only, and are irrelevant to our current research.

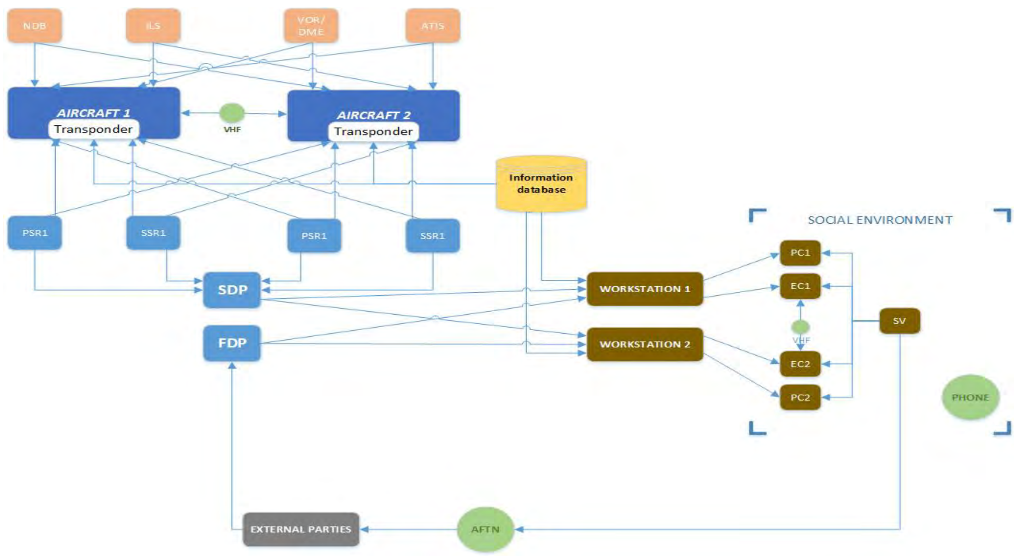


Fig. 1 The model of conventional air traffic control

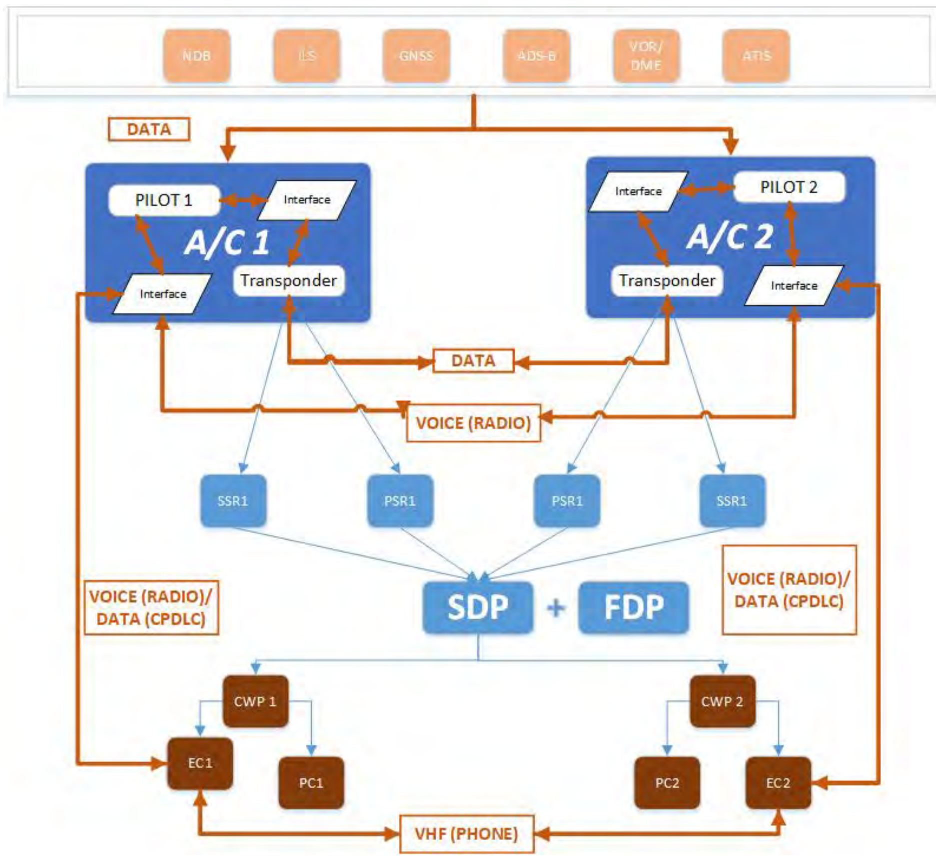


Fig. 2. Communication channels of the conventional air traffic control model

The direct connection between two arbitrary aircraft is VHF based communication, as well as an indirect link between the transponder's primary and secondary radar data. These radar data will be processed (SDP-Surveillance Data Processing), then combined with data derived from the flight plan (FDP — Flight Data Processing) to be then transmitted to the air traffic controllers' workstations (Workstation N). Executive Controller and a Planning Controller work in each workstations. A supervisor manages the controllers work. Communication between controllers is done via telephone. For a more detailed analysis of the communication channels present in the system, see Fig. 2.

### 3.2 Communication channels of conventional air traffic control

For a closer look, we have transformed our general control model, to highlight information flow channels and modes, now easier to illustrate them in the revised version. Accordingly, airplanes receive data from different navigation and airspace detection equipment and then transmit this data. The exchange of information between two aircraft can also take place through the transponders' signals. In addition, pilots can communicate on a radio tuned to a specified frequency. Air traffic controllers talk to each other through telephony. The most important element of the communication network is the pilot-controller channel. Nowadays, information exchange is done by voice communication, but there is an alternative digital solution that is referred to as CPDLC (Controller Pilot Data Link Interchange). The core of CPDLC is the communication between the air traffic controller and the pilot in the form of text messages sent over a digital channel, requesting, issuing and executing the instructions through a continuous acknowledgement system. The operation of mixed voice and text communication is ensured by an interface on the airplane for which both the pilot and the air traffic controller have direct access.

In addition, besides the interface, we demonstrated how the pilot relies on the aircraft, and we also created an interface between the pilot and the transponder. This demonstration will play a role late, when it come to remotely piloted vehicle.

In the following subsection, we are examining how these communication channels can change if remotely piloted aircraft are integrated into civilian airspace and thus explore new challenges for joint operation.

### 3.3 Air traffic control issues of LRPVs in integrated environment

Fig. 3 shows the model for the control and communication channels of the mixed operation. On the left side of the figure the communication channels of the conventional control presented earlier can be recognized, while the communication channels of LRPVs are on the right side. The issues to be answered are between the aircraft-pilot-controller three-way communication triangle, so we put emphasis on it in our research.

For a clearer illustration the pilot has been place out of the aircraft and the remote control has been displayed as a lightning symbol showing that the pilot is not sitting physically in the aircraft.

However, this solution that the pilot is not directly in the aircraft does not mean a significant change in the basic operating principle. Just as in the conventional model, two interfaces are provided on the aircraft, one for communication and for the control

of the aircraft. By default, the air traffic controller does not see any difference compared to the previous case; new interfaces and communication with the pilot centre provides this (however it is important to note that the issue of communication delays should be considered separately).
However, if we do not want to maintain a pilot-aircraft connection (for example, due to the technical difficulties presented in the previous chapters and the partial implementation of the autonomous functions such as the automatic route flight), or the connection is lost periodically, we will have to face the difficulty that the aircraft can not participate in air traffic control conflict resolution. At the same time, by providing a suitable logic interface, the air traffic controller may provide the vehicle with instructions for resolving conflicts (e.g. altitude change), which would be carried out autonomously by the aircraft while the controllers maintains the safe autonomous operation of the aircraft. This solution can be particularly useful if an aircraft is actually in an autonomous flight, so it makes the pilot workload decrease. The air traffic controller will be able to do so if the LRPV switches from remote pilot mode to autonomous control en-route. This switchover would be seen by the air traffic controller on a display and so the controller can give instructions through the aforesaid CPDLC surface.

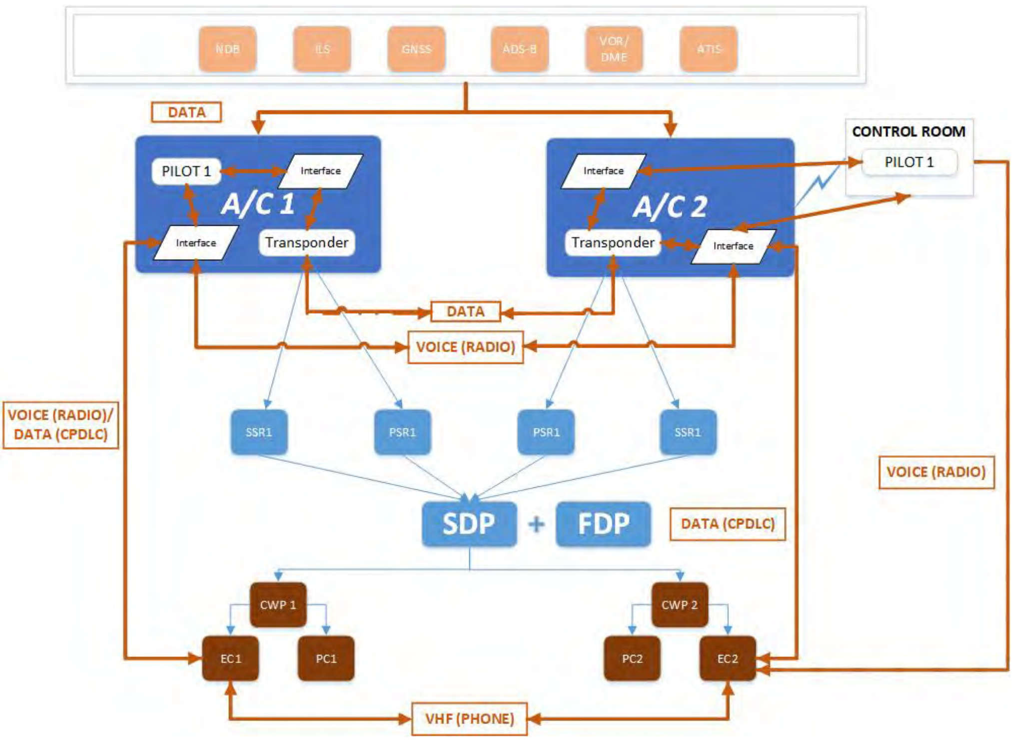


Fig. 3 Communication channels of the integrated conventional and LRPV model

The operating principle can be based on a question-response-reaction process in which the controller can give an instruction to which the aircraft responds; and there is also the possibility that the aircraft sends questions to the controller and the controller can decide whether to approve or reject the request.

The next issue is what happens when the controller loses this command-based connection with the aircraft and thus with the pilot. A solution would be the creation of a channel (or communication interface) that pilots in a remote pilot centre can connect to and communicate with a dedicated air traffic controller (here we have the premise that both the control centre and the pilot centre are well-equipped, fixed-installed facilities with basic communication capabilities). This channel is illustrated on the figure by the right side arrow line. This relationship does not exist at this time and that this research is bound to show if such a connection is needed and what could be its advantages. The specific design of the interface, its definition and the protocol for the connection can be a subject of later research.

## 4. SUMMARY OF RECOMMENDATIONS

In our research we used two main design suggestions for LRPV integration, which are the following:

1. A logical interface between the controller and the pilot shall be established, through which a controller may provide instructions (basically for emergency situations) to the aircraft, that the aircraft can accept or refuse; if it is accepted, it will be automatically executed without pilot intervention, at a required safety level guaranteed by the aircraft's own autonomous system (this function may also be interpreted in the case of piloted aircrafts using robot pilots).
2. A direct, standardized link between pilot centre and air traffic controllers shall be established, primarily with the purpose for redundancy.

## 5. ACKNOWLEDGEMENT

The professional and research work as the basis for this article was provided and supported by HungaroControl Hungarian Air Navigation Service Provider Ltd. (Support ID: HC-2017-7742); the authors would like to say their thanks herewith.

## 6. REFERENCES

[1] **Roberts, E. – Beck, A.:** Management and training programs of military drone small unmanned aircraft systems. Proceedings of Human Factors and Ergonomics Society Annual Meeting, 2017. Volume 61, Issue 1, 2017, p.1131-1135.

[2] **Pappot, M. – de Boer, R. J.:** The integration of drones in today's society. 3rd European STAMP Workshop; Procedia Engineering, Volume 128, 2015, p.54-63

[3] **Carapau, R. S. – Rodrigues, A. V. – Marques, M. M. - Lobo, V.:** Unmanned Aerial Systems in military environments: the benefits of interoperability. "Mircea cel Batran" Naval Academy Scientific Bulletin, Volume XX, Issue 1, 2017, p.43-47.

[4] **Számel, B. D. – Szabó, G.:** A légiforgalmi irányítás szisztematikus biztonsági elemzése. Közlekedéstudományi Szemle, Volume LXV, Issue 5, 2015, p.40-52. (In Hungarian)

[5] **Jiang, T. – Geller, J. – Ni, D. – Collura, J.:** Unmanned Aircraft System traffic management: concept of operation and system architecture. International Journal of Transportation Science and Technology, Volume 5, Issue 3, 2016, p.123-135.

# INVESTIGATION OF HYBRID PROPULSION SYSTEMS APPLIED ON SMALL-SIZED AIRCRAFT

**Adrià Xavier Carnerero URBAN, István Tamás MOLNÁR and Árpád VERESS**

Department of Aeronautics, Naval Architecture and Railway Vehicles,
Faculty of Transportation Engineering and Vehicle Engineering,
Budapest University of Technology and Economics
H-1111 Budapest, Műegyetem rkp. 3, Hungary

*Received: November 7, 2018*

## ABSTRACT

The reduction of fossil fuel consumption is a current major concern for transportation: the automotive sector has already implemented many solutions for replacing the conventional combustion engines, such us both hybrid and all-electric engines, which are used more frequently day by day in the current market. Nonetheless, the aircraft industry seems to be still in the early stages of development for all-electric propulsion. The logic transition of this technology is through hybrid electric propulsion. This could not only reduce the greenhouse emissions but the cost of flying. A summary, description and analysis of the possible hybrid electric configurations has been introduced in the present work. Parallel configuration is expected to be the most feasible design for adapting the current aircrafts to hybrid electric propulsion. Then, a performance analysis during cruise flight for a small-sized aircraft (4 passengers) has been performed with a modification of the conventional Breguet equation: the range is computed depending on the energy consumption instead of depending on the mass consumption. A sensitivity study of the aircraft design parameters (flight velocity, energy split factor, power split factor) considering current batteries has been presented. It has been found that if the current cruise velocity used by the aircrafts is slightly reduced, fuel reductions can be achieved by using parallel configuration by just a slight range factor reduction. From the results obtained, more flight conditions rather than the cruise can be studied. Apart from that, one can use the range model as a base for computing the performance of other hybrid configurations also.

*Keywords*: hybrid electric propulsion, parallel configuration, Breguet energy range equation, small aircraft

## 1. INTRODUCTION

The one of the most important tasks today is the reduction of fossil fuel consumption in transportation to decrease the emission for environmental protection. The automotive sector has already implemented many solutions for replacing the conventional combustion engines, such us both hybrid and all-electric engines, which are used more frequently day by day in the current market [1]. Nonetheless, the aircraft industry seems to be still in the early stages of development for hybrid electric propulsion (HEP) [2].

As the European commission states, aviation is one of the fastest-growing sources of greenhouse gas emissions [3]. Specifically, direct emissions from aviation account for more than 2% of the global greenhouse gas emissions. If no new alternatives are implemented, the International Civil Aviation Organization (ICAO) forecasts that by 2050 the total aviation emission could rise between 300-700% more. Thus, the propulsion systems of the aircraft industry should progressively change to better alternatives if these emissions are wanted to be controlled or even reduced. In fact, the European project Clean Sky will try to validate the necessary technology for achieving the environmental goals set by the Advisory Council for Aeronautics Research in Europe (ACARE) [4]. These goals are mainly the reduction of the emissions for 2050 with respect to the aircrafts used in 2000: 75% reduction in $CO_2$, 90% reduction in $NO_x$ and 65% reduction in perceived noise. In addition, some other improvements are

desired such as the total elimination of the emissions while the aircrafts are taxiing, or even the design of aircrafts, which most of their parts are recyclable.
But not only the environmental effect is the main concern regarding fossil fuels: the main cost of flying comes from fuel consumption. Nevertheless, as more electric power is used in substitution of fossil fuels, the flying business would become progressively cheaper [5].
Finally, although the aerodynamic noise produced by some parts of the aircraft such as the propeller for example cannot be removed, the high noise levels produced by gas turbines could be eliminated if only electric motors would be used [6][7].
It seems that the aircraft industry should move towards the use of more electrified motors and the substitution of the conventional combustion engines [8]. As previously stated, the automotive industry has already started to apply these changes progressively. However, aircraft are not expected to experience such drastic propulsion change in this short period of time. The main reason for it is the low energy density that characterize the current batteries [9]. In order to increase the range of an electric vehicle, more batteries are required. While in automotive vehicles the overall weight can be slightly increased if more batteries are required, the weight increase in aircrafts is totally critical. Thus, limited number of batteries can be carried, leading the application of full electric aircraft to small aircrafts with low weight and limited range [10].
Therefore, it can be assumed that until the barriers of all-electric aircrafts such us battery energy storage are solved, the logical transition goes using hybrid-electric propulsion (HEP) system, combining both internal combustion engine (ICE) and electric motor (EM). Although still far from all-electric propulsion, HEP can provide many advantages against the ICE aircrafts in terms of efficiency, environmental effects and even flight safety [7], [11]. These advantages will certainly improve as hybrid technology gets closer to all-electric propulsion and becomes less dependent on fossil fuels.

## 2. HYBRID PROPULSIONS

Hybrid propulsion is defined as a system which transmits power using two or more different propulsive sources [12]. Some examples of these propulsive sources can be combustion engines, electric motors or even fuel cells among others. During the following study, just the combination of electric motors and internal combustion engines will be considered. For this reason, every time hybrid engines are mentioned in the document it would be referred to the combination of these two propulsive sources, if not specified.
These two power sources can be combined differently to produce different performance characteristics. The possible configurations of this system will be described in the following section to compare them and extract advantages and disadvantages from each one.

### 2.1 Hybrid propulsion configurations

The two main configurations of hybrid systems are series and parallel. Nonetheless, many other combinations arise from these two structures [7]. Moreover, each configuration is able to operate in different modes: full electric mode, full fuel mode and hybrid mode whereas the battery can either be in charging mode or not among other possible modes.

### 2.1.1 Series hybrid

The main characteristic of the series configuration is the use of only the EM for powering the propeller (see Fig. 1). On the other hand, the ICE is responsible for producing electric current. The overall process of the system follows this straight-forward sequence [7]:

- The ICE receives fuel from the tank;
- The engine uses the fuel to power itself and the generator;
- Then, the generator charges the battery pack;
- Finally, the energy from the battery is sent to the EM to provide power to the propeller.

In addition, the generator can also send energy directly to the EM. In case of energy regeneration, the EM would obtain the power from the propellers to charge the battery. In this type of configuration, the ICE is not coupled to the propeller. For this reason, the engine can always be kept working under the most efficient revolutions per minute to charge the batteries. On the other hand, this means that all the power for the propeller just comes from the EM, so no extra power can be obtained by the ICE [1]. For the same reason, the ICE can be shut down and the aircraft could operate using just electric energy until the battery lasts [7].

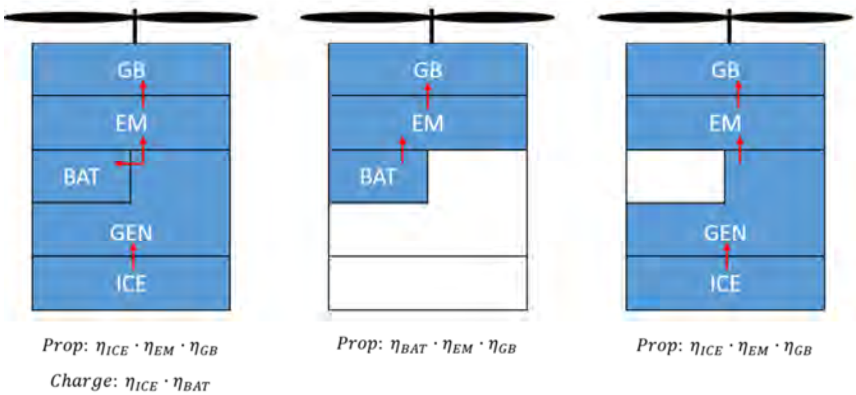


Fig. 1 Inefficiencies experienced in series configuration [13]

### 2.1.2 Parallel hybrid

While in the series configuration only the EM powers the propeller, in the parallel hybrid configuration both EM and ICE can power the propeller through a gearbox (see Fig. 2). The sequence followed by the system in order to provide power to the propeller is next [7]:

- The ICE receives fuel from the tank;
- The engine transmits the power through a transmission system to a coupler gear;
- In parallel, a battery pack sends current to the EM;
- Then, the motor transmits the power to the coupler gear;
- Finally, the coupler system transmits the power received by the motor and the engine to the propeller.

Both EM and ICE can provide power to the propeller separately or even at the same time due to the parallel configuration. For this reason, if the flight conditions require high power demands, the ICE could provide instantaneous power higher than the one that the EM itself could generate [12].
The system does not require certain auxiliary systems such as a generator after the ICE among other electrical components, meaning less weight is added to the aircraft. If the battery is desired to be charged, the EM motor itself can act as a generator. Moreover, there are less energy transfer losses [1].
On the other hand, the ICE is not running constantly at the maximum efficiency speed, meaning more fuel is wasted. In addition, due to the transmission coupler more complexity is added to the system, as the revolutions of the motor and engine should always match. In case of moving at different speeds, some kind of clutch to disengage the motor or the engine should be added [1].

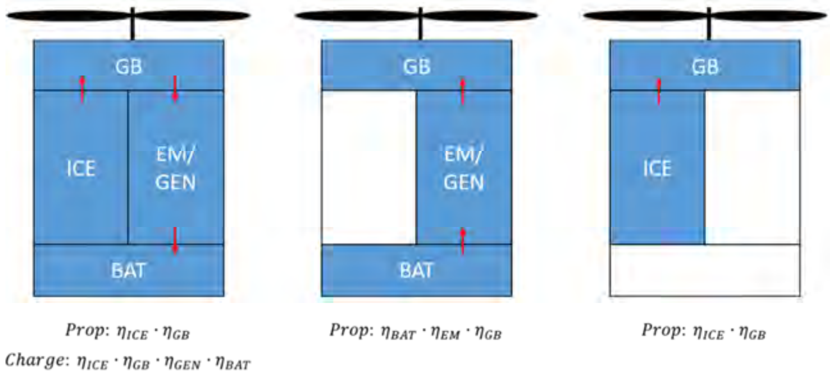


Fig. 2 Efficiencies experienced in parallel configuration [13]

### 2.2 Internal combustion engines for hybrid propulsion

The main advantages of a gas turbine are not only higher power to weight ratio, but also emits less pollutants and it requires less maintenance, as there are less moving parts than in a piston engine. Nonetheless, it has a slower respond against power demand changes as well as being more inefficient when it is not operating at design condition [14].
In this article small sized aircrafts would be the main type of aircrafts to be considered. Thus, piston engines would be the most optimal propulsive system choice, as it has been seen that gas turbines are less efficient when the size of the aircraft and motor are reduced. In addition, the fact of being part of a parallel hybrid engine system makes piston engines more suitable due to its ability to start and change its power production faster than at gas turbines.

## 3. AIRCRAFT AND PROPULSIVE SYSTEM DEFINITION

Before starting with performance calculations, a first definition of an aircraft and propulsive characteristics will be done. Initially, an aircraft used in the current market will be selected. This aircraft should have characteristics, which makes it feasible for a future adaptation with the hybrid configuration previously chosen.

After that, a study of its propeller and required power will be done, where a specific current propeller will be selected as well as doing thrust calculations for different flight speeds.

### 3.1 Aircraft selection

In order to obtain representative results, an aircraft currently used in the market will be considered for the analysis. As a first design criteria, this aircraft should not exceed more than 4 passengers, as the main goal of the article is to study HEP in small-sized aircrafts. Thus, the selected aircraft is the normal category Cessna 172 Skyhawk shown in Fig. 3.


Fig. 3 Cessna 172 Skyhawk [15]

The vehicle is a 4-seat aircraft with a maximum range of about 1185 km. Its limit speed is 302 km/h, although the maximum cruise velocity is 230 km/h [15].

### 3.2 Thrust requirements

The first steep of the aircraft analysis consists in studying the cruise performance. As all the weight data is provided by the manufacturer, the necessary lift can be easily calculated. Therefore, the drag force required to counteract for different flight velocities can be computed.

### 3.3 Propeller selection and calculation

Apart from selecting a real aircraft, a real propeller model is also used to make the results more representative. The selected propeller is the one used in the traction study done in reference [16]: propeller AV-844-1-E-C-R-(P). Nonetheless, in order to make it more similar to the propeller of the Cessna 172, just 2 blades have been taken into consideration despite this propeller is conceived as a 4-blade propeller. Following the procedure, a MATLAB code has been developed to compute the propeller performance. The input parameters of the code are the flight altitude, the flight velocity, the propeller revolutions per minute and the propeller geometry, which are constant values already given by the previously mentioned reference. The propeller revolutions have been adjusted until the desired thrust has been achieved. Then, it has been found that 1500 RPM is enough for the propeller to produce the necessary thrust. In addition, a propeller efficiency of 0.839 has been obtained at this flight conditions. This efficiency is the one used in the power calculation.

### 3.4 Power and energy split factor

Finally, two important factors are introduced. As HEP is being considered, the power provided by the ICE might not be the total power provided to the propeller, as the EM could propel it as well in a parallel configuration. In order to indicate the amount of

electric power provided to the propeller compared to the total power received by both EM and ICE, the power split factor $S$ is introduced [10].
Depending on which propulsive system is being used, $S$ can vary along the following values: $S = 0$, propeller powered with just the ICE; $S = 1$, propeller powered with just the EM and $S = ]0,1[$, propeller powered with both ICE and EM.
In addition, another design criterion for the HEP has to be introduced: the amount of fuel and batteries carried. For convenience, as in reference [10] this amount will be considered in terms of energy instead of mass. Depending on how electrified the aircraft is, the energy split factor can vary along the following values: $\psi = 0$, fuel is the only available energy; $\psi = 1$, batteries are the only available energy and $\psi = ]0,1[$, fuel and batteries are both available energies.
With these two parameters, the HEP system is totally defined. For the next sensitivity study, take into consideration how these two parameters vary in their limit cases are the following:

- Fuel conventional aircraft: $S = \psi = 0$,
- Full electric aircraft: $S = \psi = 1$,
- HEP aircraft: $S = ]0,1[$, $\psi = ]0,1[$.

## 4. RANGE FOR HYBRID ELECTRIC PROPULSION

For fuel driven conventional aircrafts, the range can be easily estimated using the Breguet equation. However, this equation is based on the mass reduction due to the fuel consumption. When using batteries, although the energy from them is consumed, the mass remains constant. For this reason, when talking about electric aircrafts other range and endurance equations which do not consider this mass loss among other aspects should be used [17].

### 4.1 Range equation for hybrid electric propulsion

Once the thrust and efficiency of the propeller have been calculated in section 3, the range can be determined. For conventional fuel powered aircrafts, the following Breguet equation can be used [10]:

$$R = \int_{W_{final}}^{W_{start}} \frac{V}{g \cdot PSFC} \frac{C_L}{C_D} \frac{1}{W} dW \tag{1}$$

Where $R$: range, $W$: weight, V: flight speed, g: gravity acceleration, PSFC: Power Specific Fuel Consumption, $C_L$ and $C_D$ are the lift and the drag coefficients respectively. This equation estimates the range of an aircraft based on the weight reduction that experiences due to the fuel consumption. Nonetheless, the batteries used to power either electric or hybrid aircrafts do not vary their mass along the flight, requiring then the use of another approach. Instead of mass reduction, the Breguet equation can be expressed in terms of energy reduction as shown in reference [10]:

$$R = \frac{\eta_{prop}}{g\left(c_P \frac{H_{fuel}}{g}(1-S) + \frac{S}{\eta_{elec}}\right)} \frac{C_L}{C_D} \frac{1}{A} \ln\left(\frac{AgE_{start} + W_{empty} + W_{payload}}{W_{empty} + W_{payload}}\right) \tag{2}$$

Where $\eta_{prop}$: propeller efficiency, $c_P$=$PSFC$ $g$, $H_{fuel}$: fuel energy density, $\eta_{elec}$: electric efficiency, $A$=f($\psi$) and $E$ is the energy.

### 4.2 Range equation considerations

Several assumptions and considerations have to be taken into account. Firstly, keep in mind that this study is made for a constant cruise flight. In addition, parallel configure-tion is the selected in the present case due to its desired features discussed in section 2. Using the previously mentioned range equation, the range can be computed for a constant cruise velocity as it will be shown in the following. Therefore, the range can be represented as a function of the power split factor $S$ and the energy split factor $\psi$.

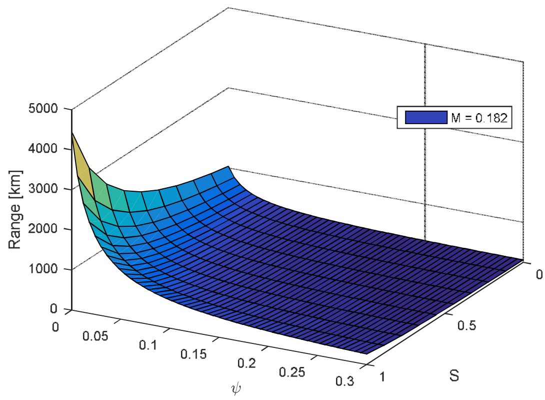


Fig. 4 Range along $\psi$ and $S$ for a constant M

As seen in Fig. 4, the range increases as the energy split factor $\psi$ gets closer to 0, meaning that the aircraft is less electrified and is more similar to a fuel powered con-ventional aircraft. As expected, the more fuel used, the larger the range. Nonetheless, it can also be observed that the range factor increases when the power split factor in-creases. This means that the more EM used for powering the propeller, the larger the range.

For this propulsive configuration, the terms in (2) regarding the fuel and ICE are larger than the ones regarding the EM and electric system. As they are dividing the range, the smaller these terms are, the larger the range is. Thus, if $S$ gets close to 1, the fuel term disappears, and the overall range becomes larger. Nevertheless, increasing the $S$ normally implies an increase in $\psi$ as well, which reduces this range value.

Other considerations regarding the power split factor $S$ and its relationship with the energy split factor $\psi$ are next:

- The power split factor $S$ is constant along the flight. This implies that the EM and the ICE are powering the propeller at a constant rate during the entire cruise flight. In reality, a parallel configuration could change the proportion of each power delivery depending on the flight requirements.
- The ICE does not charge the batteries. Although a parallel configuration can have the possibility to charge the batteries from the ICE if desired, this study won't take it into account. The starting energy from the batteries will be the only available electric energy along the flight.

- The power split factor $S$ is considered equal to the energy split factor $\psi$ during the cruise flight, which is a direct consequence of the battery energy is consumed at the same time as the fuel is consumed.

## 5. PERFORMANCE STUDY FOR HYBRID ELECTRIC PROPULSION

From equation (2), several performance parameters can be extracted depending on the selected hybridization configuration and flight conditions. For this reason, a sensitivity study will be done in the following section to understand how the performance of an aircraft varies due to the electrification of it.

### 5.1 Fuel and battery mass definition

Before defining the amount of each energy source carried in the aircraft, the propulsive system of the Cessna 172 has to be modified in order to introduce the electric systems into it. Using the same ICE as in the reality plus the addition of an EM would totally compromise the overall aircraft weight. For this reason, as a first approach a smaller ICE has been selected in order to fit with the chosen EM. The main characteristics of both propulsive systems can be summarized in Table 1.

| | Lycoming IO-145 (ICE) | EMRAX 268 (EM) |
|---|---|---|
| $\eta$ | 0.34 | 0.98 |
| $m$ [kg] | 87.5 | 20.3 |
| $P_{continious}$ [kW] | 56 | 100 |
| $H_{fuel/bat}$ [kWh/kg] | 11.90 | 0.22 |

Table 1 Lycoming IO-145 and EMRAX 268 characteristics [18][19]

Apart from the EM and the ICE, an extra 9 kg have been considered regarding the electric systems (such as the inverter), transmission and planetary gears. No extra generator is required for this configuration. This new propulsive system does not exceed the previous configuration weight (116.8 kg against the previous 117 kg engine weight from Cessna 172).

In addition, as parallel configuration is being studied, both engine and motor power can be applied at the same time, providing enough continuous power as the Cessna 172 engine usually produces during cruise flight (156 kW in total for the required 87,1 kW during cruise). Moreover, the engine and motor can provide higher peak powers, which means that they are also able to perform other flight conditions that require much more power such as take-off or climb (156 kW available in total, while the Cessna 172 engine provides 134 kW). In this case 8000 feet (2438 m) cruise height will be considered. As the maximum available mass for fuel: $m_{total}$ is known (144.7 kg) as well as both energy densities $H_{bat}$ and $H_{fuel}$, the total energy $E_{total}$ can be computed by the equation (3).

$$E_{total} = m_{total} \frac{H_{bat} H_{fuel}}{\psi H_{fuel} + (1-\psi) H_{bat}}, \tag{3}$$

Where $m$stands for the mass and $H_{bat}$ for the energy density of battery. Defining the energy split factor $\psi$ in terms of energy instead of mass means that if $\psi$ is set to 0.5, the total mass of the battery won't be equal to the total mass of the fuel, as it would be higher to have the same amount of energy as the fuel. The variation of mass along the energy split factor $\psi$ will follow the shape of Fig. 5.

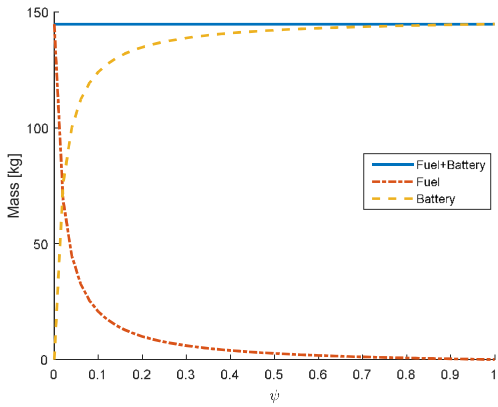


Fig. 5 Fuel mass, battery mass and total mass variation along the energy split factor ($\psi = E_{bat}/E_{total}$) for $H_{fuel} = 11{,}90\ kWh/kg$ and $H_{bat} = 0{,}22\ kWh/kg$

It can be clearly seen that after a certain value of energy split factor, the fuel mass become almost negligible while the battery mass achieves almost the maximum permitted mass for energy source.

These fast mass exchange between energy sources along the energy split factor $\psi$ is mainly due to the huge difference between energy densities of the battery and the fuel. For this reason, the total initial energy that the aircraft carries greatly decreases when the fuel is replaced by the same amount of battery mass (see Fig. 6).

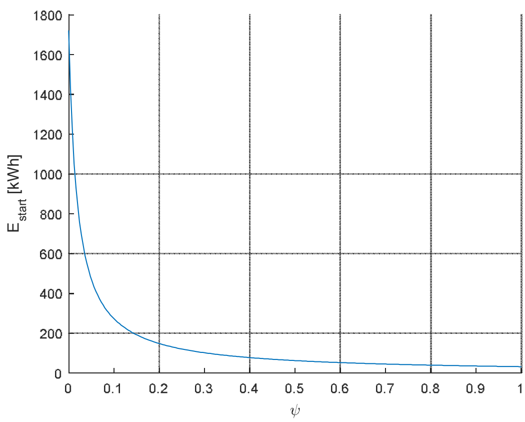


Fig. 6 Initial energy variation along $\psi$

### 5.2 Range calculation at constant Mach number

For this first analysis, the Mach number is considered constant while the energy split factor $\psi$ obtain values from a range between [0, 1]. The selected Mach is the cruise Mach number of the Cessna 172 [15]: M=0.182

Proceeding with the steps mentioned at the previous chapter, Fig. 7 presents range and endurance results for several $\psi$ values. Remember that the energy split factor $\psi$ is

studied from 0 to 1 and the power split factor $S$ is always equal to this parameter. The range and endurance decrease as $\psi$ increases. Due to the low energy density of the battery compared to the fuel, whenever $\psi$ is increased, the range rapidly decreases until some point when it is no longer interesting enough for real applications.
On the other hand, Fig. 7 shows that around energy split factor $\psi$ of 0,65, the range and endurance slightly start to increase. This behavior can be attributed to the power split factor $S$ effect. Mathematically, it can be observed how at some point the power split factor $S$ makes a greater influence than the energy split factor $\psi$ in the range. For following the explanation, the range equation (2) has been rewritten with the weights of fuel and battery inside the logarithm for convenience [10]:

$$R = \frac{\eta_{prop}}{g\left(c_P \frac{H_{fuel}}{g}(1-S)+\frac{S}{\eta_{elec}}\right)} \frac{C_L}{C_D} \frac{H_{bat}H_{fuel}}{\psi H_{fuel}+(1-\psi)H_{bat}} \ln\left(\frac{W_{bat}+W_{fuel}+W_{empty}+W_{payload}}{W_{empty}+W_{payload}}\right) \tag{4}$$

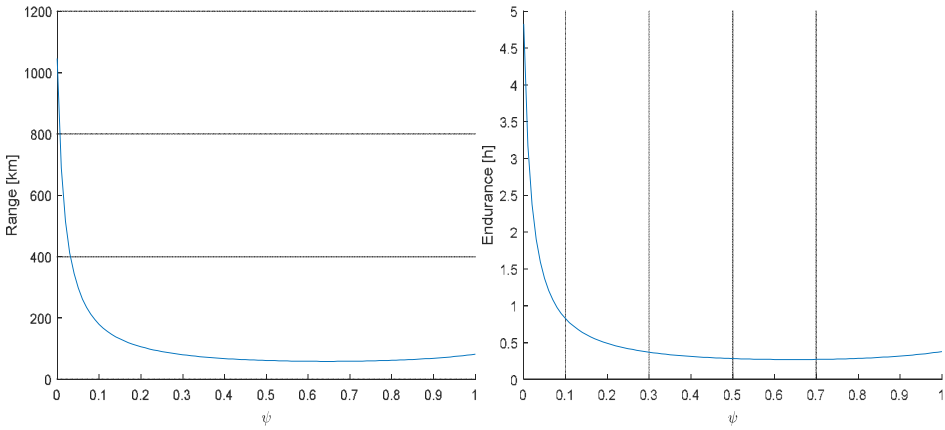


Fig. 7 Range (left) and endurance (right) along $\psi$ at constant M

## 5.3 Range calculation with variable Mach and energy split factor

Finally, both Mach number value and energy split factor will be represented to have an overall understanding of how these variables affect the range. The same procedure as in the previous analysis has been followed but without maintaining constant any of the two variables.

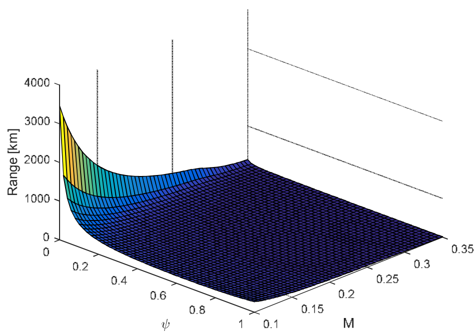


Fig. 8 1 Range along $\psi$ and $M$

Fig. 8 shows the abovementioned results: the range is increased when the Mach number and the energy split factors $\psi$ are decreased. It is easy to see that for the lowest Mach number the range factor greatly increases when the energy split factor $\psi$ gets close to 0. In addition, it is observed how the graph becomes almost plain with just a small increase of the energy split factor $\psi$.

## 6. CONCLUSIONS AND FUTURE STEPS

In order to create a more environmentally friendly and feasible aviation propulsion, aircraft technology should move towards the reduction of fuel consumption. Not only the reduction of greenhouse emissions would be reduced, but also the cost of flying would significantly decrease. Still far from the totally electrification of the aircrafts, this technology developments must transition through the development and application of HEP. Hybrid technology would not eliminate the consumption of fuel, but by slightly reduce the aircraft performance it would be able to decrease it easily with the current technology knowledge.

It seems that the easiest transition into HEP goes through parallel configurations. These designs just require the incorporation of an EM into an already known propulsion system from a current aircraft, apart from the necessary electric systems and couplers. On the other hand, series configuration would require completely new designs of the entire propulsive system, increasing the complexity and the uncertainty of its behavior and performance. In addition, parallel configuration is less heavy than the series one, apart from being more safe and powerful. Regarding the ICE, piston engines are expected to be more compatible with parallel configurations mainly due to its efficiency and ability to rapidly change its power production, especially with small sized aircrafts.

The classic Breguet equation integrates the range over the mass difference from the beginning of the flight till the end due to the consumption of the fuel. As batteries do not lose mass while being used, other equations for fully electric aircraft have been developed. However, a compromise solution between the two configurations has been used: the range equation has been integrated over the energy of the energy sources from the aircraft (fuel and battery). This is an intermediate solution which is expected to give theoretical results quite similar to the real ones, although some considerations have to be taken into account. For example, this equation depends on two essential parameters from the HEP: the power split factor $S$ and the energy split factor $\psi$ (which can be considered equal for cruise flight). According to these parameters the ICE and EM act simultaneously, constantly and during the same time along the entire flight. On the other hand, it has been assumed that the batteries are not charged during the flight, as too many inefficiencies would appear. So, this means that the starting energy from the batteries (charged on ground) is the only available electric energy along the flight.

When analyzing the range obtained for different $\psi$ configurations, it has been found that not all HEP are better than the fully electric configuration. When the mass of the battery is highly increased and there is almost no fuel mass, the range obtained by the aircraft is greatly reduced. Nonetheless, when $\psi$ keeps increasing at some point the range starts to increase. This effect, as previously explained, can be attributed to the power split factor: once the fuel mass is almost negligible, the flight becomes more efficient when most of the power comes from the EM, which means that $S$ needs to be as high as possible.

If the application requirements are not strict to the performance provided by fully fuel aircrafts, HEP could be easily implemented reducing the fuel emissions and overall flight cost. Depending on the flight demands, the design criteria should move between all the possible $\psi$ and $M$ previously studied.

The future of both HEP and fully electric aircrafts mainly remains on the development of batteries with better energy densities. Until this barrier is not surpassed, the implementation of these technologies will still be not sufficiently promising against the fully fuel conventional aircrafts. Nevertheless, battery technology is currently improving its performance much faster than what fuel systems can.

Even though this lack of high energy density on batteries, the improvement of HEP configuration concepts would provide less inefficiencies and a better overall performance of the aircraft if implemented. For example, more studies for parallel configuration should be done regarding other flight conditions such as take-off, or even analyzing how the performance of the aircraft would change if the fuel is consumed prior or after the use of the battery energy.

Moreover, this article has concentrated on the study of parallel configuration. More analysis onto other configurations such as series should be performed to extract more conclusions about which the best configuration for each of its possible applications could be.

## 7. ACKNOWLEDGEMENTS

This work was supported by Hungarian National EFOP-3.6.1-16-2016-00014 project titled by "Investigation and development of the disruptive technologies for e-mobility and their integration into the engineering education”.

## 8. REFERENCES

[1] **Ehsani, M. - Yimin, G. - Miller**, **J. M.:** “Hybrid Electric Vehicles: Architecture and Motor Drives,” Proc. IEEE, vol. 95, no. 4, 2007, p.719–728.

[2] **Friedrich, C. - Robertson**, **P. A.:** “Hybrid-Electric Propulsion for Aircraft,” J. Aircr., vol. 52, No. 1, 2015, p.176–189.

[3] “Reducing emissions from aviation | Climate Action.” [Online]. Available: https://ec.europa.eu/clima/policies/transport/aviation_en. [Accessed: 24-Feb-2018]

[4] **Darecki, M.et al.:** “Flightpath 2050,” Flightpath 2050 Eur. Vis. Aviat., 2011, p.28.

[5] **Glassock, R. - Galea, M. - Williams, W. - Glesk. T.**: “Hybrid Electric Aircraft Propulsion Case Study for Skydiving Mission,” Aerospace, vol. 4, no. 3, 2017, p. 45.

[6] **Wall, T. J. - Meyer, R.:** “A Survey of Hybrid Electric Propulsion for Aircraft,” 53rd AIAA/SAE/ASEE Jt. Propuls. Conf., 2017, p.1–15.

[7] **Lieh, J. - Spahr, E. - Behbahani, A. - Hoying**, **J.:** “Design of Hybrid Propulsion Systems for Unmanned Aerial Vehicles,” 47th AIAA/ASME/SAE/ASEE Jt. Propuls. Conf. Exhib., 2011, p.1–14.

[8] **Roof, C. - Bari, M. - Oza, A. - Chudoba**, **B.:** "The Future of Electric Aircraft," 51st AIAA Aerosp. Sci. Meet. Incl. New Horizons Forum Aerosp. Expo., 2013. p.1–10.

[9] **Trawick, D.R. - Moroniti, D. - Mavris**, **D.N.:** "Development of a Series Hybrid Propulsion System for Unmanned Aerial Vehicles," 51st AIAA/SAE/ASEE Jt. Propuls. Conf., 2015, p.1–10.

[10] **Voskuijl, M. - van Bogaert, J. - Rao**, **A.G.:** "Analysis and design of hybrid electric regional turboprop aircraft," CEAS Aeronaut. J., vol. 9, No. 1, 2018, p.15–25.

[11] **Antcliff, K.R. - Guynn, M.D. - Marien, T.V. - Wells**, **D.P.:** "Mission Analysis and Aircraft Sizing of a Hybrid-Electric Regional Aircraft," 54th AIAA Aerosp. Sci. Meet., 2016, p.1–16.

[12] **Eshani, M. - Gao, Y. - Gay, S. - Emadi**, **A.:** "Modern electric, hybrid electric and fuel cell vehicles," CRC PRESS, 2nd. Edition, 2010.

[13] **Marwa, M. - Martos, B. - Martin, S.M. - Anderson**, **R.:** "Analytic and Numeric Forms for the Performance of Propeller-Powered Electric and Hybrid Aircraft," 55th AIAA Aerosp. Sci. Meet., 2017, p.1–37.

[14] **Grosshauser**, **R.:** "Turbines vs. Reciprocating Engines," 2016. [Online]. Available:https://www.power-eng.com/articles/print/volume-120/issue-11/features/ turbines-vs-reciprocating-engines.html. [Accessed: 02-Mar-2018].

[15] **Cessna**, "Cessna 172S Skyhawk Information Manual," A Textron Company, 1998.

[16] **Molnár, I.T. - Ailer, P. - Veress, Á. - Rohács, J.- Rohács**, **D.:** "Hibrid Kisrepülőgép Propulziós Rendszer-Elemeinek Modellezésére Alkalmas Módszer Kidolgozása." Aeronautical Science Bulletins, on-line scientific journal, XXIX. year 2017. issue 3., 2017, p.317-336.

[17] **Traub**, **L. W.:** "Range and Endurance Estimates for Battery-Powered Aircraft," J. Aircr., vol. 48, No. 2, 2011, p.703–707.

[18] **Lycoming**, "Lycoming Operator's Manual," A Textron Company, 2000. [Online]. Available: http://aeroclub-lehavre.e-monsite.com [Accessed: 06-Mar-2018]

[19] **EMRAX**, "User's Manual for Advanced Axial Flux Synchronous Motors and Generators - EMRAX 268 / 268 VHML." 2017. [Online]. Available: http://emrax.com/ [Accessed: 06-Mar-2018]

# IDENTIFICATION OF SINGLE SPOOL MICRO TURBOJET ENGINE WITH FIXED EXHAUST NOZZLE AT MULTIPLE OPERATING POINTS FOR LINEAR PARAMETER VARYING CONTROL

**Károly BENEDA and Khaoula DERBEL**

Department of Aeronautics, Naval Architecture and Railway Vehicles
Faculty of Transportation Engineering and Vehicle Engineering
Budapest University of Technology and Economics
H-1521 Budapest, Hungary

*Received: November 5, 2018*

## ABSTRACT

Operation of turbojet engines is based on complex aero-thermodynamic laws, which exhibit significant nonlinearity over the entire range of regimes. This can be simplified to a linear model in a small neighborhood of a selected operating point, however, such models are not suitable for the complete range. For this reason, in such cases, where the direct nonlinear solutions would be too complex to solve, there are special methods to extend the effective range of the linear approaches by gain scheduling or linear parameter varying (LPV) control. Our present research focuses on the establishment of an LPV control. For this reason, one has to specify first the dynamic linear mathematical model of the plant to be controlled, which has been already concluded as reported in other articles. The actual phase of the investigation focuses on the identification. The authors carried out various measurements at various operating points from idle to takeoff thrust of a real micro turbojet engine of the 100N thrust class. These data can be used in the identification of the plant at different load conditions, to determine the system matrices as functions of TPR. The obtained information can be used to perform simulations to validate the model and will form the basis of an LPV control system. The present article describes the establishment of the measurements, the steps of the identification, details the progress of simulation software development. It also incorporates simulations that verify correct operation of the mathematical model.

*Keywords:* linear parameter varying control, identification, turbojet engine, fixed exhaust nozzle, turbofan power ratio, gas turbine simulation

## 1. INTRODUCTION

### 1.1 Micro turbojet engines

Several different types of gas turbines have been spread in aviation industry, ranging from the original turbojet engines through high bypass ratio turbofans and turboprops as well [1]. All of them build around a core engine comprised by compressor, combustion chamber and turbine, but the method how propulsive force is generated differs. In the present research the authors focus on micro turbojet configuration, although their propulsive efficiency is lower than the corresponding value of other types, and therefore they are not widely used in everyday air transportation [2]. However, they still have important role in secondary systems, like unmanned aerial vehicles propulsion or auxiliary power plants of sailplanes [3]. Due to their favorable simplicity they are used in hobby-built radio controlled model aircraft and can be utilized for research and education as well [4].

The particular type of micro turbojet engine on which the present research is carried out is PD-60R, which is shown in Fig. 1. This engine has originally been converted from an automotive turbocharger having 60mm compressor outlet diameter into turbojet engine. It received a custom developed combustion chamber featuring an evaporation fuel supply system rather than nozzles that would be difficult to manufacture in this size. The engine is equipped with a fixed exhaust nozzle that significantly reduces the complexity of the system, the only parameter that influences the operational condition is fuel mass flow rate.

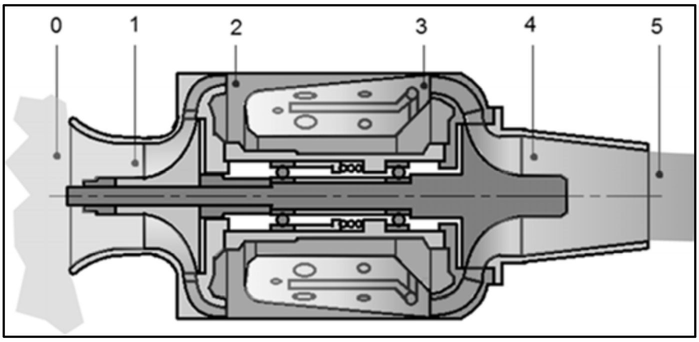


Fig. 1 Longitudinal section and aerodynamic stations of the PD-60R micro turbojet engine

The engine has a simple fuel supply system where the metering of the fuel flow is achieved through the control of rotating speed of the pump. The fuel pump is a gear-type, positive-displacement unit, designated at 12V DC supply, however, in the present application the demanded change of rotating speed is realized by pulse width modulation (PWM).

The engine has a very simple lubrication, which is of the lossy type, seldomly used in similar simple turbine engines. The fuel is a mixture of either diesel or jet fuel and turbine oil. The latter has a volume fraction of 3%. The outlet of the fuel pump is bifurcated; a small portion of the liquid is sent to the bearing chamber through an orifice which meters the amount of lubricant.

The operation of the evaporating combustion chamber is based on the heat released from burning. The fuel manifold is located at the rear of the combustion chamber and the supply tubes penetrate the chamber pointing forward. As liquid is travelling through these tubes, during normal operation the already high temperature is able to evaporate the fuel. During start, when the components are cold, preheating is required, it is solved by injecting butane gas and ignited by a glow plug. During preheat, the starter motor is commanded to maintain a minimum airflow through the unit. After the temperature in the combustion chamber has raised to a determined value, the liquid fuel supply can begin and the preheating cycle is stopped.

For initial cranking during start the engine is equipped with a three-phase BLDC electric motor, which can be controlled to various speeds according to the requirements.

### 1.2 Linear state-space model of micro turbojet engine

The state-space model of the turbojet engine has been developed earlier through the present research. This model is based on physical laws of conservation of energy and mass. In this simple structured turbine engine, there are three storage possibilities:

1. The rotor can store kinetic energy due to its motion. It can be expressed by the differential equation represented by (1), which expresses the rotor acceleration by the difference in turbine and compressor powers.

$$\dot{n} = \frac{P_T \eta_m - P_C}{\Theta(\pi/30)^2 n} \tag{1}$$

2. The combustion chamber is able to store internal energy of the gas inside. This is indicated by (2) that already shows that he relationship expressed as the change of total temperature.

$$\dot{T}_3^* = \frac{1}{c_v m_{\dot{E}}} \left[ \left( i_2^* \dot{m}_2 + H_a \eta_{\dot{E}} \dot{m}_{t\ddot{u}a} - i_3^* \dot{m}_3 \right) - c_v T_3^* \left( \dot{m}_2 + \dot{m}_{t\ddot{u}a} - \dot{m}_3 \right) \right] \tag{2}$$

3. The combustion chamber is responsible for an-other storage, the mass of the gas can be temporarily stored in this cavity, if turbine inflow and compressor outflow rates do not match. This equation is converted to the change of the total pressure, according to the ideal gas law, as represented in (3)

$$\dot{p}_3^* = \frac{p_3^*}{T_3^*} \dot{T}_3^* + \frac{R_g T_3^*}{V_{\dot{E}}} \left( \dot{m}_2 + \dot{m}_{t\ddot{u}a} - \dot{m}_3 \right) \tag{3}$$

This highly nonlinear equation system is the basis of the state space representation, where the system states are those three parameters, whose time derivatives have been introduced in (1)-(3).
The linearization of the system is provided by a perturbation model around a specified nominal operating point. Here, the changes in any variable can be expressed by the partial derivatives. So the model structure is as can be seen in (4):

$$\begin{aligned} \dot{\tilde{x}}(t) &= \mathbf{A}\tilde{x}(t) + \mathbf{B}\tilde{u}(t) \\ \tilde{y}(t) &= \mathbf{C}\tilde{x}(t) + \mathbf{D}\tilde{u}(t) \end{aligned} \tag{4}$$

The matrices of the system are composed of various partial derivatives, as represented by (5).

$$\mathbf{A} = \begin{bmatrix} \frac{\partial \dot{n}}{\partial n} & \frac{\partial \dot{n}}{\partial p_3^*} & \frac{\partial \dot{n}}{\partial T_3^*} \\ \frac{\partial \dot{p}_3^*}{\partial n} & \frac{\partial \dot{p}_3^*}{\partial p_3^*} & \frac{\partial \dot{p}_3^*}{\partial T_3^*} \\ \frac{\partial \dot{T}_3^*}{\partial n} & \frac{\partial \dot{T}_3^*}{\partial p_3^*} & \frac{\partial \dot{T}_3^*}{\partial T_3^*} \end{bmatrix} \quad \mathbf{B} = \begin{bmatrix} \frac{\partial \dot{n}}{\partial \dot{m}_{fuel}} = 0 \\ \frac{p_3^*}{m_{CC}} \\ \frac{H_a \eta_C - c_v T_3^*}{c_v m_{CC}} \end{bmatrix} \quad \mathbf{C}^T = \begin{bmatrix} \frac{\partial TPR}{\partial n} \\ \frac{\partial TPR}{\partial p_3^*} \\ \frac{\partial TPR}{\partial T_3^*} \end{bmatrix} \tag{5}$$

It must be noted, that the present research uses a novel output for controlling the engine, in contrast to conventional rotating speed or engine pressure ratio (EPR) here the Turbofan Power Ratio (TPR) can be seen, which is defined by the expression in (6):

$$TPR = \frac{p_2^*}{p_1^*} \cdot \sqrt{\frac{T_3^*}{T_1^*}} \tag{6}$$

## 1.3 Basics of linear parameter-varying control

As gas turbine engines exhibit strong nonlinear behavior throughout their operating envelope, their modeling cannot be completely ensured by linear models obtained at a single operating point. To overcome this, there are multiple solutions.

First of all, if the complete model and control structure should remain unchanged, a robust control can ensure prescribed behavior even if the plant deviates from its original state. In this situation, the fixed compensators designed through $H_2$ or $H_\infty$ methods can easily offer stability for the plant in the entire range of operation, but significant tracking errors or transient performance loss can occur by using a single controller for all circumstances [5].

On the other hand, either the model or the control structure can be varied according to the changing conditions. If the structure of the compensator remains unchanged (like PID), but control gain is scheduled it results in an off-line alteration that tries to follow the changes occurring in the plant itself as it is forced to operate under different circumstances. This results in a simple, widely-used scheme of gain scheduling [6]. These variables, which are used as a basis for scheduling, are mostly ambient conditions, like altitude, Mach number [7]. This solution has become a standard approach for turbofans [8], turboprops [9] as well as power gas turbines [10,11] in the past two decades .

Despite of the flexibility of gain scheduling, it cannot entirely guarantee stability [12]. Therefore, in the present research the third possible way handling this problem is used. In this approach the plant parameter variability has a structured description rather than an ad-hoc scheduling [5]. The linear parameter-varying (LPV) state-space description, which adds the possibility of $H_\infty$ optimization and subsequent robustness, of an uncertain plant can be written as stated in (7) and (8).

$$\dot{x} = A(p)x + B(p)u \tag{7}$$

$$y = C(p)x + D(p)u \tag{8}$$

Here the system matrices are given by set of coefficient matrices as described by (9), (10) and (11). Matrix **D** is omitted as the present model does not incorporate feedforward behavior.

$$A(p) = A_0 + p_1A_1 + p_2A_2 + \ldots + p_sA_s \tag{9}$$

$$B(p) = B_0 + p_1B_1 + p_2B_2 + \ldots + p_sB_s \tag{10}$$

$$C(p) = C_0 + p_1C_1 + p_2C_2 + \ldots + p_sC_s \tag{11}$$

The goal of this paper is to establish the coefficient matrices for the PD-60R engine.

## 2. DETERMINING COEFFICIENT MATRICES FOR THE TURBOJET ENGINE

### 2.1 Measurement of the gas turbine engine

First of all, the necessary measurement data had to be acquired in order to allow identification. The engine has been run from idle (nearly 60.000rpm) to the maximum safe operating point of approximately 115.000rpm. During the measurement, an initial PID control based on TPR was active, which has been designed for the maximum operating condition. This was a single-gain structure, and the disadvantage is evident:

one can see the oscillations (unstable condition) at idle. This should be eliminated by the LPV system later. The major parameters during the measurement are indicated in Fig. 2.

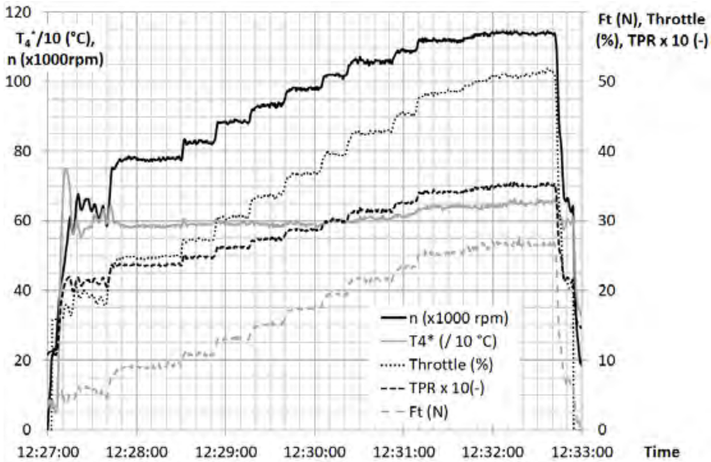


Fig. 2 Measured parameters during the identification run

According to Fig. 2, the operating mode was repeatedly changed (increased) in the form of step inputs. After each transient has been over, the steady state conditions allowed the identification of individual system matrices at the respective points. Consequently, the authors obtained ten sets of matrices, each with a more or less different members. Due to space considerations, these individual matrices are not listed here. With this data already available, the next step of matrix decomposition could take place.

## 2.2 Identification of coefficient matrices

For the initial step of the identification, one must determine which parameters should be included in the decomposition. As the measurements have been performed at ground (nearly sea level) static conditions, at this level of the research the authors do not consider the effect of ambient parameters.

According to the preliminary evaluation, which included only some of the higher operating modes in the range of TPR = 3…3.6, it was evident that the parameter for varying the system matrices should be the system output, TPR itself. Furthermore, it was also seen, that the matrix members do not linearly vary as a function of TPR. The decision was to search for the parameter matrices in the form of a second order polynomial, where $p_1$ equals to TPR and $p_2$ parameter is TPR$^2$, so the computation of e.g. system matrix $A$ can be performed using the correlation indicated in (12).

$$\mathbf{A}(TPR) = \mathbf{A_0} + TPR \cdot \mathbf{A}_1 + TPR^2 \cdot \mathbf{A}_2 \tag{12}$$

If the data is ready and the parameters are selected, the decomposition can be obtained using the next formula, presented for matrix **A** in (13). The known matrices are the multipliers on the left side, these can be obtained from the selected parameters; and the measurement offers data for the right side of the equation. The unknown, to which the equation must be solved, is the vector of parameter matrices from $\mathbf{A_0}$ through $\mathbf{A_s}$.

$$\begin{bmatrix} I & p_1(1)I & p_2(1)I & \dots & p_s(1)I \\ I & p_1(2)I & p_2(2)I & \dots & p_s(2)I \\ \vdots & & & & \vdots \\ I & p_1(r)I & p_2(r)I & \dots & p_s(r)I \end{bmatrix} \begin{bmatrix} \mathbf{A_0} \\ \mathbf{A_1} \\ \vdots \\ \mathbf{A_s} \end{bmatrix} = \begin{bmatrix} A(p(1)) \\ A(p(2)) \\ \vdots \\ A(p(r)) \end{bmatrix} \tag{13}$$

The authors have written a MATLAB® script that can quickly compose the matrices of (13), and can perform the determination of results using a Moore-Penrose pseudo-inverse, given a non-quadratic decomposition matrix.
The resulting coefficient matrices for system matrix **A** can be evaluated in Table I.

Table I. Coefficient matrices of system matrix **A**

| $\mathbf{A_0}$ | | |
|---|---|---|
| 77,64 | -154,63 | -94,18 |
| 11380 | 27992 | 863992 |
| -51,44 | -73,79 | -4295,6 |

| $\mathbf{A_1}$ | | |
|---|---|---|
| -52,56 | 101,22 | 61,30 |
| -4436,5 | -19862 | -527258 |
| 24,73 | 52,37 | 2584,3 |

| $\mathbf{A_2}$ | | |
|---|---|---|
| 7,19 | -15,58 | -1,98 |
| 865,78 | 3126,7 | 83788 |
| -4,42 | -8,22 | -419,1 |

The next step is the evaluation of accuracy: how good fit can be obtained by the present decomposition. For system matrix **A**, different behavior of members has been identified. All the nine members cannot be shown, so only two examples are taken: $A_{13}$ that exhibits an almost perfect fit throughout the complete range, and $A_{31}$, which offers good fit in the selected higher operating mode, but not for the entire range. The two examples can be evaluated in Fig. 3.

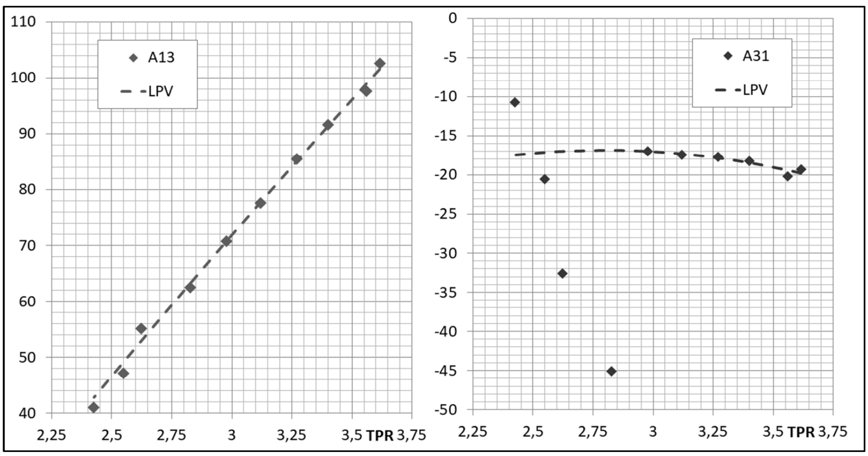


Fig. 3 Identified matrix members and regression curves of selected system matrix members

It is necessary to mention, that the members of input and output matrices, **B** and **C**, respectively, are not prone to the same behavior like $A_{31}$ in Fig. 3. These members follow an almost perfect monotonous curve, as it is indicated in Fig. 4. The members $B_1$ and $C_1$ are not shown as neither input nor output matrix has a dependency on rotating speed, the corresponding partial derivatives are both zeroes. It can be concluded, that the second order approximation results in a good fit in case of these two matrices.

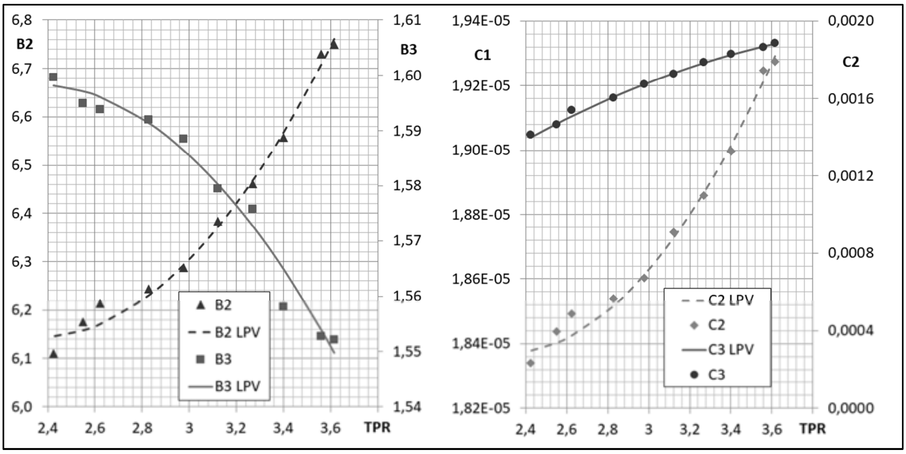


Fig. 4 Identified matrix members and regression curves of input and output matrix members

## 3. SIMULATION OF THE TURBOJET ENGINE

### 3.1 Description of Simulink® software

The dynamic simulation of the micro turbojet engine has been created in MATLAB® Simulink®, the related block diagram is shown in Fig. 5.

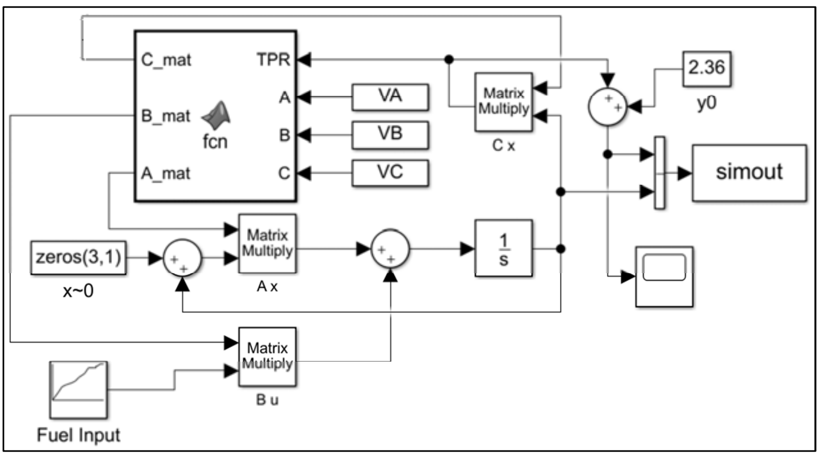


Fig. 5 Block diagram of LPV turbojet model in Simulink®

In Fig. 5, the system itself is represented by the three matrix multiplication blocks labelled as “A x”, “B u” and “C x”, respectively. According to the first correlation of (4) that describes the dynamics of the system, one has to carry out an integration in order to obtain the states themselves, this is indicated by the block labeled “1/s” in the center of the diagram. The left bottom block is the fuel input, which has been organized to simulate the values of the real measurement, it sends the required changes to the fuel flow at the appropriate time during the simulation as it happened through the real engine run. Its values are normalized to the initial fuel supply and the rest of the values are deviations in contrast to this reference. The main difference in contrast to a single operating point model is the MATLAB® function block with the label "fcn" near to the left top corner of the block diagram. This unit calculates the actual values of the matrices using **VA**, **VB** and **VC** as inputs. These are the concatenated matrices from the left side of (13), which were the unknowns and consequently the solutions of (13). The function block splits the concatenation and provides three independent parameter matrices for the LPV decomposition at the actual TPR, which is another input to this block. The outputs are then transferred to the model which uses them for the given iteration only, the computation will take place again immediately when the TPR of the actual step is obtained.

Fig. 5 also contains input constants, as the model in (4) is defined as deviation from a reference, which initialize the states (*x~0*) and output (*y0*), respectively. As the absolute value of TPR is used actively in the computation of parameter matrices, it cannot be implemented as deviation, the real initial value must be passed to this block.

The last blocks in Fig. 5 are sinks that acquire the data and provide some kind of indication. There is a scope which allows real-time monitoring of the simulation, while "simout" block saves the time series of the parameters into a workspace variable, which can be exported into e.g. Excel for comparison with the original measurement data.

Although they are not visible in Fig. 5, the configuration parameters of the simulation are also essential. As the measurement took approximately four and half minutes, the simulation stop time is set to 270 seconds. The solver is variable-step with automatic selection, which was *ode45* (Dormand-Prince) through the entire simulation. The relative tolerance has been reduced to $10^{-5}$ as numeric discrepancies have been experienced during the initial attempts. All other settings have remained automatic.

### 3.2 Comparison of simulation and measurement

After the simulation has concluded, the generated data have been moved to Excel for comparison. Due to the very detailed time steps (approx. $10^{-3}$ seconds) a reduction of the data with interpolation has been utilized.

The comparison of the measured and simulated time series can be evaluated in Fig. 6. In contrast to the model, where the turbine inlet total temperature $T_3^*$ was used as a state of the plant, the measurement allowed the acquisition of $T_4^*$ at the turbine exhaust, hence the model values were also converted to this parameter in order to allow the comparison. For rotating speed and $p_3^*$, the normalized simulation values were not biased by the initial values of the respective parameters. This was chosen intentionally by the authors, as the major part of these time series showed good agreement with the measurement, but were not accurate in the low-speed range.

It is evident that TPR and $p_3^*$ show almost perfect fit, there are major discrepancies in the series of rotating speed and turbine exhaust gas temperature $T_4^*$.

According to Fig. 6, the model calculated rotating speed does not match the measurement in the low-speed range and near to maximum power output of the engine. This means the change of this parameter is under-estimated by the model in case of low engine power.

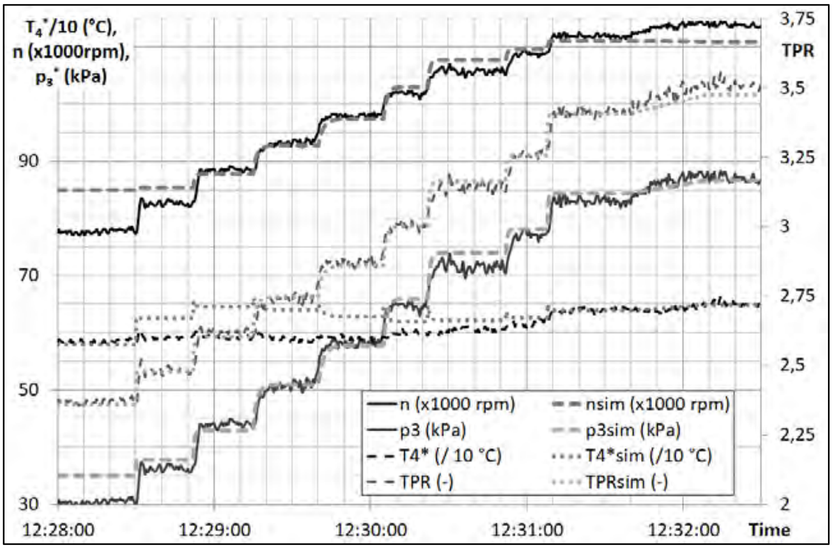


Fig. 6 Comparison of measured and simulated data

The exhaust gas temperature shows deviation in the same zone but for a more significant range. It is interesting, that the simulated variable first significantly overshoots the measured data, finally it returns and makes a perfect fit for the rest of the engine run. This means, that the model over-estimates the change of gas temperature in the TPR range of approx. 2.4 to 3, meanwhile in TPR range 3 to 3.2 there is a deficiency in contrast to reality which allows the previously overshooting value to return to the measured ones.

## 4. CONCLUDING REMARKS

The work presented in this paper has established a linear model of micro turbojet engines with parameter-varying structure in order to handle inherent nonlinearities of the plant. The authors have carried out measurements to identify values for coefficient matrices of the system. The parameter selected to govern the variation of matrices were Turbofan Power Ratio, the output of the plant, which is proportional to the thrust, and $TPR^2$. The coefficient matrices showed a good agreement with the original matrix members in the high engine power range, but a poor fit near to idle. However, the results have been accepted and a simulation was developed in MATLAB® Simulink®. The simulations showed a good correlation between measured and simulated data for almost the entire operating range of the engine, showing that the varying parameter model is able to simulate the nonlinear behavior of the engine, so this can be evaluated as a success.

As it was showed by the simulations the established model gives appropriate answer to input signals in the majority of the operating range of the engine, but still there are zones in which some of the simulated variables deviate from measured ones. Therefore, an improved model should be developed, which is based on higher order polynomial estimation of TPR to follow the changes through the entire operating range. This improvement could be elaborated together with an enhancement of the model to include changes due to different flight modes, i.e. a full flight envelope model could be obtained.

Furthermore, the measurement system for identification should be developed and a more comprehensive data acquisition for refined identification should be carried out.

## 5. REFERENCES

[1] **Flack, R.D.**: Fundamentals of Jet Propulsion with Applications. Cambridge University Press, 2005, p.637, ISBN 978-0-521-81983-1

[2] **Cwojdziński, L. – Adamski, M.**: Power Units and Power Supply Systems in UAV. Aviation, Vol. 18, No. 1, 2014, p.1-8, doi: 10.3846/16487788.2014.865938

[3] **Katolicky, Z. – Bušov, B. – Bartlová, M.:** Turbojet Engine Innovation and TRIZ. In: Proceedings of the 16th International Conference on Mechatronics - Mechatronika 2014, p.16-23, doi: 10.1109/MECHATRONIKA.2014.7018230

[4] **Savka, J. – Főző, L. – Andoga, R. – Nikolas Ivanics**: Is it Possible to Use the Experimental Identification Based on the Transition Characteristics for Micro Turbo Compressor Engines? In: XIII. New Trends in Aviation Development (NTAD), 2018, p.114-117. doi: 10.1109/NTAD.2018.8551655

[5] **Richter, H.**: Advanced Control of Turbofan Engines. Springer, New York, 2012, p.266, ISBN 978-1-4614-1170-3, doi: 10.1007/978-1-4614-1171-0

[6] **Ordonez, P. – Mills, A.R. – Dodd, T. – Liu, J.**: Formal Verification of a Gain Scheduling Control Scheme. 25th Mediterranean Conference on Control and Automation, 2017, p.259-264, doi: 10.1109/MED.2017.7984128

[7] **Martin, S. – Wallace, I. – Bates, D.G.**: Development and Validation of an Aero-engine Simulation Model for Advanced Controller Design. Proc. of IEEE American Control Conference, 2008, p.2334-2339, doi: 10.1109/ACC.2008.4586840

[8] **Bica, B. – Chipperfield, A.J. – Fleming, P.J.**: Towards fuzzy gain scheduling for gas turbine aero-engine systems: a multi-objective approach. Proceedings of IEEE International Conference on Industrial Technology, (Vol. 1), 2000, p.81-86, doi: 10.1109/ICIT.2000.854104

[9] **Pakmehr, M. – Fitzgerald, N. – Feron, E.M. – Shamma, J.S. – Behbahani, A.**: Gain Scheduled Control of Gas Turbine Engines: Stability and Verification. Journal of Engineering for Gas Turbines and Power, Vol. 136, No. 3, 2013, doi: 10.1115/1.4025637

[10] **Zaccaria, V. – Traverso, A. – Tucker, D. – Pezzini, P. – Bryden, K.M.**: Active Control of Fuel Cell Degradation in an SOFC/GT Hybrid System. Proc. of ASME Turbo Expo 2017, ISBN: 978-0-7918-5083-1, doi:10.1115/GT2017-65036

[11] **Rodriguez-Martinez, A. – Garduno-Ramirez, R. – Vela-Valdes, L.G.**: PI Fuzzy Gain-Scheduling Speed Control at Startup of a Gas-Turbine Power Plant. IEEE Transactions on Energy Conversion, Vol. 26, No. 1, March, 2011, p.310-317, doi: 10.1109/TEC.2010.2081991

[12] **Shamma, J.S. – Athans, M.**: Gain Scheduling: Potential Hazards and Possible Remedies. IEEE Control Systems Magazine, Vol. 12, No. 3, 1992, p.101-107, DOI: 10.1109/37.165527

# OPERATIONAL PROFILE OF INLAND PUBLIC TRANSPORT VESSELS

**Győző SIMONGÁTI, Csaba L. HARGITAI and Roland ZALACKÓ**

Department of Aeronautics, Naval Architecture and Railway Vehicles
Faculty of Transportation Engineering and Vehicle Engineering
Budapest University of Technology and Economics
H-1111 Budapest, Műegyetem rkp. 3., Hungary

*Received: November 6, 2018*

## ABSTRACT

Unlike seagoing merchant ships, the inland vessels operate in a wide range of propulsion power, while sailing on rivers longitudinally. Therefore, utilization of main engines are mostly partial. Because the engines run under the nominal power, both the brake specific fuel consumption (BSFC) and the total consumption can be higher than in nominal power operation, and an increase in the emissions can be expected also. The not-conventional ship propulsion systems (e.g. diesel-electric, hybrid, etc.) are getting cheaper hence they raise the possibility of economic feasibility. Selecting a ship propulsion system is a multi-criteria decision making process, which have to be supported from engineering side with operational analysis of different propulsion systems. The starting point of this analysis must be the expected or validated data based operational profile of the vessel. This article introduces the meaning of operational profile and how it can be described. The authors present an example about propulsion power utilization measurement of an inland public transport vessel. Based on the measured data the paper shows how the operational profile is defined. The article introduces the possible criteria of a multi-criterial decision making process for an optimal propulsion system design. The possible non-conventional ship propulsion systems are also introduced, and the interpretation of these for the example inland public transport vessel is presented as conclusion.

*Keywords*: inland waterway vessel, public transport vessel, propulsion system, operational profile

## 1. INTRODUCTION

A typical maritime cargo vessel operates constantly. This means that the propulsion engine (main engine) operates during almost the entire lifetime close to the nominal continuous rating, with good power utilization and efficiency. In contrast, the operation of inland vessels for public passenger transport is uneven, since the flow conditions, the speed changes, and the frequent manoeuvres. The main engine(s) operate over a wide range of partial power over their lifetime, and rated power is rarely utilized. Most of the operating time, the engine runs at partial load, which means higher specific fuel consumption and specific emissions.

The problem can also be observed in road, railway and air transport. While in aircrafts the fluctuating power utilization problem is trying to be handled by optimization of engines (eg.: [1]), in the road and rail vehicles it is trying to be handled by the development of hybrid propulsion systems (eg.: [2]).

In maritime or inland waterway vessels there are several propulsion system type, but to choose the optimal system design, the power demand distribution (or density) on a specific operation period have to be known. The time-proportional density histogram of a vessel's power consumption for an average operating cycle or period of time is called operational profile.

## 2. OPERATIONAL PROFILE OF SHIPS

The ship's operational profile is used to describe and present the ship's operation in energy terms, depicting the relationship between the total energy or power demand for

the various operating conditions and the operating time associated with the operating condition. Total power demand is the power requirement of the main engine (ie. engine of the propulsion) and the auxiliary engines (all other engines serving the operation of the ship). The operational profile can be used to determine the extent to which the rated power of the engine is utilized throughout the operating life. If the operational profile is uneven, the engine is likely to be subject to partial load, which may be detrimental to both specific fuel consumption and emissions. In such cases it is worth considering and examining the applicability and economic efficiency of other propulsion or energy systems.
There are two ways of displaying an operational profile for operational planning. One is when the relative operating time of the various typical operating states is plotted on a pie chart. It does not directly see the performance, but clearly assigns power ranges to the operating states.

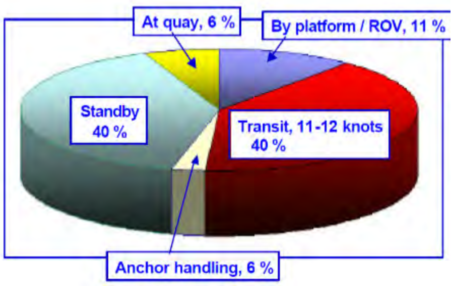


Fig. 1 Operational profile of a supply vessel Source: [3]

Another way of depicting the operational profile is to display in a bar chart, side by side the power levels for each operating state and the operating time ratio.

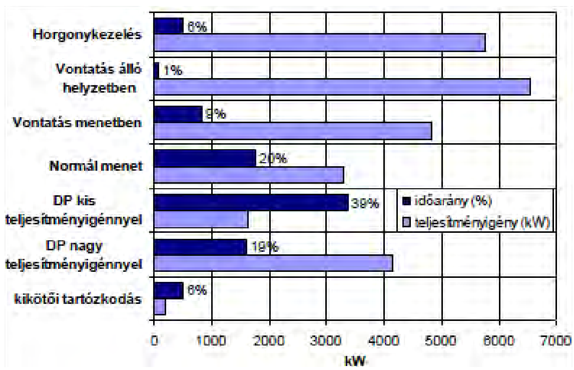


Fig. 2 Operational profile of an anchor handling vessel Source: [3]

However, for power calculations, it is better to use a power (density) histogram representation of power levels as a function of power density and distribution. In this case, the measured or calculated power-time data pairs are divided into different power ranges and the operating time ratios (expressed as a percentage) for each band can be plotted.

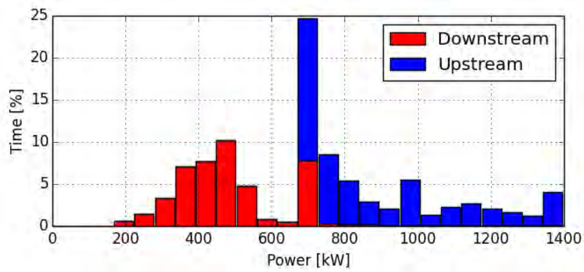


Fig. 3 Operational profile of a river cruise ship Source: [3]

It should be noted that in many cases the operational profile shows only the propulsion power. The auxiliary power is excluded or depicted separately.

The histogram representation of power utilization already indicates that the operating profile actually represents a stochastic process, and the time ratio of power utilization is influenced by many factors (probability variables). These can be grouped as follows:

- Environmental factors: In a given operating condition (eg cruise speed), the operating environment can have a major influence on energy demand.
  - wind, wind direction
  - waves
  - flows, velocity of the river
  - water depth (shallow water effect)
  - fairway width (confined water effect)
  - traffic (how much other ships need to deviate from the optimal route)
- Operating factors:
  - upstream
  - downstream
  - density of manoeuvres
- Ship loading factors:
  - amount of cargo and supplies
  - power consumption of auxiliary consumers (all consumers go at the same time)
- Driving factors:
  - charge adjustment (throttle control)
  - adherence to scheduled times for passenger ships

## 3. DESCRIBING THE OPERATIONAL PROFILE

### 3.1 Possible methods

The operational profile of a ship can be determined even by calculation or measurement. In case of a new design vessel the measurement based operational profile is not possible, since the ship is not available. It should be described by calculation, which is based on the transport task given as design boundary parameter. The transport route plan must be defined from which the planned journey time and speed-time function can be derived for a transport cycle. The required power of the ship can be calculated for each speed and loading condition (occur in the transport cycle) based on the ship resistance calculations or model test results. The operational profile can be established by applying the calculated power consumption to the planned speed-time function.

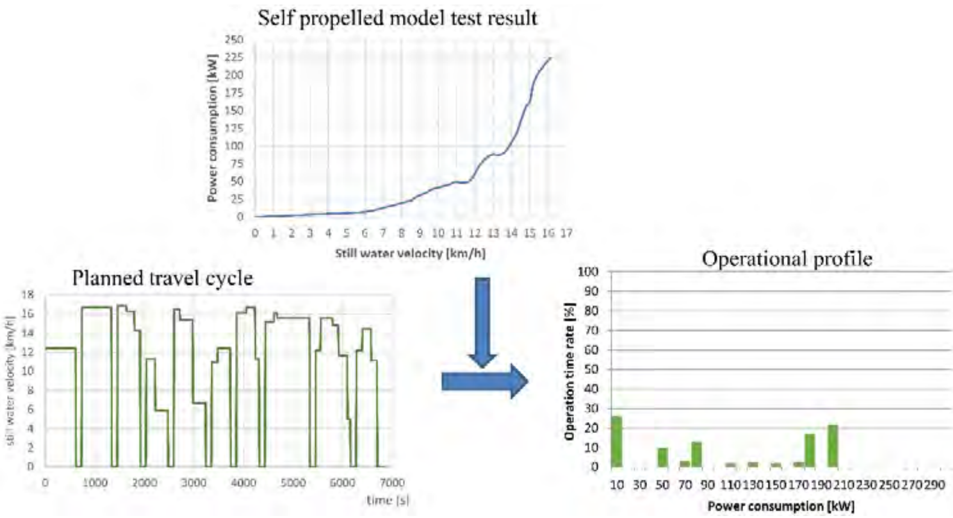


Fig. 4 Determination of the operational profile by calculation for new ships

For existing vessels, who are already in service, the calculation of operational profile follows the same methodology, except that the calculation is based not on the planned speed-time function but on the ship's log (route and speed data).

In case of an existing vessel a more accurate operational profile can be established by measurement. The power consumption data of operational profile can then be calculated from the shaft torque and RPM of the engines involved in power generation. For accurate assessment the route and speed of the ship should be precisely recorded during measurement. In the case of changing flow conditions (e.g. river navigation) the velocity relative to Earth and the still water velocity data are useful, but in most cases it is not possible to measure them accurately. The auxiliary power consumption can be measured by electric power consumption. Nevertheless the importance of auxiliary power consumption is not too significant in a cargo ship's operational profile, so a less accurate measurement does not cause serious error in the operational profile. Therefore in most cases the auxiliary power is reckoned with the ship's energy balance calculation. In this way the cost of measuring equipment can be significantly reduced.

### 3.2 Example: Determining the operational profile by measurement on an inland public transport vessel

The Department of Aeronautics, Naval Architecture and Railway Vehicles of the Budapest University of Technology and Economics carried out an experimental measurement of propulsion power on a passenger ship type BKV100, who serves in the public transport of Budapest. Based on the measured data the operational profile was determined for the environmental conditions (water level, wind, temperature, etc.) at the time of measurement.

### 3.2.1 Main properties of the tested vessel

Fig. 5 The investigated BKV100 type vessel

The investigated BKV100 type ship is a single screw passenger vessel. The main dimensions of the vessel:

| | |
|---|---|
| • Length over all ($L_{oA}$) | 24.4 m |
| • Length between pps ($L_{PP}$) | 23.25 m |
| • Breadth over all ($B_{oA}$) | 6.42 m |
| • Draft by full load ($T_{max}$) | 1.1 m |
| • Displacement in full load condition | 64.5 tons |
| • Main engine | Doosan L126 TIM |
| • Main engine power (P) | 294kW@2100 RPM |
| • Design still water speed | 18 km/h |
| • PAX: | 100 |

Her propulsion system is a single propeller system, with a diesel engine. The four wing propeller has fixed pitch and is mounted on the propeller shaft, which enters the hull through a shaft tube. The propeller shaft is connected to the thrust bearing by a rigid clutch. The thrust bearing transmit the axial force of propeller shaft (thrust) to the hull. The propulsion power is given by a diesel engine, which connects to a reduction gearbox. The propeller shaft and gearbox output shaft are parallel but not collinear. To solve this, a cardan shaft has been mounted between the gearbox shaft and thrust bearing.

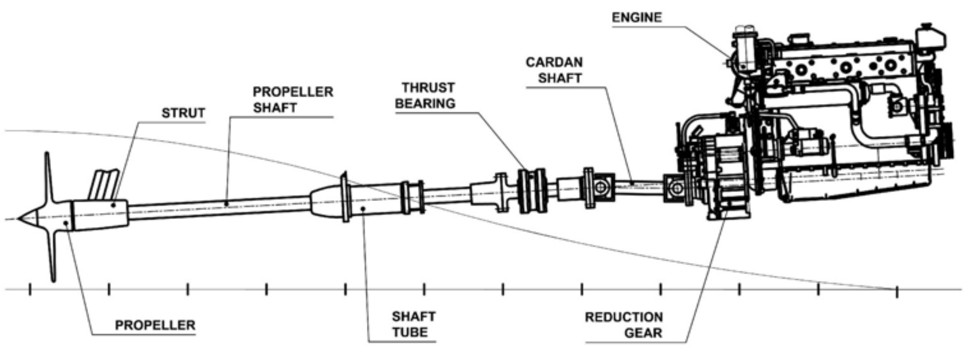


Fig. 6 Propulsion system of the tested vessel

### 3.2.2 The measuring system

To determine the operational profile on an experimental basis, the ship speed and propulsion power shall be measured during a typical operating cycle. The test vessel was equipped with a GPS receiver to record position and velocity.
The power output of the main engine has been measured with a customized device. Due to the design of the propulsion system, there is no thrust on the cardan shaft connecting the gear unit to the thrust bearing, so the mechanical power transmitted to the propeller shaft can be calculated from the torque and the shaft speed. The torque has been measured by a strain gauge glued on the cardan shaft, and the RPM of propeller shaft have been sensed by a hall sensor. Both signal have been recorded on a digital measurement unit, which rotated with the cardan shaft.

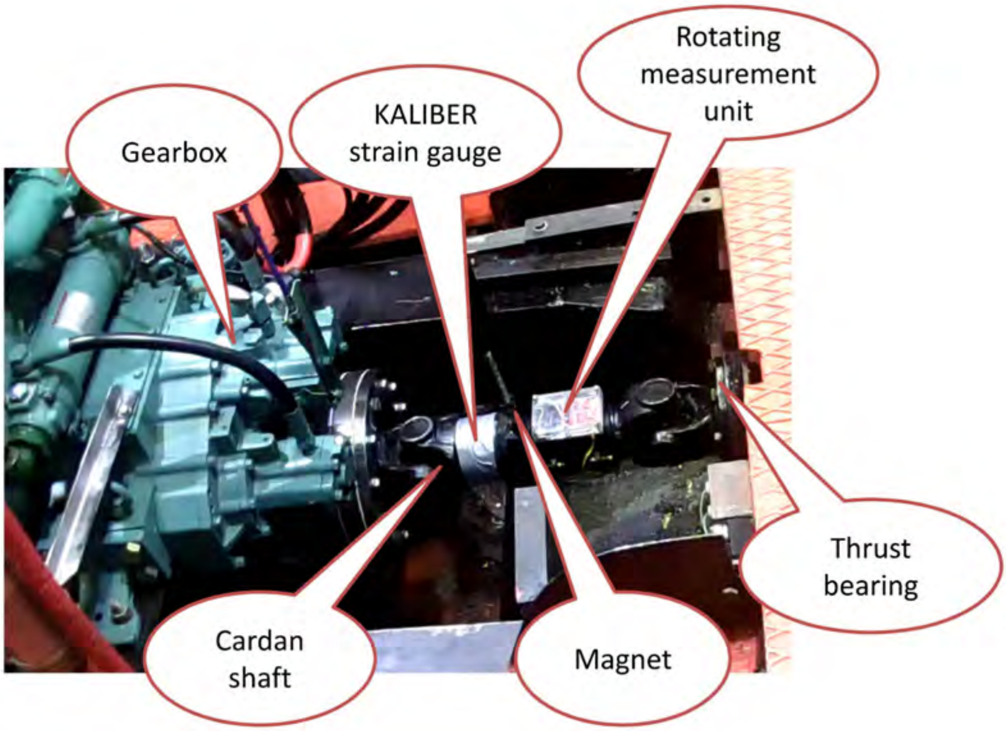


Fig. 7 Propeller shaft torque and RPM measuring system

### 3.2.3 Measured data and the operational profile

During the operational profile measurement test, the vessel ran a course that would have run in public traffic according to the schedule.

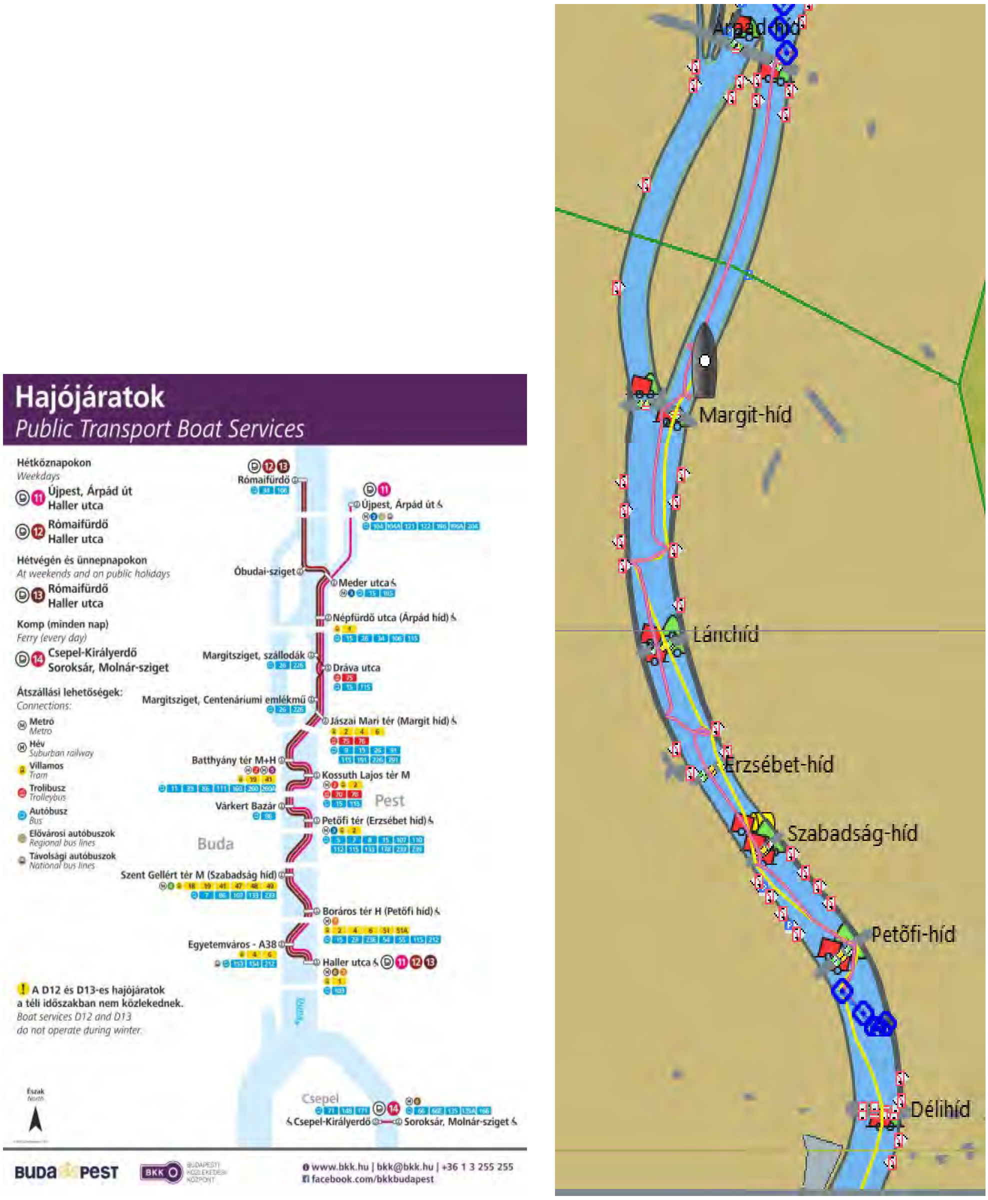


Fig. 8 The schedule and test route of the vessel

The ship has been stopped at every mooring point, but the passenger transfer time was not included into the measurement.

From the measured torque and RPM the propulsion power was easy to calculate. The speed (measured by a GPS receiver) and the propulsion power was represented in function of time (operating time record).

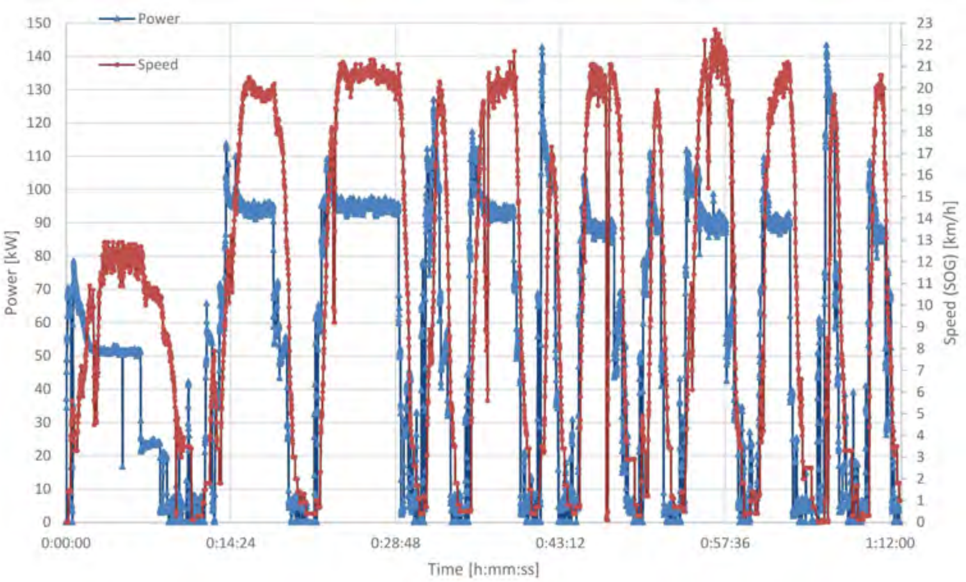


Fig. 9 Operating time record during downstream sailing

The operating profile was determined in 15kW power bands, which summarize part-time ratios over the operating cycle.

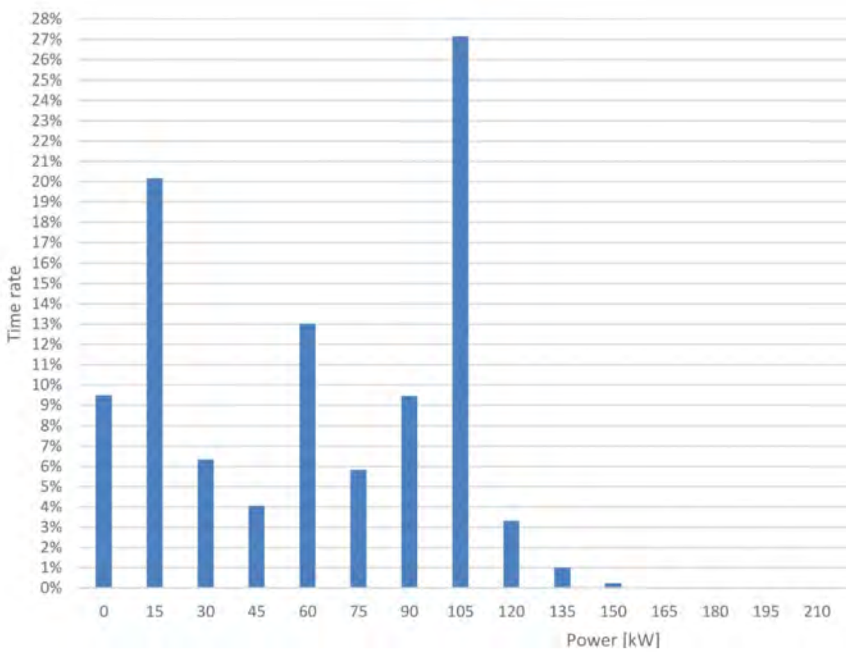


Fig. 10 Operational profile during downstream sailing

## 4. OPTIMIZATION CONSIDERATIONS FOR PROPULSION SYSTEM

Optimizing a propulsion system of an inland vessel is a very complex task. [4] There are many aspects to consider with different weights, which are sometimes contradictory. But we can use the operational profile to limit the power requirement of the propulsion system, and to support the decision making in determining the capabilities and weaknesses of each propulsion system version for a particular ship.

### 4.1 The optimization considerations

The optimization considerations can be many, especially for a special vessel like an inland public transport vessel. The aspects can be divided into two main groups:

- quantifiable
- non-quantifiable or difficult to quantify

### 4.1.1 Quantifiable considerations

Quantifiable aspects are those optimization aspects that can be predicted, calculated, or given with sufficient accuracy. They give numerically easy comparisons:

- Investment cost: The total cost of the propulsion system components and the installation or retrofitting costs can be well calculated.
- Operating costs: This includes maintenance and personnel costs. Maintenance is highly dependent on the machine, the plant, the operating staff, and the salary of the staff is not constant, but it is well-calculated data.
- Fuel costs: This item is usually classified as operating costs, but since it is a fairly large part, it is worth looking at separately as it is often the customer's primary concern to minimize fuel consumption. In terms of operating profile, it is well comparable to other systems.
- Low emission: Ratios are also expected where differences may occur due to the type of fuel used and any filters used.
- Energy use: A criterion may be the minimization of this value, which depends on the machinery, the ship's operation and the auxiliary plant.
- Redundancy: An important consideration, as in the event of a breakdown, the ship is at a great loss. The reliability of the machines can be well predicted.
- High power vs. weight and power vs. space requirements: Increasing these ratios can reduce the size of the engine compartment and reduce the size of the engine compartment. self-weight, which can mean extra payload. Its value can be calculated well due to the given machine dimensions.
- Payback time: A metric that depends on many components and can be estimated with economic accuracy.

### 4.1.2 Non-quantifiable or difficult to quantify considerations

Considerations that are either difficult to calculate or may change significantly with time are in this category.

- Availability: An important factor in the event of an unexpected failure. Time to purchase a new machine or part.
- Infrastructure: There may be bottlenecks, especially in alternative systems. Eg: a Dual Fuel motor based propulsion system requires LNG infrastructure, or a pure electric propulsion requires proper battery charging options.

### 4.2 Opportunities for selecting the optimum drive system

After defining optimization considerations of decision making process, a decision aid operation must be performed to limit the number of propulsion system variations.

The simplest method is to create a comparative table. Within the constraints and information, several possible drive system configurations must be created, all of which meet the drive system requirements. Then a table can be created to score and evaluate each configuration with respect to optimization considerations and their weight ratios. When weighing, the requirements of the customer, as well as the specifications of the ship and its propulsion system are of paramount importance. Of course, these aspects can be prioritized differently for each ship type, or the list can be expanded. Adding the weighted values in the table gives the optimum drive system with the highest or lowest rating.

Another method is to use the information technology and computers. This means that by feeding in the limitations and information available to us and choosing the necessary algorithms, we can build a model and develop a program to determine which propulsion system variation would be optimal for that particular ship.
Input data varies by ship type, but the ship's overall size, operational profile, optimization criteria and their weight, and other constraints are essential. The optimization aspects and the number of variations are large. Because we do not just want to apply our optimization model to a particular ship, we need an extremely large database. It is important that the model should be expandable so that new developments can be considered later. The model must be verified first. Successful verification can save a great deal of time and energy in selecting the optimal propulsion system for a ship.

## 5. CONCLUSIONS: ALTERNATIVE PROPULSION SYSTEM OPTIONS FOR THE TESTED BKV100 TYPE INLAND PUBLIC TRANSPORT VESSEL

### 5.1 Dual fuel or gas engines

LNG as a inland vessel fuel is gaining in importance year by year and infrastructure for inland navigation has begun. The foundation stone of the first LNG terminal was recently laid in Budapest. Dual fuel and gas engine emissions are a less than conventional diesel engines. The price of liquid natural gas is still much lower than diesel fuel. Large marine engine manufacturers (Wartsila, MAN) have already succeeded in building medium power dual-fuel engines for inland navigation. However, the maximum power requirement of the model vessel is far below these engines. The location of the fuel tank may require major structural changes and fuel filling will remain an issue for years to come. Thus, for the time being, it is not worthwhile to use a dual-fuel or gas engine powered propulsion system on the investigated BKV100 type ship.

### 5.2 Pure electric propulsion

Due to the rapid development of the batteries, there are several options for propelling the BKV100 type vessel with an electric propulsion system. This reduces operating costs, noise levels and emissions. Lowering noise levels will make travel more comfortable for passengers, and zero emissions can make more people choose this form of public transport. There are many ways to change the capacity and recharging capacity

of battery packs, as the sample ship does the same trips on a daily basis and in about the same amount of time.
Option No. 1. would be to select the capacity of battery to cover the energy requirements of a full operating cycle (upstream and downstream). In this case, only the port of departure should be equipped with a battery charger (or battery exchange point). The disadvantage of this solution may be the large mass of batteries, as this would require a significantly oversized battery pack to accommodate the additional power requirements due to fluctuations in the river water level and special cases (wind, storm, etc.).
Option No.2. would be to recharge the batteries in specific mooring points (intermediate ports during operating cycle), meaning that the batteries would be discharged and recharged more than once in a given operating cycle. In this case, a much smaller energy storage may be sufficient and the batteries can be recharged during the time of passengers getting in and out. However, this would reduce the life of the batteries and require a powerful battery charger for each mooring point.
Other options are also possible, as an intermediate state of the previous two options. This could be the case, for example, when installing an energy storage system designed for an average operating cycle and, it would be possible to charge the batteries not only at the port of departure but other mooring points, in the event of additional power requirements.
Of course, not be forgotten either case, the auxiliary power, which is not included in the operating profile, but this energy need must also be met by batteries. The average demand of auxiliary power can be considered constant during each operating cycle, so it is easy to determine. Above average demand is due to heating in winter and air conditioning in summer.

### 5.3 Diesel-electric propulsion

Due to the wide range of power requirements and the relatively high auxiliary power requirements in winter and summer, the diesel-electric drive system may be a good solution. By using several smaller generator units, you can ensure that your machines will always be able to operate around their best operating point, tailored to the current power requirements. It is easy to imagine running one engine in downstream, and two or more units running in upstream sailing. The system can meet the auxiliary power requirement and redundancy is also provided. Further benefits include quieter operation and reduced fuel consumption. On the other hand, it has higher operating costs and lower emission values than pure electric and hybrid drives.

### 5.4 Hybrid propulsion

Based on the operational profile established from the experimental results, the power demand of the BKV100 ship is not only wide-ranging, but there are some long term power-demand states that are very different from each other. Based on this, a hybrid propulsion system may be a viable alternative to a conventional propulsion system. An electric motor drive can be expedient to meet the power requirement of an electric motor with a battery pack and / or a generator set, while not neglecting the auxiliary power. As with a purely electrical system, there are many options that can lead to a good solution.

One solution could be to build the ship's propulsion system so that, in the more power demanding upstream sailing, only the generator unit operates while supplying auxiliary power and charging the battery. And during downstream sailing, a charged battery pack would satisfy the ship's total power requirement. The great advantage is that it is not necessary to have a charging station in the ports to charge the batteries. But this solution has the disadvantage of emissions and fuel consumption during upstream sailing.

Other solution is that the manoeuvre and travel operation modes are separated. In this case, the generator unit will provide power to the ship in travel operation mode, while the battery packs would provide the required power in the manoeuvre operation mode. This would result lower fuel consumption compared to the previous solution, but a reduced battery life is also expected.

## 6 REFERENCES

[1] **Bicsák, Gy. – Hornyák, A. – Veress, Á.:** Numerical Simulation of Combustion Processes in a Gas Turbine, ICNPAA 2012 World Congress: 9th International Conference on Mathematical Problems in Engineering, Aerospace and Sciences, July 10, 2012 – July 14, 2012, American Institute of Physics, Conference Proceedings, Vol. 1493, 2012, p.140-148; doi: 10.1063/1.4765482

[2] **Kiss, Cs.:** Villamos hajtású nagyvasúti vontatójárművek fejlődési irányai, Vasútgépészet, 2015, vol. III. p. (In Hungarian)

[3] HSB INTERNATIONAL, June, 2007; https://www.makmed.fr/wp-ontent/uploads/2013/02/Pusher-Tug_3x-MaK_8-M-20_Veerhaven-X_HSB_2007_Jun.pdf

[4] **Simongáti, Gy. – Hargitai, Cs. L. – Réder, T.:** A hibrid hajóhajtás alkalmazási lehetősége a folyami közforgalmú közlekedésben, Közlekedéstudományi Szemle, Vol.67 (4), 2017, p.28-45. ISSN 0023-4362 (In Hungarian)

[5] **Simongáti, Gy. – Hargitai, Cs. L.:** Hajógépek, Typotex, 2012, ISBN 978-963-279-619-2, (In Hungarian)

## SESSION FOR VEHICLE CONTROL THEORY AND INTERDISCIPLINARY SCIENCES

**FÉNYES, D. – NÉMETH, B. – GÁSPÁR, P. – ASSZONYI, M.** (Hungary)
Possibilities of Vehicle State Estimation Using Big Data Approaches ...................... 395

**SZŐTS, D. – NÉMETH, B.** (Hungary)
Challenges and Problems in the Design of Smart Intersections ................................ 403

**DALVÁRI, M. – FÉNYES, D. – MIHÁLY, A. – NÉMETH, B. – GÁSPÁR, P.** (Hungary)
Camera-Based Lateral Driver Modelling for Vehicle Control Design Purposes ....... 409

**SZALAY, J. – KŐVÁRY, B. – ARADI, SZ. – GÁSPÁR, P. –BÉCSI, T.** (Hungary)
Highway Behaviour Training through Learning Based State Choice Model............. 417

**DO, M. H. – KOENIG, D. – THEILLIOL, D.** (France+Vietnam)
Robust $H_\infty$ Proportional-Integral Observer Design for Actuator Fault Estimation ......... 425

**VU, V. T. – SENAME, O. – DUGARD, L. – PHAM, T. P. – DINH,V. P.** (France+Vietnam)
$H_\infty$/LPD Active Braking Control System to Prevent Rollover of Heavy Vehicles ........ 437

**RATHAI, K.M.M. – SENAME, O. – ALAMIR, M.** (France)
A Comparative Study of Different NMPC Schemes for Control of Semi-Active Suspension System ........................................................................ 447

**VARGA, B.** (Hungary)
Energy Aware Cruise Control for Urban Public Transport Buses ............................ 455

**HEGEDŰS, T. – NÉMETH, B. – BEDE, ZS.** (Hungary)
Control and Decision Method for Overtaking Problem in Autonomous Vehicles ......... 463

**PAPP, J. – BÁRI, G.** (Hungary)
Hardware in the Loop Test System for Teaching Model Based Design for Automotive Control ........................................................................................ 471

**PHAM, T.P. – SENAME, O. – DUGARD, L. – VU, V.T.** (France +Vietnam)
Real-Time Estimation of the Damping Force of Vehicle Electrorheological Suspension ........ 477

**DOMINA, Á. – TIHANYI, V.** (Hungary)
Comparison of Controller Systems and Motion Modelling Methods for Autonomous Vehicle Trajectory Following Practice.................................................. 487

**KOLONITS, F.** (Hungary)
Possible Cause of an Internal Level Crash, '95 Kobe Eq. ......................................... 497

**KISS, CS.** (Hungary)
Some Remarks on Designing Crankshafts................................................................ 507

**HIDAS, A.** (Hungary)
Thermal Simulation to Ensure Heat Management of Vehicle Ecus with Plastic Enclosure.......................................................................................................... 517

**POKORÁDI, L. – LÁZÁR-FÜLEP, T.** (Hungary)
Dependability of Vehicle Systems with Complex Interconnections ......................... 519

**POKORÁDI, L. – SOMOSI, V.** (Hungary)
Graph-Theoretical Investigation into Vehicle and Transportation Systems .............. 529

**FERENCZ, P.** (Hungary)
The Question of Lifetime: Extension Possibilities of Bogie Force Transmission Elements on the Basis of Condition Test Results ................................................ 539

**TULIPANT, G. – SZABÓ, A. – ZOBORY, I.** (Hungary)
Laboratory Investigation into the Noise Generated by Sliding Friction for Cast Iron and Steel Friction Pair ........................................................................... 549

# POSSIBILITIES OF VEHICLE STATE ESTIMATION USING BIG DATA APPROACHES

**Dániel FÉNYES[2], Balázs NÉMETH[1], Péter GÁSPÁR[1] and Máté ASSZONYI[2]**

[1]Systems and Control Laboratory,
Computer and Automation Research Institute,
Kende u. 13-17, Budapest, Hungary
{balazs.nemeth;gaspar.peter;}@sztaki.mta.hu

[2]Department of Control for Transportation and Vehicle Systems,
Faculty of Transportation Engineering and Vehicle Engineering
Budapest University of Technology and Economics,
Stoczek u. 2, H-1111 Budapest, Hungary

*Received: November 05, 2018.*

## ABSTRACT

Nowadays, the development of the autonomous vehicles is one of the most important challenges for the automotive industry. In general, these vehicles are equipped with numerous sensors, such as onboard-camera, lidar, radar, ultrasonic sensor, accelerometer and gyroscope. These sensors provide information about the environment and other vehicles. This information is not only processed and used directly on the car but also can be stored on internal or cloud-based memory. This collected data might contain hidden information about the motion and the dynamical behaviour of the car. This hidden information can be brought out of the datasets by using big data-based data mining approaches. The aim of the paper is to create a vehicle state estimation model based on the collected sensor data and using data mining tools. In the paper, the sensor data is collected from a high-fidelity simulation software, CarSim. The estimation model is created by the machine-learning software Weka. Finally, the created model is validated through several CarSim simulations.

*Keywords:* variable-geometry suspension, independent steering, control-oriented modeling

## 1. INTRODUCTION AND MOTIVATION

The research in the field of autonomous vehicles and intelligent transportation systems has had a fast-growing tendency in the last years. Several research institutes have focused on the new challenges posed by autonomous vehicles, while in some cases the conventional vehicle dynamical problems are extended with new perspectives. For side-slip angle estimation several methods have been developed. The conventional instruments of vehicle dynamics to measure the side-slip angle are optical sensors. Although they provide high accuracy, these sensors have relatively high costs [1]. Therefore, in several research projects filtering methods and observers are designed to estimate the side-slip angle, such as the *Kalman* filter, the *Luenberger* method and sliding mode observers, see [2], [3]. On-board sensors provide the opportunity to measure and store a lot of data regarding the vehicle states. This data may contain hidden information that can be revealed using data mining techniques. Big data was used in the prediction of vehicle slip through the combination of individual measurements of the vehicle and database information [4]. In [5] a layered neural network was developed to compute the side-slip angle. In this paper a novel application of the linear regression method on the side-slip angle estimation problem is proposed. The approach is based on big data analysis, which requires numerous signals from the automated vehicles. As a first step, the applied estimation algorithm, i.e., the ordinary linear regression method with OLS (Ordinary Least Square) subset selection, creates several different linear models using various sets of sensor signals. In the second step this algorithm compares the created models to the true model and selects the best one by determining their predictive accuracy. The advantage of the method is that it requires little on-line computation, while the complex operations are solved offline. Moreover, in the estimation method only the onboard signals of the vehicle are used, which are available without a loss in communication. The presented method is analyzed through several simulations. The structure of the paper is the following. Section II proposes the method of data collection and the mining of the linear regression information. The results are demonstrated in Section III through the variation of different parameters, such as velocity, mass and sensor noises. Finally, the contributions of the paper and the further challenges are summarized in Section IV.

## 2. BIG DATA-BASED ESTIMATION METHOD

In this paper the ordinary linear regression method with OLS subset selection is used to produce prediction models. The bases of both methods are briefly described in this section. [6]

### 2.1 Linear regression

Let's consider a dataset with n independent instances, k input variables and an output variable. The instances are written in the form of an $n\ x\ k$ design matrix $X$. Furthermore, $\zeta^*$ denotes the parameter vector of the true model, and then the output vector $y$ can be determined as

$$y = \zeta^* X + \varepsilon\ , \tag{1}$$

where $\varepsilon$ denotes the noise.

Let $\mathrm{M}(\zeta)$ denote a fitted linear model, whose unique parameter vector is $\zeta$, while $\mathrm{M}(\zeta^*)$ is the true model. The ultimate goal is to find a model $\mathrm{M}(\zeta)$, which provides the best approximation of $\mathrm{M}(\zeta^*)$. The created models are evaluated by the distances between the approximated and the true models. This distance can be calculated as

$$D\big(\mathrm{M}(\zeta^*), \mathrm{M}(\zeta)\big) = \frac{||y_{\mathrm{M}(\zeta^*)} - y_{\mathrm{M}(\zeta)}||^2}{\sigma^2}\ , \tag{2}$$

where $||\cdot||$ denotes the $L_2$ norm and $\sigma^2$ is the estimated variance of the sensor noise.

Finally, the main task is to find the model $\mathrm{M}(\zeta)$, which minimizes the distance.

$$D\big(\mathrm{M}(\zeta^*), \mathrm{M}(\zeta)\big) = min!\ . \tag{3}$$

### 2.2 OLS subset selection

The basic concept of the OLS subset selection method is to create subset models using various sets of variables. If a dataset has k variables, $k+1$ nested models ($M_j$ ) can be created, where $j = 0$ is the null model with zero variables and $j = k$ is the full model using all of the variables. In this case, an estimate of the parameter vector of $M_j$

can be determined as

$$\hat{\zeta}_{M_j} = (X'_{M_j}X_{M_j})^{-1}X'_{M_j}\mathrm{y}\ , \tag{4}$$

where $X_{M_j}$is the $n\ x\ j$ design matrix and let $P_{M_j} = X_{M_j}(X'_{M_j}X_{M_j})^{-1}X'_{M_j}$ be an orthogonal projection matrix from the original space ($k$) onto the reduced space ($j$). Then, $\hat{y}_{M_j} = P_{M_j}y$ is the estimate of $y^*_{M_j} = P_{M_j}y^*$. Since this method creates only $k+1$ subset models (instead of $2^k$, which is computationally unfeasible at increased $k$), the predefined order of the variables is a crucial point of this method. There are a set of ranking algorithms, which help determine the best predefined order of the variables, see [7], [8].

## 3. DEMONSTRATION OF THE ESTIMATION METHODS

The first step of building an estimation model is the acquisition of the appropriate training data. In this paper, the training data are collected from simulations using the high-fidelity simulation software CarSim. In the simulations, a D-class sedan passenger car has been used, whose sprung mass was 1320kg. The car has been driven along the Michigan Waterford Hill course several times at various longitudinal velocities. The measured attributes are summarized in the table below.

| **Parameter** | **Notation** |
|---|---|
| Longitudinal acceleration | $a_x$ |
| Lateral acceleration | $a_y$ |
| Yaw-rate | $\dot{\Psi}$ |
| Angular speed of wheels | $W_{i,j}(i \in \{front, rear\}, j\ \in \{left, right\})$ |
| Steering angle of front wheels | $\delta_i(i \in \{front, rear\})$ |
| Angle of steering wheel | $\delta_s$ |
| Side-slip angle | $\beta$ |

Table 1 Measured attributes of the vehicle

The sample time has been 0.01s and in this way, more than 2 million instances have been collected. Using various sets of the variables from the collected training data, 5 different estimation models have been built, as listed in Table 1. The performances of the models are evaluated by the k-fold cross-validation technique (see [9]), whose results can also be seen in Table 2.

| Model No. | Used variables | Corr. coeff. |
|---|---|---|
| 1 | $a_x$,$a_y$, $\dot{\Psi}$ | 0.9013 |
| 2 | $a_x$,$a_y$, $\dot{\Psi}$, $\delta_s$ | 0.9534 |
| 3 | $a_x$,$a_y$, $\dot{\Psi}$, $\delta_s$, $W_{f,l}$, $W_{f,r}$ | 0.9796 |
| 4 | $a_x$,$a_y$, $\dot{\Psi}$, $\delta_s$, $W_{f,l}$, $W_{f,r}$, $W_{r,l}$, $W_{r,r}$ | 0.9911 |
| 5 | $a_x$,$a_y$, $\dot{\Psi}$, $\delta_l$, $\delta_r$, $W_{f,l}$, $W_{f,r}$, $W_{r,l}$, $W_{r,r}$ | 0.9911 |

Table 2 Properties of the created models

Table 2 shows that the last two models have the best predictive accuracy. Not surprisingly, these models have exactly the same accuracy, since the two steering angles
($\delta_l, \delta_r$) and the angle of the steering wheel ($\delta_s$) are closely related to each other. Figure 1 illustrates a test scenario in which the car is driven along the test track at various velocities. Moreover, all of the models are used to predict the side-slip angle, see Figure 1.

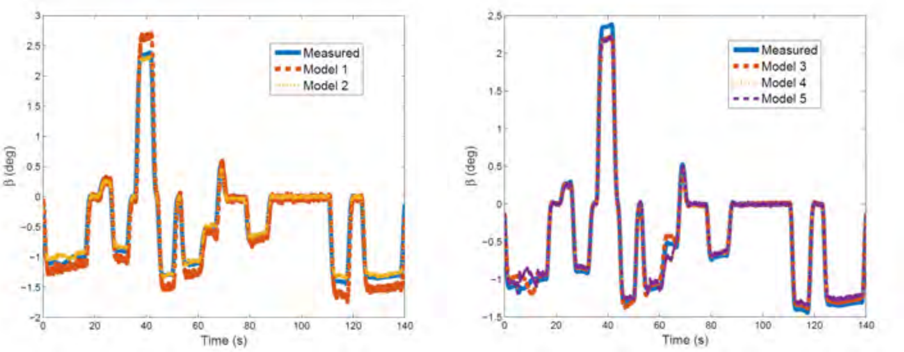


Fig. 1 Comparison of the models

It is shown that all models predict the side-slip angle accurately. Apart from a short section (65 -70s), the best prediction is given by the last two models (Model 4 and Model 5), therefore the simpler one of these models is used in the rest of the paper. In the following, the accuracy and the capability of the selected predictive model is examined in different situations.

### 3.1 Increased noise

In the first situation the impact of the increasing noise on the predictive accuracy is examined. In practice, the inertial sensors and the gyroscope are significantly affected by sensor noises, while the angular velocity of the wheels and the angle of the steering wheel can be relatively well measured. The first two sensors are disturbed by white noises, whose parameters are summarized in Table 3.

| Sensor & noise parameters | Initial values | Modified values |
|---|---|---|
| Inertial sensor: | | |
| - bias | $0.15\frac{m}{s^2}$ | $0.3\frac{m}{s^2}$ |
| - variance | $0.1^2$ | $0.2^2$ |
| Gyroscope: | | |
| - bias | $0.01\frac{rad}{s}$ | $0.02\frac{rad}{s}$ |
| - variance | $0.01^2$ | $0.02^2$ |

Table 3 Parameters of the sensors

Fig. 3 shows the result of the simulation. It can be seen that the variation of the noise has only a slight effect on the prediction. The estimated model predicts the side-slip angle accurately despite the increased noises.

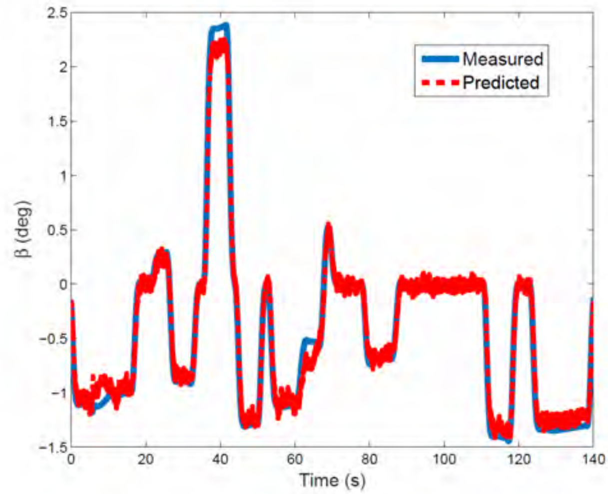


Fig. 2 Effect of increased noise

### 3.2 Variation of mass

Secondly, the effect of the variation of the car mass on the accuracy of the prediction is investigated. The initial mass of the passenger car is $m = 1320kg$. Firstly, the mass of the car is reduced to $m = 1000kg$ and then it is increased to $m = 1740kg$. The results of the changes can be seen in Figure 3. Apart from a short section, the applied model has high predictive accuracy, which means that the variation of the mass has no significant influence on the prediction. Therefore, the calculated model can resist the change in the mass.

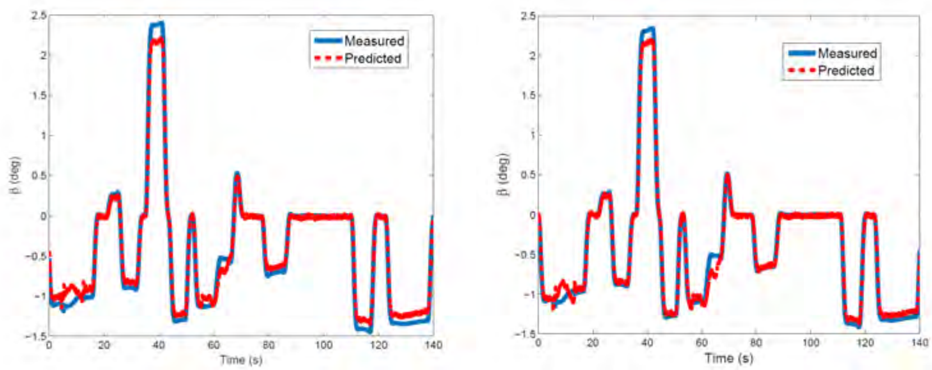


Fig. 3 Car mass: $m = 1000kg$ (left), $m = 1740kg$ (right)

### 3.3 Change of adhesion coefficient

In the third case the variation of the adhesion coefficient $\mu$ is simulated. The initial value of the adhesion coefficient is $\mu = 1$. In the simulations its value is decreased to $\mu = 0.7$ and then to $\mu = 0.4$. The results of the simulations are shown in Figure 4. In the case of $\mu = 0.7$, it can be seen that the model predicts the side-slip angle as accurately as in the normal case, see Figure 1. In the case of $\mu = 0.4$ the model also operates appropriately apart from a section between $40 - 60s$. In this section the vehicle loses its stability, since its longitudinal velocity is too high and the adhesion coefficient is too low to follow the defined path. Nevertheless, the applied model operates accurately in all other sections.

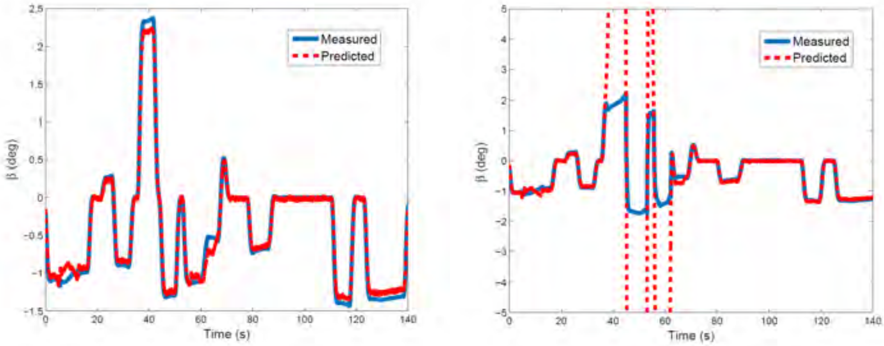


Fig. 4 Adhesion coefficient: $\mu = 0.7$ (left), $\mu = 0.4$ (right)

### 3.3 Melbourne Grand Prix Circuit

Finally, the predictive model is tested on another track. Since all of the regression models can be easily overfitted, it is important to guarantee that the calculated model operates in other cases. Therefore, in this case the passenger car is driven along the Melbourne Grand Prix Circuit at various velocities. Figure 6 shows the variation of the velocity during the simulation. The side-slip angle and its prediction are shown in Figure 7. The simulation shows that the applied model is able to predict the side-slip angle accurately. Its predictive accuracy is close to the normal case. It means that the proposed predictive model is generally able to predict the side-slip angle.

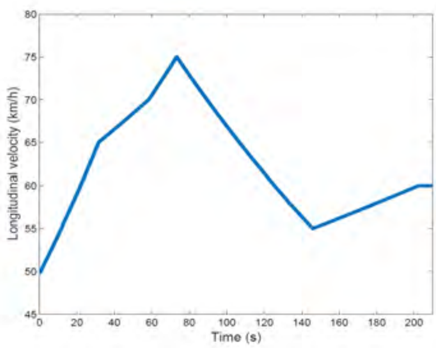


Fig. 5 Speed on Melbourne track

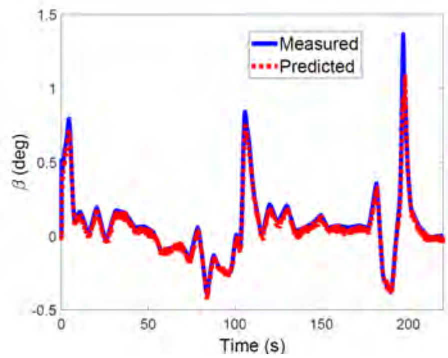


Fig. 6 Side-slip angle on Melbourne track

## 5. CONCLUSION

The paper has proposed a data-based side-slip angle estimation method for autonomous vehicles with numerous signal measurements. In the processing of the big data from the vehicle signals the linear regression algorithm has been used. The contribution of the paper is an easily implementable algorithm with a small amount of on-line computation. The proposed method can guarantee acceptably small errors in the estimation of the side-slip angle. The efficiency of the method has been analyzed through various scenarios using the high-fidelity CarSim simulator. In the future the proposed method will be verified through experimental scenarios using a real test vehicle.

## 6. ACKNOWLEDGEMENT

The research was supported by the Hungarian Government and co-financed by the European Social Fund through the project "Talent management in autonomous vehicle control technologies" (EFOP-3.6.3-VEKOP-16-2017-00001).
The research reported in this paper was also supported by the Higher Education Excellence Program of the Ministry of Human Capacities in the frame of Artificial Intelligence research area of Budapest University of Technology and Economics (BME FIKPMI/FM).
The work of Balázs Nemeth was partially supported by the János Bolyai Research Scholarship of the Hungarian Academy of Sciences and the and the ÚNKP-18-4 New National Excellence Program of the Ministry of Human Capacities.
The work of Dániel Fényes was partially supported by the ÚNKP-18-3 New National Excellence Program of the Ministry of Human Capacities.

## 7. REFERENCES

[1] **Doumiati, M. - Victorino, A. C. - Charara, A. – Lechner, D.:** Onboard real-time estimation of vehicle lateral tire road forces and sideslip angle, IEEE/ASME Transactions on Mechatronics, vol. 16, no. 4, Aug. 2011, p.601–614.
[2] **Stephant, J. - Charara, A. - Meizel, D.:** Experimental validation of vehicle sideslip angle observers, in IEEE Intelligent Vehicles Symposium, 2004, June 2004, p.150–155.
[3] **Venhovens, P. J. - Naab, K.:** Vehicle dynamics estimation using kalman filters, Vehicle System Dynamics, vol. 32, no. 2-3, 1999, p.171–184.
[4] **Jeon, J. - Lee, W. - Cho, H. J. - Lee, H.:** A big data system design to predict the vehicle slip, in 2015, 15th International Conference on Control, Automation and Systems (ICCAS), Oct. 2015, p.592–596.
[5] **Sasaki, H. - Nishimaki, T.:** A side-slip angle estmation using neural network for a wheeled vehicle, 2000.
[6] **Wang, Y. – Witten, I. H.:** Pace Regression. (Working paper 99/12). Hamilton, New Zealand: University of Waikato, Department of Computer Science., 1999.
[7] **Shibata, R.:** An optimal selection of regression variables, Biometrika, vol. 68, 1981, p.45–54.
[8] **Thompson, M.L.:** Selection of variables in multiple regression, International Statistical Society B, vol. 46, 1978, p.1–21 and 129–146.
[9] **Klauer, K.:** Model testing and selection, theory of, International Encyclopedia of the Social and Behavioral Sciences, 2001, p.9927–9931.

# CHALLENGES AND PROBLEMS IN THE DESIGN OF SMART INTERSECTIONS

**Dávid SZŐCS* and Balázs NÉMETH****

*Department of Control for Transportation and Vehicle Systems,
Faculty of Transportation Engineering and Vehicle Engineering,
Budapest University of Technology and Economics, Budapest, Hungary
H-1111 Budapest, Műegyetem rkp. 3. Hungaryr

**Systems and Control Laboratory, Institute for Computer Science and Control, Hungarian Academy of Sciences, Budapest, Hungary;

*Received: November 9, 2018*

## ABSTRACT

The main goal of the project is to assure a collusion-free passage through the intersection in the shortest possible traveling time. Firstly, the order of the incoming vehicle is proposed. Using the mentioned order, a nonlinear optimization method is proposed, with the minimum traveling time of the participants, without their collusion is guaranteed. Based on the optimized result a database is created. The second part of the optimization uses this database to solve an another type of problem, when the vehicles steps in the intersection at different moment. Also mentionable the correct choosing of initial values in this part, because it has influence to the degree of optimization. After that, most of the situations can be solved, even if the vehicles have different step-in-time parameters.

*Keywords:* autonomous vehicles, intersections, initial problem, constrained nonlinear optimization, neural networks, local-global optimization

## 1. NTRODUCTION

The interactions of autonomous vehicles in smart cities are an important research field in the autonomous vehicles. In urban areas there are large number of intersections, therefore there is a huge potential in the appropriate control of vehicles approaching the intersections. The guided control of the autonomous vehicles means a more flexible solution for vehicle interactions in intersections, which is able improve the effectiveness, simultaneously, and the safety of the traffic system.

There are several advantages using optimal control of the motions of autonomous vehicles in intersections. In a real-life traffic scenario the autonomous participants driving together with pedestrians and human-drive vehicles, thus it is inevitable to set the traffic rules clearly, which is determine the motions of the various type of travellers. Consequently, these traffic rules reduce the possibilities of autonomous vehicles and, moreover, the behaviour of the humans must be incorporated in the control of the intersection. The detection and prediction of the human behaviour are an extremely difficult and complex problem, see Li et al. (2016) [1]; *Aoude* et al. (2012) [2].

Several research have produces various results in this theme. A framework for the intersection control, which is based on queuing theory was represented by *Tachet* et al. (2016)[3]. Another paper which try to solve the problem form a different angle, a Model Predictive Control based intersection control using centralized approach for two vehicles was presented by *Riegger* et al. (2016) [4]. The quadratic programming is possibility of real time implementation compared to the convex optimization using space coordinated, see *Murgovski* et al. (2015) [5].

In this paper the challenges and problems of the motion optimization of autonomous vehicles will be shown through a base scenario which is illustrated in figure 1. The arrows show the desired way of each vehicles.

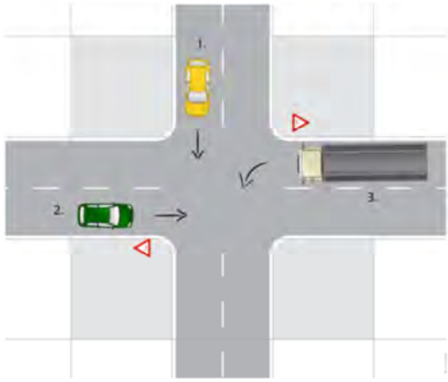


Fig. 1 The base situation - Intersection with traffic signs

It is a real-life traffic scenario, a conventional intersection with traffic signs which will be unnecessary because each vehicle will be guided from a third-party database (Fig.:2).

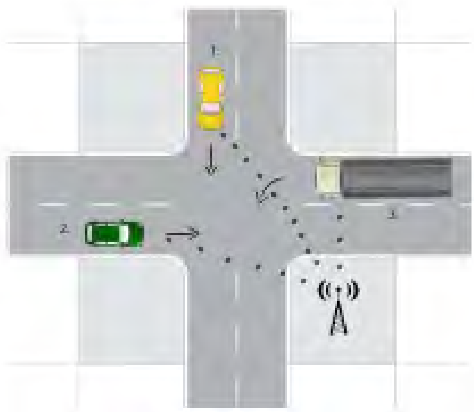


Fig. 2 Database control - Independence from traffic rules

At the third section of this paper a short description about the optimization method will be told. The efficiency of the method is presented through various simulation examples. However, the main goal of this article is to reflect the main difficulties of the mentioned optimization method. The problems will be show, through the simulation results and chosen initial values.
The performances in intersections can also lead difficulties in the control design. For example, the minimum traveling time of the vehicles can cause the deceleration of the slow heavy vehicles to provide priority for the fast passenger cars. However, the deceleration and acceleration manoeuvres of the heavy vehicles require significant amount of energy and fuel and result in decreases emission in intersections. Moreover, if the energy consumption of the vehicles is minimized, it can lead to an increase in traveling time. Since there is a contradiction between the minimization of the energy

consumption and that of traveling time, in the control of the autonomous vehicles a balance between the performances must be guaranteed.
The paper is organized as follows. In Section 2 the optimization problem together with the performance and the order of vehicles is formulated. Section 3 presents the exact method using for optimization. In Section 4 the importance of initial values will be showed through the efficiency of this method. Using the results, the being of local-global optimization cases will be presented. Finally, Section 5 summarizes the contributions of the paper and the future challenges.

## 2. OPTIMIZATION OF THE MOTION OF AUTONOMOUS VEHICLES IN INTERSECTION

In the optimization procedure applied to the intersection it is necessary to find the motion profile for all autonomous vehicles which guarantees safe approaching for them. The optimization procedure contains two tasks to be solved.

First, it is necessary to find the appropriate order of the vehicles. In this paper the goal of the intersection control is to find the minimum traveling time for each vehicle. Thus, it is required to find the order of vehicles with which the minimum traveling time for all vehicles is guaranteed. Vehicle consumptions and any other parameter with influence to the optimization is negligible in this case.

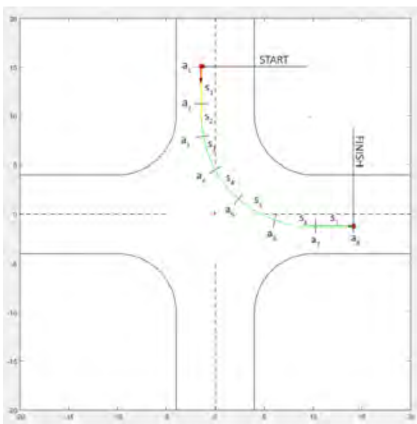


Fig. 3 Vehicle route segment

Second, the kinematics of the vehicles for the given vehicle order must be determined, e.g., the acceleration/deceleration or the velocity profile for each autonomous vehicle.

In this paper, the determination of the vehicle order is based on a rule which is defined through the experience of a large number of simulation examples. The vehicles crossing the intersection have right away based on their initial velocity and the length of their route. For example a vehicle with small initial velocity and/or long route inside of the intersection does not have right away against the fast and/or short route vehicles. In the earlier version of the optimization algorithm, problem can be solved only when the vehicle's step-in-time is the same when they reach the intersection, for now it can handle more complex situations with different reach times.

The performance of the control task is defined as the minimum traveling time for each vehicle. It is represented by the sum of traveling times of all vehicles. The avoidance of collision is guaranteed by the safe distance which must be held by the vehicles.

In order to have a continuously velocity profile (Figure 4), each vehicle route divided to seven part. (Figure 3) At each part there is an acceleration value which will be followed by the given vehicle. This value can be changed by the algorithm to find the optimal time minimum during the simulation.

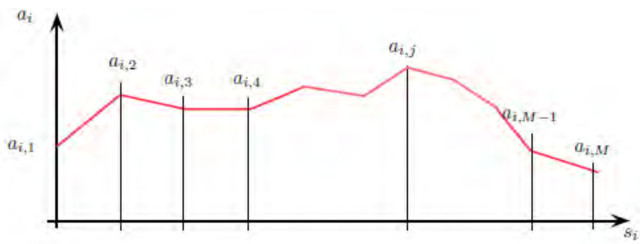


Fig. 4 Changing acceleration (ai) at each section (si)

## 4. CHALLENGES AND PROBLEMS

In this section, some of the main challenges will be described. The whole problem complexity depends on the number of participants. Each vehicle has 8 variable with which the cost function changeable. For instance, a situation with 3 vehicles means 24 variables. As mentioned before, the main goal is to reduce the travelling time to the minimum. In general, the simulation runs until it find a feasible solvation, however this result can represent a local minimum. (Figure 5)

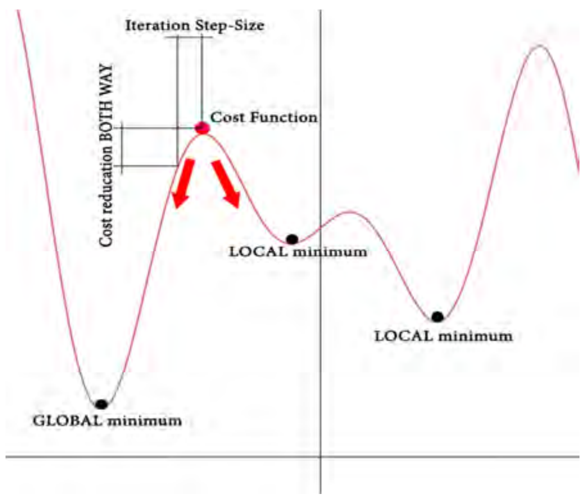


Fig. 5 Local and Global minimum problem

In Figure 5 a simplified problem has shown. In comparison with the solution to similar problems, the way of solution here is harder, because here the actual global minimum is hidden. By changing the accelerations the value of the cost function can be considered, however most of the cases, the iteration step-size is way shorter than the actual position of the global minimum, thus the solver cannot decide perfectly. It can consider only the degree of changing of the cost function and it can lead to local minimum.

The goal of the first layer is to find the vehicle order which can lead to the global optimum solution. Furthermore, the results of the vehicle order are the appropriate initial conditions in the motion optimization, which guarantees to find the global minimum traveling time in the second layer. After many simulations an initial set up made for each situation which can happen. This set up means an acceleration vector for the solver and gives it a good starting point to find mentioned global minimum. The vector based on many optimized database. The algorithm solves a situation many times but each time with a different initial velocity given to the participants. The given initial velocity changing is between 3 m/s and 8 m/s. With three vehicles this means 216 cases in one situation with a given initial step-in-time parameter. The main goal is to run a simulation and after several hours later (obviously simulation time depends on the hardware too), a database given which fulfilled with optimized scenarios of a given situation. To reach this goal, more complex inital acceleration setup has been made. As it is shown in Figure 6, two individual initial acceleration databases have been made. One of them has the attributes to solve the problem for slower cases, and the other one for the higher speed cases. At middle speed there is a „gap", where to scenario can be happened. Each dataset can solve the problem or neither one. The last one occurs less often because the fine-tuned initial acceleration setup. From the mentioned two setups an overlay has been made, which contains the attributes of both initial setup.

<table>
<tr><th colspan="3">Initial Velocity m/s</th><th rowspan="2">Initial acceleration setup for lower speeds</th><th rowspan="2">Initial acceleration setup for higher speeds</th><th rowspan="2">combo setup lower/higher speed</th></tr>
<tr><th>No.1 vehicle</th><th>No.2 vehicle</th><th>No.3 vehicle</th></tr>
<tr><td>3</td><td>3</td><td>3</td><td rowspan="8">Each case can be solved in the situation with a good optimization rate</td><td rowspan="7">Cases with bad optimization rates or can not be solved with this setup</td><td rowspan="15">Each case can be solved in the situation with a good optimization rate</td></tr>
<tr><td>3</td><td>3</td><td>4</td></tr>
<tr><td>3</td><td>3</td><td>5</td></tr>
<tr><td></td><td>.</td><td></td></tr>
<tr><td></td><td>.</td><td></td></tr>
<tr><td></td><td>.</td><td></td></tr>
<tr><td>6</td><td>3</td><td>3</td></tr>
<tr><td>6</td><td>3</td><td>4</td><td rowspan="8">Each case can be solved in the situation with a good optimization rate</td></tr>
<tr><td>6</td><td>3</td><td>5</td><td rowspan="7">Cases with bad optimization rates or can not be solved with this setup</td></tr>
<tr><td></td><td>.</td><td></td></tr>
<tr><td></td><td>.</td><td></td></tr>
<tr><td></td><td>.</td><td></td></tr>
<tr><td>8</td><td>8</td><td>6</td></tr>
<tr><td>8</td><td>8</td><td>7</td></tr>
<tr><td>8</td><td>8</td><td>8</td></tr>
</table>

Fig. 6  The optimal database setup

## 5. CONCLUSIONS

In the paper the optimal motions of autonomous vehicles for intersections and its problem have been presented. The proposed method guarantees the minimum traveling time without collisions of the vehicles. The motion design of the vehicles leads to a nonlinear constrained optimization problem. A global-local minimum problem has been found and an approaching solvation found with which most of the situation can be solved.

## 6. ACKNOWLEDGEMENT

The research was supported by the Hungarian Government and co-financed by the European Social Fund through the project "Talent management in autonomous vehicle control technologies" (EFOP-3.6.3-VEKOP-16-2017-00001).

The research reported in this paper was also supported by the Higher Education Excellence Program of the Ministry of Human Capacities in the frame of Artificial Intelligence research area of Budapest University of Technology and Economics (BME FIKPMI/FM).

The work of *Balázs Németh* was partially supported by the János Bolyai Research Scholarship of the Hungarian Academy of Sciences and the ÚNKP-18-4 New National Excellence Program of the Ministry of Human Capacities.

## 7. REFERENCES

[1] **Li, J. - He, Q. - Zhou, H. - Guan, Y. - Dai, W.:** Modeling driver behavior near intersections in hidden markov model. International Journal of Environmental. Research and Public Health, 13(12), 2016.

[2] **Aoude, G. - Desaraju, V. - Stephens, L. - How, J.:** Driver behavior classification at intersections and validation on large naturalistic data set. IEEE Transactions on Intelligent Transportation Systems, 13(2), 2012, p.724-736.

[3] **Tachet, R. - Santi, P. - Sobolevsky, S. - Ignacio Reyes-Castro, L. - Frazzoli, E. - Helbing, D. - Ratti, C.:** Revisiting street intersections using slot-based systems. 11, e0149607, 2016.

[4] **Riegger, L. - Carlander, M. - Lidander, N. - Murgovski, N. - Sjoberg, J.:** Centralized mpc for autonomous intersection crossing. In 2016 IEEE 19th International Conference on Intelligent Transportation Systems (ITSC), 2016, p.1372-1377.

[5] **Murgovski, N. - de Campos, G.R. - Sjoberg, J.:** Convex modeling of conflict resolution at traffic intersections. In 2015. 54th IEEE Conference on Decision and Control (CDC), 2015, p.4708-4713.

# CAMERA-BASED LATERAL DRIVER MODELLING FOR VEHICLE CONTROL DESIGN PURPOSES

**Máté DALVÁRI*, Dániel FÉNYES*,**
**András MIHÁLY**, Balázs NÉMETH** and Péter GÁSPÁR****

**Department of Control for Transportation and Vehicle Systems
Faculty of Transportation Engineering and Vehicle Engineering
Budapest University of Technology and Economics
H-1111 Budapest, Műegyetem rkp. 3., Hungary

**Institute for Computer Science and Control
Hungarian Academy of Sciences
H-1111 Budapest, Hungary

*Received: November 5, 2018*

## ABSTRACT

The paper proposes the modeling of a driver behavior in lateral vehicle control design purposes. Nowadays significant emphasis is placed on the development of autonomous vehicle systems which motivates to research in this area. Using a properly designed driver model during cornering ensures the comfort of the passengers and provides predictable motions for the drivers of conventional vehicles and pedestrians. In this paper the vehicle control is based on picture frames provided by an onboard mono-camera, which is used by an image processing algorithm to calculate the present and the predicted lateral errors. The identified driver model defines the instantaneous steering angle using the calculated errors and several dynamic parameters of the vehicle. One of the dynamic variables, the longitudinal speed was used as a scheduling variable to determine the actual operating region of the system. The formulated driver model is verified through a real-time running simulator software, where the measured values of the steering angles can be compared with calculated ones. The simulation showed the accuracy and reliability of the formulated driver model.

*Keywords:* camera-based system, driver identification, lateral autonomous vehicle control

## 1. INTRODUCTION

One of the main motivations of my research is the fact of emphasis of developing autonomous vehicle systems are increasing due to the many expected advantages using autonomous driving system instead of real human drivers. For instance, quicker reaction time in emergency, longer distance can be driven simultaneously by an autonomous vehicle other free activities are available for the driver during travel, etc.
Copying the driving style of real human drivers during cornering is required from an autonomous driver model. It can provide comfort for the passengers and gives predictable movements for the drivers of conventional vehicles and pedestrians. Researchers have been concerned about how to describe models of human driving in the past years. Depending on the applications different driver models are available today.
In one of the previous researches by Gaspar et al. (2018) the modeling of the human behavior connected with the lateral control of the vehicle. The controlled steering angle based on two steering components calculated from four different type of input signals. This method takes into consideration that the most important human sensor is the visual channel while driving, therefore it emphasizes the visible predicted lateral errors, furthermore it also considers the actual lateral error and yaw-error. The visual channel is ensured by a mono-camera. My research was influenced by this paper. Other research by David et al. (2012) the driver model based on the effect of the steering

torque feedback and the neuromuscular dynamics comprising arm inertia, muscles and stretch reflex dynamics. The model represents a path-following task at constant speed. The influence of the steering torque feedback, scale of the muscle conditions and reflex for the path-following bandwidth were examined. A cost function was also used for tuning between path-following accuracy and control activity. A different solution toward autonomous lateral vehicle guidance was proposed by Stefan et al. (1986) using a neuro-controller. Instead of a complex driver model parameterization, a neural network was trained by few thousands of human-driving measurements without knowing the physical car parameters. The neural network gets the information from an image processing system mounted on the car. The advantage of this method that the identification of the driver was not created with complicated dynamic equations, but the disadvantages that a big amount of data is needed for a precise neural network and the physics behind the driver model is not recognizable. Different driver models were created based on physical equations by Manfred et al. (2007) as well.
In this research a camera-based lateral driver model was proposed for lateral vehicle control. The next sections of the paper describe the mono-camera based lane detection system, the required lateral errors, the identification of the driver model and the results of the simulations.

## 2. SENSING THE ENVIRONMENT

The most significant sensing channel of human during driving is the visual channel leaving behind others like vestibular system and somatosensory system remarking that they have also not negligible roles on the sensing system. Regarding the importance of the visual channel the source of input signals of the planned driver model is ensured by a mono-camera mounted on the vehicle and processed by an image processing system.

### 2.1 Image processing system

Gathering the actual lane is necessary to determine the required input data for the driver model. Designing a new lane recognition algorithm is not part of the task, therefore an existed one is utilizable, in this case the Visual Perception Using Monocular Camera image processing system from Matlab was chosen. Firstly, the image processing system performs an image transformation from the original view to a bird-view where the lanes appear as straight lines. Secondly the image system finds number of points on the picture at the significant intensity differences, then the algorithm fits curve to these points. Where the intensity difference is significant, like between lane markers and road surfaces, then more candidate points are located. The lane detection was tested on a road real-time, see Figure 1, where the recognized red and green curves candidate the edge of the lanes.

### 2.2 Desired signals from the camera image processing system

The driver model needs four different input signals to calculate the actual steering angle. The four processed input signals are the next:

- The current lateral error between the actual front position of the vehicle and the reference trajectory (middle of the lane), see Figure 2. a.

- The current yaw-angle error between the angle of the vehicle and the heading angle of the reference trajectory, see Figure 2. a.
- The lateral error between the reference trajectory and the predicted position of the vehicle at $T_1$ and $T_2$ prediction time, see Figure 2. b.


Fig. 1 Testing lane detection system in real time

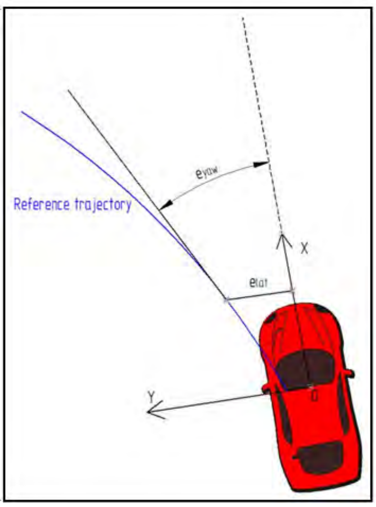


Fig. 1. a Actual lateral and. yaw-angle error

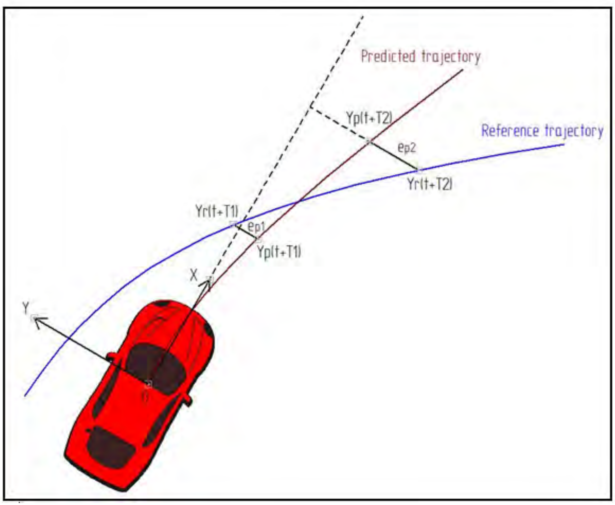


Fig. 2.b Predicted lateral error

To get the predicted lateral error the image processing system has to determine the reference trajectory and the predicted position of the vehicle continuously. The reference trajectory is the middle of the lane and it's calculated from the detected lines of the actual lane. For calculating of the predicted position of the vehicle the equations are below by Robin et al. 2008, see (1) and (2):

$$\vec{x}(t) = \begin{pmatrix} x & y & \theta & v & w \end{pmatrix}^T \quad , \tag{1}$$

where t is the current time, x and y are the coordinates, θ is the yaw-rate, v is the longitudinal speed, ω is the angular speed.

$$\vec{x}(t+T)=\begin{pmatrix} \frac{v}{\omega}\sin(\omega T+\theta)-\frac{v}{\omega}\sin(\theta)+x(t) \\ -\frac{v}{\omega}\cos(\omega T+\theta)+\frac{v}{\omega}\sin(\theta)+y(t) \\ \omega T+\theta \\ v \\ \omega \end{pmatrix}, \tag{2}$$

where T is the prediction time.

## 3. DESIGNING AND IDENTIFICATION OF THE DRIVER MODEL

### 3.1 Structure of the driver model

The closed loop controller is shown in Figure 3. The Image processing unit represents the vehicle including the camera and the steering actuator manages the frames from the camera and other measured physical quantities in order to get the 4 lateral error signals. The identified Driver model block represents the driver's steering behavior and calculates the actual necessary steering angle based on the error signals. The longitudinal speed was used as a scheduling variable.

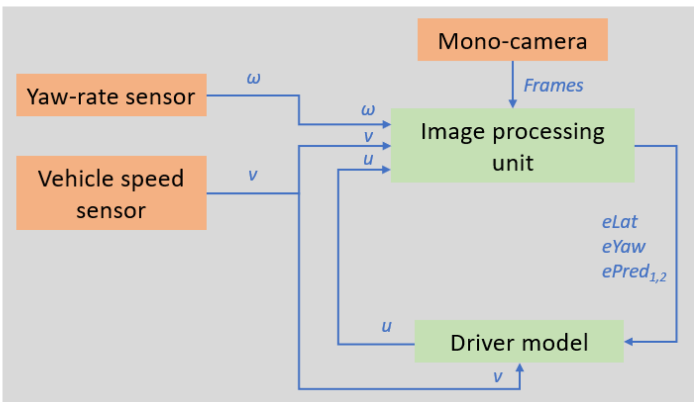


Fig. 3 Structure of the lateral controller

The idea of defining the driver model is to weight the four error signals separately one by one with control parameters. The influence of the different errors can be implemented simply representing the driver's behavior. To get the actual proper steering angle, two steering components were calculated and were summarized for a final output signal as by Gaspar et al. (2018), see (3) and (4):

$$\delta_A = K_1 \cdot eLat + K_2 \cdot eYaw, \tag{3}$$

where eLat is the actual lateral error, eYaw is the actual yaw-angle error and $K_j$, j∊{1, 2, 3, 4} are the required control parameters.

$$\delta_B = K_3 \cdot ePred_1 \cdot sign(ePred_1) + K_4 \cdot ePred_2 \cdot sign(ePred_2), \tag{4}$$

where $ePred_i$, i∊{1, 2} are the predicted lateral errors at $T_i$, i∊{1, 2} prediction time.

### 3.2 Identification of the driver model

In the identification procedure the representation of the human driving behavior is the designated task. The longitudinal speed was used as a scheduling variable ensuring the performance of the system in a chosen speed interval. Therefore, the identification of the driver model was done on constant longitudinal speeds for gaining the control parameters for each exact speed.
The applied identification procedure in order:

1. At the first, the vehicle was driven along a road with bends and straight lines using the CarMaker simulation software to get the steering reference data.
2. With the image processing system using a mono-camera the data of the four kind of lateral errors were determined, see Figure 4.

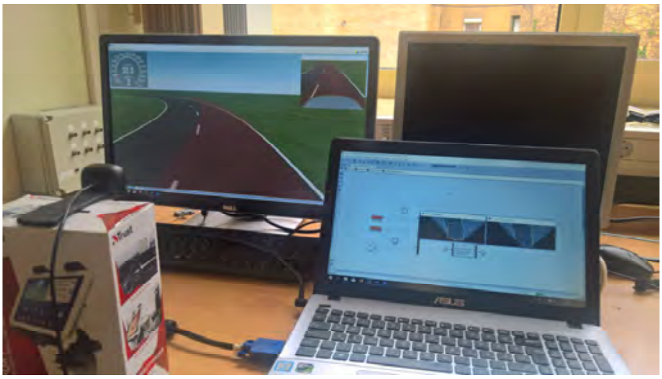

Fig. 4 Identification process, calculating the lateral errors

3. $K_i$, $i \epsilon (1, 2, 3, 4)$ control parameters were determined for each discrete longitudinal speed by minimalizing the equation, see (5), in more detailed form see (6):

$$\sum \left(\delta - \delta_{ref}\right)^2 = min! \tag{5}$$

where $\delta$ is the calculated steering angle and $\delta_{ref}$ is the reference steering angle.

$$\sum \left((K_1 \cdot eLat + K_2 \cdot eYaw + K_3 \cdot ePred_1 + K_4 \cdot ePred_2) - \delta_{ref}\right)^2 \tag{6}$$

## 4. RESULTS AND SIMULATIONS

In this section the proposed lateral driver control is demonstrated by CarMaker/Matlab based simulations. The calculated trajectory followed the entire reference trajectory, see Figure 5. a. In sharp bends the driver model creates a distinct trajectory than the reference providing a more comfortable cornering behavior for the driver, see Figure 5. b, while the vehicle safely stays on its own lane.
Using the lateral driver model, the reference steering angle was nearly completely followed by the calculated steering angle, the differences only serve the purpose to provide a more suitable corning trajectory for a better comfort of the driver, see Figure 6.

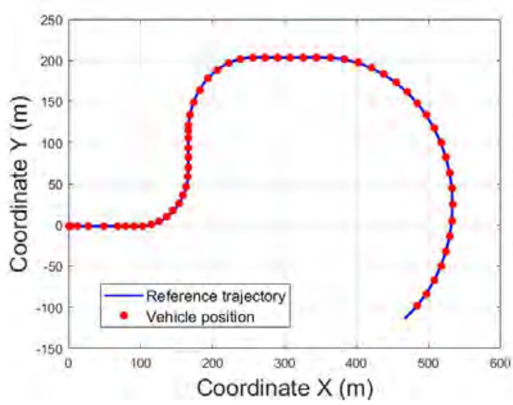


Fig. 2. a Entire trajectory

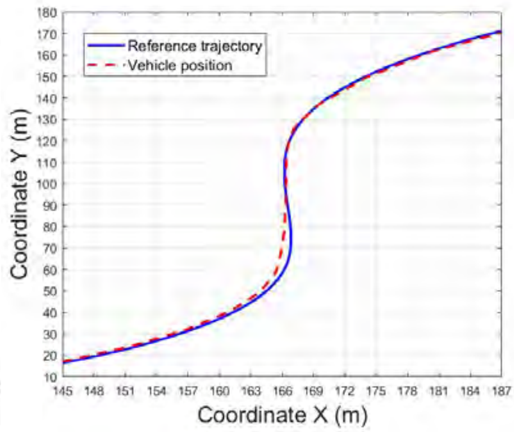


Fig. 5. b Sharp bends

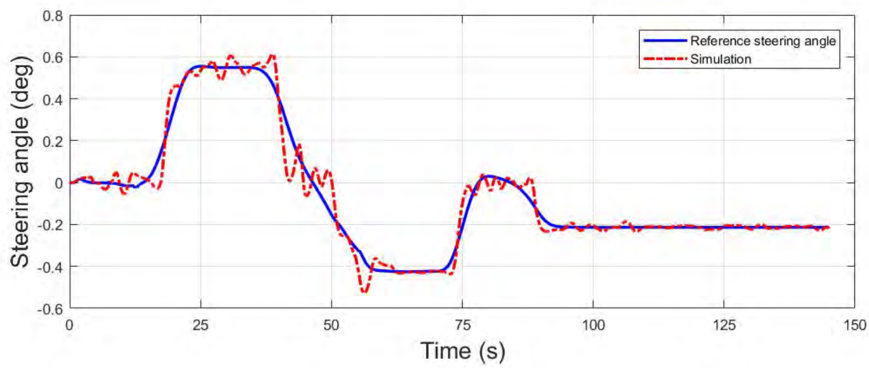


Fig. 3 Steering angle comparison

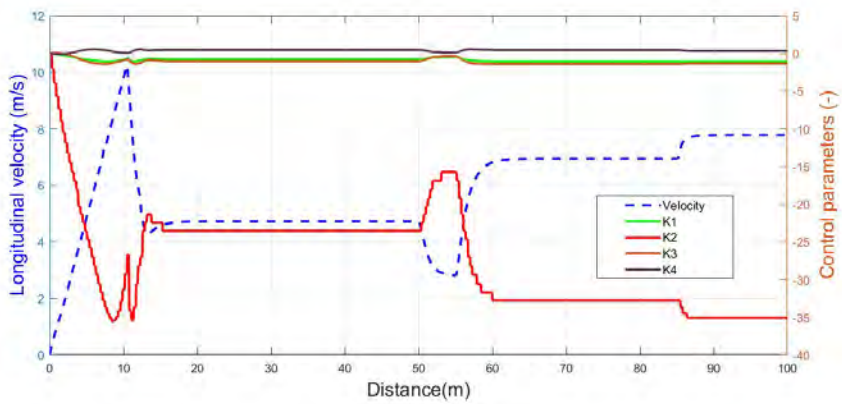


Fig. 4 Control parameters depending on the longitudinal speed

To ensure the performance of the system the longitudinal speed was used as a scheduling variable. The identified $K_i$ control parameters among the discrete speeds were determined by interpolation and based on the actual speed the parameters were successfully controlled to the necessary values, see Figure 7.

## 5. CONCLUDING REMARKS

The proposed paper has been shown that with an appropriate lateral driver model based on the driver's behavior, a more realistic and convenient cornering trajectory is achievable for the driver. The simulations verified that the steering control could follow the reference signal sufficiently and was able to modify the trajectory during the cornering. Moreover, the model properly could handle the steering control to the effect of the changing longitudinal speed. The simplicity of the driver model can assist the control system to operate real-time efficiently, nevertheless a more sophisticated driver model or combination of different driver models may can be beneficial for a more strength and accurate driver model system.

## 6. ACKNOWLEDGEMENT

The research was supported by the Hungarian Government and co-financed by the European Social Fund through the project "Talent management in autonomous vehicle control technologies" (EFOP-3.6.3-VEKOP-16-2017-00001).
The research reported in this paper was also supported by the Higher Education Excellence Program of the Ministry of Human Capacities in the frame of Artificial Intelligence research area of Budapest University of Technology and Economics (BME FIKPMI/FM).
The work of Balázs Nemeth was partially supported by the János Bolyai Research Scholarship of the Hungarian Academy of Sciences and the and the ÚNKP-18-4 New National Excellence Program of the Ministry of Human Capacities.

## 7. REFERENCES

[1] **Péter, G. – Balázs, N. – Gergely, S.**: Design and Verification of Autonomous Steering Control Based on Driver Modeling. European Control Conference (ECC), Limassol, 2018, p.953-958.

[2] **David, J.C.:** A path-following driver-vehicle model with neuromuscular dynamics, including measured and simulated response to a step in steering angle overlay. Department of Engineering, University of Cambridge, Trumpington Street, Cambridge, 2012, p.573-596.

[3] **Neusser, S. - Nijhuis, J. - Spaanenburg, L. - Höfflinger, B. - Franke, U. - Fritz, H.**: Neurocontrol for lateral vehicle guidance. IEEE Micro, 1993, p.57-66.

[4] **Manfred, P. – Johannes, E.:** Driver models in automobile dynamics application, Vehicle System Dynamics. International Journal of Vehicle Mechanics and Mobility, 2007, p.699-741.

[5] **Robin, S. - Eric, R. - Gerd W.:** Comparison and Evaluation of Advanced Motion Models for Vehicle Tracking. Information Fusion, 11th International Conference, 2008.

# HIGHWAY BEHAVIOUR TRAINING THROUGH LEARNING BASED STATE CHOICE MODEL

**János SZALAY, Bálint KŐVÁRI, Szilárd ARADI, Péter GÁSPÁR and Tamás BÉCSI**

Department of Control for Transportation and Vehicle Systems,
Faculty of Transportation Engineering and Vehicle Engineering
Budapest University of Technology and Economics
H-1111 Budapest, Műegyetem rkp. 3., Hungary

*Received: November 5, 2018*

## ABSTRACT

Automated highway driving solutions are reaching the commercially available vehicles, though with restricted functionalities. The research presents a mixed simulation model, where the behavior planning of a vehicle can be designed with interactive traffic environment, the traffic is modelled with classic microscopic approach, though the vehicle to be controlled uses more complex model. The control of the vehicle is based on a hierarchical state machine approach, where the model can choose from different basic behavior schemes, like lane keeping, lane changing etc. with underlying low-level control for all states. The paper shows the performance of the classic state choice models and compares it to a machine learning based approach, where the state transition decisions are controlled by a neural network structure.

*Keywords: Machine learning, highway behaviour*

## 1. INTRODUCTION

The paper presents the statistical comparison of a rule-based and a machine learning based approach on fully automated highway driving (AHD). The purpose is to assess the limitations and weaknesses of the different methods and to explore the possibilities of using such techniques on this complex control task, because it is arguable which formula will be able to reach the required level of safety. To establish the performance evaluation the paper provides a general walkthrough on the environment. There are many simulators and environments intended for research in the field of autonomous driving, such as CARLA [1] or TORCS [2], though neither was proper for our research needs, therefore the presented study also consist a newly developed simplified highway simulation. The environment has three substantial portions: vehicle model, sensor model, traffic model.

| ID | Meaning | Elements | Default |
|---|---|---|---|
| 0,1 | Front Left Lane | *dx, dv* | 500,0 |
| 2,3 | Front Ego Lane | *dx, dv* | 500,0 |
| 4,5 | Front Right Lane | *dx, dv* | 500,0 |
| 6,7 | Rear Left Lane | *dx, dv* | 500,0 |
| 8,9 | Rear Ego lane | *dx, dv* | 500,0 |
| 10,11 | Rear Right Lane | *dx, dv* | 500,0 |
| 12 | Left Safety Zone | *Occup[0,1]* | - |
| 13 | Right Safety Zone | *Occup[0,1]* | - |
| 14 | Vehicle lateral position | *Pos [m]* | - |
| 15 | Vehicle heading | *th[rad]* | - |
| 16 | Vehicle speed | *v [m/s]* | - |

Table.1: State vector for the ego vehicle

More details on the model can be found in our previous works [1] [2]. The vehicle model is a rigid kinematic bicycle model where the tire slip is neglected, thus the lateral motion exclusively influenced by the geometric parameters [3] [4]. The sensor information is based on common automotive sensors such as camera and radar based systems. Environment information contains ego vehicle position and heading relative to the lane and also the relative distance and velocity of the vehicles in the ego and neighboring lanes. Table 1. shows the components of the state vector.

IDs [0-11] gives the relative distances and relative speeds of the surrounding vehicles. If the lane does not exist or it is unoccupied the default - [500,0] - values are used. IDs [12,13] present the occupancy of the both safe zones of the ego vehicle while [14-16] provide the lateral position relative to the center of the rightmost lane, the vehicle's heading relative to the orientation of the lane and the ego vehicle's speed also. Fig. 1 visualizes the sensor information in order to help the better understanding.

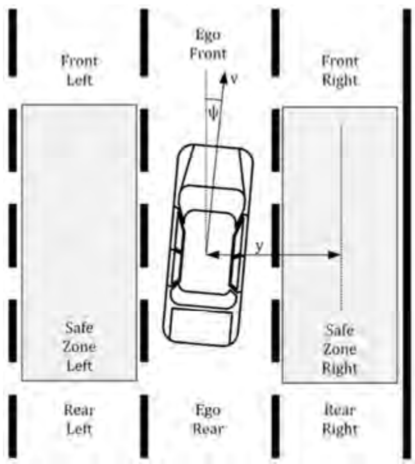


Fig. 1 Sensor model of the ego vehicle

The traffic model is microscopic and is fully parametrized, the number of the lanes, traffic density in each lane – mean and deviation – the needed speed of the vehicles in the form of mean and deviation also. The goal of this approach is to produce diverse traffic situations. The controlled vehicle is chosen after a warm up stage which is essential to make the traffic close to real. Other participants of the traffic are controlled by a two level hierarchical controller [7]. On the first level it choses from strategic goals e.g. avoid collision, keep right, maximize speed, perform a lane changing maneuver if it is needed, on the next level it creates actions - in a form of acceleration, deceleration and steering - to realize the chosen goal. Fig. 2 displays a snapshot on the environment. The implementational details and structures of the environment resembles to the well known and widely used OpenAI gym format [7].
Section 2 describes the design steps of the comparison system. Section 3 explains the result of the statistical comparison and Section 4 considers the possible improvements.

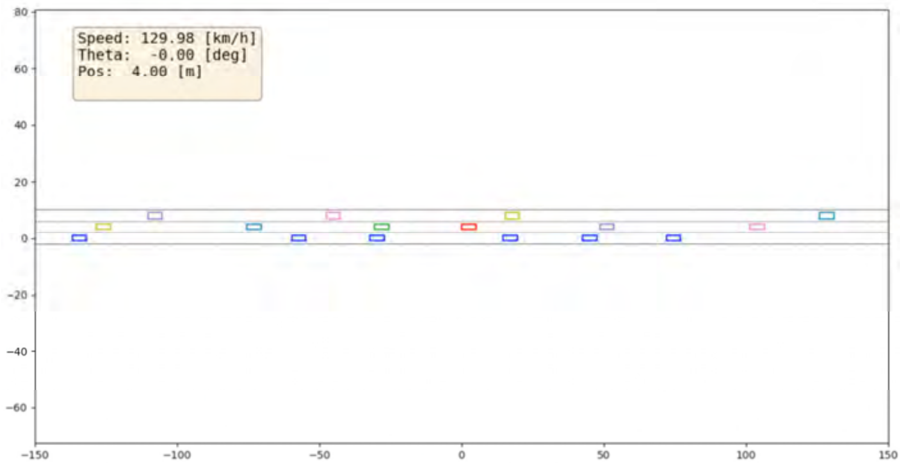


Fig. 2 Snapshot on the environment

## 2. THE CREATION OF THE COMPARISON SYSTEM

The original system has an important component which is responsible for the decision-making process, in this new system the purpose is to replace the rule-based method with a neural network. Fig. 3 shows the conceptual structure of the designed system.

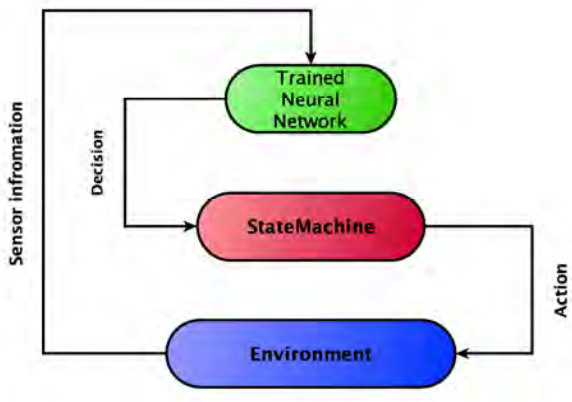


Fig. 3 Decision loop

The input is the same sensor information vector like in the original system, while the output is a discrete decision about what kind of action is needed in order to solve the current traffic situation, represented by the sensor information. The possible decisions are: slow down, speed up, change left, change right, steady flow. A state-machine component realizes these actions in the form of accelerations or decelerations and steering angles.

When a system needs to choose from a discrete set of decisions - based on sensor information - the task is called a multiclass classification. For the realization, the supervised training of an Artificial Neural Network (ANN) were chosen.

In supervised learning one feeds the neural network with input-output pairs and it learns the function that maps the input to the output. To reach high accuracy the training process needs a large amount of pre-processed training data, for this task, we uses the original system to produce raw data for the pre-processing.

## 2.1 Data Pre-Processing

The first step in the pre-processing is the collection of eligible amounts of data, with respect to the fact that in order to achieve the best performance, the decision space has to be covered evenly.

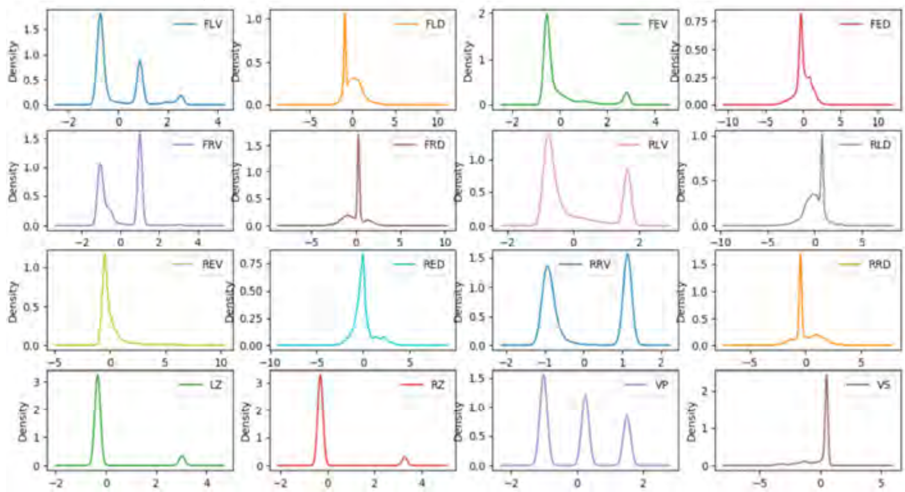


Fig. 4 Rescaling of inputs

This is followed by examination of input effects, hence to find the less important components of the sensor information vector in order to decrease the size of the input, thus indirectly the time of the training process. The only sensor information that we omitted is the vehicle heading, because the neural network only need samples from decision-making points and the vehicle heading only changes under the lane changing maneuver, but it can not be interrupted because of the dynamics of the system.

Moreover, we had to rescale the dataset because, most of the sensor information have different intervals and it decreases the accuracy of the neural network. We used standardization which transforms the attributes into Gaussian like distribution. Finally, we shuffled the dataset to fit the chosen batch size in the training process. The result of the rescaling is shown on Fig. 4.

## 2.2 Training & Testing

Training a neural network takes a long a time, because there are a lot of parameter (e.g. epoch, batch size, number of layers, size of the layers, optimizer, loss function, activation function) that we have to adjust, but we never know what will be the best for our specific task, so in order to save time we just train on lower number of data until we got a promising result, then we can start the training with the whole dataset.

Testing the trained neural network's accuracy is the first step of the performance evaluation. In our case we used *KfoldCrossValidation*, this method provides a wider percept about the accuracy of the network then the classic train-test split method. This method unfold our dataset into k-folds then chooses one fold for testing and trains the network with the remaining folds and repeats this process k times. Finally, we get the mean accuracy and the standard deviation of the trainings, this makes the result more reliable. If the accuracy is high enough, we can continue the evaluation with the confusion matrixes. The confusion matrix shows us which decision the neural network mix with. Despite of a high accuracy we should check the distribution of the inaccuracy between the different decisions, because if it concentrates in one particular decision type it could be mean that the neural network have not learnt that specific type. Fig. 5 shows the confusion matrix of this task.

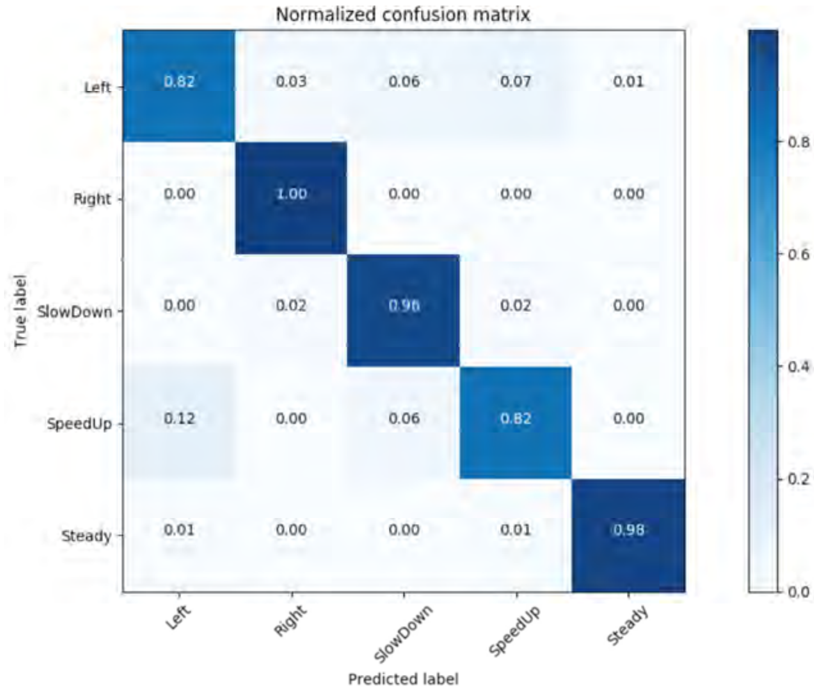


Fig. 5 Normalized confusion matrix of the training process

### 2.3 Results

After the training process we replaced the decision-making component with the trained network and measured the performance in safety, speed maximization and in keeping right, then we compared it to the original rule-based system. The comparison is based on the same size of test run in the environment and the statistical evaluation is based on the sensor information recorded during the test run.

| | The rule based system | Neural Network (5) | |
|---|---|---|---|
| Safety | 0 | 13 | Colission from LaneChanging |
| | 39 | 262 | Numeber of Lanechanging |
| | 0 | 2 | Colission from Follow |
| Speed | 120 | 130 | Mean |
| | 70% | 78% | 120<v<140 |
| | 67% | 69% | 125<v<135 |
| Keep right | 43% | 67% | Left lane |
| | 29% | 21% | Middle lane |
| | 28% | 11% | Right lane |

Fig. 6 Comparison of system performances

As Fig. 6 shows the rule-based system is safer and stays in the right lane more than the neural network based system, though it handles the speed better. What is also significant that the NN based system changes lane nearly six times more than, the original system and it stays in the right lane twice less. This suggest, that the lane changing condition of the original system is too strict and because of that it must slow down in scenarios when the NN based system changes the lane and keeps its high speed. The main drawback of the NN based system is the situations that lead to collisions. The collisions from lane changing has two different reasons, the first scenario is when the ego vehicle stays in the middle lane and it tries to change right, but it starts the maneuver in the wrong moment and it bumps into the front vehicle in the target lane. The second scenario is, when the ego vehicle stays in the left lane and lefts the highway, this mostly occurs when the ego vehicle's velocity is higher then the speed limit. The confusion matrix of Fig. 5 gives a hint on this behavior.

It shows that the network mixes the speed up decision with the change left decision. The another reason is that the ego vehicle lefts the state-space defined by the dataset used for training by mixing up the speed up and slow down decisions, because the rule-based system, where we obtained the training data always keeps the speed limit. The problem with mixing up the speed up and slow down decisions is also causes the collisions from following of the front vehicle.

## 3. CONCLUSION

Most of the failures of the neural network came from inaccuracy which may lead to data pre-processing. The reason is that the scenarios where the ego vehicle causes a collision is under represented in the training dataset, because when we collected the data for training, we just collected the same number of lane changing decision from every lane into every possible direction, but a lane changing can occur in several different situations in one lane into one direction and this is also true for the other decision types. So, to solve that issue we should find all the occurrences of the traffic situations attached to the decisions. We can achieve that by using unsupervised learning methods for data clustering (e.g. K-nearest neighbor). In the future work we should collect the training data more carefully in order to represent all the scenario equally to reach higher accuracy.

## 9. REFERENCES

[1] **Dosovitskiy, A. - Ros, G. - Codevilla, F. - Lopez, A. - Koltun, V.:** „CARLA: An open urban driving simulator" arXiv preprint arXiv:1711.03938, 2017.

[2] **Wymann, B. - Espi'e, E. - Guionneau, C. - Dimitrakakis, C. - Coulom, R. - Sumner, A.:** „Torcs, the open racing car simulator" 2000. [Online]. Available: http://torcs. sourceforge. net.

[3] **Bécsi, T. - Aradi, S. - Fehér, Á. - Szalay, J. - Gáspár, P.:** „Highway Environment Model for Reinforcement Learning" IFAC-PapersOnLine, vol. 51, 2018, p.429-434.

[4] **Aradi, S. - Bécsi, T. - Gáspár, P.:** „Policy Gradient Based Reinforcement Learning Approach for Autonomous Highway Driving," in 2018 IEEE Conference on Control Technology and Applications (CCTA), 2018.

[5] **Kong, J. - Pfeiffer, M. - Schildbach G. - Borrelli, F.:** „Kinematic and dynamic vehicle models for autonomous driving control design" in 2015 IEEE Intelligent Vehicles Symposium (IV), 2015.

[6] **Polack, P. - Altché, F - d'Andréa-Novel, B. - La Fortelle, A.:** „The kinematic bicycle model: A consistent model for planning feasible trajectories for autonomous vehicles?" in 2017 IEEE Intelligent Vehicles Symposium (IV), 2017.

[7] **Fang, X. - Pham, H. A. - Kobayashi, M.:** „Pd controller for car-following models based on real data," in Proceedings of 1st Human-Centered Transportation Simulation Conference, 2001.

[8] **Brockman, G. - Cheung, V. - Pettersson, L. - Schneider, J. - Schulman, J. - Tang, J. - Zaremba, W.:** „Openai gym" arXiv preprint arXiv:1606.01540, 2016.

# ROBUST $H_\infty$ PROPORTIONAL INTEGRAL OBSERVER DESIGN FOR ACTUATOR FAULT ESTIMATION

**Manh-Hung DO [1], Damien KOENIG [1] and Didier THEILLIOL [2]**

[1] Univ. Grenoble Alpes, CNRS, Grenoble INP*, GIPSA-lab, F-38000 Grenoble, France.
E-mail: {manh-hung.do, damien.koenig}@gipsa-lab.grenoble-inp.fr

[2] University of Lorraine, CRAN, UMR 7039, Campus Sciences, B.P.70239,
F-54506 Vandoeuvre-les-Nancy Cedex, France.
E-mail: didier.theilliol@univ-lorraine.fr
* Institute of Engineering Univ. Grenoble Alpes

*Received: November 5, 2018*

## ABSTRACT

The main contribution of this paper is the design of robust H∞ proportional-integral (PI) observers for actuator fault estimation, applied to uncertain linear time-invariant system. The observer design is based on the PI observer, combining the $H_\infty$ norm to deal with system uncertainties and disturbance attenuation. Then the application to the suspension system is presented in order to highlight the performance of the proposed estimator.

*Keywords*: Observers, Fault detection, Uncertain linear systems, Semi-active suspension, Linear time-invariant (LTI), Robust estimation.

## 1. INTRODUCTION

The parametric uncertainty has always been an interesting topic for research (see [1]) due to its negative effects on system stability and observer performance. To solve this kind of time-varying and bounded uncertainty, most methods are based on the linear matrix inequality (LMI) optimization, which is obtained from the Lyapunov stability function. In [2], the observer design problem was addressed by applying the projection lemma and the Schur complement to linear discrete-time linear switched system in presence of uncertainties. Another solution was then introduced in [3] and [4], in which the majoration lemma (see [5]) was applied to deal with system uncertainties while the H∞ norm attenuated the influence of disturbance. However, these approaches have certain disadvantages. Firstly, the increase in the number of uncertainties will lead to numerous sub-spaces (for projection lemma) or a complexity growth in LMI solution (for majoration lemma). Secondly, there is always a static error between the system state and its estimation due to the use of classical proportional observer. To deal with above issues, proportional-integral (PI) observer, whose structure and robustness were studied in [6] and [7], was applied to estimate the system states and faults of the descriptor system in [8]. In [9], the uncertainties in state matrices were treated by majoration lemma and the fault was estimated by the H∞ PI observer. Nevertheless, its LMI solution may encounter some numerical problems to achieve the asymmetrical stability.

Meanwhile, for the suspension application, the fault estimation strategy has been developed since many years. In [10], the actuator fault was estimated by using H∞ filtering technique. In [11], the parity space and frequency-based estimator were implemented to estimate the actuator fault. In [12], a comparison between different estimation methods, such as fast adaptive fault estimation (FAFE), parameter adaptive observer, and switched linear parameter-varying observer, has been studied for actuator fault. However, the robustness of observer against uncertainties has not been taken into account in the above approaches.As a result, there is a need to overcome the drawbacks of previous methods. Hence, the contribution of paper is the implementation of H∞ synthesis to simply deal with the impact of parametric uncertainty on the actuator fault estimation, thus reducing the complexity of LMI optimization. In which, the proposed observer design is based on the mathematical model inspired from the vehicle suspension system.

The paper is organized as follows. Firstly, the problem formulation is presented in Section 2. In Section 3, under the disturbance and fault occurrence, the observer design problem against system uncertainties is solved by using LMI optimization. The simulation result is illustrated in Section 4. Finally, the conclusion with remarks and future work are presented in Section 5.

Notations: $\mathbb{R}^n$ and $\mathbb{R}^{m\times n}$ represent respectively the n dimensional Euclidean space and the set of all $m\times n$ real matrices; $X^T$ is the transposed of matrix X; $X>0$ is real symmetric positive definite matrix; 0 and I denote zeros and identity matrix with appropriate dimensions; and the symbol $(*)$ denotes the transposed block in the symmetric position.

## 2. PROBLEM FORMULATION

### 2.1 Suspension Modelling

The quarter-car, or the semi-active suspension in the platform, can be modeled by a mass-spring-damper system. In which:

- The sprung mass $m_s$ represents a quarter of the chassis body
- $z_s$ is the vertical displacement around the equilibrium point of $m_s$;
- The sprung mass $m_{us}$ represents wheel/tire of the vehicle
- $z_{us}$ is the vertical displacement around the equilibrium point of $m_{us}$;
- The semi-active suspension is composed of a spring with the stiffness coefficient $k_s$ and a controllable damper with the damping coefficient c, where $c_{min} \le c \le c_{max}$;
- The tire is modeled by a spring with the stiffness coefficient $k_t$;
- The road profile $z_r$ is considered as unknown input d for the suspension.

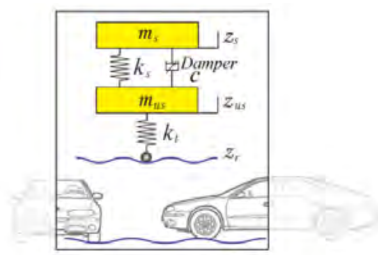


Fig. 1 The quarter-car model

The suspension dynamics are described by the following equations [13]:

$$\begin{cases} m_s\ddot{z}_s = -k_s(z_s - z_{us}) - F_c \\ m_{us}\ddot{z}_{us} = k_s(z_s - z_{us}) + F_c - k_t(z_{us} - z_r) \end{cases}, \qquad (1)$$

where $F_c = c\,\dot{z}_{def}$ is the damper force; $z_{def} = z_s - z_{us}$ is the displacement (deflect-tion) between the chassis and the tire position; and $\dot{z}_{def}$ is the deflection speed.
In order to obtain LTI model of suspension system, the damper force $F_c$ is decomposed into 2 components:

$$F_c = c\dot{z}_{def} = c_0\dot{z}_{def} + u \tag{2}$$

In which, u is the model input corresponding to the varying part of semi-active damper force $F_c$; $c_0$ is the nominal value of damper, corresponding to a passive damper when there is no control input u.
According to [14] in case of semi-active suspension, the authors chose $c_0 = (c_{min} + c_{max})/2$ as the nominal damping value, so the control input u in (1) is supposed to be limited in symmetric region $[-u^*_{max}, u^*_{max}]$ where $u^*_{max} = (c_{max} - c_{min})\dot{z}_{def}/2$.
Two available outputs are supposed to be available: $z_{def}$ is the displacement; and $\ddot{z}_{us}$ is the tire acceleration and there is the actuator fault $f_a$ in the damper actuator input u.
The faulty LTI model has been considered for the study as: [13] [14]

$$\begin{cases} \dot{x} &= Ax + Bu + E_d d + E_f f_a \\ y &= Cx + Du + F_d d + F_f f_a \end{cases}, \tag{3}$$

in which, $x = [z_s \;\; \dot{z}_s \;\; z_{us} \;\; \dot{z}_{us}]^T$ is the state vector; $y = [z_{def} \;\; \ddot{z}_{us}]^T$ is the output vector; d is the road profile $z_r$ considered as unknown input; u is the control input;

$$A = \begin{bmatrix} 0 & 1 & 0 & 0 \\ -\dfrac{k_s}{m_s} & -\dfrac{c_0}{m_s} & \dfrac{k_s}{m_s} & \dfrac{c_0}{m_s} \\ 0 & 0 & 0 & 1 \\ \dfrac{k_s}{m_{us}} & \dfrac{c_0}{m_{us}} & -\dfrac{kt + k_s}{m_{us}} & -\dfrac{c_0}{m_{us}} \end{bmatrix}; E_d = \begin{bmatrix} 0 & 0 & 0 & \dfrac{k_t}{m_{us}} \end{bmatrix}^T,$$

$$C = \begin{bmatrix} 1 & 0 & -1 & 0 \\ \dfrac{k_s}{m_{us}} & \dfrac{c_0}{m_{us}} & -\dfrac{kt + k_s}{m_{us}} & -\dfrac{c_0}{m_{us}} \end{bmatrix}; F_d = \begin{bmatrix} 0 & \dfrac{k_t}{m_{us}} \end{bmatrix}^T; B = \begin{bmatrix} 0 & -\dfrac{1}{m_s} & 0 & \dfrac{1}{m_{us}} \end{bmatrix}^T;$$

$$D = \begin{bmatrix} 0 & \frac{1}{m_{us}} \end{bmatrix}^T; E_f = B; F_f = D$$

## 2.2 System presentation

The damping coefficient c is uncertain parameter varying between $c_{min}$, $c_{max}$ and its nominal parameter $c_0$. That leads to the uncertainties existing in the state matrices A and C of (3). As a result, the following system is considered for the study:

$$\begin{cases} \dot{x} &= (A + \Delta A)x + Bu + E_d d + E_f f_a \\ y &= (C + \Delta C)x + Du + F_d d + F_f f_a \end{cases} \tag{4}$$

- $x \in R^{n_x}$ is the state vector; $y \in R^{n_y}$ is the measurement output vector; $u \in R^{n_u}$ is the input vector; $d \in R^{n_d}$ is the disturbance vector; $f_a \in R^{n_f}$ is the actuator fault to be estimated.
- Matrices A, B, C, D, $E_d$, $E_f$, $F_d$ and $F_f$ are all known constant matrices with appropriate dimensions, which correspond to the nominal system defined in (3).

- The terms $\Delta A$ and $\Delta C$ are time-varying parameter matrices corresponding to uncertainties of nominal system. They can be represented as: $\Delta A = \bar{A}\theta$ and $\Delta C = \bar{C}\theta$, where $\bar{A}$ and $\bar{C}$ are defined as:

$$A_\theta = \begin{bmatrix} 0 & 0 & 0 & 0 \\ 0 & -\frac{1}{m_s} & 0 & \frac{1}{m_s} \\ 0 & 0 & 0 & 0 \\ 0 & \frac{1}{m_{us}} & 0 & -\frac{1}{m_{us}} \end{bmatrix}; \; C_\theta = \begin{bmatrix} 0 & 0 & 0 & 0 \\ 0 & \frac{1}{m_{us}} & 0 & -\frac{1}{m_{us}} \end{bmatrix}; \tag{5}$$

and $\theta$ is the variation of damping coefficient "c", where $\theta = 0$ when the system works correctly in nominal mode or without the uncertainty, otherwise $-\Delta c_0 \leq \theta \leq \Delta c_0$ with $\Delta c_o = (c_{max} - c_{min})/2$.

The paper's interest is to find an observer design which can deal with the uncertainty generated by the varying dynamics of damping coefficient and estimate the actuator fault $f_a$.

In order to achieve the above objectives, the system (4) can be rewritten as:

$$\begin{cases} \dot{x} & = Ax + Bu + [E_d \;\; A_\theta] \begin{bmatrix} d \\ \theta x \end{bmatrix} + E_f f_a \\ y & = Cx + Du + [F_d \;\; C_\theta] \begin{bmatrix} d \\ \theta x \end{bmatrix} + F_f f_a \end{cases} \tag{6}$$

Choosing $w = \begin{bmatrix} d \\ \theta x \end{bmatrix}$ as the new disturbance vector. The system (6) is simplified as:

$$\begin{cases} \dot{x} & = Ax + Bu + E_{dw} w + E_f f_a \\ y & = Cx + Du + F_{dw} w + F_f f_a \end{cases} \tag{7}$$

Where $E_{dw} = [E_d \;\; A_\theta]$ and $F_{dw} = [F_d \;\; C_\theta]$.

The observer design for system (7) is presented in next section.

## 3. ROBUST H∞ PI OBSERVER DESIGN

**Assumption 1**. As discussed in [8] and [15], the faults are considered to be bounded and supposed to be in low frequency domain, i.e., $\dot{f} \approx 0$. In fact, most system faults, such as an actuator stuck and offsets in sensor outputs, exist in this zone (see [16] and [17]).

To estimate the fault, an augmented state is considered, so the $H_\infty$ PI observer has the representation:

$$\begin{cases} \dot{\hat{x}} & = A\hat{x} + Bu + L_P(y - \hat{y}) + E_f \hat{f}_a \\ \dot{\hat{f}}_a & = L_I(y - \hat{y}) \\ \hat{y} & = C\hat{x} + Du + F_f \hat{f}_a \end{cases} \tag{8}$$

Where $L_P$ and $L_I$ are the proportional and integral gains of the PI observer, respectively.

The state estimation error $e_x$ and fault estimation error $e_f$ are defined as:

$$\begin{cases} e_x = x - \hat{x} \\ e_f = f_a - \hat{f}_a \end{cases} \tag{9}$$

Using (7) and (8), the dynamics of estimation errors are given by:

$$\begin{cases} \dot{e}_x = \dot{x} - \dot{\hat{x}} = (A - L_P C)e_x + (E_f - L_P F_f)e_f + (E_w - L_P F_w)w \\ \dot{e}_f = \dot{f} - \dot{\hat{f}} = -L_I C e_x - L_I F_f e_f - L_I F_w w \end{cases} \tag{10}$$

In other words,

$$\begin{cases} \dot{e} &= (A_a - L_a C_a)e + (E_{wa} - L_a F_w)w \\ e_f &= C_{af} e \end{cases} . \tag{11}$$

where:

- Estimation error : $e = \begin{bmatrix} e_x \\ e_f \end{bmatrix}$
- $A_a = \begin{bmatrix} A & E_f \\ 0 & 0 \end{bmatrix}, L_a = \begin{bmatrix} L_P \\ L_I \end{bmatrix}, E_{wa} = \begin{bmatrix} E_w \\ 0 \end{bmatrix}, C_a = [C \quad F_f], C_{af} = [0_{n_x} \quad I_{n_f}]$

**Assumption 2**. In order that the PI observer (8) exists, the pair $(A_a, C_a)$ in (11) is assumed to be detectable, which can be demonstrated as the following condition (see [8])

$$\text{rank}\begin{bmatrix} sI - A_a \\ C_a \end{bmatrix} = \text{rank}\begin{bmatrix} sI - A & -E_f \\ 0 & sI_{n_f} \\ C & F_f \end{bmatrix} = n_x + n_f \ \forall \ \text{Re}(s) \geq 0$$

The objective of H∞ PI observer is to attenuate the influence of disturbance $w$ on actuator fault estimation error (see [8])

$$\min_\gamma \|T_{e_f w}\| = \min_\gamma \frac{\|e_f\|_2}{\|w\|_2} \leq \gamma \tag{12}$$

**Theorem 1**. The observer (11) is asymptotically stable if there exist a symmetric positive definite matrix P and a matrix Q which satisfy the following LMI:

$$\begin{bmatrix} PA_a + A_a^T P + QC_a + C_a^T Q^T & E_{wa} + QF_w & C_{af}^T \\ (*) & -\gamma^2 I & 0 \\ (*) & (*) & -I \end{bmatrix} < 0 \tag{13}$$

The gain of the observer is then calculated by:

$$\begin{bmatrix} L_P \\ L_I \end{bmatrix} = L_a = -P^{-1}Q \tag{14}$$

**Proof:** The candidate Lyapunov function $V = e^T P e \ (P > 0)$ is chosen. Consequently,

$$V = \dot{e}^T P e + e^T P \, \dot{e} \tag{15}$$

$$= e^T (PA_a + A_a^T P - PL_a C_a - C_a^T L_a^T P)e + e^T (PE_{wa} + PL_a F_w)w + w^T (E_{wa}^T P + F_w^T L_a^T P)e \ .$$

The condition (12) can be expressed as:

$$\dot{V} + e_f^T e_f - \gamma^2 w^T w \leq 0 \, . \tag{16}$$

Using $Q = -PL_a$, the left-hand side of (16) becomes

$$\dot{V} + e_f^T e_f - \gamma^2 w^T w$$
$$= [e^T \quad w]\begin{bmatrix} PA_a + A_a^T P + QC_a + C_a^T Q^T + C_{af}^T C_{af} & E_{wa} + QF_w \\ (*) & -\gamma^2 I \end{bmatrix}\begin{bmatrix} e \\ w \end{bmatrix} \tag{17}$$

A sufficient condition for both stability of observer (8) and disturbance objective (16) is that:

$$\begin{bmatrix} PA_a + A_a^T P + QC_a + C_a^T Q^T + C_{af}^T C_{af} & E_{wa} + QF_w \\ (*) & -\gamma^2 I \end{bmatrix} < 0 \ \forall \begin{bmatrix} e \\ w \end{bmatrix} \neq 0 \tag{18}$$

Applying the Schur Complement to above inequality, (13) is obtained, which completes the proof.

## 4. APPLICATION TO SUSPENSION MODEL

### 4.1 Model & Observer Parameter

For the simulation purpose, the following parameters are chosen:

TABLE 1
SUSPENSION PARAMETER

| Parameters | Unit | Value | Description |
|---|---|---|---|
| $m_s$ | Kg | 2.578 | A quarter-car chassis mass |
| $m_{us}$ | Kg | 0.485 | Rear tire mass |
| $k_s$ | N/m | 349 | Suspension stiffness |
| $c_{min}$ | Ns/m | 18 | Minimum damping coefficient |
| $c_{max}$ | Ns/m | 85 | Maximum damping coefficient |
| $k_t$ | N/m | 3067.5 | Tire stiffness |

Based on the above parameter, Yalmip toolbox [18] and Sedumi solver [19] allow obtaining the optimal H∞ performance of the PI observer: $\gamma = 0.0141$. The gains of PI observer are presented as followings:

$$L_P = \begin{bmatrix} -41.8691 & -0.0010 \\ 27.5365 & -0.0010 \\ -39.3964 & -0.0010 \\ -42.6490 & 0.9990 \end{bmatrix}, \tag{19}$$

$$L_I = [-1230.5514 \quad -0.0001]\,. \tag{20}$$

### 4.2 Frequency Analysis

As the matrices $A_\theta$ and $C_\theta$ in (5) have the first and third columns be the zeros columns, there is no direct transfer from element $\theta x_1$ and $\theta x_3$ of varying vector $\theta x$. Therefore, the frequency analysis will only concentrate on the road profile d, and the other 2 varying element $\theta x_2$ and $\theta x_4$.

The impact of d on fault estimation error $e_{f_a}$ is studied in the frequency **from 0 to 20 Hz** as the road profile spectrum stays in this domain (see [13]). In the Fig. 2, the Bode diagram has a peak at 1.05Hz, which reflects the most important influence of road profile on estimation result (-63.4dB).

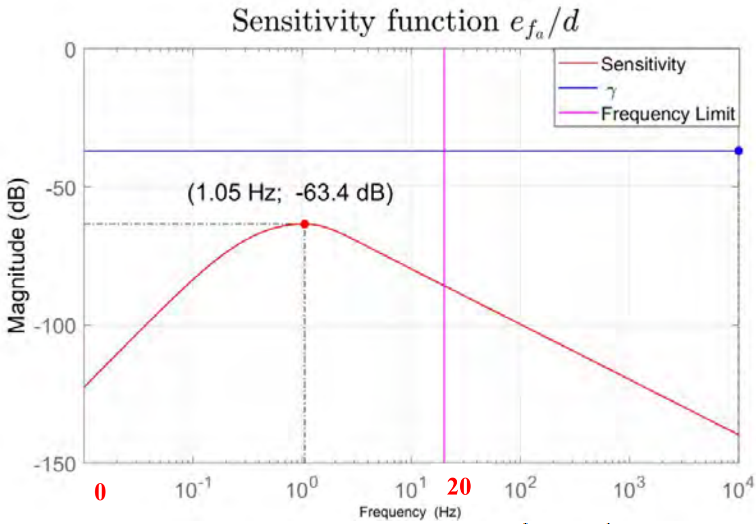


Fig. 2 Sensitivity function $|e_{f_a}/d|$

In Fig. 3 and Fig.4, the sensitivities decrease significantly from 1 Hz ($10^0$ Hz). The higher the frequency, the less impact of parameter variation/uncertainty on the estimation error. Moreover, the amplitude of sensibilities is below the curve of $\gamma$, which verifies the H∞ synthesis mentioned in (12).

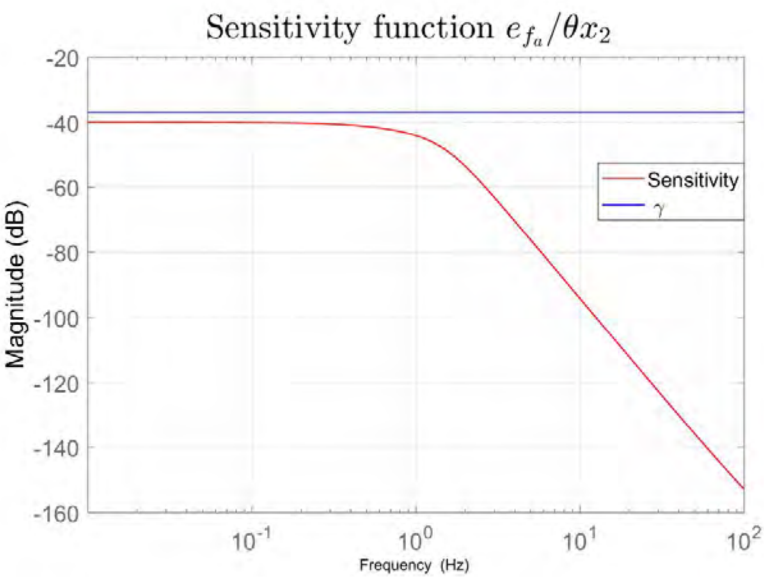


Fig. 3 Sensitivity function $|e_{f_a}/\theta x_2|$

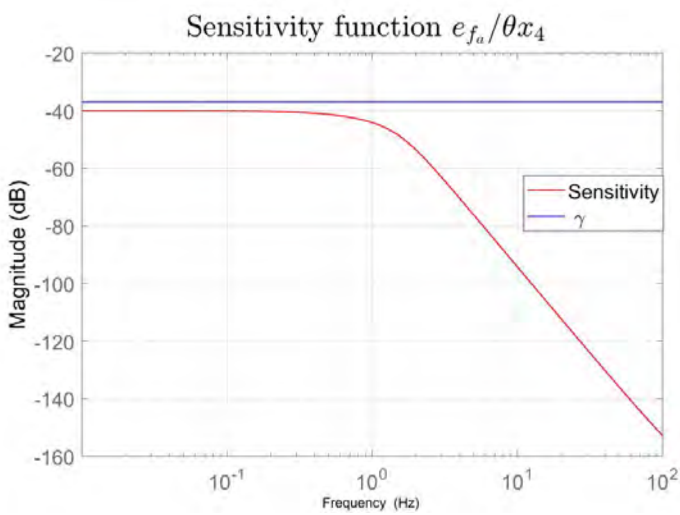


Fig. 4 Sensitivity function $|e_{fa}\ /\theta x_4|$

The relation between the real and estimated fault is represented by the complementary sensitivity $T_{\hat{f_a} fa}$ in Fig. 5. In which, the $|T_{\hat{f_a} fa}| = |\hat{f_a}\ /\ fa| = 0$ (dB), i.e. $\hat{f_a} \approx fa$, from 0 to 0.1 Hz, so the fault $f_a$ may be estimated by the use of H∞ PI observer if its bandwidth is less than 0.1 Hz (or slow-varying fault in this study)

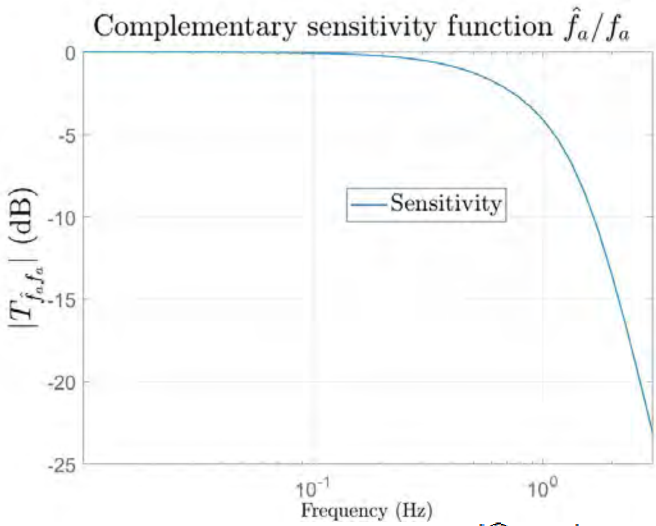


Fig. 5. Sensitivity function $|\hat{f_a}\ /\ fa|$

### 4.3 Simulation condition

The following conditions are considered for the simulation in Matlab:

- Simulation time: t = 25 s.
- Road profile d: is modeled as a sinus signal. The frequency $f_c$ is chosen as 1.05 Hz, which represents one of the worst case that the suspension has to handle.

$$d = z_r = \sin(2\,\pi\, f_c) \quad (cm) \tag{21}$$

- Fault scenario: abrupt fault is considered according to assumption 1.

$$f_a = \begin{cases} -6\,, & 5\,s \leq\ t \leq 10\,s \\ -4\,, & 15\,s \leq\ t \leq 20\,s \\ 0, & \text{otherwise} \end{cases} \tag{22}$$

- Variation of damping coefficient $\theta$ ($-\Delta c_0 \leq \theta \leq \Delta c_0$ as mentioned in (4)):
  - **Case 1:** $\theta$ is considered as an exponentially decreasing function, which demonstrates the uncertainty due to the mechanical degradation of damper:

$$\theta = K(e^{-0.03t} - 1) \tag{23}$$

with $K = 60\%\Delta c_0$ representing the 60% degradation comparing to the nominal value $c_0$. In other words, when $t \to \infty, \theta \to -0.6\Delta c_0$.

  - **Case 2:** $\theta$ is a sinusoid function representing high dynamics of damping coefficient, maybe caused by the temperature of fluid inside the damper.

$$\theta = K\sin(2\pi\, 5) \tag{24}$$

The analysis of both cases will allow verifying the impact of $\theta x$ on the estimation error $e_{f_a}$ in low and high frequency, mentioned in Bode diagrams Fig 3 and 4.

### 4.4 Simulation result

In Fig. 6 and Fig. 7, under the existence of road profile, the robust H∞ PI observer allows the estimation of the actuator fault with the rising time about 1 seconds.

In the case 1 (Fig. 6), due to the rise of degradation, the impact of uncertainty on estimation result increases along the simulation time course. In fact, there exists a stronger variation in the amplitude of the estimated actuator fault in the zone [15, 20] s, comparing to that of [5, 10] s. Moreover, it is worth to noting that at low frequency, only an attenuation of -40dB (0.01 in Fig.3 and Fig.4) can be achieved, so the

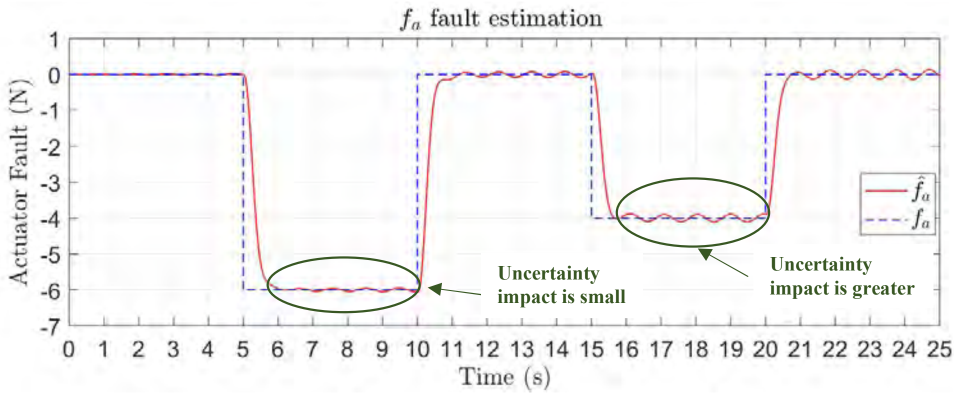


Fig. 6 Actuator fault estimation result in case 1.

amplitude of uncertainty has great impact on estimation error.

In the case 2 (Fig. 7, high frequency domain), for the sinus signal with 5 Hz, the attenuation observed in Fig. 3 and Fig. 4 reaches up to -75dB (1.8e-4). As a result, the actuator estimation get a better result with less disturbance comparing to case 1.

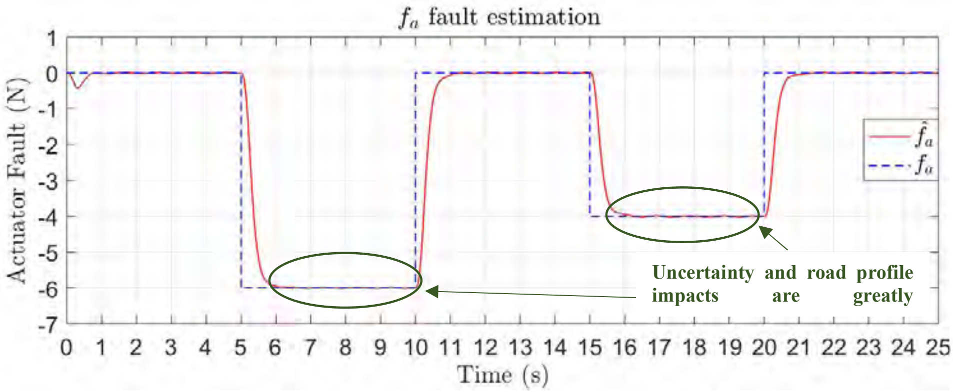


Fig. 7 Actuator fault estimation result in case 2.

In general, although the proposed method has limited estimation results due to the value of uncertainty in low frequency zone, it still works well in high frequency with great attenuation of disturbance impact on error.

## 5. CONCLUSION

By considering the uncertainty as a system disturbance, the robust H∞ PI observer not only attenuates the influence of damping coefficient's variation, but also estimates the actuator fault in suspension system. The observer design process is simple and its performance has been also been proven by the simulation result. For future work, a comparison in estimation quality between the robust H∞ PI observer and H∞ unknown input observer will be studied.

## 6. ACKNOWLEDGEMENT

The paper is supported by European project 15016, in the collaboration with GIPSA-lab, France and their partners.

## 7. REFERENCES

[1] **Jabbari, F. - Benson, R. W.:** "Observers for stabilization of systems with matched uncertainty," Dynamics and Control, vol. 2, 1992, p.303-323.

[2] **Nouailletas, R. - D. Koenig - Mendes, E.:** "LMI design of a switched observer with model uncertainty: Application to a hysteresis mechanical system," in Decision and Control, 2007 46th IEEE Conference on, 2007.

[3] **Abbaszadeh, M. - Marquez, H. J.:** "Robust H∞ observer design for a class of nonlinear uncertain systems via convex optimization," in American Control Conference, 2007. ACC'07, 2007.

[4] **Abbaszadeh, M. - Marquez, H. J.:** "LMI optimization approach to robust $H_\infty$ filtering for discrete-time nonlinear uncertain systems," in American Control Conference, 2008, 2008.

[5] **Wang, Y. - Xie, L. - Souza, C. E.:** "Robust control of a class of uncertain nonlinear systems," Systems & Control Letters, vol. 19, 1992, p.139-149.

[6] **Wojciechowski, B.:** "Analysis and synthesis of proportional-integral observers for single-input-single-output time-invariant continuous systems," Gliwice, Poland, 1978.

[7] **Shafai, B. - Carroll, R. L.:** "Design of proportional-integral observer for linear time-varying multivariable systems," in Decision and Control, 1985, 24th IEEE Conference, 1985.

[8] **Marx, B. – Koenig, D. - Georges, D.:** "Robust fault diagnosis for linear descriptor systems using proportional integral observers," in Decision and Control, 2003. Proceedings. 42nd IEEE Conference, 2003.

[9] **Do, M.H. - Koenig, D. - Theilliol, D.:** "Robust H∞ Proportional-Integral Observer for Fault Diagnosis: Application to Vehicle Suspension," IFAC-PapersOnLine, vol. 51, no. 24, pp. 536--543, 2018.

[10] **Varrier, S. - Vivas-Lopez, C. A. - Jorge de-J, L.S. - Koenig, D. J. - Martinez, J. - Morales-Menendez, R. - etr al.:** "Applicative fault tolerant control for semi-active suspension system: Preliminary results," in Control Conference (ECC), 2013 European, 2013.

[11] **Hernandez-Alcantara, D. - Tudon-Martinez, J. C. - Amézquita-Brooks, L. - Vivas-Lopez, C. A. - Morales-Menéndez, R.:** "Modeling, diagnosis and estimation of actuator faults in vehicle suspensions," Control Engineering Practice, vol. 49, 2016, p.173-186.

[12] **Nguyen, M. Q. - Sename, O. - Dugard, L.:** "Comparison of observer approaches for actuator fault estimation in semi-active suspension systems," in Control and Fault-Tolerant Systems (SysTol), 2016, 3rd Conference, 2016.

[13] **Savaresi, S. M. - Poussot-Vassal, C. - Spelta, C. - Sename, O. - Dugard, L.**: Semi-active suspension control design for vehicles, Elsevier, 2010, p. 60-68.

[14] **Do, A. L. - Da Silva, J. M. G. - Sename, O. - Dugard, L.:** "Control design for LPV systems with input saturation and state constraints: an application to a semi-active suspension," in Decision and Control and European Control Conference (CDC-ECC), 2011, 50th IEEE Conference, 2011.

[15] **Hamdi, H. - Rodrigues, M. - Mechmeche, C. - Theilliol, D. - Braiek, N. B.:** "Fault detection and isolation in linear parameter-varying descriptor systems via proportional integral observer," International journal of adaptive control and signal processing, vol. 26, 2012, p.224-240.

[16] **Isermann, R.:** Fault-diagnosis systems: an introduction from fault detection to fault tolerance, Springer Science & Business Media, 2006.

[17] **Alwi, H. - Edwards, C. - Tan, C. P.:** Fault detection and fault-tolerant control using sliding modes, Springer Science & Business Media, 2011.

[18] **Lofberg, J.:** "YALMIP: A toolbox for modeling and optimization in MATLAB," in Computer Aided Control Systems Design, 2004 IEEE International Symposium, 2004.

[19] **Sturm, J. F.:** "Using SeDuMi 1.02, a MATLAB toolbox for optimization over symmetric cones," Optimization methods and software, vol. 11, 1999, p.625-653.

[20] **Koenig, D. - Marx, B. - Varrier, S.:** "Filtering and fault estimation of descriptor switched systems," Automatica, vol. 63, 2016, p.116-121.

# H∞/LPV ACTIVE BRAKING CONTROL SYSTEM TO PREVENT ROLLOVER OF HEAVY VEHICLES

**Van Tan VU[1], Olivier SENAME[2], Luc DUGARD[2], Thanh-Phong PHAM[2], and Van Phong DINH[3]**

[1]Department of Automotive Mechanical Engineering,
University of Transport and Communications, Hanoi, Vietnam
E-mail: vvtan@utc.edu.vn
[2]Univ. Grenoble Alpes, CNRS, Grenoble INP*, GIPSA-lab, 38000 Grenoble, France
*Institute of Engineering Univ. Grenoble Alpes
E-mail: {olivier.sename, luc.dugard, thanh-phong.pham2}@gipsa-lab.grenoble-inp.fr
[3]Department of Applied Mechanics, SME, Hanoi University of Technology, Hanoi, Vietnam
E-mail: phong.dinhvan@hust.edu.vn

*Received: November 5, 2018*

## ABSTRACT

Rollover of heavy vehicles is an important road safety problem world-wide. Several active control schemes have been proposed to prevent rollover, such as active steering, active suspension, active anti-roll bars, with the active braking system being the most common method used for vehicles. In this paper, the active braking system is combined with the passive suspension system. The grid-based LPV approach is used to synthesize the $H_\infty$/LPV controller which is self-scheduled by two varying parameters: the forward velocity and the normalized load transfer at the rear axle. The parameter dependent weighting function for the lateral acceleration is used in order to allow for the vehicle performance adaptation to the risk of rollover. Simulation results are performed in the frequency domain, and emphasize the efficiency of the proposed methodology.

*Keywords:* Vehicle dynamics, Active braking control system, Rollover, $H_\infty$ control, Linear Parameter Varying (LPV) system.

## 1. INTRODUCTION

### 1.1 Context

Active Braking System (ABS) is the general concept of controlled braking on vehicles, such as Electronic Brake System (EBS), Anti-lock Braking System (ABS), Advanced Emergency Braking System (AEBS), Autonomous Emergency Braking (AEB) [1], [2]. The active braking system was introduced to the automotive industry in the 1950s with the goal to improve braking performance. For a long time, hydraulic brake systems dominated the market however the main disadvantage is the noticeable oscillation of the wheel slip around a reference value. Today, electromechanical actuators are becoming common and will most probably replace totally hydraulic brakes in the near future, along with the development of X-by-wire technology. These actuators allow the application of a smoother and continuous braking action on the brake pads [3]. The evolution of braking systems in the automotive field is well described in Fig 1. We can see that, since electronics have been integrated into vehicles, the advances in the development of active vehicle control systems have been inextricably linked to advances in sensors and actuators technology [4]. The effect of the controlled suspension is only to keep the vehicle body perpendicular to the road, since it cannot reduce the lateral tyre force component. Therefore, the role of active braking system in order to avoid the vehicle rollover situation is very important [5-7].

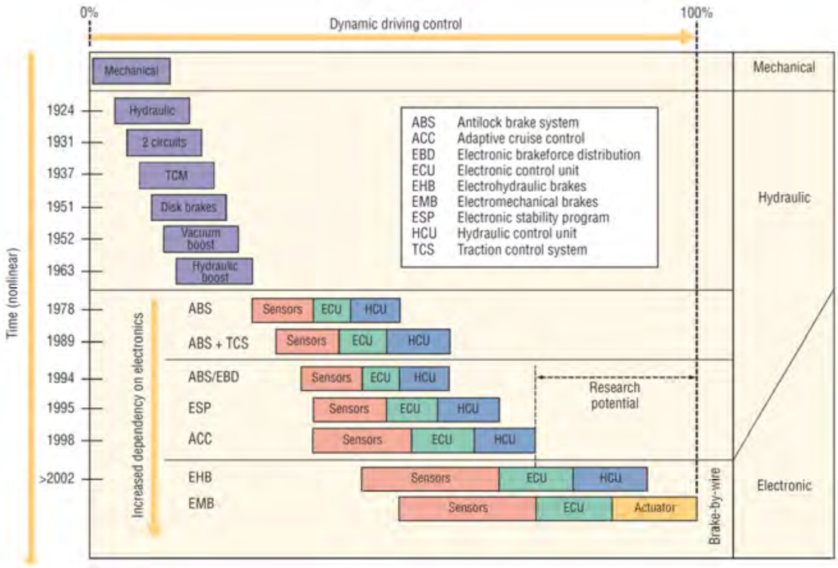


Fig. 1 The evolution of braking systems [4].

## 1.2 Related works

In the literature one can find the following references related to improved roll stability:

- In [8], a combined control structure between the active anti-roll bar system and the active braking system was proposed. The best part of this solution is that, in a normal driving situation, only the active anti-roll bar system is working and the active braking system is only activated when the vehicle comes close to a rollover situation.
- In [3], a robust control algorithm for an anti-lock brake system is proposed. The method used is based on the static-state feedback of the longitudinal slip and does not involve controller scheduling with changing vehicle speed or road adhesion coefficient estimation.

## 1.3 Paper contributions

Based on the idea in [8], here the authors would like to present preliminary research results on the active braking system with the aim of preventing the vehicle rollover phenomenon. Hence this paper contributes the following elements:

- The active braking system is designed based on the control signal being the yaw moment control, which is generated by the difference in braking force at 4 wheels. This allows the controller to be synthesized more easily than when considering the braking force at each wheel.
- The grid-based LPV approach is used to synthesize the $H_\infty$/LPV controller self-scheduled by two varying parameters: the forward velocity and the normalized load transfer at the rear axle. The parameter dependent weighting function for the lateral acceleration is used in order to allow for the vehicle performance adaptation to the risk of rollover.

The paper is organised as follows: Section 2 presents the yaw-roll model of a single unit heavy vehicle. Section 3 develops the $H_\infty$/LPV control synthesis for an active braking system to prevent rollover. Section 4 introduces the grid-based LPV approach. Section 5 presents some simulation results in the frequency domain. Finally, some conclusions are drawn in section 6.

## 2. VEHICLE MODELING

The yaw-roll model of a single unit heavy vehicle for studying the active anti-roll bar system is presented in [9]. Here, this model is suitably modified for the active braking system by using the yaw moment control $M_z$ as shown in Fig 2 [10]. The parameters and variables of the yaw-roll model are detailed in Table 1. The motion differential equations are formalized as follows:

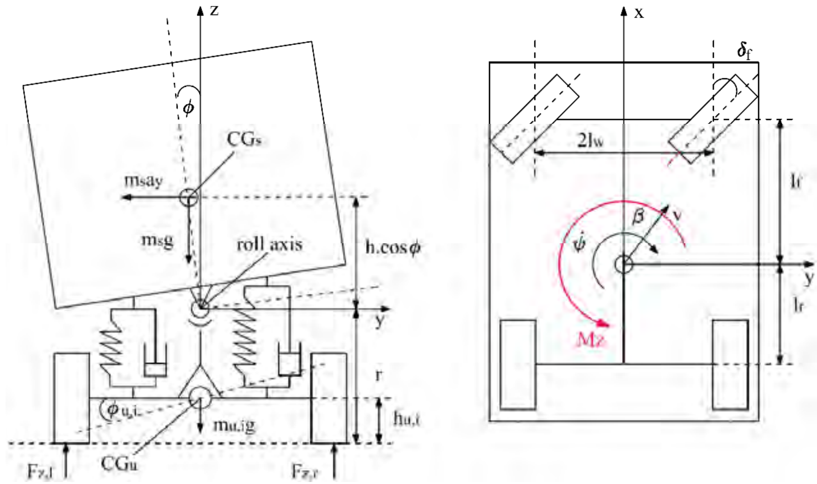


Fig. 2 Yaw-Roll model of a single unit heavy vehicle [8].

$$\begin{cases} mv(\dot{\beta}+\dot{\psi}) - m_s h \ddot{\phi} = F_{yf} + F_{yr} \\ -I_{xz}\ddot{\phi} + I_{zz}\ddot{\psi} = F_{yf} l_f - F_{yr} l_r + M_z \\ (I_{xx} + m_s h^2)\ddot{\phi} - I_{xz}\ddot{\psi} = m_s g h \phi + m_s v h(\dot{\beta}+\dot{\psi}) - k_f(\phi - \phi_{uf}) - b_f(\dot{\phi} - \dot{\phi}_{uf}) + M_{ARf} \\ \qquad - k_r(\phi - \phi_{ur}) - b_r(\dot{\phi} - \dot{\phi}_{ur}) + M_{ARr} \\ -rF_{yf} = m_{uf} v(r - h_{uf})(\dot{\beta}+\dot{\psi}) + m_{uf} g h_{uf} \phi_{uf} - k_{tf}\phi_{uf} + k_f(\phi - \phi_{uf}) + b_f(\dot{\phi} - \dot{\phi}_{uf}) + M_{ARf} \\ -rF_{yr} = m_{ur} v(r - h_{ur})(\dot{\beta}+\dot{\psi}) - m_{ur} g h_{ur} \phi_{ur} - k_{tr}\phi_{ur} + k_r(\phi - \phi_{ur}) + b_r(\dot{\phi} - \dot{\phi}_{ur}) + M_{ARr} \end{cases} \quad (1)$$

where $F_{yf,r}$ are the lateral tyre forces and $M_{ARf,r}$ the moments of the passive anti-roll bar system impact the un-sprung and sprung masses at the two axles [10].

The yaw moment control $M_z$ generated by the active braking system. The driving throttle is constant during a lateral manoeuver and the forward velocity depends only on the brake forces at the four wheels ($F_b$). The differential equation of the forward velocity is:

$$m\dot{v} = -4F_b \quad (2)$$

The motion differential equations (1)-(2) can be rewritten in the LPV state-space representation with the forward velocity as the varying parameter ($\rho_1 = v$) as follows:

$$\dot{x} = A(\rho_1).x + B_1(\rho_1).w + B_2(\rho_1).u \tag{3}$$

with the state vector $x = \begin{bmatrix} \beta & \dot{\psi} & \phi & \dot{\phi} & \phi_{uf} & \phi_{ur} & v \end{bmatrix}^T$, the exogenous disturbance $w = \begin{bmatrix} \delta_f \end{bmatrix}^T$

and the control input $u = \begin{bmatrix} M_Z \end{bmatrix}^T$.

Table 1: Variables and Parameters of the yaw-roll model [8].

| Symbols | Description | Value | Unit |
|---|---|---|---|
| $m_s$ | Sprung mass | 12487 | kg |
| $m_{u,f}$ | Unsprung mass on the front axle | 706 | kg |
| $m_{u,r}$ | Unsprung mass on the rear axle | 1000 | kg |
| $m$ | The total vehicle mass | 14193 | kg |
| $v$ | Forward velocity | - | km/h |
| $v_{wi}$ | Components of the forward velocity | - | km/h |
| $h$ | Height of CG of sprung mass from roll axis | 1.15 | m |
| $h_{u,i}$ | Height of CG of unsprung mass from ground | 0.53 | m |
| $r$ | Height of roll axis from ground | 0.83 | m |
| $a_y$ | Lateral acceleration | - | $m/s^2$ |
| $\beta$ | Side-slip angle at center of mass | - | rad |
| $\psi$ | Heading angle | - | rad |
| $\dot{\psi}$ | Yaw rate | - | rad/s |
| $\alpha$ | Side slip angle | - | rad |
| $\phi$ | Sprung mass roll angle | - | rad |
| $\phi_{u,i}$ | Unsprung mass roll angle | - | rad |
| $\delta_f$ | Steering angle | - | rad |
| $C_f$ | Tire cornering stiffness on the front axle | 582 | kN/rad |
| $C_r$ | Tire cornering stiffness on the rear axle | 783 | kN/rad |
| $k_f$ | Suspension roll stiffness on the front axle | 380 | kNm/rad |
| $k_r$ | Suspension roll stiffness on the rear axle | 684 | kNm/rad |
| $b_f$ | Suspension roll damping on the front axle | 100 | kN/rad |
| $b_r$ | Suspension roll damping on the rear axle | 100 | kN/rad |
| $k_{tf}$ | Tire roll stiffness on the front axle | 2060 | kNm/rad |
| $k_{tr}$ | Tire roll stiffness on the rear axle | 3337 | kNm/rad |
| $I_{xx}$ | Roll moment of inertia of sprung mass | 24201 | $kgm^2$ |
| $I_{xz}$ | Yaw-roll product of inertial of sprung mass | 4200 | $kgm^2$ |
| $I_{zz}$ | Yaw moment of inertia of sprung mass | 34917 | $kgm^2$ |
| $l_f$ | Length of the front axle from the CG | 1.95 | m |
| $l_r$ | Length of the rear axle from the CG | 1.54 | m |
| $l_w$ | Half of the vehicle width | 0.93 | m |
| $\mu$ | Road adhesion coefficient | 1 | - |

## 3. THE H∞/LPV SYNTHESIS FOR AN ACTIVE BRAKING SYSTEM

### 3.1. The H∞/LPV control design

In this section, the H∞/LPV control design is presented for the active braking system in heavy vehicles to prevent rollover in emergency situations. In Fig 3 the H∞/LPV control structure includes the nominal model $G(\rho_1)$, the controller $K(\rho_1, \rho_2)$, the performance output $z$, the control input $u$, the measured output $y$, and the measurement noise $n$. $\delta_f$ is the steering angle (disturbance signal), set by the driver. The measured output is $y = [a_y,\ \dot{\phi}]$. The input scaling weight $W_\delta$, chosen as $W_\delta = 0.02$. The weighting functions $W_{n1}$ and $W_{n2}$ are selected as: $W_{n1} = W_{n2} = 0.02$, which accounts for small sensor noise models in the control design.

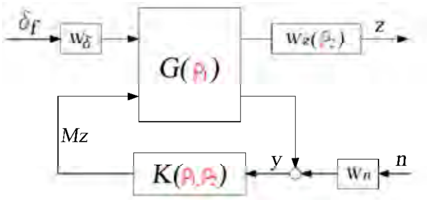


Fig. 3 Closed-loop interconnection structure of the active braking system.

The parameter dependent weighting function $W_z$ represents the performance output and is chosen as $W_z = diag\left[\dfrac{\tau_1 s+\tau_2}{\tau_3 s+\tau_4}, \rho_2 \dfrac{\zeta_1 s^2+\zeta_2 s+\zeta_3}{\zeta_4 s^2+\zeta_5 s+\zeta_6}\right]$. The purpose of this weighting function is to keep the yaw moment $M_z$ and the lateral acceleration $a_y$ as small as possible over the desired frequency range to over *4 rad/s*, which represents the limited bandwidth of the driver [8,11]. The varying parameter is defined as $\rho_2=f(|Rr|)$.

**3.2. The solution of the H$_\infty$/LPV control problem**

According to Fig 3, the concatenation of the nonlinear model (3) with the performance weighting functions has a partitioned representation in the following form:

$$\begin{bmatrix} \dot{x}(t) \\ z(t) \\ y(t) \end{bmatrix} = \begin{bmatrix} A(\rho) & B_1(\rho) & B_2(\rho) \\ C_1(\rho) & D_{11}(\rho) & D_{12}(\rho) \\ C_2(\rho) & D_{21}(\rho) & D_{22}(\rho) \end{bmatrix} \begin{bmatrix} x(t) \\ w(t) \\ u(t) \end{bmatrix} \tag{4}$$

where the exogenous input $w(t)=[\delta_f,\ n]$, the control input $u(t)=[M_z]$, the measured output vector $y = [a_y,\ \dot{\phi}]$ and the performance output vector $z(t)=[M_z\ a_y]^T$.

The LPV model of the active braking system (4) uses the varying parameters $\rho=[\rho_1;\ \rho_2]$, which are known in real time. The parameter $\rho_1= v$ is measured directly, while the parameter $\rho_2=f(|Rr|)$ can be calculated by using the measured roll angle of the unsprung mass at the rear axle $\phi_{ur}$.

## 4. THE GRID-BASED LPV APPROACH

The LPV system in the equation (10) is conceptually represented by a state-space system $S(\rho)$ that depends on a time varying parameter vector $\rho \in P_\rho$. A grid-based LPV model of this system is a collection of linearizations on a gridded domain of parameter values [12]. For general LPV systems, this conceptual representation requires storing the state-space system at an infinite number of points in the domain of $\rho$. For each grid point $\hat{\rho}_k$, there is a corresponding LTI system ($A(\hat{\rho}_k)$, $B(\hat{\rho}_k)$, $C(\hat{\rho}_k)$, $D(\hat{\rho}_k)$), which describes the dynamics of $S(\hat{\rho}_k)$ when $\hat{\rho}_k$ is held constant. It is worth noting that $\hat{\rho}_k$ represents a constant vector corresponding to the $k^{th}$ grid point, while $\rho_i$ is later used to denote the $i^{th}$ element of the vector $\rho$. All the linearized systems on the grid have identical inputs $u$, outputs $y$ and state vectors $x$. Together they form an LPV system approximation of $S(\rho)$ [13], [14].

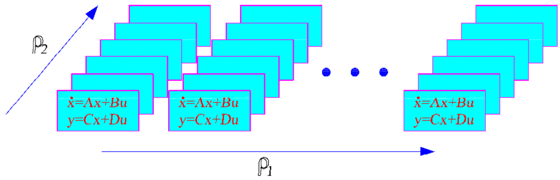


Fig. 4 LPV models defined on a rectangular grid.

The grid-based LPV approach is pictorially represented in Fig 4, with the example of such a system that depends on two parameters ($\rho_1, \rho_2$). The grid-based LPV approach approximates this conceptual representation by storing the LPV system as a state-space array defined on a finite, gridded domain. In this paper, we use the grid-based LPV approach and the LPVTools™ presented in [15] to synthesize the $H_\infty$/LPV active braking control system. It requires a gridded parameter space for the two varying parameters $\rho = [\rho_1, \rho_2]$.

The $H_\infty$ controllers are synthesized for 10 grid points of the forward velocity in the range $\rho_1 = v = [40\ km/h;\ 130\ km/h]$ and 5 grid points of the normalized load transfer at the rear axle in a range $\rho_2 = f(|Rr|) = [0;\ 1]$. The grid points and the LPV controller synthesis using LPVTools™ are expressed by the following commands:

```
rho1 = pgrid('rho1',linspace(40/3.6,130/3.6,10));
rho2 = pgrid('rho2',linspace(0,1,5));
[Klpv,normlpv] = lpvsyn(H,nmeas,ncont).
```

## 5. SIMULATION RESULTS ANALYSIS

The parameters of the yaw-roll model of a single unit heavy vehicle are detailed in Table 1. To evaluate the effectiveness of the active braking system on the prevention of vehicle rollover in the frequency domain, the two following cases will be considered as:

- **1st case:** the varying parameters $\rho_1 = v$ varies from *40 km/h* to *130 km/h* and $\rho_2 = 0.8$;
- **2nd case**: the varying parameters $\rho_2 = [0, 0.8, 1]$ varies and $\rho_1 = v = 80\ km/h$.

### 5.1 1st case: the varying parameters $\rho_1 = v$ varies from *40 km/h* to *130 km/h* and $\rho_2 = 0.8$

Vehicle rollover often occurs when the forward velocity is higher than *60 km/h*. Therefore, in this case, the authors consider the varying parameter of the forward velocity $\rho_1 = v$ from *40 km/h* to *130 km/h*, while the varying parameter $\rho_2$ is kept constant at 0.8.

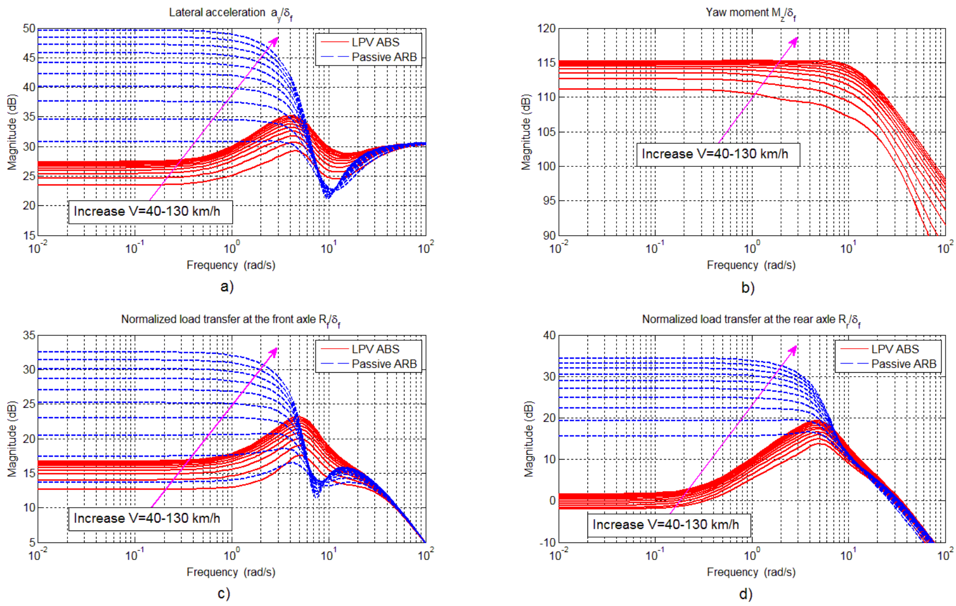


Fig. 5 1st case: transfer function magnitude of (a) the lateral acceleration $\frac{a_y}{\delta_f}$, (b) the yaw moment $\frac{M_Z}{\delta_f}$, (c, d) the normalized load transfers $\frac{R_{f,r}}{\delta_f}$ at the two axles.

The objective of the $H_\infty$/LPV active braking control design is to prevent the vehicle rollover in an emergency situation with the considered frequency range to over *4 rad/s*. Fig 5 shows the transfer function magnitude of (a) the lateral acceleration, (b) the yaw moment, and (c, d) the normalized load transfers at the two axles. We can see that the $H_\infty$/LPV active braking control system reduces significantly the lateral acceleration and the normalized load transfers in the specified frequency range. By penalizing the lateral acceleration, the lateral tyre forces are reduced, therefore the normalized load transfers are also reduced.

### 5.2 2nd case: the varying parameters $\rho_2$= [0, 0.8, 1] varies and $\rho_1$=v =80 km/h.

In this case, the forward velocity is kept constant at $\rho_1=v=80\ km/h$, while the varying parameter $\rho_2$ is surveyed at the three values: $\rho_2=0$, $\rho_2=0.8$, $\rho_2=1.0$. Fig 6 shows the simulation results in the frequency domain of the lateral acceleration, the yaw moment, as well as the normalized load transfers at the two axles. They show clearly the effect of the varying parameter $\rho_2$ to prevent vehicle rollover in the frequency range to over *4 rad/s*. When the varying parameter $\rho_2$ increases, the lateral acceleration and the normalized load transfers at the two axles decrease, which means that the active braking system can adapt to the rollover situation by increasing $\rho_2$. The reduction of the transfer function magnitude of the lateral acceleration and of the normalized load transfers when $\rho_2$= [0, 0.8, 1], compared to the passive anti-roll bar, is summarized in Table 2.

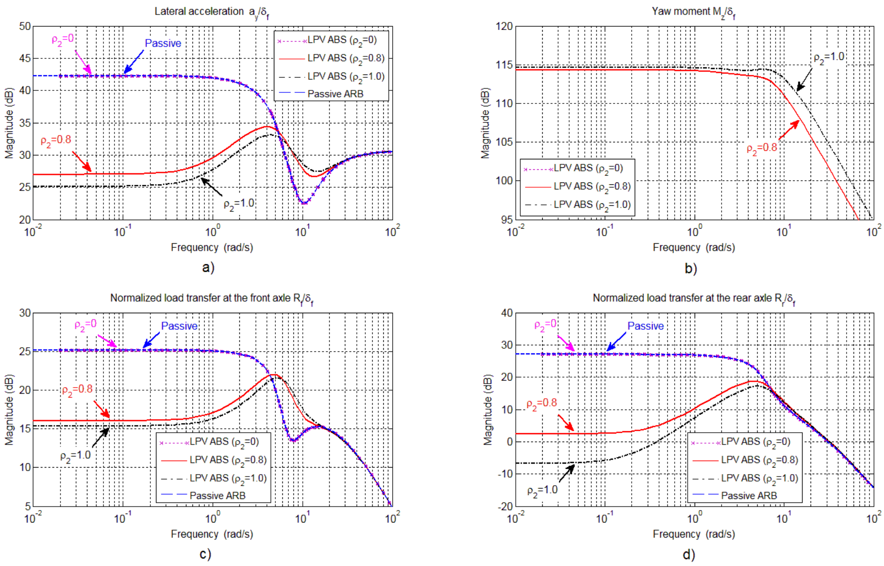


Fig. 6 2[nd] case: transfer function magnitude of (a) the lateral acceleration $\frac{a_y}{\delta_f}$, (b) the yaw moment $\frac{M_Z}{\delta_f}$, (c, d) the normalized load transfers $\frac{R_{f,r}}{\delta_f}$ at the two axles.

Table 2: Reduction of the magnitude of the transfer functions compared to the passive anti-roll bar system.

| Transfer functions | $\rho_2 = 0$ | $\rho_2 = 0.8$ | $\rho_2 = 1$ |
|---|---|---|---|
| $\frac{a_y}{\delta_f}$ | *0* | *16 dB* | *18 dB* |
| $\frac{R_f}{\delta_f}$ | *0* | *9 dB* | *10 dB* |
| $\frac{R_r}{\delta_f}$ | *0* | *25 dB* | *34 dB* |

## 6. CONCLUSIONS

This paper proposes the first preliminary results on the combination of the active braking system and the passive anti-roll bar system for a single unit heavy vehicle. The grid-based LPV approach is used to synthesize the $H_\infty$/LPV active braking controller, which is self-scheduled by two varying parameters. The parameter dependent weighting function for the lateral acceleration is used in order to allow for the vehicle performance adaptation to the risk of rollover. The simulation results in the frequency domain emphasize the efficiency of the proposed methodology.

In normal situations the active braking system is in "off" mode, but when the normalized load transfer at the rear axle reaches its limit, the active braking system will be activated, thus improving the vehicle behaviour. Hence in the future, a braking monitor will be needed in order that the $H_\infty$/LPV active braking control system will satisfy simultaneously the two objectives, which are the prevention of vehicle rollover and the increased stability at the smooth switching points.

## 7. ACKNOWLEDGEMENTS

The authors acknowledge the support of the project "Intelligent and autonomous vehicles for improving transport and road safety in Vietnam" from the French Embassy in Vietnam.

## 8. REFERENCES

[1] **Leen, G. – Donal, H.**: Expanding Automotive Electronic Systems. Computer 35(1), 2002, p.88-93.

[2] **D'alfio, N. - Morgando, A. – Sorniotti, A.:** Electro-hydraulic brake systems: design and test through hardware-in-the-loop simulation. Vehicle System Dynamics: International Journal of Vehicle Mechanics and Mobility 44(0), 2006, p.378-392.

[3] **Caglar, B. - Kose, E. - Anla, G.:** Robust control of anti-lock brake system. Vehicle System Dynamics: International Journal of Vehicle Mechanics and Mobility 45(3), 2007, p.217-232.

[4] **Savaresi, S. - Mara, T.:** Active Braking Control Systems Design for Vehicles. Springer, 2010.

[5] **Palkovics, L. - Semsey, Á. – Gerum, E.:** Roll-Over Prevention System for Commercial Vehicles - Additional Sensorless Function of the Electronic Brake System. Vehicle System Dynamics: International Journal of Vehicle Mechanics and Mobility 32(4-5), 1999, p.285-297.

[6] **Morrison, G. – Cebon, D.**: Combined emergency braking and turning of articulated heavy vehicles. Vehicle System Dynamics: International Journal of Vehicle Mechanics and Mobility 55(5), 2017, p.725-749.

[7] **Vu, V. T. - Sename, O. - Dugard, L. – Gáspár, P.:** Enhancing roll stability of heavy vehicle by LQR active anti-roll bar control using electronic servovalve hydraulic actuators. Vehicle System Dynamics: International Journal of Vehicle Mechanics and Mobility 55(9), 2017, p.1405-1429.

[8] **Gáspár, P. - Bokor, J. – Szászi, I.:** The Design of a Combined Control Structure to Prevent the Rollover of Heavy Vehicles. European Journal of Control 10(2), 2004, p.148-162.

[9] **Gáspár, P. - Bokor, J. – Szászi, I.:** Reconfigurable control structure to prevent the rollover of heavy vehicles. Control Engineering Practice 13(6), 2005, p.699-711.

[10] **Vu, V. T.:** Enhancing the roll stability of heavy vehicles by using an active anti-roll bar system. PhD thesis, University Grenoble Alpes, 2017.

[11] **David, S. – Cebon, D.:** Active Roll Control of Single Unit Heavy Road Vehicles. Vehicle System Dynamics: International Journal of Vehicle Mechanics and Mobility 40(4), 2003, p.229-270.

[12] **Arnar, H. - Seiler, P. – Packard, A.:** LPVTools: A Toolbox for Modeling, Analysis, and Synthesis of Parameter Varying Control Systems. First IFAC Workshop on Linear Parameter Varying Systems. France, 2015.

[13] **Andres, M. – Balas, G. J.:** Development of Linear-Parameter-Varying Models for Aircraft. Journal of Guidance, Control, and Dynamics 27(2), 2004, p.218-228.

[14] **Simon, H.:** Generating structured LPV-models with maximized validity region. IFAC World Congress - 19th IFAC WC 2014. Cape Town, South Africa.

[15] **Arnar, H. - Seiler, P. – Balas, G. J.:** LPV aeroservoelastic control using the LPVTools toolbox. AIAA Atmospheric Flight Mechanics. United States, 2013.

# A COMPARATIVE STUDY OF DIFFERENT NMPC SCHEMES FOR CONTROL OF SEMI-ACTIVE SUSPENSION SYSTEM

**Karthik Murali Madhavan RATHAI, Olivier SENAME and Mazen ALAMIR**

Univ. Grenoble Alpes, CNRS, Grenoble INP, GIPSA-lab,
F-38000 Grenoble, France
{karthik.murali-madhavan-rathai, olivier.sename, mazen.alamir}@gipsa-lab.grenoble-inp.fr

*Received: November 5, 2018.*

## ABSTRACT

Control of semi-active suspension system for vertical dynamics of automobiles plays a vital role in guaranteeing comfort and safety for the on-board passengers. The seemingly simple task of control poses to be daunting under the presence of multiple nonlinearities, physical constraints and specification over objective satisfaction of the system and thereby, it is of paramount importance to account for these issues during control system design for better efficiency and prolonged endurance of the suspension system. Amongst the existing several control methodologies, predictive control techniques serves as a promising approach in dealing with the aforementioned issues. In this paper, we present several nonlinear model predictive control (NMPC) schemes and a detailed performance analysis of the methods. The incorporated NMPC schemes are the direct methods – single shooting, multiple shooting and collocation methods. The different methods were tested in simulation under MATLAB environment.

*Keywords:* Vehicle dynamics, Non-linear model predictive control, Suspension systems, Optimal control

## 1. INTRODUCTION

In the recent years, study on advanced control methods for automotive systems has gained a huge momentum and most of the automotive industries has embarked in research and development and implementation of better control algorithms for improved passenger comfort and safety and as well as vehicle's performance in terms of energy efficiency, pollution reduction etc. This sudden surge in interest is partly in response to the advent of autonomous vehicles and it has also been the key driving factor for automotive companies to strive for optimal performance. Conditioned upon the aforementioned requirements both objectively and subjectively, optimal control methods fares much better than other control methods due to the systematic approach embodied in its design to tackle the above issues. In order to implement optimal control in practice, model predictive control (MPC) formulation of the optimal control problem (OCP) provides the necessary feedback control framework to work seamlessly in real-time and real-world. The crux of the MPC scheme is the receding horizon method, where an OCP is solved online at every sampling instant. Despite the enormous benefits of the method, one of the major downside is the computational requirements for solving the underlying optimization problem of the OCP at every sampling period. However, given the exponential growth of computational power and easy/cheap availability of computing resources, the chasm between the two is closing in and the method seems promising in the near future.

The main ingredients of the MPC problem are a) the objective function, b) system constraints and c) the system dynamics [1] and when any of the ingredients induce any nonlinearity, the problem is known as nonlinear MPC (NMPC). In general, the NMPC problem can be solved in three prongs which are a) Direct methods (discretize then optimize), b) Indirect methods (optimize then discretize) and c) Dynamic programming [2]. This paper utilizes the direct methods approach, however irrespective of the method adopted the problem requires a nonlinear programming (NLP) solver to deduce the optimal solution for the NMPC problem. The direct methods can be broadly classified as single shooting, multiple shooting and collocation methods. Despite the fact that all the three methods solve the same problem, the solutions sought varies due to the difference in the problem formulation. The NLP solver that yields the solution might return different local minima solution for different cases. Under special case of convex problems, the solution of all the methods tends to be the same. In this paper, the subject of focus is on a comparative study on NMPC direct methods for control of semi-active suspension system for a quarter car model. The nonlinearity is induced due to the inherent dissipativity characteristics of the semi-active damper system [3],[4].

The paper is organized as follows. Section 2 describes the mathematical model of the quarter car model equipped with semi-active suspension system. Section 3 and Section 4 details the NMPC design requirements and direct methods formulation. Section 5 expounds the simulation results obtained and finally, the paper is concluded with conclusions and future works in Section 6.

## 2. MATHEMATICAL MODELLING

The quarter-car model system equipped with semi-active suspension system shown in Fig.1 are given by the following set of equations

$$\begin{cases} \mathrm{m_s}\ddot{\mathrm{z}}_\mathrm{s} = -\mathrm{k_s}(\mathrm{z_s} - \mathrm{z_{us}}) - \mathrm{F} \\ \mathrm{m_{us}}\ddot{\mathrm{z}}_\mathrm{us} = \mathrm{k_s}(\mathrm{z_s} - \mathrm{z_{us}}) + \mathrm{F} - \mathrm{k_t}(\mathrm{z_{us}} - \mathrm{z_r}) \\ \mathrm{F} = \mathrm{f_c}\tanh\left(a_1\dot{z}_{def} + a_2 z_{def}\right)u + c_{nom}\dot{z}_{def} + k_{nom}z_{def} \end{cases} \tag{1}$$

Where, $\mathrm{m_s}$, $\mathrm{m_{us}}$, $\mathrm{k_s}$, $\mathrm{k_t}$ are the sprung mass, unsprung mass, stiffness coefficient of the suspension system and stiffness coefficient of the tyre respectively. $\mathrm{z_s}$, $\mathrm{z_{us}}$, $\mathrm{z_r}$, $\dot{z}_{def}= \dot{z}_s - \dot{z}_{us}$, $z_{def}= \mathrm{z_s} - \mathrm{z_{us}}$ are the chassis mass displacement, unsprung mass displacement, road profile displacement, deflection velocity and displacement between the chassis and the tyre respectively. The force exerted due to the suspension system is given by the Guo's [5] nonlinear equation F with $\mathrm{f_c}$, $a_1$, $a_2$, $c_{nom}$, $k_{nom}$ the appropriate parameters for the force model. The input for the system is $u$, which is the PWM duty cycle (DC) signal that drives the damper system. The nonlinear dynamics of the system is compactly expressed with $\dot{x} = f(x, u, w)$, where $x = [\mathrm{z_s}, \ \mathrm{z_{us}}, \dot{z}_s, \dot{z}_{us}]^T$, $w = \mathrm{z_r}$ the road disturbance acting on the system and $u$ is the PWM-DC signal.

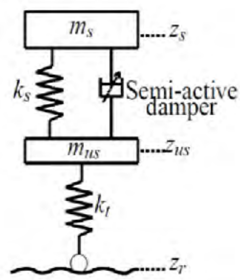


Fig.1 The quarter-car model

The parameters for the mathematical model are utilized from the INOVE test platform. The INVOVE test platform [6], shown in Fig.2 is a 1:5-scaled baja style racing car which consists of 4 controllable Electro-Rheological (ER) dampers and 4 DC motors to generate different road profiles for each wheel corner. The numerical values of the parameter are listed in the reference herein [3].

Fig. 2 INOVE test platform

## 3. NMPC DESIGN REQUIREMENTS

### 3.1 Objective requirements

In this paper, the chosen objective design for the semi-active suspension pertains to comfort objective. The prime goal of the comfort based objective design is to minimize the vertical acceleration of the chassis [7] i.e. $\ddot{z}_s$. For a given look ahead period $T_l$, the objective is defined with

$$J_{com}\big(x(t), u(t)\big) = \int_o^{T_l} l(x(t), u(t), t)dt \tag{2}$$

Where, $l(x(t), u(t), t) = (\ddot{z}_s(t))^2$ which is obtained from equation (1).

### 3.2 Constraint requirements

The constraints incorporated into NMPC problem are:

- Semi-active damper input constraint: Minimum and maximum saturation force of the semi-active damper system i.e. $|F| \leq F_{max}$.
- State constraint: Minimum and maximum stroke displacement of the suspension system i.e. $|z_{def}| \leq z_{max}$.
- PWM-DC input constraint: The PWM-DC input $u$ is constrained in the set $u \in [u_{min}, u_{max}]$.
- Road disturbance: The road profile is treated constant over the horizon i.e. $\dot{z}_r = 0$. This can be appended as an additional state variable and the augmented dynamics of the system can be expressed with $\dot{\tilde{x}} = f(\tilde{x}, u)$, where $\tilde{x} = [z_s, z_{us}, \dot{z}_s, \dot{z}_{us}, z_r]^T$.

The list of constraints can be compactly expressed with $h(\tilde{x}, u) \leq 0$ , which is the mixed nonlinear input and state constraints of the system. Thus, given the objective and the constraints of the system, the OCP to be solved at every time instant with initial condition $\tilde{x}(0)$ for the NMPC problem is defined with

$$\begin{cases} \min_{\tilde{x}(.),u(.)} J_{com}\big(\tilde{x}(t),u(t)\big) \\ \text{subject to :} \\ \tilde{x}(0)=\tilde{x}_0 \\ \dot{\tilde{x}}(t)=f\big(\tilde{x}(t),u(t)\big), t\in[0,T_l] \\ h(\tilde{x}(t),u(t)) \le 0,\ t\in[0,T_l] \end{cases} \tag{3}$$

## 4. NMPC DIRECT METHODS FORMULATION

The OCP of the NMPC scheme (3) leads to an infinite dimensional problem and it is cumbersome and in most cases it is impractical to implement. The direct methods, transcribes the problem into a finite dimensional problem, which yields an approximate solution to (3) by virtue of NLP solvers. In order to set the transcription procedure, the following assumptions are taken into consideration [8]:

### 4.1 Assumptions

- The input $u(t), \forall t \in [0, T_l]$ is finitely parameterized by piecewise constant vector $\mathcal{U}$ at an integer multiple of the sampling period $T_s$ over the horizon. With this representation, the input can be expressed with $u(t) = \mu(t, \mathcal{U})$, which is a piecewise continuous input signal.
- The dynamics (defined by the ODE in (3)) of the system is numerically simulated for the given input signal $u(t) = \mu(t, \mathcal{U})$, which is compactly expressed with $\tilde{x}(t) = \phi(t; \mathcal{U}, \tilde{x}(0))$, which is evaluated at $N$ discrete time instants $T_d = \{t_1, t_2, \dots, t_N\} \subset [0, T_l]$. The time stamps $T_d$ typically corresponds to the integer multiple of the sampling period and it is utilized to discretize the dynamics, objective function and the constraint functions listed in (3). The ODE solver utilized in this paper is a 4$^{\text{th}}$ order Runge-Kutta (RK) solver. With the aforementioned assumptions, the generic NLP framework for the direct method is expressed with

$$\begin{cases} \min_w F(w) \\ \text{subject to :} \\ G(\tilde{x}_0, w) = 0 \\ H(w) \le 0 \end{cases} \tag{4}$$

Where, $w$ is the optimization variable which depends upon the direct method formulation utilized.

**Remark 1.** The ODE solver mentioned in the assumption is to be considered as a computer code and not in terms of algebraic equations. The ODE solver is a simulator which takes the numerical input trajectory $u(t) = \mu(t, \mathcal{U})$ and outputs the numerical state trajectory which is utilized in the objective and constraint functions for the NLP problem mentioned in (4). Thus, the objective and the constraint functions is embedded with the ODE solver code and is ought to be deemed as computer codes (function code). Under conditions of twice differentiability of all the functions (codes) listed in (3), the Jacobians and Hessians for the NLP solver are numerically obtained by methods such as finite differences, algorithmic differentiation etc. [9] (also known as oracles in optimization parlance) and this information aids the optimization procedure. Thanks to MATLAB's "fmincon" routine which automatically computes the derivatives from the objective and constraint functions.

### 4.2 Direct single shooting

The direct single shooting method also known as sequential method eliminates the dynamics equality constraint in (3) by forward simulation and thus, removing the state variables from the OCP NMPC problem. This reduces the optimization problem only to the input variables $\mathcal{U}$, which is obtained from the following NLP problem.

$$\begin{cases} \min\limits_{\mathcal{U}} \sum_{k=1}^{N} l(\phi(t_k;\mathcal{U},\tilde{x}(0)),\mu(t_k,\mathcal{U}))(t_k-t_{k-1}) \\ \qquad\qquad\qquad \text{subject to :} \\ h(\phi(t_k;\mathcal{U},\tilde{x}(0)),\mu(t_k,\mathcal{U})) \le 0,\ t_k\in T_d \end{cases} \tag{5}$$

The objective is discretized by means of Riemann sum at time stamps $T_d$. The states are replaced with the ODE simulator evaluated at these time stamps in the objective as well as the constraints. The optimal solution $\mathcal{U}^*$ obtained from (5) and the first input $\mathcal{U}^*(0)$ is injected into the system and the process is repeated in receding horizon manner.

### 4.3 Direct multiple shooting

The direct multiple shooting method also known as simultaneous method retains the state variables as optimization variables and this increases the number of decision variables in the optimization formulation in (3). The ODE solver simulates the system over multiple time intervals i.e. $[t_{k-1},t_k], \forall\ k=\{1,2,\ldots,N\}$ simultaneously and the final state value $\tilde{x}(t_k)$ for the simulation in the each interval $[t_{k-1},t_k]$ is stipulated to obey the dynamics of the system, which is enforced by equality constraints. The NLP optimization problem is formulated as

$$\begin{cases} \min\limits_{\mathcal{U},\{\tilde{x}(t_1),\tilde{x}(t_2),\ldots\tilde{x}(t_N)\}} \sum_{k=1}^{N} l(\tilde{x}(t_k),\mu(t_k,\mathcal{U}))(t_k-t_{k-1}) \\ \qquad\qquad\qquad \text{subject to :} \\ h(\tilde{x}(t_k),\mu(t_k,\mathcal{U})) \le 0,\ t_k\in T_d \\ \tilde{x}(t_{k+1})-\phi(t_k;\mathcal{U},\tilde{x}(t_k))=0, t_k\in T_d \\ \tilde{x}(t_0)=\tilde{x}(0) \end{cases} \tag{6}$$

The optimal solution for the above optimization problem yields both the optimal state trajectory and optimal input sequence. As per the standard receding horizon policy, the first input $\mathcal{U}^*(0)$ is applied to the system and repeated in the future. The benefits of utilizing direct multiple shooting methods include a) Better simulator stability with unstable system, b) Parallelizability of ODE simulation, c) Structural properties of the Hessian matrices aid the optimization routine. However the flip side is that the optimization is carried out over an increased number of variables and a good initialization for the NLP solver is required for faster convergence to the optimal/sub-optimal solution (this can be ameliorated by warm start procedure).

### 4.4 Direct collocation

Direct collocation methods are extension to the simultaneous methods, where the ODE simulator is expunged from the multiple shooting formulation (6) and is replaced with algebraic equality constraints enforced at the collocation points. The optimization problem is expressed with

$$\begin{cases} \min\limits_{\mathcal{U},\{\tilde{x}(t_1),\tilde{x}(t_2),\ldots\tilde{x}(t_N)\}} \sum_{k=1}^{N} l(\tilde{x}(t_k),\mu(t_k,\mathcal{U}))(t_k - t_{k-1}) \\ \text{subject to :} \\ h\big(\tilde{x}(t_k),\mu(t_k,\mathcal{U})\big) \leq 0,\ t_k \in T_d \\ \Psi(\tilde{x}(t_{k+1}),\tilde{x}(t_k),\mu(t_k,\mathcal{U})\big) = 0,\ k = 0,\ldots,N-1 \\ \tilde{x}(t_0) = \tilde{x}(0) \end{cases} \tag{7}$$

The fundamental difference between (6) and (7) is Ψ (Implicit solver), which satisfies the dynamics of the system at the collocation points. Direct collocation methods are typically suited for stiff systems and implicit RK methods are popularly adopted in optimal control literature. This introduces additional algebraic variables which are casted as equality constraints in (7). In this paper, vis-à-vis to the system considered, trapezoid collocation method is utilized to enforce the dynamics constraints at the collocation points.

## 5.SIMULATION RESULTS

The NMPC methods were implemented in MATLAB environment and NLP solver utilized was the "fmincon" routine. The sampling period $T_s$ was chosen to be 5ms and the look ahead period $T_l$ as 15ms. The input parameterization $\mathcal{U}$ was chosen to be a constant signal over the horizon. The "fmincon" solver was set to sequential quadratic programming (SQP) mode with maximum number of Newton iteration as 3. The road profile utilized was a chirp signal with an amplitude of 2.5mm and a frequency sweep from 1Hz to 8Hz for a duration of 25s.

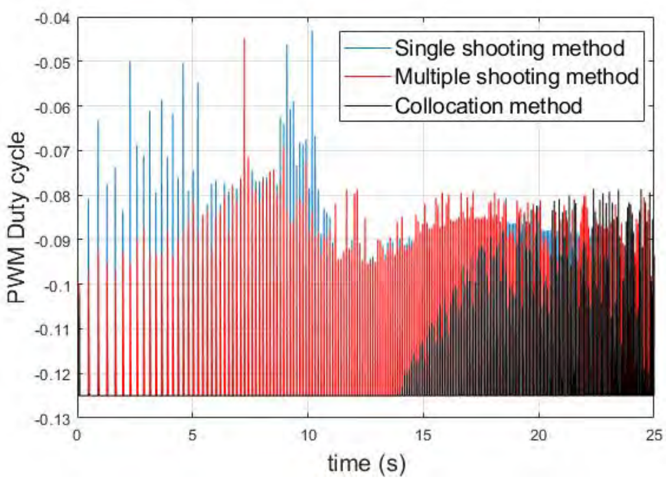


Fig. 3 PWM duty cycle input

Fig.3 displays the PWM-DC computed from the NMPC methods. Clearly, it is evident that the input profiles are not the same for the methods due to the difference in the problem formulation.

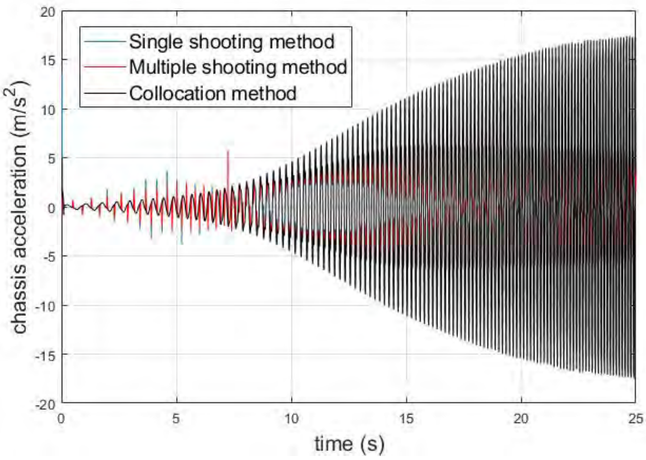


Fig. 4 Chassis acceleration $\ddot{z}_s$

Fig.4 displays the chassis acceleration for the system. From the plot is evident that the solution for the single shooting, multiple shooting and collocation method are nearly equal in performance, however the collocation method tends to be have better greater RMS value in comparison with the other two methods. However, this is subjected to choice of the collocation method utilized in the problem formulation. The RMS values of the acceleration is listed in the table Table I. The dissipativity constraints are illustrated in Fig.5.

| NMPC method | RMS value (m/s^2) |
|---|---|
| Single shooting | 6.9020 |
| Multiple shooting | 6.8808 |
| Collocation | 6.9685 |

Table I Chassis acceleration RMS values

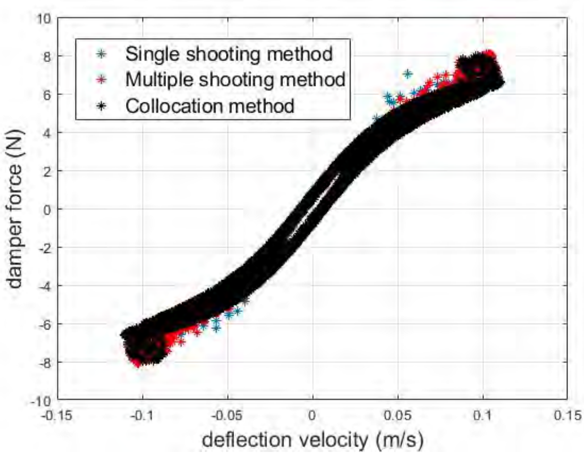


Fig. 5 Dissipativity constraint

## 6. CONCLUSION AND FUTURE WORKS

In this work, a comparative simulation study is conducted on the different popular NMPC methods and its integration with a quarter car model equipped with semi-active suspension system. The work is conducted in the spirit of learning, exploring and investigating different NMPC methods and its suitability for automotive systems. In the future works, real-time implementation of the above methods are to be conducted to validate the real-time feasibility and viability in the INOVE test platform at GIPSA-lab, Grenoble.

## 7. ACKNOWLEDGEMENT

This work was supported within the ITEA3 European project, 15016 EMPHYSIS (Embedded systems with physical models in the production code software).

## 8. REFERENCES

[1] **Mazen, A.**: Stabilization of nonlinear systems using receding-horizon control schemes: a parametrized approach for fast systems. Vol. 339. Springer, 2006.

[2] **Rawlings, J. – Blake, David Q. Mayne – Diehl, M.**: Model Predictive Control: Theory, Computation, and Design. Nob Hill Publishing, 2017.

[3] **Rathai, K. M. M. – Mazen, A. – Sename, O. – Tang, R.**: "A Parameterized NMPC Scheme for Embedded Control of Semi-active Suspension System." IFAC-PapersOnLine 51, No. 20, 2018, p.301-306.

[4] **Savaresi, S. M. – Poussot-Vassal, Ch. – Spelta, C. – Sename, O. – D ugard, L.**: Semi-active suspension control design for vehicles. Elsevier, 2010.

[5] **Shuqi, G. – Yang, Sh. – Cunzhi Pan.**: "Dynamic modeling of magnetorheological damper behaviors." Journal of Intelligent material systems and structures 17, No. 1, 2006, p.3-14.

[6] **Vivas-Lopez, C. – Hernández, D. – Nguyen, M.Q. – Fergani, S. - Buche, G. – Sename, O. – Dugard, L. – Morales-Menéndez, R.**: "INOVE: a testbench for the analysis and control of automotive vertical dynamics." Proceedings of the 14th MINI Conference on Vehicle System Dynamics, Identification and Anomalies (VSDIA 2014) (Ed. by prof. I. Zobory), BME EJJT, Budapest, 2015, p.403-413.

[7] **Rathai, K. M. M. – Sename, O. – Alamir, M.:** Reachability based model predictive control for semiactive suspension system. In Fifth Indian Control Conference (ICC) 2019, IIT Delhi, India.

[8] **Johansen, Tor A.**: "Introduction to nonlinear model predictive control and moving horizon estimation." Selected topics on constrained and nonlinear control 1, 2011, p.1-53.

[9] **Griewank, A – Walther, A.**: Evaluating derivatives: principles and techniques of algorithmic differentiation. Vol. 105. Siam, 2008.

# ENERGY AWARE CRUISE CONTROL FOR URBAN PUBLIC TRANSPORT BUSES

**Balázs VARGA**

Department of Control for Transportation and Vehicle Systems
Faculty of Transportation Engineering and Vehicle Engineering
Budapest University of Technology and Economics
Stoczek J. u. 2, H-1111 Budapest, Hungary

*Received: November 5, 2018*

## ABSTRACT

This paper presents a multi-objective velocity control scheme for electric urban public transport buses. An efficient public transport system shall balance between multiple conflicting objectives. This work focuses on two of these: timetable adherence and energy efficiency. For timetable adherence a discrete-time model is given for longitudinal bus dynamics. Then, an energy consumption model is formulated for electric public transport vehicles. The model discusses the share of resistances and the effect of recuperation. The proposed control algorithm estimates an optimal velocity profile towards the next bus stop using a distributed, shrinking horizon model predictive controller (MPC). Due to the piecewise nature of the energy consumption model, the optimization employs some heuristic search algorithms. Simulation results show that considering energy efficiency as a control objective results in smoother decelerations towards the desired bus stop.

*Keywords:* Public transport, Velocity control, Energy consumption

## 1. INTRODUCTION

Electrification of public transport buses poses as an attractive choice to minimize air pollution in cities. Electric vehicles release no local emissions, are quieter, more energy efficient and simpler, which can lead to less maintenance. Battery capacity and efficient charging are the main bottlenecks in the spread of electric public transport buses. Using them energy efficiently is vital. Eco-cruise control techniques are intensively researched: look ahead strategies are proposed to enhance energy efficiency of vehicles in [1], [2], [3]. Operating a public transport vehicle on its designated lane punctually is a fundamental demand from both the public and the service provider. There are two prominent control methods: velocity control [4] and holding [5]. With the emergence of highly automated and autonomous vehicles accurate velocity control can be achieved. This means the energy consumption of these vehicles can be significantly reduced with careful planning. The proposed shrinking horizon model predictive control algorithm selects an optimal trajectory of an electrified public transport vehicle between two stops, considering a prescribed timetable and the total energy consumed. The remainder of the paper is as follows. In the system modeling two models are proposed: i) a bus following model that describes the longitudinal motion of the bus and ii) a physical based energy consumption model. Both models are extended for a short time horizon and fit into a single objective function. In Section 3, the proposed control algorithm is tested via simulations under static conditions. Finally, Section 4 concludes the findings of this paper.

## 2. SYSTEM MODELLING

The proposed bus velocity control algorithm creates an optimal trajectory within a predefined prediction horizon, considering the schedule and the total energy consumed. To this end, two models are formulated. First, the longitudinal movement of a bus describing operations on a line is derived. The model is augmented with a reference trajectory based on an idealized schedule. Then, the shrinking horizon model predictive scheme is introduced. Next, an energy consumption model, based on the longitudinal velocity and acceleration of the vehicle is introduced, considering regenerative braking. This model is then fit into model predictive framework, resulting in a more realistic approach for penalizing control input, albeit turning the cost function into a piecewise-linear one.

### 2.1 Longitudinal bus following model

Public transport buses operate on a predefined route. The longitudinal movement along the route is characterized by the following discrete-time model:

$$x(k+1) = x(k) + v(k)\Delta t, \tag{1}$$
$$v(k+1) = v(k) + a(k)\Delta t, \tag{2}$$
$$a(k) = \frac{1}{\tau}(v_{des}(k) - v(k)), \tag{3}$$

where position $x(k+1)$ and velocity $v(k+1)$ denote the states over the period of $[k\Delta t, (k+1)\Delta t]$ with discrete time step index $k$ and sampling time $\Delta t$. $v_{des}(k)$ is the desired velocity (velocity setpoint) at time step $k$. $\tau$ is a model parameter capturing the sensitivity of vehicles to the change of their desired velocity. According to [6] it shall be calibrated between $1.25\ s$ and $2.5\ s$. Too small values would result in unrealistic acceleration or deceleration towards the desired velocity. The proposed model can be rewritten into state-space form $X(k+1) = AX(k) + Bu(k)$ with $v_{des}(k)$ being the controlled variable:

$$\begin{bmatrix} v(k+1) \\ x(k+1) \end{bmatrix} = \begin{bmatrix} 1 - \frac{\Delta t}{\tau} & 0 \\ \Delta t & 1 \end{bmatrix} \begin{bmatrix} v(k) \\ x(k) \end{bmatrix} + \begin{bmatrix} \frac{\Delta t}{\tau} \\ 0 \end{bmatrix} v_{des}(k). \tag{4}$$

Timetable tracking is incorporated into the model via an additional error term $z_{tt}(k+1) = \mathrm{CX(k)} + r(k)$.

$$z_{tt}(k+1) = \begin{bmatrix} 0 & -1 \end{bmatrix} \begin{bmatrix} v(k) \\ x(k) \end{bmatrix} + x_{ref}(k), \tag{5}$$

where $x_{ref}(k)$ is an idealised reference trajectory based on the timetable of the bus. The timetable is a set of points in the time-space diagram (i.e. the bus shall be at a given stop at a given time). The reference trajectory (in time-space) between each stop is a straight line, however, these intermittent points are not used by the controller.

The control-oriented model is used as basis of a shrinking horizon model predictive controller. The goal of the controller is calculating an optimal velocity profile along its route in an energy efficient way.

### 2.2 Timetable tracking cost function

The shrinking horizon MPC prediction length depends on the scheduled travel time to the next bus stop. The interval between the actual $t_0$ and the desired arrival time to the next stop $t_{ETA}$ is split into $N$ equidistant time samples, see Fig. 1. In every time step the prediction horizon decreases by one. By the last time step the bus shall arrive at the desired stop. To avoid small or even negative horizon lengths (due to lateness or being close to the stop) the horizon length is bounded by a lower bound $N_{min} = 5$.

$$N = \min\left\{N_{min}, \frac{t_{ETA}-t_0}{\Delta t}\right\}. \tag{6}$$

Next, the vehicle dynamics model in Eq. (4) and the error term in Eq. (5) are extended for $N$ horizon length.

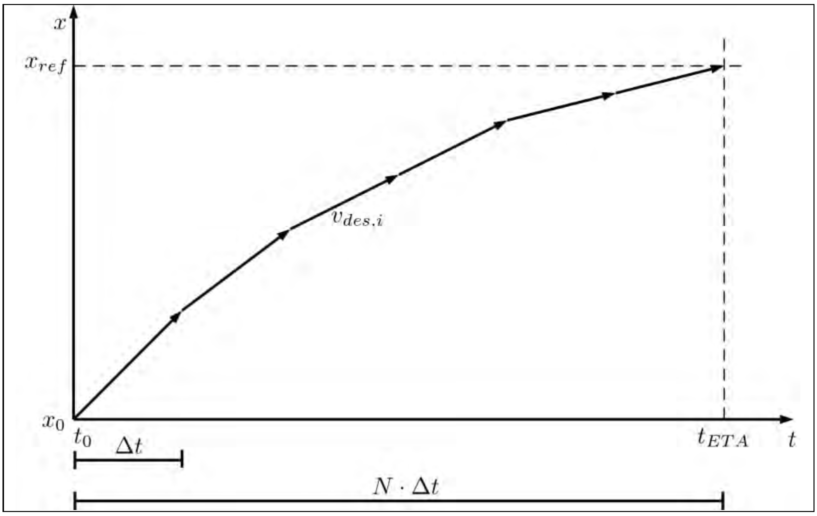


Fig. 1 MPC horizon length calculation

$$x(k) = \mathcal{A}X(k) + \mathcal{B}u(k) =$$
$$= \begin{bmatrix} X(k+1|k) \\ X(k+2|k) \\ \vdots \\ X(k+N|k) \end{bmatrix} = \begin{bmatrix} A \\ A^2 \\ \vdots \\ A^N \end{bmatrix} X(k) + \begin{bmatrix} B & 0 & \cdots & 0 \\ AB & B & & 0 \\ \vdots & \vdots & \ddots & \vdots \\ A^{N-1}B & A^{N-2}B & \cdots & B \end{bmatrix} \begin{bmatrix} u(k|k) \\ u(k+1|k) \\ \vdots \\ u(k+N-1|k) \end{bmatrix}, \tag{7}$$

$$z_{tt}(k) = \mathcal{C}x(k) + \mathcal{D}r(k) =$$
$$\begin{bmatrix} z_{tt}(k+1|k) \\ z_{tt}(k+2|k) \\ \vdots \\ z_{tt}(k+N|k) \end{bmatrix} = \begin{bmatrix} C & 0 & \cdots & 0 \\ 0 & C & & 0 \\ \vdots & \vdots & \ddots & \vdots \\ 0 & 0 & \cdots & C \end{bmatrix} x(k) + \begin{bmatrix} 1 & 0 & \cdots & 0 \\ 0 & 1 & & 0 \\ \vdots & \vdots & \ddots & \vdots \\ 0 & 0 & \cdots & 1 \end{bmatrix} \begin{bmatrix} r(k|k) \\ r(k+1|k) \\ \vdots \\ r(k+N-1|k) \end{bmatrix}. \tag{8}$$

The cost function to be minimised in the optimisation is sought in the following quadratic form:

$$J(k) = \frac{1}{2}\left(z_{tt}(k)Qz_{tt}(k) + u(k)Ru(k)\right), \tag{9}$$

where $z_{tt}(k)$ is the predicted error between the actual and the reference trajectory of the bus. $u(k)$ is the control input at every time iteration. $Q$ and $R$ are weighting matrices, penalizing the deviation from the reference and the magnitude of the control input, respectively. The state vector $x(k)$ does not appear directly in the cost function

Eq. (9). By inserting Eq. (7) into Eq. (8) and performing some algebraic reformulations, the cost function in Eq. (9) turns into:

$$J_{tt}(k) = \frac{1}{2}\mathcal{u}^T(\mathcal{B}^T\mathcal{C}^T Q\mathcal{C}\mathcal{B} + R)\mathcal{u} + (X^T\mathcal{A}^T\mathcal{C}^T Q\mathcal{C}\mathcal{B} + \mathcal{r}^T(k)\mathcal{D}^T Q\mathcal{C}\mathcal{B})\mathcal{u}, \quad (10)$$

subject to:

$$|z_{tt}(k+N|k)| < \varepsilon, \quad (11)$$

$$v_{min} < v_{des}(k) < v_{max}. \quad (12)$$

Eq. (11) suggests that the bus shall be at the next bus stop (within a small $\varepsilon$ range) by the last time step $N$. As an additional constraint for the optimization, it is assumed that the control input is limited (Eq. (12)): the lower limit $v_{min} = 0\frac{km}{h}$, since negative velocity is not allowed, $v_{max} = 50\frac{km}{h}$ is the legal speed limit on the link.

## 2.3 Energy consumption model

Next, an energy consumption model is formulated for electric vehicles with regenerative braking. The model considers the share of resistances and the power needed to accelerate in every time step $k$ as well as the recuperated energy during braking [7]. The power at the wheels $P_w(k)$ consists of five terms:

$$P_w(k) = P_r(k) + P_g(k) + P_d(k) + P_a(k) + P_b(k). \quad (13)$$

In the followings, the meaning of each loss is discussed.

- $P_r(k)$ is the rolling resistance.

  $$P_r(k) = \mu\, m\, g \cos(\theta)\, v(k), \quad (14)$$

  where $m = 18000\ kg$ is the total vehicle mass, $g = 9.81\frac{m}{s^2}$ is the gravitational constant, $\mu = 0.01$ is the rolling resistance factor, $\theta$ is the road inclination and $v(k)$ is the instantenous velocity of the vehicle.
- $P_g(k)$ is the extra power required when driving uphill or downhill.

  $$P_g(k) = m\, g \sin(\theta)\, v(k). \quad (15)$$
- $P_d(k)$ is the power to overcome the air drag.

  $$P_d(k) = \frac{1}{2}\, c_w\, \rho\, A_f v^3(k), \quad (16)$$

  where $c_w = 0.6$ is the drag coefficient, $\rho = 1.293\frac{kg}{m^3}$ is the density of air and $A_f = 8.2\ \mathrm{m}^2$ is the face area of the vehicle.
- $P_a(k)$ is the power to accelerate.

  $$P_a(k) = m\, v(k)\, a^+(k). \quad (17)$$

  For convenience, acceleration and deceleration are distinguished with $a^+(k)$ and $a^-(k)$, respectively.
- $P_b(k)$ is the power regenerated during braking.

  $$P_b(k) = m\, v(k)\, a^-(k)\, \eta_{reg}, \quad (18)$$

  where $\eta_{reg}$ is the efficiency of regenerative braking. Its value greatly varies on the intensity of braking, i.e. the usage of friction brakes.

Next, the drivetrain losses are analysed. Fig. 2. depicts the losses of an electric powertrain. The efficiency at each stage of the powertrain is summarised in Table 1.

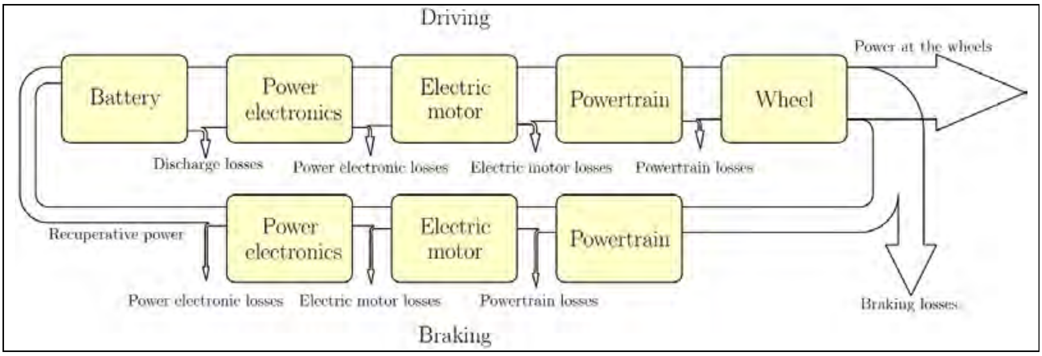


Fig. 2 Sankey diagram of an electric powertrain

| | | |
|---|---|---|
| Battery discharge efficiency | $\eta_{batt}$ | 93 % |
| Power electronics efficiency | $\eta_{pe}$ | 97 % |
| Electric motor efficiency | $\eta_{mot}$ | 95 % |
| Mechanical efficiency | $\eta_{pt}$ | 98 % |
| Regeneration efficiency | $\eta_{reg}$ | 50 % |

Table 1. Powertrain efficiencies

The power to move the vehicle for time step $k$ equals:

$$P(k) = \frac{P_r(k)+P_g(k)+P_d(k)+P_a(k)}{\eta_{batt}\cdot\eta_{pe}\cdot\eta_{mot}\cdot\eta_{pt}} + P_b(k)\cdot\eta_{batt}\cdot\eta_{pe}\cdot\eta_{mot}\cdot\eta_{pt}. \tag{19}$$

The total energy consumption along the prediction horizon is $E(k) = \sum_{k=1}^{N} P(k)$.

## 2.4 Energy aware cost function

The next aim is to reformulate the model in Eq. (19) such that it can be fit into a cost function to penalize energy consumption of the vehicle along its route. In Eq. (19) only $P_a(k)$ and $P_b(k)$ are functions of the control input $v_{des}(k)$ through the acceleration as in Eq. (3). The other terms are independent from $v_{des}(k)$, they only offset the cost and can be omitted. Weighting the cost function is much easier when only the most significant terms (i.e. acceleration and deceleration) are left. Weighting the total energy consumption would work towards slowing down the bus as lower velocity means lower energy consumption. On the other hand, weighting acceleration directly penalises rapid accelerations and decelerations which is the most significant portion of energy consumption.

Let's couple the efficiencies together as $\eta_a = \eta_{batt}\eta_{pe}\eta_{mot}\eta_{pt}$ and $\eta_b = \eta_{batt}\eta_{pe}\eta_{mot}\eta_{pt}\eta_{reg}$ and substitute Eq. (3) into Eq. (17) and Eq. (18).

$$P_a{}'(k) = -\frac{mv^2(k)}{\tau\,\eta_a} + \frac{mv(k)}{\tau\,\eta_a}v_{des}(k), \tag{20}$$

$$P_b{}'(k) = -\frac{\eta_b mv^2(k)}{\tau} + \frac{\eta_b mv(k)}{\tau}v_{des}(k). \tag{21}$$

Eq. (20) and Eq. (21) are linear functions of $v_{des}(k)$ and the independent parts can be omitted. Extending $P_a'(k)$ and $P_b'(k)$ to $N$ horizon results in the total energy consumed or regenerated as:

$$E_a(k) = \frac{m}{\tau\,\eta_a} u^T(k) S x(k), \tag{22}$$

$$E_b(k) = \frac{m\,\eta_b}{\tau} u^T(k) S x(k), \tag{23}$$

where $S$ is a row selector matrix for the velocity $v(k)$ over the prediction horizon: $S = diag\{[1 \quad 0] \dots [1 \quad 0]\}$. Note that $x(k)$ contains only the predicted velocities and not the actual one. Therefore $S$ shall be shifted left. Next, insert $x(k) = \mathcal{A}X(k) + \mathcal{B}u(k)$ into Eq. (22) and Eq. (23) and introduce $K_a = \frac{m}{\tau\,\eta_a} S$ and $K_b = \frac{m\,\eta_v}{\tau} S$.

$$E_a(k) = u^T(k) K_a \mathcal{A} X(k) + u^T(k) K_a \mathcal{B} u(k), \tag{24}$$

$$E_b(k) = u^T(k) K_b \mathcal{A} X(k) + u^T(k) K_b \mathcal{B} u(k). \tag{25}$$

The power to accelerate and the regenerated power are quadratic polynomials of the control input $u(k)$. To obtain a cost function, introduce weighting coefficients $W_a$, $W_b$, $V_a$, $V_b$.

$$J_e^+(k) = u^T(k) K_a \mathcal{B} W_a u(k) + X^T(k) \mathcal{A}^T K_a^T V_a u(k), \tag{26}$$

$$J_e^-(k) = u^T(k) K_b \mathcal{B} W_b u(k) + X^T(k) \mathcal{A}^T K_b^T V_b u(k), \tag{27}$$

For the sake of simplicity, the selection between $J_e^+(k)$ and $J_e^-(k)$is depending on the acceleration or deceleration (the relation of $v(k)$ and $v_{des}(k)$) at every iteration at time step. The piecewise quadratic cost function can be written as follows:

$$\min_u \begin{cases} J_e^+(k) & if\ v(k+i|k) \le v_{des}(k+i|k) \\ J_e^-(k) & if\ v(k+i|k) > v_{des}(k+i|k) \end{cases}, \quad \forall i \in [1..N], \tag{28}$$

subject to:

$$a_{min} \le \frac{1}{\tau}\left(v_{des}(k) - v(k)\right) \le a_{max}\,. \tag{29}$$

The acceleration and deceleration are bounded by $a_{min}$ and $a_{max}$ to avoid physically infeasible values.

Finally, resulting cost function becomes

$$J(k) = J_{tt}(k) + J_e(k). \tag{30}$$

$J_e(k)$ is piecewise due to the separation of acceleration and deceleration. This turns the optimisation into a non-smooth problem which can be solved with a variety of optimisation tools, in this example sequential quadratic programming (SQP) method is chosen [8]. The free parameter in the optimization is the desired velocity of the bus.

## 3. SIMULATION RESULTS

The proposed control algorithm is tested from two aspects. First, the shape of a predicted trajectory is analysed from a static point in space-time. Then, the total energy saving achieved by the control algorithm is concluded.

In the first simulation the vehicle predicts $60\,sec$ ahead, and the next stop is $450\,m$ away. A timetable tracking strategy – where only $J_{tt}$ is considered – is compared to the energy aware control (Fig. 3.). If energy cost is not considered, the accelerations and decelerations are steeper, and the vehicle accelerates to the maximum velocity. Since the timetable is not tight, it waits with the departure from the stop. In a realistic scenario it would be highly undesirable, since the prediction does not consider future obstacles such as a traffic light or a slower vehicle ahead. This strategy shall be augmented with an additional constraint to rather wait at the next stop instead of in the previous one. If energy consumption is costed, velocity profiles become smoother, with a long coasting phase before the stop. The prediction utilizes the long time between the two stops and arrives just in time. If the vehicle is slowed down by some obstacle it still can correct the prediction in the next time step and arrive on time.

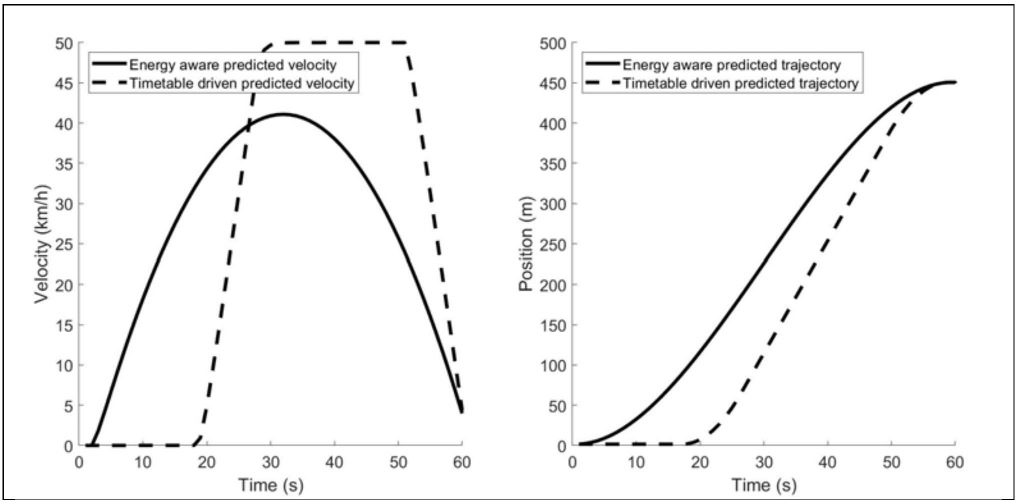


Fig. 3 Velocity and trajectory prediction from a fixed point

Taking energy consumption into account when planning the vehicle's trajectory results in 19,8% energy saving. It is achieved by smoother accelerations and the exploitation of regenerative braking. In realistic scenarios, however, this improvement is much modest, since several disturbances act on the vehicle and it cannot exactly follow the prescribed profile. In addition, due to the nature of the MPC controller, only the first time-step is used as control input, the rest is discarded.

## 4. CONCLUSIONS

This paper presented a velocity control algorithm to drive public transport buses between stops in an energy efficient way. With the help of a linear bus following model and an energy consumption model for electric vehicles with regenerative braking, a model predictive controller was formulated. The energy consumption model is based on the longitudinal motion of the vehicle and considers the share of resistances and efficiencies in the drivetrain. The piecewise linear (in the control input) model leads to an objective function penalizing rapid accelerations and encouraging long coasting phases before coming to a stop. Simulation results suggest that significant energy saving can be achieved by planning the trajectory of the vehicle ahead.

## 5. ACKNOWLEDGEMENTS

The research reported in this paper was supported by the Higher Education Excellence Program of the Ministry of Human Capacities in the frame of Artificial Intelligence research area of Budapest University of Technology and Economics (BME FIKPMI/FM)

## 6. REFERENCES

[1] **Mihály, A. – Németh, B. – Gáspár, P.**: Real-time Look-ahead Cruise Control Simulator. Periodica Polytechnica Transportation Engineering. Vol 46 (1), 2018, p.11-16.

[2] **Hellström, E. – Åslund, J. – Nielsen, N.**: Design of an efficient algorithm for fuel-efficient look-ahead control. Control Engineering Practice. Vol 18 (11), 2010, p.1318-1327.

[3] **Basso, R. – Lindroth, P. – Kulcsár, B. – Egart, B.**: Traffic aware electric vehicle routing. IEEE 19th International Conference on Intelligent Transportation Systems (ITSC). 2016, p.416-421.

[4] **Varga, B. – Tettamanti, T. – Kulcsár, B.**: Optimally combined headway and timetable reliable public transport system. Transportation Research Part C: Emerging Technologies, Vol. 92, 2018, p.1-26.

[5] **Xuan, Y. – Argote, J. – Daganzo, C. F.:** Dynamic bus holding strategies for schedule reliability: Optimal linear control and performance analysis. Transportation Research Part B: Methodological. Vol 45 (10), 2011, p.1831-1845.

[6] **Helbing, D. – Tilch, B.**: Generalized force model of traffic dynamics. Physical Review E, 58(133), 1998, p.1-6.

[7] **Guzzella, L. – Sciarretta, A. – et. al.**: Vehicle Propulsion Systems. Vol. 3, Springer-Verlag, Berlin, 2013.

[8] **Nocedal, J. – Wright, S. J.**: Numerical Optimization. Springer-Verlag, New York, 2006.

# CONTROL AND DECISION METHOD FOR OVERTAKING PROBLEM IN AUTONOMOUS VEHICLES

**Tamás HEGEDŰS*, Balázs NÉMETH** and Zsuzsanna BEDE***

*Department of Control for Transportation and Vehicle Systems
Faculty of Transportation Engineering and Vehicle Engineering
Budapest University of Technology and Economics
Stoczek utca. 2, H-1111 Budapest, Hungary

**Systems and Control Laboratory
Institute for Computer Science and Control
Kende utca 13-17, H-1111 Budapest, Hungary

*Received: November 6, 2018*

## ABSTRACT

In this paper we deal with an overtaking and lane change strategy for autonomous vehicles. The algorithm is divided into two main layers. The upper layer is responsible for the decision making (e.g lane changing). Before decision-making we predict the motion of other participants and divide the road into discrete sets in each interval, then we compute the probability of occupancy. Considering the state of the motion of ego vehicle we can compute the probability of collision. After assigning a graph points to discrete elements, the probability of collision is ordered to the graph edges, then we determine the route with the smallest cost. The decision-making algorithm is not able to control the vehicle, so it is necessary to design a traceable trajectory for the vehicle. Since we have a series of points to be reached for the future, this can be used as a reference vector for the trajectory design algorithm. One Model Predicitve Controller (MPC) is responsible for the design of the trajectory so we can obtain limitations to several states to ensure comfort and security. Extending the algorithm, we can compute the longitudinal movement as well. In this paper the decision-making and the trajectory planning algorithm is presented, and the whole model validated in CarMaker.

*Keywords*: autonomous, overtaking, line change maneuver, motion prediction

## 1. INTRODUCTION

Overtaking maneuvers are maybe the most dangerous maneuvers among autonomous vehicles. During controlling the vehicle, we must pay attention to number of things simultaneously, such as accelerations of the vehicles, pedestrians movement etc. First, we estimate the motion of the surrounding vehicles, using this information we can predict the future position of the other participants. Because of the rapidly changing traffic conditions the prediction process could be difficult and inaccurate. In the next step collision free overtaking trajectory is planned, which has to fulfill several requirements, the most important is not to endanger the own and the other participants safety. Besides the safety requirements the comfort is highly important for the passengers, so several factors must be limited, such as longitudinal/lateral accelerations.

In the recent years, several different approaches have been developed for the design of overtaking trajectories. The minimization of lateral jerk using polynomial equations presented in [1]. In [2] can be seen a collision free overtaking trajectory planning using Model Predictive Control (MPC). A nonlinear adaptive control method is proposed in [3] has an advantage, that unnecessary the exact knowledge about the other vehicle. The movement prediction of other participants is closely related with the design of overtaking trajectory [4]. Estimation of the future environment is necessary in decision-making process (e.g. line changing).

Many different methods have been developed to make prediction as accurate as possible, such as Dynamic Bayesian Networks [5] and Markov chain models [6]. According to another approach, the prediction is based on past similarities using the pre-recorded data [7]. In this paper, one method is presented which is able to evaluate the given traffic situation and make a decision about the next maneuver. After the decision making we can generate the reference vector and using one Model Predictive Control (MPC) we can compute the optimal input signal considering the given limitations.

## 2. MOTION PREDICTION AND DECISION MAKING

In case the vehicles are equipped with Vehicle-to-Vehicle communication technology information about their states can be sent easily to each other. However, based on this data the next maneuver cannot be determined because of the rapidly changing traffic conditions. Therefore, we used the probability-based method to determine the future position of the vehicles. The longitudinal and the lateral prediction are computed separately and finally combined.

*Longitudinal prediction*

Since, the driver can change the velocity of the vehicle all the time, we must consider the possible acceleration values. We perform the prediction in the given T time horizon, which is divided into equidistant *n* time sets. Using it, future positions can be computed of the surrounding vehicles, for every time step. Assuming Gaussian distribution the probability density function reads:

$$f_{long}(x) = \frac{1}{\sigma\sqrt{2\pi}} e^{\frac{-(x-\mu)^2}{2\sigma^2}}. \tag{1}$$

Where the mean values are $\mu_i = v_0 t_i$. Defining the standard deviation, the possible acceleration/deceleration values can be considered. $a_{possible} \in [a_{min}, a_{max}]$ assuming $|a_{min}| = |a_{max}|$. Thus the future positions of the vehicle can be computed for every time step, for the given interval. The longitudinal steps are defined as $s_i = t_i v$.

$$P_{long}(s_i, s_j) = \int_{s_i}^{s_j} f_{long}(x\,)dx. \tag{2}$$

*Lateral prediction*

In the average traffic condition beside the speed, the lateral position of the vehicle can be changed. In the following, the lane changing maneuver is modelled using four clothoid segments with similar parameters.

The maneuver can be characterized by the lateral acceleration because it includes the velocity of the vehicle, and the actual radius of the trajectory. Determining the $y$ projection of the trajectory in addition of the given lateral accelerations where $a_{lat}$ varies between 0.1 … 4.6 $m/s^2$. The initial velocity set to 25 $m/s$ and the length of the segment is 250m. The trajectories approximated with linear functions (Fig. 1).

In the following, probabilities are assigned for each acceleration values, but first the probability density function has to be determined. The probability of the lateral movement of the vehicle can be described by Gamma-distribution function as in [11].

$$f(x, \alpha, \beta) = \frac{\beta^{\alpha} x^{\alpha-1} e^{-\beta x}}{\Gamma(\alpha)} . \qquad (3)$$

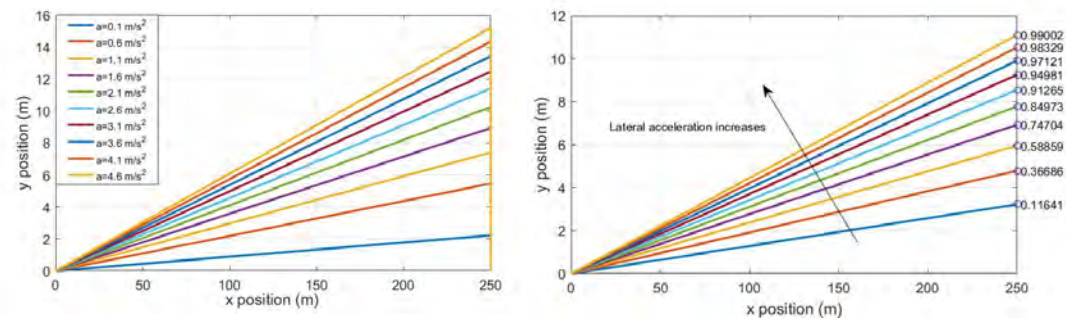


Fig. 1 (a) Trajectories with different lateral accelerations.
(b) Lateral acceleration with probabilities

The values of $\alpha = 2,\ \beta = 2.8$ are fixed and the values are set to satisfy the comfort level of the passengers [8]. Using the above-mentioned function, the probability can be computed between two given lateral acceleration values.

$$P_{lat}(a_{lat,min}, a_{lat,max}) = \int_{a_{lat,min}}^{a_{lat,max}} f_{lat}(x)dx \qquad (4)$$

Since the relationship between the lateral acceleration and the lateral position have been already computed (Fig. 1) the probabilities can be expressed between two lateral position as

$$P_{lat}(y_{min}, y_{max}) = \int_{y_{min}}^{y_{max}} f_{lat}(x)dx \qquad (5)$$

Fig. 1. b. shows the probability values on the right side. This probability values are computed between zero and the given accelerations. The lateral displacement ($y$) is divided into N equidistant sets. $y_i = y_s n,\quad n = 1 \dots N$ where $y_s = \frac{y}{N}$. Using the acceleration values, the probabilities for lateral positions can be computed.

*Combining probabilities*

In this section the predictions are combined. The most important step is to determine the probability of the start of the overtaking, which is achieved through sigmoid-function [10].

$$P_{over}(\lambda) = \frac{1}{1 + e^{-m\lambda}}, \qquad where\ \ \lambda = \frac{v_{prev} - v_0}{d} \qquad (6)$$

Where $d$ is the distance between the cars, $v_{prev}$ closer, and $v_0$ is the velocity of further car. The typical overtaking time gap is 1.5 s [9], the $m$ parameter is set to 1.5, so when the value of $\lambda$ is 1.5, the probability will be high enough. The sigmoid function determines the willingness of overtake when the $\lambda = 0$, this means that the velocity of the two vehicles are similar, the probability of overtaking is 50%. If $\lambda$ increases, the willingness increasing as well, while if $\lambda < 0$ the willingness decreases. Using these the prediction map can be computed.

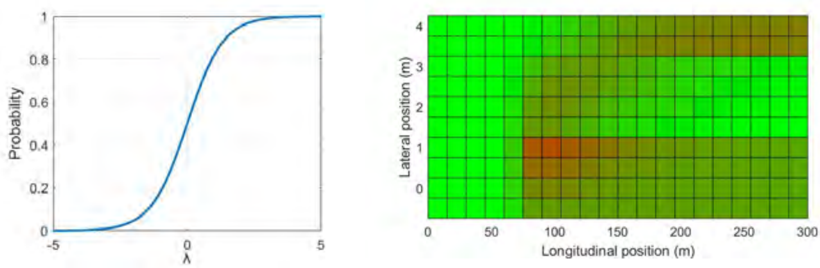


Fig. 2 (a) Sigmoid function, (b) Prediction map

Fig. 2 b shows the result of the prediction. The velocity of ego vehicle is 28 m/s and the velocity of the car in front is 26 m/s. The distance between them 16 m, and the overtaking willingness is 50 %. The main purpose of the decision-making algorithm is to guarantee the collision free trajectory. One graph point was assigned to every area element then the points are connected, considering the possible movement of the vehicle. In the next step weights of the edges are determined based on the probabilities of the prediction map, to solve the optimization problem, Dijkstra algorithm is used [12]. This algorithm provides the reference vector for the control layer in the following.

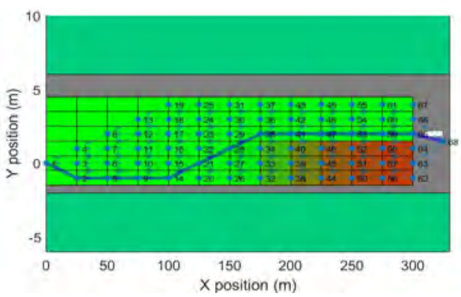


Fig. 3 Example for decision making

## 3. SIMULATION

The simulation was made using CarMaker, where the following traffic situation was defined. The reference vector is not suitable for controlling the vehicle, therefore a MPC is used for longitudinal control and another one for lateral control. The input vector of the control layer is the reference vector introduced before, using that the optimal solution is calculated. The first input signal is used then the whole process repeats. Fig. 4 shows the initial conditions where the reference velocity is 20 m/s. The velocities of the surrounding vehicles were constant during the simulation. In this simulation the prediction horizon is set to 50, and the sample time to 0.1s.

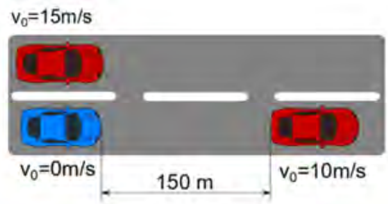


Fig. 4 Simulation situation

The simulation was run in case of parallel traffic conditions where in addition the controlled vehicle two other vehicles participated.

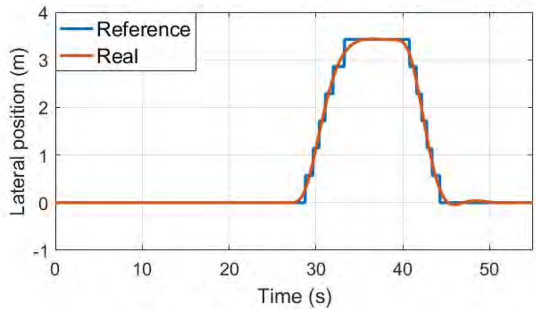


Fig. 5 Lateral position of the controlled vehicle

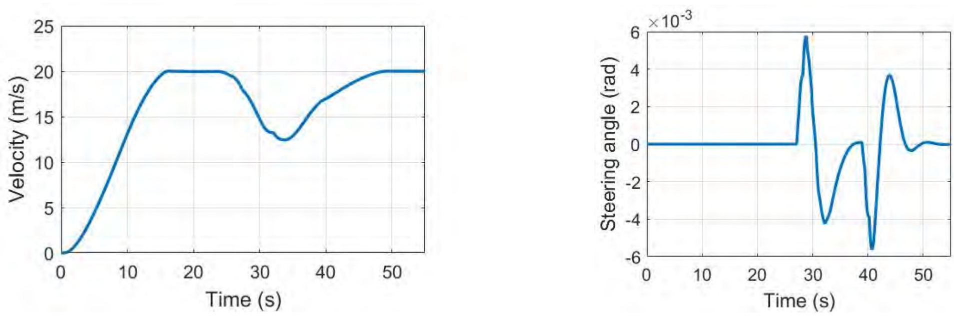


Figure. 6 (a) velocity, (b) steering angle during simulation

As Fig. 5 presents, the blue line is computed by graph-based decision-making algorithm, and the red one is the real trajectory. As it was mentioned, the reference vector is not suitable for controlling the vehicle since the result of decision making process is limited to some discrete values. During the simulation the vehicle reached the allowed velocity then slowed down due to traffic conditions, this can be seen in Fig. 6.

## 4. CONCLUSION

In this paper the graph-based decision-making method was presented where the edge weights of the directed graph were computed using the prediction probabilities. The reference route and velocity vector were determined using one greedy algorithm. The control of the vehicle was MPC based strategy, where given limitation for the acceleration and velocity was considered.

Since the motion of surrounding vehicles is involved in the trajectory planning, collision free route can be computed.

## 5. ACKNOWLEDGEMENT

The research was supported by the Hungarian Government and co-financed by the European Social Fund through the project "Talent management in autonomous vehicle control technologies" (EFOP-3.6.3-VEKOP-16-2017-00001).

The research reported in this paper was also supported by the Higher Education Excellence Program of the Ministry of Human Capacities in the frame of Artificial Intelligence research area of Budapest University of Technology and Economics (BME FIKPMI/FM).

The work of *Balázs Nemeth* was partially supported by the János Bolyai Research Scholarship of the Hungarian Academy of Sciences and the and the ÚNKP-18-4 New National Excellence Program of the Ministry of Human Capacities.

## 6. REFERENCES

[1] **Shamir, T.:** How should an autonomous vehicle overtake a slower moving vehicle: design and analysis of an optimal trajectory, IEEE Transactions on Automatic Control, vol. 49, no. 4, April 2004, p.607–610.

[2] **Berntorp, K.**: Path planning and integrated collision avoidance for autonomous vehicles, in 2017 American Control Conference (ACC), May 2017, p.4023–4028.

[3] **Petrov, P. – Nashashibi, F.:** Modeling and nonlinear adaptive control for autonomous vehicle overtaking, IEEE Transactions on Intelligent Transportation Systems, vol. 15, no. 4, Aug 2014, p.1643–1656.

[4] **Carvalho, A. - Lef´evre, S. - Schildbach, G. - Kong, J. – Borrelli, F.:** Automated driving: The role of forecasts and uncertainty - A control perspective, European Journal of Control, vol. 24, 2015, p.14–32.

[5] **Gindele, T. - Brechtel, S. – Dillmann, R.:** A probabilistic model for estimating driver behaviors and vehicle trajectories in traffic environments, in 13th International IEEE Conference on Intelligent Transportation Systems, Sept 2010, p.1625–1631.

[6] **Althoff, M. - Mergel, A.:** Comparison of markov chain abstraction and monte carlo simulation for the safety assessment of Autonomous cars, IEEE Transactions on Intelligent Transportation Systems, vol. 12, no. 4, Dec 2011, p.1237–1247.

[7**] Okamoto, K. - Berntorp, K. - Cairano, S. D.:** Similarity-based vehicle-motion prediction, American Control Conference (ACC), May 2017, p.303–308.

[8] **Xu, J. - Yang, K. - Shao, YM. - Lu,GY.:** An Experimental Study on Lateral Acceleration of Cars in Different Environments in Sichuan**,** China, 2014.

[9] **Farah, H. - Bekhor, S. - Polus, A. – Toledo, T.:** A passing car acceptance model for two-lane rural highways, Israel Institute of Technology, Haifa, 2009.

[10] **Wissing, C. - Nattermann, T. - Glander, K.H. - Hass, C. – Bertram, T.:** Lane Change Prediction by Combining Movement and Situation based Probabilites, TU Dortmund University, 2017.

[11] **Mahapatra, G. – Kumar, A.:** Dynamic Parameters of Vehicles under Heterogeneous Traffic Stream with No Lane Discipline: An Experimental Study, Department of Civil Engineering, Indian Institute of Technology Guwahati, India, 2018.

[12] **Tsitsiklis, J. N.**: Efficient algorithms for globally optimal trajectories, IEEE Transactions on Automatic Control, 40(9, Sep 1995, p.1528-1538.

# HARDWARE IN THE LOOP TEST SYSTEM FOR TEACHING MODEL BASED DESIGN FOR AUTOMOTIVE CONTROL

**János PAPP and Gergely BÁRI**

Department of Vehicle Technologies
John von Neumann University
H-6000 Kecskemét, Hungary

*Received: November 9, 2018.*

## ABSTRACT

This paper introduces a Hardware in the Loop (HiL) test environment, which is developed for teaching undergraduate vehicle engineers. The aim was to extend the lectures with experiences gained, while solving a practical problem based project. The task for the student is to develop a gearshift mechanism automation system. This has to be done with model-based design, using V-model methodology, with low level and vehicle level simulation, and in real time hardware simulation environment as well. The students have a limited time to absolve this task, so the developed hardware and software package is designed to help them spend the highest possible amount of time on the high level design, and get experience with the methodology. The developed system consist of a gear shifter mechanism with linear actuators with sensor feedback to be able to design and test a controller. This is controlled via a fast prototyping hardware solution. This controller is integrated to a real time vehicle HiL test system. With this project one can learn top-down design, control algorithm design, component and system simulation practices. Our aim was to have a project, which is enough for a thesis for a bachelor degree. For the minimum allowed level of completion is achievable for a student with lack of knowledge at the beginning. A motivated student with higher approach can work on it more easily, because the task have many levels of depth to it. For example, after one have low fidelity models and rough estimation of the real system, one can find ways to improve it. In addition, one can find different field of interest and work more with that, for example actuator modelling, control software design or vehicle simulation. We also modified a regular serial car to be able to accommodate this system. We set a reward for the students to keep them motivated during the whole duration. If the developed system meets minimum requirements, one can demonstrate in simulation, and in HiL testing all functionality, than it can be put inside the car, and can be tested in real life. Students participated in this project, gained a lot of knowledge in the mentioned topics and proved the project's worthiness in education.

*Keywords:* Hardware in the Loop testing, model based design, teaching design methods

## 1. INTRODUCTION

Vehicles complexity nowdays are increasing in a rapid paste, and in the future this trend with the automation of the driver will continue. For those who are designing these systems it is a rapidly transforming world too. The field of desciplines needed for these task are spreading out. Engineers with multidisciplinary knowledge are needed for the industry. The vehicle engineering field is one of this example. To address this need we think teaching design processes of automotive control is very important.

Modern vehicle systems have to comply with a large set of requirement, for example regulatory standards. From the economic perspective, these have to be cost effective and to be designed in the shortest time possible. Acomplising these simulatanously is proved to be a very difficult task [1]. We can use model based design, which is well suited for these task, thus they are widely used in the automitve industry [2].

For this, we want to prepare vehicle engineering students to be able to work effectivle in these environments. We would like to give them practical knowledge and opportunity to practise these desgin processes, which are required for independent work. For this we designed projects for students, and with this the need is risen for an environment to design the software and hardvare part of the tasks. Further along the task requirements, and the built system will be shown.

## 2. PROJECT REQUIREMENTS

The project, in this case the theses, for vehicle enginering student has multiple objectives. Firstly, we would like to show the basics of model based design. For designing models and complex systems the V-modell design methodolgy is used in the industry. This has advantages that it helps to keep track of the project, and the need for testing is visually well represented [3] as you can see on Fig. 1.

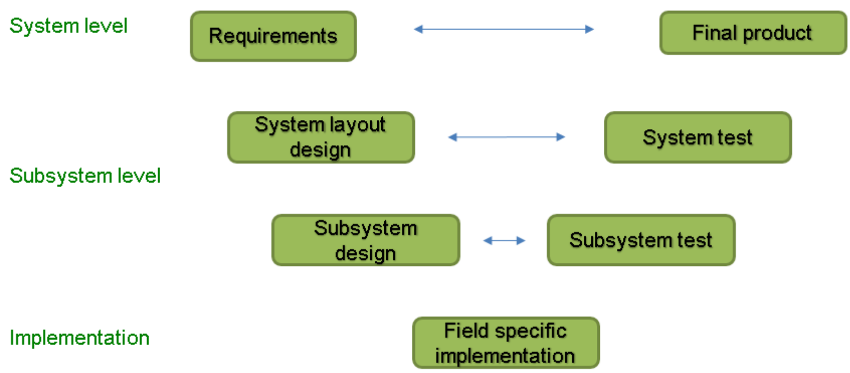


Fig. 1 V-modell

Designing a complex system, in most cases have a control unit, with a software [4]. These have to be thorougly tested, which is a huge challenge. Using the V-modell methodogy we can devide the problems to subtasks and test them on muliple levels [3]. Secondly, be practical and close to real world challenges as possible. Thirdly we would like to avoid deep rooted problems in other fields than vehicle engineering, such as design and manufacturing an electric system.

We suggest the requirements below for these objectives:

Hardware part
- Basic 3D CAD designing
- Building a simple-cheap hardware

Software part
- Easy control problems in high level programming software
- Use rapid prototype systems

Multilayer design
- Testable system
- Several iteration of the V-model
- Design, implement, test repeat several times

avoid not the above in scope of vehicle engineering

## 3. TEACHING ENVIRONMENT

Hardware in the Loop (HiL for short) test systems help design and test processes [5]. We can see a detailed description of a complex system in [6]. With this, we can test subsystems in different combination, with different levels of simulation. For this project we designed and built a HiL test system to acomplish the requirements mentioned above. This system is made of several units. We use linear actuators with DC motors to actuate a manual gearbox in a passenger vehicle as plant.

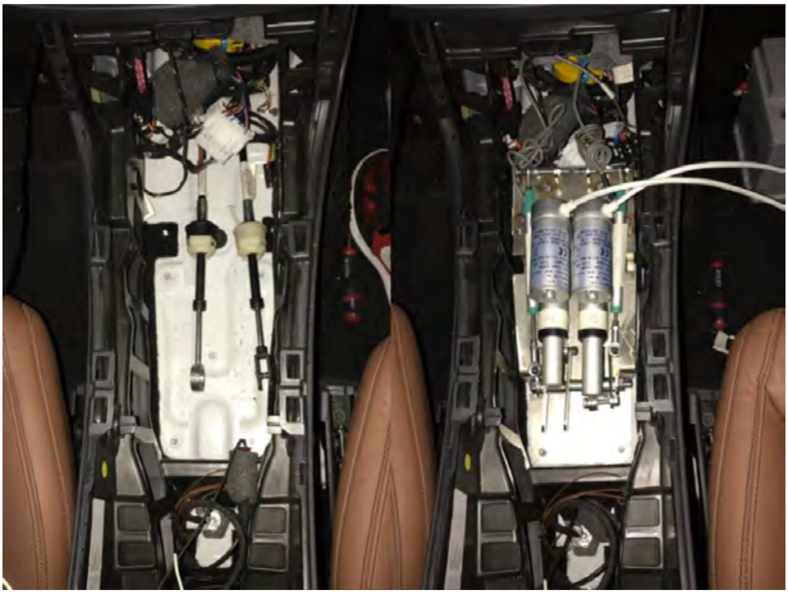

Fig. 2 Automation of Manual Gearbox

The actuators are driven by the dSpace RapidPro unit [7]. With RapidPro hardware we can control relays, DC motors, AC motors. We can implement a PWM control loop as well for more precise control. This device is connected to a dSpace MicroAutobox II [8] (Electronic Control Unit, ECU) device that can run any Matlab / Simulink [9] model, which is a high level language and useful for practise system level design. The output of this device controls the motor drive electronics, measures the motor current, the voltage, and the status of the transmission control via linear potentiometers. It is possible to create a closed-loop control or to create a higher level of complex logic required for the operation of the manual gerabox. This system can be installed and tested by a student in a real vehicle. The device is also integrated with an additional system. This system extends a Vehicle Dynamic Simulation with Inmotion node from IPG [11], which can execute real time simulation, this have several interfaces that are very usefull.

Testing the control algorithm on different levels is possible with this system. Firstly desktop simulation with Simulink (Level 1). After successful demonstration of the models and controls, the student can advance further with deploying the control software to the ECU (Level 2). Using vehicle simulations for the dinamics as well as the control algorithm and plant model in IPG Carmaker software [10] (3 Level). Than

Level 4, with full system control software with the real plant, with closed loop control with full vehicle simulation. Finally, Level 5 is in real vehicle with protype hardware and software, and testing the vehicle with hardware and software in real test cases.
The important part is: one can understand the needs for testing, and after every level a vaidation have to done, which can be fed back to the design process. Succesfully completing a level is necessary for advancing further, so it gives feedback also to the student, and keeps them motivated during the whole project. You can see the different levels and correspondent hardware (dark gray), and software component in (light gray) on Fig. 3.

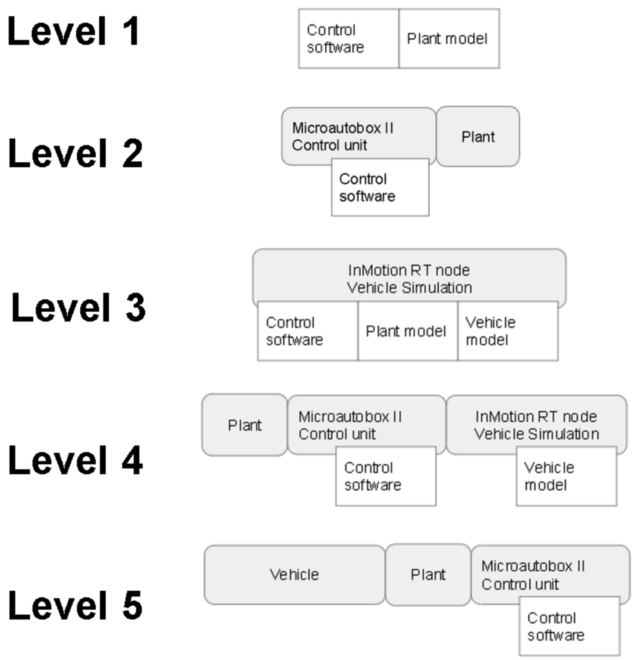


Fig. 3 Test system levels

## 4. TECHING ENVIRONMENT TEST

We tried two projects with this environment. First was a vehicle electrifacation project, where a power management module with the ECU was desgined and implemented. Second project was manual gearbox automation, which lead to the project description for the student thesis. During these example projects the necessary cable harnesses, and interface software components are made. The students for their projects only got the environment and not the completed projects examples.

## 5. CONCLUSION

We set out requirements for a teaching environment to help the education of model based design for automotive control tasks. We built the environment and tested with example projects. Until now only two student got a task similar to what we mentioned above. Only the second one used this completed environment. We saw in their work and thesis that we achieved these goal. In the future we would like to advance this further to a subject for broader audience, as well as collecting more objective feedback analysing the effects of using this environment.

## 6. ACKNOWLEDGMENTS

The research presented in this paper was carried out as part of the EFOP-3.6.2-16-2017-00016 project in the framework of the New Széchenyi Plan. The completion of this project is funded by the European Union and co-financed by the European Social Fund.

## 7. REFERENCES

[1] **Pelliccione, P. - Knauss, E. - Heldal, R. - Magnus Ågren, S. - Mallozzi, P. - Alminger, A. - Borgentun, D.:** Automotive Architecture Framework: The experience of Volvo Cars, Journal of Systems Architecture, Volume 77, 2017, Pages 83-100, ISSN 1383-7621, https://doi.org/10.1016/j.sysarc.2017.02.005.

[2] **Oestersötebier, F. - Abrishamchian, F. - Lankeit, Ch. - Just, V. - Trächtler, A.:** Approach for an Integrated Model-based Design of Intelligent Dynamic Systems Using Solution and System Knowledge, Procedia Technology, Volume 26, 2016, Pages 436-446, ISSN 2212-0173, https://doi.org/10.1016/j.protcy.2016.08.056.

[3] **Ohata, A. - Butts, K. R.:** Improving Model-based Design for Automotive Control Systems Development, IFAC Proceedings Volumes, Volume 41, Issue 2, 2008, p. 1062-1065, ISSN 1474-6670, ISBN 9783902661005, https://doi.org/10.3182/20080706-5-KR-1001.00182.

[4] **Kumar, P. – Jegan, A.:** Systematic Approach in V-Model Development Cycle for an Automotive Embedded Control System, Journal of Advance in Electronic and Electric Engineering. ISSN 2231-1297, Vol.3, No.4, 2015, p.465-470.

[5] **Chen, X. - Salem, M. - Das, T. - Chen, X.:** (2008). Real Time Software-in-the-Loop Simulation for Control Performance Validation. Simulation. 84, p.457-471. 10.1177/0037549708097420.

[6] **Soltani, A. - Assadian, F.:** A Hardware-in-the-Loop Facility for Integrated Vehicle Dynamics Control System Design and Validation, IFAC-PapersOnLine, Volume 49, Issue 21, 2016, p.32-38, ISSN 2405-8963, https://doi.org/ 10.1016/ j.ifacol.2016.10.5

[7] RapidPro harver, https://www.dspace.com/en/pub/home/products/hw/rapidpro.cfm

[8] MicroAutoBox II hardver, https://www.dspace.com/en/pub/home/ products/hw/ micautob.cfm

[9] Mathworks Matlab Simulink softver, https://www.mathworks.com/products/ simulink.html

[10] IPG Automotive, Carmaker softver, https://ipg-automotive.com/products-services/simulation-software/ carmaker/

[11] IPG Automotive, InMotion RT node hardver, https://ipg-automotive.com/ products-services/real-time-hardware/ xpack4-technology/

# REAL-TIME ESTIMATION OF THE DAMPING FORCE OF VEHICLE ELECTRORHEOLOGICAL SUSPENSION

**Thanh-Phong PHAM[a,b], Olivier SENAME[a], Luc DUGARD[a] and Van Tan VU[c]**

[a] Univ. Grenoble Alpes, CNRS, Grenoble INP, GIPSA-lab, 38000 Grenoble, France
[b] Faculty of Electrical and Electronic Engineering,
University of Technology and Education,
The University of Danang, 550000 Danang, Vietnam
[c] Department of Automotive Mechanical Engineering,
University of Transport and Communications, Hanoi, Vietnam
*thanh-phong.pham2@gipsa-lab.grenoble-inp.fr*
*olivier.sename@gipsa-lab.fr*
*luc.dugard@gipsa-lab.fr*
*vvtan@utc.edu.vn*

*Received: November 5, 2018*

## ABSTRACT

The real-time estimation of damper force plays key role for control and diagnosis of suspension systems for road vehicles. In this paper, we consider a semi-active electrorheological (ER) suspension system. First, a nonlinear quarter-car model is proposed using the dynamic nonlinear model of ER damper. The estimation of the damper force is developed through a $H_2$ observer whose objective is to minimize the effects of bounded unknown road profile disturbances and measurement noises on the estimation errors of the state variables. Finally, the observer performances are assessed experimentally using the INOVE platform from GIPSA-lab (1/5-scaled real vehicle). Both simulation and experimental results illustrates the effectiveness of proposed observer in the ability of estimating the damper force in real-time.

*Keywords:* Semi-active suspension, automotive systems, $H_2$ observer, damper force estimation

## 1. INTRODUCTION

Over the years, semi-active suspensions are now widely used in vehicle applications due to their advantages compared to active and passive suspensions ([1] and references therein). Main issues concern the design of control algorithms based on a reduced number of sensors to improve passenger's comfort and road holding. Many control approaches were proposed in the literature (see [2] [3] and a review in [4]). Some control design methodologies considered the damper force as the control input of the suspension system, then using an inverse model for the implementation (see for instance [5], [6]). Other authors use force tracking control schemes in order to attain control objectives (see [3]). Indeed, the damper force signal plays an important role in control synthesis.

Therefore, damper force estimation methodologies were proposed (see [7], [8], [9], [10], [11]), tackling difficult and expensive damper force measurement in practice. In [10], parallel *Kalman* filters were developed to estimate the damper force without considering the dynamic behavior of the semi-active damper. Authors in [7] presented the $H_\infty$ damper force observer using a dynamic nonlinear model of the ER damper. Moreover, in [9], authors introduced an LPV-$H_\infty$ filter to estimate the damping force using deflection and deflection velocity signals. As well, based on accelerometers, a full-car observer using the linearized model of the damper was proposed in [12] and gave interesting results both simulations and experiments. Despite these achievements, the damping force observer based on the dynamic nonlinear model of semi-active ER suspension system, is still an open problem.

In this paper, an $H_2$ observer is proposed in order to estimate the damper force in the presence of unknown road profile input and measurement noises. The design of the observer is based on a nonlinear suspension model consisting of a quarter-car vehicle model, augmented with a first order dynamical nonlinear damper model. The contributions of this paper are the following:

- An $H_2$ observer is designed to estimate the damper force, minimizing the effect of unknown disturbances on the estimation error.
- The observer is implemented on a 1/5 scaled vehicle test-bench. Both simulation and experimental results illustrate the efficiency of the algorithm.

The paper is organized as follows. Firstly, the quarter-car system modeling is presented in section 2. The central part of this paper, namely, the observer design, is detailed in section 3. To demonstrate the effectiveness of the observer, the simulation and experiment works are given in the section 4. The conclusion is finally drawn in section 5.

## 2. QUARTER-CAR SYSTEM MODELLING

This section introduces the quarter-car model equipped with a semi-active ER suspension system as shown in the Figure 1.

First, a phenomenological model considering the dynamic and nonlinear characteristic of semi-active ER damper is illustrated. Based on *Guo*'s model, the dynamic nonlinear model of ER damper is represented as follows:

$$\begin{cases} F_d = k_0 x_d + c_0 \dot{x}_d + F_{ER} \\ \tau \dot{F}_{ER} + F_{ER} = f_c . u_{nl} \end{cases} \tag{1}$$

where $u_{nl} = u.\tanh\left(k_1\, \hat{x}_d + c_1 \dot{\hat{x}}_d\right)$; $u$ is the duty cycle of the PWM signal; $k_0$, $k_1$, $c_0$, $c_1$, $f_c$, $\tau$ , the parameters of the model (1) are shown in Table 1.

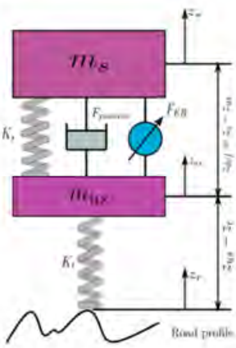


Fig. 1 Quarter-car model with semi-active suspension

Second, the well-known quarter model consists of the sprung mass ($m_s$), the unsprung mass ($m_{us}$), the suspension components located between $m_s$ and $m_{us}$ and the tire which is modelled as a spring with stiffness ($k_t$). As depicted in Fig. 1, by applying the second law of Newton for motion, the system dynamics around the equilibrium are given as:

$$\begin{cases} m_s \ddot{z}_s = -F_s - F_d \\ m_{us} \ddot{z}_{us} = F_s + F_d - F_t \end{cases} \tag{2}$$

where $F_s = k_s(z_s - z_{us})$ is the spring force, $F_t = k_t(z_{us} - z_r)$ is the tire force, and the damper force $F_d$ is given as in (1) with $x_d = z_s - z_{us}$

Replacing (1) into (2), one obtains

$$\begin{cases} m_s\ddot{z}_s = -(k_s + k_0)(z_s - z_{us}) - c_0(\dot{z}_s - \dot{z}_{us}) - F_{ER} \\ m_{us}\ddot{z}_{us} = (k_s + k_0)(z_s - z_{us}) + c_0(\dot{z}_s - \dot{z}_{us}) + F_{ER} - k_t(z_{us} - z_r) \\ \dot{F}_{ER} = -\frac{1}{\tau}F_{ER} + \frac{f_c}{\tau}u_{nl} \end{cases} \tag{3}$$

where $z_s$ and $z_{us}$ are the displacements of the sprung and unsprung masses, respectively and $z_r$ is the road profile input.

By selecting the system states as $x = [x_1, x_2, x_3, x_4, x_5]^T = [z_s - z_{us}, \dot{z}_s, z_{us} - z_r, \dot{z}_{us}, F_{ER}]^T$ and the measured outputs as $y = [\ddot{z}_s, \ddot{z}_{us}]^T$, the state-space representation of the system dynamics (3) is as follows

$$\begin{cases} \dot{x} = Ax + Bu_{nl} + D_1\omega \\ y = Cx + D_2\omega \end{cases} \tag{4}$$

where $A = \begin{bmatrix} 0 & 1 & 0 & -1 & 0 \\ -\frac{k_0+k_s}{m_s} & -\frac{c_0}{m_s} & 0 & \frac{c_0}{m_s} & -\frac{1}{m_s} \\ 0 & 0 & 0 & 1 & 0 \\ -\frac{k_0+k_s}{m_{us}} & \frac{c_0}{m_{us}} & -\frac{k_t}{m_{us}} & -\frac{c_0}{m_{us}} & \frac{1}{m_{us}} \\ 0 & 0 & 0 & 0 & -\frac{1}{\tau} \end{bmatrix}$, $B = \begin{bmatrix} 0 \\ 0 \\ 0 \\ 0 \\ \frac{f_c}{\tau} \end{bmatrix}$,

$C = \begin{bmatrix} -\frac{k_0+k_s}{m_s} & -\frac{c_0}{m_s} & 0 & \frac{c_0}{m_s} & -\frac{1}{m_s} \\ -\frac{k_0+k_s}{m_{us}} & \frac{c_0}{m_{us}} & -\frac{k_t}{m_{us}} & -\frac{c_0}{m_{us}} & \frac{1}{m_{us}} \end{bmatrix}$, $D_1 = \begin{bmatrix} 0 & 0 \\ 0 & 0 \\ -1 & 0 \\ 0 & 0 \\ 0 & 0 \end{bmatrix}$, $D_2 = \begin{bmatrix} 0 & 0.01 \\ 0 & 0.01 \end{bmatrix}$,

$\omega = \begin{pmatrix} \dot{z}_r \\ n \end{pmatrix}$, where $\dot{z}_r$ is road profile derivative and $n$ is measurement noises

Table 1: Parameter values of the quarter-car model equipped with an ER damper

| Parameter | Description | value | Unit |
|---|---|---|---|
| $m_s$ | Sprung mass | 2.27 | kg |
| $m_{us}$ | unsprung mass | 0.25 | kg |
| $k_s$ | Spring stiffness | 1396 | N/m |
| $k_t$ | Tire stiffness | 12270 | N/m |
| $k_0$ | Passive damper stiffness coefficient | 170.4 | N/m |
| $c_0$ | Viscous damping coefficient | 68.83 | N.s/m |
| $k_1$ | Hysteresis coefficient due to displacement | 218.16 | N.s/m |
| $c_1$ | Hysteresis coefficient due to velocity | 21 | N.s/m |
| $f_c$ | Dynamic yield force of ER fluid | 28.07 | N |
| τ | Time constant | 43 | ms |

## 3. OBSERVER DESIGN

In this section, an $H_2$ observer is developed to estimate the damping force. The unknown input ω (which includes the road profile disturbance and the sensor noises) is considered as an unknown disturbance. Therefore, an $H_2$ observer is proposed to minimize the effect of this unknown disturbance on the state estimation error $(x - \hat{x})$.
The $H_2$ observer for the quarter-car system (4) is of the following form:

$$\dot{\hat{x}} = Ax + L(y - C\hat{x}) + B\hat{u}_{nl} \ , \tag{5}$$

where $\hat{x}$ is the estimated state vector. The observer gain $L$ is determined in the next steps
The state estimation error is defined as:

$$e(t) = x(t) - \hat{x}(t) \ . \tag{6}$$

Differentiating $e(t)$ with respect to time leads to

$$\dot{e} = \dot{x} - \dot{\hat{x}} = (A - LC)e + (D_1 - LD_2)\omega \quad . \tag{7}$$

Let $T_{e\omega}(s) = \big(sI - (A - LC)\big)^{-1}W$ be the transfer function between state estimation error $e$ and the unknown disturbance $\omega$. The $H_2$ observer design objective is as follows:

- The system (7) is stable for $\omega = 0$ (8)
- $\|T_{e\omega}(s)\|_2$ is minimized for $\omega \neq 0$

The following theorem reformulates the above objective into an LMI framework
**Theorem 1:** Consider the system (7). Given a positive scalar $\gamma_2$, if there exist a symmetric positive definite matrix $P$ and a matrix $Y$ satisfying the LMI (9)

$$\begin{pmatrix} PA + A^TP - YC - (YC)^T & PD_1 - YD_2 \\ D_1^TP - (YD_2)^T & -I \end{pmatrix} < 0$$
$$\begin{pmatrix} P & I \\ I & \gamma_2 I \end{pmatrix} > 0 \tag{9}$$

then, the observer gain $L$ determined from $L = P^{-1}Y$ ensure that the objective (8) is attained.
The theorem is proven by applying the generalized $H_2$-norm for the system (7).

## 4. SIMULATION AND EXPERIMENT RESULTS

### 4.1 Synthesis results and frequency domain analysis

Solving theorem 1, we obtain the gain $\gamma_2 = 2.9 \times 10^{-5}$ and the observer gain

$$L = \begin{bmatrix} 3.7 \times 10^{-6} & -3.7 \times 10^{-5} \\ 1.1 \times 10^{-4} & -0.0011 \\ 2.7 \times 10^{3} & -2.7 \times 10^{4} \\ -0.1 & 1 \\ 1.9 \times 10^{-8} & -1.9 \times 10^{-7} \end{bmatrix}$$

The resulting attenuation of the sensor noises and road profile disturbance on the state estimation error, subject to the minimization problems, is shown in Fig. 2. These results emphasize the good attenuation level of the measurement noises and unknown road profile effect on the estimation errors of the estimated states, since the largest sensor noise and road profile disturbance amplification of the 5 errors, over the whole frequency range, are -176dB and -217dB, respectively.

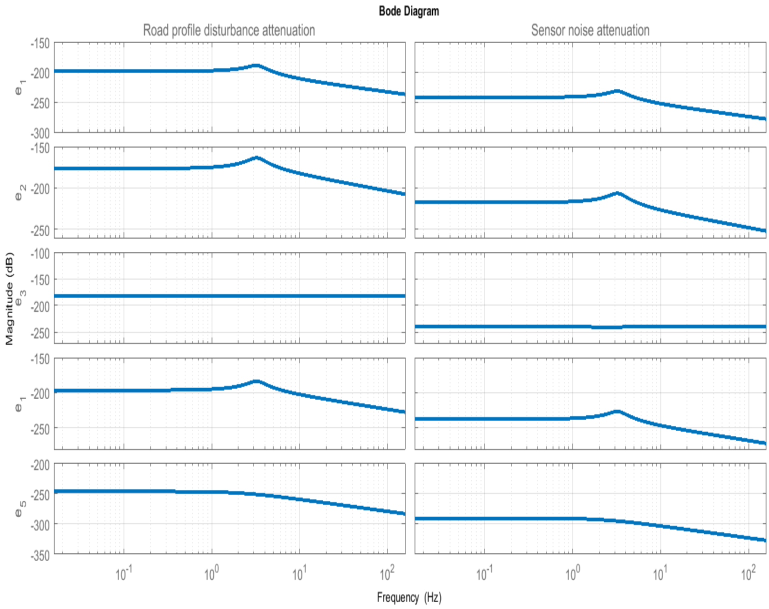


Fig. 2  Bode diagram of the estimation error system (7)

## 4.2 Simulation

To demonstrate the effectiveness of the proposed design, the simulations are made with the nonlinear quarter-car model presented in Section 2. The following initial conditions of the proposed approach are considered:

$$x_0 = [0 \quad 0 \quad 0 \quad 0 \quad 0]^T$$
$$\hat{x}_0 = [0.01 \quad 0.1 \quad 0.001 \quad 0.1 \quad 1]^T$$

Four simulation scenarios are used to evaluate the performance of the observer as follows:

*Scenario 1:*

- The road profile is a sequence of sinusoidal bumps $z_r = 15\sin(4\pi t)\ (mm)$.
- The duty cycle of the PWM signal is $u = 0.1$.

*Scenario 2:*

- The road profile is $z_r = 15\sin(14\pi t)\ (mm)$.
- The duty cycle is $u = 0.1$.

*Scenario 3:*

- The road profile is chirp signal
- The duty cycle is $u = 0.1$.

*Scenario 4:*

- An ISO 8608 road profile signal (Type C) is used.
- The duty cycle is $u = 0.1$.

The simulation results of two tests are shown in the Fig. 3, Fig. 4, Fig. 5 and Fig. 6

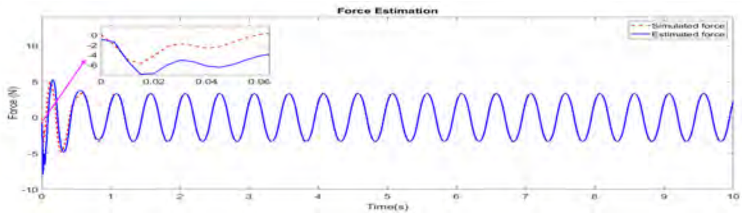


Fig. 3 Simulation scenario 1: Simulated force vs. estimated force

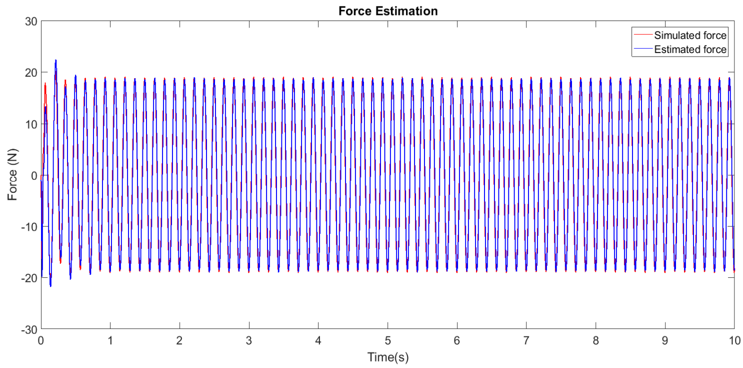


Fig. 4 Simulation scenario 2: Simulated force vs. estimated force

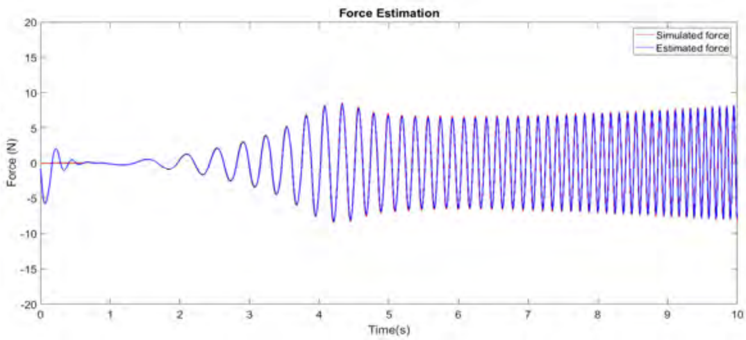


Fig. 5 Simulation scenario 3: Simulated force vs. estimated force

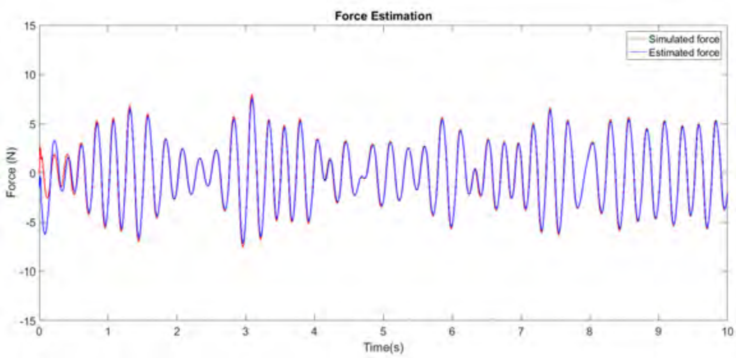


Fig. 6 Simulation scenario 4: Simulated force vs. estimated force

The effectiveness of the damper force observer is clearly seen in the Fig. 3-Fig. 6 where the estimated force converges towards the simulated one, after a short transient period of 1s.

### 4.3 Experiment

The observer is implemented on the 1/5 scaled car testbed INOVE at Gipsa-lab, presented in Fig. 7.


Fig. 7 INOVE testbed at GIPSA-lab

The test-bench consists of 4 semi-active ER suspensions controlled in real-time by an xPC target and a host computer. The target PC is connected to the host computer via Ethernet communication standard. Each corner of the system has a DC motor to generate various road profiles. The damping force estimation algorithm is applied at the rear-left quarter car of the INOVE vehicle.

Here, the damping force observer is performed for the rear-left corner whose available sensors are the un-sprung mass accelerometer, the sprung mass accelerometer the damping force sensor, the position sensors to measure the suspension deflection, the road profile and the un-sprung mass position.

In this experimental test, the duty cycle $u$ of the PWM signal is constant (u = 0.1) and the real road profile is a sinusoidal wave, shown in Fig. 8. The experiment result of the observer is presented in Fig. 9. The result illustrates the good accuracy of the proposed observer.

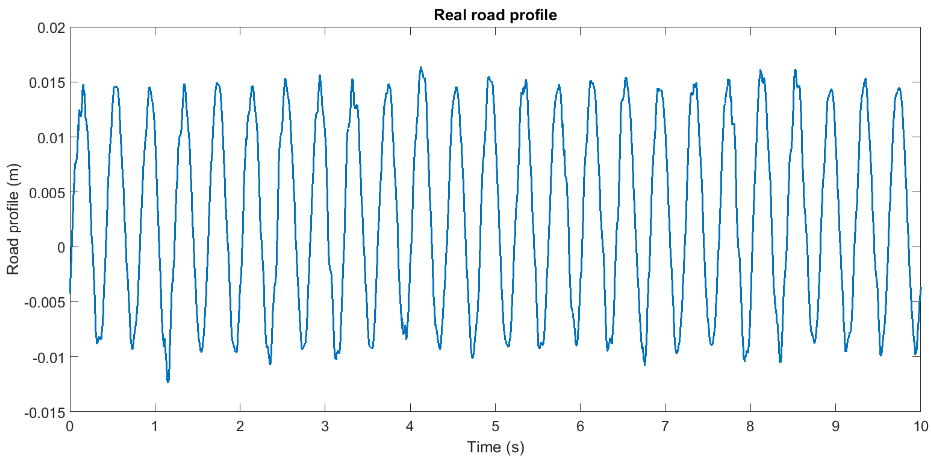


Fig. 8 Real road profile

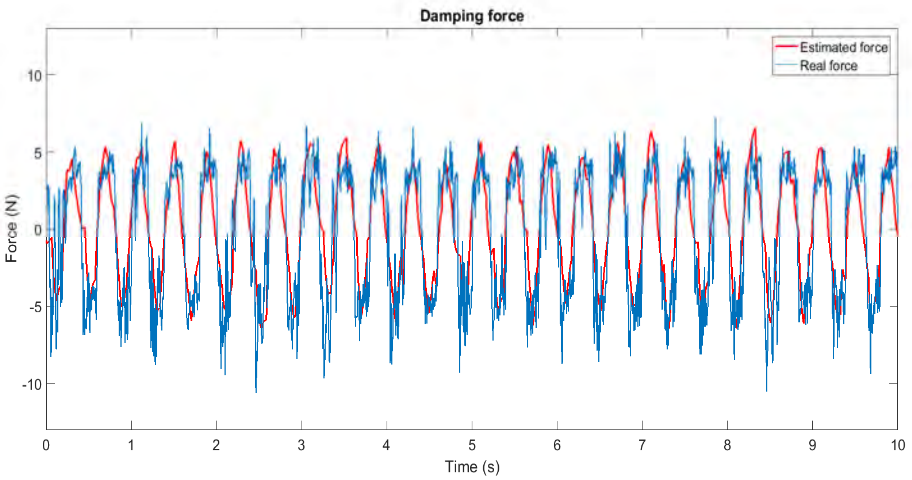


Fig. 9 Experiment: real force vs. estimated force

## 5. CONCLUSION

This paper proposed an $H_2$ observer to estimate the damping force, with the use of the dynamic nonlinear model of the ER damper. First, the quarter-car system was represented with a phenomenological model of damper. Second, an $H_2$ observer was designed, illustrating a good estimation result of the damper force. The estimation error was minimized the effect of the unknown inputs (road profile disturbance and measurement noises) by using the $H_2$-norm. Both simulation and experiment results demonstrate the ability and the accuracy of the proposed model to estimate the damper force of the ER semi-active damper.

## 6. REFERENCES

[1] **Savaresi, S.M. - Poussot-Vassal. C. – Spelta, C. - Sename. O. – Dugard,L.:** Semi-active suspension control design for vehicles. Elsevier, 2010.

[2] **Poussot-Vassal, C. - Sename, O. - Dugard, L. - Gaspar, P. - Szabo, Z. - Bokor, J.:** A new semi-active suspension control strategy through *lpv* technique. Control Engineering Practice, 2008, p.1519-1534.

[3] **Priyandoko, G. - Mailah, M. - Jamaluddin, H.**: Vehicle active suspension system using skyhook adaptive neuro active force control. Mechanical systems and signal processing, 2009, p.855-868.

[4] **Poussot-Vassal, C. - Spelta, C. - Sename, O. - Savaresi, S.M. - Dugard, L.:** Survey and performance evaluation on some automotive semi-active suspension control methods: A comparative study on a single-corner model. Annual Reviews in Control, 2012, p.148-160.

[5] **Do, A.L. - Sename, O. - Dugard, L.:** An *lpv* control approach for semi-active suspension control with actuator constraints. In American Control Conference (ACC), 2010, p.4653-4658.

[6] **Nguyen, M.Q. - da Silva, J.G. - Sename, O. - Dugard, L.:** Semi-active suspension control problem: Some new results using an LPV/$H_\infty$ state feedback input constrained control. IEEE 54th Annual Conference on Decision and Control (CDC), 2015, p.863-868.

[7] **Estrada-Vela, A. - Alcantara, D.H. - Menendez, R.M. - Sename, O. - Dugard, L.**: $H_\infty$ observer for damper force in a semi-active suspension. IFAC-PapersOnLine, 2018, p.764-769.

[8] **Reichhartinger, M. - Falkensteiner, R. - Horn, M.:** Robust estimation of forces for suspension system control. In Joint 9th IFAC Symposium on Robust Control Design and 2nd IFAC Workshop on Linear Parameter Varying Systems, 2018.

[9] **Tudon-Martinez, J.C. - Hernandez-Alcantara, D. - Sename, O. - Morales-Menendez, R. - de J. Lozoya-Santos, J.:** Parameter-dependent $H_\infty$ filter for lpv semi-active suspension systems. In Joint 9th IFAC Symposium on Robust Control Design and 2nd IFAC Workshop on Linear Parameter Varying Systems, 2018.

[10] **Koch, G. - Kloiber, T. - Lohmann, B**.: Nonlinear and filter based estimation for vehicle suspension control. 49th IEEE Conference on Decision and Control (CDC), 2010, p.5592-5597.

[11] **Rajamani, R. - Hedrick, J.K.:** Adaptive observers for active automotive suspensions: theory and experiment. IEEE Transactions on control systems tech-nology, 1995, p.86-93.

[12] **Dugard, L. - Sename, O. - Aubouet, S. - Talon, B.:** Full vertical car observer design methodology for suspension control applications. Control Engineering Practice, 2012, p.832-845.

# COMPARISON OF CONTROLLER SYSTEMS AND MOTION MODELLING METHODS FOR AUTONOMOUS VEHICLE TRAJECTORY FOLLOWING PRACTICE

**Ádám DOMINA and Viktor TIHANYI**

Department of Automotive Technologies
Faculty of Transportation and Vehicle Engineering
Budapest University of Technology and Economics
H-1111 Budapest, Műegyetem rkp. 3., Hungary

*Received: November 5, 2018*

## ABSTRACT

Nowadays the self-driving vehicles are one of the most focused technology in the current industrial and science researches, both commercial and passenger vehicles. This technology increases the safety, functionality, efficiency, and reliability in every part of the vehicle industry. A well-constructed autonomous vehicle is able to reduce the chance of an accident this is one of the most important reason of the expansion of them. Today functionalities above level two, automation according to SAE standard is not allowed because of legal situation and technical immaturity of the technology. Precise motion control is essential to enable such highly automated vehicles. In this work we are focusing on the trajectory following solutions, would like to create a complete path following solution, which provides accurate control in various conditions. To reach this goal, first different control algorithms developed, based on simulations where the vehicle models was adjusted to a particular real demonstrator vehicle. Both dynamic and kinematic bicycle model was used to simulate the motion of the vehicle. Two different path following algorithms and both kinematic and dynamic vehicle models were implemented in MATLAB Simulink simulation environment. Thereafter the controllers was tested and compared in simulation environment, the differences between the controllers and vehicle models was analysed.

*Keywords:* autonomous vehicle, controller, path following, tracking, vehicle model, bicycle model

## 1. INTRODUCTION

Nowadays, the vehicle industry developments are mainly concentrated on autonomous vehicles. It is driven by a reduction in the number and severity of accidents and fuel consumption. Autonomous vehicles and driving support systems [1], [2] all serve this purpose. In order to achieve this, the automation level of vehicles needs to be increased and the deployment of intelligent infrastructure is indispensable. An important, safety-critical task of automated vehicles is to plan and follow the route.

In this paper, different trajectory following controllers are implemented. The operation of the controllers is required to be tested in a software environment before testing them on the real vehicle. To do this, a vehicle model has been implemented, preferably in the same software environment as the controller, thus facilitating the testing in a virtual environment. The vehicle model must be able to simulate the movement of the real vehicle, the higher the speeds needed to simulate the movement of the vehicle the more accurate and detailed the model is needed. There are kinematic and dynamic vehicle models, kinematic models only describe the spatial motion of the vehicle, how the vehicle moves, and does not deal with the forces that cause the movement. Dynamic vehicle models rely on vehicle-acting forces describe the behaviour of the vehicle under the effect of the forces. Based on these, simpler, kinematic models are typically used at low vehicle speeds and more complex dynamic models at higher speeds. Beside kinematic models, those are easy to implement, the computational requirements are

low, the dynamic models are more complex, require more computing power, but give more accurate results.
The controllers designed here are used on a Smart demonstration vehicle with low speed, typically up to 20-25 km/h. The most common model for this movement is the bicycle model, which also has a kinematic and dynamic version. The purpose of this paper is to examine the differences between different vehicle models for different path following controllers, so both kinematic and dynamic vehicle models have been implemented. The dynamic model includes only the lateral dynamics of the vehicle. The longitudinal dynamics was neglected because the vehicle is typically used at constant speeds.
To test the controller in a software environment, vehicle models and controllers are first implemented and then the vehicle model parameters are aligned to the real vehicle. After that, the controller is tested and the controller parameters tuned.

## 2. KINEMATIC BICYCLE MODEL

The bicycle model is derived from a four-wheeled vehicle by replacing the two wheels on one axle of the vehicle with one wheel at the half of the gauge. The wheelbase of the vehicle does not change. The resulting model is a one-way vehicle model, or as it is called bicycle model. The geometry of the model is characterized by two values, one is the wheelbase and the other is the steering angle. The steering angle is derived from the Ackermann geometry. The essence of Ackermann geometry is that the steered wheels of the vehicle are steered at different angles in order to ensure the geometrically correct rolling radius for each wheel. However, the bicycle model has only one front wheel, the steering angle of this is the arithmetic mean of the steering wheel angles of the real vehicle, see Fig. 1.

$$\delta_0 = \frac{\delta_1+\delta_2}{2} \ . \qquad (1)..$$

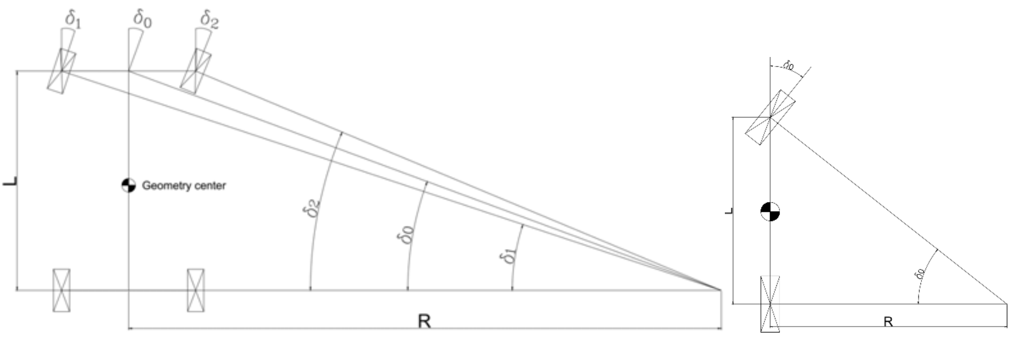


Fig. 1 Deriving the bicycle model

The motion of the kinematic model is described with a single equation that defines the yaw-rate of the vehicle as a function of the speed and the steering angle:

$$\dot{\psi} = \frac{v_x}{R} = \frac{v_x * tan(\delta)}{L} \ , \qquad (2)$$

where $v_x$ is the speed of the vehicle, in the car-fixed coordinate system, R is the turning radius, $\delta$ is the steering angle (marked $\delta_0$ in Fig. 1, and $\delta$ in Fig. 2), L is the wheelbase. Yaw-rate is the angular velocity of the vehicle around the z-axis. Fig. 2 shows the kinematics of the bicycle model.

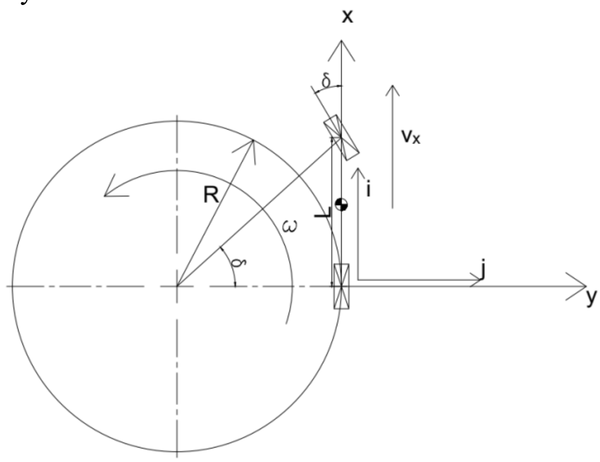


Fig. 2 Kinematics of bicycle model

Equation (2) describes the connection between the longitudinal and lateral motion of the vehicle. Knowing this, the longitudinal and lateral speed of the vehicle can be calculated in the ground-fixed coordinate system.

## 3. DYNAMIC BICYCLE MODEL

The dynamic vehicle model takes into account the lateral forces acting on the vehicle, the longitudinal velocity is assumed to control separately. Fig. 3 shows the dynamic bicycle model, $\alpha_f$ and $\alpha_r$ are the sideslip angles at the front and rear wheels, $\beta$ is the sideslip angle of the vehicle, $l_f$ and $l_r$ are the distances between the centre of gravity point of the vehicle and the front and rear axles.

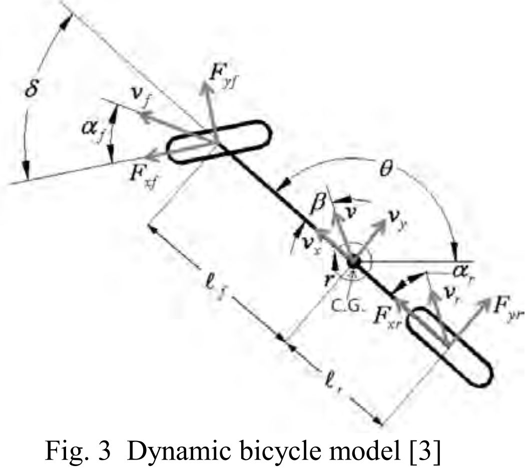


Fig. 3 Dynamic bicycle model [3]

$\Theta$ is the heading angle of the vehicle, the first derivative of this is the yaw-rate, $v_f$ and $v_r$ are the velocity of the front and rear wheels. C.G. is the centre of gravity.
The side slip of the wheels is caused by lateral forces acting on the vehicle during cornering. The motion of the vehicle is described by two equations, the longitudinal forces acting on the vehicle are neglected. The first equation describes the lateral forces (3), the second describes the yaw moments around C.G. point (4).

$$F_{yf}\,cos(\delta) - F_{xf}\,sin(\delta) + F_{yr} = m(\dot{v}_y + v_x\omega), \tag{3}$$

$$l_f\big(F_{yf}\,cos(\delta)\big) - l_r\big(F_{yr} - F_{xf}sin(\delta)\big) = I_z\dot{\omega}\ , \tag{4}$$

where m is the mass, $I_z$ is the yaw inertia of the vehicle, $\dot{\omega}$ is the yaw-rate.
The slip angles of the tires are given by (5) and (6)

$$\alpha_f = tan^{-1}\left(\frac{v_y + l_f\omega}{v_x}\right) - \delta, \tag{5}$$

$$\alpha_r = tan^{-1}\left(\frac{v_y - l_r\omega}{v_x}\right). \tag{6}$$

At small sideslip angles, the force generated by the wheels is linearly proportional to the slip angle, shown in Fig. 4.

$$F_{yf} = -c_f\alpha_f, \tag{7}$$

$$F_{yr} = -c_r\alpha_r\,. \tag{8}$$

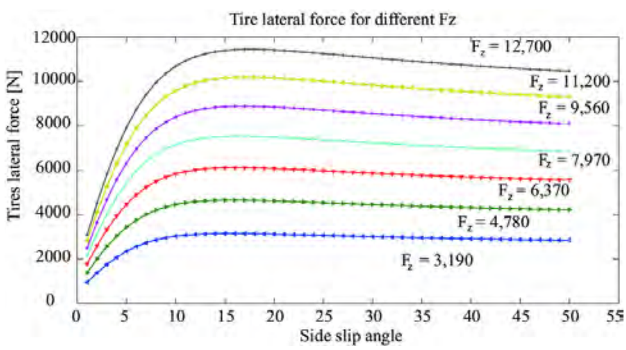


Fig. 4 The lateral force – sideslip angle connection [4]

In equation (7) and (8) $c_f$ and $c_r$ are the cornering stiffness of the front and rear tires. $F_{xf}$=0, because the longitudinal dynamics is neglected. Substituting equations (3)-(8), resulting (9) and (10) describes the motion of the vehicle.

$$\dot{v}_y = \frac{-c_f\left[tan^{-1}\left(\frac{v_y + l_f\omega}{v_x}\right) - \delta\right]cos(\delta) - c_r\,tan^{-1}\left(\frac{v_y - l_r\omega}{v_x}\right)}{m} - v_x\omega\ , \tag{9}$$

$$\dot{\omega} = \frac{-l_f c_f \left[ tan^{-1}\left(\frac{v_y + l_f \omega}{v_x}\right) - \delta \right] cos(\delta) + l_r c_r \, tan^{-1}\left(\frac{v_y - l_r \omega}{v_x}\right)}{I_z} , \qquad (10)$$

## 4. PURE PURSUIT CONTROLLER

The first geometric path following controller is the widely used Pure Pursuit controller [5]. The principle is fitting a semi-circle through the current configuration of the vehicle and the reference point on the path, with an L distance before the vehicle. L distance called look-ahead distance, this is the only tuningable parameter of the controller. The fitted circle is tangent to the heading of the vehicle, at the rear axle, see Fig. 5.

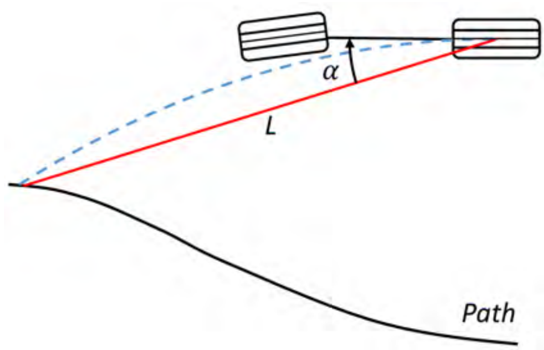


Fig. 5 Pure pursuit geometry

The necessary turning radius R, and the steering angle $\delta$, which is the output of the controller, can be calculated:

$$R = \frac{L}{2sin(\alpha)}, \qquad (11)$$

$$\delta = tan^{-1}\left(\frac{W}{R}\right) . \qquad (12)$$

## 5. STANLEY CONTROLLER

The other geometric path following controller is the Stanley controller [6], which was first used in 2005, at the DARPA Grand Challenge. Fig. 6 shows the geometry of the controller. The control strategy is to point the front wheel towards the path. The component of the velocity of the front wheel is normal to the path, and proportional to the distance between the wheel and the path. The controlled variable is the position of the front wheel, $\bar{t}$ is the tangent unit vector of the path, where the distance between wheel and path is minimal, e is the distance. The path tangent vector and the distance e are always perpendicular. $\Theta_e$ is the angle between the heading of the vehicle and the unit-vector $\bar{t}$, $v_f$ is the velocity of the front wheel.

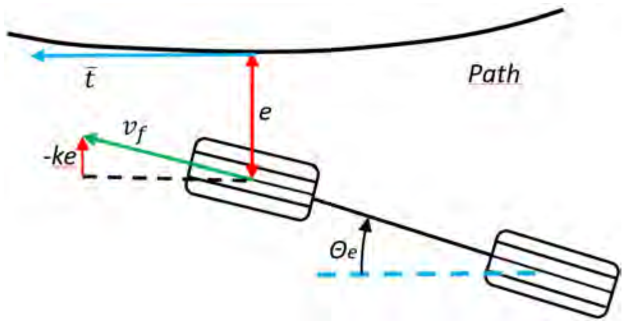


Fig. 6 Stanley geometry

The time derivative of the e error is:

$$\dot{e} = v_f sin\,(\Theta_e + \delta), \tag{13}$$

which can be controlled by the steering angle. Replacing $\dot{e}$ with –k·e, (13) can written in a new form:

$$v_f sin\,(\Theta_e + \delta) = -ke. \tag{14}$$

The controller can be tuned by k factor. The steering angle can be expressed from (14), assuming small angles, the sine function can be replaced by tangent function:

$$\delta = tan^{-1}(-ke/v_f) - \Theta_e. \tag{15}$$

## 6. SIMULATION RESULTS, CONTROLLER COMPARISON

Both controllers have been tested with both vehicle models, making a total of 4 different versions. Testing was done on the same reference path, so the results can be easily compared Fig. 7. The vehicle speed start from 10 km/h, increases until 50 km/h, in 10 km/h steps. The lookahead distance at Pure Pursuit controller is 5 meter, the “k” factor at Stanley controller is -4.

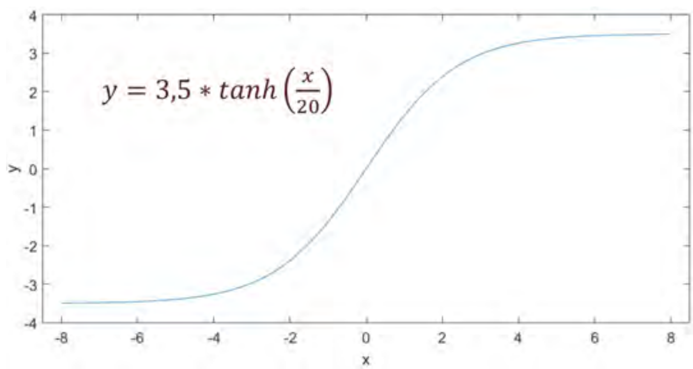


Fig. 7 Reference path

In the figures below, the reference path is marked in black, the track run by the front wheel of the vehicle is red and the rear wheel track is marked blue.

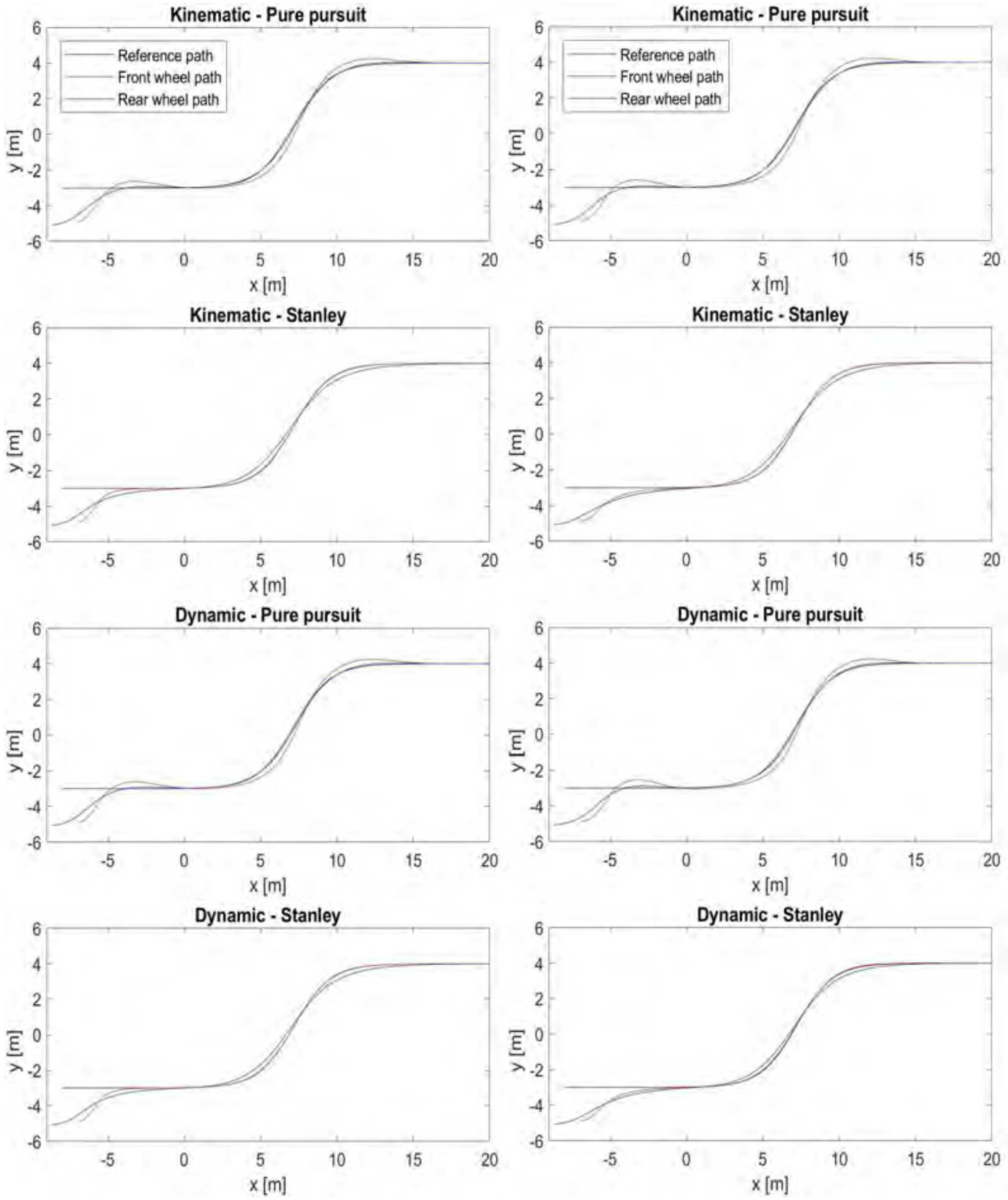


Fig. 8 Results at 10 km/h (left) and at 20 km/h (right)

As it is shown in Fig. 8, Fig. 9, Fig. 10, with the speed increasing, the vehicle is increasingly deviates from the path. There are two defective forms of motion, the overshoot and the oscillation. The overshoot is a delay in the cornering, the vehicle starts the cornering just after went over the turn. At the kinematic model, the lack of the dynamics of the vehicle make it unsuitable for motion modelling at higher speed, limit of applicability is 20 km/h. At low speed ranges, 0-20 km/h, this model gives satisfying results, there are minimal differences between kinematic and dynamic model, the kinematic model is good for small speed simulation, for example parking manoeuvres.

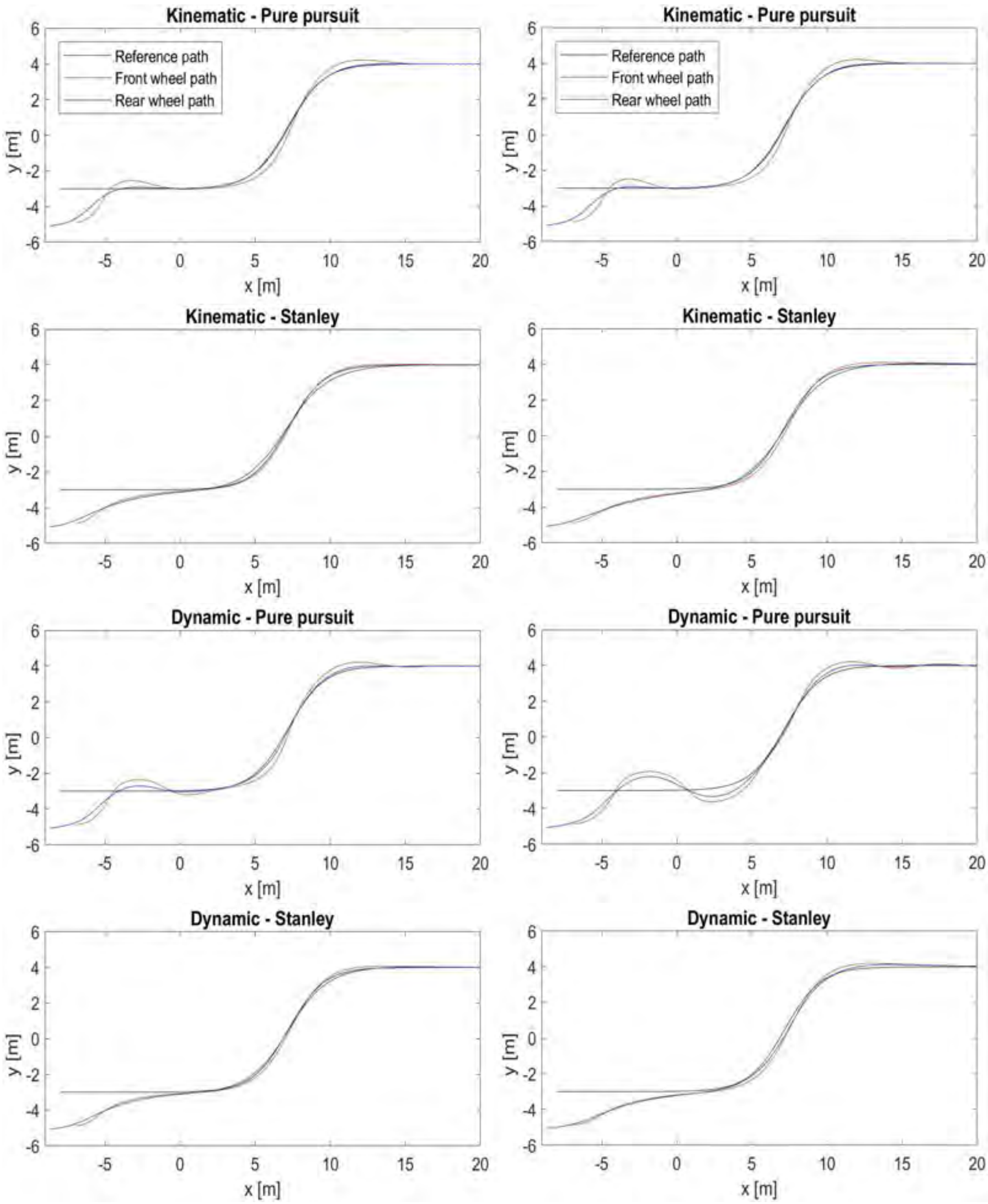


Fig. 9 Results at 30 km/h (left) and at 40 km/h (right)

The dynamic model calculates more accurate the lateral behaviour of the vehicle, this can be seen well above 40 km/h, at pure pursuit controller. The dynamic model shows more better the oscillation around the path, than the kinematic model. At 50 km/h with pure pursuit controller, the oscillation is so great that path tracking in not feasible, the kinematic model just shows overshoot at the corners.

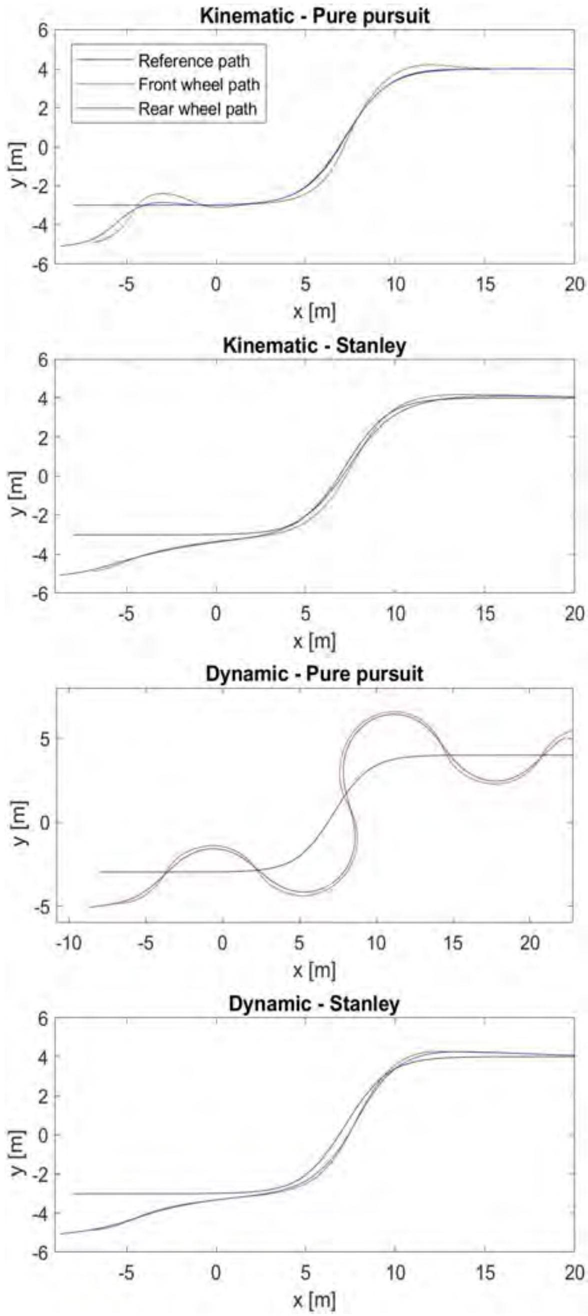


Fig. 10 Results at 50 km/h

Considering the path following controllers, the “Pure pursuit” shows oscillation around the path, at higher speeds, this is caused by the extent of the lookahead distance. The oscillation can be reduced by increasing look-ahead, but this would result larger lateral difference from the path. The Stanley controller shows more accurate path following, at higher speed it shows overshooting. The lack of this controller is too unsuitable for reverse driving, and the further increase of the k factor results oscillation around the path.

## 10. ACKNOWLEDGMENT

The project has been supported by the European Union, co-financed by the European Social Fund. EFOP-3.6.2-16-2017-00002.

## 11. REFERENCES

[1] **Lengyel, H. - Szalay, Zs.**: The Significance and Effect of the Traffic System Signaling to the Environment, Present and Future Traffic, Proceedings of the 4th International Congress of Automotive and Transport Engineering, January 2019, p.847-856.

[2] **Lengyel, H. - Szalay, Zs.**: Traffic sign anomalies and their effects to the highly automated and autonomous vehicles, 35th International Colloquium on Advanced Manufacturing and Repair Technologies in Vehicle Industry, 2018, p.193-204.

[3] **Snider, J. M.**: Automatic Steering Methods for Autonomous Path Tracking, Robotics Institute, Carnegie Mellon University, Pittsburgh, Pennsylvania, February 2009.

[4] **Farhat, A. - Hernandez - Alcantara, D. - Koeig, D. – Morales-Menendez, R.:** Tire Force Estimation using a Proportional Integral Observer, 13$^{th}$ European Workshop on Advanced Control and Diagnostics (ACD 2016); doi:10.1088/1742-6596/783/1/012014.

[5] **Paden, B. - Cap, M.- Yong, S. Z -. Yershov, D. - Frazzoli**, **E.:** "A survey of motion planning and control techniques for self-driving urban vehicles", IEEE Transactions on Intelligent Vehicles, vol. 1, June 2016, p.33-55.

[6] **Amer, N. H. - Zamzuri, H. - Hudha, K. - Kadir, Z. A.**: Modelling and Control Strategies in Path Tracking Control for Autonomous Ground Vehicles: A Review of State of the Art and Challenges, J Intell Robot Syst 86: 2017, p.225-254.

# POSSIBLE CAUSE OF AN INTERNAL LEVEL CRASH, '95 KOBE EQ

**Ferenc KOLONITS**

Budapest University of Technology and Economics
Faculty of Transportation Engineering and Vehicle Engineering
Department of Aeronautics, Naval Architecture and Railway Vehicles
Muegyetem rkp 3, Budapest H-1111 Hungary
kolonf@mail.iif.hu
+36(1)463 1939, fax +36(1)463 3080

*Received: November, 6, 2018*

## ABSTRACT

On 1.17, 1995, a great earthquake struck the Kobe-Osaka area (Hyogo-ken Nambu Hansin Daishinsai). It caused great damage both in building structures and human lives. The geology of the area has been being prone to generate EQs, not less than four tectonic plates are meeting here. Therefore, the cause of damages and rules of construction are of prominent interest there, and subject to continuous development. Specific attention has to be given to local anomalies differing with the general "continuous" picture. One of them is the collapse of sixth floor of Kobe Old City Hall, while ones above and under survived without visible damage. There were manifold "root cause" supposed. One may say, the 6-8$^{th}$ floors were annexed later – however, they erected together in 1957. Worth of consideration were that the higher part of the building had been constructed as RC instead of SRC. A further cause to look after were the impact of reflected shear waves from top to down – but the effect does not change along the length of the floor. A possible after-effect of the war bombing can be put aside, because those were made not by ground-breaking explosives, but with incendiary bombs not changing the soil structure. The most promising way for further consideration is the looking at higher vibration modes. The development of fractures has to be re-iterated. As the paper Hong Zuo*, Fangwen Wang* & Teng Hou: An Equivalent Strain Gradient Theory for Evolvement of Damage in Void Material (13th International Conference on Fracture June 16–21, 2013, Beijing, China) describes, the procedure in a body, containing internal cavities, goes as follow. An internal cavity generates stress concentration. At a sufficiently high level, crack(s) start and further on, the cavities merge. The crack starts at the location of maximal equivalent (Hencky) strain and follows its gradient. The frame of the City Hall building can be treated as a one-dimensional beam. The first, second and third modes can be calculated and Huber-v.Mises-Hencky stresses along with Hencky strain had been analyzed in a previous conference paper. The 2. and 3. eigenmodes do not put up any peculiarity around the 6th floor, the first mode is of dominant size and showing local maxima at the top of 6th columns. Therefore, that might be considered as a possible originator of a crash of the sixth floor.

*Keywords:* earthquake, Kobe, SRC building, mid-level crash

## 1. THE SEISMIC EVENT

At 5:47, 01.17.1995, a sizeable earthquake of about 15 s duration struck the Japanese city Kobe and its area. Richter magnitude 7.2, Mercalli intensity X-XII, 5000 dead, 26000 wounded and 300000 de-housed, cumulated damage 95…147 md USD. Not less than four tectonic plates met there. The Eurasian and Philippine Sea ones form the Nankai trough between and the Median Tectonic Line along the region. The Kobe-Osaka area resembles as if straddling a powder keg. The course of events had been registered and analyzed in the literature [1]…[5]. However, some details deserve further attention due new publications appearing in the meantime. Since then, there had been seismic events of higher level, say Fukushima, but Kobe exemplified a wide variety of objects concerned. Fukushima as structure withstood a higher-level EQ, there its influence on nuclear process turned out to be critical. The variety mentioned above indirectly pointed at by the high Mercalli intensity and moderate Richter magnitude. This can show that a good part of area stricken is of low resistance structures. Besides of modern buildings and infrastructure, there was an Old City area, really razed down.

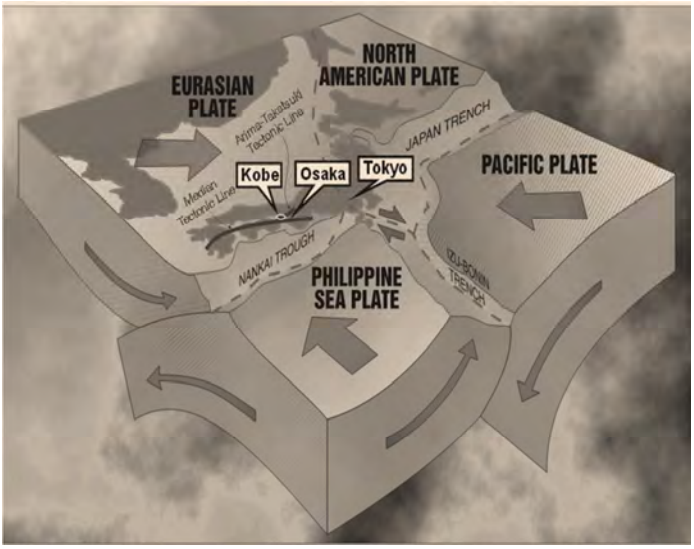


Fig. 1 The tectonic structure around Kobe

## 2. THE CHARACTERISTICS OF THE EARTHQUAKE

The effects of a seismic event can be represented with response spectra, i.e. maximal displacement etc. as function of eigen-frequency of the structure concerned.

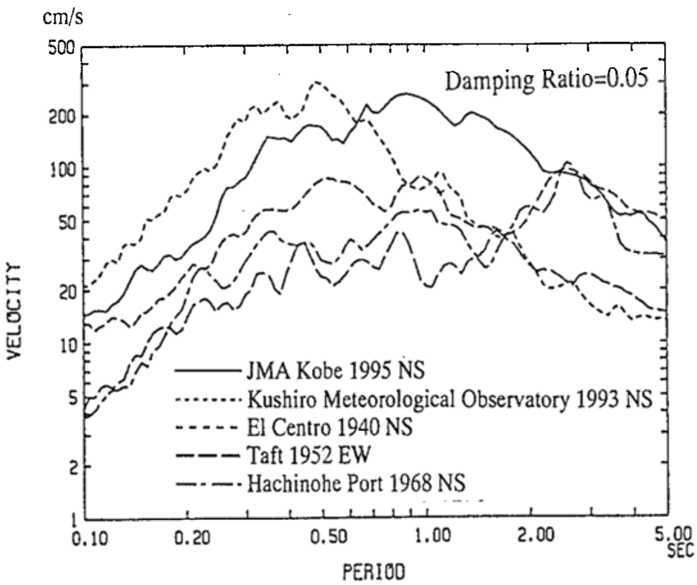


Fig. 2 Surface velocity response spectra

The Fig.2 shows that the Kobe EQ is powerful enough with respect to usual reference EQs. A distinctive feature is that long periods put up high response values, i.e. structures with low eigen-frequencies would be more shaken. This is the case of traditional Japanese houses with flexible bamboo piles and heavy roof more stable against taifun. On the other hand, these results lower eigenvalues and higher EQ loads – that is, why the Old Kobe area suffered great damages.


Fig. 3 Damaged buildings of various ages

The damage picture reflects the customs and standards of planning/building time. Typical milestones are shown on Fig.3. The part Nr.1 shows a traditional structure. As mentioned above, it most likely ends in a total crash. Following the catastrophic EQ in 1923, began a systematic work of summarizing the rules for a safer practice and continuously including lessons might be drawn. The experiences and theory development led to establish better based design rules in the 60-70th years. The item Nr.2 had been built already under them. It stood against the impact, with some mid-height damage or collapse. In 1981, the theory and technology being further developed, the rules followed them again. The high buildings could survive then with no visible damage.


Fig. 4 Typical deteriorations on RC structures

The over-all damage would appear as consequence of constituent ones. Fig.4. shows some typical cases of. They can be considered mostly buckling and shear. Fig.5 depicts a more complex case, where the over-all deformation would build up from those of (homogenous) substructures. One of the most interesting damage cases is the localized one of Kobe Old City Hall. There, the 6$^{th}$ storey completely wiped out, while the other levels did not shown conspicuous fault.

Fig. 5 Complex damage of substructures

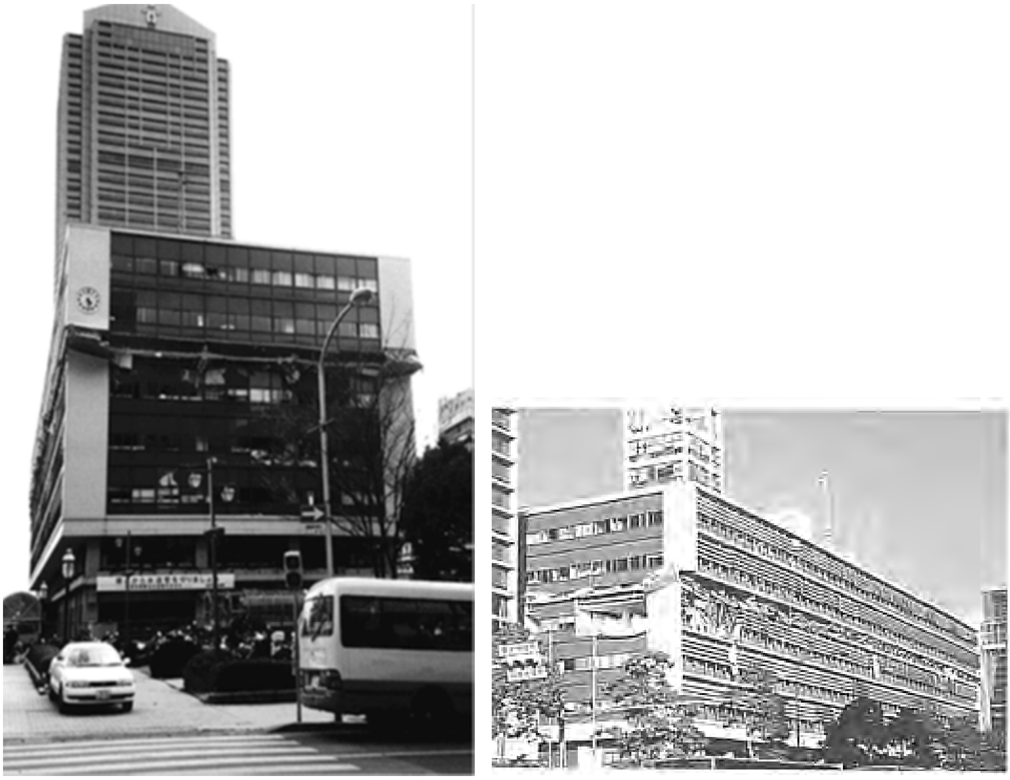

Fig. 6 Crash of the Old City Hall

Fig.6 shows the Old City Hall from two directions. The $6^{th}$ storey crashed and the part upwards shifted as a whole.

## 3. THE SIMPLIFIED MODEL OF THE CITY HALL

The frame of the building consists of 8 horizontal storey plates and 72 vertical columns. The plates are relatively stiff, they would move horizontally, the columns underwent double bending. The M masses of floors, beams etc. are evenly distributed among the 72 columns of inter-storey support. The final model will be a vertical beam of elastic columns with point masses, clamped at the bottom, free at roof level. Details from an approximate calculation are shown in Tab.1. Here, M means the mass of the storey parts, L the heights, and $a{*}a$ the cross section area of the substituting beam, respectively. The numbering there refers to the levels. In the last two columns, $\omega$ and T are the eigen-frequencies and cycle times, numbered in sequence.
Previous analysis [6] showed, that the responses pertaining to eigen-forms 2,3 and higher, are less than 20% of the first one. Thus, influence of the first eigen-form seems to be decisive.
The Fig. 8 shows the spectral displacement spectrum. It can be seen that in the first eigen-form an overwhelming response were given.

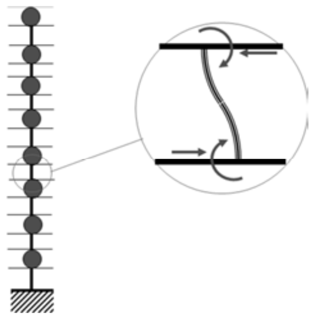

Fig. 7 Beam-and-point-mass model of the City Hall

**Table 1.** Storey data of Kobe City Hall and angular eigen-frequencies/cycle times

| Nr | M[kg] | L[m] | a[m] | ω[1/s] | T[s] |
|---|---|---|---|---|---|
| 1 | 27479.2 | 4.15 | 1 | 13.789 | 0.4557 |
| 2 | 31598.6 | 4.2 | 1 | 32.544 | 0.1931 |
| 3 | 31598.6 | 3.65 | 0.85 | 52.581 | 0.1195 |
| 4 | 31598.6 | 3.65 | 0.85 | 71.104 | 0.0884 |
| 5 | 31598.6 | 3.65 | 0.85 | 83.356 | 0.0754 |
| 6 | 31598.6 | 3.65 | 0.65 | 109.80 | 0.0572 |
| 7 | 31598.6 | 3.65 | 0.65 | 139.02 | 0.0452 |
| 8 | 26645.8 | 3.8 | 0.6 | 158.69 | 0.0396 |

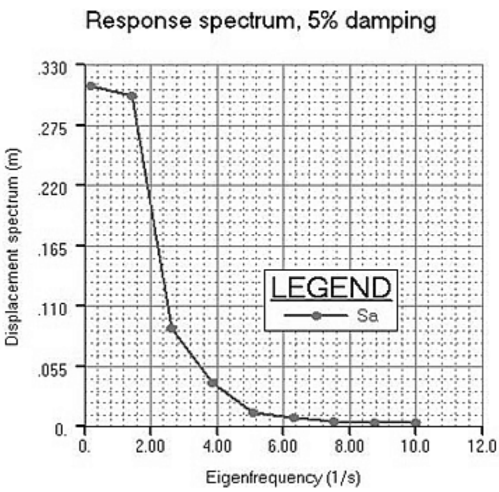


Fig. 8 Displacement spectrum of the model on Fig.7.

The modal analysis had been reconstructed with MSC Patran/Marc. The first eigen-form is shown on Fig. The first natural frequency is 2.37392, the one from the Tab. calculation were 2.1944 (difference 8%). At the 6$^{th}$ storey there is a more intense local deformation.

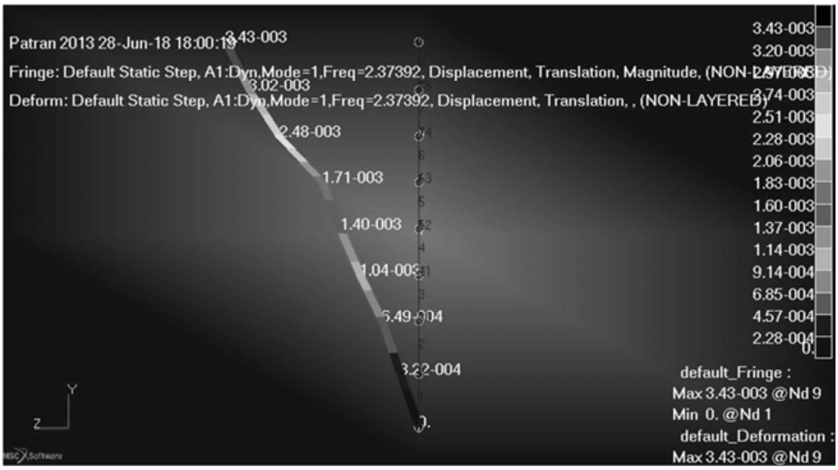


Fig. 9 Deformed shape of the model in the first eigen-form

## 4. POSSIBLE CAUSE OF THE "ISOLATED LOCAL" DAMAGE

### 4.1 Theories

- The 6-8$^{th}$ floors are structurally differing with the ones beneath. It had been thought that they were annexed later. However, all the building had been erected together in 1957. A structural difference was that the SRC had been continued upwards RC.
- The horizontal EQ shear waves could be reflected from the top of the building and the interference with the following ones might generate overload. A similarity can be thought with the HESH armor piercing shot. That generates a pressure wave on the armor, which turns around to traction on the inner surface and this generates an internal crack. However, if a shear wave turned around, the nature of risk remains essentially the same.
- An idea has been emerged, that the intensive bombing in the final phase of WW2 changed the soil properties beneath. There are examples, where alterations made by human or natural processes exerted influence on EQ characteristics (i.e. the lake sediment under Mexico City). However, the bombing had been made by incendiary attacks. These had been fatal for buildings and human lives but cannot change the soil structure.
- There had been remarks made that higher eigen-forms may influence the special behavior of the 6$^{th}$ floor. However, above it has been shown, that these influence is small if any related to the first one.

### 4.2 Looking for possible sources of damage

Theories are there enough, and further ones are *in statu nascendi*. A conference paper [7] offers a possibility to adapt it onto the damage process at hand. The starting step is a fatigue test of a plate stripe with two bored holes and pulsated along its length. The result as can be awaited is a pattern of cracks starting from the holes and meeting each other up to break.

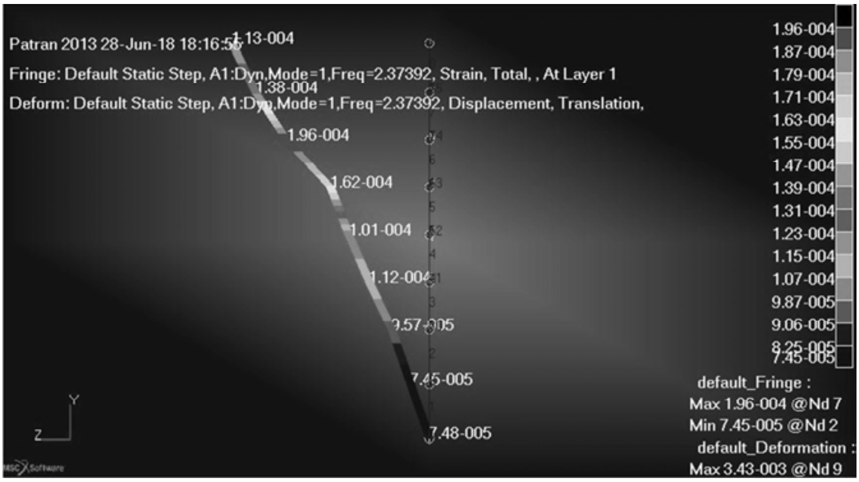


Fig. 10 The total strain in the first eigen-form

The material is seemingly continuous, but its microstructure puts up crystals and voids. These voids are prone to form stress concentrations and cracks can start from. The fundamental question of fracture mechanics is, where begins a crack and in what a direction continues. The results led to a consequence, instead of classical criteria based on stress, these processes are governed by equivalent strain (This latter cannot be fully identified from the paper, most likely its structure is similar to the von Mises stress). The theorem pronounced: a crack begins where the equivalent strain is a local maximum, and it propagates in the direction of negative gradient of.

Fig.10. shows the MSC Marc strain result of the first eigen-form, summarized according von Mises rule. At the top of the 6th floor, the strain shows up local maximum, up- and downwards the strains are diminishing. The RC structure contains voids enough. According the above outlined theory, the top of the 6th floor is susceptible to incipient cracking. On the other hand, this is a typical deterioration form of concrete.

## 5. SUMMARY

The analysis of a seemingly special fault gave an interesting by-product. Engineering structural analysis mostly based on stresses and damage forms related to. There are structures, however, mostly built of more rigid materials, where crack developments and fracture mechanics approach are decisive. Most likely, the special damage of Old City Hall of Kobe had been at least partially caused by such effects. Apart from the example set by this event, that calls attention a more systematic study of strain effects being preferable.

## 6. REFERENCES

[1] The January 17, 1995 Kobe earthquake, *EQE Summary Report*, April 1995

[2] *INCEDE Newsletter*, Special Issue, January 1995

[3] **Housner, G.W.:** Strong ground motion,. in: *Earthquake Engineering*. Ed.by Wiegel, R.L. Prentice-Hall Inc.Englewood Cliffs, N.J. Chap. 4, 1970, p.75-91.

[4] **Kanda, J.:** Building damages due to the 1995 Hyogoken-Nambu Earthquake (Paper S1-5-1) *Int.Symp. on seismic safety relating to NPP*, Kobe, Japan, 03.03-05.1997

[5] **Banon, H.:** Prediction of seismic damage in reinforced concrete frames, *Doctoral work*, Department of Civil Engineering, MIT, 1980.

[6] **Kolonits, F. – Csák, B.:** Theoretical Considerations and Practical Trends for Aseismic Buildings, *Vibration Problems ICOVP 2011, the 10th Int. Conference on Vibration Problems,* Proceedings in Physics 139, Springer, 2011, p.107-112.

[7] **Zuo, H. – Wang, F.W. – C Hou,T. :** An Equivalent Strain Gradient Theory for Evolvement of Damage in void Material, *13th International Conference on Fracture*, June 16-21, 2013, Beijing, China

# SOME REMARKS ON DESIGNING CRANKSHAFTS

**Csaba KISS**

Department of Railway Vehicles, Aircraft and Ships
Faculty of Transportation Engineering and Vehicle Engineering
Budapest University of Technology and Economics
H-1521 Budapest, Hungary

*Received:June 15, 2018*

## ABSTRACT

Designing a crankshaft is even now a very complex and complicated task. In four miscellaneous group the influencing factors can be classified. In the first group the factors associated with the materials are taken into consideration (composition, basis of failure etc.). The second group embodies the issues in connection with the manufacturing process (method, heat treatment, surface roughness etc.). The environmental and operational effects are taken into account in the third group (temperature effect, stress state, loading system, analysis of forces and moments loading the crankshaft etc.). The design parameters of the crankshaft are in the fourth group: size, shape, speed etc. This paper would like to draw the attention on the importance of this parameters, because a FEM-analysis and its results can not directly reflect on these effects, although they have a very great influence on the crankshaft life cycle, fatigue and damage accumulation.

Keywords: *crankshaft, design, material, manufacturing, stress, fatigue, FEM-analysis*

## 1. INTRODUCTION

The crankshaft of an internal combustion engine is undoubtedly one of the most important part of it. It basically determines the reliability and the life cycle of the engine. The complicated design of the crankshaft and the loadings acting on it make a little bit challenging the design process. Although over the decades several methods have been elaborated for designing a very rugged and reliable crankshaft several parameters and effects strongly influencing the adequate design of the crankshaft remained and in this article these attributes will be addressed.

## 2. INTRODUCTORY REMARKS

It is well known that the basic ageing process of the crankshaft is the fatigue caused by the varying forces and moments. If the basic characters of the loadings of a crankshaft are analysed than it can be stated that the forces are the radial, tangential forces, the supporting forces at the journal and the crankpin bearings, at the mounting surfaces of the crankcase respectively. The moments are the useful moment of the engine due to the tangential forces, the loading moment exerted by the driven machine, the tilting moment coming from the normal component of the resultant forces acting on the piston. Some additional loads can originate from the operational circumstances and the vibratory effects which have to be carefully analysed and computed. In this paper the attention is primarily devoted to the strength problems. The crankshafts nowadays are manufactured from alloyed, high-strength steel or high-strength nodular cast iron. To take into consideration of the material parameters needs a very careful investigation and sometimes very deep practical experiences.

## 3. LOAD-STATE DISTRIBUTION FUNCTION

The most realistic and reliable basis of the designing of a crankshaft is the so-called load-state distribution function of the engine. Such a function can be seen in Figure 1.

It had been elaborated based on the data gained from a diagnostic data logger of a diesel-electric locomotive.

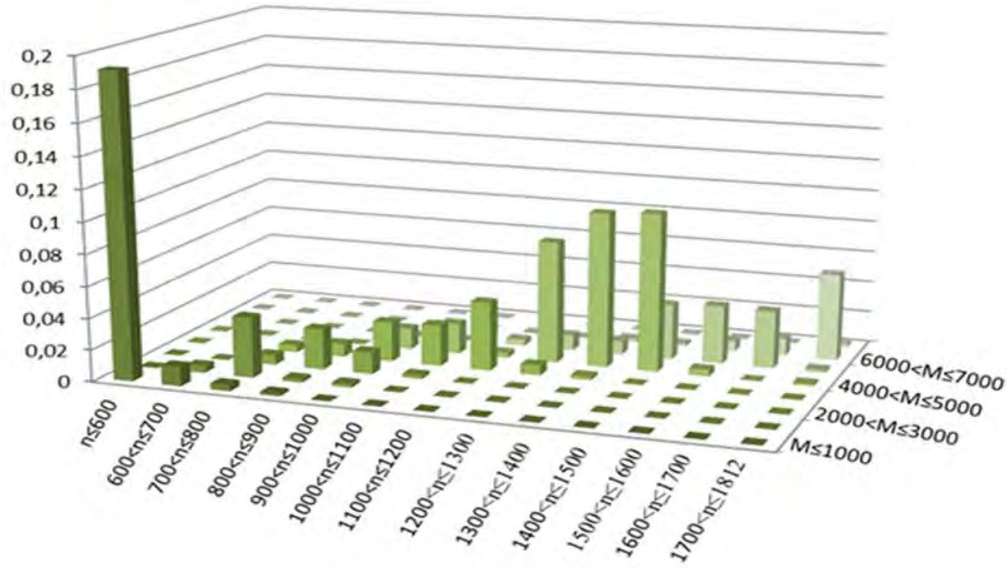


Fig. 1 An example of a load-state distribution function [1]

The heigths of the columns give the relative frequencies of the load-states above the external characteristics of the engine. It can and must be stated, that the results are in compliance with the practical experiences.

From the mean effective pressure of the engine and the RPM of the engine the working cycle can be derived. Every column in the Fig. 1. determines a load-state of the engine and taking into consideration the internal characters of the engine (gas-exchange process, valve timing, the parameters of crank mechanism etc.) the loading of the crankshaft can be computed.

## 4. THE MATERIAL CHARACTERISTICS

Now two material grade are used for manufacturing a crankshaft. The most important material is the alloyed high-strength steel which is generally press-forged. The other one is the high-strength nodular cast iron which is used for moderate stresses and quite balanced loadings.

In Fig. 2. the well-established Ramberg-Osgood material law can be seen for the two material grades with the data of [2]. Based on the curves the strain-hardening effect of the materials can be recognized. An important consequence is that the assumption of the linearity is only for the relatively small deflections adequate. But the attention should here be drawn that the material parameters should be very carefully determined.

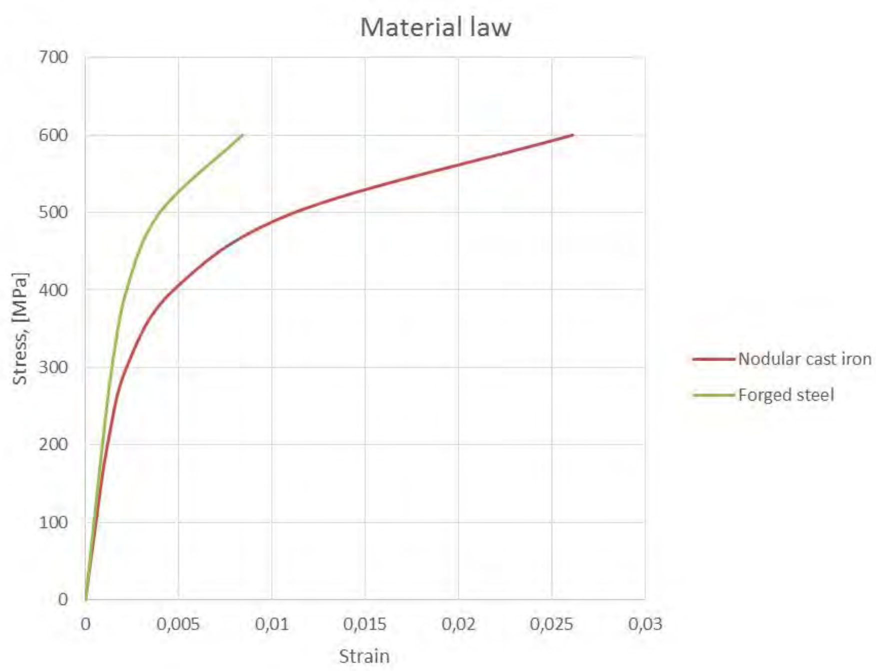


Fig. 2 The Ramberg-Osgood material law for forged steel and nodular cast iron [2.]

## 5. ANALYSIS OF THE STRESS STATE

On the basis of the loadings of the crankshaft the stress state of the cross section being computed can be analyzed.

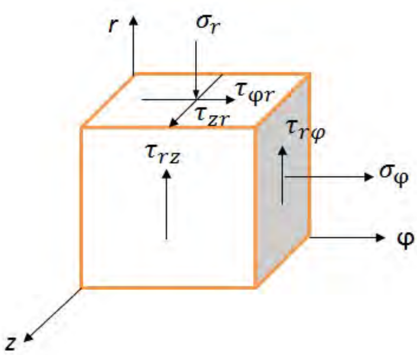


Fig. 3 The stress state on the infinitesimal cubicle in the middle of the crankpin

Due to the relatively complicated shape of the crankshaft its stress state is quite complex. In the Fig. 3. the stress state of the crankshaft for the middle of the crankpin is depicted in polar-coordinates. It can be recognized that it is a multi-axial stress state.

It has been mentioned that the basic ageing phenomenon of the crankshaft is the mechanical fatigue due to the fact that the loadings have a strong time-dependence and angular position dependence.
In the following homogeneous, isotropic materials are considered.

## 6. DIMENSIONING APPROACHES

The dimensioning methods can be classified into two main categories:

1. deterministic approach,
2. probabilistic approach.

### 6.1. The deterministic approach

Within the first category the following three subcategories can be identified:

1. stress-life (fatigue strength approach),
2. strain-life (fatigue life approach),
3. fracture mechanics (damage tolerant approach).

Generally speaking the stress-life approach is used mainly for the high-cycle fatigue, the strain-life approach is applied preferably for the low-cycle fatigue.
The standing point of the fracture mechanics is that there can be material defects in a raw material too. That is the reason why this method is referred to a damage-tolerant approach. In the next figure some of the fatigue criteria used in the practice is visualized which is naturally applied in the case of the stress-life approach. It is well impressive that there are relatively large differences between the several curves.

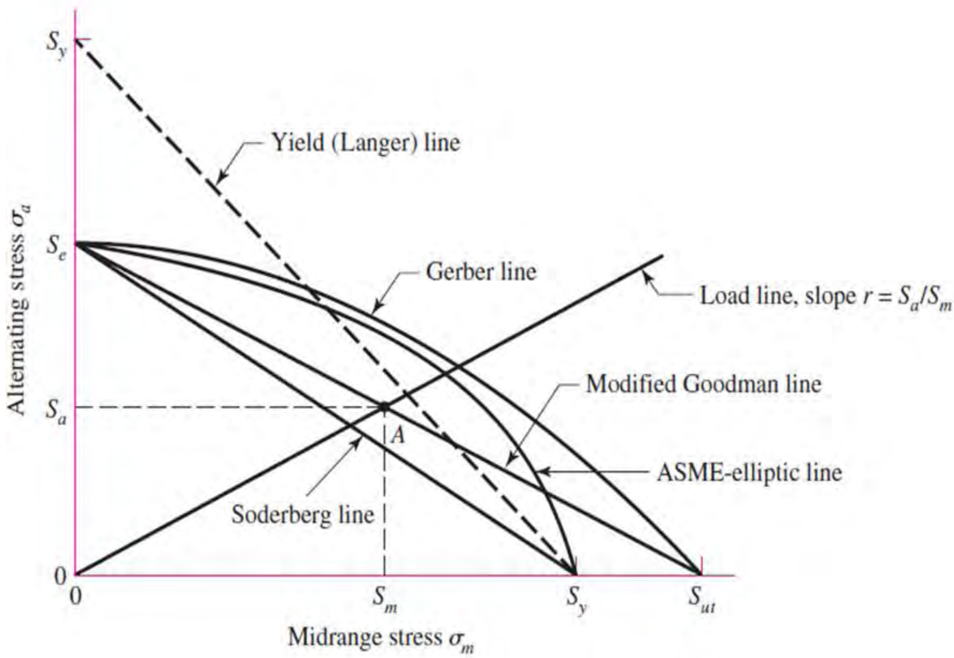


Fig. 4 The miscellaneous fatigue criteria used in the technical practice [4]

In the figure the *S* letter stand here for the several material strengths. The $\sigma$ provide the stresses exerted by the loadings in the material.

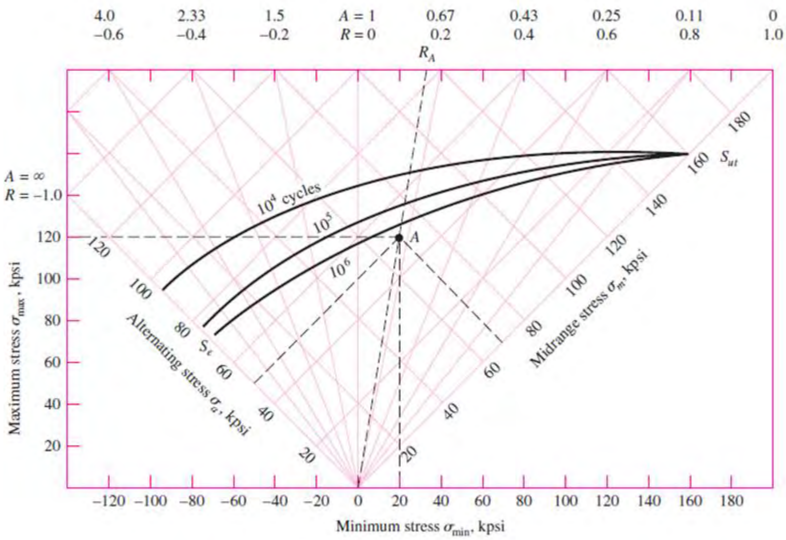


Fig. 5 Master fatigue diagram for an alloyed steel [4]

As an example in Fig. 5. the so-called master fatigue diagram of an alloyed steel is depicted in normalized scales. It is a very compact and informative summary of the fatigue parameters.

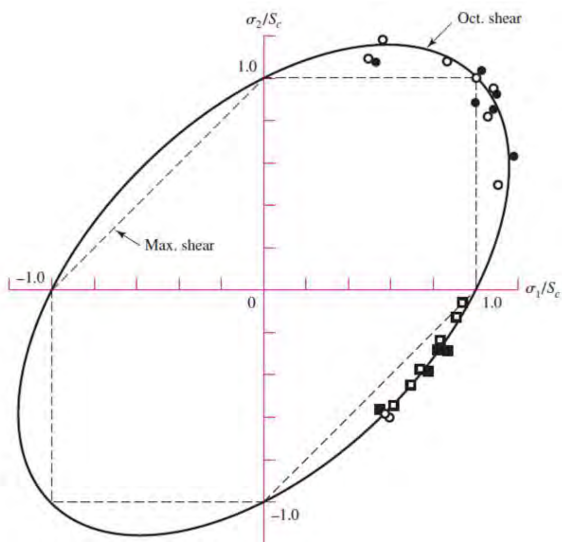


Fig. 6 The stress theories versus normalized equivalent stress [4]

In case of a plane stress state the several stress theories are depicted in the same diagram. The attention should be drawn that the choice of the stress theory (for example the hydrostatic stress sensitivity, out-of-phase conditions etc.) to be used needs to be thoroughly thought over.

In case of such a material which behaves different when being tensioned or compressed, as it is the case of the nodular cast iron and partially alloyed steels further investigation should be made whose results can be shown in Fig. 7.

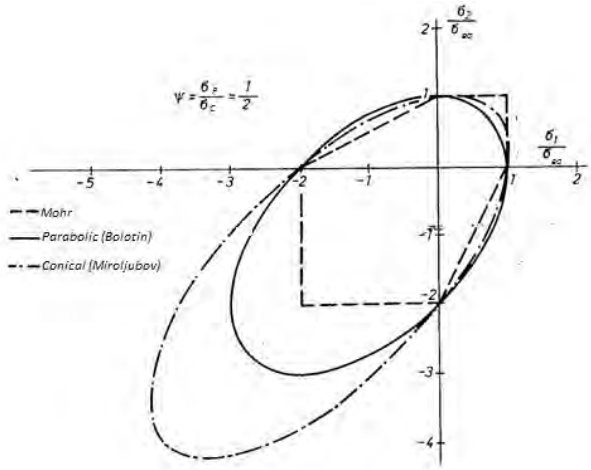


Fig. 7 The stress theories versus normalized equivalent stress in case of asymmetrical material behaviour [5]

The Miroljubov and Bolotin stress theories take into account the hydrostatis stress and the octahedral shear stress but Bolotin made the assumption that the equivalent stress is proportional the square of the octahedral shear stress. In the picture the $\psi$ gives the ratio of the ultimate tension strength and the ultimate compression strength.
The envelopes of the allowable stresses are shown in Fig. 6 and 7, corresponding to the stress theories and material characteristics used here.

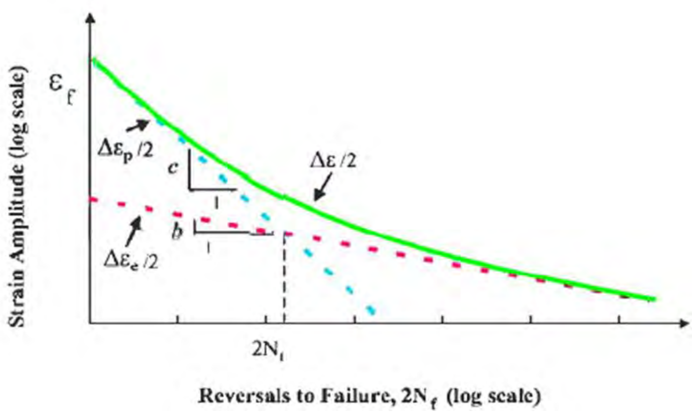


Fig. 8 Strain amplitude versus reversals to failure [6]

It has been mentioned that the strain-life approach is primarily usable for the low-cycle fatigue computation. In this case the total strain is divided into two parts namely the elastic and plastic strain. The following equation is the most known relationship called

Coffin-Manson equation for taking into consideration the material parameters and the stress:

$$\frac{\Delta\varepsilon}{2} = \frac{\sigma_f^{'}}{E} \cdot (2 \cdot N)^b + \varepsilon_f^{'} \cdot (2 \cdot N)^c,$$

where

- the *fatigue ductility coefficient* $\varepsilon_f'$ is the true strain corresponding to fracture in one reversal. The plastic-strain line begins at this point,
- *the fatigue strength coefficient* $\sigma_f'$ is the true stress corresponding to fracture in one reversal. Note that the elastic-strain line begins at $\sigma_f'/E$,
- *the fatigue ductility exponent c* is the slope of the plastic-strain line and is the power to which the life 2*N* must be raised to be proportional to the true plastic strain amplitude. If the number of stress reversals is 2*N*, then *N* is the number of cycles,
- *the fatigue strength exponent b* is the slope of the elastic-strain line, and is the power to which the life 2*N* must be raised to be proportional to the true-stress amplitude.

This relation shows how the strains and stresses can be interconnected.
The fracture mechanics reflects to the fact that a material ready for installation contains a some extent of defects. In other words the ageing process is considered to be basically a crack-propagation process. To conduct this another types of material parameters should be determined for numerical calculations.

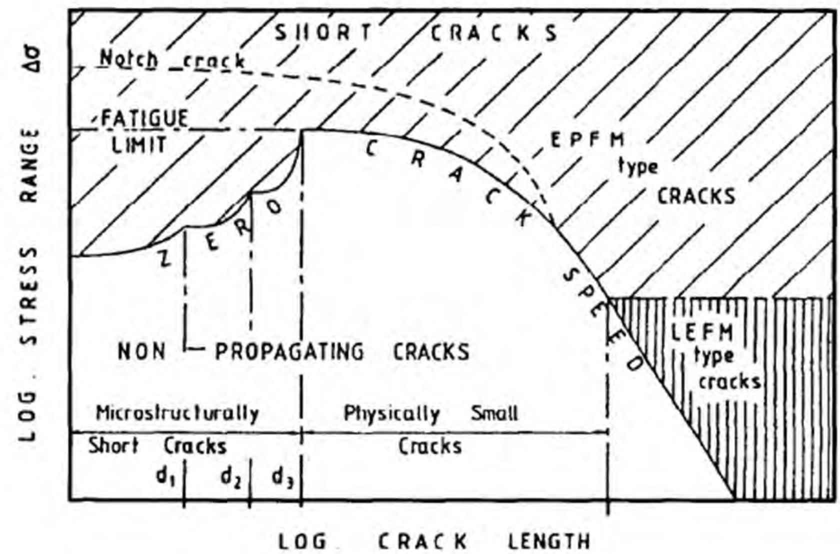


Fig. 9 The modified Kitagawa-Takahashi diagram [7]

In Fig. 9. a special summary is given about the zones differing from each other in the crack length and the stress ranges in the log-log scales.

## 6.2. The probabilistic approach

The most advanced and a relatively new method is the probabilistic approach. It tries to take into account all uncertainties associated with the loadings, the stress state, the stress gradients, the crack initiation, the fatigue process, the damage accumulation, the processing of experimental data etc.

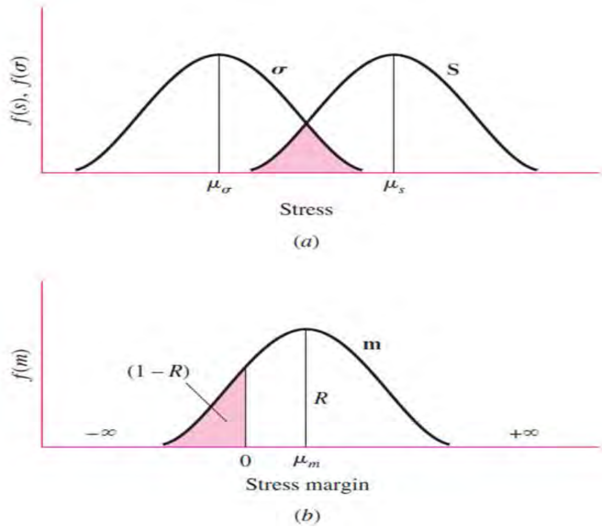


Fig. 10 Probability density functions for stress and strain [8]

In the deterministic approach the safety factor corresponds to the strength reserve. But in the opposite way when the probabilistic way is used the difference between the strength and the stress is the margin of safety. If it is negative the part is expected to fail. Based on this the reliability of a component can be interpreted as the probability that the margin of safety is higher than zero.

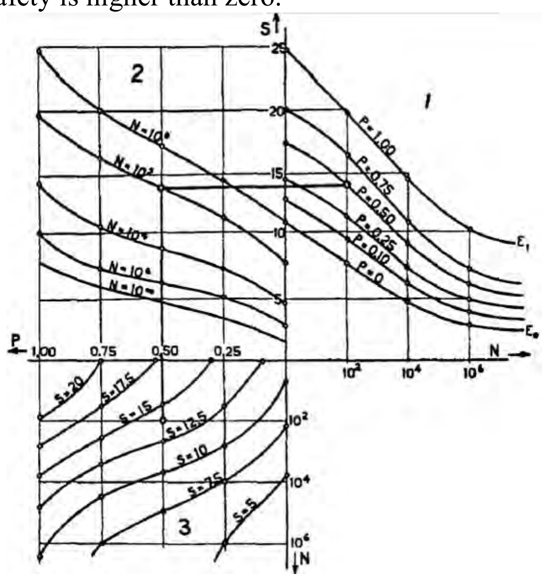

Fig. 11 The complete fatigue diagram [8]

In the probabilistic approach the three basic questions are to be answered:
1. Fracture possibility,
2. Stress over one cycle,
3. Life-cycle, the total number of the load cycles survived.

In Fig. 11 the complete fatigue diagram is shown. In this diagram *P* stands for the fracture possibility, S stands for stress over one cycle and *N* is the life-cycle.

## 7. CONCLUDING REMARKS

On the basis of our investigations the following conclusions can be drawn:
1. The crankshaft is a very complicated and one of the most important component of an engine.
2. This component needs to be designed in a very comprehensive manner.
3. The choice of the adequate methods and parameters is vital for designing a rugged, reliable crankshaft.
4. Although several methods had been elaborated for the crankshaft design, no general method can be given for the dimensioning.
5. Over the design process every choice has to be done very carefully.
6. In the near future the even greater importance of the probabilistic method can be expexted.

## 8. REFERENCES

[1] **Gargya, A.:** Operational experiences of a repowered diesel locomotive M62, 2012 Diploma thesis

[2] **Fatemi, A. – Williams, J. – Montazersagdh, F.:** Fatigue Performance Evaluations of Forged Steel versus Ductile Cast Iron Crankshaft: A Comparative Study, University of Toledo, August, 2007

[3] **Suresh, S.:** Fatigue of Materials, 2nd Edition, Cambridge University Press, 2002

[4] **R. G. Budynas, J. K. Nisbett:** Shigley’s Mechanical Engineering Design, 9th Edition, McGraw-Hill, 2010

[5] **Muttnyánszky, Á. et al:** Szilárdságtan (Strength theory), Tankönyvkiadó, Budapest, 1981. (in Hungarian)

[6] **Suresh, S.:** Fatigue and Fracture presentation, MIT, 2000

[7] **Fatemi, A. – Yang, L.:** Cumulative fatigue damage and life prediction theories: a survey of the state of the art for homogeneous materials, Elsevier Science Ltd. 1988

[8] **Weibull, W.:** A statistical representation of fatigue failures in solids, Transactions of The Royal Institute of Technology, Stockholm, 1949

# THERMAL SIMULATION TO ENSURE HEAT MANAGEMENT OF VEHICLE ECUS WITH PLASTIC ENCLOSURE

**Anna HIDAS**

Budapest University of Technology and Economics,
Faculty of Transportation Engineering and Vehicle Engineering
Department of Aeronautics, Naval Architecture and Railway Vehicles,
H-1111 Budapest, Stoczek u. 6. Bldg. J., 427, Hungary
E-Mail: ahidas@vrht.bme.hu
Phone: +36 30 2051773

## ABSTRACT

Electronic Control Units (ECUs) are critical components of the vehicle operation, as they control important safety functions such as the Anti-lock Braking System (ABS). Thus they have to meet several criteria: they have to be able to operate even in harsh conditions while environmental implications and the suitability for high volume manufacturing should be taken into consideration as well. Therefore heat management becomes a central problem, since it has a significant impact on the reliability and durability of the system. Electronic modules in vehicles are usually sealed to prevent moisture or dust from entering the unit. Thus convection cooling of the system is compromised and conduction becomes the dominant way of taking the heat away from the Printed Circuit Board (PCB). Normally the heat is transferred through the enclosure of the ECU to the vehicle structural body. It can be seen that the materials used in the ECU are an important part of the thermal considerations, choosing a good conductor as the enclosure material eases thermal management of the system. Even so manufacturers would like to reduce product cost, and for that reason substitute the metal (e.g. aluminium) parts with economically better performing - cheaper and lighter - plastic parts, even though their thermal properties are not ideal. In such situations it is extremely important to analyse whether the new design can still accurately take the heat away from the electronic components. Thermal simulation of the system can be a key in the redesign process, in case a fast and reliable simulation tool is available to check the thermal performance of different concepts. Here a simulation process is presented along with validation to demonstrate its capabilities of predicting system behaviour in the described situation. Therefore the original design was simulated, and the simulation results were validated with several measurements. Through this process the accuracy of the simulation was ensured, and the new design could be evaluated with the help of the introduced simulation method.

# DEPENDABILITY OF VEHICLE SYSTEMS WITH COMPLEX INTERCONNECTIONS

**László POKORÁDI and Tímea LÁZÁR-FÜLEP**

Donát Bánki Faculty of Mechanical and Safety Engineering
Óbuda University
H-1081 Budapest, Hungary

*Received: November 5, 2018*

## ABSTRACT

The issue of safety is of increasing importance also in the automotive industries. This includes making driving and the components, their architecture safer. This latter, system safety, depends strongly on the failure probability of individual components and how it handles dif-ferent faults, errors and failures. In wide interpretation, under the notion of dependability, system safety expresses operation without catastrophic events harming users and the environ-ment, while reliability and availability present the continuity in system readiness. Reliability is more precised concerning its time dependence from which availability can be derived. In today's automotive industry, companies are organized into simultaneous engineering teams to develop their new products. The new way of doing business enables some companies to develop their new products quicker, cheaper with higher quality and reliability. In the past years there has been the tendency to increase the safety of vehicles by introducing intelligent assistance systems that help the driver to cope with critical driving situations. These functions are characterized by the active control of the driving dynamics by distributed assistance systems, which therefore need a reliable communication network. Electronic components controlling these functions, are safety-critical. However, the assistance functions deliver only an add-on service in accordance with a fail-safe strategy for the electronic components. If there is any doubt about the correct behaviour of the assistance system, it will be switched off. For by-wire systems without a mechanical back-up a new dimension of safety requirements for automotive electronics is reached. After a fault the system has to be fail-operational until a safe state is reached.
In this paper different available methods are going to be presented investigating the adaptability to vehicle systems with complex interconnections.

*Keywords:* reliability, safety, vehicle system, complex interconnection

## 1. INTRODUCTION

This paper is closely connected to EFOP project called Dynamics and Control of Autonomous Vehicles meeting the Synergy Demands of Automated Transport Systems (EFOP-3.6.2-16-2017-00016), in which the following research consortium is taking part: Széchenyi István University, Neumann János University, Dunaújvárosi University and Óbudai University [6].

The aim of the research is to elaborate mathematical methods and procedures which support design of technical systems and system elements with increasing complexity introduced in autonomous vehicles and transportation systems taking into operational safety and maintenance risk factors into account. This includes investigation of reliability and development of the joint risk assessment methods of vehicle sensor networks.

Nowadays one of the most important social issues is safety reliability and risk. These highly affect engineers and experts who design and operate different technical systems based on their specializations.

The main research aim of the authors is elaborating and studying applicability of different mathematical solutions and well-algorithmizable models for supporting decision making in reliability and safety engineering of vehicle systems with complex interconnections e.g. vehicle sensor networks. Beyond introducing the project the paper presents the topics mentioned above.

Determinate target of the project is to improve research and development conditions in human resources and services. In order to provide proper dissemination and long term financing strong cooperation with economic sphere is inevitable thus it is need to be strengthened and facilitated.

Long term goal of common research of the consortium partners is that with common force they can have a more active and initiative role in creating knowledge based economics and enhancing research and development potential in Hungarian higher education. Based on the created new knowledge bases participation and cooperation in international networks is initiated. Short term goals are cooperation in network and forming common research groups by harmonizing capacities of which synergic effects can multiply the actual individual potentials of the institutions [6].

Concrete goal of the research is that the partner institutions gain significant results in control and communication of autonomous vehicle and vehicle systems. Seven joint research areas were assigned by the partners, which are structured in three main research directions. The method is based on integrated approach and interactions of related research problems focusing on cooperation based on mutual strengths and common human resource development.

According to different technical-economic analyses the following prerequisites are needed for autonomous transport with reliable and available operation:

- On-board environmental observation technologies working properly in different conditions.
- High precision localization technologies, which can complete sensor data with geographical information during decision making and organize, select and prepare them for the perception system according to their spatial connection.
- Communication technologies which make information connection among traffic players, the related infrastructure and the environmental elements in general.
- Perception methods, which enable to analyze decision making situations in real time based on sensor and communication data and support control system adapted to the given situation.
- Low level vehicle control algorithms with complex, local controlling operation of each vehicle including actuator operation by real time decision making based on perception algorithms in order to fulfill the transport mission safely determined for the vehicle at a required performance.
- High level vehicle control making vehicle group control possible along general aspects by and in the interest of real time complex traffic control solutions and achievement of global optimum conditions.
- Application of innovative materials, vehicle drive and fuels with better adaptability to total automatization.

The goals are defined by the scientific application and they are unambiguously determined also adjusted to concrete project goals.

In this paper two different available methods are going to be presented investigating the reliability to vehicle sensors as systems with complex interconnections.

## 2. DEPENDABILITY AS GENERAL RELIABILITY

In wide interpretation, under the notion of dependability (general reliability), inspiring trust in system service, system safety expresses operation without catastrophic events harming users and the environ-ment, while reliability and availability present the continuity in system readiness. Reliability is more precised concerning its time dependence from which availability can be derived [11].

To increase reliability of a given system more features and parameters of reliability can be determined in order make it measurable. The following notions give an insight into these system features: Reliability has several kinds of definitions and all of them give a general operation statement about system functioning: ‘the probability that…’ ‘a unit will function normally when used according to specified conditions for at least a stated period of time’ or ‘a component (or system) can perform a required function under stated conditions for a given period of time’.

There is a quite wide range of calculation with time concerning failure from different aspects. The following determinations are also used in evaluation, e.g. Mean Time Between Critical Failures (MTBCF), Time Between Failure (TBF). Determining the Mean Time Between Failures (MTBF) for highly redundant systems is an extremely tedious, if not math-ematically difficult process. These systems are typically characterized by hierarchical application of nonidentical component (k of n) reliability calculations. Multiple levels in the hierarchy and large values of k and n make this calculation nearly intractable.

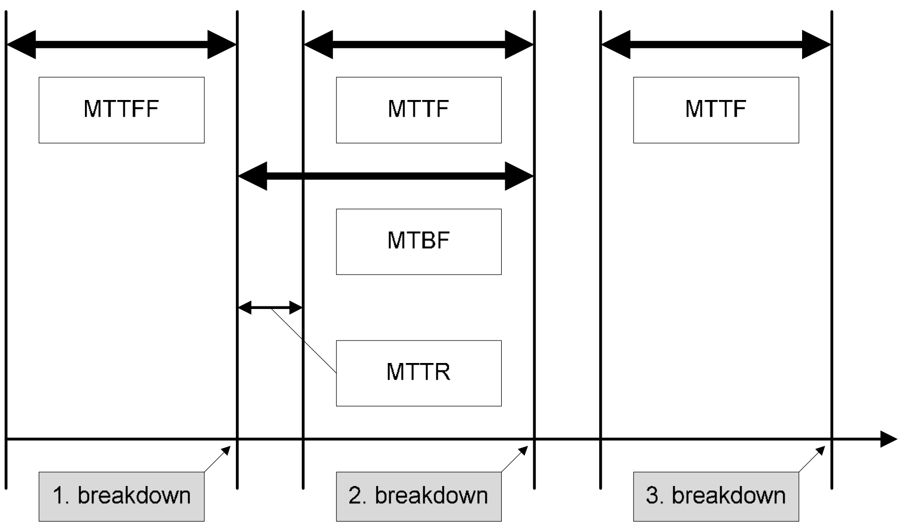


Fig. 1 System lifecycle statistical parameters

The Fig. 1 illustrates the measures like MTTFF (Mean Time To First Failure), MTTF

(Mean Time To Failure), MTBF, MTTR (Mean Time Between Repair).
A system with high reliability may not necessarily be highly fault-tolerant. It is desirable to have a redundant system reconfigured so that it can tolerate a large number of faults. In many critical applications, fault-tolerance has been essential architectural attribute for achieving high reliability. Redundancy is provided on a massive scale in critical systems requiring ultra-high reliability. The massively redundant schemes are of two types: fault masking and standby redundancy. Interestingly, in these schemes, the number of faults that are tolerated is very small compared to the number of redundant modules employed. This implies a large cost to reliability ratio.
Design redundancy requires that a failure in one function does not impair the system's ability to reconfigure to an equivalent back-up function. Redundancy can be used at hardware level, software level or in time, but it is now well-accepted that computer systems cannot achieve the required reliability and fault-tolerance without employing redundancy in their structures. Differences can be made between active ('hot') and passive ('cold') operation implementations. While the former means simultaneously functioning in the 'background', the latter interprets inactive functionality, which is switched on when the primary means of performing the function fails.
Because electronics can fail suddenly and without warning, redundant and fault-tolerant systems are traditionally used for safety-critical functions, such as in aerospace. The obvious benefit of redundancy is that it provides a back-up to a failed component. In avionics safe-life systems are required since there should not be possibility of error due to faults. As it is well-known, no aircraft has ever remained in the sky, so it should continue flight until it can land.

## 3. SYSTEMS WITH COMPLEX INTERCONNECTION

The sensors used in automotives can be modelled as Bridge Structure Systems (BSS). The BSS shown in Figure 2 has five elements, $A$; $B$; $C$; $D$; $E$. Their reliability can be characterized by reliability ri i∈L and probability of failure: $p_i$ $i \in L$ , where $L$ is set of Latin characters $A$; $B$; $C$; $D$; $E$.

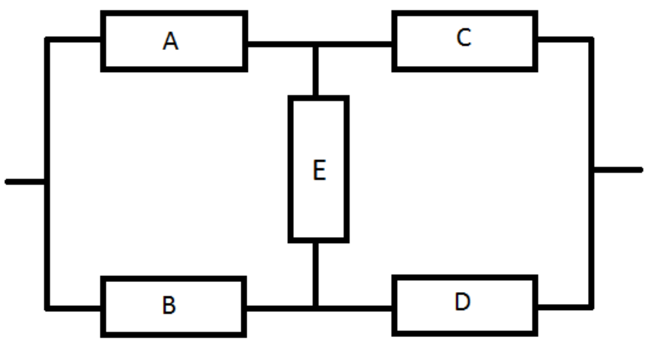


Fig. 2 Reliability Block Diagram of BSS

| *i* | A | B | C | D | E | System | $Q_i$ |
|---|---|---|---|---|---|---|---|
| 1 | 0 | 0 | 0 | 0 | 0 | 0 | $p_A\, p_B\, p_C\, p_D\, p_E$ |
| 2 | 1 | 0 | 0 | 0 | 0 | 0 | $r_A\, p_B\, p_C\, p_D\, p_E$ |
| 3 | 0 | 1 | 0 | 0 | 0 | 0 | $p_A\, r_B\, p_C\, p_D\, p_E$ |
| 4 | 1 | 1 | 0 | 0 | 0 | 0 | $r_A\, r_B\, p_C\, p_D\, p_E$ |
| 5 | 0 | 0 | 1 | 0 | 0 | 0 | $p_A\, p_B\, r_C\, p_D\, p_E$ |
| 6 | 1 | 0 | 1 | 0 | 0 | 1 | $r_A\, p_B\, r_C\, p_D\, p_E$ |
| 7 | 0 | 1 | 1 | 0 | 0 | 0 | $p_A\, r_B\, r_C\, p_D\, p_E$ |
| 8 | 1 | 1 | 1 | 0 | 0 | 1 | $r_A\, r_B\, r_C\, p_D\, p_E$ |
| 9 | 0 | 0 | 0 | 1 | 0 | 0 | $p_A\, p_B\, p_C\, r_D\, p_E$ |
| 10 | 1 | 0 | 0 | 1 | 0 | 0 | $r_A\, p_B\, p_C\, r_D\, p_E$ |
| 11 | 0 | 1 | 0 | 1 | 0 | 1 | $p_A\, r_B\, p_C\, r_D\, p_E$ |
| 12 | 1 | 1 | 0 | 1 | 0 | 1 | $r_A\, r_B\, p_C\, r_D\, p_E$ |
| 13 | 0 | 0 | 1 | 1 | 0 | 0 | $p_A\, p_B\, r_C\, r_D\, p_E$ |
| 14 | 1 | 0 | 1 | 1 | 0 | 1 | $r_A\, p_B\, r_C\, r_D\, p_E$ |
| 15 | 0 | 1 | 1 | 1 | 0 | 1 | $p_A\, r_B\, r_C\, r_D\, p_E$ |
| 16 | 1 | 1 | 1 | 1 | 0 | 1 | $r_A\, r_B\, r_C\, r_D\, p_E$ |
| 17 | 0 | 0 | 0 | 0 | 1 | 0 | $p_A\, p_B\, p_C\, p_D\, r_E$ |
| 18 | 1 | 0 | 0 | 0 | 1 | 0 | $r_A\, p_B\, p_C\, p_D\, r_E$ |
| 19 | 0 | 1 | 0 | 0 | 1 | 0 | $p_A\, r_B\, p_C\, p_D\, r_E$ |
| 20 | 1 | 1 | 0 | 0 | 1 | 0 | $r_A\, r_B\, p_C\, p_D\, r_E$ |
| 21 | 0 | 0 | 1 | 0 | 1 | 0 | $p_A\, p_B\, r_C\, p_D\, r_E$ |
| 22 | 1 | 0 | 1 | 0 | 1 | 1 | $r_A\, p_B\, r_C\, p_D\, r_E$ |
| 23 | 0 | 1 | 1 | 0 | 1 | 1 | $p_A\, r_B\, r_C\, p_D\, r_E$ |
| 24 | 1 | 1 | 1 | 0 | 1 | 1 | $r_A\, r_B\, r_C\, p_D\, r_E$ |
| 25 | 0 | 0 | 0 | 1 | 1 | 0 | $p_A\, p_B\, p_C\, r_D\, r_E$ |
| 26 | 1 | 0 | 0 | 1 | 1 | 1 | $r_A\, p_B\, p_C\, r_D\, r_E$ |
| 27 | 0 | 1 | 0 | 1 | 1 | 1 | $p_A\, r_B\, p_C\, r_D\, r_E$ |
| 28 | 1 | 1 | 0 | 1 | 1 | 1 | $r_A\, r_B\, p_C\, r_D\, r_E$ |
| 29 | 0 | 0 | 1 | 1 | 1 | 0 | $p_A\, p_B\, r_C\, r_D\, r_E$ |
| 30 | 1 | 0 | 1 | 1 | 1 | 1 | $r_A\, p_B\, r_C\, r_D\, r_E$ |
| 31 | 0 | 1 | 1 | 1 | 1 | 1 | $p_A\, r_B\, r_C\, r_D\, r_E$ |
| 32 | 1 | 1 | 1 | 1 | 1 | 1 | $r_A\, r_B\, r_C\, r_D\, r_E$ |

Table I Truth Table of BSS

Table II. shows the probabilities of failure of elements the investigated BSS [8]. The elements have only two – operating and non-operating – states. In case of operating state an item is performing its required function. If an item is in non-operating state, it is not performing its required function. Sum of probabilities of operating and non-operating should be unity:

$$p_i + r_i = 1 \quad . \tag{1}$$

One of the approaches to correctly compute the unreliability of BSS is the summation of the probabilities of all non-operating system states of the investigated sensor. A table listing the probability of each possible state for a system is frequently referred to a truth table. The elements and the complete system can be operating (designated as the 1 state) or non-operating ones (designated as the 0 state).

The possible system states are summarized in the form of a truth table, shown in Table I., with each element being assigned either an operating or a non-operating state. The $Q_j\ , j \in N$ column lists the probabilities of each of the system states. Since the table covers all of the possible combinations, the sum of all of the state probabilities should be 1.

The state probabilities resulting in an operating system are included in the rows 6; 8; 11; 12; 14; 15; 16; 22; 23; 24; 26; 27; 28; 30; 31 and 32. The

$$R_{sys} = Q_6 + Q_8 + Q_{11} + Q_{12} + Q_{14} + Q_{15} + Q_{16} + Q_{22} + Q_{23} + Q_{24} + Q_{26} + Q_{27} + Q_{28} + Q_{30} + Q_{31} + Q_{32} \tag{2}$$

sum of the operating system state probabilities included in this column is the reliability of the system. The Table II shows system reliabilities $R_{sys}$ in case of different reliabilities of element $r_i$.

| $r_i$ | $R_{sys}$ |
|---|---|
| 0.90 | 0.9785 |
| 0.95 | 0.9948 |
| 0.99 | 0.9998 |

Table II System Reliabilities in Cases of Different Reliabilities of Elements

## 4. MONTE-CARLO SIMULATION

Aleatory uncertainty is an inherent variation associated with the investigated vehicle system or its environment. It is also called as variability, irreducible, random uncertainty or (in the control theory) parametric one. Aleatory uncertainty is primarily associated with objectivity. Its possible „engineering“ sources:

- incorrect measuring;
- measuring noises;
- discretization;
- strong statistical information;
- sparse statistical information;
- using of linguistic data;
- selecting the appropriate database;
- manufacturing anomalies.

One of the most well-known probabilistic uncertainty investigation methods is the Monte Carlo simulation. The “classical” Monte Carlo simulation is used as an uncertainty analysis of a deterministic calculation because it yields a distribution describing the probability of alternative possible values about the nominal (designed) point. The name Monte-Carlo was applied to this class of mathematical methods by scientists working on the development of nuclear weapons during the Manhattan Project in Los Alamos. All Monte-Carlo Simulations have the following common features:

1) A known *f(x)* probability density function over the set of system inputs.
2) Random sampling of inputs based on the distribution specified in feature 1) and simulation of the system under the selected inputs.
3) Numerical aggregation of experimental data collected from multiple simulations conducted according to feature 2).

| | | | |
|---|---|---|---|
| **Gauss distribution** | | | |
| **A** | mean: 0.73 | deviation: 0,021 | |
| **C** | mean: 0.70 | deviation 0,025 | |
| **Weibull-distribution** | | | |
| **B** | location: 0.53 | shape: 1.5 | scale: 0.07 |
| **D** | location: 0.57 | shape: 2.0 | scale: 0.06 |
| **Uniform distribution** | | | |
| **E** | min.: 0.60 | max.: 0.80 | |

Table III. Used Distribution of Reliabilities of Elements

Numerical experiments of Monte-Carlo Simulation lead us to run the simulation on many sampled inputs before we can infer the values of the most interesting system performance measures. At its heart it is a computational procedure in which a performance measure is estimated using samples drawn randomly from a population with appropriate statistical properties. The selection of samples, in turn, requires an appropriate random number generator.
During our investigation the number of samples was 500 000. The table III. shows the used distribution and their data. Fig. 3 shows histograms of simulation.
The results of Monte-Carlo Simulation method can be used:
- for analyzing of reliability of bridge structure senzors;
- for estimating the availability and Required Number for Spare Part depending on required estimating uncertainty;
- for assessing the Numbers of Failures depending on required estimating uncertainty.

## 5. CONCLUDING REMARKS

The Dynamics and Control of Autonomous Vehicles meeting the Synergy Demands of Automated Transport Systems (EFOP-3.6.2-16-2017-00016) project was introduced in this paper. Within the project the Óbudai University, Institute of Mechatronics and Vehicle Engineering is examining sensor networks and systems including their reliable and safe operation.
The aim of the Authors' research is to elaborate mathematical methods and procedures which support design of technical systems and system elements with increasing complexity introduced in autonomous vehicles and transportation systems taking into

operational safety and maintenance risk factors into account. This includes investigation of reliability and development of the joint risk assessment methods of vehicle sensor networks.

The first results of our project form Óbuda University can be read in papers [1]; [2]; [3]; [4] ; [5]; [7]; [9]; [10]; [12]; [13]; [14] and [15].

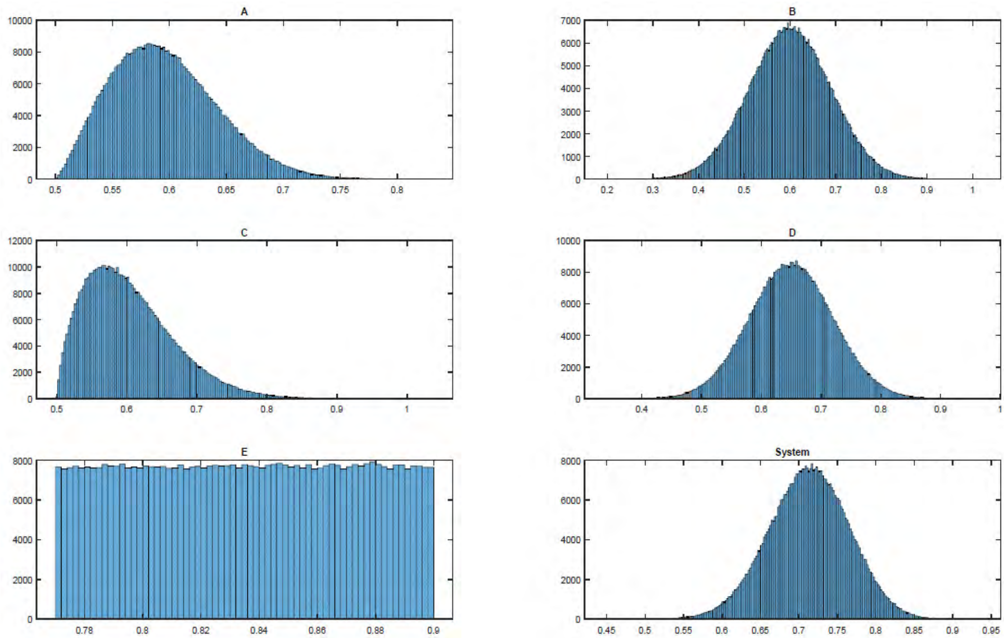


Fig. 3 Inputs and Result of Monte-Carlo Simulation

## ACKNOWLEDGEMENT

The research presented in this paper was carried out as part of the EFOP-3.6.2-16-2017-00016 project in the framework of the New Széchenyi Plan. The completion of this project is funded by the European Union and co-financed by the European Social Fund.

## 6. REFERENCES

[1] **Berecz, É.Cs. - Kiss, G.**: Dangers in Autonomous Vehicles. Proc. of the IEEE 18th International Symposium on Computational Intelligence and Informatics (CINTI 2018), 2018, p.263-268.

[2] **Drexler, D.Á. - Takács, Á. - Galambos, P. - Rudas I.J. – Haidegger, T.:** Handover Process Models of Autonomous Cars Up To Level 3 Autonomy. Proc. of the IEEE 18th International Symposium on Computational Intelligence and Informatics (CINTI 2018), 2018, p.307-312.

[3] **Koncz, A. – Pokorádi, L.**: Usage in Automotive Industry. Proc. of the IEEE 18th International Symposium on Computational Intelligence and Informatics (CINTI 2018), 2018, p.257-262.

[4] **Lázár-Fülep, T.:** Few Words about Reliability of Vehicle Systems with Complex Interconnections. Proc. of the IEEE 18th International Symposium on Computational Intelligence and Informatics (CINTI 2018), 2018, p.273-276.

[5] **Nagy, I. - Tuloki, Sz.:** Fault Analysis and System Modelling in Vehicle Engineering. Proc. of the IEEE 18th International Symposium on Computational Intelligence and Informatics (CINTI 2018), 2018, p.313-319.

[6] Pályázati felhívás a felsőoktatási rendszer K+F+I szerepvállalásának növelésére: Tematikus kutatási hálózati együttműködések – EFOP-3.6.2-16.

[7] **Pokorádi, L. – Ványi, G.:** Sensitivity analysis of FMEA as possible ranking method in risk prioritization Politechnical University of Bucharest Scientific Bulletin. Series D: Mechanical Engineering 80:(3) 2018, p.165-176.

[8] **Pokorádi, L.:** Failure Probability Analysis of Bridge Structure Systems. Proc. of the 10th Jubilee IEEE International Symposium on Applied Computational Intelligence and Informatics, 2015, p.319 – 322.

[9] **Pokorádi, L.:** Graph model-based analysis of technical systems IOP Conference Series: Materials Science and Engineering Volume 393, Issue 1,

[10] **Pokorádi L.:** Methodology of Advanced Graph Model-based Vehicle Systems' Analysis. Proc. of the IEEE 18th International Symposium on Computational Intelligence and Informatics (CINTI 2018), 2018, p.325-328.

[11] **Pokorádi, L. - Fülep, T.:** Reliability in Automotive Engineering by Fuzzy Rule-Based FMEA Proc. of the FISITA 2012, p.793-800.

[12] **Szénási, S. - Felde, I. - Kertész, G. – Nádai, L.:** Comparison of Road Accident Black Spot Searching Methods. Proc. of the IEEE 18th International Symposium on Computational Intelligence and Informatics (CINTI 2018), 2018, p.247-250.

[13] **Szénási, S. - Felde, I. - Kertész, G. – Nádai, L.:** Road Accident Black Spot Localisation using Morphological Image Processing Methods on Heatmap. Proc. of the IEEE 18th International Symposium on Computational Intelligence and Informatics (CINTI 2018), 2018, p.251-256.

[14] **Tóth, L. - Kiss, G.**: The Relationship between Standard and Autonomous Vehicles. Proc. of the IEEE 18th International Symposium on Computational Intelligence and Informatics (CINTI 2018), 2018, p.269-272.

[15] **Tuloki, Sz. – Nagy, I.**: Mapping and Security Analysis of Sensor Network for Electric Vehicles. Proc. of the XXIIIrd International Scientific Conference of Young Engineers, 2018, p.243-247.

# GRAPH-THEORETICAL INVESTIGATION INTO VEHICLE AND TRANSPORTATION SYSTEMS

**László POKORÁDI[1] and Vilmos SOMOSI[2]**

[1]Óbuda University Institute of Mechatronics and Vehicle Engineering
H-1081 Budapest Népszínház u. 8, Hungary
pokoradi.laszlo@bgk.uni-obuda.hu
[2]HungaroControl Hungarian Air Navigation Services
H-1185 Budapest, Igló u. 33
vilmos.somosi@hungarocontrol.hu

*Received: November 5, 2016*

## ABSTRACT

Vehicle and transportation systems generally have network structures. During mathematical model-based analysis and synthesis of these systems, it is a key issue the determination of existence of interconnection between the subsystems and components. In cases of integrated and complex systems their exposures can be difficult task because of complexity of interconnections. Graph theory is a well-known mathematical tool; to study interconnections between components of network structure systems. The main aim of the paper is to show an easy-usable algorithm for determination of existence of interconnection (connection matrix) between the network structure system-components. The paper shows the proposed methodology theoretically and through two case studies demonstrating its possibilities of use.

*Keywords:* transportation; vehicle systems; graph theory; interconnection

## 1. INTRODUCTION

Graphs are models to study interconnections between components of network structure systems. Graph theory is the historical mathematical background of the modern network's science. Graph theory is one of the tools of the efficient mathematic modelling of the transport and communication systems. The first significant step in the network analysis is the exploration and visualization of the relationship (dependency) between the elements, which can also represent complex interactions among them.

The paper of Lázár-Fülep is closely connected to EFOP project called Dynamics and Control of Autonomous Vehicles meeting the Synergy Demands of Automated Transport Systems (EFOP-3.6.2-16-2017-00016), in which the following research consortium is taking part: Széchenyi István University, Neumann János University, Dunaújvárosi University and Óbudai University. The aim of the research mentioned above is to elaborate mathematical methods and procedures which support design of technical systems and system elements with increasing complexity introduced in autonomous vehicles and transportation systems taking into operational safety and maintenance risk factors into account [3]. This includes investigation of reliability and development of the joint risk assessment methods of vehicle sensor networks [4] [10].

There is a vast literature on graph theory and its applications, including many articles and books. In the book Finke [2] there is a comprehensive theoretical background. Péter has shown a new model developed for complex road networks [7].

The publication of *Somosi* and *Pokorádi* introduced the special data connectivity of surveillance systems for Hungarian Air Navigation Service Provider's (HungaroControl) remote en-route Air Traffic Services in Kosovo upper airspace by by Graph-analysis which is an efficient tool for modelling such a complex transport and communication networks [8].

The paper [6] dealt with a solution of the power supply providers' practical problem. Its Authors give answer to the question that if an equipment fails in the network then consequently, how many customers are affected by the blackout.

The aim of *Pokorádi*'s paper [9] was to show a new, easy-usable algorithm for the determination of existence of interconnection between the network structure system-components or states of technical processes. The proposed method is adaptable to the model sensor networks in automotive engineering and to the investigations of their uncertainties and reliability.

In paper of *Nagy* and *Tuloki* a real, fully electric vehicle's sensor and communication network system (Nissan Leaf Z0) is explored, then the wheel speed sensor operation is analyzed, drawing attention to the sensor faults and fault error spreading in the network. Furthermore, the vehicle's system model will be created and shown, how the sensor faults are built-in into this model [4].

The aims of this paper is to show a methodology of determination of interconnection between the system-components theoretically and its possibilities of use by case studies.

The outline of the paper is as follows: Section 2 shows theoretical background of graph-modell based investigation of systems shortly. Section 3 presents two case studies to demonstrate possibilities of use of proposed method. Section 4 summarizes the paper, outlines the prospective scientific work of the Authors.

## 2. GRAPH THEORETICAL BACKGROUND

A graph $G = (N,L,f)$ is a 3-tuple (a triple) consisting of a set of nodes $N$, a set of links $L$, and a mapping function $f : L \rightarrow N \times N$, which maps links into pairs of nodes. Nodes directly connected by a link are called *adjacent* nodes.

The direct links are ignored in the graph's adjacency matrix $\mathbf{A}$ – which shows the number of links directly connecting node $i$ to node $j$.

The connection matrix $\mathbf{Z}$ contains a 1 in row $i$ column $j$ if one or more links connect node $i$ to node $j$. In other words, connection matrix shows that can we get at node $j$ from node $i$. For example, the connection matrix can be used for troubleshooting or to determine "sink states" of technical processes in engineering practice.

It is obvious that element of the *k-th* power matrix $\mathbf{A}^k$ of matrix $\mathbf{A}$ shows the number of independent $k$-long paths from node $i$ to node $j$.

The element $\mathbf{H}_k$ of

$$\mathbf{H}_k = \sum_{n=1}^{k} \mathbf{A}^n \tag{1}$$

summarized the matrix of power matrices shows the number of independent, maximum $k$-long paths from node i to node j.

Let us generate signum matrix $\mathbf{S}_k$ of $\mathbf{H}_k$ using following function:

$$\mathbf{S}_k = sign\ \ \mathbf{H}_k \quad s_{ij}^{[k]} = sign\ h_{ij}^{[k]} \quad . \tag{2}$$

If

$$\mathbf{A}^k = \mathbf{N} \quad , \tag{3}$$

where **N** is zero (null) matrix, then the length of the longest path of graph is $k$ - *1*. The equality

$$\mathbf{S}_k = \mathbf{J} \ , \tag{4}$$

where **J** is matrix of ones, means that all nodes have connection with all other ones.
It is obvious too, that the longest path (circuit which connects all nodes) of graph has equal number of its nodes of graph denoted m.
Applying the above mentioned three conditions, the connection matrix calculation method can be represented by flowsheet of Fig. 1.

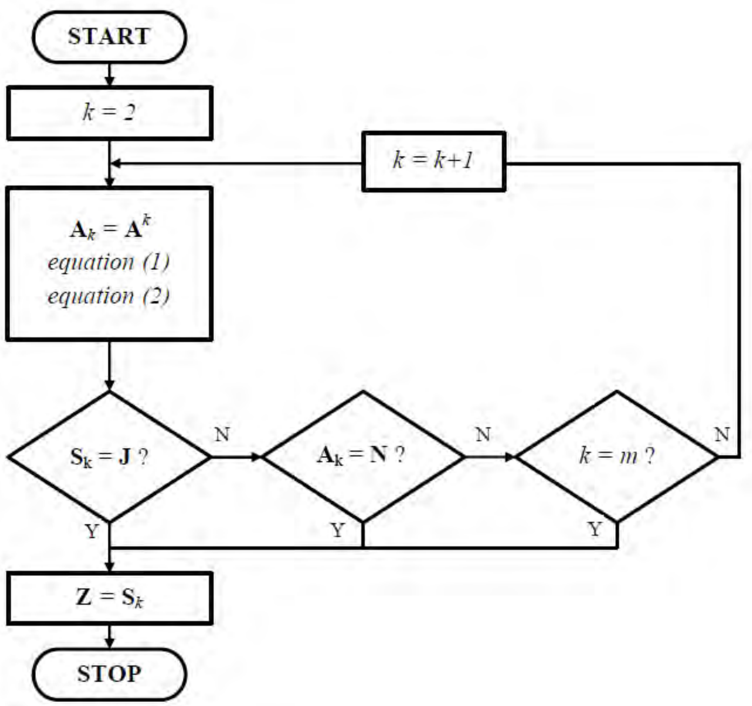


Fig. 1 Block Diagram of Connection Matrix Determination

The connection matrix **Z** shows the interconnection between nodes. But, based upon the investigation of the connection matrix, the

$$\mathbf{e} = \left[ \mathrm{e_k} \right] \quad \mathrm{e_k} = \sum_{\mathrm{j=1}}^{\mathrm{m}} \mathrm{z_{jk}} \tag{5}$$

exposure vector **e**, and

$$\mathbf{i} = \left[ i_k \right] \quad i_k = \sum_{j=1}^{m} z_{kj} \tag{6}$$

impact vector **i** can be determined.
The exposure vector e represents the exposedness of nodes, in other words which node depend on the other ones mostly. The impact vector i shows which node(s) ha(s)ve affect to other ones in the highest degree.

## 3. CASE STUDIES

To demonstrate possibilities of this method described above, we show two case studies. Firstly a vehicle system (Mi-8 helicopter's pneumatic brake system) will be investigated by above mentioned graph-theoretical method. Than connection matrix of network of surveillance radars for Kosovo upper airspace air traffic control service will be determined and analysed.

### 3.1. Pneumatic Brake System of Mi-8 Helicopter

The helicopter Mi-8 Hip pneumatic brake system shown in Fig. 2 by examining the braked state of the system.

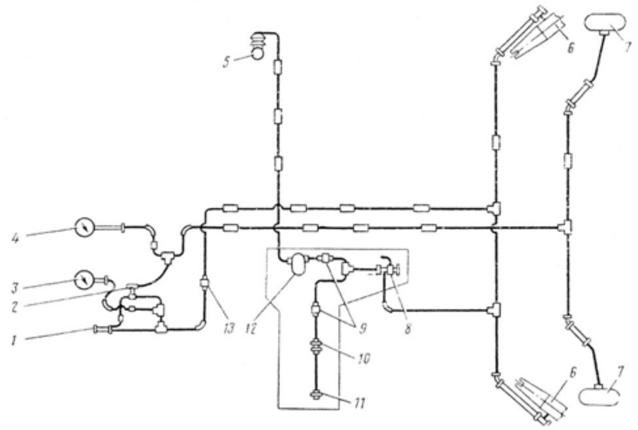


Fig. 2 Schematic Diagram of Pneumatic Brake System of Helicopter Mi-8 Hip

1 – UP-7 control equipment; 2 – UPO3/2 control equipment; 3;4 – pressure gauges; 5 – AK 50 air compressor; 6 – compressed air tanks; 7 – wheel-brakes; 8 – AD 50 pressure-adjusting knob; 9 – one-way valve; 10;13 – filters; 11 – refuelling device; 12 –settler.

When analysing the braked state of pneumatic brake system, it can be observable that the elements 10, 12 and 13 are considered passive. The filters do not play role in the braked steady state of the system; even the on-board refuelling device 11 has a role only during system maintenance. The one-way valves 9 can also be regarded as passive. But, as they determine the direction of the flow of compressed air in a given pipe section, the graph describing the operation of the system is "directed".
Based on the above considerations and the analysis of the function of the components, the graph model of the system can be seen in Fig. 3, using numbering of schematic diagram.

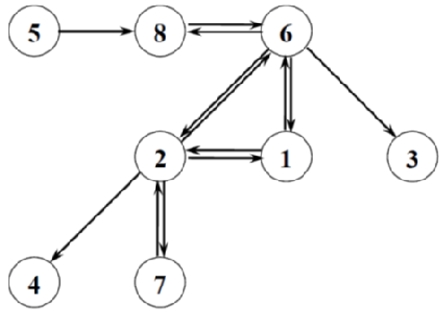


Fig. 3 Graph Model of Pneumatic Brake System of Helicopter Mi-8 Hip.

The adjacent matrix of system:

$$\mathbf{A}=\begin{bmatrix}0&1&0&0&0&1&0&0\\1&0&0&1&0&1&1&0\\0&0&0&0&0&0&0&0\\0&0&0&0&0&0&0&0\\0&0&0&0&0&0&0&1\\1&1&1&0&0&0&0&1\\0&1&0&0&0&0&0&0\\0&0&0&0&0&1&0&0\end{bmatrix}. \qquad (7)$$

The connection matrix:

$$\mathbf{Z}=\begin{bmatrix}1&1&1&1&0&1&1&1\\1&1&1&1&0&1&1&1\\0&0&0&0&0&0&0&0\\0&0&0&0&0&0&0&0\\1&1&1&1&0&1&1&1\\1&1&1&1&0&1&1&1\\1&1&1&1&0&1&1&1\\1&1&1&1&0&1&1&1\end{bmatrix}. \qquad (8)$$

The exposure vector:

$$\mathbf{e}^{\mathrm{T}}=\begin{bmatrix}6&6&6&6&0&6&6&6\end{bmatrix}. \qquad (9)$$

The impact vector:

$$\mathbf{i}^{\mathrm{T}}=\begin{bmatrix}7&7&0&0&7&7&7&7\end{bmatrix}. \qquad (\underline{1}\cancel{1}0)$$

The following conclusions can be deduced from the results of graph modelling and analysis:

- the exposure vector e shows that the air compressor 5 is not affected by a failure of another element of the system, seeing that $e_5 = 0$;
- exposedness of other elements are the same – see equation;
- the impact vector i also illustrates that derangement of the pressure gauges 3 and 4 has no effect on the operation of the other elements, because $i_3 = i_4 = 0$;
- impact of other elements are the same.

### 3.2. Kosovo Upper Airspace Air Traffic Control System

The en-route Air Traffic Services (ATS) in the Kosovo Upper Airspace (Flight Level 205 to Flight Level 660) are provided by HungaroControl Hungarian Air Navigation Service Provider (ANSP) located in a non-neighbouring country 700 km away from the Area of Responsibility. This unique service provision from Budapest Area Control Centre (ACC) is based on purchased data and services of the already existing infrastructure of the ANSPs operating in the adjacent countries of Kosovo. The remote ATS requires full coverage of the Kosovo airspace by redundant networks and connectivity between significant elements i.e. data-sources (radar and radio sites), flight data processing, and controller working positions (user endpoints):

- network of surveillance radars;
- Air-Ground communication lines;
- Ground-Ground communication lines (between ATS units).

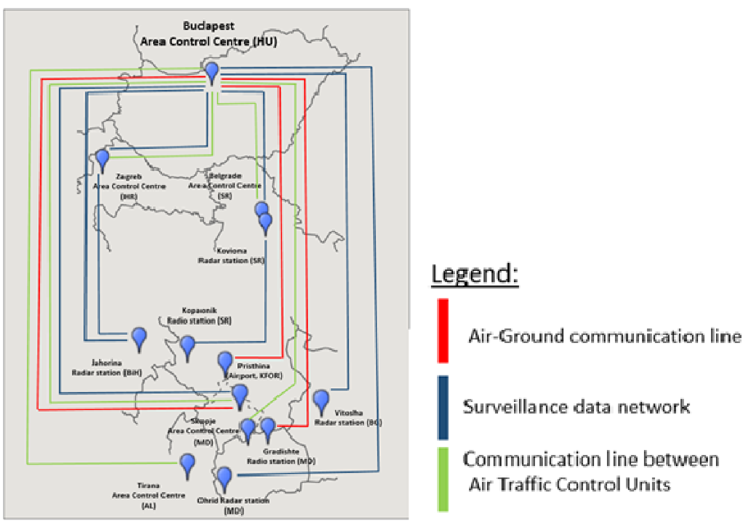


Fig. 4 Datalinks of Kosovo Upper Airspace Air Traffic Services

The absolut radar coverage on certain flight levels in the area are presented in Fig. 5 (measures on FL205, FL340, FL410 calculated by EUROCONTROL software)[1].

[1] Flight Level 205-340-410 (6200m – 10500m – 13000m)

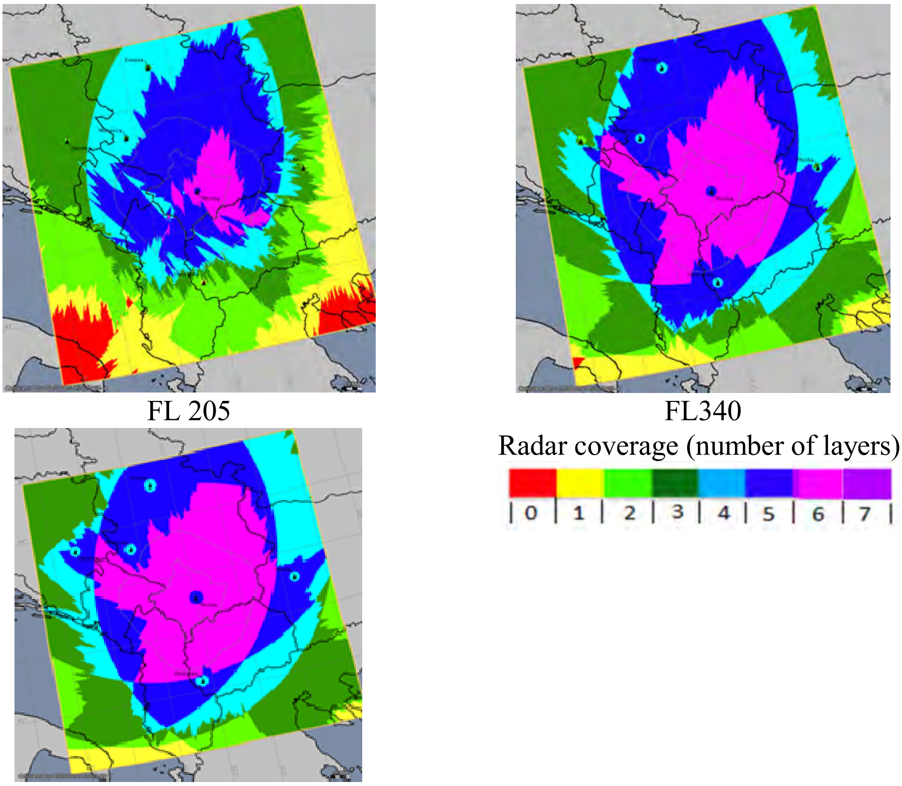


Fig. 5 Radar coverage in Kosovo airspace

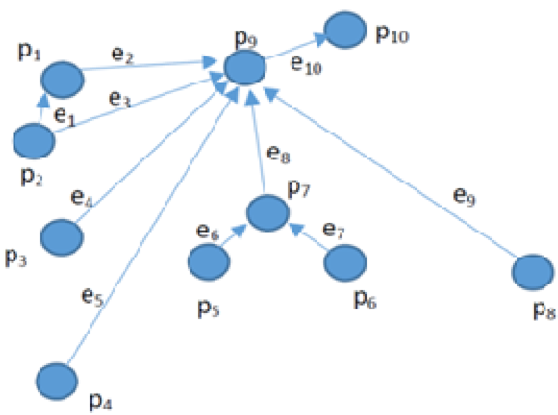


Fig. 6 Graph Model of Sureveillance Data Network

P1 – Zagreb ACC (HR); P2 – Jahorina radar station (BiH); P3 –Pristina radar station (KOS); P4 – Ohrid radar station (MD); P5 – Koviona radar station (SRB); P6 – Murtenica radar station (SRB) ; P7 – Belgrade ACC; P8 –Vitosha radar station (BG); P9 – HungaroControl flight data processing system (MRTS & RFS); P10 – HungaroControl air traffic controllers positions; e1 – e10 – data connectivity

The adjacent matrix of system:

$$\mathbf{A} = \begin{bmatrix} 0 & 0 & 0 & 0 & 0 & 0 & 0 & 0 & 1 & 0 \\ 1 & 0 & 0 & 0 & 0 & 0 & 0 & 0 & 1 & 0 \\ 0 & 0 & 0 & 0 & 0 & 0 & 0 & 0 & 1 & 0 \\ 0 & 0 & 0 & 0 & 0 & 0 & 0 & 0 & 1 & 0 \\ 0 & 0 & 0 & 0 & 0 & 0 & 1 & 0 & 0 & 0 \\ 0 & 0 & 0 & 0 & 0 & 0 & 1 & 0 & 0 & 0 \\ 0 & 0 & 0 & 0 & 0 & 0 & 0 & 0 & 1 & 0 \\ 0 & 0 & 0 & 0 & 0 & 0 & 0 & 0 & 1 & 1 \\ 0 & 0 & 0 & 0 & 0 & 0 & 0 & 0 & 0 & 0 \\ 0 & 0 & 0 & 0 & 0 & 0 & 0 & 0 & 0 & 0 \end{bmatrix}. \qquad (\underline{2}\cancel{1}1)$$

The analysis of the Graph-model by matrix algebra methodolgy also verified that $P_9$ node (data processor) is a key element requires redunancy. Occurrence of significant failure or outage in ATM systems has a very low level of risk, but shall not be ignored. One example of an extreme emergency situation is the blackout of the air traffic control tower at Liszt Ferenc International Airport on 07 December 2012 (broken heating pipe caused water damage and short circuit), when airport operations were terminated due to lack of radio-communication and malfunction of controlling systems [5].

Another regional example of the vis-major situation is the Zagreb ACC ($P_1$ node on the Graph) failure occured on 30 July 2014. The heavy thunderstorm caused severe flooding, lightning strike and power failure in the operations facility. Disruption in air traffic service provision caused airspace closure and air traffic was onloaded to surrounding ACCs. Airspace was reopened after T+2 hours with 25% capacity reduction and 50% after T+4 hours, while the full (100%) capacity was reached in 2 days [1].

The connection matrix:

$$\mathbf{Z} = \begin{bmatrix} 0 & 0 & 0 & 0 & 0 & 0 & 0 & 0 & 1 & 1 \\ 1 & 0 & 0 & 0 & 0 & 0 & 0 & 0 & 1 & 1 \\ 0 & 0 & 0 & 0 & 0 & 0 & 0 & 0 & 1 & 1 \\ 0 & 0 & 0 & 0 & 0 & 0 & 0 & 0 & 1 & 1 \\ 0 & 0 & 0 & 0 & 0 & 0 & 1 & 0 & 1 & 1 \\ 0 & 0 & 0 & 0 & 0 & 0 & 1 & 0 & 1 & 1 \\ 0 & 0 & 0 & 0 & 0 & 0 & 0 & 0 & 1 & 1 \\ 0 & 0 & 0 & 0 & 0 & 0 & 0 & 0 & 1 & 1 \\ 0 & 0 & 0 & 0 & 0 & 0 & 0 & 0 & 0 & 1 \\ 0 & 0 & 0 & 0 & 0 & 0 & 0 & 0 & 0 & 0 \end{bmatrix}. \qquad (\underline{3}\cancel{1}2)$$

The exposure vector:

$$\mathbf{e}^{\mathrm{T}} = \begin{bmatrix} 1 & 0 & 0 & 0 & 0 & 0 & 2 & 0 & 8 & 9 \end{bmatrix} \ . \tag{13}$$

HungaroControl can handle the implacts of an unexpected failure or damage of the ATM systems (certain or all elements of the critical infrastructure), or a pre-planned capacity decrease (due to maintentance work or overhaul) by a coordination process with close cooperation of stakeholders (communication network and radar service providers) by checking the operational status of the systems and the connection lines and harmonizing the timing of the necessary maintenance tasks.

Establishment of redundant radar coverage in the Area of Responsibility requires detailed preliminary calculations and assessments in different layers (flight levels), while level of redunancy (e.g. number of radars for coverage, independent data connections) shall minimise/eliminate safety risks. The purchased data provided by redundant sensors (primary and secondary radars) from adjacent countries also determine unit costs (en-route fees that airspace users pay for ATS provision). System maintenance and development plans should be synchronized and coordinated (in accordance with the contractual obligations).

## 5. SUMMARY, FUTURE WORK

This paper showed sortly an algorithm to determine the connections between the network structure system's components or states of technical processes. Using the proposed method it is possible to determine the connection matrix of investigated systems if its adjacent matrix is known.

The first case study demonstrated possibility of use of method shown in section 2. It is true that the investigated vehicle system is not too complicated. But, in case of a more complex system, like a bigger graph, deducing conclusions is not easy, therefore the application of the proposed method is necessary.

In his future work, the Author proposes to develop other mathematical models and tools to investigate vehicle sensory networks for investigation of their reliability and dependability based on investigation of *Tuloki* and *Nagy* [4] [10].

The second case study introduced graph modeling-based analisys of network of surveillance radars of Kosovo upper airspace air traffic control system.

In the aim of the complete modelling of the Kosovo ATS solution, further assessments are required, as the Multi Radar Tracking System (Kosovo Automated and Integrated ATM System – KATIAS, $P_7$ point in the chart) has three redunant elements: Master and Slave and their backup systems (Radar Fallback System – RFS).

Feasibility of remote ATS tachnology also requires analysis of the linkage between the above mentioned data processing systems and the air traffic controllers working position ($P_9$ and $P_8$ points with $e_9$ link in the Graph-model). In reality $P_8$ means 4 wokring positions in HungaroControl's operations room: 1-1 EC (Executive Controller) and 1-1 PC (Planning Controller) positions to provide 2 sectors in the Kosovo airspace.

## 6. ACKNOWLEDGEMENT

The research presented in this paper was carried out as part of the EFOP-3.6.2-16-2017-00016 project in the framework of the New Széchenyi Plan. The completion of this project is funded by the European Union and co-financed by the European Social Fund.


## 7. REFERENCES


[1] AIRportal.hu: Ferihegy Tower blackout: Bezárták a repülőteret. http://www.airportal.hu/ap/viewtopic.php?t=10877 (01.08.2016.).

[2] **Finke, G.**: Operations research and networks, John Wiley & Sons, Hoboken, 2002.

[3] **Lázár-Fülep, T.**: Few Words about Reliability of Vehicle Systems with Complex Interconnections, Proc. of the 18th IEEE International Symposium on Computational Intelligence and Informatics, CINTI 2018, p.273 – 276.

[4] **Nagy, I. - Tuloki, Sz**.: Fault Analysis and System Modelling in Vehicle Engineering, Proc. of the 18th IEEE International Symposium on Computational Intelligence and Informatics, CINTI 2018, p. 313 – 317.

[5] Network Manager: Monthly Network Operations Report. Analysis – July 2014. https://www.eurocontrol.int/sites/default/files/publication/performance/201407/network-operations-report-july-2014-analysis.pdf (02.01.2017.)

[6] **Pálfi, J. - Holcsik, P. - Pokorádi, L.**: Determination of Customer Number by Matrix Operations in Case of Network Failure, Proc. of SACI 2018, p.555-560.

[7] **Péter, T. - Szabó, K.**: A new network model for the analysis of air traffic networks Periodica Polytechnica, Transportation Engineering, 2012, p.39–44.

[8] **Pokorádi, L. – Somosi, V.**: A Koszovói magaslégtéri irányítási rendszer gráf-modellezése, HADMÉRNÖK 2017/4, p.239-251. (In Hungarian)

[9] **Pokorádi, L.**: Graph model-based analysis of technical systems, IOP CONFERENCE SERIES: MATERIALS SCIENCE AND ENGINEERING 393:(1) Paper 012007. 2018, 8 p.

[10] **Tuloki, Sz. – Nagy, I.**: Mapping and Security Analysis of Sensor Network for Electric Vehicles, Proc. of the XXIII$^{rd}$ International Scientific Conference of Young Engineers, 2018, p.243-247.

# THE QUESTION OF LIFETIME: EXTENSION POSSIBILITIES OF BOGIE FORCE TRANSMISSION ELEMENTS ON THE BASIS OF CONDITION TEST RESULTS

**Péter FERENCZ**

Department of Railway Vehicles, Aircraft and Ships
Faculty of Transportation Engineering and Vehicle Engineering
Budapest University of Technology and Economics

H-1521 Budapest, Hungary

*Received: November 7, 2018*

## ABSTRACT

The actual railway vehicle maintenance issues have changed compared to the last century. Market participants can also provide a satisfactory response to repair functions. Of course, it is unchanged that each operator works with different circumstances, environmental impacts may be different, and the mileage is greatly influenced by these. Market players therefore offer customized repair services. Customization is done on the basis of test results, especially the various ratings of the force transfer elements are the subject of consideration when, for example, the overhaul of the bogie is due. The line of thought described here covers the method by which a good estimate of the service life of a component can be given, depending on the size of the railway fleet operated.

*Keywords*: bogie revision, tailor made products, part lifetime determination, deterioration curve, fleet size, risk maintenance strategy, component lifetime extension, customized repair technical content, service fleet size dependent repair

## 1. INTRODUCTION

More and more emphasis is placed on the development of state-of-the-art testing systems that create modern railway vehicle maintenance strategies. Operators are increasingly looking for sustainable, reliable, low-cost solutions. The Original Equipment Manufacturer already determines the revision cycle time of the running gears and bogies at the time of manufacture, but of course, as new products, the technical content and cycle time of the revision may differ depending on the operating conditions. This train of thoughts provides a comprehensive analysis of possible data collection methods for related operations, possible ways and principles for determining the continued usability of individual components.

By way of example, mention is made of rubber-metal elements used in both primary and secondary suspension elements, parts of longitudinal force transfer elements, rubber-metal elements, which may remain in the function of even one revision cycle, up to an additional one million running kilometers. Based on the test parameters of each component, test procedures can be developed and, in the light of the test results, if the component has the option of continued usability, additional simple technological steps may be taken, including the involvement of component manufacturers to determine the features and criteria of a component for further usability, or just need to be replaced. For each parameter, further usability criterion values are determined, which results in a diagnostic database for a series of tests and their results. In addition to rubber-metal elements, the subject of the study, including the rating of wheel-mounted brake discs, and the comparability of parameters of the same type of system components operated by several other operators, is also included.

## 2. PURPOSE OF TESTS

The purpose of the state-of-the-art vehicle maintenance philosophy is to monitor the operation of individual components as individuals and keep them in operation until certain parameters reach their operational limit values or exceed the criteria.
The basic goal of study can be specified as to create better vehicle parameter features with focusing on the application and the application of diagnostic processes in maintenance. The characteristic space of parameters shown in Fig. 1 for general treatment of system deterioration describes the stochastic process of system deterioration. Parameter space 'P' is set of vectors, in which set the time-dependent parameter variations emerge as in-space curves:

$$\mathbf{p}(t)\ . \tag{1}$$

The sub-vectors of $\mathbf{p}(t)$ contain the masses, moments of inertia, stiffness, damping and unique operational characteristics of the considered vehicle-dynamical system.
Determining the actual technical configuration of dynamical system the goal is to settle, the time dependent motion-state vector as time-function:

$$\mathbf{Y}(t)\ . \tag{2}$$

The continuous slow deterioration in technical state is time-dependent and is reflected also in the variations with time of the parameter vector $\mathbf{p}(t)$.

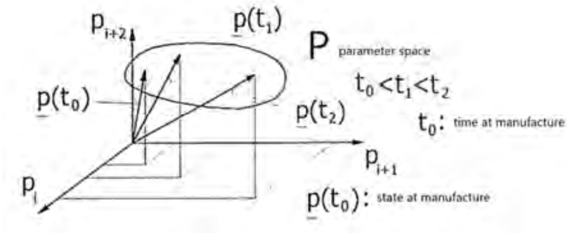


Fig. 1 Characteristic space of parameters [1]

With application of above designations, the change of technical change (i.e. sub-system feature of wheel profile alteration) can be represented by the following mapping:

$$\mathbf{p}(t) = \mathcal{W}_t\, \mathbf{Y}(0)\ . \tag{3}$$

Here, the $\mathcal{W}_t$ represents the *technical state deterioration* (can be the wear) *operator* (on the basis of description [2] p.255). Thus the actual technical state is fed back to the initial motion state $\mathbf{Y}(0)$ of the dynamical system considered.
On the basis of the above described principle, the original manufacturers of bogies and their components provide life expectancy and replacement cycle data. The individual tests may be carried out by the manufacturers of the components or by another independent company, respectively. Uniform test results are classified into three simple categories. The purpose of such a simple classification is to determine whether a given part can be used without restriction, for further use, or, where appropriate, for no longer to be used.
It is necessary to distinguish "special" damages from the process of damage due to normal operational failure. These are exceptional issues that need to be treated as out-

liers when evaluating results as a statistical population. Of course, these component parts fall into a clearly unavailable category, but they do not form part of a large number of outages due to operational wear.
Consequently, the results of these tests provide the basis for further usability classification. For example, components that were previously considered mandatory by the previous manufacturer's specifications for revision, and the results of the tests may indicate that they may serve as a further revision cycle time, result in significant cost reductions. These have an impact on future computable costs, on their distribution and on the realization of the total life cycle cost. Certain technological steps, maintenance and repair tasks of the maintenance can be reworded or rescheduled.
The following can be reported along the lines of traditional maintenance strategy. The physical process of normal damage, the process of destruction, deterioration, is controlled by test tasks. The regularity of tasks defined for each subspace group gives a cycle. Compared to the status-based strategy, the Critical Criteria for specific tests must be designed to exit traditional task lists as compared to the standard tasks. The task list defined for a specific component group at a given time is made as a technical content depending on the inspection and test results. The age of vehicles is also a determining factor. If we want to define the first technical (approx. 1 million km) or second revision technical data for certain group of components like bogies from production, the vehicle fleet size and age matters. The Life Cycle Cost (LCC) of a given component group is assessed and determined by the method of determining the life of the parts assigned to the product. Production (design) data is possible by reconsidering data from certain substructures, such as component level lifetime extensions. Usually, this process should be adapted to the individual number of individuals in the fleet.
The following method can be considered as the deterioration of the natural state of the components and the classic description of the statistical evaluation of the process of system degradation. Fig. 2 illustrates the progress of the process over time, for example, the process of natural wear propagation. The curve consists of three main sections divided by two inflection points, so the derivative of the first section is negative, the middle and the third are positive. The rate of change of function (1) is described by the following expression, which gives the following velocity.

$$v_z = (z_2-z_1)/(t_2-t_1) = dz/dt \quad . \tag{4}$$

The second inflection point of the quasi-linear portion of the function (Fig. 2) gives the lifetime measure.

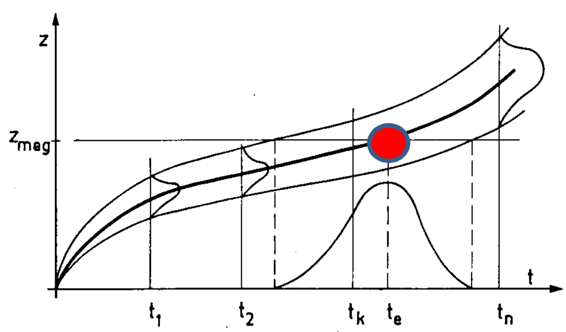

Fig. 2 Deterioration function of part

Examination of a sample group consisting of parts of the same type gives the bunches of individual curves assigned to each sample, and the batch expected value process as a function can be used to determine the purpose of the test, the reference point of which is the red point.

The permissible component life (2) can be expressed as:

$$t_e = z_{meg}/v_z \, . \tag{5}$$

As used in (2), "$z_{meg}$" means the maximum allowable limit, such as the limit of a wear process.

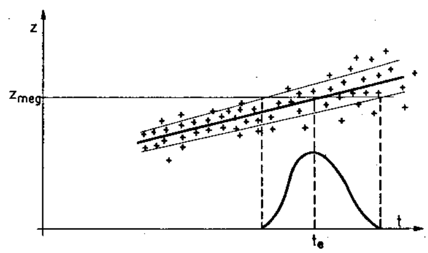


Fig. 3 Statistic results of limit [5]

Thus, the determination of the limit value for a group of samples is the purpose of the statistical evaluation. The deterioration criterion for the maximum or allowable state is at the intersection point of the expected value function of the quasi-linear scale limit values and the expected value of the plurality of inflection points.
This leads to an optimization process, the results of which are the "lifetime" action parameters on basis of MINIMUM RISK! and MAXIMUM QUALITY!
The basic question is, on the basis of a test at a given moment, is it possible to establish that each component or group of parts can be used for another revision cycle?
How does the reliability and safety of the components change, so does the structure, and the system?
Optimization boundary conditions, such as safety, warranty liability, original manufacturer specifications, operating conditions, method of determining original lifetime cost, and implementation of the bogie review process must be taken into account.

## 3. COMPONENT GROUPS THAT SHALL BE CONSIDERED

The full range of power transfer elements, rods, rubber-metal elements, bushings, silent blocks, longitudinal and transverse force transmission components can be considered as test subjects. Particularly important for rubber-metal elements, where static load-performance tests are performed repeatedly to provide primary results. The measured characteristics of the spring are to be compared with the original values of the original factory characteristic and the spreading range. The results of the compari-

son, the difference and the degree of agreement give the input information of the mentioned usability categorization.
There are rubber-metal element units that can be considered as generally usable after the results of the tests, and then a new test method, such as a special visual inspection of the element in question, or a comparison with a “picture-catalog”, is a normal new technology for the eventual revision. This makes it possible to judge a necessary exchange. Suspension system elements must always be subjected to a characteristic test. The testing of the primary spring elements, mostly steel coil springs, is based on a comparison method and the stiffness parameter of the test is carried out in the range defined in the nominal working point (s). Damper units need to be qualified based on their full operating characteristics.

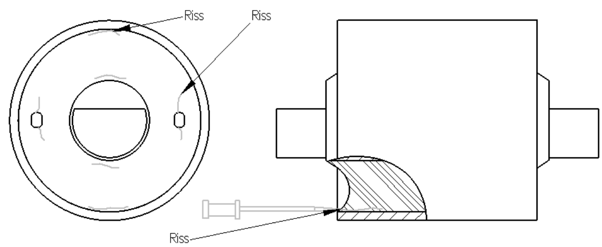


Fig. 4 Example of features to be checked on axle guide bearing bush [4]

Both axle bearings and brake discs provide a broad base for testing and creating a diagnostic database. There are two main categories between the parts and parts that can be tested. All types of rubber-metal elements and dampers are considered to be "**rather uncertain**" because the mapping, modeling and measurement of the deterioration process is more complex. Wheel discs, brake disc wear rings, axle bearings are “easy-to-test” materials, these can be labeled as "**less uncertain**" because of their definite limitations on their usability, such as wear propagation limits.

## 3. TEST RESULTS AND APPLICATION

In the simple category described, a method associated with the test results of the bogie components is ranked and evaluated. Generally, the sample size is so low that the certainty of the result is low in that the "true" value is calculated based on the "deterioration" function described above, with simple expected value defined. The result is as follows. "Test revisions” carried out for each type of component groups, even bogies in the certain fleet. By replacing these certain parts, a complete condition examination is performed on the dismantled parts. Assessing the state of deterioration by positioning it on the "deterioration curve”, then examining original components by specialist OEMs or independent experts follow. The primary question is whether the fault found or the picture of the situation is abnormal, so outlier, or the normal condition is deterioration faced? In the event that the “normal” deterioration condition is identified, the criteria for continued usability are determined by the safety criteria. What is a reliable test method for a particular part? What is the result? Should a decision be made in addition to a low sample number, and even if that "result point" is located in the quasi-linear phase of the damage process?

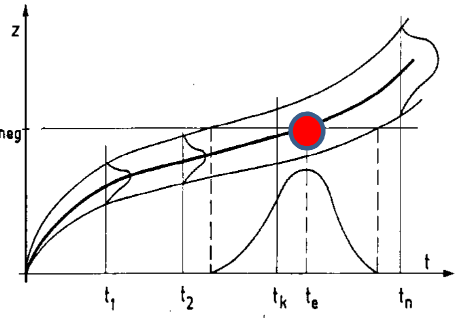


Fig. 5 Worst and the best fit case

In addition to the test results, the available operating data for the “more certain” result is to be taken into account. These are usually the results of vehicle maintenance inspection tasks, which can be collected as preliminary data for repairing or revising bogies or parts. After the test revision, the operator, the original manufacturer and the suppliers shall be informed of the results. The results can be feedback, the technical content of the maintenance or the repair can be changed, which can be considered as a lifetime change. Thus, the test results of the components described above are evaluated in two different ways.

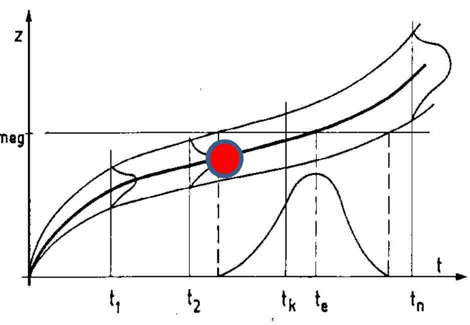


Fig. 6 Worst and the best fit case

The uncertainty arises from the fact that the position on the result curve is not known at which point of the quasi-linear phase situated. It may be in the immediate vicinity of an inflection point. Depending on the characteristics of the component group, the so-called "**more uncertain**" and "**less uncertain**" categories are derived. The theory is expanded to include the additional attribute applied to the categories, the “**worst-case**” and the “**best-fit**” categories.

Fig. 5 illustrates the "worst case" case, so the result is considered to be still in good condition and replaced at the end of its usability. Fig. 6 illustrates the "best fit" case, the test results are considered good, and the degree of continued usability can reach or exceed the next revision cycle time. Fig. 6 illustrates the "best fit" case, the test results are considered good, and the degree of continued usability can reach or exceed the next revision cycle time.

## 4. CONTRADICTION OF RESULTS APPLY IN MIRROR OF FLEET SIZE

The size of the operating fleet is a very important factor. Take an example of a fleet of 100 train units, in which a train consists of 2 driven and 4 running bogies. In addition to this "big" fleet operator, also at a "small" fleet operator company shall be compared to with i.e. 5 same train units, but contracted for 100% availability performance. Which parameters are used and how the decision parameter criteria for above described test procedure to be defined? Examining the reliability of each bogie element by type can be generalized, which is highly dependent on the size of the fleet. Of course, for a small fleet, one of the elements of the 10 bogies of the 5 trains can be tested with greater reliability than the whole of the 100 trains. The reliability of the test results ultimately affects the extent to which the original manufacturer's specifications can be deviated from and the reliability of the technical content of the revision ahead.
A "small" operator with 5 train units is more likely not to have spare bogie units, so the loss of an unexpected operation of a part, even for the entire train, is much more costly, even in terms of lifetime cost. The company operating the "small" fleet is at greater risk with the continued operation of "old" parts.

The following simple example illustrates the effect of fleet size.

**Sample brake down analysis of a „SMALL" OPERATOR FLEET**

**Quantity of the operated trainsets is: 5**
**Bogie type distribution in trainset:**

Driven bogie 2 units,
Jacobs trailer 3 units
Sum:
Driven bogie 10 units
Jacobs trailer 15 units

**The most important RISK of the certain type of fleet is:**
brake down of 1 trainset has strong influence on fleet availability.

**Yearly mileage performance of the fleet is : 450 000 – 600 000 km**
**Auxiliary fleet float conditions are:**

No or low amount of spare sub-systems or components, or bogies;
Strong sensitivity on process LEAD time shall be considered.
Sensitivity on COST reduction is high, keeping trains at 100% availability.
Resultant fleet availability sensitivity:

$$AS = 1 / 5 = 20\% \tag{6}$$

**The „Less uncertain" items are** considered to be exchanged in case no possibility to reach the next revision cycle period.

**For the „Rather uncertain" items the a**pplication of „**WORST or BEST FIT CASE** abstraction" applied depending mainly on experiences with certain part usage in other applications.
Despite the simple reliability factor of i.e. tested axle guide bearing units case for driven bogies is:

$$R = 4 / 10*4 = 0{,}1 \rightarrow 10\% \tag{7}$$

Besides on increment sensitivity of the parameter is:

$$S = 1 / 10*4 = 2{,}5\% \tag{8}$$

**Sample break down analysis of a „BIG" OPERATOR FLEET**

**Quantity Operated trainsets is: 105**
**Bogie type distribution in trainset:**
Driven bogie 2 units
Jacobs trailer 3 units
Sum:
Driven bogie 210 units
Jacobs trailer 315 units

**The most important RISK of the certain type of fleet is:**
The unexpected brake down or malfunction of a component in higher amount.

**Yearly mileage performance is: 180 000 – 250 000 km**
**Auxiliary fleet float conditions are:**
Significant amount of spare sub-systems or components, or bogies.
Sensitivity on process LEAD time lower then small fleet operator
Sensitivity on COST reduction with keeping items on further usage.
Resultant fleet availability sensitivity:

$$AS = 1 / 105 = 0{,}95\% \tag{9}$$

**The „Less uncertain" items are** considered to be further used even in case no possibility to reach the next revision cycle period but a certain further mileage.

**For the „Rather uncertain" items of** Application of „**BEST FIT CASE** abstraction" applied relying on maintenance check and higher certainty, less sensitivity.
Despite the simple reliability factor of i.e. tested axle guide bearing units case for driven bogies is:

$$R = 4 / 210*4 = 0{,}0047 \rightarrow 0{,}47\% \tag{10}$$

Besides on increment sensitivity of the parameter is:

$$S = 1 / 210*4 = 0{,}12\% \tag{11}$$

## 5. TO ENSURE THE DECISIONS

On basis of the above described data flow, the „small fleet operator" decision point are influenced by other risks comparing to the „big fleet operator". The dependency of on „AS" sensitivity value is high at a small fleet. Thus even the „less uncertain" parts and groups, even in case of existing possibility of further usage are considered to be ex-

changed, i.e. the wheels or brake discs, in order to not to stop any of the train out of the fleet.
The „big fleet operator" decides strongly relying on the size and features of the available exchange float of parts, even a higher quantity of complete spare bogie units. Therefore, the risk is considered more depending on a certain part failure in a high quantity. The „less uncertain" type of items is always considered to be further used. The technical content of revision process can be adjusted in accordance with the test results.
So the application and evaluation in general can be described as simple question. Where is a certain result located on the lifetime – technical state deterioration curve? The decision shall be ensured with a process based on the statistical evaluation of test results. Reference distribution (i.e. designed, simulated, on recent tests carried out feature) shall be considered to compare the evaluated empirical distribution (refer to [3] p. 13). The degree of similarity between distributions to be used to indicate the degree of sensitivity between the references, expected values, and measured by values. The *Kolmogorov-Smirnov* test statistics measured here directly as the maximum vertical distance between the two distribution functions, shown on same graph (see Fig. No.7). The test statistics can be calculated using:

$$T_1 = \sup | S_1(x) - S_2(x) | , \tag{12}$$

where with supremum indication the equation represents the greatest absolute difference between the distributions.

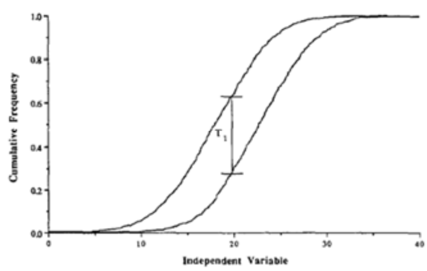


Fig. 7  Example of the determination of K-S statistic [3]

To end up the analysis method, certain maximum limit of $T_1$ to be defined in an evaluation of a certain parameter that features the deterioration of system. This parameter $T_1$ provides the criteria of decision described in the above chapters and ensures the stability (boundary conditions) of optimization.

## 5. CONCLUDING REMARKS

- Bogie force transmission elements as defined groups have possibility for further usage comparing to OEM determined revision cycle, lifetime extension, this possibility provides identification of decision points within overhaul, diagnostic technologies;
- The optimization has the main goal of risk minimization besides cost minimization;

- The remained „effective” lifetime is depending on the optimization boundary conditions;
- The fleet size has contradiction feature in decision making of components further usability;
- Part-group dependent decision making method is settled;
- The decision shall be ensured, for this the proposal of usage parameter sensitivity test of Kolmogorov-Smirnov method implemented;
- On basis of thoughts unique, customized revision technical content can be provided on each unit of bogies, or even vehicles.

## 6. REFERENCES

[1] **Zobory, I. – Benedek, T. – Győri, J.:** Vehicle Diagnostics. Lecture Notes. BME Budapest, 2004. (in Hungarian);

[2] **Zobory, I.:** Prediciton of Wheel/Rail Profile Wear, Vehicle System Dynamics, Vol.28 (1997), p.221-259.

[3] **Hamby, D. M.:** A review of techniques for parameter sensitivity analysis of environmental models, Westinghouse Savannah River Company, SC 29808, U.S.A.

[4] **Ferencz, P.:** Lifetime extension possibilities of Stadler bogie force transmission elements on the basis of test results, Proceedings of the 10$^{th}$ International Conference on Railway Bogies (BOGIE’16), (Ed. by Prof. I. Zobory), Scientific Society of Mechanical Engineers (SSME/GTE), Budapest, 2017, p.357-366.

[5] **Sólyomvári, K. – Ferencz, P.:** Maintenance and Repair of Railway Vehicles c. course lecture notes, BME Department of Railway Vehicles, Aircraft and Ships Budapest, 2007 – 2018.

# LABORATORY INVESTINGATION INTO THE NOISE GENERATED BY SLIDING FRICTION IN CASE OF CAST IRON AND STEEL FRICTION PAIRS

**Gergely TULIPÁNT, András SZABÓ and István ZOBORY**

Department of Aeronautics, Naval Architecture and Railway Vehicles
Faculty of Transportation Engineering and Vehicle Engineering
Budapest University of Technology and Economics
H-1111 Budapest, Műegyetem rkp. 3, Hungary

*Received: November 5, 2018*

## ABSTRACT

This paper presents the relationships evaluated from laboratory experiments carried out on the friction analysing roller test bench at the Group of Railway Vehicles and Vehicle System Analysis at the BME. In the course of investigating the friction coefficient and specific wear processes parallel also noise measurements were carried out.

*Keywords:* friction coefficient, noise measurement, temperature measurement.

## 1. INTRODUCTION

This paper presents the relationships evaluated from laboratory experiments carried out on the friction analyzing roller test bench at the Group of Railway Vehicles and Vehicle System Analysis at the BME. In the course of investigating the friction coefficient and specific wear processes parallel also noise measurements were carried out. For the different constant contact pressure and sliding velocity setting conditions also the noise-pressure was evaluated parallel with the brake-block pressure, sliding velocity and temperature measurements. The noise measurements results showed positive correlation with the maximum temperature values arising on the friction interface (the so called hot spot temperatures). Furthermore the stochastic character of the experimental results was taken into consideration, by pointing out the statistical parameters of the measured time functions. Also a frequency analysis has been carried out taking into consideration combined investigation results into the friction and wear, as well as into noise loading processes. A conjecture emerged concerning the possibility of estimating also important material characteristics (e.g. thermal conductivity) by means of analyzing the numerical characteristics of the quasi-steady friction and noise processes.

## 2. TEST BENCH FOR TRIBOLOGICAL MEASUREMENT

The investigation into the tribological properties of sliding friction pairs emerging in the operation processes of railway vehicles belongs to the field of interest of the Group of Railway Vehicles and Vehicle System Analysis. In the framework of this research topic a test bench has been developed for examining the friction coefficient and specific wear of cast-iron and steel material pair. In the course of several measurements it has been recognized that the tribological characteristics of the sliding friction process are in certain correlation with the noise generated by the sliding frictional and also the rolling processes realized on the test bench mentioned. In Fig. 1 the test bench equipped with the proper measuring system for analyzing the correlations between the frictional and wear characteristics, as well as between the temperature processes and the noise radiated from the friction interfaces.

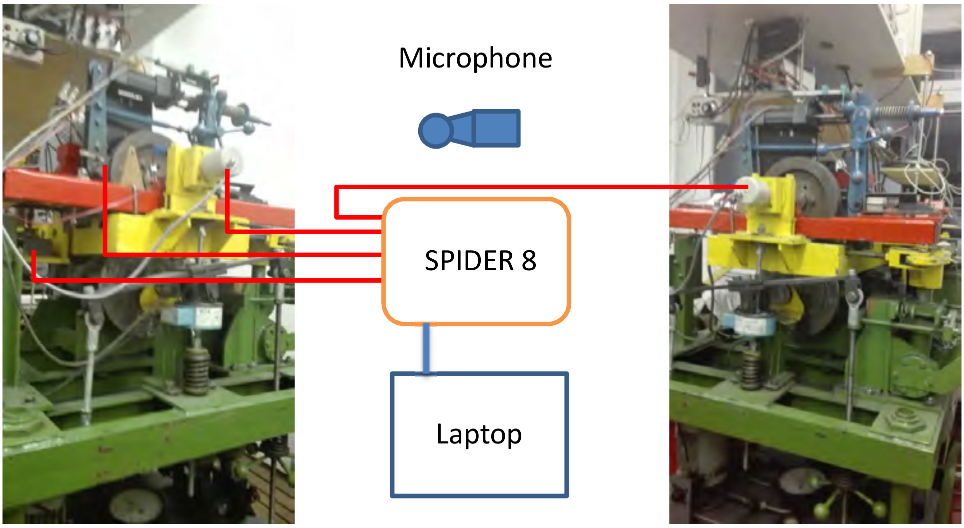


Fig. 1 The roller test bench for investigation into the frictional processes.

## 3. NOISE MEASUREMENT TO CARACTERISE THE FRICTION PROCESS

The microphone for receiving the noise load signal has been located at a given short distance from the frictional/rolling noise generating sources. The basic task of the investigation was to determine the quantitative characteristics of the correlation between the generated noise and the tribological characteristics (sliding speed, brake-block pressure and contact temperature) experienced at certain pairs (regions) of the contacting sliding friction pair.

The distance between the microphone and the sliding surface of the wheel and the brake block attacking it was 200 mm. The noise pressure was continuously registered by using magnetic data carrier, thus the file consisting of the time dependent noise pressures in unit of measure of dB was proper for combined processing together with the files of measured data of the frictional processes.

The frictional processes were followed by registering the frictional coefficient variation with time and the that the of temperature at a point of the brake block in the close neighborhood of the leading edge of the block and the sliding surface of the brake block pressed on the rotating wheel driven by the so called “rail wheel” through rolling contact.

On the basis of several former experiments it turned out that the actual heat state of the brake block, especially the position variation of the hot spots along the arc of contact highly influences the frequency of the friction noise generated in the course of the friction examinations carried out by using the labor-equipment called “roller test bench for friction examinations”. In Fig. 2 the positions of the hot spots experienced in the course of our laboratory examinations are shown. In some cases the hot spot is single and is situated close to the leading edge of the brake block. The noise generated was of higher frequency if the hot spot was situated close to the leading (input) edge. In the figures of the second raw in the left figure part the bifurcation of the hot spots can be recognized, i.e. the hot spot that some instances before was situated at the center site of the brake block bifurcated into two individual hot spots moving slowly towards the leading and the trailing edges of the brake block.

Fig. 2 The position of the hot spots on the contact interface in the course of the thermo-elastic instability process

After some instances the motion direction of the hot spots changes and merging of the two hot spots takes place in the central site of the brake block, see the figure part in the middle of the second row. Further on the hot spot begins to move to the leading edge (edges) again, and the process described above appears again in repeated form.
The process described above is the so called "thermo-elastic instability". As a feast rule one can formulate that the friction noise becomes of higher frequency if the contacting hot spots arrive at the close neighborhood of the leading (input) edge, and be-

comes of lower frequency if the motion of the hot spot achieves the central site of the brake block.

## 4. MEASUREMENT RESULTS CONCERNING THE FRICTION OF CAST-IRON/STEEL FRICTION PAIR UNDER HIGH TEMPERATURE CONDITIONS

The results of the measurements are shown in Fig. 3. One can easily recognize the stair like function of the mean brake block pressure ($p$) variation with time, which function reflects the stage-wise increasing cycles with controlled constant mean brake block pressures. In correlation with the increasing mean brake block pressures also the variation of the measured brake block temperature close to the leading edge of the brake block shows time increasing mean trends around which trend the appearance of the thermo-elastic instability phenomenon can be recognized.

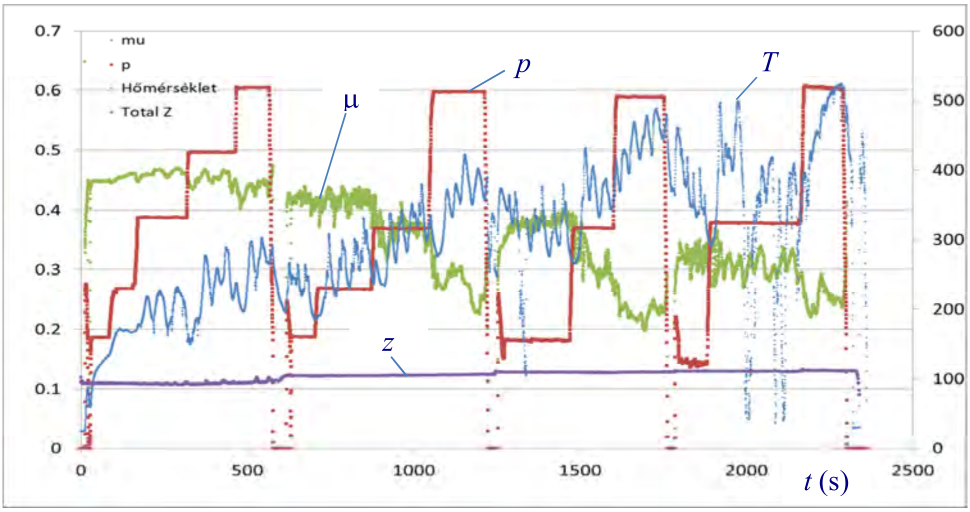


Fig. 3 The measured quantities varying with time for the four load cycles.

At constant mean pressures (pressure stairs) the quasi-periodic temperature variations showed with sharp maximum peaks and moderately rounded minimum extrema. The sequential cycles of the experiment were carried out with controlled constant sliding velocities. This fact explains the ever increasing braking power and as a result the ever increasing trends in the contact temperature at the position of the thermo-couple. From Fig. 3 the combined effect of the mean contact pressure and the sliding velocity can be read off. The combined effect of the increasing braking power is reflected in the variation of the mean coefficient of sliding friction. It is characteristic that with increasing mean pressures and increasing local temperature trends the coefficient of friction is of decreasing character.

In Fig. 3 also the variation with time of the noise pressure in unit of measure dB is indicated for all the four load cycles concerning constant (controlled) sliding velocity levels. In the following chapter the mentioned correlation between the noise level and the measured local temperature will be analyzed for the first load cycle, i.e. time interval [200,600] (in seconds).

Since the most important functional relationship is the friction coefficient vs. sliding speed function, in Fig. 4 the measured scattering friction coefficient values are indicated concerning the controlled sliding velocity levels set in. Each point belongs to the above explained mean pressure levels and certain measured local temperature values. All the same the tendency of the sliding velocity dependents of the average friction coefficient can be recognized: decreasing friction coefficient values belong to increasing sliding velocity values.

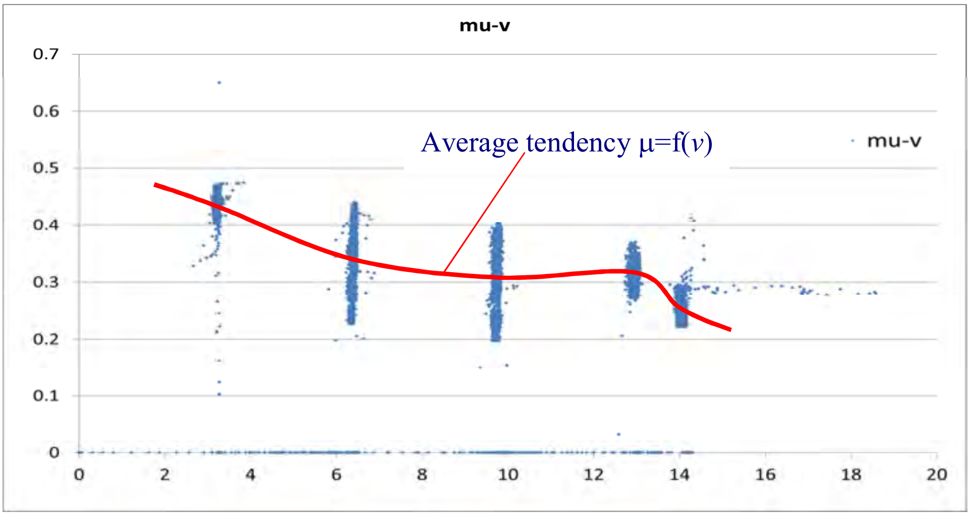


Fig. 4 Scattering measurement results: friction coefficient values varying with sliding velocity in m/s. Each point reflects varying mean pressures and local temperatures measured

## 5. NOISE MEASUREMENT RESULTS TAKEN PARAREL TO THE TRIBILOGICAL TEMPERATURE PROCESS

It has been mentioned that an analysis was intended to evaluate the correlation between the local temperature and the noise pressure recognized in the course of the experiments.

In Fig. 5 two time functions are shown, namely the measured local temperature in the close neighborhood of the leading edge of the brake block and the noise pressure measured at a distance of 200 mm from the sliding surfaces. Two noise peaks has been chosen for frequency analysis.

The first assigned temperature peak begins at 420 second and the noise pressure intensively increases up to the top of the peak characterized by 98 dB at 430 second. Concerning the correlated temperature process the contact temperatures show an intensive increase for the initial time 430 s, and initial temperature 235 C° up to the top temperature peak characterized by 290 C° at the time 435 s. The noise measuring equipment made it possible to evaluate the spectrum of the noise components of different frequencies.

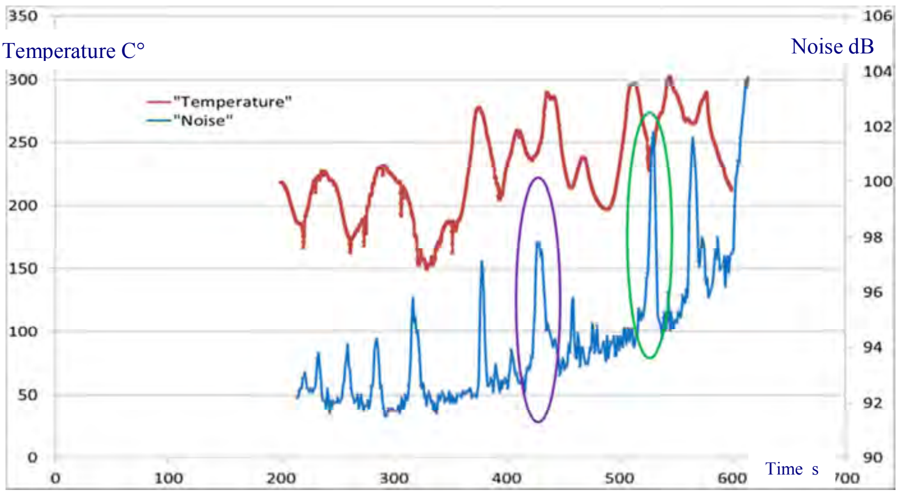


Fig. 5 The measured local temperature and the noise pressure vs. time functions. Two noise peaks assigned for frequency analysis

In Fig. 6 the two spectra belonging to the initial time (430 s) prior to the temperature peak and to the time of the top of the peak (maximum) at time 435 s are visualized in a combined diagram.

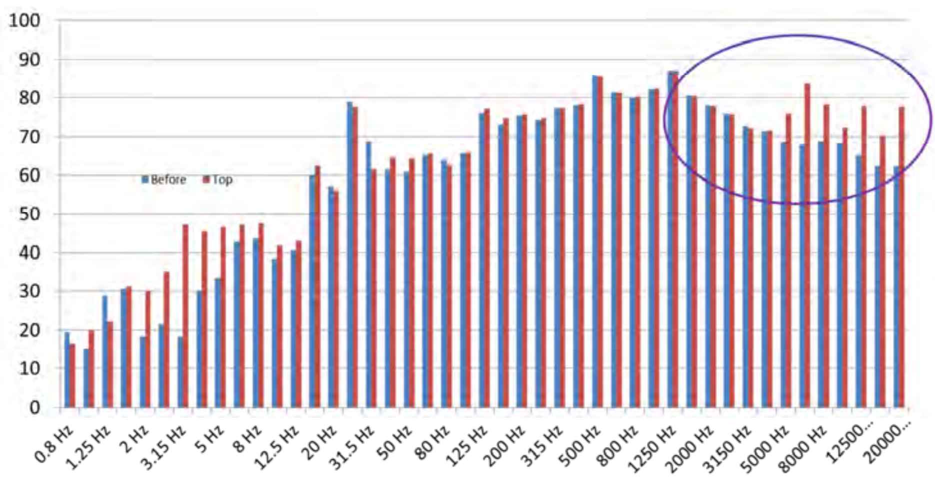


Fig. 6 Two spectra belonging to the time point pair identifying the initial and maximum temperatures of the peak considered.

In the diagram a column-pair belongs to each frequency value analyzed. The left column belongs to the initial time instant of the intensive increase in temperature while the right one belongs to the time instant of the achieved peak temperature. The inten-

sive noise increasing emerges in the high frequency range 5 kHz to 20 kHz indicated by an ellipse in the Figure.
The second assigned temperature peak begins at 530 second and the noise pressure intensively increases up to the top of the peak characterized by 102 dB at 540 second. Concerning the correlated temperature process the contact temperatures shows an intensive increase for the initial time 535 s, and initial temperature 225 C° up to top of the temperature peak characterized by 300 C° at the time 550 s. In Fig. 7 the two spectra belonging to the initial time (535 s) prior to the temperature peak and to the time of the top of the peak (maximum) at time 550 s are visualized in a combined diagram.
In the spectrum again a column-pair belongs to each frequency value analyzed. The left column belongs to the initial time instant of the intensive increase in temperature while the right one belongs to the time instant of the achieved peak temperature. The intensive noise increasing emerges in the high frequency range 1 kHz to 20 kHz indicated by an ellipse in the Figure.

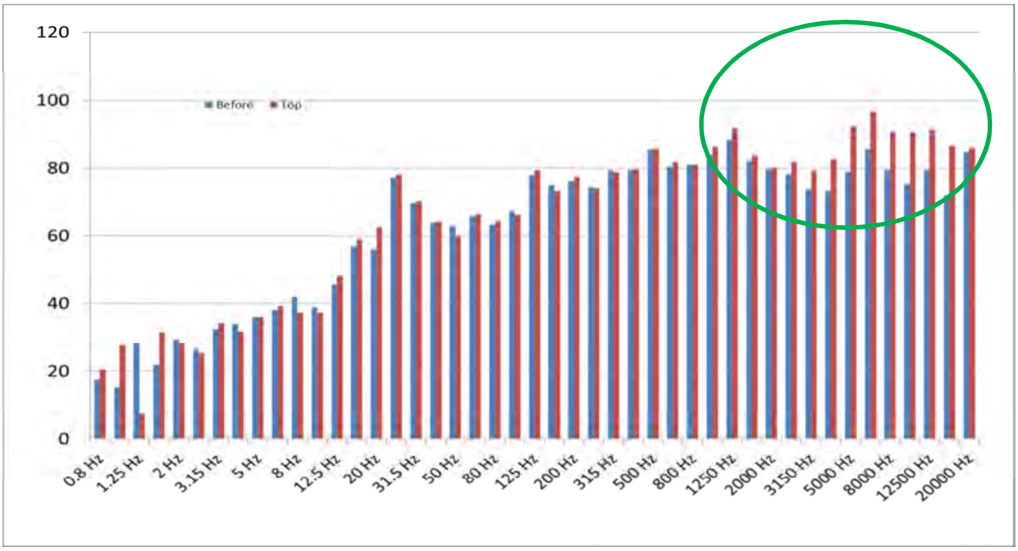


Fig. 7 Two spectra belonging to the time point pair identifying the initial and maximum temperatures of the peak considered.

## 6. CONCLUDING REMARKS

Based on the processing of the measurement results the following conclusions can be drown:

- At the low sliding speed levels there is an expressed relation between the location of the noise peaks and the intensive increase in contact temperature at the leading edge (entry point) of the brake block in case of piece-wise constant pressure levels.
- A characteristic increase in the sliding friction induced noise level is experienced in the frequency interval over 1200 Hz.
- In the considered experience environment (driving of the wheel by rolling contact) the noise generated by the rolling due to the corrugation of the rolling

surfaces disturbingly covers the noise generated by the sliding friction contact of the wheel and the break block.

## 7. REFERENCES

[1] **Johnson, K. L.**: Contact Mechanics. Cambridge University Press, Cambridge. 1986.
[2] **Ambrózy, A.**: Elektronikus zajok. Műszaki Könyvkiadó. Budapest, 1972. (In Hungarian)

# ADVERTISEMENTS

BUDAPEST UNIVERSITY OF TECHNOLOGY AND ECONOMICS

# Faculty of Transportation Engineering and Vehicle Engineering

Budapest University of Technology and Economics (BME) was founded in 1782, and is one of the largest higher educational institutions in the field of engineering in Central Europe with about 24.000 students and 1200 teachers and researchers. The university holds an international reputation for excellence in engineering.

One main priority research area is dedicated to the Vehicle Technology, Transportation and Logistics. The Faculty's mission defines the undertaking of high level of scientific activity, research and development, offering expertise and consultation to transport and vehicle industry companies, logistics providers and to industrial policy makers. Concerning the research potential the Faculty has participated in several international research projects, 9 FP7 projects and more than 20 project proposals in the Horizon 2020 European research programme.

Our main research fields in automotive technology are the following:

**Engine and driveline research area**

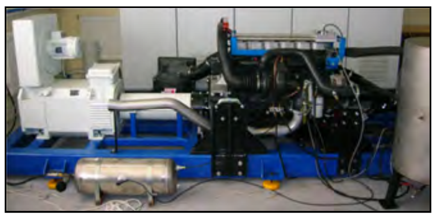

- Comprehensive simulation and computation experiences
- Engine and component analysis
- Powertrain simulation
- Transmission analysis
- Alternative fuels: CNG, hydrogen, biofuels

**Chassis and electronics research area**

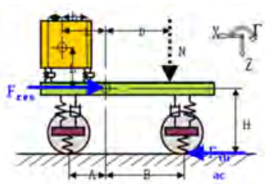

- System overview
- Active and semi-active suspensions
- Development of brake systems
- Steering system design
- Brake system based vehicle dynamical controller

**Vehicle operation research area**

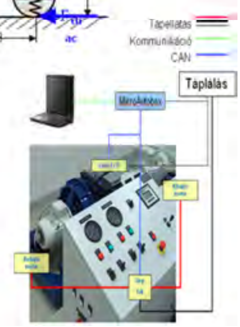


- Developments related to vehicle recycling
- Irregular vehicle operation – accident analysis
- Monitoring vehicle operation – FMS development
- Reliability analysis and system redundancy

# BME BUDAPEST UNIVERSITY OF TECHNOLOGY AND ECONOMICS

## BME ITS NONPROFIT Plc.

## ACTIVITY AREAS:

- ***TRANSPORTATION AND VEHICLE RESEARCH***
- ***TRANSPORTATION AND VEHICLE SYSTEM DESIGN***
- ***COST-BENEFIT ANALYSIS***
- ***EVALUATION***
- ***PROJECT MANAGEMENT***
- ***FISIBILITY STUDY***
- ***RISK ANALYSIS***
- ***RAILWAY NOBO & DEBO ANALYSIS***

***Certification of Vehicle Systems***

***Certification of Track Systems and Buildings***

***Certification of Electric Energy Supply Systems***

***Certification of Railway Operation***

***Postal Address:*** **H-1111 BUDAPEST, XI. Műegyetem rkp. 3.**

***Directorate*****: BUDAPEST, XI. Műegyetem rkp. 3., bldg. K. floor 1. No. 71.**

***Phone*****: (36-1) 463 3797** ***Fax*****: (36-1) 463 3798** ***E-mail*****: bmeits@bmeits.hu**

# MKSZ Hungarian Transport Association

Professional Association of Hungarian Local Public Transport Operators was founded in 1998. It was renamed in 2011 as Hungarian Transport Association. The Association represents numerous transport professional issues and brings together undertakings working in local public transport, takes part in legislation preparations and represents the common interests of its members. Presently, its main objective is to take part in preparation of launching operation of vehicles with different alternative tractions. Its president is Dr. Gyula Várszegi. Number of members is growing, it includes now 9 major transport undertakings:

## *Budapest Transport Privately Held Corporation*

BKV carries 1.4 billion passengers a year and operates 5 branches (bus, tram, metro, suburban railway, trolleybus) in an integrated system. Beyond these, it operates other modes primarily of touristic importance, like cogwheel railway, funicular, chairlift and river boat services. BKV preserves the heritage from its own history and from its predecessors by maintaining two museums as well as by operating nostalgic transport services.

## *BKV Railway Vehicle Repair and Service Ltd.*

The company was established in 1997 and deals with repair and production of main parts and other special components of tram, suburban railway and metro vehicles. Its activity has been extended in recent years by production of railway switches as well as overall modernisation of buses and trolleybuses. Regular vocational trainings have been carried out at the company's premises since its founding.

## *INTER TAN-KER Closed Public Limited Company*

The legal predecessor of our company, INTER TAN-KER Kft., was founded in 2002. Today, the company's core business is in the field of transport, in turn carrying out the operator's activities. INTER TAN-KER Zrt. regards it as its mission to help the work of the government and local governments as well as multinational, small and medium-sized enterprises in the field of transport with comprehensive solutions. In order to further develop transport in Hungary, we are open to understanding and supporting the goals of our partners by involving our own and external resources. We would like to maintain our key role by meeting the various needs of Hungarian and international transport and introducing innovative solutions. During our activities, it is our guiding principle to satisfy our partners' needs beyond their expectations and to further facilitate their work and make it more effective.

## *Szeged Transport Company Ltd.*

Public transport of Szeged is currently provided by two operators (the municipality owned Szeged Transport Company and the state owned Tisza Volán Share Holding Company). Szeged Transport Company operates trams and trolleybuses, furthermore it runs pay parking system and an automated parking house.


WE MAKE
MOBILITY SAFE
www.knorr-bremse.hu

# Wheel slide protection system MGS3

## Optimized WSP control for shorter stopping distances even in extreme weather conditions

**Decades of experience and ongoing technical improvement enable Knorr-Bremse to offer state-of-the-art wheel slide protection.**

### Additional features of high performance MGS3

- Multi-mode switch over WSP control between low and extremly low adhesion for shorter stopping distances
- Higher pneumatic performance for shorter ventilation times
- One system for all markets: easier homologation of trains
- eNozzle functionality: electronic adaption to different brake cylinder volumes for less commissioning efforts
- Improved system control and diagnostic by pressure sensor integration

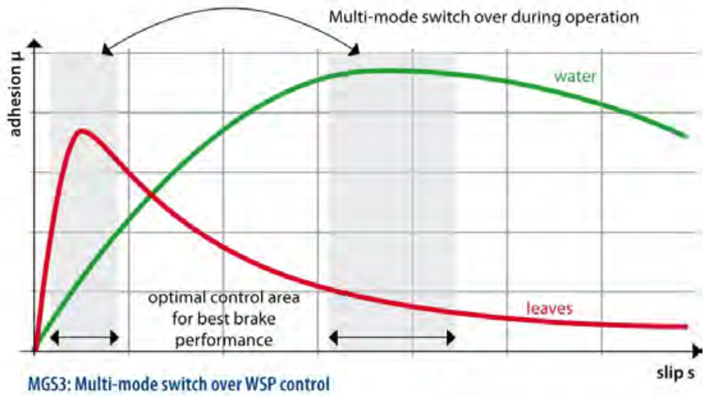


MGS3: Multi-mode switch over WSP control for different track conditions

### Multisensor

- One multifunctional sensor for WSP and COMORAN system
- Measuring speed, acceleration and temperature
- Output signal: Rectangular current signal, polarity reversal protected, permanently shortcircuit protected
- Temperature range: $-40\,°C \leq T \leq +100\,°C$ (optionally extended to cover low temperature requirements)

### High Performance Anti-Skid Valve

- One valve for all market requirements
- Integrated pressure sensor
- Operating pressure: max. 6.5 bar
- Temperature range: $-40\,°C \leq T \leq +70\,°C$ (optionally extended to cover low temperature requirements)

### Application example: MGS3 integrated in ESRA Evolution Control Unit

- Interface to typical train network systems such as MVB, CANopen, RS485 HDLC, Ethernet protocol variants etc.)
- Service and maintenance interface (Ethernet)
- Data Log function with large storage volume
- Temperature range: $-40\,°C \leq T \leq +70\,°C$ (optionally extended to cover low temperature requirements)
- Additional integrated functions such as:
  - Control for electromagnetic track brake and sanding
  - Speed signal output
  - Distance counter


STADLER
KÜLÖNVONAT
H-START
415 062
MAKING
RAIL TRAVEL FUN
www.stadlerrail.com


Routine for others. Creation for us.
E-MOBILITY
AUTONOMOUS TRUCK
ECO-EFFICIENCY
At Knorr-Bremse we all work for shaping tomorrow's transportation. Together.
We imagine and create the smart systems that make trucks the safest participants of road traffic.
Knorr-Bremse produces and develops brake and driver assistant systems of commercial vehicles.
The reliability of these systems are key to each participant of the traffic so for us as well.
We bring these systems to life in the trucks of the future.
Routine for others. Creation for us. We create the trucks of the future.
join us!
www.joinus.hu
R&D CENTER


SIEMENS
Vectron
In a changing world,
flexibility is our standard.
Driving mobility through sustainable transformation.
www.siemens.com/mobility

**GRAMPET DEBRECENI VAGONGYÁR KFT.**
**H-4034 DEBRECEN, HÉT VEZÉR U. 24/B.**
WWW.VAGONGYAR.HU ☎+36 52 889 100 FAX: +36 52 889 199 INFO@VAGONGYAR.HU

*Wheelset workshop*

- Maintenance of spare parts (e.g. buffing and draw gear, mechanical brakes, springs)
- Overhaul wheelsets IL, IS1, IS2 and IS3
- Assembly of new wheelsets
- Manufacturing welding constructions

**OUR COSTUMERS ARE FROM:**

- Hungary
- Germany
- Austria
- Switzerland
- France
- Romania

*Rebuilduing Hbbills*

**CERTIFICATES, AUTHORIZATIONS:**

- ECM Maintenance delivery function
- ISO 9001:2008
- VPI
- DIN EN ISO 3834-2
- EN 15085-2
- DIN EN 27201-7
- AD 2000 – Merkblatt HP0
- RID 6.8.2.1.23
- AFER (Zaes 68 m3, Eaos, Uagps 562, Uagps 535, Habis, Habfis)

*Building Ro-La*

# N O T E S :